

Rare Lepton Decays  
and  
**Differentiable Hadronization Models**

From Signatures of New Physics to Data-Driven Event Generation

A dissertation submitted to the  
Graduate College  
of the University of Cincinnati  
in partial fulfillment of the  
requirements for the degree of

*Doctor of Philosophy*

in the Department of Physics  
of the College of Arts and Sciences  
by

**Tony Menzo**  
B.S. The Ohio State University

October 2025

Committee Chair: Jure Zupan, Ph.D.

# Abstract

This dissertation is partitioned into two parts: phenomenological studies focused on rare lepton decays as probes of heavy and light new physics, and the development of differentiable, data-driven hadronization models. Part I develops the phenomenology of new physics signatures stemming from rare charged lepton flavor violating decays probed by experiments at the intensity frontier. These include interactions mediated by both high-scale effective operators and light new physics, manifesting in multi-lepton final states ( $\mu \rightarrow 5e$ ), elastic nuclear transitions ( $\mu \rightarrow e$  conversion), baryon-number-violating muon capture, and time-dependent signals from ultralight dark matter ( $\mu \rightarrow e\phi, \tau \rightarrow \ell\phi$ ). Part II develops two distinct strategies for advancing differentiable and data-driven hadronization models. One involves comprehensive reweighting frameworks for hadronization that enable efficient uncertainty estimation, facilitate parameter tuning, and interface naturally with differentiable programming paradigms. The other introduces machine-learning-based methods for extracting microscopic fragmentation dynamics directly from macroscopic observables through the deformation of existing models – effectively providing solutions to the inverse problem of hadronization. Altogether, these studies advance the interpretability, flexibility, and precision of theoretical predictions for both high-intensity and high-energy experiments.



# Acknowledgements

Thinking about the last five years, I have a tremendous amount of gratitude, appreciation, and awe for the people, places, ideas, and knowledge I've had the opportunity to interact with. It has been a true adventure in both physics and life. In many ways, this dissertation reflects a small portion of the knowledge gained during my time as a graduate student.

If I haven't made it clear in the rest of this document, despite my best efforts, let me crystallize a point for posterity: the work presented here stems from a *collective* learning experience between myself and collaborators. Chief among those, and to whom I owe the most thanks, is Jure Zupan. Your physics intuition is legendary and even after many years of working with you, I think it would take many more years to probe the breadth and depth of your knowledge. You are a world-class physicist, an even better person, and your mentorship has been invaluable. In a similar vein, I also owe many thanks to Phil Ilten. Your algorithmic/programmatic style to physics has made a deep impression on how I think about the subject. Your computational particle physics course, where we first met, will remain as one of the most enlightening experiences of my entire ‘formal’ education. Since then, our work together over the many years has been a genuine pleasure. To the many physicists who have positively and persistently shaped my experiences and views on physics as a graduate student, namely, Manuel Szewc, Steve Mrenna, Christian Bierlich, Ahmed Youssef, Michael Wilkinson, Ben Assi, Paddy Fox, Maxim Pospelov, Matheus Hostert, Yotam Soreq, Wick Haxton, Evan Rule, Ken McElvain, Innes Bigaran, Julia Gehrlein, Yuval Grossman, Ben Nachman, Simon Knapen, Joachim Brod, Chaja Baruch, Inbar Savoray, Duncan Roja, Ranit Das, Abhishek Banerjee, and Rikab Gambhir – thank you for the many conversations and permeated knowledge. To the physicists who I have never met directly, but interacted with indirectly through papers, textbooks, etc. – thank you for expanding my mind. I'd like to also give a special thank you to Alex Kagan, to whom I owe my whole graduate school experience, as well as Will (Coach) Mathes, who first prophesized (and encouraged) my path towards a doctorate many years ago. Last, but not least, I'd like to thank Stuart Raby for pointing my wandering mind towards particle physics during my last year of undergrad – I will always be grateful to have learned the subject from a true grandmaster.

To my lifelong friends, Mark Beshara, Jason Huang, Yash Maniya, Gokul Raghavan, Vishwa Rohera, Kevin Troung, Ram Vilku, and Denny Vroom – you guys render ‘the grind’ bearable. To quote, “... I couldn’t have asked for a better group of ballers.” [1].

To my mom, Valerie, and my dad, Roy, thank you for giving me the opportunity to experience the journey that is life. A special thank you to Nanna (JoAnn/JT) – your support over the years made this work possible. To my siblings and their families – Alex, Sophie, Gunner, Adrien, and Tom – thank you for keeping me grounded and motivating greatness; you guys are my people. To Ketan, Beena, Amy, Baa (Pravina), and the whole Kadakia family, your constant presence and home away from home has a special place in my heart.

To my dog, Wilson, many of our daily walks and fetch sessions have simultaneously acted as a time for physics sandboxing, where many ideas/confusions have been born, raised, and gone to die – you have been one of the brightest sources of happiness for me. Finally, to the most important person in my life, my beautiful wife and best friend, Feni, who allows me to do what I love, despite its challenges. *All* that I do, is dedicated to you.

# List of Publications and Preprints

To all of my collaborators listed explicitly below, thank you for your ideas, patience, and contagious enthusiasm. Physics is better – and certainly more fun – when done as a team.

## Part I is based upon the following works:

- [2] – Matheus Hostert, **TM**, Maxim Pospelov, Jure Zupan, “New physics in multi-electron muon decays.” Journal of High Energy Physics 2023.10 (2023): 1-22. [[arXiv:2306.15631](#)] (Chapter 2)
- [3] – Wick Haxton, Kenneth McElvain, **TM**, Evan Rule, Jure Zupan, “Effective theory tower for  $\mu \rightarrow e$  conversion.” JHEP 11 (2024) 076. [[arXiv:2406.13818](#)] (Chapter 3)
- [4] – Patrick J. Fox, Matheus Hostert, **TM**, Maxim Pospelov, Jure Zupan, “Muon-induced baryon number violation.” Phys.Rev.D 110 (2024) 7, 075015. [[arXiv:2407.03450](#)] (Chapter 4)
- [5] – Innes Bigaran, Patrick Fox, Yann Gouttenoire, Roni Harnik, Gordan Krnjaic, **TM**, Jure Zupan, “Direct detection of ultralight dark matter via charged lepton flavor violation.” [[arXiv:2503.07722](#)] (Chapter 5)

## Part II is based upon the following works:

- [6] – Phil Ilten, **TM**, Ahmed Youssef, Jure Zupan, “Modeling hadronization using machine learning.” SciPost Physics, 14(3), 027 (2023). [[arXiv:2203.04983](#)] (Chapter 8)
- [7] – Christian Bierlich, Phil Ilten, **TM**, Stephen Mrenna, Manuel Szwec, Michael Wilkinson, Ahmed Youssef, Jure Zupan, “Reweighting Monte Carlo Predictions and Automated Fragmentation Variations in Pythia 8.” SciPost Physics 16.5 (2024): 134. [[arXiv:2308.13459](#)] (Chapter 7)
- [8] – Christian Bierlich, Phil Ilten, **TM**, Stephen Mrenna, Manuel Szwec, Michael Wilkinson, Ahmed Youssef, Jure Zupan, “Towards a data-driven model of hadronization using normalizing flows.” SciPost Physics 17.2 (2024): 045. [[arXiv:2311.09296](#)] (Chapter 8)
- [9] – Christian Bierlich, Phil Ilten, **TM**, Stephen Mrenna, Manuel Szwec, Michael Wilkinson, Ahmed Youssef, Jure Zupan, “Describing Hadronization via Histories and Observables for Monte Carlo Event Reweighting.” SciPost Phys. 18 (2025) 2, 054. [[arXiv:2410.06342](#)] (Chapter 8)
- [10] – Nick Heller, Phil Ilten, **TM**, Stephen Mrenna, Benjamin Nachman, Andrzej Siódmodk, Manuel Szwec, Ahmed Youssef, “Rejection Sampling with Autodifferentiation – Case study: Fitting a Hadronization model.” [[arXiv:2411.02194](#)] (Chapter 7)
- [11] – Benoit Assi, Christian Bierlich, Phil Ilten, **TM**, Stephen Mrenna, Manuel Szwec, Michael Wilkinson, Ahmed Youssef, Jure Zupan, “Characterizing the hadronization of parton showers using the HOMER method.” [[arXiv:2503.05667](#)] (Chapter 8)
- [12] – Benoit Assi, Christian Bierlich, Phil Ilten, **TM**, Stephen Mrenna, Manuel Szwec, Michael Wilkinson, Ahmed Youssef, Jure Zupan, “Posthoc reweighting of hadron production in the Lund string model.” [[arXiv:2505.00142](#)] (Chapter 7)

Additional works, consisting of projects that I am very fond of, but did not have a clear embedding into the overall structure of this dissertation, are listed here for completeness:

- [13] – Adam Davis, **TM**, Ahmed Youssef, Jure Zupan, “The earth mover’s distance as a measure of CP violation.” Journal of High Energy Physics 2023.6 (2023): 1-42. [[arXiv:2301.13211](#)]
- [14] – Chaja Baruch, Patrick Fitzpatrick, **TM**, Yotam Soreq, Sokratis Trifinopoulos, Jure Zupan, “Searching for exotic scalars at fusion reactors.” [[arXiv:2502.12314](#)]

# Contents

<b>Abstract</b>	i
<b>Acknowledgements</b>	iii
<b>List of Publications and Preprints</b>	iv
<b>List of Figures</b>	x
<b>List of Tables</b>	xvi
<b>Conventions</b>	xvii

<b>I Rare Lepton Decays</b>	1
<b>1 Introduction</b>	2
1.1 Lore – Theory . . . . .	4
1.2 Lore – Experiment . . . . .	7
1.2.1 Modern experimental frontiers . . . . .	10
1.2.1.1 Example estimate of new physics reach at the energy frontier . . . . .	11
1.2.1.2 Example estimate of new physics reach at the intensity frontier . . . . .	12
1.3 The Electroweak Theory of Leptons . . . . .	13
1.3.1 The Lagrangian . . . . .	15
1.3.2 Electroweak symmetry breaking via the Higgs mechanism . . . . .	16
1.3.3 Neutrino masses . . . . .	18
1.4 Accidental symmetries . . . . .	19
1.4.1 CLFV beyond the Standard Model . . . . .	22
1.5 Experimental searches for CLFV . . . . .	23
1.5.1 Current bounds on $\mu$ 's . . . . .	23
1.5.2 Current bounds on $\tau$ 's . . . . .	24
1.5.3 MEG ( $\mu \rightarrow e\gamma$ ) . . . . .	25
1.5.4 Mu3e ( $\mu \rightarrow 3e$ ) . . . . .	26
1.5.5 Mu2e, COMET ( $\mu N \rightarrow eN$ ) . . . . .	27
<b>2 New physics in multi-electron muon decays</b>	29
2.1 Standard model decays . . . . .	29
2.2 Exotic muon decay . . . . .	31

2.2.1	A dark sector model . . . . .	32
2.2.2	Signal rate: $\mu \rightarrow 5e$ . . . . .	33
2.3	Constraints . . . . .	34
Muon lifetime: . . . . .	34	
Neutrinoless muon decays: . . . . .	34	
Higgs decays: . . . . .	35	
$\mu \rightarrow e\gamma$ : . . . . .	35	
$\mu \rightarrow 3e$ : . . . . .	36	
2.4	Experimental reach . . . . .	36
2.4.1	Backgrounds . . . . .	36
Decays with missing energy: . . . . .	36	
Accidental backgrounds: . . . . .	37	
2.4.2	Simulation . . . . .	38
2.4.3	Sensitivity . . . . .	40
Sensitivity to SM decays: . . . . .	40	
Sensitivity to exotic decays: . . . . .	42	
2.4.4	Future directions . . . . .	44
2.5	Conclusions . . . . .	44
<b>3</b>	<b>An effective theory tower for <math>\mu \rightarrow e</math> conversion</b>	<b>47</b>
3.1	The effective tower . . . . .	47
3.2	Weak effective theory . . . . .	49
3.3	Nuclear effective theory . . . . .	51
3.3.1	Kinematics . . . . .	51
3.3.2	NRET basis . . . . .	53
3.4	Matching quarks and gluons to nucleons . . . . .	56
3.4.1	Nucleon matrix elements . . . . .	56
3.4.2	Covariant nucleon-level interactions . . . . .	57
3.4.3	The NRET . . . . .	58
3.5	Predictions from UV models . . . . .	63
3.5.1	Bounds on UV Wilson coefficients . . . . .	63
3.5.2	Leptoquarks . . . . .	64
3.5.3	ALP exchanges . . . . .	71
3.6	Public code: MuonBridge . . . . .	72
3.7	Conclusions . . . . .	78
<b>4</b>	<b>Muon-induced baryon number violation</b>	<b>80</b>
4.1	Particle production in muon capture . . . . .	80
4.2	The effective operator . . . . .	85
4.3	UV completions . . . . .	88
4.3.1	Triplet-triplet-singlet model . . . . .	90
4.3.1.1	Off-shell $\Phi$ . . . . .	91
4.3.1.2	On-shell $\Phi$ . . . . .	92
4.3.2	More models . . . . .	93
Alternative scenarios for $\Phi$ produced on-shell. . . . .	93	
Production of kaons. . . . .	94	
Alternative dark photon couplings. . . . .	94	

Models that lead to $\mu^- n$ annihilation. . . . .	95
4.3.3 Loop-induced processes . . . . .	95
Proton decay. . . . .	95
Neutron decay. . . . .	96
$n - \chi$ mixing. . . . .	97
4.4 The signature . . . . .	99
4.5 Constraints . . . . .	101
4.5.1 Proton decay . . . . .	101
Scaling with energy release: . . . . .	102
MadGraph estimates: . . . . .	103
4.5.2 Neutron stars . . . . .	104
4.6 Conclusions . . . . .	107
<b>5 Direct detection of ultralight dark matter with CLFV</b>	<b>109</b>
5.1 Ultralight dark matter . . . . .	110
5.2 ULDM with flavor violating couplings . . . . .	111
5.3 UV realization(s) . . . . .	114
5.3.1 Non-Abelian pseudo-NGBs . . . . .	114
5.3.1.1 An example realization: $SU(3)_L \times SU(3)_R \rightarrow SU(3)_V$ . . . . .	116
5.3.1.2 Other examples . . . . .	118
5.4 Observing periodic signals . . . . .	119
5.4.1 Numerical examples . . . . .	121
5.5 Astrophysical and laboratory constraints . . . . .	122
5.6 Additional details related to observing periodic signals . . . . .	123
5.6.1 Coherent (“slow”) oscillations . . . . .	124
5.6.2 Incoherent (“fast”) oscillations . . . . .	127
5.6.3 Time-independent signal . . . . .	128
5.6.4 Discussion of time-dependent results . . . . .	129
5.6.4.1 Experimental details . . . . .	130
5.7 Conclusions . . . . .	132
<b>II Differentiable Hadronization Models</b>	<b>133</b>
<b>6 Introduction</b>	<b>134</b>
6.1 Monte Carlo Event Generators . . . . .	134
6.2 Landscape of hadronization models . . . . .	137
<i>Artru–Mennessier</i> . . . . .	137
<i>Lund</i> . . . . .	137
<i>Feynman and Field</i> . . . . .	138
<i>Cluster</i> . . . . .	138
<i>UCLA</i> . . . . .	138
<i>Statistical</i> . . . . .	138
<i>Coalescence</i> . . . . .	139
6.3 The Lund string model . . . . .	139
6.3.1 The $q\bar{q}$ string . . . . .	139
6.3.2 Hadronizing a $q\bar{q}$ string . . . . .	140

6.3.2.1	Incorporating transverse momentum . . . . .	145
6.3.2.2	The $q\bar{q}$ hadronization as a data-structure . . . . .	146
6.3.3	Hadronizing a $qg\bar{q}$ string . . . . .	148
6.4	Machine learning and differentiable event simulation . . . . .	149
<b>7</b>	<b>The reweighting revolution</b>	<b>151</b>
7.1	Statistical reweighting . . . . .	152
7.2	Automated hadron kinematic variations . . . . .	153
7.2.1	Accept-reject sampling . . . . .	153
7.2.2	Alternative accept-reject sampling . . . . .	154
7.2.3	Kinematic reweighting in the Lund string model . . . . .	155
7.2.4	Reweighting metrics . . . . .	156
7.3	Automated hadron production variations . . . . .	157
7.3.1	Flavor reweighting in the Lund string model . . . . .	159
7.3.1.1	Incorporating rejection weights a.k.a. filtering . . . . .	161
7.3.2	From analytic to stochastic weights . . . . .	163
7.4	Autodifferentiable kinematic reweighting . . . . .	164
7.4.1	Fitting a hadronization model . . . . .	164
7.4.2	Observables . . . . .	166
7.4.3	Results . . . . .	167
7.4.3.1	Loss landscapes . . . . .	168
Pseudo- $\chi^2$ . . . . .	169	
1D Wasserstein distance . . . . .	169	
Multi-dimensional sliced Wasserstein distance . . . . .	169	
7.4.3.2	Confidence Intervals . . . . .	170
7.5	Conclusions . . . . .	171
<b>8</b>	<b>Data-driven hadronization models</b>	<b>173</b>
8.1	MAGIC . . . . .	174
8.1.1	Fine-tuning microscopic fragmentation kinematics . . . . .	176
8.2	HOMER . . . . .	181
8.2.1	Details about the HOMER method . . . . .	182
8.2.1.1	Step 1: event classifier . . . . .	183
The unbinned scenario. . . . .	183	
The binned scenario. . . . .	184	
8.2.1.2	Step 2: inference of fragmentation weights . . . . .	185
8.2.1.3	Step 3: HOMER output . . . . .	190
8.2.2	High-level observables . . . . .	192
8.2.3	Extracting fragmentation functions with HOMER: unbinned high-level observables . . . . .	192
8.2.3.1	Results: Steps 1 (classifier) and 2 (regressor) . . . . .	193
8.2.4	HOMER with gluons . . . . .	194
8.2.4.1	Increase in information gap and decrease in effective statistics . . . . .	194
8.2.4.2	Varying initial states . . . . .	195
8.2.4.3	Selecting the hyperparameter $\sigma_s$ . . . . .	196
8.3	Conclusions . . . . .	197

<b>A Estimating decay rates and scattering cross sections</b>	<b>235</b>
<b>B Additional details on matching and form factor numerics</b>	<b>238</b>
B.1 Intermediate results for WET to NRET matching . . . . .	238
B.1.1 From WET to covariant nucleon interactions . . . . .	238
B.1.2 NRET decomposition of covariant interactions . . . . .	240
B.2 Numerical value of nucleon form factors . . . . .	241
B.3 WET translation . . . . .	242
<b>C Normalizing flows</b>	<b>249</b>
C.1 One-dimensional normalizing flows . . . . .	251
C.2 Two-dimensional flows . . . . .	252
<b>D Observables</b>	<b>254</b>

# List of Figures

1.1	The Feynman diagram for $\mu \rightarrow e\gamma$ in the SM with non-zero neutrino masses. . . . .	21
1.2	Generic depiction of CLFVing BSM interactions (left: photonic, right: contact) shown for example in the context of $\mu N \rightarrow eN$ . Pink lines and vertices indicate UV-agnostic BSM particles and interactions. . . . .	22
2.1	<b>Left:</b> Example of one contributing Feynman diagram for the SM ‘super’-Michel decay $\mu \rightarrow eeee\nu\nu$ . <b>Right:</b> Example of one contributing Feynman diagram for SM ‘ultra’-Michel decay $\mu \rightarrow eeeee\nu\bar{\nu}$ . . . . .	30
2.2	The leading neutrinoless $\mu \rightarrow eeeee$ contribution in the higgsed $U(1)_d$ model presented in section 2.2.1. . . . .	33
2.3	Transverse (top) and longitudinal (bottom) event displays showing an example of a simulated SM five-track $\mu^+ \rightarrow 3e^+ 2e^- 2\nu$ decay event at Mu3e. The blue heatmap within the double-cone target of each panel represents the modeled $x, y$ , and $z$ probability densities of muon decays within the double-cone target. . . . .	39
2.4	The number of electrons or positrons that are reconstructed as short tracks (left) and long tracks (right) for $\mu^+ \rightarrow 3e^+ 2e^-$ (pink) and $\mu^+ \rightarrow 3e^+ 2e^- 2\nu$ (blue) decays. We show the new-physics decays for $m_{\gamma_d} = 30$ MeV and $m_{h_d} = 90$ MeV. A short track is defined by $N_{\text{hits}} \geq 4$ and a long track as $N_{\text{hits}} \geq 6$ . Solid lines show the total branching ratio for short or long tracks. Dashed lines have an additional requirement that at least two <i>electrons</i> be reconstructed as either short or long tracks. Dotted lines have yet another requirement on the missing energy $E_{\text{miss}}$ , defined as the difference between the total energy of short tracks and the muon mass. The hatched bands indicate the MC statistical uncertainty. . . . .	41
2.5	Left panel shows the reconstructed missing energy distribution for $\mu^+ \rightarrow 3e^+ 2e^-$ ( $m_{\gamma_d} = 30$ MeV and $m_{h_d} = 90$ MeV) compared with the $\mu^+ \rightarrow 3e^+ 2e^- 2\nu$ SM rate. Solid histograms include the requirement of exactly 5 reconstructed short tracks. In the right panel we show the reconstructed total electron energy distribution. In this case, solid histograms require exactly 5 reconstructed short-tracks and $E_{\text{missing}} < 10$ MeV. . . . .	41
2.6	The Mu3e reach for $\mu^+ \rightarrow e^+(h_d \rightarrow \gamma_d \gamma_d)$ decays as a function of $m_{\gamma_d}$ and $y_{\mu e} = y_{e\mu}$ for various choices of $m_{h_d}$ , assuming a sensitivity of $\mathcal{B}(\mu^+ \rightarrow e^+ h_d) < 10^{-12}$ after signal selection described in section 2.4.2. We fix $\varepsilon = 10^{-4}$ and $\alpha_D = \alpha/10$ . Dashed lines indicate regions where the scalar quartic coupling $\lambda > \sqrt{4\pi}$ for this particular choice of $\alpha_D$ . The limit based on a comparison of the total muon lifetime $\tau_\mu$ and independent determinations of $G_F$ is shown as a dark grey region ( $\mathcal{B} < 2 \times 10^{-3}$ ) and the limit from Ref. [15] is shown in the light grey region ( $\mathcal{B} < 4 \times 10^{-6}$ ). . . . .	42

2.7	The reconstructed masses of the dark photon (left) and the dark higgs (right) for various fixed masses before signal selection cuts (solid lines) and after signal selection cuts (filled histograms). After selection, the resulting resolution on the dark photon mass is approximately $\sigma_{m_{\gamma_d}}/m_{\gamma_d} = 2.3\%$ and $\sigma_{m_{h_d}}/m_{h_d} = 1.5\%$ for the dark higgs mass. The total branching ratio for the signal was fixed to $7 \times 10^{-13}$ in both panels. . . . .	43
2.8	The reconstructed missing energy for $\mu^+ \rightarrow e^+e^+e^-e^-\bar{\nu}_\mu\nu_e$ and $\mu^+ \rightarrow e^+e^+e^-\bar{\nu}_\mu\nu_e$ events in Mu3e. For the former, the filled histograms show the subset of events with three, four, and five reconstructed short tracks, requiring exactly two reconstructed electrons. For the latter, we show the total rate downscaled by a factor of $10^{-4}$ . This points to a naive estimate of 3e events where one of the positrons undergoes Bhabha scattering to produce a four-track final state. . . . .	45
3.1	The effective field theories — and their respective thresholds — relevant for describing $\mu \rightarrow e$ conversion, as well as the corresponding computer codes (in grey boxes). The <b>MuonBridge</b> repository, introduced as part of this manuscript, consists of the interconnected packages <b>MuonConverter</b> , <b>Mu2e_NRET</b> , and <b>Elastic</b> (orange boxes). . . . .	48
3.2	A graphical representation of how different WET operators eq. (3.1) contribute to the $\mu \rightarrow e$ conversion rate, in which we keep the terms that remain in the $v_N, v_\mu \rightarrow 0$ limit, as well as the coherently enhanced but velocity-suppressed contribution from the $W_{\Phi''\Phi''}$ response function. The NRET coefficients $c_i^N$ receive contributions from WET Wilson coefficients $\hat{C}_i^{(d)}$ , as denoted with the corresponding colored circles (only the $c_i^N$ that contribute to the numerically leading response functions are considered). These then enter the leptonic response factors $R_{OO'}^{\tau\tau'}$ that multiply various nuclear response functions, as indicated. For instance, $\hat{C}_1^{(5)}$ contributes to $c_1^N, c_4^N$ and $c_6^N$ , and these lead to $W_{MM}^{\tau\tau'}, W_{\Sigma'\Sigma'}^{\tau\tau'}, W_{\Sigma''\Sigma''}^{\tau\tau'}$ nuclear responses. . . . .	61
3.3	The energy scales probed by dimension-six SMEFT operators assuming the projected experimental limits of the future Mu2e and COMET experiments, $B(\mu^- + \text{Al} \rightarrow e^- + \text{Al}) < 10^{-17}$ . The notation is as in [16, 17]. . . . .	65
3.4	Diagram for tree-level contributions to $\mu \rightarrow e$ conversion mediated by scalar leptoquark $R_2$ . Leptoquark superscripts indicate the electric charge of the exchanged particle. . . . .	66
3.5	A decomposition of the $\mu \rightarrow e$ conversion rate in terms of contributions from different nuclear response components classified by the type of response ( $OO'$ ) as well as the isoscalar/isovector component ( $\tau\tau'$ ), for $^{27}\text{Al}$ target, at a single representative point in the parameter space of the $R_2$ leptoquark model, eq. (3.67). . . . .	69
3.6	A comparison of the isoscalar nuclear response components over $2 \times 10^4$ parameterizations of the $R_2$ leptoquark model introduced in eqs. (3.67) and (3.68). Each of the 18 dimensionless complex parameters $y_{2ij}^{RL,LR}$ are randomly sampled over the unit complex circle and the leptoquark mass is held fixed at 5000 TeV. The color denotes the logarithm of the ratio of the summed isoscalar components and the sum of isovector components for all contributing nuclear responses. Whenever the scalar response contributions fall below $\approx 98\%$ of the total rate, the gray lines are used to illustrate how the components are distributed. The $\mu \rightarrow e$ conversion rates for the shown points lie in the range $10^{-17} < B(\mu^- + \text{Al} \rightarrow e^- + \text{Al}) < 10^{-11}$ (we do not denote which of the points are already excluded). . . . .	70

3.7	A simplified overview of the mapping and matching computations performed by <b>wilson + MuonBridge</b> for a UV theory defined by a single CLFV SMEFT operator with a Wilson coefficient set to $1/\Lambda^2$ at scale $\mu_{\text{UV}} = \Lambda$ . The red lines denote the largest contributions to the WET coefficients and are chosen by selecting all coefficients with an absolute value within one order-of-magnitude of the largest coefficient.	77
4.1	A schematic of the different particle production mechanisms in muon capture. Each quadrant corresponds to a different rule for baryon and lepton flavor number conservation or (apparent) violation.	81
4.2	The scenario for muon-induced (apparent) baryon number violation considered in this work (eq. (4.14)). On the left, we show the muon capture on protons, and on the right, the tree-level proton decay channel. In both cases, the dark photon $A'$ can be either on or off shell.	84
4.3	The energy spectrum for electrons and positrons produced in exotic muon capture for a few choices of dark particle masses. Couplings are fixed as indicated in the left panel of each row. On the left, we show the individual electron/positron energies, and on the right, their combined energy. The usual $\mu \rightarrow e$ conversion electron energy is shown as a narrow green band around $E_{e^-}^{\text{cap}} \simeq 104.98$ MeV, and the region where muon decay-in-orbit dominates is shaded in gray [18].	85
4.4	Same as fig. 4.3 but for $\alpha_D \ll 1$ and $d_{\text{tr}} = 10^{-3}$ GeV $^{-1}$ . The $\chi_2 \rightarrow \chi_1 e^+ e^-$ transition is induced by the tensor interaction of eq. (4.15) and leads to a preference for more energy-asymmetric $e^+ e^-$ .	86
4.5	The left diagram shows the UV completion of section 4.3 that realizes the contact interaction $G_{\mu p}$ of eq. (4.14). A heavy di-quark $T_1$ and a lepto-quark $T_2$ scalar couple to an intermediate-mass gateway particle $\Phi$ . The diagram on the right shows how the gateway particle $\Phi$ can be produced on-shell in muon capture with a third-body rescattering ( $Z$ represents a nucleus of atomic number $Z$ ).	90
4.6	Loop induced proton decay from the triplet-singlet model.	95
4.7	Neutron mixing with $\chi_2$ generated at the two-loop level. At an additional loop, the mixing between $\chi_1$ and $n$ is generated by an $A'$ line.	97
4.8	Estimates of the lifetime of a free proton (left) and neutron (right) as a function of the mass of the lightest dark particle $\chi_1$ for benchmark (I). The bottom panel illustrates the scaling of the lifetime with respect to the energy release $Q$ , which is proportional to the nucleon mass minus the sum of the masses of all final state particles that are on shell, see eqs. (4.51) and (4.52). The nucleon lifetime $\tau_N^{\min}$ and its respective energy release $Q_{\min}$ are calculated for the smallest value of $\chi_1$ mass shown in the figure. We do not include loop-level proton decay channels which may dominate at the largest masses.	100
4.9	The normalized true total visible energy spectrum (energy of the $e^+ e^+ e^-$ system) in $p \rightarrow eee\nu\nu\chi_1\chi_0$ decays for two choices of dark photon masses. The distributions look similar for the same benchmarks when using transition moments instead ( $\alpha_D \rightarrow d_{\text{tr}}$ ), although the total lifetimes increase.	101
4.10	The momentum of the individual final state particles in $p \rightarrow eee\nu\nu\chi_1\chi_0$ decays for two choices of dark photon masses. Here the final state positrons $e_1^+$ and $e_2^+$ are distinguished at the event level by the magnitude of the three-momenta, with $e_2^+$ always being assigned to the larger momenta.	103

5.1	Present and projected constraints on LFV couplings $f/\sqrt{C_{\mu e}}$ (left) and $f/\sqrt{C_{\tau \ell}}$ (right) for time-binned and single-bin analyses, as a function of the scalar mass, $m_\phi$ – see eqs. (5.10) and (5.12). <b>Left:</b> Present constraint from TWIST [19, 20] is shaded in yellow. The projected single-bin (dashed line) and time-binned (solid line) analysis reach from Mu3e [21, 22] are shown in purple. The astrophysical bound on $f/\sqrt{C_{\mu e}}$ from SN1987A [23, 24] is shown here as a dot-dashed green line – see main text for details. <b>Right:</b> The constraints on $f/\sqrt{C_{\tau \ell}}$ from present and projected Belle-II analyses [25] are shown here in blue: current $62.8 \text{ fb}^{-1}$ time-integrated constraint is shaded, single-bin constraint is a dashed line and projected time-binned constraint is a solid line; the $50 \text{ ab}^{-1}$ projected time-binned constraint is a dot-dashed line. The projected constraints from FCC-ee Tera-Z run [26] are shown in red: dotted line for single-bin analysis, and red solid line for time-binned analysis. The constraints on $C_{\tau \mu}$ and on $C_{\tau e}$ (denoted collectively here as $C_{\tau \ell}$ ) almost completely overlap on this logarithmic scale. . . . .	112
5.2	Model contribution to $\ell_i \rightarrow \ell_j \phi'$ , where the interaction with the background classical field ( $\phi_c$ ) is denoted in red. . . . .	114
5.3	The 90% confidence upper limit on the signal branching $\mathcal{B}_{\text{sig}}$ obtained from a time-dependent analysis, as a function of bin size $\Delta t$ (solid, dashed-dotted lines) for different $\phi$ masses at Mu3e (left) and Belle II (right), using the same assumptions as in Fig. 5.1. The dotted vertical lines denote approximately when the oscillatory signal for each mass is resolved, $\Delta t \sim m_\phi^{-1}$ . The horizontal dashed black line denotes the upper limit for a time-independent, single-bin, analysis. . . . .	120
5.4	Same as fig. 5.3 for the full integrated luminosity at Belle-II (left) as well the projection for FCC-ee (right). . . . .	125
6.1	A cartoon illustration of a single fragmentation during $\bar{q}q$ hadronization. . . . .	140
6.2	A depiction of the $q\bar{q}$ string in momentum space. See the text for details. . . . .	142
6.3	Schematic detailing the different components of a simulated run. String breaks are grouped into fragmentation chains, while collections of rejected and accepted fragmentation chains form fragmentation histories. Observable events are obtained from the last, accepted fragmentation chain. A collection of multiple events is a run. . . . .	148
7.1	Observable distributions for hadron multiplicity $N_h$ at three distinct parameterizations of the Lund $a, b$ parameters, using a sample of $N = 10^6$ events. Dotted histograms denote the reweighed distributions. . . . .	154
7.2	The reweighting metrics defined in eq. 7.9 over the $(a, b)$ parameter plane for the <b>Model 1</b> and <b>Model 2</b> base parameterizations denoted by the red dots. The green star denotes the ‘experimental’ or target parameterization. For both metrics, values closer to zero imply better coverage and effective statistics. . . . .	157
7.3	Illustration of the decision flow in the simple case of string breaks without di-quarks. There are three possibilities, $u\bar{u}$ , $d\bar{d}$ , and $s\bar{s}$ , the latter with a probability $\rho/(2+\rho)$ , and the two former with a probability of 1/2, given that no $s\bar{s}$ pair was produced. All probabilities can be read off directly from the decision flow chart. . . . .	160
7.4	Flowchart depicting the introduction of rejection/filtering in a simplified example beginning with an $s$ -quark end-point. In this toy example, vector mesons and the $\eta'$ meson are not included, so a string break following an $s$ -quark can only result in an $\eta$ (for $s\bar{s}$ breaks) or kaons (for $u\bar{u}$ or $d\bar{d}$ breaks). Because of this simplification, this example does not conserve isospin. . . . .	162

7.5	Observable distributions the classifier score $\mathcal{S}$ (right) at three distinct parameterizations of the Lund $a, b$ parameters, using a sample of $N = 10^6$ events. Dotted histograms denote the reweighted distributions. . . . .	166
7.6	An example of the two-dimensional Lund $a$ and $b$ parameter plane loss landscape for the pseudo- $\chi^2$ loss defined in eq. (7.23). The red dot denotes the initial base parameterization from which we reweigh from and the green cross denotes the target parameterization from which the observable distribution was generated from. Both subplots are generated by computing the loss and gradients over a grid of 100 $(a, b)$ pairs. For each parameterization the losses and gradients are averaged over four mini-batches of $5 \times 10^4$ events for a total ‘batch size’ of $2 \times 10^5$ events. . . . .	168
7.7	Two-dimensional Lund $a$ and $b$ parameter plane loss landscape for one-dimensional and sliced Wasserstein distances over various dimensionalities of low and high-level observables, with the same grid and mini-batching as in fig. 7.6. . . . .	170
7.8	The 95% confidence ellipses on $a, b$ parameters estimated from 1,000 bootstrapped training runs over 300 epochs and identical tuning hyperparameters. Demonstrates the increasing accuracy of slicing over multiple low and high-level observables, from only $N_h$ (red), $\{\mathcal{S}_1, N_h\}$ (blue), and $\{\mathcal{S}_1, \mathcal{S}_2, N_h\}$ (purple). . . . .	171
8.1	A comparison between the (histograms) PYTHIA and (solid lines) MLHAD NF generated single emission $p_z$ distributions produced at four different fixed values of $m_\perp$ which were not used in the training of the model. . . . .	175
8.2	(left) Comparison of hadron multiplicity distributions generated with (orange) PYTHIA and the (blue) MLHAD NF, constructed from hadronizations of $10^5$ strings, all with an initial energy of $E_{\text{string}} = 100 \text{ GeV}$ and an energy cutoff of $E_{\text{cutoff}} = 25 \text{ GeV}$ . (right) Scaling of average hadron multiplicity $\langle N_h \rangle$ is given as a function of the starting string energy. Each marker represents an averaging of hadron multiplicity over the hadronization of $5 \times 10^3$ strings. The dotted lines show the average multiplicity $\langle N_h \rangle$ and the bands the corresponding $1\sigma$ range. . . . .	177
8.3	<b>Left:</b> Comparison between the single emission kinematic distribution $p_z$ of the (blue dashed) base model, the (green dashed-dotted) distribution used to generate $\mathbf{y}_{\text{exp}}$ , and (red) an ensemble of solutions learned using MAGIC. <b>Right:</b> Comparison of hadronization-chain level hadron multiplicity between the (blue) base, (red) one of the fine tuned, and the (green) target distributions where each histogram is constructed from $5 \times 10^5$ hadronization chains. The mean of each histogram is shown as a vertical dashed line. . . . .	180
8.4	Summary flowchart of the HOMER method. Here $\mathcal{C}$ is the event-level classifier and $\mathcal{R}$ is the weight-level regressor that transforms the event-level weights into string break-level weights. . . . .	191
8.5	<b>Left:</b> Performance of the Step 1 classifier depicted in the context of reweighting performance of the total hadron multiplicity, $n_f$ . We see very nice agreement between the HOMER-reweighted (yellow) simulation (blue) compared to the desired data distribution (red). For more details on the curves labeled ‘Classifier’, ‘Inference’, ‘Best NN’ see ref. [27]. <b>Right:</b> Distributions for the fragmentation function averaged over all string break variables except (left) $z$ . We see that the HOMER extracted fragmentation function (yellow) agree nicely with the fragmentation function used to generate the synthetic data (red). All weights are from the model trained with the unbinned high-level observables. . . . .	193
8.6	Flowchart of the modified Step 2 for the HOMER method with gluons. . . . .	195

- C.1 (top) Schematic of the input and output of the NF architecture. Here  $\mathbf{x}_i$  and  $\hat{\mathbf{z}}$  represent, respectively, the input and output samples obtained from the network when mapping in the forward direction and  $\mathbf{z}$  and  $\hat{\mathbf{x}}_i$  represent, respectively, input and output samples of the network obtained when traversing the network in the backward direction. The backward direction is used for event generation while the forward direction is used for training. The forward (backward) direction consists of a series of  $n$  successive transformations  $f_{i+1}(\mathbf{z}_i)$  ( $f_i^{-1}(\mathbf{x}_i)$ ). . . . . 249

# List of Tables

4.1	Proton decay channels and the corresponding constraints on the dark sector mass spectrum that we impose so as to forbid them at tree level. The naive scaling of each decay channel, assuming all final state particles are relativistic, is shown in the right-most column. Generalization to non-relativistic final state particles is straightforward – see section 4.5.1 for more details. . . . .	89
A.1	Propagators and polarization tensors for spin-0, 1/2, and 1 particles. . . . .	237
B.1	Dirac forms of the CLFV amplitudes $\mathcal{L}_{\text{int}}^j$ are related to linear combinations of the Pauli forms (the operators $\mathcal{O}_i$ ). Bjorken and Drell spinor and gamma matrix conventions are used. Here $\chi_e = (\xi_s \quad \vec{\sigma}_L \cdot \hat{q} \xi_s)^\top$ , $\chi_\mu = (\xi_s \quad 0)^\top$ , and $N = (\xi_s \quad \frac{\vec{\sigma}_N \cdot \vec{v}_N}{2} \xi_s)^\top$ . The Dirac forms are expanded to first order in $\vec{v}_N$ to maintain consistency with their use between Schrödinger wave functions. . . . .	243
B.2	Nonrelativistic reduction of tensor currents and their correspondence to the upper-component operators $\mathcal{O}_i$ . . . . .	244
B.3	As in table B.1, but listing the additional terms generated for scalar- and vector-mediated interactions when the linear expansion in velocities includes $\vec{v}_\mu$ , so that $\chi_\mu = \left( \xi_s \frac{\vec{\sigma}_L \cdot \vec{v}_\mu}{2} \xi_s \right)$ . . . . .	245
B.4	As in table B.2, but listing the additional terms generated for tensor-mediated interactions when the linear expansion in velocities includes $\vec{v}_\mu$ . . . . .	245
B.5	Numerical values of input parameters that enter the expressions for matrix elements of vector, axial, scalar, pseudoscalar, and tensor quark currents, CP-even and CP-odd gluonic currents, as well as the CP-even and CP-odd Rayleigh operators. See the main text and appendix D of [3] for details and references. . . . .	246
B.6	The WCxf-compatible operators and Wilson coefficient naming schemes for MuonConverter (left) and the WET-3 JMS basis [28] (right). The translation between the two bases can be found in table B.7. . . . .	247
B.7	The translation between the MuonConverter basis and the WET-3 JMS basis. . . . .	248

# Conventions

We will use the following conventions throughout unless specified otherwise:

- The Minkowski spacetime metric with signature

$$g_{\mu\nu} = \begin{pmatrix} +1 & 0 & 0 & 0 \\ 0 & -1 & 0 & 0 \\ 0 & 0 & -1 & 0 \\ 0 & 0 & 0 & -1 \end{pmatrix} \quad (1)$$

where  $\mu, \nu = 0, 1, 2, 3$ .

- The Pauli matrices,  $\sigma_i$ , given by

$$\sigma_1 = \begin{pmatrix} 0 & 1 \\ 1 & 0 \end{pmatrix}, \quad \sigma_2 = \begin{pmatrix} 0 & -i \\ i & 0 \end{pmatrix}, \quad \sigma_3 = \begin{pmatrix} 1 & 0 \\ 0 & -1 \end{pmatrix}. \quad (2)$$

- The Dirac gamma matrices in the *chiral basis*

$$\gamma^\mu = (\gamma^0, \gamma^i) = \begin{pmatrix} 0 & \sigma^\mu \\ \bar{\sigma}^\mu & 0 \end{pmatrix}, \quad i = 1, 2, 3, \quad (3)$$

$$\gamma^5 \equiv i\gamma^0\gamma^1\gamma^2\gamma^3 = \begin{pmatrix} -\mathbf{1}_{2\times 2} & 0 \\ 0 & \mathbf{1}_{2\times 2} \end{pmatrix} \quad (4)$$

where

$$\sigma^\mu = (\mathbf{1}_{2\times 2}, \sigma_i), \quad \bar{\sigma}^\mu = (\mathbf{1}_{2\times 2}, -\sigma_i). \quad (5)$$

# **Part I**

## **Rare Lepton Decays**

# Chapter 1

## Introduction

*“We do not know what the rules of the game are; all we are allowed to do is to watch the playing. Of course, if we watch long enough, we may eventually catch on to a few of the rules. The rules of the game are what we mean by fundamental physics.”*

Richard Feynman

The Standard Model (SM) of particle physics is widely supported by all high energy data. To date, there exists no statistically significant<sup>1</sup>, i.e.,  $>“5\sigma”$  and independently confirmed<sup>2</sup> experimental deviations from its theoretical predictions. To achieve this level of agreement with experimental data the SM requires a total of 19 - 26 input parameters  $\Theta_{\text{SM}}$ :

$$\Theta_{\text{SM}} = \Theta_{\text{SM}}^{m_\nu=0} + \Theta_{\text{SM}}^{m_\nu \neq 0}, \quad \text{with} \quad (1.1)$$

$$\Theta_{\text{SM}}^{m_\nu=0} = \{g_1, g_2, g_3, y_u^i, y_d^i, y_\ell^i, m_h, v, \theta_{12}, \theta_{23}, \theta_{13}, \delta\} \quad (1.2)$$

$$\Theta_{\text{SM}}^{m_\nu \neq 0} = \{m_\nu^i, \vartheta_{12}, \vartheta_{23}, \vartheta_{13}, \delta_D \text{ (or } \delta_M^1, \delta_M^2\text{)}\} \quad \text{where} \quad (1.3)$$

- $g_1, g_2, g_3$  are the local  $SU(3) \times SU(2) \times U(1)$  gauge couplings,
- $y_u^i, y_d^i, y_\ell^i$  are Yukawa couplings of the SM fermions to the Higgs. Each Yukawa has three copies denoting different flavors  $i = 1, 2, 3$  for a total of 9 parameters.
- $m_h, v$  determine the properties of the Higg’s potential and the strength of spontaneous symmetry breaking (SSB). And finally,

---

<sup>1</sup>There are, however, a number of tensions ( $\geq “3\sigma”$  significance) between theory predictions and experimental measurements, see section 1.2 for more details.

<sup>2</sup>There are measurements which eclipse the discovery threshold for significance, however, these measurements are either in broad disagreement with other experimental measurements such that global averages are insignificant or unable to be replicated independently. For more details, see section 1.2

- $\theta_{12}, \theta_{23}, \theta_{13}, \delta$  correspond to the Cabibo-Kobayashi-Maskawa (CKM) mixing angles,  $\theta_{ij}$ , and phase,  $\delta$ , related to the strength of mixing between mass and flavor eigenstates.

For non-zero neutrino masses, we include an additional 7 parameters

- $m_\nu^i$  are three neutrino masses
- $\vartheta_{12}, \vartheta_{23}, \vartheta_{13}$  are the neutrino mixing parameters present in the Pontecorvo-Maki-Nakagawa-Sakata (PMNS) matrix.
- $\delta_D$  is a single phase appearing in the PMNS matrix, assuming neutrinos are Dirac particles. If neutrinos are Majorana particles, two independent phases  $\delta_M^1, \delta_M^2$  can appear in the PMNS matrix.

Each of these parameters are determined from experimental measurements. Given a set of 19–26 independent measurements, a simultaneous global fit can be performed to determine  $\Theta_{\text{SM}}$ . Once the parameters are fixed, the SM makes thousands of predictions. This overconstrained property of the SM is an incredible feature of the model – a 19 parameter fit can correctly predict thousands of physical observables. Albeit encoded in the somewhat elaborate but explicit mathematical framework of Lagrangian-Hamiltonian mechanics and quantum field theory, this feature is an interesting example of physical information compression.

While these parameters are the minimal set required to make a numerical prediction at a fixed energy scale, comparing this numerical prediction to the results of an experiment often requires a larger set of parameters that incorporate non-perturbative physics and detector effects. In practice many experimental measurements require the use of event simulations to validate detector components, estimate efficiencies, model backgrounds, etc. These event simulations are built on top of the parameters in eqs. (1.2) and (1.3) and, in almost all cases, also have additional parameters that must be fixed or *tuned* to data. For example, PYTHIA [29, 30], a widely used general purpose Monte Carlo event generator for high-energy collisions, has a default (MONASH [31]) tune of  $\mathcal{O}(50)$  parameters<sup>3</sup>. With this tune, PYTHIA produces simulations that are in broad agreement with data across many experimental measurements.

A large portion of literature in particle phenomenology focuses on the observable implications of utilizing more or less parameters than those outlined above for the SM. More parameters can allow for new observable phenomena or alleviate tensions with experimental data. For example, models based on supersymmetry (SUSY) such as the Minimal Supersymmetric Standard Model (MSSM)<sup>4</sup> trade more tuneable parameters for a richer set of collider signatures and phenomenological predictions (which, to date, have alluded all collider searches). This brand of

---

<sup>3</sup>Many of these parameters can be highly correlated or reside in completely orthogonal experimental sectors, reducing the effective number of ‘tuneable’ parameters.

<sup>4</sup>Supersymmetry and the MSSM have been extensively reviewed in Refs. [32, 33] (see also the Supersymmetry section of the PDG [34]) and originate in the early constructions of Wess, Zumino, and Fayet [35, 36].

phenomenology is typically referred to as incorporating new physics (NP) beyond the SM (BSM) (also known as “bottom-up” model building) and motivates new experimental searches which can then place strict constraints on possible new physics (in the case of non-observation) – this will be the main phenomenology of focus in part I.

Reducing the number of parameters is also highly desirable and widely studied. Encoding the predictions of the SM into a more “efficient” mathematical framework is a hallmark of UV completions like Grand Unified Theories (GUT’s)<sup>5</sup>, attempting to embed the SM into more fundamental mathematical representations of larger local gauge groups, reducing the number of independent gauge interactions.

A more radical approach to parameter counting appears in string theory where the parameters of the Standard Model are not inserted by hand but arise from the geometric and topological data of compactified extra dimensions (also known as “top-down” model building). For example, in flux compactifications of type IIB string theory, discrete choices of quantized fluxes and moduli stabilization determine the effective four-dimensional couplings and mass scales at low energies [42, 43]. The number of consistent compactifications (reflecting the many possible flux and geometry configurations) is enormous and results in an enormous number distinct vacua estimated to be on the order of  $\mathcal{O}(10^{500})$  [44, 45]. This landscape represents a conceptual shift in the notion of parameter counting itself, rather than introducing or reducing a finite set of free parameters, the theory admits a vast discretuum of possible low-energy realizations, each with its own effective parameters determined by geometry and fluxes. In this way, parameter counting shifts from tuning within one theory to charting the space of vacua and developing ‘observables’ that break degeneracies among otherwise indistinguishable low-energy vacua descended from a unified high-dimensional theory.

## 1.1 Lore – Theory

Structurally, the SM is an effective field theory (valid for energies  $E \gtrsim 100$  GeV) built upon a quantum field theoretic formulation of Poincare invariant, locally gauge invariant representations of field excitations in space and time. The theory manages to place the electromagnetic, strong, and weak forces of nature into a single cohesive theoretical framework. The reconciliation of the SM with the force of *gravity*, is a very active field of research. The SM’s observable predictions primarily come in the form of quantities known as cross sections,  $\sigma$ , and decay widths,  $\Gamma$  (or branching ratios  $\mathcal{B}$ ), oftentimes expressed differentially with respect to convenient experimental observables such as the kinematics of the outgoing final state. Interacting quantum field theories are constructed as perturbative expansions around free field theories – a feature which manifests directly in the way observables are computed. Generically, observables

---

<sup>5</sup>Grand Unified Theories have been extensively reviewed in Refs. [37, 38] and originate in the early constructions of Pati, Salam, Georgi, Glashow, Fritzsch, and Minkowski [39–41].

can be thought of as a *weighted phase space sampling*, i.e., a phase space configuration whose weight is reported in the form of a perturbative Taylor expansion around a small parameter  $\alpha$ . Observables can then, in principle, be reported to arbitrary precision (up to computability – the computational complexity of the computation grows roughly factorially in the total number of individual contributions to the sum order by order in the  $\alpha$  expansion) although they are typically reported at some order in the expansion parameter  $\alpha$ . Schematically the prediction for an observable  $O$  is given by:

$$O \sim \int d\Phi_n \times |\mathcal{M}(\Phi_n)|^2 \quad (1.4)$$

where  $d\Phi_n$  is the Lorentz-invariant phase space element for an  $n$ -body final state with mass dimension  $[d\Phi] = 2(n - 2)$ . In practice, the matrix element,  $\mathcal{M}$ , is computed order by order in  $\alpha$

$$\mathcal{M} \sim \mathcal{M}^{(0)} + \alpha \mathcal{M}^{(1)} + \alpha^2 \mathcal{M}^{(2)} + \cdots + \alpha^\infty \mathcal{M}^{(\infty)}. \quad (1.5)$$

This expansion is manifested explicitly in the language of *Feynman diagrams* with the leading-order,  $\mathcal{O}(\alpha)$ , referred to as the tree-level Feynman diagram contribution, second order,  $\mathcal{O}(\alpha^2)$ , as the one-loop Feynman diagram contribution, etc.

The sum in eq. (1.5) may, and generically will be beyond tree-level, contain many divergent terms – loop diagrams contain unbounded integrals over internal momenta,  $k$ , of the form

$$\int \frac{d^4 k}{(2\pi)^4} \mathcal{I}(k, \{p_i\}) \quad (1.6)$$

where  $\mathcal{I}$  is the loop-integrand dependent on the internal,  $k$ , and external momenta  $\{p_i\}$  of the diagram. There are roughly two types of divergences:

- **UV-divergences:** in the limit of  $k \rightarrow \infty$ , given  $\mathcal{I} \sim k^n$ , the integral will diverge for  $n \geq -4$

$$\int \frac{d^4 k}{(2\pi)^4} k^n \sim \int_0^\infty k^{n+3} dk \quad (1.7)$$

- **IR-divergences:** in the limit of  $k \rightarrow 0$ , given  $\mathcal{I} \sim 1/k^m$ , the integral will diverge for  $m \leq 4$  (in four dimensions)

$$\int \frac{d^4 k}{(2\pi)^4} \frac{1}{k^m} \sim \int_0^\infty k^{3-m} dk \quad (1.8)$$

The high-momentum modes of the internal loop momentum “pollute” the relevant low-scale behavior and produce infinite results when integrated. One way to get around this is to regulate the integrals – that is, to simply not allow high-momentum modes to contribute above a cutoff scale  $\Lambda$

$$\int_0^\Lambda (\dots) dk \quad (1.9)$$

effectively rendering all loop-divergences finite<sup>6</sup>. In practice, for various reasons, this crude cutoff prescription is replaced with more sophisticated regularization prescriptions, the most practical being dimensional regularization (dim-reg) [46]. The key observation is that in  $D < 4$  spacetime dimensions the UV divergences in eq. (1.7) become finite (similarly for IR divergences e.g. eq. (1.8) but in  $D > 4$ ). In the case of UV divergences, for example, ‘shifting’ the number spacetime dimensions  $D \rightarrow 4 - 2\epsilon$  for  $\epsilon > 0$  where  $\epsilon$  is an arbitrary infinitesimal parameter, causes all divergences to appear as  $1/\epsilon$  poles which can then be explicitly removed by counter-terms in a minimal subtraction scheme (MS [47],  $\overline{\text{MS}}$  [48]). Technically, we first define bare couplings and fields, which absorb the divergences appearing in loop diagrams to become a renormalized cousin i.e. a redefinition of the original bare coupling once counter-terms have been subtracted.

Note that shifting the dimension of spacetime will also alter the mass dimension of the fields appearing in the Lagrangian. For example,

$$[\phi] = 1 - \epsilon, \quad [\psi] = \frac{3}{2} - \epsilon \quad (1.10)$$

where  $\phi$  and  $\psi$  represent scalar and fermion fields, respectively. Naively, this would ‘dimensionify’ what would be dimensionless couplings the interaction Lagrangian in  $D = 4$ . To keep couplings dimensionless, we can introduce an arbitrary dimensionful parameter into the Lagrangian,  $\mu$ , conventionally referred to as the renormalization scale, which will book-keep the  $\epsilon$ -induced scale dependence of the couplings

$$\lambda\phi^4 \rightarrow (\lambda\mu^{2\epsilon})\phi^4, \quad y\phi\bar{\psi}\psi \rightarrow (y\mu^\epsilon)\phi\bar{\psi}\psi, \quad \dots \quad (1.11)$$

Implicitly, this makes every prediction of the theory dependent on the arbitrary choice of renormalization scale – any variation in  $\mu$  will shift theoretical predictions. Instinctually, physical observables shouldn’t be dependent on the choice. We can enforce this prior via a constraint on the bare couplings,  $\{\lambda_0, g_0, m_0, \dots\}$ , of the theory

$$\frac{d}{d\mu}\{\lambda_0, g_0, m_0, \dots\} = 0. \quad (1.12)$$

Because the bare parameters are related to renormalized ones via multiplicative renormalization (e.g.,  $\lambda_0 = Z_\lambda\mu^{2\epsilon}\lambda$ , etc., where  $Z_\lambda$  is the counterterm), this condition induces differential equations for the renormalized couplings. Differentiating both sides and using the chain rule,

---

<sup>6</sup>Interestingly, even if all loop diagrams are regulated successfully, a separate divergence stems from a factorial growth in the number of contributions to the series in eq. (1.5) causing the sum to be asymptotic. This means that any finite value of  $\alpha$  produces a divergent sum (even for perturbative  $\alpha!$ ). Despite the generic non-convergent behavior, the predictions from the “low-order” expansion are highly accurate with the factorial growth dominating only at higher orders in the  $\alpha$  expansion – often in the regime that is not computable with modern techniques. The exact crossing point is, of course, model-dependent.

one finds that the renormalized parameters must vary with  $\mu$ :

$$\mu \frac{d\lambda}{d\mu} = \beta_\lambda(\lambda), \quad \mu \frac{dm}{d\mu} = m\gamma_m(\lambda), \quad \dots \quad (1.13)$$

where the beta functions,  $\beta$ , and anomalous dimensions,  $\gamma$ , encode the scale-dependence of the couplings. To make predictions requires an initial condition, namely, the parameters need to be measured at some reference scale. Once the boundary condition is set, the solutions to eq. (1.13) describe the trajectory to all other scales.

In the renormalization prescription outlined above, it turns out that for local operators with mass dimension  $d \leq 4$ , the required number of counter-terms is finite — at the loop level, each operator can only produce operators of the same ‘structure’ as those contained in the theory. In another sense, the quantum correction to the theory *close* onto itself. Because of this, theories which only contain operators up to dimension-4 are termed *renormalizable*.

Higher dimensional operators with mass dimension  $d > 4$ , on the other hand, require an infinite number of counter-terms to absorb the divergences they generate — the theory no longer closes onto itself under renormalization. Such theories are termed *non-renormalizable* in the traditional sense. Nonetheless, non-renormalizable theories are still predictive when treated as effective field theories (EFTs), valid below some cutoff scale  $\Lambda$  at which the UV physics becomes important. In this framework, all operators consistent with the symmetries of the low-energy theory are included, with higher-dimensional terms suppressed by powers of  $\Lambda$ :

$$\mathcal{L}_{\text{EFT}} = \mathcal{L}_{\text{ren.}} + \sum_i \frac{c_i^{(5)}}{\Lambda} \mathcal{O}_i^{(5)} + \sum_j \frac{c_j^{(6)}}{\Lambda^2} \mathcal{O}_j^{(6)} + \dots \quad (1.14)$$

where  $c_i^{(5)}, c_j^{(6)}, \dots$  are  $\mathcal{O}(1)$  coefficients typically referred to as *Wilson coefficients*. The expansion is organized as a power series in  $E/\Lambda$ , where  $E$  is the characteristic energy of the process. Truncating at a fixed order yields a finite number of parameters and controlled theoretical errors, enabling systematic low-energy predictions without knowledge of the full UV dynamics.

## 1.2 Lore – Experiment

The predictions of the SM has been extensively tested experimentally. It is one of the most comprehensively tested models in the history of science. The experimental confirmation of the Standard Model proceeded through a series of landmark discoveries, many of which validated theoretical predictions made decades earlier. The positron, predicted by Dirac in 1928, was first observed by Anderson in 1932 using a cloud chamber exposed to cosmic rays [49, 50]. The muon was discovered in 1936 and was initially mistaken for the predicted meson in Yukawa’s theory of the strong nuclear force [51]. The discovery of the pion came a decade later (1947), validating Yukawa’s model of nuclear binding [52, 53]. Parity violation in weak interactions was

confirmed by Wu et al. in 1957, an experimental milestone that motivated the chiral structure of the electroweak theory [54]. The discovery of the neutrino, inferred from nuclear beta decay in the 1930s, was realized experimentally by Cowan and Reines in 1956 [55]. The existence of quarks was first inferred from hadron spectroscopy, but gained strong experimental support from deep inelastic scattering experiments at SLAC (late 1960s), which revealed point-like substructure in the proton consistent with partons (quarks) [56, 57]. The charm quark was discovered simultaneously by two groups in 1974 via the  $J/\psi$  resonance, independently observed by two collaborations: the MIT-BNL experiment at Brookhaven National Laboratory, who named the resonance the “ $J$ ” particle [58], and the SLAC-LBL collaboration, who called it the “ $\psi$ ” [59]. The bottom quark was discovered in 1977 [60], and the top quark, predicted to complete the third generation, was observed at the Tevatron in 1995 [61, 62]. The discovery of the  $W^\pm$  and  $Z$  bosons in 1983 at CERN by the UA1 and UA2 collaborations confirmed the central predictions of electroweak unification [63, 64]. Later, the precise measurements of their masses and widths at LEP and SLC further validated the SM at the loop level [65]. The Higgs boson, the final missing piece of the SM, was discovered in 2012 by the ATLAS and CMS experiments at the LHC, almost five decades after its original proposal [66, 67].

As mentioned at the beginning of this chapter, while there are no experimental results which have crossed the “discovery” threshold, there are a number of measurements in tension with the SM predictions:

- **Flavor physics anomalies:** measurements related to lepton flavor universality violation in semileptonic  $B$ -meson decays, such as  $R_{K^{(*)}}$  and  $R_{D^{(*)}}$  deviate from the SM expectations [68–71]. These discrepancies suggest potential lepton flavor universality violation beyond the SM, with combined significance currently around the  $3 - 4\sigma$  level.
- **Cabibbo-angle anomaly (Cabibbo-angle universality violation):** There is a persistent tension arising from the extraction of the CKM matrix element  $V_{ud}$  from superallowed nuclear beta decays and neutron decay measurements. Current determinations show roughly a  $3\sigma$  tension with the theoretical expectation of CKM unitarity (the requirement that  $|V_{ud}|^2 + |V_{us}|^2 + |V_{ub}|^2 = 1$ ), indicating potential violations of Cabibbo universality or systematic theoretical uncertainties [72–74].
- **$W$ -boson mass measurement:** Recent precision measurements of the  $W$ -boson mass by the CDF collaboration have shown significant deviations from the SM prediction, differing by approximately  $7\sigma$  from the theoretical expectation based on global electroweak fits [75]. However, these results are yet to be independently confirmed by other experiments, and thus remain under scrutiny [76, 77]. For potential new physics contributions explaining this positive mass discrepancy, see our work in [78].

- **ATOMKI anomaly:** Observations from the ATOMKI experiment involving nuclear transitions of excited  $^8\text{Be}$  and  $^4\text{He}$  nuclei reveal excesses in electron-positron angular distributions at certain energies. These anomalies have been interpreted as possible signatures of a new boson (often referred to as the “X17 particle”) with a mass around 17 MeV [79–81]. The significance of this deviation is reported around  $6.8\sigma$ , however, the signal remains unconfirmed. Dedicated searches by the PADME [82], MEG-II [83] and NA64 [84, 85] collaborations have so far reported no significant signals, placing stringent constraints on the X17 parameter space.
- **“Neutron lifetime puzzle”:** Measurements of the free neutron lifetime using two distinct experimental techniques — the *bottle* method, which confines ultracold neutrons in material or magnetic traps and measures the disappearance rate, and the *beam* method, which counts decay products from a well-characterized neutron beam — yield values differing by  $\sim 8\text{s}$  ( $\tau_n^{\text{bottle}} \approx 879.4\text{s}$  versus  $\tau_n^{\text{beam}} \approx 888.0\text{s}$ ). This discrepancy corresponds to a  $\sim 4\sigma$  tension [86, 87]. At face value, it could indicate exotic, BSM decay channels such as  $n \rightarrow \chi + \gamma$  into a dark sector [88, 89], or alternatively, point to unaccounted-for systematic effects in one or both measurement techniques.

Many modern experiments measuring against SM theory predictions have entered a ‘precision era’, indicating ultra-precise sensitivity to non-SM behavior and probing higher order terms in the matrix element expansion in eq. (1.5). For example, a recent measurement of the muons magnetic moment in the form of the  $(g - 2)_\mu$  observable,  $a_\mu$ , was reported with a precision of 127 ppb =  $127 \times 10^{-9}$  relative precision  $\approx$  (uncertainty/measured value) [90]

$$a_\mu = 1165920705(148) \times 10^{-12} \text{ (127 ppb)}. \quad (1.15)$$

Comparing this measurement with a similarly recent update to theory calculation of hadronic vacuum polarization diagrams now show agreement with the experimental value within relative uncertainties, relieving a long-standing  $\sim 4\sigma$  tension to  $< 1\sigma$

$$\Delta a_\mu \equiv a_\mu^{\text{exp}} - a_\mu^{\text{th}} = (384 \pm 637) \times 10^{-12}. \quad (1.16)$$

The SM computation required to compare to this precision measurement requires the inclusion of meaningful theoretical contributions from higher-order QED corrections at the five-loop level [91].

Precision electroweak observables, such as the  $Z$  boson mass, width, and asymmetry parameters, have been measured at electron-positron colliders like LEP and SLC [65]. For instance, the mass of the  $Z$  boson is determined to impressive precision:

$$M_Z = 91.1876 \pm 0.0021 \text{ GeV}. \quad (1.17)$$

This precision has allowed stringent tests of radiative corrections and indirect constraints on the Higgs boson mass prior to its discovery.

Similarly, the Fermi constant,  $G_F$ , which governs the strength of the weak interaction, is known precisely from muon lifetime measurements [92]:

$$G_F = 1.1663787(6) \times 10^{-5} \text{ GeV}^{-2}. \quad (1.18)$$

This parameter normalizes all low-energy charged-current weak processes, entering directly into matrix elements for muon decay, nuclear beta decay, and semileptonic meson transitions. Alongside  $M_Z$  and  $\alpha_{\text{EM}}$ , it forms a minimal input set for the electroweak sector, and serves as a reference point for testing the internal consistency of the SM through global electroweak fits. Deviations in processes involving weak vertices thus provide sensitive indirect probes of new physics.

Finally, the electromagnetic coupling,  $\alpha_{\text{EM}}$ , extracted from low-energy Thomson scattering, quantum Hall measurements, and the magnetic moment of the electron  $(g - 2)_e$ , is one of the most precisely known parameters in the SM [93, 94]:

$$\alpha_{\text{EM}}^{-1} = 137.035999084(21). \quad (1.19)$$

Its precise value enables sub-permille level predictions for QED and electroweak observables, making it an essential input for high-precision SM tests and similarly to  $(g - 2)_\mu$ , potentially sensitive to loop-level effects from new physics.

### 1.2.1 Modern experimental frontiers

Modern tests of the SM, and thereby searches for new physics beyond the SM, can be broadly categorized into three distinct experimental frontiers with different theoretical implications and constraints:

1. The **energy frontier** or collider-based approaches attempting to directly produce heavy exotic states from high energy collisions (LHC – CMS, ATLAS, LHCb).
2. The precision or **intensity frontier** probe weakly coupled physics i.e. rare interactions through intense particle fluxes (Mu2e, COMET, Mu3e, MEG, NA62, Belle-II, etc.) or large volumes of nuclei with background-free signatures (Super-Kamiokande, Hyper-Kamiokande, SNO, DUNE, etc.).
3. The astrophysical or **cosmic frontier** probes new physics through observational deviations in cosmological, stellar, and galactic evolution, arising from modifications to the well-established correlations between Standard Model (SM) processes and the predictions of the  $\Lambda$ CDM cosmological model.

All three approaches are complimentary and can probe vastly different effective new physics scales,  $\Lambda$ , typically referred to as the “reach” of an experiment or measurement. As a benchmark model for estimating and comparing the reach at the energy and intensity frontiers, we can consider new physics from a dimension-6 four-fermion contact operator

$$-\mathcal{L} \supset \frac{C_{(6)}}{\Lambda^2} (\bar{\psi}_1 \Gamma_A \psi_2) (\bar{\psi}_3 \Gamma_B \psi_4) \quad (1.20)$$

where  $\psi_{1,2,3,4}$  denote generic fermionic field content i.e. SM or BSM fields and  $\Gamma_{A,B}$  denote arbitrary Lorentz invariant structures.

### 1.2.1.1 Example estimate of new physics reach at the energy frontier

At the energy frontier the reach is measurement dependent – as a simple example, consider the direct production from an  $e^+e^-$  collision of the SM forbidden final state  $e^\pm\mu^\mp$  sourced by the following dimension-6 operator:

$$\mathcal{L}_{ee\mu e} = -\frac{C_{(6)}}{\Lambda^2} (\bar{e}e)(\bar{\mu}e). \quad (1.21)$$

The naive scaling of this cross section can be estimated using the techniques from appendix A resulting in

$$\sigma_{e^+e^- \rightarrow \mu^\mp e^\pm} \sim \frac{C_{(6)}^2}{64\pi} \frac{s}{\Lambda^4}. \quad (1.22)$$

The total number of expected events depends on the integrated luminosity

$$N_{ee\mu e} = \sigma_{e^+e^- \rightarrow \mu^\mp e^\pm} \times \mathcal{L}_{\text{int}} \times \varepsilon \quad (1.23)$$

where  $\mathcal{L}_{\text{int}} = \int \mathcal{L} dt$  and  $\varepsilon$  is the detection efficiency. Assuming no SM background and no observed signal events, Poisson statistics tells us that  $N_{ee\mu e} \leq 3$  at a 95% confidence-level (CL). This allows us to place a constraint on the cross section

$$\sigma_{ee\mu e}^{95\% \text{ CL}} \leq \frac{3}{\mathcal{L}_{\text{int}} \varepsilon} \quad (1.24)$$

and subsequently an estimate for the reach

$$\Lambda \gtrsim \left( \frac{C_{(6)}^2}{192\pi} \times \sqrt{s} \times \mathcal{L}_{\text{int}} \right)^{1/4}. \quad (1.25)$$

Importantly, eq. (1.25) shows that there are two ways for a collider based experiment to increase their new physics potential – increase the center of mass energy or the luminosity. The OPAL collaboration at LEP searched for this channel [95] and placed a 95% CL upper limit on the cross section across three COM energy regimes. The most constraining of which comes from the

$200 \leq \sqrt{s} \leq 209$  GeV region containing an integrated luminosity of  $322.2 \text{ pb}^{-1}$  and  $\mu e$  detection efficiency of  $\varepsilon = 55.8 \pm 0.7\%$ . With these numbers and the expressions above we can estimate the expected upper limit on the cross section

$$\sigma_{ee\mu e}^{95\% \text{CL}} \lesssim 17 \text{ fb} \left( \frac{322.2 \text{ pb}^{-1}}{\mathcal{L}_{\text{int}}} \right) \left( \frac{0.558}{\varepsilon} \right). \quad (1.26)$$

The actual upper limit reported by OPAL was  $\sigma_{ee\mu e}^{95\% \text{CL}} \leq 22 \text{ fb}$ .

$$\Lambda \gtrsim 148 \text{ GeV} \left( \frac{\sqrt{s}}{204.5 \text{ GeV}} \right)^{1/2} \left( \frac{17 \text{ fb}}{\sigma_{ee\mu e}^{95\% \text{CL}}} \right)^{1/4}. \quad (1.27)$$

The LHC is capable of producing proton-proton ( $pp$ ) collisions at a center-of-mass energy of  $\sqrt{s} \approx 14$  TeV. The new physics reach from direct production lower than this due to the compositeness of the proton  $p \equiv uud$ . Roughly, the reach can be estimated as  $\Lambda \sim \sqrt{s}/3 \sim 5$  TeV. The reduction roughly corresponds to the fact that at 14 TeV, the partons (gluons and quarks) inside of the proton are the interacting degrees of freedom, not the proton itself. Each parton roughly carries an equal proportion of the energy and momentum of the proton (the exact amount of energy each parton carries inside of the proton is more accurately described by its parton distribution function (PDF)).

Precision measurements can also be performed at collider based experiments. In these measurements, new physics manifests as contributions to the total rate of a process. The precision on the measurement can then be used to infer a new physics scale based on the next decimal digit of the measurement. If new physics were present, it would then influence the next digit and produce a discrepancy as precision improves.

### 1.2.1.2 Example estimate of new physics reach at the intensity frontier

The reach of the intensity frontier is fundamentally set by the total number of observed events, or equivalently, the total number of unobserved events. If a large number of statistically independent events are observed and the signal process is not seen after accounting for the total amount of expected background events, it can be concluded that the event occurs with a probability roughly smaller than  $1/(\text{number of observations})$ . For example, at experiments searching for rare muon decays, such as  $\mu \rightarrow 3e$ , limits on branching ratios are approximately set by the “single event sensitivity” (non-observation), i.e.  $N_{\text{sig}} \lesssim 1$  (based on an approximately background-free search) after measuring  $N_{\text{obs}}$  muon decays (and ignoring possible detection efficiencies associated with the detector)

$$\mathcal{B}(\mu^+ \rightarrow e^+ e^- e^+) \equiv \frac{\Gamma(\mu \rightarrow 3e)}{\Gamma(\mu)} \lesssim \frac{1}{N_{\text{obs}}}. \quad (1.28)$$

Based on the naive argument above, assuming an operator of the form in eq. (1.21), the rate for the exotic three-body decay is given roughly by dimensional analysis as

$$\Gamma_{\mu \rightarrow 3e} \approx \frac{C_{(6)}^2}{144\pi^3} \frac{m_\mu^5}{\Lambda^4}. \quad (1.29)$$

The effective new physics scale probed by an experiment, such as Mu3e, observing a total of  $N_\mu \approx 10^{15}$  muon decays with non-observation is then, assuming  $C_{(6)} \simeq 1$ ,

$$\Lambda \gtrsim 2 \times 10^3 \text{ TeV} \left( \frac{N_\mu}{10^{15}} \right)^{1/4} \left( \frac{10^{-19} \text{ GeV}}{\Gamma_\mu} \right)^{1/4}. \quad (1.30)$$

Muons are inherently sensitive to new physics scales  $\gtrsim$  TeV. A fun limit<sup>7</sup>, which emphasizes the importance of muons as high-scale probes of new physics, is  $N_\mu \rightarrow 1$ , *i.e.*, observing a single muon decay that isn't the  $\mu \rightarrow 3e$  signal naively probes a new physics scale of  $\sim$  TeV. The small width of the muon combined with the fact that its SM couplings and mass live where we (humans) can produce, capture, and manipulate large quantities of it, solidifies the muons unique role in precision tests of the SM and searches for new physics<sup>8</sup>.

In part I we will be primarily interested in rare leptonic (mostly muon) decays – specifically those which violate charged lepton flavor number. Below we will introduce the mathematical formulation of the leptonic Standard Model and outline how an approximate accidental global symmetry causes charged-lepton-flavor-violating (CLFV) rates in the SM to be approximately “forbidden”. We will also then describe how new physics can produce observable CLFV signals. Finally we will describe a subset of a vast number of experiments searching for CLFV signals for which motivate the phenomenology in the following chapters of Part I.

### 1.3 The Electroweak Theory of Leptons

The Electroweak Theory of Leptons or the *Leptonic Standard Model* (LSM) is a chiral gauge theory first discussed by Sheldon Glashow in 1961 [96]. The model attempts to unify the electromagnetic and weak interactions. Glashow's model introduced electroweak gauge group and the concept of a weak mixing angle. The model didn't, however, address the issue of mass generation. In 1967, Steven Weinberg [97]; and separately Abdus Salam [98], resolved the issue of mass generation by embedding a Higgs mechanism [99–102] into Glashow's model.

The LSM is defined by the following ingredients [103, 104]:

- The local gauge symmetry

$$SU(2) \otimes U(1)_Y \quad (1.31)$$

---

<sup>7</sup>Thank you Jure, for pointing this out.

<sup>8</sup>I think a modern phenomenologists take on the famous quote by Isidor Rabi, “Who ordered that?”, would be something like “Can we get some more of that?”.

whose generators are defined as  $T_a, a = 1, 2, 3$  for  $SU(2)$  and the weak hypercharge operator  $Y$  for  $U(1)_Y$  satisfying

$$[T_a, T_b] = i\epsilon_{abc}T_c \quad (1.32)$$

$$[T_a, Y] = 0. \quad (1.33)$$

These operators take values on the LSM fields, assigned below.

- The leptonic field content, consisting of three families or *flavors* ( $e, \mu, \tau$ ) of three left-handed Weyl spinor fields for a total of nine independent field degrees of freedom (18 component degree of freedom). Each flavor is a copy of the same gauge representation i.e. each is assigned the same quantum charges under the gauge group. All three families are then uniquely defined through the definition of a single flavor:

$$\ell \equiv \begin{pmatrix} \nu_e \\ e \end{pmatrix}, \bar{e} \quad (1.34)$$

with charges

$$T_a \ell = \frac{1}{2} \tau_a \ell, \quad T_a \bar{e} = 0, \quad (1.35)$$

$$Y \ell = -\ell, \quad Y \bar{e} = +2 \bar{e}. \quad (1.36)$$

where  $\tau_a, a = 1, 2, 3$ , are the  $2 \times 2$  Pauli matrices given in Eq. 2. Note that with this assignment of quantum numbers, the electric charge operator is given by the relation

$$Q = T_3 + \frac{Y}{2}. \quad (1.37)$$

We will adopt the common shorthand notation to denote the transformation of the fields under the gauge group

$$\ell \sim \mathbf{2}_{-1}, \quad \bar{e} \sim \mathbf{1}_{+2}. \quad (1.38)$$

For phenomenological and historical purposes it is often more convenient to use four-component Dirac notation. The Dirac four-component electron and neutrino fields, for example, are given by

$$\Psi_e \equiv \begin{pmatrix} e_L \\ e_R \end{pmatrix} = \begin{pmatrix} e \\ i\sigma_2(\bar{e})^* \end{pmatrix}, \quad \Psi_\nu \equiv \begin{pmatrix} \nu_e \\ 0 \end{pmatrix} = P_L \Psi_\nu \equiv \Psi_{\nu,L}. \quad (1.39)$$

It will be useful to also define how Dirac spinors transform in terms of Weyl spinors under the discrete symmetries  $\mathbf{C}, \mathbf{P}, \mathbf{T}$  corresponding to charge, parity, and time reversal

transformations, respectively. Consider a generic Dirac spinor

$$\Psi \equiv \begin{pmatrix} \psi_L \\ \psi_R \end{pmatrix} = \begin{pmatrix} \chi_1 \\ i\sigma_2\chi_2^* \end{pmatrix}, \quad \text{we have} \quad (1.40)$$

$$\mathbf{C} : \Psi^C \equiv C(\bar{\Psi})^\top = i\gamma_2\Psi^* = \begin{pmatrix} \chi_2 \\ i\sigma_2\chi_1^* \end{pmatrix} \quad \text{i.e. } \chi_1 \leftrightarrow \chi_2 \quad (1.41)$$

$$\mathbf{P} : \Psi^P(t, \vec{x}) \equiv \gamma_0\Psi(t, -\vec{x}) = \begin{pmatrix} \psi_R \\ \psi_L \end{pmatrix} \quad \text{i.e. } \chi_L \leftrightarrow \chi_R \quad (1.42)$$

$$\mathbf{T} : \Psi^T(t, \vec{x}) \equiv \gamma^1\gamma^3\Psi^*(-t, \vec{x}) = \begin{pmatrix} i\sigma_2\chi_1^* \\ -\chi_2 \end{pmatrix} \quad \text{i.e. } \chi_1 \leftrightarrow i\sigma_2\chi_1^*, \quad \chi_2 \leftrightarrow i\sigma_2\chi_2^* \quad (1.43)$$

where we have used  $\bar{\Psi} \equiv \gamma^0\Psi^\dagger$  and  $C \equiv i\gamma^0\gamma^2$ .

- A single complex scalar field

$$\phi = \begin{pmatrix} \phi^+ \\ \phi^0 \end{pmatrix} \quad (1.44)$$

with charges

$$T_a\phi = \frac{1}{2}T_a, \quad Y\phi = \phi \quad \text{or equivalently } \phi \sim \mathbf{2}_{+1}. \quad (1.45)$$

- Spontaneous symmetry breaking at some scale  $\Lambda_{\text{EW}}$

$$SU(2) \otimes U(1)_Y \xrightarrow{\Lambda_{\text{EW}}} U(1)_{\text{EM}}. \quad (1.46)$$

Given the above local gauge symmetries and field content, the leading order, renormalizable model can be constructed by enumerating all dimension-4 Lorentz and gauge invariant terms that may appear in the Lagrangian.

### 1.3.1 The Lagrangian

The local symmetry in eq. (1.31) comes with  $(2^2 - 1) + 1 = 4$  vector gauge bosons – three associated with the generators of  $SU(2)$  (transforming under the adjoint representation),  $W_\mu^a$  with  $a = 1, 2, 3$ , and one with the generator of  $U(1)_Y$ ,  $B_\mu$ . The gauge fields have charges

$$T_a W_{\mu,b} = -i\epsilon_{abc}W_\mu^c, \quad YW_{\mu,a} = 0 \quad (1.47)$$

$$T_a B_\mu = 0, \quad YB_\mu = 0 \quad (1.48)$$

or equivalently

$$W_\mu^a \sim \mathbf{3}_0, \quad B_\mu \sim \mathbf{1}_0. \quad (1.49)$$

The interactions between the fermionic field content and the gauge bosons is fully determined by the covariant derivative

$$D_\mu \equiv \partial_\mu + igT_a W_\mu^a + ig' \frac{Y}{2} B_\mu. \quad (1.50)$$

The gauge field strengths are given by

$$W_{\mu\nu} = \partial_\mu W_\nu - \partial_\nu W_\mu + ig[W_\mu, W_\nu] \quad (1.51)$$

where  $W_\mu \equiv T_a W_\mu^a$ . The full gauge-fermion Lagrangian for one family of leptons is then given concisely in Weyl notation as

$$\mathcal{L}_{\text{gauge-fermion}} = \ell^* i\bar{\sigma}_\mu D^\mu \ell + \bar{e}^* i\bar{\sigma}_\mu D^\mu \bar{e} - \frac{1}{2} \text{Tr}(W_{\mu\nu} W^{\mu\nu}) - \frac{1}{4} B_{\mu\nu} B^{\mu\nu} \quad (1.52)$$

or equivalently in Dirac notation

$$\begin{aligned} \mathcal{L}_{\text{gauge-fermion}} = & \bar{\Psi}_{\nu,L} i\gamma^\mu \partial_\mu \Psi_{\nu,L} + \bar{\Psi}_e i\gamma^\mu \partial_\mu \Psi_e \\ & - \frac{g}{\sqrt{2}} (W_-^\mu \bar{\Psi}_e \gamma_\mu P_L \Psi_\nu + W_+^\mu \bar{\Psi}_\nu \gamma_\mu P_L \Psi_e) \\ & + e A^\mu \bar{\Psi}_e \gamma_\mu \Psi_e \\ & - \frac{g}{2 \cos \theta_W} Z^\mu (\bar{\Psi}_\nu \gamma_\mu (g_V^\nu - \gamma_5 g_A^\nu) \Psi_\nu + \bar{\Psi}_e \gamma_\mu (g_V^e - \gamma_5 g_A^e) \Psi_e) \\ & - \frac{1}{2} \text{Tr}(W_{\mu\nu} W^{\mu\nu}) - \frac{1}{4} B_{\mu\nu} B^{\mu\nu}. \end{aligned} \quad (1.53)$$

### 1.3.2 Electroweak symmetry breaking via the Higgs mechanism

Generically speaking, chiral theories cannot contain massive fermions. The Higg's mechanism [99–102] is a model building trick that allows for a chiral theory to achieve massive fermions via symmetry breaking. The mechanism relies on embedding the want-to-be-massive fermions into a vectorial subgroup of the full chiral gauge group. In this way, the breaking of the symmetry group can always be oriented in such a way to provide mass to the desired fermions.

To be explicit, the scalar  $\phi$  can be coupled to the electron and neutrino via the gauge invariant Yukawa operator

$$\begin{aligned} -\mathcal{L}_{\phi e} = & \lambda_e \bar{e} \phi^\dagger \ell + \text{h.c.} \\ = & \lambda_e \bar{e} (\phi^{+\dagger} \nu_e + \phi^{0\dagger} e) + \text{h.c.} \end{aligned} \quad (1.54)$$

If we could force the components of  $\phi$  to align such that

$$\phi^0 = \frac{v}{\sqrt{2}}, \quad \phi^+ = 0, \quad (1.55)$$

the neutrino would remain massless, the electron would obtain a mass

$$m_e = \frac{\lambda_e v}{\sqrt{2}}, \quad (1.56)$$

and  $SU(2) \otimes U(1)_Y$  would break to  $U(1)_{\text{QED}}$  producing three pseudo-Nambu-Goldstone (massive gauge) bosons (in the limit where  $g, g' \neq 0$ ). All of these desirable features can be achieved via the following scalar sector

$$\mathcal{L}_\phi = (D_\mu \phi)^\dagger (D^\mu \phi) - V(\phi), \quad \text{where} \quad (1.57)$$

$$V(\phi) = \frac{\lambda}{2} \left( \phi^\dagger \phi - \frac{v^2}{2} \right)^2. \quad (1.58)$$

Minimization of the potential in eq. (1.58), produces the field minimum  $\phi_*$  satisfying

$$\left. \frac{\partial V(\phi)}{\partial \phi} \right|_{\phi=\phi_*} = 0. \quad (1.59)$$

The minimum requires  $\phi$  to obtain a vacuum expectation value (VEV) via the constraint

$$\phi_*^\dagger \phi_* = \frac{v^2}{2}. \quad (1.60)$$

As a complex scalar field,  $\phi$  has four degrees of freedom

$$\phi = \begin{pmatrix} \phi^+ \equiv \phi_1 + i\phi_2 \\ \phi^0 \equiv \phi_3 + i\phi_4 \end{pmatrix}. \quad (1.61)$$

The potential in eq. (1.58) triggers spontaneous symmetry breaking (SSB) of the SM gauge group, or in other words, forces the Higgs field to ‘choose a direction’ in field space. We are free to choose the direction of this breaking – an  $SU(2)_L$  rotation can always bring us to a desired direction. A convenient direction, alluded to in eq. (1.55), that outputs explicit values of fermion masses occurs in the so-called unitary gauge where

$$\phi(x) \rightarrow \frac{1}{\sqrt{2}} \begin{pmatrix} 0 \\ h(x) + v \end{pmatrix}. \quad (1.62)$$

In this gauge only  $\phi_3(x) \equiv h(x)$  survives, the other three degrees of freedom are gauged away and reappear in the longitudinal modes of the now massive gauge bosons. Note that now, the physical Higg’s boson,  $h$ , is a real scalar field.

### 1.3.3 Neutrino masses

In 1998, SuperKamiokande found a discrepancy between the expected and measured flux of muon neutrinos from the atmosphere [105]. Three years later in 2001, the Sudbury Neutrino Observatory (SNO) independently confirmed a similar discrepancy using expected and measured fluxes of solar neutrinos [106]. These discoveries confirmed that a neutrino with an initial flavor,  $\alpha$ , produced at  $t_i$  has a non-zero probability to oscillate into a neutrino of a different flavor,  $\beta$  at time  $t_f$ . From a theory standpoint, these measurements are explained neatly by giving neutrinos a small, but non-zero, mass.

Of course, in the electroweak theory neutrinos are, by definition, massless (due to the non-inclusion of a left-handed anti-neutrino – see eq. (1.39)). A number of popular modifications to the SM exist in the literature that provide neutrino mass generation. The simplest extension is to add field content in the form of a left-handed anti-neutrino Weyl spinor field transforming as a singlet under all LSM charges

$$\bar{\nu}, \quad \Psi_\nu = \begin{pmatrix} \nu_e \\ i\sigma_2 \bar{\nu}_e^* \end{pmatrix} \quad (1.63)$$

We can now write an additional Yukawa term in addition to eq. (1.54) after defining an equivalent  $SU(2)$ -transformed reparameterization of the Higgs field with opposite hypercharge to that in eq. (1.44)

$$\tilde{\phi} \equiv i\sigma_2 \phi^* = \begin{pmatrix} (\phi^0)^* \\ (\phi^+)^* \end{pmatrix}, \quad \tilde{\phi} \sim \mathbf{2}_{-1} \quad (1.64)$$

allowing for terms of the form

$$\begin{aligned} -\mathcal{L}_{\phi\nu} &= \lambda_\nu \bar{\nu}_e \tilde{\phi}^\dagger \ell + \text{h.c.} \\ &= \lambda_\nu \bar{\nu}_e (\phi^0 \nu_e + \phi^+ e) + \text{h.c.} \end{aligned} \quad (1.65)$$

After spontaneous symmetry breaking the neutrino will obtain a mass similarly to the electron

$$m_\nu = \frac{\lambda_\nu v}{\sqrt{2}}. \quad (1.66)$$

Because neutrino masses are much smaller than the charged lepton masses, the Yukawa coupling,  $\lambda_\nu$ , will need to be extremely small and unnatural. This motivates a slightly more general parametrization of neutrino masses using effective operators.

Generically, when an accidental symmetry is found to be broken, the easiest way to parameterize the new physics without committing to a UV completion is to add the lowest order non-renormalizable operator that generates the desired feature. In the context of neutrino mass, the

lowest order operator dimension-5 and commonly referred to as the Weinberg operator

$$-\mathcal{L}_{\text{Weinberg}} = \frac{c_{(5)}}{\Lambda} (\tilde{\phi}^\dagger \ell) (\tilde{\phi}^\dagger \ell) \quad (1.67)$$

or equivalently in Dirac notation

$$-\mathcal{L}_{\text{Weinberg}} = \frac{c_{(5)}}{\Lambda} (\overline{\Psi}_e^C \epsilon \phi) (\Psi_e \epsilon \phi) \quad (1.68)$$

where  $\Lambda \gg v$  is a new physics scale where this operator is generated. Below the electroweak symmetry breaking scale

$$\tilde{\phi}(x) \rightarrow \frac{1}{\sqrt{2}} \begin{pmatrix} h(x) + v \\ 0 \end{pmatrix} \quad (1.69)$$

and neutrinos obtains a mass

$$m_\nu = \frac{c_{(5)}}{2} \frac{v^2}{\Lambda}. \quad (1.70)$$

Regardless of the mechanism for neutrino mass generation, the fact that neutrinos have a non-zero mass have far-reaching phenomenological implications on the low-energy predictions of the SM.

## 1.4 Accidental symmetries

In the previous sections, we only discussed a single family of leptons,  $e, \bar{e}, \nu_e$ . Experiment tells us that we should have two additional copies of ‘electron-like states’ with the same interactions and consecutively larger masses. Thus, the SM also includes two additional leptonic flavors, muons  $\mu$ , and tau leptons (or tauons)  $\tau$ , which can be straightforwardly incorporated by copying all ‘ $e$ ’ terms in the Lagrangian and replacing  $e \rightarrow \mu$  or  $e \rightarrow \tau$ . With additional flavors, eq. (1.54) can be written more generally as

$$-\mathcal{L}_{\phi l} = \lambda_{ij}^l \bar{l}_i \phi^\dagger \ell_j^l \quad (1.71)$$

where  $i, j \in \{e, \mu, \tau\}$  and the Yukawa matrix  $\lambda_{ij}^l$  is an arbitrary complex  $3 \times 3$  matrix, note that this implies the different lepton flavors can mix in this basis, which should be the case since there is no symmetry preventing it. However, in practice, we can always choose a basis where  $\lambda_{ij}^l$  is diagonal and real. After SSB we get a charged lepton mass term of the form

$$m_{ij}^l \equiv \frac{\lambda_{ij}^l v}{\sqrt{2}} \delta_{ij} = \begin{pmatrix} m_e & 0 & 0 \\ 0 & m_\mu & 0 \\ 0 & 0 & m_\tau \end{pmatrix} \quad (1.72)$$

where

$$m_e = 0.51099895000(15) \text{ MeV}, \quad m_\mu = 105.6583755(23) \text{ MeV}, \quad m_\tau = 1776.93(09) \text{ MeV}. \quad (1.73)$$

Small neutrino masses disturb this story slightly, introducing additional flavor structure into the leptonic sector. Conventionally, we choose a basis in which the charged lepton mass matrix is diagonal, so that all flavor misalignment is attributed to the neutrino sector. This misalignment gives rise to the physical phenomenon of neutrino mixing, encoded in the PMNS matrix.

If we neglect neutrino masses for a moment and consider the kinetic terms in eq. (1.52) and mass terms in eq. (1.72) we see that the LSM has an accidental global symmetry in the charged lepton sector

$$G_{\text{LSM}}^{\text{global}} \equiv U(1)^3 = U(1)_e \otimes U(1)_\mu \otimes U(1)_\tau. \quad (1.74)$$

These  $U(1)$  factors are known as electron, muon, and tau number, respectively – or collectively as *charged lepton number*. All three quantum numbers are exactly conserved in the LSM. In principle we can also equivalently use any set of three orthogonal vectors in  $U(1)^3$ . For example, defining the total lepton number as  $L \equiv L_e + L_\mu + L_\tau$ , an equivalent ‘anomaly-aligned’ basis useful for phenomenological studies is given by [107]

$$G_{\text{LSM}}^{\text{global}} = U(1)_L \otimes U(1)_{\mu-\tau} \otimes U(1)_{\mu+\tau-2e}. \quad (1.75)$$

The  $U(1)_{\mu-\tau}$ , along with  $U(1)_{e-\tau}$  and  $U(1)_{e-\mu}$ , are the only additional combinations of SM field content which keep the theory  $(\text{SM} + U(1)_{L_i-L_j})$  non-anomalous after gauging (without adding more BSM fermion content) [108, 109]. Many BSM models exploit this and promote these global symmetries to local ones – bringing along an additional gauge boson, commonly denoted as  $Z'_\mu$ , which has a number of well-studied phenomenological signatures [110]. While all three charged-lepton-number differences are equivalent from the perspective of anomalies,  $U(1)_{\mu-\tau}$  is the most commonly considered case in the literature due to better alignment with neutrino phenomenology and overall weaker constraints [111]. If we allow for additional field content in the form of  $n$   $U(1)_{L_i-L_j}$ -charged right-handed neutrinos,  $N_R$ , and consider vector-like charge assignments in the lepton sector, a continuous family non-anomalous configurations can be found using constrained linear combinations parameterized as [112]

$$\alpha(L_i - L_j) + \beta(L_j - L_k) \quad (1.76)$$

and constrained by

$$3\alpha\beta(\beta - \alpha) = \sum_n Q_n^3 \quad (1.77)$$

where  $Q_n$  denotes the  $U(1)_{L_i-L_j}$  charge of the right-handed neutrino. This effectively allows for any linear combination of  $L_i - L_j$  to be gauged and remain anomaly free, given that the

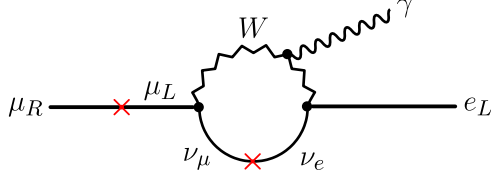


FIGURE 1.1: The Feynman diagram for  $\mu \rightarrow e\gamma$  in the SM with non-zero neutrino masses.

appropriate amount of right-handed neutrinos have been added to the theory (and engineered to de-couple at low-energies to maintain consistency with current bounds). The  $U(1)_L$  is approximately conserved in the SM, up to sphaleron transitions at very large energies and irrelevant for low-energy phenomenology. And finally,  $U(1)_{\mu+\tau-2e}$  is simply determined from the orthogonality requirement.

As mentioned above, neutrino masses induce flavor oscillations and indicate that  $U(1)_{\mu-\tau} \otimes U(1)_{\mu+\tau-2e}$  is not conserved in nature. Practically speaking, the charged-lepton-flavor-violating processes induced by neutrino oscillations are severely suppressed by a Glashow-Iliopoulos-Maiani (GIM) mechanism in the lepton sector. For example, Dirac neutrinos induce the  $\Delta(L_\mu - L_e) = 2$  CLFVing process  $\mu \rightarrow e\gamma$  at one-loop (as well as  $\tau \rightarrow \mu\gamma, \tau \rightarrow e\gamma$ ) as shown in fig. 1.1 with a branching ratio of [113]

$$\mathcal{B}(\mu \rightarrow e\gamma) \simeq \frac{\Gamma_{\mu \rightarrow e\gamma}}{\Gamma_{\mu \rightarrow e\nu\bar{\nu}}} = \frac{3\alpha_{\text{EM}}}{32\pi} \left| \sum_{j=2,3} U_{\mu j} \frac{\Delta m_{je}^2}{M_W^2} U_{je}^\dagger \right|^2 \approx 10^{-54} \quad (1.78)$$

where

$$\Gamma_{\mu \rightarrow e\nu\bar{\nu}} = \frac{G_F^2}{192\pi^3} m_\mu^5 \times I\left(\frac{m_e^2}{m_\mu^2}\right) \quad \text{with} \quad I(r_e) = 1 - 8r_e - 12r_e^2 \ln r_e + 8r_e^3 - r_e^4 \quad (1.79)$$

is the dominant muon ‘Michel’ decay channel with  $\mathcal{B}(\mu \rightarrow e\nu\bar{\nu}) \approx 1$ . Plugging in numbers, we find the muon width to be

$$\Gamma_\mu \simeq 3 \times 10^{-19} \text{ GeV}. \quad (1.80)$$

The branching ratio in eq. (1.78) renders CLFV in the SM, for all practical purposes, experimentally unobservable. For example, at a state-of-the-art muon stopping rate of  $\approx 10^{10}$  Hz, the SM predicts the observation of a single  $\mu \rightarrow e\gamma$  event every  $\approx 10^{36}$  years. Other SM processes, such as  $\mu \rightarrow eee$  or  $\mu N \rightarrow eN$  are further suppressed by factors of  $\alpha_{\text{EM}}$  [113, 114]

$$\mathcal{B}(\mu \rightarrow eee) \simeq \frac{\alpha_{\text{EM}}}{3\pi} \left( \log \frac{m_\mu^2}{m_e^2} - 3 \right) \times \mathcal{B}(\mu \rightarrow e\gamma) \quad (1.81)$$

$$\mathcal{C}(\mu N \rightarrow eN) \simeq \alpha_{\text{EM}} \times \mathcal{B}(\mu \rightarrow e\gamma).$$

More generally **charged lepton flavor violation** (CLFV) describes any process which conserves total lepton number  $L$  but violates  $U(1)_{\mu-\tau} \otimes U(1)_{\mu+\tau-2e}$  and involves no radiation in the

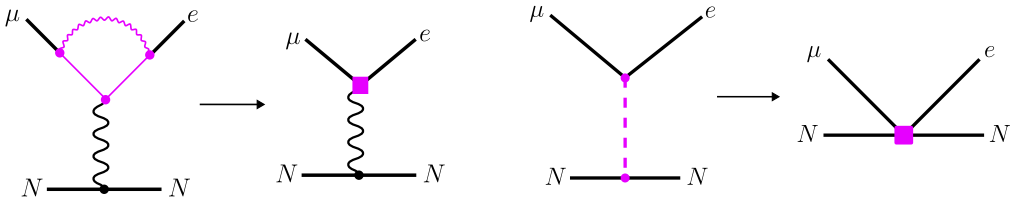


FIGURE 1.2: Generic depiction of CLFVing BSM interactions (left: photonic, right: contact) shown for example in the context of  $\mu N \rightarrow e N$ . Pink lines and vertices indicate UV-agnostic BSM particles and interactions.

form of neutrinos. New physics contributions to these processes and their associated signatures at a variety of experiments will be the main focus of part I.

#### 1.4.1 CLFV beyond the Standard Model

There are a large number of BSM models – including but not limited to those incorporating supersymmetry, compositeness, leptoquarks, heavy neutrinos, a second Higgs doublet, a heavy  $Z'$ , or dark matter – which naturally induce charged lepton flavor violation (CLFV), making current experimental bounds on CLFV processes one of the most stringent constraints on the space of viable models.

In the context of heavy new physics sourcing the CLFV, the corresponding diagrams can be generally classified by their short-range or long-range characteristics. Long-distance, or *photonic*, mechanisms (see, for example, fig. 1.2 top) are mediated by the exchange of a virtual photon between the nucleus and the  $\mu$ - $e$  leptonic current and are generically related to the  $\mu \rightarrow e\gamma$  decay. Short-distance, or *non-photonic*, mechanisms (see, for example, fig. 1.2 bottom) involve effective four-fermion interactions between quarks and leptons mediated by heavy intermediate particles at tree-level or a the one-loop-level via box diagrams. Each of these mechanisms, photonic and non-photonic, can also be encapsulated into model-agnostic effective field theories which can help facilitate model discrimination. At  $d = 6$ , the Standard Model Effective field theory (SMEFT) contains 888 operators which violate charged lepton number [16, 115, 116]. Some CLFV rates can even probe some  $d = 8$  operators [117, 118]. In particular, in chapter 3 we will explicitly develop a tower of effective field theories for computing  $\mu N \rightarrow e N$  conversion rates.

CLFV can also be sourced by light new physics [24]. Unlike heavy new physics, light new physics can remain dynamical at the relevant experimental energies and, as a result, their contributions cannot be captured by simple contact interactions. Instead, the resulting kinematics and differential distributions depend on the mass, spin, and couplings of the light mediator. For example, if CLFV is mediated by a light vector or scalar, the phase space can exhibit resonant enhancements when the invariant mass of a subset of final-state leptons matches the mediator mass (see chapters 2 and 4). Furthermore, the Lorentz structure of the interaction can leave

distinctive imprints in angular distributions [119], opening up new handles to disentangle signal from background and to extract properties of the underlying theory.

Additionally, light new physics can participate in both on- and off-shell processes and may induce visible or invisible final states depending on its decay modes. This can significantly alter the experimental strategy for detection. In many cases, traditional inclusive CLFV observables, which are optimized under the assumption of contact interactions, lose sensitivity and make more differential or exclusive observables essential. Accordingly, a robust search program for CLFVing light new physics requires dedicated efforts to go beyond total rate measurements and to consider the full kinematic information available to the detector.

New physics signatures involving light new physics in rare muon decays will be discussed at length in chapters 2, 4 and 5. Recently, in ref. [120] we discuss the sensitivity of fixed-target experiments to  $\tau$ -sourced CLFVing light new physics.

## 1.5 Experimental searches for CLFV

As discussed in detail above, CLFV decays in the SM are approximately forbidden. Inversely, any experimental measurement confirming CLFV necessarily and unambiguously implies BSM physics. Searches for these SM-forbidden channels offer as extremely precise tests of the SM and form the basis of many experimental studies searching for BSM physics.

### 1.5.1 Current bounds on $\mu$ 's

In the context of muons, the prospect of observing CLFV has promoted many advancement in the research and development of high intensity muon beams and accompanying experimental techniques. These developments have allowed for constraints on the rate of  $\mu \rightarrow e$  conversion to improve by roughly 12 orders of magnitude over the last 75 years. In the context of muonic systems, past and current searches for CLFV can be categorized by search channel, with experimental sensitivities reported in branching  $\mathcal{B}$  or capture  $\mathcal{C}$  ratios

$$\mathcal{B}(\mu \rightarrow eX) \equiv \frac{\Gamma(\mu \rightarrow eX)}{\Gamma(\mu)}, \quad \mathcal{C}(\mu N \rightarrow eN) \equiv \mathcal{C}(N) \equiv \frac{\Gamma(\mu N \rightarrow eN)}{\Gamma(\mu N \rightarrow \text{all captures})}. \quad (1.82)$$

For example, muons decaying to three electrons ( $\mu^+ \rightarrow e^+e^-e^+$ ) has been searched for at SINDRUM ( $\mathcal{B}(\mu \rightarrow 3e) < 10^{-12}$ ) [121] and will continue to be searched for at Mu3e (projected  $\mathcal{B}(\mu \rightarrow 3e) < 10^{-16}$ ) [122], muons decaying to an electron plus a photon ( $\mu \rightarrow e\gamma$ ) was searched for at MEG ( $\mathcal{B}(\mu \rightarrow e\gamma) < 4.2 \times 10^{-13}$ ) [123] and MEG-II (projected  $\mathcal{B}(\mu \rightarrow e\gamma) < 6 \times 10^{-14}$ ) [124], and finally captured muons decaying to an electron within the field of a nucleus ( $N\mu^- \rightarrow Ne^-$  where  $N$  is a nucleus of atomic mass  $A$  and atomic number  $Z$ ) has been searched for at SINDRUM II ( $\mathcal{C}(\text{Ti}) < 4.3 \times 10^{-12}$  and  $\mathcal{C}(\text{Au}) < 7 \times 10^{-13}$ ) [125] and TRIUMF ( $\mathcal{C}(\text{Ti}) <$

$4.6 \times 10^{-12}$ ) [126] and will continue to be searched for at DeeMe (projected  $\mathcal{C}(\text{C}) < 10^{-13}$  and  $\mathcal{C}(\text{SiC}) < 10^{-14}$ ) [127], COMET (projected  $\mathcal{C}(\text{Al}) < 7 \times 10^{-15}$ ) [128], and the experiment Mu2e [129]. The Mu2e experiment, located at Fermilab, is expected to achieve the most sensitive limits on nuclear  $\mu \rightarrow e$  conversion – further improving the leading constraints set by SINDRUM-II by an additional four-orders-of-magnitude within the next five years (projected  $\mathcal{C}(\text{Al}) < 2.87 \times 10^{-17}$ ).

### 1.5.2 Current bounds on $\tau$ 's

Compared to muons, producing and isolating large quantities of taus is much harder. The current most effective method involves high-luminosity  $e^+e^-$  colliders operating near the  $\tau$ -pair production threshold (e.g., Belle II at  $\sqrt{s} \sim 10.6$  GeV), where  $e^+e^- \rightarrow \tau^+\tau^-$  occurs with an appreciable cross section. Other  $\tau$  production channels involve cascade decays of heavy flavor mesons, particularly semileptonic  $B \rightarrow D^{(*)}\tau\nu_\tau$  and leptonic  $D_s^+ \rightarrow \tau^+\nu_\tau$  decays, which yield taus at the few percent level but typically within more complex and less reconstructible final states. Additionally,  $\tau$ 's can also be produced by running  $e^+e^-$  machines at the  $\Upsilon(4S)$  resonance. Moreover, because  $m_\tau > m_\pi, m_K$ , the  $\tau$ 's decay hadronically  $\approx 65\%$  of the time, leading to larger backgrounds and making CLFVing processes more challenging to isolate experimentally. The short lifetime of the  $\tau$  further complicates direct detection and tagging of its decay products – with the most effective mitigation being the use of asymmetric beams such that the outgoing final states are highly boosted. Sensitivities to CLFVing  $\tau$  decays are typically reported in terms of branching ratios

$$\mathcal{B}(\tau \rightarrow \ell X) \equiv \frac{\Gamma(\tau \rightarrow \ell X)}{\Gamma(\tau)} \quad \text{where } \ell = e, \mu. \quad (1.83)$$

For example, current leading limits on  $\tau \rightarrow 3\ell$  have been set by the Belle II experiment (all limits are at the 90% CL):

$$\begin{aligned} \mathcal{B}(\tau^- \rightarrow e^-e^+e^-) &< 2.7 \times 10^{-8} & [130] \\ \mathcal{B}(\tau^- \rightarrow e^-\mu^+\mu^-) &< 2.7 \times 10^{-8} & [130] \\ \mathcal{B}(\tau^- \rightarrow e^+\mu^-\mu^-) &< 1.7 \times 10^{-8} & [130] \\ \mathcal{B}(\tau^- \rightarrow e^-\mu^-e^+) &< 1.8 \times 10^{-8} & [130] \\ \mathcal{B}(\tau^- \rightarrow e^-\mu^+e^-) &< 1.5 \times 10^{-8} & [130] \\ \mathcal{B}(\tau^- \rightarrow \mu^-\mu^+\mu^-) &< 1.9 \times 10^{-8} & [131]. \end{aligned} \quad (1.84)$$

A preliminary sensitivity analysis of the  $\tau \rightarrow 5\mu$  has also been conducted in the context of the LHCb experiment with sensitivity estimated to be  $\mathcal{B}(\tau^- \rightarrow \mu^-\mu^+\mu^-\mu^+) < 4.2 \times 10^{-8}$ . Belle-II has also performed a search for  $\tau \rightarrow \ell\phi$  [25, 132] and place a  $m_\phi$ -dependent 90% CL upper

limit on the branching fraction. Finally, BaBar has also placed bounds on  $\tau \rightarrow \ell\gamma$  finding  $\mathcal{B}(\tau^\pm \rightarrow e^\pm\gamma) < 3.3 \times 10^{-8}$  and  $\tau^\pm \rightarrow \mu^\pm\gamma < 4.4 \times 10^{-8}$  [133].

As rare muon decay experiments such as MEG, Mu3e, and Mu2e will be the main focus for the phenomenological studies in the rest of part I, below we summarize the generic experimental setups.

### 1.5.3 MEG ( $\mu \rightarrow e\gamma$ )

The MEG experiment (and successor MEG-II), based at the Paul Scherrer Institute (PSI), utilizes a continuous anti-muon,  $\mu^+$ , beam incident on a layered polyethylene-polyester film stopping target to search for the CLFVing decay  $\mu^+ \rightarrow e^+\gamma$  [123, 124, 134]. Once stopped, the anti-muon either decays via the SM Michel decay,  $\mu^+ \rightarrow e^+\nu\bar{\nu}$ , or via the CLFV decay of interest,  $\mu^+ \rightarrow e^+\gamma$ . The latter produces a mono-energetic positron and photon, each with energy

$$E_{e^+} = E_\gamma = m_\mu/2 \approx 52.8 \text{ MeV}, \quad (1.85)$$

emitted back-to-back in the muon rest frame. These kinematic features form the backbone of MEG's signal identification strategy.

The primary backgrounds in MEG originate from 1. radiative muon decays with internal conversion,  $\mu^+ \rightarrow e^+\nu_e\bar{\nu}_\mu\gamma$ , where the neutrinos carry away little energy and the positron-photon pair can mimic the CLFV signature, and 2. accidental coincidences between a Michel positron and a photon from unrelated processes (e.g., bremsstrahlung or positron annihilation-in-flight), both of which are significant due to the continuous high-rate beam environment. The accidental background rate scales quadratically with the instantaneous muon rate and ultimately dominates the sensitivity at high intensities.

Anti-muon production is facilitated by the general-purpose high intensity proton accelerator at PSI running in the  $\pi E5$  channel. Protons incident on the production Target E (consisting of a rotating graphite wheel) produce stopped surface pions that can subsequently decay to anti-muons that are captured, collimated, and directed to the stopping target [135].

The MEG detector is composed of several highly optimized subsystems designed to precisely reconstruct the positron and photon. Positrons are tracked using a set of low-mass drift chambers immersed in a gradient magnetic field ranging from 1.27 T to 0.49 T (in the radial direction), produced by a superconducting COBRA (COnstant Bending RAdius) magnet. This geometry ensures that positrons of a given momentum follow trajectories of constant projected bending radius, independent of the emission angle, allowing for efficient tracking over a wide angular acceptance.

Photons are detected in a large C-shaped liquid xenon (LXe) calorimeter that wraps around one side of the stopping target, covering a large solid angle in the photon emission direction

but not fully enclosing the target. The calorimeter measures the energy, timing, and conversion point of incident photons via scintillation light read out by photomultiplier tubes (in MEG) or silicon photomultipliers (in MEG II). The combined positron and photon timing resolution is  $\sim 100$  ps, with spatial resolutions on the order of a few mm and energy resolution at the few percent level, sufficient to reject the vast majority of background events.

A dedicated timing counter, located outside the tracking volume, provides precise timing information for positrons and enables suppression of accidental backgrounds through time coincidence requirements. Additional background reduction is achieved via fiducial cuts, track quality cuts, and requirements on the relative directions and energies of the positron and photon.

The experiment operated at a continuous muon stopping rate of  $\sim 3 \times 10^7$  Hz and was able to set the most stringent limit on  $\mu^+ \rightarrow e^+\gamma$  to date,  $\mathcal{B}(\mu^+ \rightarrow e^+\gamma) < 4.2 \times 10^{-13}$  at 90% CL [123]. Its upgrade, MEG II, aims to improve sensitivity by an order of magnitude through a combination of increased beam intensity, improved detector granularity, and enhanced resolution in all subsystems [124].

#### 1.5.4 Mu3e ( $\mu \rightarrow 3e$ )

The Mu3e experiment [122], also based at PSI (right next to MEG), utilizes the same continuous anti-muon beam but now incident on a hollow double cone aluminum target to stop muons (at a rate of  $\sim 2.5 \times 10^7$  Hz) and record there decay products. The experiment is specifically designed to search for the approximately SM forbidden,  $\mu^+ \rightarrow e^+e^-e^+$  channel. Because the muons decay at rest, the smoking gun signature is the reconstruction of a  $e^+e^-e^+$  system whose spatial components of momenta sum to zero and whose energies sum to the mass of the muon,  $m_\mu$

$$\left| \sum_i p_i \right| = m_\mu, \quad i = e_1^+, e^-, e_2^+. \quad (1.86)$$

The two main sources of background stem from 1. the possibility of mutually exclusive tracks, i.e. many independent Michel decays  $\mu \rightarrow e\nu\bar{\nu}$ , in the detector satisfying the signature in eq. (1.86) i.e. combinatorial background and 2. radiative muon decays,  $\mu \rightarrow e\nu\bar{\nu}(\gamma \rightarrow ee)$ , where energy-loss from the radiated neutrinos is small and the photon converts internally (within the target) to an electron-positron pair. Backgrounds from Bhabha pair production in the target and detector also contribute a large number of low energy electrons which can pair with Michel electrons to fake a 3e signal – these can largely be mitigated by a cut on electron-positron pair invariant mass. Backgrounds stemming from the SM ‘super-Michel’ decay  $\mu \rightarrow 3e2\nu$  can be mitigated by cuts on missing energy. In principle pion contaminants from the beam can also mimic the signal via the  $\pi \rightarrow eeee\nu$  and  $\pi \rightarrow \mu\nu(\gamma \rightarrow ee)$  channels, however low levels of pion contamination and small branching fractions render these background negligible.

The primary active layers surrounding the double cone target are modeled as four thin cylinders centered around the double-cone target. In addition to these layers, Mu3e plans to install recurler components, extending the outermost cylinders up and downstream of the target, thereby increasing the probability of detecting tracks that curl back at large distances from the stopping target. The inner and outer trackers as well as the double-cone stopping target are immersed in a uniform 1 T magnetic field aligned with the beam axis. Timing information is provided by two complementary subsystems: a scintillating fiber (SciFi) detector wrapped around the central pixel layers, and a scintillating tile detector integrated into the recurler components. Together, they aim to achieve a time resolution of  $\sim 100$  ps per track, sufficient to disentangle pile-up and suppress combinatorial backgrounds. Importantly for the phenomenological studies in part I, charged particles exiting the double-cone stopping target must have a transverse momentum of at least  $\approx 10 - 12$  MeV to traverse all central detector pixel layers and be reconstructed with the standard track-finding algorithms.

### 1.5.5 Mu2e, COMET ( $\mu N \rightarrow eN$ )

The Mu2e experiment [129, 136, 137], based at Fermilab, utilizes a pulse muon,  $\mu^-$ , beam incident on thin aluminum foil targets to stop (at a rate of  $\sim 1.5 \times 10^{10}$  Hz) and capture individual muons into atomic orbits to form muonic atoms. The experiment is designed to detect the CLFVing direct conversion of the muon in orbit to an electron. Once securely captured by a nucleus, the muon quickly ( $\sim 10^{-13}$  seconds) cascades down to the  $1s$  atomic orbital via Auger and x-ray emissions. In the  $1s$  ground state, the muon can either 1. decay in orbit (via a Michel decay  $\mu \rightarrow e\bar{\nu}_e\nu_\mu$ ), 2. be captured by the nucleus ( $\mu^- p \rightarrow n\nu_\mu$ ), or 3. convert into an electron. If the muon is converted, the outgoing electron is mono-energetic with energy

$$E_{\mu \rightarrow e}(N) = m_\mu - E_b(N) - \frac{E^2}{2m_N} \quad (1.87)$$

where  $m_\mu$  is the muon mass,  $E_b$  is the muonic binding energy, and the last term describes the energy loss from nuclear recoil<sup>9</sup>. Because the electron energy is roughly equivalent to the muon mass, it resides well above the end of the Michel spectrum (52.8 MeV) and thus provides a distinct signal within the detector. Reducing the background for this mono-energetic electron spectrum drives many of the design decisions of the Mu2e detector. The principle backgrounds considered by Mu2e are muon decays-in-orbit, radiative muon capture ( $\mu^- Al \rightarrow \nu Mg(\gamma \rightarrow e^+ e^-)$ ), delayed processes due to slowly spiraling particles from the beam line, prompt processes occurring nearly synchronously with the arrival of the a particle at the stopping target i.e. radiative pion capture ( $\pi^- N \rightarrow N^*(\gamma \rightarrow e^+ e^-)$ ), high energy electrons and muons from

---

<sup>9</sup>For example, in aluminum (the chosen target material of Mu2e) the conversion energy is  $E_{\mu \rightarrow e}(Al) \approx 104.97$  MeV.

cosmic rays, and accidental backgrounds from track reconstruction errors induced by additional activity in the detector.

The experiment consists of three major portions distinguished and categorized efficiently by the names of the three solenoids used in the experiment, namely, the production, transport, and detection solenoids. The production portion of the experiment involves the injection of accelerated protons from the Fermilab delivery ring that are incident, at an angle and in the opposite direction of the production solenoid, on a production target of aluminum stabilized NbTi immersed in a graded magnetic field (4.6 T to 2.5 T). The production target produces pions and muons that are then fed, via the graded magnetic field, into the transport solenoid. Transport is facilitated by an S-shaped superconducting solenoid to efficiently transport low energy muons towards the detector. The detector contains an aluminum stopping target (consisting of 34, 100  $\mu\text{m}$  thick aluminum sheets with 50 mm of separation between each sheet) that is also immersed in a graded magnetic field, decreasing from 2 T to 1 T along the direction of the beamline. The graded field plays an important role both as a ‘filter’ that reduces potential signal contamination (from Michel decay electrons and beam-related backgrounds) and also as a reflector of potential signal electrons traveling in the opposite direction of the tracker/calorimeter that effectively doubles the geometric acceptance of the detector. The tracker and calorimeter are both immersed in a uniform magnetic field of 1T and surround a central region with no instrumentation due to the absence of signal electrons in this region, ensured by the upstream graded magnetic field. Mu2e utilizes a number of background mitigation strategies that allow the experiment to run with approximately zero SM-background. The most relevant for the phenomenological studies in the rest of part I being that 1. electrons from the stopping target with transverse momenta  $< 90$  MeV do not reach the tracker and 2. all tracks must have a momentum  $p$  within the range  $103.75 \text{ MeV} < p < 105.0 \text{ MeV}$  to be accepted as signal.

The rest of part I will be organized as follows: in chapter 2 we consider the SM  $\mu \rightarrow eeeee\nu\bar{\nu}$  decay as well as new physics contributions to the  $\mu \rightarrow eeeee$  in the context of the Mu3e experiment, in chapter 3 we describe an effective theory tower for describing  $\mu \rightarrow e$  conversion rates in the field of nuclei relevant for experiments like Mu2e and COMET, in chapter 4 we consider exotic baryon-number violating muon capture in the context of Mu2e, and finally, in chapter 5 we consider time-dependent signatures induced by ultralight dark matter with flavor violating couplings.

# Chapter 2

## New physics in multi-electron muon decays

**Preface:** This chapter is based on the published work in [2] with Matheus, Maxim, and Jure. The Mu3e experiment described in section 1.5.4 is expected to collect a total of  $\approx 10^{15}$  stopped muon over its running time. The main idea of the project was to understand if there were any other decay modes with branching ratios  $> 10^{-15}$  that Mu3e could be sensitive to. It turns out that with these statistics you can expect to see  $\mathcal{O}(100s)$  of the (never-before-observed)  $\mu \rightarrow 5e2\nu$  SM process. Subsequently, new physics models producing the SM-forbidden  $\mu \rightarrow 5e$  could produce an excess of events on top of this background – we estimate these rates and report the new physics reach for the  $5e$  channel at Mu3e.

### 2.1 Standard model decays

The enormous statistics expected to be collected by the upcoming muon experiments will enable the study of tiny radiative muon decay modes. These decay channels have important implications in their own right. Apart from testing QED at high orders in  $\alpha$ , they can also be important search channels for certain dark sector models. In what follows, we discuss the muon decay to five tracks with missing energy, i.e., muon decays with double internal photon conversions.

We estimate the branching ratios for the SM  $\mu \rightarrow 3e\bar{\nu}\nu$  (fig. 2.1 left) and  $\mu \rightarrow 5e\bar{\nu}\nu$  (fig. 2.1 right) decays using MADGRAPH5\_AMC@NLO [138] to leading order in  $G_F$  and  $\alpha$ . We find

$$\mathcal{B}(\mu^+ \rightarrow e^+ e^+ e^- \bar{\nu}_\mu \nu_e) = (3.601 \pm 0.005) \times 10^{-5}, \quad (2.1)$$

$$\mathcal{B}(\mu^+ \rightarrow e^+ e^+ e^- e^+ e^- \bar{\nu}_\mu \nu_e) = (3.929 \pm 0.001) \times 10^{-10}, \quad (2.2)$$

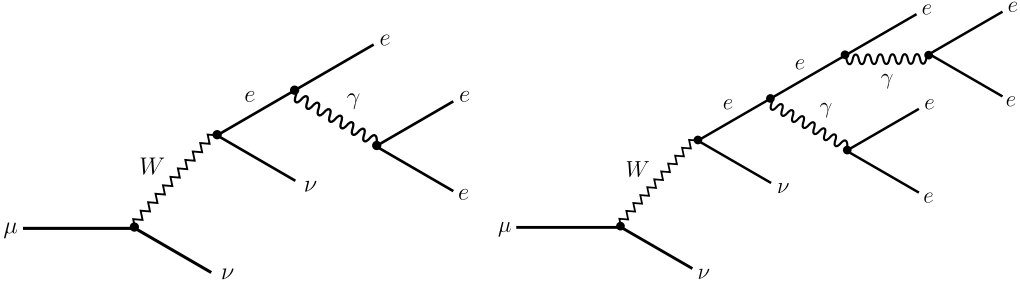


FIGURE 2.1: **Left:** Example of one contributing Feynman diagram for the SM ‘super’-Michel decay  $\mu \rightarrow eeee\nu\bar{\nu}$ . **Right:** Example of one contributing Feynman diagram for SM ‘ultra’-Michel decay  $\mu \rightarrow eeeee\nu\bar{\nu}$ .

where the quoted uncertainty is from the MC only. The electron mass is included to avoid infrared divergences, but the uncertainties in the masses and couplings are not taken into account.<sup>1</sup> The  $\mu^+ \rightarrow e^+e^+e^-\bar{\nu}_\mu\nu_e$  process has already been calculated previously [140–142] since it is an important background to the main physics goal of the Mu3e experiment, the search for neutrinoless  $\mu^+ \rightarrow e^+e^+e^-$  decays. It is also of interest in connection with the  $\mu^+ \rightarrow \bar{\nu}_\mu\nu_e e^+\gamma_d \rightarrow \bar{\nu}_\mu\nu_e e^+e^+e^-$  dark sector mode, where an additional vector particle (*e.g.* the dark photon) is radiated in the decay process [143]. The analysis of sensitivity to  $\gamma_d$  has been performed by the Mu3e collaboration [21]. In addition, it is expected that the SM rate, eq. (2.1), previously studied in [144], will be observed with enormous statistics.

The SM 5e mode, eq. (2.2), has not been calculated/discussed before, to the best of our knowledge. The rate is very small, but perhaps not hopeless with the statistics planned to be collected by Mu3e. The  $\mu \rightarrow 5e2\nu$  decay occurs at order  $\Gamma \propto \mathcal{O}(G_F^2\alpha^4)$ , where  $G_F$  is the Fermi constant. The corresponding partial decay width,  $\Gamma \sim \mathcal{O}(10^{-19} \text{ eV})$ , would be the smallest measured decay rate involving the second and third-generation particles.

To be observable, the five charged tracks should have sufficient energy to escape the Mu3e target and fall within the detector acceptance. A simple estimate of the observable branching ratio can be found by requiring the transverse momentum of each electron and positron to be larger than the experimental threshold,  $p_{T,\text{th}} \sim 10 \text{ MeV}$ . We find

$$\mathcal{B}\left(\mu^+ \rightarrow e^+e^+e^-e^+\bar{\nu}_\mu\nu_e \mid \text{all } p_{e^\pm}^{\text{T,true}} > 10 \text{ MeV}\right) = (1.4 \pm 0.1) \times 10^{-14}, \quad (2.3)$$

where  $p_{e^\pm}^{\text{T,true}}$  is the true transverse momentum of individual electrons and positrons in the muon rest frame. Here “true” refers to the value of the quantity before any experimental smearing is applied, and should be contrasted with the “reconstructed” quantities on which we apply cuts in section 2.4. For completeness, we also quote the branching ratio for a threshold of 10 MeV

---

<sup>1</sup>The SM input parameters are  $m_\mu = 105.658 \text{ MeV}$ ,  $m_e = 510.999 \text{ keV}$ ,  $\alpha^{-1}(\mu = 0) = 137.036$ ,  $G_F = 1.16638 \times 10^{-5} \text{ GeV}^{-2}$ , and  $\Gamma_\mu = 2.99598 \times 10^{-16} \text{ MeV}$  [139].

on the true *total* momentum,

$$\mathcal{B}(\mu^+ \rightarrow e^+ e^+ e^- e^- \bar{\nu}_\mu \nu_e | \text{all } p_{e^\pm}^{\text{true}} > 10 \text{ MeV}) = (9.5 \pm 0.2) \times 10^{-13}, \quad (2.4)$$

where  $p_{e^\pm}^{\text{true}}$  is the true momentum of individual electrons and positrons in the muon rest frame. With the transverse-momentum cut, the above indicates that Mu3e should observe about 35 events in 300 days of continuous running at a rate of  $10^8$  muon stops per second, *i.e.*, about  $2.5 \times 10^{15}$  muon decays. We revisit these estimates in Section 2.4.3 with our simulation, showing that requiring five observable tracks leads to an even smaller branching ratio.

Another relevant regime of the SM rate is when the neutrinos carry a small amount of energy. Such phase-space configurations are highly disfavored in this decay since internal photon conversion tends to produce soft  $e^+ e^-$  pairs. Nevertheless, it can represent a background to neutrinoless decay modes, as discussed in more detail in section 2.4.1. The rate is a steeply falling function of the missing energy, so we quote two cases,

$$\mathcal{B}(\mu^+ \rightarrow e^+ e^+ e^- e^- \bar{\nu}_\mu \nu_e | E_{\text{missing}}^{\text{true}} < 20 \text{ MeV}) = (8.9 \pm 0.3) \times 10^{-14}, \quad (2.5)$$

$$\mathcal{B}(\mu^+ \rightarrow e^+ e^+ e^- e^- \bar{\nu}_\mu \nu_e | E_{\text{missing}}^{\text{true}} < 10 \text{ MeV}) = (1.1 \pm 0.2) \times 10^{-15}, \quad (2.6)$$

where  $E_{\text{missing}}^{\text{true}}$  is the true energy of the two neutrinos in the muon rest frame. As we will see, this rate, even after accounting for detector resolution effects, is far too low and does not constitute a worrisome background to neutrinoless exotic decays.

Finally, we note that muon decays to dark sector particles can also induce  $5e2\nu$  final states. For example, muon-specific forces [145–148] could induce the  $\mu^+ \rightarrow \bar{\nu}_\mu \nu_e e^+ S$  decay, where the dark scalar can then decay to four tracks,  $S \rightarrow 2e^+ 2e^-$ , through a cascade of decays involving other dark particles as intermediate states. If the decay/fragmentation of  $S$  is fast, such a channel will not be picked up by the proposed missing momentum/missing energy searches [149, 150]. While a more detailed analysis of such decay modes lies outside the scope of the present manuscript, we emphasize that the decay rate, eq. (2.2), should be added to the list of physics goals pursued by the Mu3e experiment. For the remainder of the manuscript, we focus on the experimentally cleaner decay mode, the neutrinoless  $\mu \rightarrow 5e$  decay, which can be induced in dark sector scenarios.

## 2.2 Exotic muon decay

Previous dark sector searches at muon facilities focused on a single visible or invisible resonance. The TWIST and PIENU results provide the best limits on two-body decays to invisible particles, constraining  $\mathcal{B}(\mu^+ \rightarrow e^+(X \rightarrow \text{inv})) < \mathcal{O}(10^{-5})$  [19, 151]. The MEG experiment searched for  $\mu^+ \rightarrow e^+(X \rightarrow \gamma\gamma)$ , providing the best limits on this branching ratio at the level of  $\mathcal{O}(10^{-11})$  for

$20 < m_X < 45$  MeV [134], much above the SM background from double radiative muon decays,  $\mathcal{B}(\mu^+ \rightarrow \bar{\nu}_\mu \nu_e e^+ \gamma\gamma; E_{\text{missing}} < 10 \text{ MeV}) = 1.2 \times 10^{-14}$  [142], where the missing energy  $E_{\text{missing}}$  is required to be small. At SINDRUM, constraints on  $\mathcal{B}(\mu^+ \rightarrow e^+(X \rightarrow e^+e^-)) < \mathcal{O}(10^{-12})$  were placed, depending on the value of  $m_X$  [152]. The Mu3e experiment will be well positioned to improve on the latter. Below, we extend this list of phenomenologically interesting dark sector signatures by considering a cascade decay into the dark sector,  $\mu^+ \rightarrow e^+(h_d \rightarrow \gamma_d \gamma_d \rightarrow 2(e^+e^-))$ .

### 2.2.1 A dark sector model

Our benchmark model consists of a higgsed dark abelian gauge group  $U(1)_d$  coupled to the SM through kinetic mixing between the dark photon and the ordinary photon and through lepton-flavor-violating dimension-five operators. That is, the Lagrangian of the model is given by  $\mathcal{L} = \mathcal{L}_{\text{SM}} + \mathcal{L}_{\text{DS}} + \mathcal{L}_{\text{LFV}}$ , where  $\mathcal{L}_{\text{SM}}$  is the SM Lagrangian and

$$\mathcal{L}_{\text{DS}} = (D_\mu \phi)^\dagger D^\mu \phi - \frac{1}{4} F_d^{\mu\nu} F_{d\mu\nu} - \frac{\varepsilon}{2} F_d^{\mu\nu} F_{\mu\nu} - \mu^2 (\phi^\dagger \phi) - \lambda (\phi^\dagger \phi)^2, \quad (2.7)$$

with  $F_d^{\mu\nu}$  the dark photon field strength tensor, while  $D^\mu \phi = (\partial^\mu - ig_d \gamma'_d \mu) \phi$ , and we set for simplicity the mixed quartic,  $\mathcal{L}_{\text{DS}} \supset \lambda' (\phi^\dagger \phi)(H^\dagger H)$  to zero. The dark scalar  $\phi$  develops a vev,  $\phi = (v_d + h_d)/\sqrt{2}$ , giving the dark photon a mass  $m_{\gamma_d} = g_d v_d$ . After the usual field redefinitions [153], we end up with the massive physical dark photon,  $\gamma_d$ , the massless photon  $\gamma$ , and the light scalar  $h_d$ .

The LFV interactions are mediated by the dimension-five operators

$$\mathcal{L}_{\text{LFV}} = -\frac{C_{ij}}{\Lambda} \phi (\bar{L}_i H) \ell_j + \text{h.c.}, \quad (2.8)$$

where  $\Lambda$  is the cut-off of the effective theory,  $L_i$  ( $\ell_i$ ) are the left-handed (right-handed) SM lepton doublets (singlets), and the summation over generation indices  $i, j = 1, 2, 3$  is understood. After  $\phi$  and  $H$  obtain the vevs, the masses of the charged leptons are given by the sum of the SM Yukawas

$$\mathcal{L}_{\text{SM}} \supset -\lambda_{ij} (\bar{L}_i H) \ell_j + \text{h.c.}, \quad (2.9)$$

and the dimension-five terms in eq. (2.8), giving

$$\text{diag}(m_\ell) = V_L \left( \lambda + C \frac{v_d}{\sqrt{2}\Lambda} \right) V_R^\dagger \frac{v}{\sqrt{2}}, \quad (2.10)$$

where  $V_{L,R}$  are the unitary matrices that diagonalize the mass matrix. Note that the same unitary transformation also diagonalizes the Higgs couplings to leptons. After mass diagonalization, the interaction Lagrangian in the physical basis is given by

$$\mathcal{L} \supset -m_\ell \bar{\ell}_L \ell_R \left( 1 + \frac{h}{v} \right) - y_{ij} \bar{\ell}_L \ell_R h_d \left( 1 + \frac{h}{v} \right) + \text{h.c.}, \quad (2.11)$$

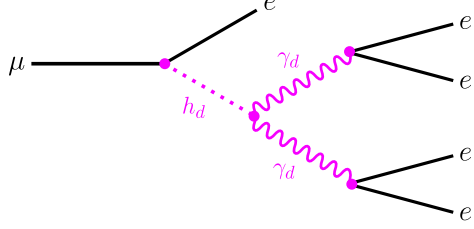


FIGURE 2.2: The leading neutrinoless  $\mu \rightarrow eeeee$  contribution in the higgsed  $U(1)_d$  model presented in section 2.2.1.

where  $y = V_L C V_R^\dagger v / (\sqrt{2} \Lambda)$ .

### 2.2.2 Signal rate: $\mu \rightarrow 5e$

The dimension-five flavor-violating couplings eq. (2.8) in the higgsed dark abelian  $U(1)_d$  extension of the SM will lead to the  $\ell_i \rightarrow \ell_j h_d$  decays if these are kinematically allowed. In this manuscript we focus on the  $\mu \rightarrow e h_d$  transition, where the dark scalar  $h_d$  further decays promptly into two dark photons, each of which decays to an  $e^+ e^-$  pair,  $h_d \rightarrow (\gamma_d \rightarrow e^+ e^-)(\gamma_d \rightarrow e^+ e^-)$ , as shown in fig. 2.2. This  $\mu \rightarrow 5e$  decay can well be the leading signature of such a higgsed dark  $U(1)_d$ , if the dark gauge coupling is large enough such that the  $h_d \rightarrow \gamma_d \gamma_d$  decay dominates. The  $\mu \rightarrow 5e$  cascade decay is kinematically allowed for  $m_{h_d} < m_\mu - m_e$  and  $m_{h_d} > 2m_{\gamma_d}$ .

The branching ratio for the  $\mu \rightarrow e h_d$  decay is given by

$$\mathcal{B}(\mu \rightarrow e h_d) = \frac{1}{\Gamma_\mu} \left[ (|y_{\mu e}|^2 + |y_{e \mu}|^2) [1 + r_e^2 - r_{h_d}^2] + 4 \text{Re}(y_{\mu e} y_{e \mu}) r_e \right] \frac{m_\mu}{32\pi} \lambda^{1/2}(1, r_e^2, r_{h_d}^2), \quad (2.12)$$

where  $\Gamma_\mu$  is the muon decay width,  $\lambda(x, y, z)$  is the Källen function, while  $r_{e, h_d} = m_{e, h_d} / m_\mu$ . Assuming  $\mathcal{B}(h_d \rightarrow \gamma_d \gamma_d) \approx \mathcal{B}(\gamma_d \rightarrow e^+ e^-) \approx 1$ , and neglecting the electron mass, the  $\mu \rightarrow 5e$  branching ratio is then

$$\mathcal{B}(\mu^+ \rightarrow e^+ h_d \rightarrow e^+ 2(e^+ e^-)) = 3.5 \times 10^{-3} \left( \frac{\sqrt{|y_{\mu e}|^2 + |y_{e \mu}|^2}}{10^{-9}} \right)^2 (1 - r_{h_d}^2)^2. \quad (2.13)$$

As we will discuss, the above numerical example for  $y_{\mu e, e \mu}$  is safely below the current experimental bounds discussed in section 2.3.

To a good approximation, the dark scalar decay is prompt as long as the dark coupling is sizeable. The partial decay width is given by [154],

$$\Gamma_{h_d \rightarrow 2\gamma_d} = \frac{\alpha_d}{8} \frac{m_{h_d}^3}{m_{\gamma_d}^2} f(m_{\gamma_d} / m_{h_d}), \quad (2.14)$$

where  $f(r) = (1 - 4r^2 + 12r^4)\sqrt{1 - 4r^2}$ . In the limit of  $h_d \rightarrow \gamma_d \gamma_d$  dominating the decay width, this then also gives the lifetime of the dark Higgs,

$$c\tau_{h_d} = 270 \text{ fm} \times \left(\frac{\alpha}{\alpha_D}\right) \left(\frac{90 \text{ MeV}}{m_{h_d}}\right) \left(\frac{3}{m_{h_d}/m_{\gamma_d}}\right)^2 \frac{1}{f(m_{\gamma_d}/m_{h_d})}. \quad (2.15)$$

On the other hand, the dark photon decays back to the SM particles through the kinetic mixing parameter,  $\varepsilon \lesssim 10^{-3}$ , and, therefore, may have an observable displacement within the experiment. In the mass range of interest,  $2m_e < m_{\gamma_d} \lesssim (m_\mu - m_e)/2$ , the dark photon always decays back to electron-positron pairs,  $\gamma_d \rightarrow e^+e^-$ , with the decay width [154]

$$\Gamma_{\gamma_d \rightarrow e^+e^-} = \frac{\alpha \varepsilon^2 m_{\gamma_d}}{3} (1 - 4r_e^2)^{1/2} (1 + 2r_e^2), \quad (2.16)$$

giving the  $\gamma_d$  lifetime of

$$c\tau_{\gamma_d}^0 = 0.27 \text{ mm} \times \left(\frac{10^{-4}}{\varepsilon}\right)^2 \left(\frac{30 \text{ MeV}}{m_{\gamma_d}}\right) \frac{1}{g(m_e/m_{\gamma_d})}, \quad (2.17)$$

where  $g(r) = (1 + 2r^2)\sqrt{1 - 4r^2}$ . Most dark photons would still decay within the stopping target for the above parameters, leading to no significant modification of the  $\mu^+ \rightarrow 3e^+ 2e^-$  signals. For smaller kinetic mixing parameters  $\varepsilon \ll 10^{-4}$ , other constraints from beam-dump and fixed-target experiments exclude the mass range of interest [155]. Therefore, in our discussion, we will always assume that the dark photons decay promptly inside the Mu3e target.

## 2.3 Constraints

The  $y_{\mu e, e\mu}$  LFV couplings of the dark Higgs are constrained by a few other probes, with the most relevant constraints reviewed below. However, these bounds are not very stringent and do not significantly limit the possible strength of the  $\mu \rightarrow 5e$  signal.

**Muon lifetime:** Simply requiring that the  $\mu \rightarrow 5e$  decay does not saturate the muon decay width ( $\Gamma_{\mu \rightarrow e h_d} < \Gamma_\mu$ ), gives  $\sqrt{|y_{\mu e}|^2 + |y_{e\mu}|^2} < 1.7 \times 10^{-8}$ , which by itself is already quite constraining. Note that a factor of  $\mathcal{O}(30)$  tighter bound on  $(|y_{\mu e}|^2 + |y_{e\mu}|^2)^{1/2}$  can be extracted from the consistency of the Fermi constant extracted from the muon lifetime measurement confronted with other determinations of  $G_F$  [78, 156].

**Neutrinoless muon decays:** An experiment at Lawrence Berkeley Laboratory performed several searches for rare muon decays, including the channel  $\mu^+ \rightarrow e^+ \gamma\gamma$  [15]. The detector constituted a cylindrical NaI crystal that surrounded the muon target. The constraint was based on an inclusive requirement that the entire energy collected in the NaI crystal reconstruct

the muon mass. This results in a limit on neutrinoless muon decays to any number of electrons and photons, from which we conclude that  $\mathcal{B}(\mu^+ \rightarrow 3e^+ 2e^-) < 4 \times 10^{-6}$ . Other searches for the two-photon mode were performed at an experiment in TRIUMF [157], at the Crystal Box detector at Los Alamos [158], and more recently at the MEG [134] experiment at PSI. Neither of these limits directly applies to the  $5e$  mode due to the ability of the detectors to differentiate between charged and neutral particles. A similar argument applies to recasts of  $\mu \rightarrow e\gamma$  searches [159].

In principle, the annihilation of muonium  $\mu^+ e^- \rightarrow \gamma_d \gamma_d \rightarrow 2e^+ 2e^-$  can also provide a limit on our model, though the rate is suppressed by the wave function overlap. We are not aware of any searches for this channel. The analogous  $\mu^+ e^- \rightarrow \gamma\gamma$  decay has been constrained in Ref. [160], but their limit does not directly apply to the final state with charged particles.

**Higgs decays:** The Higgs Yukawas are diagonal in the mass basis, (2.11), so that the  $h \rightarrow \mu e$  decays are forbidden. Flavor-violating Higgs decays are possible, if they are accompanied by an emission of a dark Higgs,  $h \rightarrow \mu e h_d$ . Such three-body decays will smear the  $\mu e$  invariant mass distribution and thus a reduced signal in the  $h \rightarrow \mu e$  searches at the LHC. While the full recasting of the bounds is beyond the scope of this paper, we can get a rough estimate of the exclusion by assuming that the effect is similar in size to what was found for the  $h \rightarrow \tau \mu \phi$  decays, with  $\phi$  an invisible particle, in Ref. [161]. Under this approximation, the bound  $\mathcal{B}(h \rightarrow \mu e) < 4.4 \times 10^{-5}$  [162] (see also [163]) would imply  $(|y_{\mu e}|^2 + |y_{e\mu}|^2)^{1/2} \lesssim 0.03$ .

In principle, there is also sensitivity to  $h_d - \mu\mu$  coupling,  $y_{\mu\mu}$ , from the measured  $h \rightarrow \mu\mu$  branching ratio,  $\mathcal{B}(h \rightarrow \mu\mu) = (2.6 \pm 1.3) \times 10^{-4}$  [164]. Some of the  $h \rightarrow \mu\mu h_d$  bremsstrahlung decays would pass experimental cuts and be part of the  $h \rightarrow \mu\mu$  signal. Taking as a rough estimate that the efficiency of the experimental cuts is similar as for  $h \rightarrow \tau \mu \phi$  [161], this would then lead to a very weak bound,  $y_{\mu\mu} \lesssim \mathcal{O}(0.1)$ .

$\mu \rightarrow e\gamma$ : The LFV Yukawa couplings of  $h_d$  in eq. (2.11) mediate  $\mu \rightarrow e\gamma$  decays at the one-loop level via the effective Lagrangian [165]

$$\mathcal{L}_\gamma = \frac{em_\mu}{8\pi^2} (c_L \bar{e} \sigma^{\alpha\beta} P_L \mu + c_R \bar{e} \sigma^{\alpha\beta} P_R \mu) F_{\alpha\beta} + \text{h.c.}, \quad (2.18)$$

where  $c_{L,R}$  are dimensionful Wilson coefficients. The rate for  $\mu \rightarrow e\gamma$  is given by

$$\Gamma_{\mu \rightarrow e\gamma} = \frac{\alpha m_\mu^5}{64\pi^4} (|c_L|^2 + |c_R|^2), \quad (2.19)$$

where, assuming  $y_{\mu\mu} \gg y_{ee}$  for simplicity, and  $m_e \ll m_{h_d} \ll m_\mu$  the Wilson coefficient  $c_L$  can be expressed as

$$c_L \approx \frac{1}{8m_\mu^2} y_{\mu e}^* \left[ \text{Re}(y_{\mu\mu}) \left( -5 + \frac{2\pi^2}{3} \right) - i\text{Im}(y_{\mu\mu}) \right] \quad (2.20)$$

and  $c_R$  given equivalently with the substitution  $y_{\mu e}^* \rightarrow y_{e\mu}$ . Using the final limits from MEG [123] constraining  $\mathcal{B}(\mu \rightarrow e\gamma) < 4.2 \times 10^{-13}$  and assuming  $\text{Im}(y_{\mu\mu}) = 0$ , we obtain

$$y_{\mu\mu} \sqrt{|y_{\mu e}|^2 + |y_{e\mu}|^2} < 5.1 \times 10^{-12}. \quad (2.21)$$

$\mu \rightarrow 3e$ : The decay  $\mu \rightarrow eh_d$ , followed by  $h_d \rightarrow e^+e^-$  decay, gives a constraint on a combination of  $y_{\mu e}$  and  $y_{ee}$  couplings. We are interested in the regime, where  $h_d \rightarrow \gamma_d\gamma_d$  dominates so that only a small fraction of  $h_d$  decays through the  $h_d \rightarrow e^+e^-$  channel. The  $h_d \rightarrow e^+e^-$  branching ratio, in the regime where  $\mathcal{B}(h_d \rightarrow \gamma_d\gamma_d) \approx 1$ , is

$$\mathcal{B}(h_d \rightarrow e^+e^-) \simeq \frac{4|y_{ee}|^2 m_{\gamma_d}^2}{g_d^2 m_{h_d}^2} \frac{1}{f(m_{\gamma_d}/m_{h_d})}, \quad (2.22)$$

where for simplicity we took the limit  $m_e \ll m_{h_d}$ . The bound  $\mathcal{B}(\mu \rightarrow 3e) < 1.0 \times 10^{-12}$  then translates to

$$(|y_{\mu e}|^2 + |y_{e\mu}|^2)^{1/2} < 5 \times 10^{-6} \times \left( \frac{10^{-9}}{|y_{ee}|} \right) \left( \frac{g_d}{0.1} \right) \left( \frac{m_{\gamma_d}}{5 \text{ MeV}} \right) \left( \frac{30 \text{ MeV}}{m_{h_d}} \right). \quad (2.23)$$

Note that this simple scaling of the bound is valid for  $m_{\gamma_d} \sim \mathcal{O}(m_{h_d})$  as long at  $|y_{ee}| \ll g_d$ .

## 2.4 Experimental reach

In this section, we address the experimental reach of Mu3e to the five-track channels. We start with a general discussion of the expected backgrounds to  $\mu^+ \rightarrow 3e^+ 2e^- 2\nu$  and  $\mu^+ \rightarrow 3e^+ 2e^-$  measurements at Mu3e in section 2.4.1. We leave a more detailed background rate estimate for future studies within the Mu3e collaboration. In the remainder of the section, we present our assumptions behind our sensitivity estimates. Section 2.4.2 describes our simplified numerical simulation of Mu3e. We then present the selection criterion and resulting efficiencies for both SM and new-physics decays in section 2.4.3. We then present a few future directions that can improve upon our sensitivity estimates in section 2.4.4.

### 2.4.1 Backgrounds

**Decays with missing energy:** Backgrounds from  $\mu^+ \rightarrow 3e^+ 2e^- 2\nu$  may be mitigated by exploring the different kinematics of the neutrinoless  $\mu^+ \rightarrow 3e^+ 2e^-$  decay. Of greatest significance is the cut on the reconstructed missing energy, or equivalently, on the reconstructed energy of the five-electron system. The left panel in fig. 2.5 shows the missing energy distribution of the signal and the background. The signal events are compatible with no missing energy within the momentum resolution of the detector. Using our simulation, we find that a cut on the missing

energy of 10 MeV can suppress the  $\mu^+ \rightarrow 3e^+ 2e^- 2\nu$  background down to the  $\mathcal{O}(10^{-15})$  level. This is compatible with the branching ratios in eqs. (2.5) and (2.6).

Due to the significant missing energy carried by neutrinos, most electron and positron tracks are too soft to be reconstructed as short or long tracks — they do not travel far enough in the transverse direction. As shown in the right panel in fig. 2.5, this is particularly true for the electron tracks, which are a product of internal photon conversion. While this hurts the sensitivity to the SM decays, it becomes an advantage in searches for the exotic decays.

**Accidental backgrounds:** Interactions of Michel decay positrons with the target and detector material are an important source of backgrounds to the  $\mu \rightarrow 3e$  signal [122], and therefore should be carefully estimated for the  $\mu \rightarrow 5e$  channel. For the  $3e$  channel, it was shown by the Mu3e collaboration that this background can be fully mitigated, *i.e.*, reduced to below 0.2 events per  $10^{15}$  muon decays using kinematics, timing, and position cuts. For the  $5e$  channel, such cuts are also expected to be important since the momenta of the five tracks also need to sum up to zero. The  $5e$  channel, however, has an advantage compared to the  $3e$  one: the  $5e$  event contains two negatively charged tracks in the event, which is much less common in the experiment. To take advantage of this feature, a good understanding of the charge misidentification capabilities of Mu3e will be crucial. However, even if/when positrons get misreconstructed as electrons, the kinematic, positional, and timing cuts remain available.

In what follows, we provide a naive and conservative estimate of the total number of accidental backgrounds per  $10^{15}$  muon decays, following a similar prescription to the one outlined in ref. [143]. We neglect Compton scattering and photon conversion within the target and detector material, which are subdominant compared to Bhabha scattering. The possible sources of accidental backgrounds are

1. A  $\mu \rightarrow 3e2\nu$  decay in combination with a proximal Michel decay, where the ejected positron immediately Bhabha scatters on an electron within the target material,

$$N_{\mu \rightarrow 3e2\nu + \text{Bhabha}} = N_\mu \times (R_\mu \delta t) \times P_p \times (\mathcal{B}_{\mu \rightarrow 3e2\nu} \mathcal{B}_{\mu \rightarrow 1e2\nu}) \times P_{\text{Bhabha}} \approx 10^3. \quad (2.24)$$

Alternatively, one could also consider a single Michel decay in combination with a  $\mu \rightarrow 3e2\nu$  decay, where the Bhabha scattering is initiated by one of the two positrons produced in  $\mu \rightarrow 3e2\nu$ . This brings the total rate to approximately  $3 \times 10^3$  events, before any kinematical cuts, and assuming that the positrons from  $\mu \rightarrow 3e2\nu$  can produce visible  $e^+e^-$  Bhabha pairs as often as the Michel positrons.

2. Three Michel decays where two of the three positrons have Bhabha scattered with electrons within the target material,

$$N_{3M + \text{Bhabha}} = \frac{1}{2} N_\mu \times (R_\mu \delta t)^2 \times P_p^2 \times (\mathcal{B}_{\mu \rightarrow 1e2\nu})^3 \times P_{\text{Bhabha}}^2 \approx 10^{-1}. \quad (2.25)$$

3. A Michel decay in combination with two radiative Michel decays, where the two photons convert into electron-positron pairs within the target, and the two positrons from these conversions remain undetected,

$$N_{3M_\gamma} = \frac{2}{3} N_\mu \times (R_\mu \delta t)^2 \times P_p^2 \times (\mathcal{B}_{\mu \rightarrow 1e2\nu} \mathcal{B}_{\mu \rightarrow 1e2\nu 1\gamma}^2) \times P_\gamma^2 \approx 10^{-3}. \quad (2.26)$$

4. Five Michel decays with two positrons misidentified as electrons,

$$N_{5M} = \frac{1}{12} N_\mu \times (R_\mu \delta t)^4 \times P_p^4 \times (\mathcal{B}_{\mu \rightarrow 1e2\nu})^5 \times P_{e^+ \rightarrow e^-}^2 \approx 10^{-4}. \quad (2.27)$$

Above, the total number of muons was assumed to be  $N_\mu = 10^{15}$ , with  $R_\mu = 10^8/\text{s}$  the stopped muon rate,  $\delta t = 2.5 \times 10^{-10} \text{ s}$  the average time resolution,  $P_p = 10^{-2}$  the vertex timing resolution suppression factor (taken as the quoted suppression power of the fiber detectors [122]),  $P_{e^+ \rightarrow e^-} = 0.45\%$  the charge misidentification probability,  $\mathcal{B}_{\mu \rightarrow 1e2\nu} \approx 1$ ,  $\mathcal{B}_{\mu \rightarrow 1e2\nu\gamma} \approx 0.014$  ( $E_\gamma > 10 \text{ MeV}$ ) [139],  $P_{\text{Bhabha}} \approx 10^{-4}$  is the conditional probability for an observable Bhabha scattered  $e^+e^-$  pair given a positron from within the target (from Tab. 22.2 of ref. [122]), while  $P_\gamma = 8 \times 10^{-4}$  is the assumed photon conversion probability within the target. Note that the above estimates hold in the limit  $R_\mu T \gg 1$  where  $T$  is the duration of the measurement (roughly  $\pi \times 10^7 \text{ s}$  for phase I of Mu3e to which also the above choices of parameters apply).

In addition to the coincident combination of Bhabha processes and radiative modes of muon decays, two electrons can also be observed when an electron produced in  $\mu^- \rightarrow 3e2\nu$  decays undergoes Møller scattering or initiates trident production in the material. Because the number of high-momentum electrons in the experiment is far smaller than that of positrons, we expect these channels to be subdominant to the background sources listed above.

In their  $3e$  sensitivity estimates, the Mu3e collaboration also included a cut on the lowest invariant pairwise  $e^+e^-$  mass in order to suppress Bhabha pair production backgrounds in the window from 5 MeV to 10 MeV. This will limit the sensitivity to new physics for dark photon masses within this range if such a cut is still necessary for the  $5e$  channel. While a full detector simulation, including material effects and vertex reconstruction, is needed in order to accurately assess the loss in sensitivity due to these backgrounds, we do expect the double coincidence in  $e^+e^-$  invariant masses to be a sufficiently strong discriminator such that one could efficiently search for new-physics events.

#### 2.4.2 Simulation

To study the sensitivity of Mu3e to muon decays with five tracks, we built a fast MC of the detector and simulate  $\mu^+$  decays using MADGRAPH5\_AMC@NLO for  $\mu^+ \rightarrow 3e^+ 2e^- 2\nu$  and the PHASESPACE [166] package for  $\mu^+ \rightarrow 2e^+ 1e^-$ . We simulate a total of 13 million events for the former and 1 million for the latter. The simulation distributes muons inside the target,

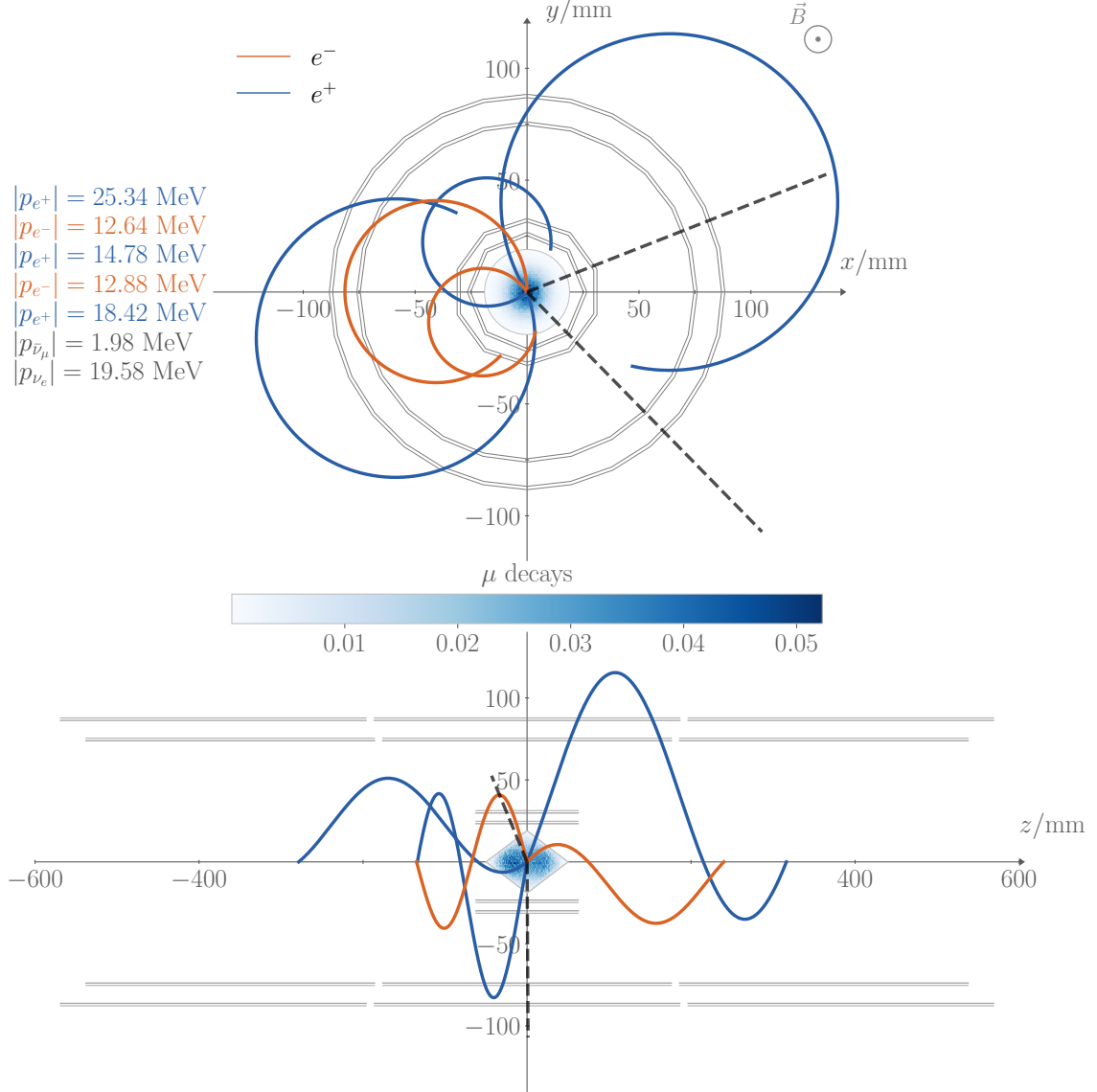


FIGURE 2.3: Transverse (top) and longitudinal (bottom) event displays showing an example of a simulated SM five-track  $\mu^+ \rightarrow 3e^+ 2e^- 2\nu$  decay event at Mu3e. The blue heatmap within the double-cone target of each panel represents the modeled  $x$ ,  $y$ , and  $z$  probability densities of muon decays within the double-cone target.

modeled as a hollow double-cone structure. The target's maximum radius is 19 mm, and its total length is 100 mm. The  $z$  position of the decays inside the target is sampled according to Fig. 6.3 of ref. [122] that shows the simulated stopping distribution along the  $z$ -direction of the double-cone target. The  $x$  and  $y$  positions are sampled according to the transverse beam profile modeled as a two-dimensional Gaussian with widths  $\sigma_x = 7.50$  mm and  $\sigma_y = 8.74$  mm. The probability density of muon decays inside the target is shown as a heatmap in the event displays in fig. 2.3.

Each electron and positron trajectory with the initial position  $(x_0, y_0, z_0)$  and momentum  $(p_x, p_y, p_z)$  is determined by the equations of motion

$$x(t) = x_0 + \frac{p_y}{Bq} \left\{ 1 - \cos \left( \frac{Bq}{m} t \right) + \frac{p_x}{p_y} \sin \left( \frac{Bq}{m} t \right) \right\}, \quad (2.28)$$

$$y(t) = y_0 + \frac{p_x}{Bq} \left\{ -1 + \cos \left( \frac{Bq}{m} t \right) + \frac{p_y}{p_x} \sin \left( \frac{Bq}{m} t \right) \right\} \quad (2.29)$$

$$z(t) = z_0 + \frac{p_z}{m} t, \quad (2.30)$$

where  $B$  is the magnitude of the magnetic field ( $B = 1.0$  T) directed along the beamline,  $q$  is the electric charge, and  $m$  is the particle mass. The particles follow a helical trajectory with radius  $R = p_T/B$ , where  $p_T \equiv ((p_x)^2 + (p_y)^2)^{1/2}$  is the total momentum in the  $x - y$  plane, transverse to the beam pipe. The trajectory length is determined by the point at which the particle exits the detector barrels in the  $z$  direction, defined as the end of the longest reculer cylinder. We neglect any particle losses inside the barrel. Having determined the trajectory in the  $x - y$  plane, we count the number of intersections between each track and the active components of the detector, each defining a hit. The primary active layers are modeled as four thin cylinders centered around the double-cone target. From the innermost to the outermost layers, the cylinders have radii of 23.3 mm, 29.8 mm, 73.9 mm, and 86.3 mm, and extents of 124.7 mm, 124.7 mm, 351.9 mm, and 372.6 mm. In addition to these layers, Mu3e plans to install reculer components, extending the outermost cylinders up and downstream of the target, thereby increasing the probability of detecting tracks that curl back at large values of  $z$ . We replicate the two outermost cylinders with a shifted  $z$  location to account for these. The gap between the end of the outermost detector and the reculer is assumed to be 20 mm.

The momentum resolution of the tracks depends on the number of hits for a given trajectory. Tracks with at least 4 hits constitute a short track, and the resolution is  $\sigma_p/p \sim 5\%$ . We smear them according to the resolution in Fig. 19.2 of ref. [122]. The resolution can be far better for long tracks, defined by tracks with 6 and 8 hits, ranging from  $\sigma_p/p \sim 0.5\%$  to  $\sigma_p/p \sim 3\%$ . We smear these tracks following Fig. 19.3 of ref. [122]. Our analysis assumes that the energy losses are fully accounted for and that the detection time is not used. We have checked that our setup reproduces the correct reconstruction gaps in the  $\cos \theta$  and  $p_e$  plane, in accordance with Fig. 19.4 of ref. [122].

#### 2.4.3 Sensitivity

**Sensitivity to SM decays:** While we do not use a full background simulation, we can still make a few low-level requirements that suppress intrinsic muon-decay backgrounds to the exotic  $\mu^+ \rightarrow 3e^+ 2e^-$  decays. For the SM rate  $\mu^+ \rightarrow 3e^+ 2e^- 2\nu$ , we require that all five tracks are reconstructed as short tracks ( $n_{\text{hits}} \geq 4$  for each track). In other words, all tracks are required to cross at least four layers of the detector. This automatically imposes a momentum threshold

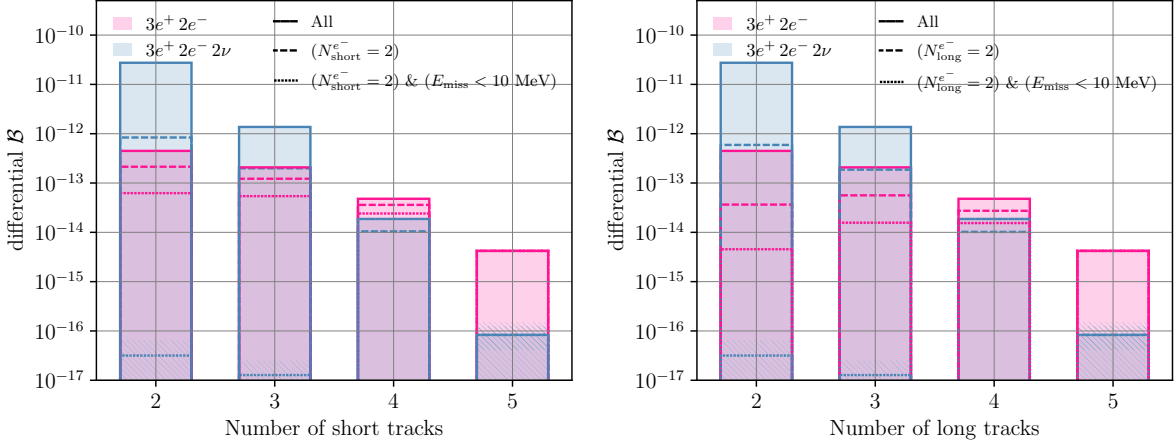


FIGURE 2.4: The number of electrons or positrons that are reconstructed as short tracks (left) and long tracks (right) for  $\mu^+ \rightarrow 3e^+ 2e^-$  (pink) and  $\mu^+ \rightarrow 3e^+ 2e^- 2\nu$  (blue) decays. We show the new-physics decays for  $m_{\gamma_d} = 30 and  $m_{h_d} = 90. A short track is defined by  $N_{\text{hits}} \geq 4$  and a long track as  $N_{\text{hits}} \geq 6$ . Solid lines show the total branching ratio for short or long tracks. Dashed lines have an additional requirement that at least two *electrons* be reconstructed as either short or long tracks. Dotted lines have yet another requirement on the missing energy  $E_{\text{miss}}$ , defined as the difference between the total energy of short tracks and the muon mass. The hatched bands indicate the MC statistical uncertainty.$$

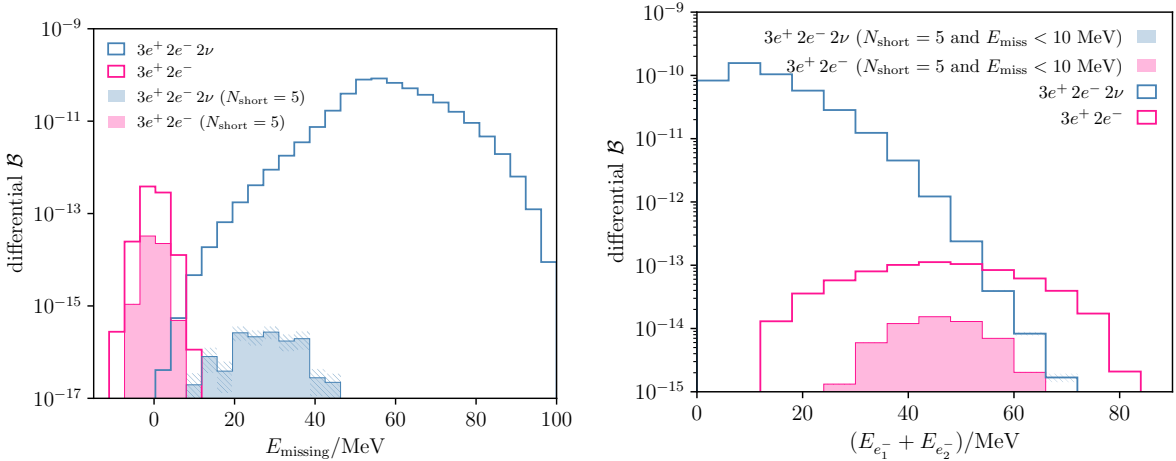


FIGURE 2.5: Left panel shows the reconstructed missing energy distribution for  $\mu^+ \rightarrow 3e^+ 2e^-$  ( $m_{\gamma_d} = 30 and  $m_{h_d} = 90) compared with the  $\mu^+ \rightarrow 3e^+ 2e^- 2\nu$  SM rate. Solid histograms include the requirement of exactly 5 reconstructed short tracks. In the right panel we show the reconstructed total electron energy distribution. In this case, solid histograms require exactly 5 reconstructed short-tracks and  $E_{\text{missing}} < 10.$$$

of about 10 MeV for each charged track and already significantly reduces background with missing energy as shown in fig. 2.4. Our simulation shows that the resulting branching ratio for five short-track events from the process  $\mu^+ \rightarrow e^+ e^+ e^- e^- \bar{\nu}_\mu \nu_e$  is about  $\mathcal{B} \sim 2 \times 10^{-15}$ , much below the value in eq. (2.3), which uses truth-level cuts. This loss in rate is due to the steep dependence of the rate on the transverse-momentum threshold and the muon decay position within the target. Whether this five-track rate is detectable or not will rely on the

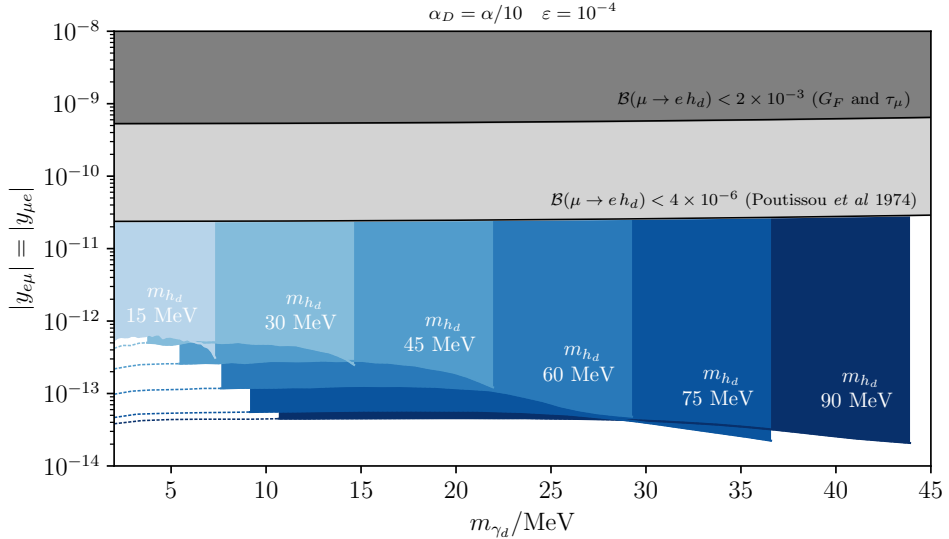


FIGURE 2.6: The Mu3e reach for  $\mu^+ \rightarrow e^+(h_d \rightarrow \gamma_d \gamma_d)$  decays as a function of  $m_{\gamma_d}$  and  $y_{\mu e} = y_{e\mu}$  for various choices of  $m_{h_d}$ , assuming a sensitivity of  $\mathcal{B}(\mu^+ \rightarrow e^+ h_d) < 10^{-12}$  after signal selection described in section 2.4.2. We fix  $\varepsilon = 10^{-4}$  and  $\alpha_D = \alpha/10$ . Dashed lines indicate regions where the scalar quartic coupling  $\lambda > \sqrt{4\pi}$  for this particular choice of  $\alpha_D$ . The limit based on a comparison of the total muon lifetime  $\tau_\mu$  and independent determinations of  $G_F$  is shown as a dark grey region ( $\mathcal{B} < 2 \times 10^{-3}$ ) and the limit from Ref. [15] is shown in the light grey region ( $\mathcal{B} < 4 \times 10^{-6}$ ).

resulting efficiencies of the five-track reconstruction algorithm and the accidental and beam-induced backgrounds. We also note that even when all tracks have sufficient energy to fall within the detector acceptance, the amount of missing energy in these events is still significant, as shown in fig. 2.5. We comment on potential alternative directions to detect the SM rate in section 2.4.4.

**Sensitivity to exotic decays:** Similarly to the SM decays above, to estimate the sensitivity of Mu3e to the neutrinoless channel, we impose the requirement that all five tracks are within the experimental acceptance. Since the exotic mode has no missing energy, we further require that  $E_{\text{missing}} < 10$  MeV, similarly to the sensitivity studies for  $\mu^+ \rightarrow 2e^+ 1e^-$ . The impact of this last cut on the new-physics rate as well as on the intrinsic SM background is shown in fig. 2.5. Even though the MC statistics are small in this region of phase space, we can readily conclude that the combination of applied cuts is exceedingly stringent, pushing the estimated intrinsic background branching ratio to  $\mathcal{O}(10^{-15})$  or lower at no significance cost to the signal efficiency.

We quote the sensitivity of Mu3e to lepton-flavor-violating decays with five tracks requiring a total of  $10^3$  new-physics events per  $10^{15} \mu^+$  decays after the signal selection discussed above. We believe that this requirement is extremely conservative. Firstly, the signal selection criteria can be relaxed by exploiting charge identification (most new-physics events have two visible electron

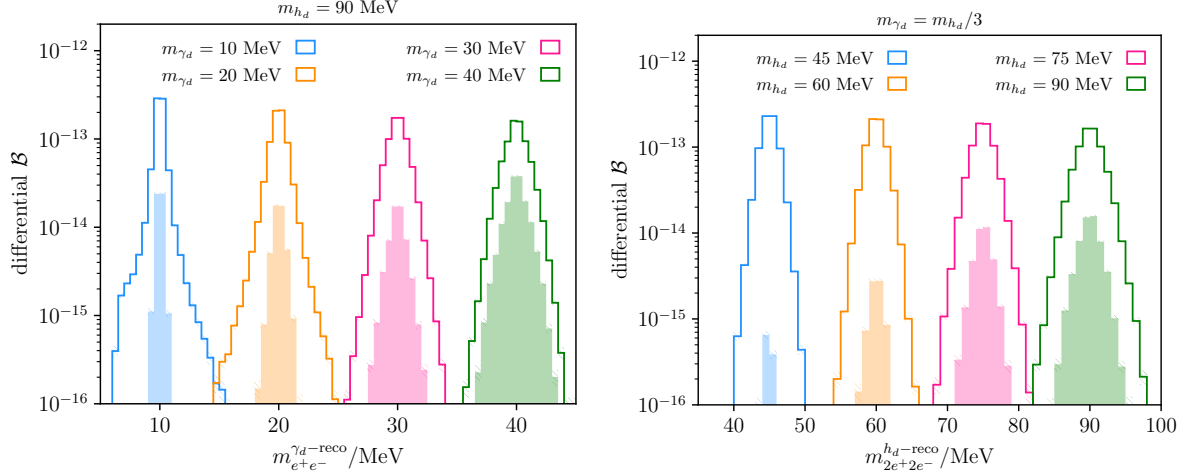


FIGURE 2.7: The reconstructed masses of the dark photon (left) and the dark higgs (right) for various fixed masses before signal selection cuts (solid lines) and after signal selection cuts (filled histograms). After selection, the resulting resolution on the dark photon mass is approximately  $\sigma_{m_{\gamma_d}}/m_{\gamma_d} = 2.3\%$  and  $\sigma_{m_{h_d}}/m_{h_d} = 1.5\%$  for the dark higgs mass. The total branching ratio for the signal was fixed to  $7 \times 10^{-13}$  in both panels.

tracks), significantly boosting the signal efficiency. Secondly, while we do not simulate accidental, beam-induced, and charge-misidentification backgrounds, our discussion in section 2.4.1 indicates that even before any kinematical requirements, these backgrounds are not expected to be larger than about a thousand events. Therefore, if the power of kinematical background rejection that was found for the  $3e$  channel is of similar size also for the  $5e$  channel, then the  $\mu \rightarrow 5e$  search should be background free for branching ratios as low as  $10^{-15}$ . Nevertheless, all our results are based on a signal rate of 1000 events, post-selection.

The reach of Mu3e in the parameter space of the dark higgsed  $U(1)_d$  model, discussed in section 2.2.1, is shown in fig. 2.6 for different values of  $m_{h_d}$  and  $m_{\gamma_d}$ . We fix the kinetic mixing parameter to  $\varepsilon = 10^{-4}$ , below the reach of the prompt decay searches, and above the limits set by the beam-dump searches at FASER [167] and other beam-dump experiments [168–170]. We also fix the dark coupling to  $\alpha_D = \alpha/10$  for illustration, although the decay rate is mostly insensitive to the exact choice of this parameter. In the regions of parameter space where this choice leads to a breakdown of perturbativity for the scalar quartic coupling,  $\lambda > \sqrt{4\pi}$ , we draw the experimental sensitivity with a dashed line. No previous experimental search for this channel exists to the best of our knowledge, so Mu3e can provide the best limits on  $|y_{e\mu}|^2 + |y_{\mu e}|^2$  for  $m_{h_d} < m_\mu - m_e$  and  $m_{\gamma_d} < m_{h_d}/2$ . In the case of a discovery, Mu3e could measure the dark photon and dark scalar masses, depending on the observed signal rate. We show the reconstructed dark photon and scalar masses in fig. 2.7.

#### 2.4.4 Future directions

Finally, we also comment on the possibility that searching for exotic multi-lepton production need not require five tracks. Depending on the charge misidentification capabilities, two electron tracks should already constitute a sufficiently-exotic final state. In that case, the selection criterion of requiring exactly five tracks in the event may be relaxed to requiring *at most* five tracks but exactly two electrons. For instance, with this more flexible selection, reconstructing an  $e^+e^-e^+e^-$  event with a missed positron as missing energy may be sufficient. With the alternative strategy to require two negatively charged tracks and relax the requirement on the total number of tracks, the observable branching ratios can be much larger. Requiring only two positrons and two electrons boosts the observable branching ratio to  $7 \times 10^{-14}$ . Similarly, requiring only one positron and two electrons recovers another order of magnitude, with a branching ratio of  $8 \times 10^{-13}$ .

The backgrounds to these three- and four-tracks selections will likely be larger. For instance, mis-reconstructed  $\mu^+ \rightarrow e^+e^+e^-\bar{\nu}_\mu\nu_e$  events will likely overwhelm the three-track channel due to the unavoidable missing energy. We also note that three-track  $5e$  decays are unlikely to be a background to the  $\mu^+ \rightarrow e^+e^+e^-$  signal thanks to the two electrons and the significant amount of missing energy. Nevertheless, the four-track  $5e$  decays may very well be within the Mu3e reach. The dominant background will likely be from  $\mu^+ \rightarrow e^+e^+e^-\bar{\nu}_\mu\nu_e$  decays with a single Bhabha scatter. Assuming the conservative numbers in section 2.4.1, this gives about  $8 \times 10^6$  events before any kinematical cuts. This number is probably much smaller as the positrons from these decays are softer than Michel ones and will produce observable  $e^+e^-$  pairs less often. We show the missing energy distribution for different track requirements in fig. 2.8. As a guide to the eye, we also show the  $\mu^+ \rightarrow e^+e^+e^-\bar{\nu}_\mu\nu_e$  rate downscaled by  $10^{-4}$ , representing the rate for  $3e$  events with an observable Bhabha pair. The latter must be significantly suppressed to successfully measure the  $5e$  decays through a four-track with two electrons signal selection. Having identified the need for more flexible signal definitions to enhance the observable SM rate, we leave a detailed study of efficiencies and backgrounds to the collaboration.

## 2.5 Conclusions

The next generation of high-intensity experiments involving muons is poised to reach new levels of sensitivity to lepton flavor violation, down to  $\mathcal{B} \sim 10^{-15}$ . Typically, these experiments are designed with one particular physics goal and measurement in mind, such as  $\mu^+ \rightarrow e^+e^+e^-$  decay in the case of the Mu3e experiment. However, the low-background environment, high intensity, and detector capabilities can turn these experiments into sensitive probes of dark sectors, putting them at the forefront of sensitivity to dark photons, dark scalars, or axion-like particles.

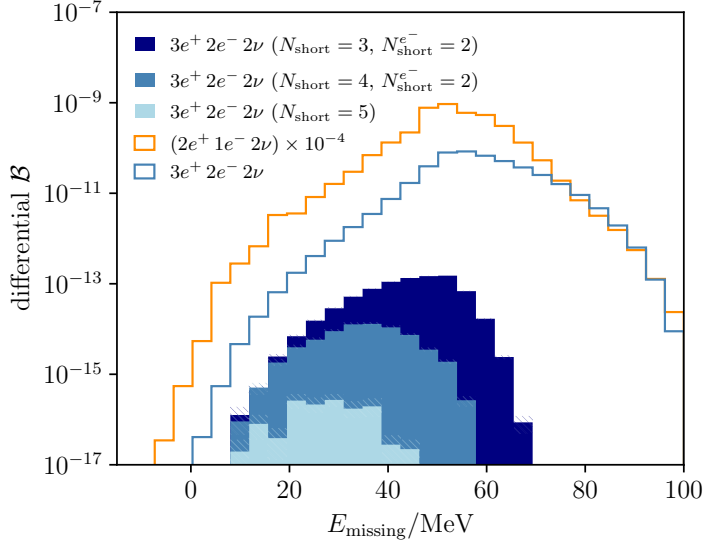


FIGURE 2.8: The reconstructed missing energy for  $\mu^+ \rightarrow e^+ e^+ e^- e^+ e^- \bar{\nu}_\mu \nu_e$  and  $\mu^+ \rightarrow e^+ e^+ e^- \bar{\nu}_\mu \nu_e$  events in Mu3e. For the former, the filled histograms show the subset of events with three, four, and five reconstructed short tracks, requiring exactly two reconstructed electrons. For the latter, we show the total rate downscaled by a factor of  $10^{-4}$ . This points to a naive estimate of 3e events where one of the positrons undergoes Bhabha scattering to produce a four-track final state.

In this work, we have analyzed the scenario of muon decay to 5 charged tracks,  $\mu^+ \rightarrow e^+ e^+ e^- e^+ e^-$ . In the Standard Model, such a decay mode (accompanied by the emission of two neutrinos) is highly suppressed by powers of  $\alpha$  resulting in a total branching ratio of  $4 \times 10^{-10}$ . The observable branching ratio will depend on the selection strategy, ranging from  $\mathcal{O}(10^{-15})$  for five-short-track events to  $\mathcal{O}(10^{-13})$  for events two observable electrons and two observable positrons. In contrast, the higgsed  $U(1)_1$  dark sector model we consider, generates a cascade of decays, resulting in a high multiplicity of electrons and positrons without further suppression by coupling constants. Therefore, such dark sectors may induce the  $3e^+ 2e^-$  decay signature with rates far above those of the SM backgrounds. In particular, as shown in fig. 2.5, the SM decays do not pose a threat to  $\mu \rightarrow 5e$  new physics searches since the branching ratio for the SM  $\mu \rightarrow 5e 2\nu$  decay with  $E_{\text{missing}} < 10$  MeV is of the order of  $\mathcal{O}(10^{-15})$  or below.

The Mu3e collaboration currently does not have a dedicated study of a signal composed of five charged tracks. To that end, we have performed a simplified simulation of the Mu3e detector to determine a realistic signal efficiency. The requirement to have multiple energetic particles reduces the signal efficiency for the  $\mu \rightarrow 5e$  signature down to the level of  $\mathcal{O}(0.1\% - 1\%)$ , depending on the masses of the dark particles, indicating a resulting sensitivity to branching ratios of order  $\mathcal{B}(\mu^+ \rightarrow 3e^+ 2e^-) \sim 10^{-12}$  in the most optimistic background-free case. For the dark sector masses in the tens of MeV range, the Mu3e sensitivity would translate to a probe of the lepton-flavor-violating muon-electron-dark Higgs coupling at the level  $|y_{\mu e, e\mu}| < 10^{-13}$  and below, as shown in fig. 2.6. Recalling that such couplings originate from dimension-five operators, eq. (2.8), we arrive at the future sensitivity of Mu3e to new physics scales  $\Lambda$  as high

as  $\Lambda \propto 10^{15} - 10^{16}$  GeV. We conclude by encouraging the Mu3e collaboration to perform a dedicated study of “5e” physics channels, both in the neutrinoless new physics channel and in the SM channel, where neutrinos carry additional missing energy away.

# Chapter 3

## An effective theory tower for $\mu \rightarrow e$ conversion

**Preface:** This chapter closely follows the published work in [3] with Evan, Wick, Ken, and Jure. The goal of this paper was to connect a recently formulated non-relativistic nuclear-level EFT (NRET) for  $\mu \rightarrow e$  conversion [171] (by Evan, Wick, and Ken) to high-scale sources of CLFV. To do this we built a tower of sequentially matched EFTs that run and match dimension-6 CLFV-ing SMEFT operators from the UV down to the nuclear scale, where the  $\mu \rightarrow e$  conversion rate can then be computed using the NRET.

Compared to Mu3e and MEG, the study of CLFVing  $\mu \rightarrow e$  signatures at Mu2e (described in section 1.5.5) are complicated by the use of muons  $\mu^-$  rather than anti-muons  $\mu^+$ . Positively charged muons incident on a stopping target will penetrate the target and slowly come to rest via Coulomb exchanges with the material. Negatively charged muons, on the other hand, will penetrate the target and slow until becoming trapped by a potential well of a nucleus within the material. Once, trapped, the muon quickly (in roughly  $10^{-13}$  seconds) gets pulled towards the nucleus and reaches a stable configuration in the  $1s$  orbital. Because the new physics sourcing the CLFV  $\mu \rightarrow e$  signature could originate from interactions with the partons in the nucleus or the electron cloud – it is important to understand how these parton level-interactions manifest at the level of the nucleus. Here we accomplish this through a sequential matching of multiple effective field theories, referred to as an EFT tower.

### 3.1 The effective tower

In this chapter, we develop a bottom-up approach for  $\mu \rightarrow e$  conversion, with the corresponding tower of EFTs shown in fig. 3.1. Starting from a UV theory and integrating out heavy mediators, one recovers the SM augmented by higher dimension operators — the so-called Standard

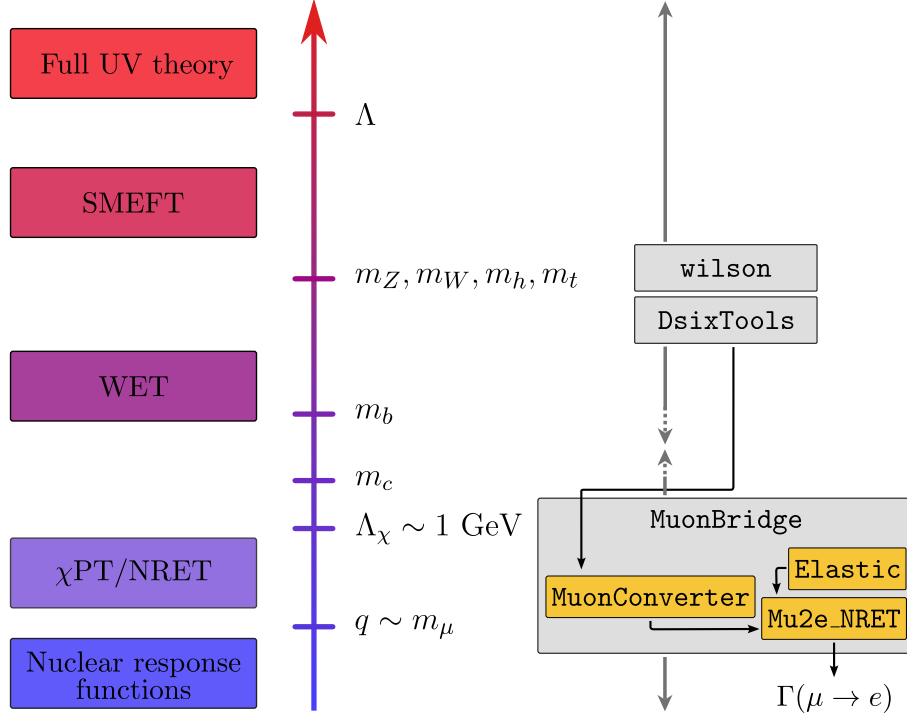


FIGURE 3.1: The effective field theories — and their respective thresholds — relevant for describing  $\mu \rightarrow e$  conversion, as well as the corresponding computer codes (in grey boxes). The `MuonBridge` repository, introduced as part of this manuscript, consists of the interconnected packages `MuonConverter`, `Mu2e_NRET`, and `Elastic` (orange boxes).

Model Effective Field Theory (SMEFT). Only a subset of SMEFT operators are relevant for the problem at hand — those that induce  $\mu \rightarrow e$  transitions. At the electroweak scale the  $Z$  and  $W$  gauge bosons, the Higgs, and the top quark are integrated out, giving rise to Weak Effective Theory (WET) describing CLFV interactions with currents constructed from quark, gluon or electromagnetic gauge fields, containing either five (above  $b$  quark mass), four (above roughly the  $c$  quark mass) or three ( $u$ ,  $d$ ,  $s$ ) active quark flavors. As our default choice we take the three-flavor WET at  $\mu = 2$  GeV, a scale choice most commonly used in lattice QCD evaluations of the hadronic matrix elements. The three-flavor WET can be matched nonperturbatively onto covariant nucleon-level interactions, describing physics below  $\Lambda_\chi \approx m_\rho \approx 1$  GeV, where the dynamics due to the omitted degrees of freedom (such as the vector meson resonances) is included through the momentum exchange dependence of the single-nucleon form factors. Because  $\mu \rightarrow e$  is characterized by the three-momentum transfer of size  $q \approx m_\mu$ , a more efficient NRET can then be obtained by nonrelativistic reduction. The NRET basis is compatible with the standard nonrelativistic many-body methods, like the shell model, that are typically employed in nuclear response function evaluations.

The prerequisite nuclear-level NRET was developed recently in refs. [171, 172], together with the accompanying public code `Mu2e_NRET_v1`, available in `Mathematica` and `Python`. In this work, we introduce an updated code, `Mu2e_NRET_v2`, with two major changes. First, we extend the code to include the leading muon-velocity-suppressed contributions, which were calculated in

ref. [172] but not included in `Mu2e_NRET_v1`. Second, to facilitate the matching between NRET and WET, we extend the set of covariant scalar- and vector-mediated interactions discussed in ref. [172] to include tensor mediators. In addition, we provide a new open-source code `MuonConverter` (also available in `Python` and `Mathematica`), that facilitates the connection between NRET and WET and provides an interface to SMEFT through optional linking to dedicated external codes `wilson` [173] and `DsixTools` [17, 174], see fig. 3.1.

To allow for independent usage, `MuonConverter`, `Mu2e_NRET`, and `Elastic` — a database of shell-model one-body density matrices that are required for the evaluation of NRET nuclear form factors — are integrated together within a single parent repository, `MuonBridge`, containing documentation, examples, and the appropriate instructions for assembling the independent components, depending on the specific goals of user.

The rest of the chapter is organized as follows: In section 3.2 we introduce a convenient WET operator basis up to dimension 7 for use in  $\mu \rightarrow e$  conversion calculations. Section 3.3 describes the NRET basis of 26 operators that arises in an expansion to linear order in  $\vec{v}_N$  and  $\vec{v}_\mu$ , and the matching from WET to the NRET is performed in section 3.4. As an illustration, in section 3.5 we perform the EFT matching for two new physics models where  $\mu \rightarrow e$  conversion is mediated by either heavy leptoquarks or light axion-like particles (ALPs). Finally, in section 3.6 we describe the `MuonBridge` repository.

Appendix B contains further technical details and intermediate results. Explicitly appendix B.1 contains intermediate results for WET to NRET matching, including the mapping from WET onto the covariant Dirac basis of 32 operators used as an intermediate step in the matching. Details on the numerical evaluation of nucleon form factors are presented in appendix B.2. Finally, in appendix B.3 we give the translation between our WET basis and the dimension-6 WET three-flavor basis of ref. [175], which is used by the `MuonConverter` to interface with other existing SMEFT/WET software.

## 3.2 Weak effective theory

The tower of EFTs in fig. 3.1 relates UV-scale physics to the nuclear scale where  $\mu \rightarrow e$  conversion experiments are performed. In this manuscript, we focus on the last three steps in the ladder of EFT matchings: the Weak Effective Theory (WET) at  $\mu = 2\text{ GeV}$ , the matching to NRET, and the prediction of conversion rates for nuclear targets of experimental interest using state-of-the-art shell-model methods to evaluate nuclear response functions. The formalism for relating the UV physics at an arbitrary high scale  $\Lambda$  to the WET at  $\mu = 2\text{ GeV}$  is, on the other hand, well developed [175–181] and available in the form of public codes [173, 174, 182].

The part of the WET Lagrangian at  $\mu = 2$  GeV relevant for describing the  $\mu \rightarrow e$  conversion process is given by<sup>1</sup>

$$\mathcal{L}_{\text{eff}}^{\text{WET}} = \sum_{a,d} \hat{\mathcal{C}}_a^{(d)} \mathcal{Q}_a^{(d)}, \quad (3.1)$$

where the  $\mathcal{Q}_a^{(d)}$  are CLFV operators of mass dimension  $d$  (defined below) and the  $\hat{\mathcal{C}}_a^{(d)}$  are dimensionful Wilson coefficients. By introducing an energy scale  $\Lambda_{\text{CLFV}}$  associated with the CLFV physics, we can express these dimensionful Wilson coefficients in terms of dimensionless  $\mathcal{O}(1)$  Wilson coefficients  $\mathcal{C}_a^{(d)}$  as

$$\hat{\mathcal{C}}_a^{(d)} = \frac{\mathcal{C}_a^{(d)}}{\Lambda_{\text{CLFV}}^{d-4}}. \quad (3.2)$$

In what follows, we retain operators up to and including dimension 7. The full set of dimension-5 operators consists of the magnetic and electric dipoles,

$$\mathcal{Q}_1^{(5)} = \frac{e}{8\pi^2} (\bar{e}\sigma^{\alpha\beta}\mu) F_{\alpha\beta}, \quad \mathcal{Q}_2^{(5)} = \frac{e}{8\pi^2} (\bar{e}\sigma^{\alpha\beta}i\gamma_5\mu) F_{\alpha\beta}, \quad (3.3)$$

where  $F_{\alpha\beta}$  is the electromagnetic field strength tensor. The dimension-6 operators are

$$\mathcal{Q}_{1,q}^{(6)} = (\bar{e}\gamma_\alpha\mu)(\bar{q}\gamma^\alpha q), \quad \mathcal{Q}_{2,q}^{(6)} = (\bar{e}\gamma_\alpha\gamma_5\mu)(\bar{q}\gamma^\alpha q), \quad (3.4)$$

$$\mathcal{Q}_{3,q}^{(6)} = (\bar{e}\gamma_\alpha\mu)(\bar{q}\gamma^\alpha\gamma_5 q), \quad \mathcal{Q}_{4,q}^{(6)} = (\bar{e}\gamma_\alpha\gamma_5\mu)(\bar{q}\gamma^\alpha\gamma_5 q). \quad (3.5)$$

$$\mathcal{Q}_{5,q}^{(6)} = (\bar{e}\mu)(\bar{q}q), \quad \mathcal{Q}_{6,q}^{(6)} = (\bar{e}i\gamma_5\mu)(\bar{q}q), \quad (3.6)$$

$$\mathcal{Q}_{7,q}^{(6)} = (\bar{e}\mu)(\bar{q}i\gamma_5 q), \quad \mathcal{Q}_{8,q}^{(6)} = (\bar{e}i\gamma_5\mu)(\bar{q}i\gamma_5 q), \quad (3.7)$$

$$\mathcal{Q}_{9,q}^{(6)} = (\bar{e}\sigma^{\alpha\beta}\mu)(\bar{q}\sigma_{\alpha\beta}q), \quad \mathcal{Q}_{10,q}^{(6)} = (\bar{e}i\sigma^{\alpha\beta}\gamma_5\mu)(\bar{q}\sigma_{\alpha\beta}q). \quad (3.8)$$

The quark label  $q = u, d, s$  denotes one of the three light quark flavors. We assume that the CLFV interaction responsible for  $\mu \rightarrow e$  conversion is flavor-conserving in the hadronic sector.

The dimension-7 basis includes 8 operators that couple to gauge bosons

$$\mathcal{Q}_1^{(7)} = \frac{\alpha_s}{12\pi} (\bar{e}\mu) G^{a\alpha\beta} G_{\alpha\beta}^a, \quad \mathcal{Q}_2^{(7)} = \frac{\alpha_s}{12\pi} (\bar{e}i\gamma_5\mu) G^{a\alpha\beta} G_{\alpha\beta}^a, \quad (3.9)$$

$$\mathcal{Q}_3^{(7)} = \frac{\alpha_s}{8\pi} (\bar{e}\mu) G^{a\alpha\beta} \tilde{G}_{\alpha\beta}^a, \quad \mathcal{Q}_4^{(7)} = \frac{\alpha_s}{8\pi} (\bar{e}i\gamma_5\mu) G^{a\alpha\beta} \tilde{G}_{\alpha\beta}^a, \quad (3.10)$$

$$\mathcal{Q}_5^{(7)} = \frac{\alpha}{12\pi} (\bar{e}\mu) F^{\alpha\beta} F_{\alpha\beta}, \quad \mathcal{Q}_6^{(7)} = \frac{\alpha}{12\pi} (\bar{e}i\gamma_5\mu) F^{\alpha\beta} F_{\alpha\beta}, \quad (3.11)$$

$$\mathcal{Q}_7^{(7)} = \frac{\alpha}{8\pi} (\bar{e}\mu) F^{\alpha\beta} \tilde{F}_{\alpha\beta}, \quad \mathcal{Q}_8^{(7)} = \frac{\alpha}{8\pi} (\bar{e}i\gamma_5\mu) F^{\alpha\beta} \tilde{F}_{\alpha\beta}, \quad (3.12)$$

where  $G_{\alpha\beta}^a$  is the gluon field strength tensor and  $\tilde{G}_{\alpha\beta} = \frac{1}{2}\epsilon_{\alpha\beta\mu\nu}G^{\mu\nu}$  is its dual.<sup>2</sup> The electromagnetic dual  $\tilde{F}_{\alpha\beta}$  is similarly defined. In order to complete the basis of dimension-7 CLFV

<sup>1</sup>Our basis at  $\mu = 2$  GeV follows from [183], though we choose instead the operator basis with currents of definite parity. We keep only the subset of operators that give rise to  $\mu \rightarrow e$  transitions and assume this is the only flavor-violating effect.

<sup>2</sup>We use the convention  $\epsilon_{0123} = +1$ .

operators, we introduce the following four-fermion operators with derivatives acting inside the lepton currents

$$\mathcal{Q}_{9,q}^{(7)} = (\bar{e} \overset{\leftrightarrow}{i\partial_\alpha} \mu) (\bar{q} \gamma^\alpha q), \quad \mathcal{Q}_{10,q}^{(7)} = (\bar{e} i\gamma_5 \overset{\leftrightarrow}{i\partial_\alpha} \mu) (\bar{q} \gamma^\alpha q), \quad (3.13)$$

$$\mathcal{Q}_{11,q}^{(7)} = (\bar{e} \overset{\leftrightarrow}{i\partial_\alpha} \mu) (\bar{q} \gamma^\alpha \gamma_5 q), \quad \mathcal{Q}_{12,q}^{(7)} = (\bar{e} i\gamma_5 \overset{\leftrightarrow}{i\partial_\alpha} \mu) (\bar{q} \gamma^\alpha \gamma_5 q), \quad (3.14)$$

$$\mathcal{Q}_{13,q}^{(7)} = \partial^\alpha (\bar{e} \gamma^\beta \mu) (\bar{q} \sigma_{\alpha\beta} q), \quad \mathcal{Q}_{14,q}^{(7)} = \partial^\alpha (\bar{e} \gamma^\beta \gamma_5 \mu) (\bar{q} \sigma_{\alpha\beta} q), \quad (3.15)$$

$$\mathcal{Q}_{15,q}^{(7)} = \partial^\alpha (\bar{e} \gamma^\beta \mu) (\bar{q} i\sigma_{\alpha\beta} \gamma_5 q), \quad \mathcal{Q}_{16,q}^{(7)} = \partial^\alpha (\bar{e} \gamma^\beta \gamma_5 \mu) (\bar{q} i\sigma_{\alpha\beta} \gamma_5 q), \quad (3.16)$$

where  $\bar{e} \overset{\leftrightarrow}{i\partial_\nu} \mu = \bar{e} i\partial_\nu \mu - \bar{e} \overset{\leftarrow}{i\partial_\nu} \mu$ .

Instead of the operators  $\mathcal{Q}_{13,q}^{(7)}, \dots, \mathcal{Q}_{16,q}^{(7)}$ , one could use equations of motion to write a more symmetric operator basis, with the derivatives acting on the quark currents

$$\mathcal{Q}_{13,q}^{(7)} = -(\bar{e} \gamma^\alpha \mu) (\bar{q} \overset{\leftrightarrow}{iD_\alpha} q) + 2m_q \mathcal{Q}_{1,q}^{(6)}, \quad (3.17)$$

$$\mathcal{Q}_{14,q}^{(7)} = -(\bar{e} \gamma^\alpha \gamma_5 \mu) (\bar{q} \overset{\leftrightarrow}{iD_\alpha} q) + 2m_q \mathcal{Q}_{2,q}^{(6)}, \quad (3.18)$$

$$\mathcal{Q}_{15,q}^{(7)} = -(\bar{e} \gamma^\alpha \mu) (\bar{q} i\gamma_5 \overset{\leftrightarrow}{iD_\alpha} q), \quad (3.19)$$

$$\mathcal{Q}_{16,q}^{(7)} = -(\bar{e} \gamma^\alpha \gamma_5 \mu) (\bar{q} i\gamma_5 \overset{\leftrightarrow}{iD_\alpha} q). \quad (3.20)$$

This reformulation demonstrates that our dimension-7 basis is equivalent to the basis in ref. [183] (when restricted to those operators that can mediate  $\mu \rightarrow e$  conversion). Our basis is chosen to make the evaluation of hadronic matrix elements straightforward.

### 3.3 Nuclear effective theory

The  $\mu \rightarrow e$  conversion process results in momentum exchanges typical of the nuclear scale, where the natural degrees of freedom for describing the strong interaction are nucleons. To make contact with experiments, the CLFV light-quark operator basis of section 3.2 must be matched to the basis of CLFV single-nucleon operators. Just as the WET basis is organized by a power-counting in mass dimension, the NRET basis must also be organized through an expansion in small dimensionless parameters. Before introducing the single-nucleon CLFV basis, we briefly review how the physics of  $\mu \rightarrow e$  conversion motivates the particular form of the nuclear-scale effective theory [171, 172] used in this work.

#### 3.3.1 Kinematics

The  $\mu^-$  that gets captured in the nuclear Coulomb field quickly de-excites to the  $1s$  orbital. The muon's binding energy  $E_\mu^{\text{bind}}$  (defined to be positive) and the muon's wave function  $\psi_\mu$  can be determined by numerically solving the Dirac equation for a potential sourced by the

experimentally known nuclear charge distribution. To the precision we work, screening and other corrections arising from the Coulomb potential of the surrounding electron cloud can be ignored.

We are interested in  $\mu \rightarrow e$  transitions where the nucleus remains in the ground state.<sup>3</sup> The three-momentum  $\vec{q}$  of the outgoing electron is then given by

$$\vec{q}^2 = \frac{M_T}{m_\mu + M_T} \left[ \left( m_\mu - E_\mu^{\text{bind}} \right)^2 - m_e^2 \right], \quad (3.21)$$

where we keep the first correction in  $m_\mu/M_T$ , with  $M_T$ ,  $m_\mu$ , and  $m_e$  being the masses of the target nucleus, muon, and electron, respectively. Once the energy of the electron is known, the outgoing electron wave function can be obtained from numerical solutions of the Dirac equation in the Coulomb field generated by the extended nuclear charge. As the momentum transfer from the leptons to the nucleus is sufficient to require retention of several electron partial waves, this has the potential to significantly complicate calculations. Fortunately, the Coulomb-distorted waves can be very well approximated by much simpler plane waves, evaluated for a shifted effective momentum  $q_{\text{eff}}$  determined from the average value of the Coulomb potential near the nucleus [172]. Numerically, the difference between  $q$  and  $q_{\text{eff}}$  is  $\approx 5\%$  in  $^{27}\text{Al}$ .

To motivate the form of the nuclear-scale effective theory, we note that:

1. The outgoing electron is highly relativistic, with  $E_e \approx m_\mu$ : the correction due to the muon binding energy  $E_\mu^{\text{bind}}$  is small ( $E_\mu^{\text{bind}} \approx 0.463$  MeV in  $^{27}\text{Al}$ ). The electron velocity — defined in the NRET as the Galilean-invariant velocity with respect to the center of mass of the final-state nucleus — thus has magnitude 1 (in units of  $c$ ) and direction  $\hat{q}$ , the latter of which is, in principle, an observable. This leaves only the nonrelativistic velocities of the bound-state nucleons and muon to be treated as operators, a task ideally suited for NRET methods.
2. Relativistic corrections for the bound muon are roughly proportional to  $Z\alpha/2$ . For light nuclei such as  $^{27}\text{Al}$ , the muon is highly nonrelativistic, so that its Dirac wave function is dominated by its Schrödinger-like upper component. The muon's velocity operator  $\vec{v}_\mu$  thus enters the NRET as a correction generated by the suppressed lower component of the Dirac solution. In the NRET,  $\vec{v}_\mu$  is defined as the Galilean-invariant velocity associated with the motion of the bound muon with respect to the center of mass of the initial-state nucleus. The effects of  $\vec{v}_\mu$  are limited to small numerical changes in nuclear form factors: the  $\vec{v}_\mu$  operator plays no role in the selection rules that determine the nuclear response functions.

---

<sup>3</sup>Experimentally, this is the preferred option as the resulting conversion electrons will be at the endpoint of the SM background from  $\mu \rightarrow e\nu\bar{\nu}$  decays. In  $\mu \rightarrow e$  conversions where the nucleus transitions to an excited state, the less energetic outgoing electron must compete with a larger SM background but may provide additional information about the underlying CLFV mechanism [184].

3. Nucleons bound in a nucleus are only mildly relativistic, with typical velocities  $v_{\text{avg}} \approx 0.1$ . We can therefore perform a nonrelativistic expansion of the nuclear charges and currents. In the NRET, the nucleon velocity operator  $\vec{v}_N$  stands for the set of  $A - 1$  independent nucleon Jacobi velocities, e.g., the Galilean-invariant velocities  $\vec{v}_N \equiv \{(\vec{v}_2 - \vec{v}_1)/\sqrt{2}, (2\vec{v}_3 - (\vec{v}_1 + \vec{v}_2))/\sqrt{6}, \dots\}$ , where  $\vec{v}_i$  is velocity operator for the  $i$ -th nucleon and  $A$  is the nucleon number. See [172, 185] for details.

The available Hermitian operators that enter into the construction of the NRET CLFV operators are:  $i\hat{q}$  where  $\hat{q}$  is the velocity of the outgoing ultra-relativistic electron, the nucleon velocity operator  $\vec{v}_N$ , and the respective lepton and nucleon spin operators,  $\vec{\sigma}_L$  and  $\vec{\sigma}_N$ . Extending this set of building-block operators to include the muon velocity operator  $\vec{v}_\mu$  generates the relativistic corrections associated with the lower component of the muon's Dirac wave function.

### 3.3.2 NRET basis

Working to the first order in the nucleon velocity  $\vec{v}_N$  and neglecting the muon velocity  $\vec{v}_\mu$ , there are 16 independent CLFV single-nucleon operators [171, 172],

$$\mathcal{O}_1 = 1_L 1_N, \quad \mathcal{O}'_2 = 1_L i\hat{q} \cdot \vec{v}_N, \quad (3.22a)$$

$$\mathcal{O}_3 = 1_L i\hat{q} \cdot [\vec{v}_N \times \vec{\sigma}_N], \quad \mathcal{O}_4 = \vec{\sigma}_L \cdot \vec{\sigma}_N, \quad (3.22b)$$

$$\mathcal{O}_5 = \vec{\sigma}_L \cdot (i\hat{q} \times \vec{v}_N), \quad \mathcal{O}_6 = i\hat{q} \cdot \vec{\sigma}_L i\hat{q} \cdot \vec{\sigma}_N, \quad (3.22c)$$

$$\mathcal{O}_7 = 1_L \vec{v}_N \cdot \vec{\sigma}_N, \quad \mathcal{O}_8 = \vec{\sigma}_L \cdot \vec{v}_N, \quad (3.22d)$$

$$\mathcal{O}_9 = \vec{\sigma}_L \cdot (i\hat{q} \times \vec{\sigma}_N), \quad \mathcal{O}_{10} = 1_L i\hat{q} \cdot \vec{\sigma}_N, \quad (3.22e)$$

$$\mathcal{O}_{11} = i\hat{q} \cdot \vec{\sigma}_L 1_N, \quad \mathcal{O}_{12} = \vec{\sigma}_L \cdot [\vec{v}_N \times \vec{\sigma}_N], \quad (3.22f)$$

$$\mathcal{O}'_{13} = \vec{\sigma}_L \cdot (i\hat{q} \times [\vec{v}_N \times \vec{\sigma}_N]), \quad \mathcal{O}_{14} = i\hat{q} \cdot \vec{\sigma}_L \vec{v}_N \cdot \vec{\sigma}_N, \quad (3.22g)$$

$$\mathcal{O}_{15} = i\hat{q} \cdot \vec{\sigma}_L i\hat{q} \cdot [\vec{v}_N \times \vec{\sigma}_N], \quad \mathcal{O}'_{16} = i\hat{q} \cdot \vec{\sigma}_L i\hat{q} \cdot \vec{v}_N. \quad (3.22h)$$

This operator basis matches closely the one previously derived for dark matter direct detection [185]; we distinguish with a prime the operators for which there are significant differences. The NRET operators  $\mathcal{O}_i$  are understood to act between Pauli spinors  $\xi_s$  for muon, electron, and nucleons. The leptonic current operators  $1_L$  or  $\vec{\sigma}_L$  couple the  $1s$  muon wave function to the various distorted partial waves comprising the outgoing electron's wave function.

The corresponding effective interaction can be expressed as

$$\mathcal{L}_{\text{eff}}^{\text{NRET}} = \sum_{N=n,p} \sum_{i=1}^{16} c_i^N \mathcal{O}_i^N + \dots, \quad (3.23)$$

where ellipses denote omitted corrections due to operators generated by  $\vec{v}_\mu$ , two-body currents that arise in nuclear systems, etc. We refer to the numerical coefficients  $c_i^N$  as the low-energy

constants (LECs) of the NRET. They are the analogs of the Wilson coefficients  $\hat{c}_a^{(d)}$  in the WET Lagrangian, eq. (3.1), and carry dimensions of  $1/(\text{mass})^2$ . Strictly speaking, the LECs are functions of  $\vec{q}^2$ ; however, for a given target the momentum transfer in  $\mu \rightarrow e$  conversion is a fixed quantity determined by kinematics, as in eq. (3.21). As a result, the NRET LECs are genuine constants capable of encoding the exact momentum dependence that arises, for example, from the exchange of light mediators with  $m^2 \lesssim \vec{q}^2$ . Thus, the NRET formalism is ideally suited to describe not just heavy mediators but also light new physics such as the CLFV axion-like-particle scenario considered below in section 3.5.3.

In eq. (3.23) we have also introduced the index  $N$  to allow for the CLFV physics to couple differently to protons vs. neutrons. Equivalently, we can work in terms of isoscalar and isovector operators

$$\mathcal{L}_{\text{eff}}^{\text{NRET}} = \sum_{\tau=0,1} \sum_{i=1}^{16} c_i^\tau \mathcal{O}_i t^\tau + \dots, \quad (3.24)$$

where  $c_i^0 = (c_i^p + c_i^n)/2$ ,  $c_i^1 = (c_i^p - c_i^n)/2$ , and  $t^0 = 1$ ,  $t^1 = \tau_3$  are the isospin matrices.

Working to first order in the nucleon velocity  $v_N$  and neglecting the muon velocity  $v_\mu$ , the  $\mu \rightarrow e$  conversion rate is given by [171, 172]

$$\begin{aligned} \Gamma(\mu \rightarrow e) &= \frac{1}{2\pi} \frac{q_{\text{eff}}^2}{1 + q/M_T} |\phi_{1s}^{Z_{\text{eff}}}(\vec{0})|^2 \\ &\times \sum_{\tau,\tau'} \left\{ \left[ R_{MM}^{\tau\tau'} W_{MM}^{\tau\tau'}(q_{\text{eff}}) + R_{\Sigma''\Sigma''}^{\tau\tau'} W_{\Sigma''\Sigma''}^{\tau\tau'}(q_{\text{eff}}) + R_{\Sigma'\Sigma'}^{\tau\tau'} W_{\Sigma'\Sigma'}^{\tau\tau'}(q_{\text{eff}}) \right] \right. \\ &+ \frac{q_{\text{eff}}^2}{m_N^2} \left[ R_{\Phi''\Phi''}^{\tau\tau'} W_{\Phi''\Phi''}^{\tau\tau'}(q_{\text{eff}}) + R_{\tilde{\Phi}'\tilde{\Phi}'}^{\tau\tau'} W_{\tilde{\Phi}'\tilde{\Phi}'}^{\tau\tau'}(q_{\text{eff}}) + R_{\Delta\Delta}^{\tau\tau'} W_{\Delta\Delta}^{\tau\tau'}(q_{\text{eff}}) \right] \\ &\left. - \frac{2q_{\text{eff}}}{m_N} \left[ R_{\Phi''M}^{\tau\tau'} W_{\Phi''M}^{\tau\tau'}(q_{\text{eff}}) + R_{\Delta\Sigma'}^{\tau\tau'} W_{\Delta\Sigma'}^{\tau\tau'}(q_{\text{eff}}) \right] \right\}, \end{aligned} \quad (3.25)$$

where

$$R_{MM}^{\tau\tau'} = c_1^\tau c_1^{\tau'*} + c_{11}^\tau c_{11}^{\tau'*}, \quad (3.26)$$

$$R_{\Sigma''\Sigma''}^{\tau\tau'} = (c_4^\tau - c_6^\tau)(c_4^{\tau'} - c_6^{\tau'})^* + c_{10}^\tau c_{10}^{\tau'*}, \quad (3.27)$$

$$R_{\Sigma'\Sigma'}^{\tau\tau'} = c_4^\tau c_4^{\tau'*} + c_9^\tau c_9^{\tau'*}, \quad (3.28)$$

$$R_{\Phi''\Phi''}^{\tau\tau'} = c_3^\tau c_3^{\tau'*} + (c_{12}^\tau - c_{15}^\tau)(c_{12}^{\tau'*} - c_{15}^{\tau'*}), \quad (3.29)$$

$$R_{\tilde{\Phi}'\tilde{\Phi}'}^{\tau\tau'} = c_{12}^\tau c_{12}^{\tau'*} + c_{13}^\tau c_{13}^{\tau'*}, \quad (3.30)$$

$$R_{\Delta\Delta}^{\tau\tau'} = c_5^\tau c_5^{\tau'*} + c_8^\tau c_8^{\tau'*}, \quad (3.31)$$

$$R_{\Phi''M}^{\tau\tau'} = \text{Re}[c_3^\tau c_1^{\tau'*} - (c_{12}^\tau - c_{15}^\tau)c_{11}^{\tau'*}], \quad (3.32)$$

$$R_{\Delta\Sigma'}^{\tau\tau'} = \text{Re}[c_5^\tau c_4^{\tau'*} + c_8^\tau c_9^{\tau'*}], \quad (3.33)$$

and  $\phi_{1s}^{Z_{\text{eff}}}(\vec{0})$  is the  $1s$  wave function of a muonic atom with effective charge  $Z_{\text{eff}}$ , evaluated at the origin. The leptonic response functions  $R_i^{\tau\tau'}$  are bilinears in the NRET LECs. The specific combinations define what can (and thus what cannot) be determined about CLFV from elastic  $\mu \rightarrow e$  conversion. Note that the nuclear response functions  $W_i^{\tau\tau'}$  depend on the modified momentum of the outgoing electron wave  $q_{\text{eff}}$ .

In the long wavelength limit,  $q_{\text{eff}} \rightarrow 0$ , the coherently enhanced response function  $W_{MM}^{\tau\tau}$  counts the number of protons and neutrons in the nucleus, while  $W_{\Sigma'\Sigma'}^{\tau\tau'}$  and  $W_{\Sigma''\Sigma''}^{\tau\tau'}$  measure the transverse and longitudinal nuclear spin responses, respectively. The velocity-dependent response functions  $W_{\Phi''\Phi''}^{\tau\tau'}, W_{\tilde{\Phi}'\tilde{\Phi}'}^{\tau\tau'},$  and  $W_{\Delta\Delta}^{\tau\tau'}$  appear in the rate formula multiplied by a factor of  $q_{\text{eff}}^2/m_N^2$ , reflecting their origin as responses sensitive to the composite structure of the nucleus, generated by operators like the orbital angular momentum  $\vec{\ell}$ . As such, contributions from these responses vanish in the limit of a point-like nucleus,  $q_{\text{eff}} \rightarrow 0$ .

One of these response functions,  $W_{\Phi''\Phi''}^{\tau\tau'}$ , becomes coherent in nuclei like  $^{27}\text{Al}$  where one of two spin-orbit partner shells  $j = \ell \pm 1/2$  is occupied [185]. The response  $\Phi''$ , which is generically associated with tensor mediators, corresponds to the longitudinal projection of the nuclear spin-velocity current  $\vec{v}_N \times \vec{\sigma}_N$  and can interfere with the charge multipole operator  $M$ . (Similarly, there can be interference between the transverse-magnetic response  $\Delta$  and the transverse-electric response  $\Sigma'$ .) In  $^{27}\text{Al}$ , which is a nearly ideal target for maximizing the coherence of  $\Phi''$ , the interference term  $W_{\Phi''M}^{00}$  contributes  $\approx 5\%$  of the total response (for equal NRET coefficients, e.g.,  $c_1^0 = c_3^0$ ). Along with the usual coherent coupling to nuclear charge, these two distinct sources of nuclear enhancements of operators lead to a hierarchy in the associated response functions for  $^{27}\text{Al}$ . In the case of isoscalar couplings — assuming that the relevant NRET coefficients are roughly equal in magnitude — the hierarchy is

$$W_{MM}^{00} \sim \mathcal{O}(A^2) \gg \frac{q_{\text{eff}}}{m_N} W_{M\Phi''}^{00} \gg \left\{ W_{\Sigma'\Sigma'}^{00}, W_{\Sigma''\Sigma''}^{00}, \frac{q_{\text{eff}}^2}{m_N^2} W_{\Phi''\Phi''}^{00} \right\} \gg \left\{ \frac{q_{\text{eff}}^2}{m_N^2} W_{\Delta\Delta}^{00}, \frac{q_{\text{eff}}^2}{m_N^2} W_{\tilde{\Phi}'\tilde{\Phi}'}^{00} \right\}. \quad (3.34)$$

This assumes, as is the case for  $^{27}\text{Al}$ , that the nuclear ground state carries angular momentum  $j \geq 1$ , so that all nuclear response functions can contribute. The above hierarchy of nuclear response functions illustrates that the nucleus can alter the naïve nucleon-level counting based on the small parameter  $|\vec{v}_N|$ ; coherence can elevate operators to be of the allowed strength.

The six response functions (and the two interference terms) constitute the most general set of symmetry-allowed nuclear response functions. That is, the constraints of the nuclear ground state — angular momentum, parity, and time-reversal — restrict the operators that can contribute to the elastic  $\mu \rightarrow e$  conversion process, so that the 16 leading single-nucleon operators embed into just six nuclear response functions and two interference terms. The general form is generated at  $\mathcal{O}(v_N)$ ; the extension to  $\mathcal{O}(v_\mu)$  adds small form factor corrections, but does not change any of the essential features of the CLFV physics.

If one includes all first-order effects of velocity, whether associated with the nucleon or muon, the NRET operator basis in eq. (3.23) expands to [172]

$$\mathcal{L}_{\text{eff}}^{\text{NRET}} = \sum_{N=n,p} \sum_{i=1}^{16} c_i^N \mathcal{O}_i^N + \sum_{N=n,p} \sum_{i \in I} b_i^N \mathcal{O}_i^{f,N}, \quad (3.35)$$

where the second sum is over ten new operators linear in  $\vec{v}_\mu$ , indexed by the set  $I = \{2, 3, 5, 7, 8, 12, 13, 14, 15, 16\}$ , which arise from the muon's lower component,

$$\mathcal{O}_2^{f'} = i\hat{q} \cdot \frac{\vec{v}_\mu}{2} 1_N, \quad \mathcal{O}_3^f = i\hat{q} \cdot \left[ \frac{\vec{v}_\mu}{2} \times \vec{\sigma}_L \right] 1_N, \quad (3.36a)$$

$$\mathcal{O}_5^f = \left( i\hat{q} \times \frac{\vec{v}_\mu}{2} \right) \cdot \vec{\sigma}_N, \quad \mathcal{O}_7^f = \frac{\vec{v}_\mu}{2} \cdot \vec{\sigma}_L 1_N, \quad (3.36b)$$

$$\mathcal{O}_8^f = \frac{\vec{v}_\mu}{2} \cdot \vec{\sigma}_N, \quad \mathcal{O}_{12}^f = \left[ \frac{\vec{v}_\mu}{2} \times \vec{\sigma}_L \right] \cdot \vec{\sigma}_N, \quad (3.36c)$$

$$\mathcal{O}_{13}^{f'} = \left( i\hat{q} \times \left[ \frac{\vec{v}_\mu}{2} \times \vec{\sigma}_L \right] \right) \cdot \vec{\sigma}_N, \quad \mathcal{O}_{14}^f = \frac{\vec{v}_\mu}{2} \cdot \vec{\sigma}_L i\hat{q} \cdot \vec{\sigma}_N, \quad (3.36d)$$

$$\mathcal{O}_{15}^f = i\hat{q} \cdot \left[ \frac{\vec{v}_\mu}{2} \times \vec{\sigma}_L \right] i\hat{q} \cdot \vec{\sigma}_N, \quad \mathcal{O}_{16}^{f'} = i\hat{q} \cdot \frac{\vec{v}_\mu}{2} i\hat{q} \cdot \vec{\sigma}_N, \quad (3.36e)$$

with the  $b_i^N$  the associated LECs. Although there are only 10 additional operators, they are labeled in analogy with the 16 upper component operators:  $\mathcal{O}_i \leftrightarrow \mathcal{O}i^f$  under the exchange  $\vec{v}_N \leftrightarrow \vec{v}_\mu/2$ . Here we employ  $\vec{v}_\mu/2$  because this operator, when acting on the muon's upper Dirac component, generates the lower component. The complete expression for  $\Gamma(\mu \rightarrow e)$  with all velocities handled through linear order is given in Eq. (B3) of ref. [172]. The new public computer codes discussed in section 3.6 are the first to properly include the effects of  $\vec{v}_\mu$ .

## 3.4 Matching quarks and gluons to nucleons

We turn next to the nonperturbative matching from WET to NRET, starting with single nucleon matrix elements.

### 3.4.1 Nucleon matrix elements

For the nucleon matrix elements, we use a notation closely resembling that of refs. [186, 187]<sup>4</sup>

---

<sup>4</sup>The difference is in the definitions of the tensor form factors,  $\hat{F}_{T,i}^{q/N} \equiv F_{T,i}^{q/N}/m_q$ , where  $F_{T,i}^{q/N}$ , with  $i = 0, 1, 2$ , are the form factors in [186, 187]. This choice reflects the normalization of the tensor current operators in WET basis, section 3.2. For scalar and pseudoscalar form factors  $F_S^{q/N}$ ,  $F_P^{q/N}$  we keep the  $m_q$  prefactors in the currents, since the form factors thus defined are more precisely known. Note that the definitions of  $F_{\tilde{\gamma}}$  and  $F_{\tilde{G}}$  form factors include minus signs in order to match [186, 187], where the  $\epsilon^{0123} = +1$  convention was used.

$$\langle N' | \bar{q} \gamma^\mu q | N \rangle = \bar{u}'_N \left[ F_1^{q/N}(q_{\text{rel.}}^2) \gamma^\mu - \frac{i}{2m_N} F_2^{q/N}(q_{\text{rel.}}^2) \sigma^{\mu\nu} q_\nu \right] u_N , \quad (3.37)$$

$$\langle N' | \bar{q} \gamma^\mu \gamma_5 q | N \rangle = \bar{u}'_N \left[ F_A^{q/N}(q_{\text{rel.}}^2) \gamma^\mu \gamma_5 - \frac{1}{2m_N} F_{P'}^{q/N}(q_{\text{rel.}}^2) \gamma_5 q^\mu \right] u_N , \quad (3.38)$$

$$\langle N' | m_q \bar{q} q | N \rangle = F_S^{q/N}(q_{\text{rel.}}^2) \bar{u}'_N u_N , \quad (3.39)$$

$$\langle N' | m_q \bar{q} i \gamma_5 q | N \rangle = F_P^{q/N}(q_{\text{rel.}}^2) \bar{u}'_N i \gamma_5 u_N , \quad (3.40)$$

$$\langle N' | \frac{\alpha_s}{12\pi} G^{a\mu\nu} G_{\mu\nu}^a | N \rangle = F_G^N(q_{\text{rel.}}^2) \bar{u}'_N u_N , \quad (3.41)$$

$$\langle N' | \frac{\alpha_s}{8\pi} G^{a\mu\nu} \tilde{G}_{\mu\nu}^a | N \rangle = -F_{\tilde{G}}^N(q_{\text{rel.}}^2) \bar{u}'_N i \gamma_5 u_N , \quad (3.42)$$

$$\begin{aligned} \langle N' | \bar{q} \sigma^{\mu\nu} q | N \rangle &= \bar{u}'_N \left[ \hat{F}_{T,0}^{q/N}(q_{\text{rel.}}^2) \sigma^{\mu\nu} - \frac{i}{2m_N} \gamma^{[\mu} q^{\nu]} \hat{F}_{T,1}^{q/N}(q_{\text{rel.}}^2) \right. \\ &\quad \left. - \frac{i}{m_N^2} q^{[\mu} k_{12}^{\nu]} \hat{F}_{T,2}^{q/N}(q_{\text{rel.}}^2) \right] u_N , \end{aligned} \quad (3.43)$$

$$\langle N' | \frac{\alpha}{12\pi} F^{\mu\nu} F_{\mu\nu} | N \rangle = F_\gamma^N(q_{\text{rel.}}^2) \bar{u}'_N u_N , \quad (3.44)$$

$$\langle N' | \frac{\alpha}{8\pi} F^{\mu\nu} \tilde{F}_{\mu\nu} | N \rangle = -F_{\tilde{\gamma}}^N(q_{\text{rel.}}^2) \bar{u}'_N i \gamma_5 u_N . \quad (3.45)$$

Here we shortened  $\langle N' | = \langle N(k_2) |$ ,  $| N \rangle = | N(k_1) \rangle$ ,  $\bar{u}'_N = \bar{u}_N(k_2)$ ,  $u_N = u_N(k_1)$  and introduced  $q^\mu = k_1^\mu - k_2^\mu$ ,  $k_{12}^\mu = k_1^\mu + k_2^\mu$ , with

$$q_{\text{rel.}}^2 \equiv q_\mu q^\mu \simeq -|\vec{q}|^2 \equiv -q^2 . \quad (3.46)$$

Compared to ref. [186], the definition of the momentum exchange  $q^\mu$  differs by a sign (but the definitions of form factors coincide). For covariant derivative we use  $D_\mu \psi = (\partial_\mu + ieQ_\psi A_\mu)\psi$ , where  $Q_\psi$  is the electric charge. The antisymmetrized tensors are defined as  $\gamma^{[\mu} q^{\nu]} = \gamma^\mu q^\nu - \gamma^\nu q^\mu$ , and similarly for  $q^{[\mu} k_{12}^{\nu]}$  and  $\gamma^{[\mu} \not{q} \gamma^{\nu]}$ . For CP-violating light new physics, additional form factors appear on right-hand sides (RHS) of eqs. (3.37), (3.38) and (3.43). These are expected to be small and are discussed in appendix C of [3]. The numerical values of the form factors for  $\mu \rightarrow e$  conversion in  ${}^{27}\text{Al}$  are derived in appendix B.2.

### 3.4.2 Covariant nucleon-level interactions

To facilitate matching between nuclear NRET and WET, we follow ref. [172] and introduce an intermediate step — a set of covariant single-nucleon operators and corresponding LECs. We denote the resulting interaction as

$$\mathcal{L}_{\text{eff}}^{\text{cov}} = \sum_{N=n,p} \sum_{j=1}^{32} d_j^N \mathcal{L}_{\text{int}}^{j,N} . \quad (3.47)$$

The Lorentz covariant operators  $\mathcal{L}_{\text{int}}^{j,N}$  are listed in appendix B.1.2, in the first columns of tables B.1 and B.2. The operators in table B.1 appear in ref. [172], where all covariant interactions generated from scalar or vector mediators were enumerated. Here, we extend this set to include tensor-mediated interactions, listed in the first column of table B.2.

The WET is matched onto  $\mathcal{L}_{\text{eff}}^{\text{cov}}$ , relating the LECs of the former to the CLFV coefficients  $d_j^N$  of the nucleon-level interaction that we employ below  $\Lambda_\chi$ . In this nonperturbative matching, we use the definitions of the nucleon matrix elements in eqs. (3.37) and (3.45), with the corresponding results for  $d_j^N$  coefficients listed in appendix B.1.1, eqs. (B.1) and (B.32). The  $d_i^N$  coefficients — expressed in the proton/neutron basis — are readily converted into the isospin basis via

$$d_i^0 = \frac{1}{2} (d_i^p + d_i^n), \quad d_i^1 = \frac{1}{2} (d_i^p - d_i^n). \quad (3.48)$$

### 3.4.3 The NRET

Because the momentum scale in  $\mu \rightarrow e$  conversion is set by  $m_\mu \ll m_N$ , we can perform a nonrelativistic reduction of the covariant operators,  $\mathcal{L}_{\text{int}}^{j,N}$ , to obtain the NRET. This reduces the number of nucleon-level operators while generating an interaction compatible with standard nuclear calculations, which are typically nonrelativistic. Since we consider only elastic  $\mu \rightarrow e$  conversion, and since the nuclear recoil energy  $\approx m_\mu^2/M_T$  is extremely small, the reduction can be done with  $q^0 \equiv 0$ .

The relativistic reduction of operators  $\mathcal{L}_{\text{int}}^{1-20}$  — the interactions arising from scalar and vector mediators — to their corresponding NRET forms was done in ref. [172]. For convenience those results are summarized in appendix B.1.2, with the resulting  $\mathcal{O}_i^N$  and  $\mathcal{O}_i^{f,N}$  displayed in tables B.1 and B.3, respectively. The corresponding results from the nonrelativistic reduction of 12 new tensor-mediated interactions are given in tables B.2 and B.4, respectively. (We note that certain tensor operators were also considered recently in [188].) The final columns of these tables relate the relativistic  $\{d_i^N\}$  to the appropriate  $\{c_i^N, b_i^N\}$  NRET LEC combinations.

Combining with the results for the  $d_i^N$  in appendix B.1.1, we then obtain for the  $c_i^N$

$$\begin{aligned} c_1^N &= -\frac{\alpha}{\pi q} \hat{\mathcal{C}}_1^{(5)} \sum_q Q_q F_1^{q/N} + \sum_q \hat{\mathcal{C}}_{1,q}^{(6)} F_1^{q/N} + \sum_q \frac{1}{m_q} \hat{\mathcal{C}}_{5,q}^{(6)} F_S^{q/N} \\ &\quad - \frac{q}{m_N} \sum_q \hat{\mathcal{C}}_{9,q}^{(6)} (\hat{F}_{T,0}^{q/N} - \hat{F}_{T,1}^{q/N} + 4\hat{F}_{T,2}^{q/N}) \\ &\quad + \hat{\mathcal{C}}_1^{(7)} F_G^N + \hat{\mathcal{C}}_5^{(7)} F_\gamma^N + (q + m_+) \sum_q \hat{\mathcal{C}}_{9,q}^{(7)} F_1^{q/N} \\ &\quad - \frac{q^2}{2m_N} \sum_q \hat{\mathcal{C}}_{13,q}^{(7)} \left[ \hat{F}_{T,0}^{q/N} - \hat{F}_{T,1}^{q/N} + \left( 4 + \frac{q^2}{m_N^2} \right) \hat{F}_{T,2}^{q/N} \right], \end{aligned} \tag{3.49}$$

$$c_2^N = i \left[ \sum_q \hat{\mathcal{C}}_{1,q}^{(6)} F_1^{q/N} + m_+ \sum_q \hat{\mathcal{C}}_{9,q}^{(7)} F_1^{q/N} + \frac{q^2}{2m_N} \sum_q \hat{\mathcal{C}}_{13,q}^{(7)} (\hat{F}_{T,1}^{q/N} - 4\hat{F}_{T,2}^{q/N}) \right], \tag{3.50}$$

$$c_3^N = -2 \sum_q \hat{\mathcal{C}}_{9,q}^{(6)} \hat{F}_{T,0}^{q/N} - q \sum_q \hat{\mathcal{C}}_{13,q}^{(7)} \left( \hat{F}_{T,0}^{q/N} + \frac{q^2}{m_N^2} \hat{F}_{T,2}^{q/N} \right), \tag{3.51}$$

$$\begin{aligned} c_4^N &= -\frac{\alpha}{2\pi m_N} \hat{\mathcal{C}}_1^{(5)} \sum_q Q_q (F_1^{q/N} + F_2^{q/N}) - \frac{q}{2m_N} \sum_q \hat{\mathcal{C}}_{1,q}^{(6)} (F_1^{q/N} + F_2^{q/N}) \\ &\quad - \sum_q \hat{\mathcal{C}}_{4,q}^{(6)} F_A^{q/N} + 2 \sum_q \hat{\mathcal{C}}_{9,q}^{(6)} \hat{F}_{T,0}^{q/N} - \frac{q}{2m_N} (m_+ - q) \sum_q \hat{\mathcal{C}}_{9,q}^{(7)} (F_1^{q/N} + F_2^{q/N}) \\ &\quad + i(m_- - q) \sum_q \hat{\mathcal{C}}_{12,q}^{(7)} F_A^{q/N} - q \sum_q \hat{\mathcal{C}}_{13,q}^{(7)} \left[ \hat{F}_{T,0}^{q/N} + \frac{q^2}{4m_N^2} \hat{F}_{T,1}^{q/N} \right], \end{aligned} \tag{3.52}$$

$$\begin{aligned} c_5^N &= -\frac{\alpha}{\pi q} \sum_q \hat{\mathcal{C}}_1^{(5)} Q_q F_1^{q/N} - \sum_q \hat{\mathcal{C}}_{1,q}^{(6)} F_1^{q/N} \\ &\quad - (m_+ - q) \sum_q \hat{\mathcal{C}}_{9,q}^{(7)} F_1^{q/N} - \frac{q^2}{2m_N} \sum_q \hat{\mathcal{C}}_{13,q}^{(7)} (\hat{F}_{T,1}^{q/N} - 4\hat{F}_{T,2}^{q/N}), \end{aligned} \tag{3.53}$$

$$\begin{aligned} c_6^N &= -\frac{\alpha}{2\pi m_N} \sum_q \hat{\mathcal{C}}_1^{(5)} Q_q (F_1^{q/N} + F_2^{q/N}) - \frac{q}{2m_N} \sum_q \hat{\mathcal{C}}_{1,q}^{(6)} (F_1^{q/N} + F_2^{q/N}) \\ &\quad - \frac{qm_+}{4m_N^2} \sum_q \hat{\mathcal{C}}_{4,q}^{(6)} F_{P'}^{q/N} - \frac{q}{2m_N} \sum_q \frac{1}{m_q} \hat{\mathcal{C}}_{8,q}^{(6)} F_P^{q/N} + \frac{q}{2m_N} \left( \hat{\mathcal{C}}_4^{(7)} F_G^N + \hat{\mathcal{C}}_8^{(7)} F_{\tilde{\gamma}}^N \right) \\ &\quad - \frac{(m_+ - q)q}{2m_N} \sum_q \hat{\mathcal{C}}_{9,q}^{(7)} (F_1^{q/N} + F_2^{q/N}) - iq \sum_q \hat{\mathcal{C}}_{12,q}^{(7)} \left( F_A^{q/N} - \frac{m_+ m_-}{4m_N^2} F_{P'}^{q/N} \right) \\ &\quad - q \sum_q \hat{\mathcal{C}}_{13,q}^{(7)} \left( \hat{F}_{T,0}^{q/N} + \frac{q^2}{4m_N^2} \hat{F}_{T,1}^{q/N} \right) + iq \sum_q \hat{\mathcal{C}}_{16,q}^{(7)} \hat{F}_{T,0}^{q/N}, \end{aligned} \tag{3.54}$$

$$c_7^N = \sum_q \hat{\mathcal{C}}_{3,q}^{(6)} F_A^{q/N} + (m_+ + q) \sum_q \hat{\mathcal{C}}_{11,q}^{(7)} F_A^{q/N}, \tag{3.55}$$

$$\begin{aligned} c_8^N &= i \frac{\alpha}{\pi q} \sum_q \hat{\mathcal{C}}_2^{(5)} Q_q F_1^{q/N} - \sum_q \hat{\mathcal{C}}_{2,q}^{(6)} F_1^{q/N} \\ &\quad + i(m_- - q) \sum_q \hat{\mathcal{C}}_{10,q}^{(7)} F_1^{q/N} - \frac{q^2}{2m_N} \sum_q \hat{\mathcal{C}}_{14,q}^{(7)} (\hat{F}_{T,1}^{q/N} - 4\hat{F}_{T,2}^{q/N}), \end{aligned} \tag{3.56}$$

$$\begin{aligned}
c_9^N &= i \frac{\alpha}{2\pi m_N} \sum_q \hat{\mathcal{C}}_2^{(5)} Q_q (F_1^{q/N} + F_2^{q/N}) - \frac{q}{2m_N} \sum_q \hat{\mathcal{C}}_{2,q}^{(6)} (F_1^{q/N} + F_2^{q/N}) \\
&\quad - \sum_q \hat{\mathcal{C}}_{3,q}^{(6)} F_A^{q/N} - 2i \sum_q \hat{\mathcal{C}}_{10,q}^{(6)} \hat{F}_{T,0}^{q/N} \\
&\quad + i \frac{(m_- - q)q}{2m_N} \sum_q \hat{\mathcal{C}}_{10,q}^{(7)} (F_1^{q/N} + F_2^{q/N}) - (m_+ - q) \sum_q \hat{\mathcal{C}}_{11,q}^{(7)} F_A^{q/N} \\
&\quad - q \sum_q \hat{\mathcal{C}}_{14,q}^{(7)} \left( \hat{F}_{T,0}^{q/N} + \frac{q^2}{4m_N^2} \hat{F}_{T,1}^{q/N} \right), \tag{3.57}
\end{aligned}$$

$$\begin{aligned}
c_{10}^N &= i \sum_q \hat{\mathcal{C}}_{3,q}^{(6)} \left( F_A^{q/N} - \frac{q m_-}{4m_N^2} F_{P'}^{q/N} \right) + \frac{q}{2m_N} \sum_q \frac{1}{m_q} \hat{\mathcal{C}}_{7,q}^{(6)} F_P^{q/N} - 2 \sum_q \hat{\mathcal{C}}_{10,q}^{(6)} \hat{F}_{T,0}^{q/N} \\
&\quad - \frac{q}{2m_N} \left( \hat{\mathcal{C}}_3^{(7)} F_G^N + \hat{\mathcal{C}}_7^{(7)} F_\gamma^N \right) + im_+ \sum_q \hat{\mathcal{C}}_{11,q}^{(7)} \left( F_A^{q/N} - \frac{q m_-}{4m_N^2} F_{P'}^{q/N} \right) \\
&\quad - q \sum_q \hat{\mathcal{C}}_{15,q}^{(7)} \hat{F}_{T,0}^{q/N}, \tag{3.58}
\end{aligned}$$

$$\begin{aligned}
c_{11}^N &= \frac{\alpha}{\pi q} \sum_q \hat{\mathcal{C}}_2^{(5)} Q_q F_1^{q/N} - i \sum_q \hat{\mathcal{C}}_{2,q}^{(6)} F_1^{q/N} - \sum_q \frac{1}{m_q} \hat{\mathcal{C}}_{6,q}^{(6)} F_S^{q/N} \\
&\quad + \frac{q}{m_N} \sum_q \hat{\mathcal{C}}_{10,q}^{(6)} \left( \hat{F}_{T,0}^{q/N} - \hat{F}_{T,1}^{q/N} + 4\hat{F}_{T,2}^{q/N} \right) - \mathcal{C}_2^{(7)} F_G^N - \mathcal{C}_6^{(7)} F_\gamma^N \\
&\quad - (m_- + q) \sum_q \hat{\mathcal{C}}_{10,q}^{(7)} F_1^{q/N} + i \frac{q^2}{2m_N} \sum_q \hat{\mathcal{C}}_{14,q}^{(7)} \left[ \hat{F}_{T,0}^{q/N} - \hat{F}_{T,1}^{q/N} + \left( 4 + \frac{q^2}{m_N^2} \right) \hat{F}_{T,2}^{q/N} \right], \tag{3.59}
\end{aligned}$$

$$c_{12}^N = -2 \sum_q \hat{\mathcal{C}}_{10,q}^{(6)} \hat{F}_{T,0}^{q/N} + q \sum_q \hat{\mathcal{C}}_{15,q}^{(7)} \hat{F}_{T,0}^{q/N}, \tag{3.60}$$

$$c_{13}^N = -2i \sum_q \hat{\mathcal{C}}_{9,q}^{(6)} \hat{F}_{T,0}^{q/N} + q \sum_q \hat{\mathcal{C}}_{16,q}^{(7)} \hat{F}_{T,0}^{q/N}, \tag{3.61}$$

$$c_{14}^N = -i \sum_q \hat{\mathcal{C}}_{4,q}^{(6)} F_A^{q/N} - (m_- + q) \sum_q \hat{\mathcal{C}}_{12,q}^{(7)} F_A^{q/N}, \tag{3.62}$$

$$c_{15}^N = iq \sum_q \hat{\mathcal{C}}_{14,q}^{(7)} \left( \hat{F}_{T,0}^{q/N} + \frac{q^2}{m_N^2} \hat{F}_{T,2}^{q/N} \right) + q \sum_q \hat{\mathcal{C}}_{15,q}^{(7)} \hat{F}_{T,0}^{q/N}, \tag{3.63}$$

$$c_{16}^N = i \frac{\alpha}{\pi q} \sum_q \hat{\mathcal{C}}_2^{(5)} Q_q F_1^{q/N} - iq \sum_q \hat{\mathcal{C}}_{10,q}^{(7)} F_1^{q/N}, \tag{3.64}$$

where all the form factors are understood to be evaluated at  $q_{\text{rel}}^2 = -q_{\text{eff}}^2$ , and we defined

$$m_\pm = m_\mu \pm m_e. \tag{3.65}$$

Similarly, one can express the  $b_i^N$  coefficients in terms of  $\hat{\mathcal{C}}_i^{(d)}$ . While the  $b_i^N$  coefficients are included in our numerical results, as well as in the **MuonBridge** computer code, they generate only subleading corrections. As a result, they are not relevant to the present qualitative discussion, and we do not show their matching explicitly.

Note that the NRET LECs  $c_i^N$  are in general complex. First of all, the Wilson coefficients  $\hat{\mathcal{C}}_i^{(d)}$  can be complex, given that the lepton-flavor-violating WET operators in eq. (3.1) are not

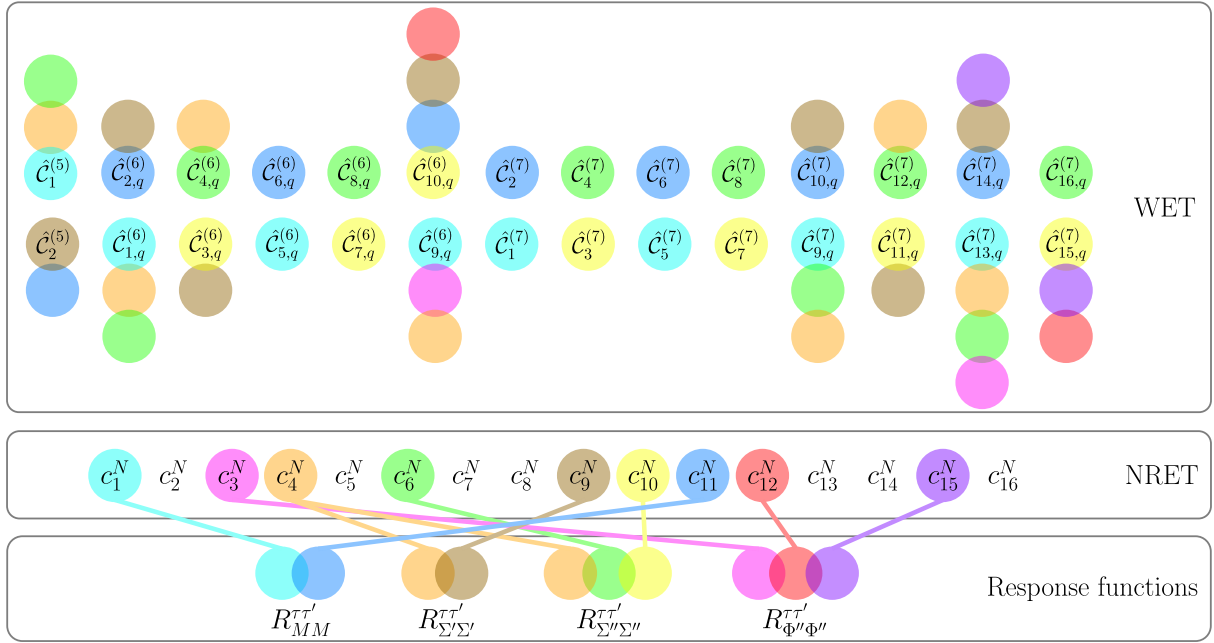


FIGURE 3.2: A graphical representation of how different WET operators eq. (3.1) contribute to the  $\mu \rightarrow e$  conversion rate, in which we keep the terms that remain in the  $v_N, v_\mu \rightarrow 0$  limit, as well as the coherently enhanced but velocity-suppressed contribution from the  $W_{\Phi''\Phi''}$  response function. The NRET coefficients  $c_i^N$  receive contributions from WET Wilson coefficients  $\hat{C}_i^{(d)}$ , as denoted with the corresponding colored circles (only the  $c_i^N$  that contribute to the numerically leading response functions are considered). These then enter the leptonic response factors  $R_{OO'}^{\tau\tau'}$ , that multiply various nuclear response functions, as indicated. For instance,  $\hat{C}_1^{(5)}$  contributes to  $c_1^N, c_4^N$  and  $c_6^N$ , and these lead to  $W_{MM}^{\tau\tau'}, W_{\Sigma'\Sigma'}^{\tau\tau'}, W_{\Sigma''\Sigma''}^{\tau\tau'}$  nuclear responses.

hermitian (note though, that they are defined in such a way that they would have been hermitian, had the leptonic currents been flavor conserving). However, even if  $\hat{C}_i^{(d)}$  are taken to be real, the  $c_i^N$  are still complex in general, due to the appearance of explicit factors of  $i$  in eqs. (3.49) and (3.64). These can be traced back to the fact that  $i\hat{q}$  used to construct the NRET operators actually represents two operators, the electron velocity and the three-momentum transfer, see the discussion in Appendix A of ref. [172].

Using the results for  $c_i^N$  in eqs. (3.49) and (3.64), together with the rate formula in eq. (3.25) and the known nuclear response functions,  $W_a^{\tau\tau'}$ , one can obtain predictions for the  $\mu \rightarrow e$  conversion rate in terms of the WET Wilson coefficients  $\hat{C}_i^{(d)}$ . Here, we focus on the leading contribution to  $\Gamma(\mu \rightarrow e)$ , i.e., those terms that are nonzero in the  $v_N, v_\mu \rightarrow 0$  limit, supplemented by the coherently enhanced but velocity suppressed contribution from the  $W_{\Phi''\Phi''}$  response function, which in general contributes at the same level as the spin-dependent nuclear response functions, cf., eq. (3.34). The graphical representation of how the WET Wilson coefficients  $\hat{C}_i^{(d)}$  map onto the leading prediction for the  $\mu \rightarrow e$  conversion rate is shown in fig. 3.2.

We make several phenomenologically relevant observations:

- Dimension-5 WET operators  $Q_{1,2}^{(5)}$ , i.e., the transition magnetic and electric moments, induce the coherently enhanced spin-independent,  $W_{MM}^{\tau\tau'}$ , as well as the spin-dependent,

$W_{\Sigma'\Sigma'}^{\tau\tau'}$ ,  $W_{\Sigma''\Sigma''}^{\tau\tau'}$ , nuclear responses. At dimension 6 also  $W_{\Phi''\Phi''}^{\tau\tau'}$  is generated (although only from  $\hat{C}_{9,q}^{(6)}$  and  $\hat{C}_{10,q}^{(6)}$ ).

- Even if only a single Wilson coefficient  $\hat{C}_i^{(d)}$  is nonzero, this always results in a nonzero contribution from at least one of the numerically leading nuclear response functions.
- All 16 NRET operators are generated by the dimension  $d \leq 7$  WET basis. At dimension  $d \leq 6$ , all NRET operators except  $\mathcal{O}_{15}^N$  are generated.
- Not all NRET operators  $\mathcal{O}_i^N$  in eq. (3.35) contribute to the above numerically leading nuclear response functions:  $c_5^N$ ,  $c_8^N$ , and  $c_{13}^N$  contribute only to numerically subleading nuclear responses, whereas  $c_2^N$ ,  $c_7^N$ ,  $c_{14}^N$ , and  $c_{16}^N$  do not contribute at all to elastic  $\mu \rightarrow e$  conversion due to the parity and time-reversal properties of the nuclear response functions that they generate [172].
- Working at this numerically leading order, certain WET Wilson coefficients contribute to just a single NRET operator:<sup>5</sup> the Wilson coefficients  $\hat{C}_{5,q}^{(6)}, \hat{C}_1^{(7)}, \hat{C}_5^{(7)}$  only contribute to  $c_1^N$ ;  $\hat{C}_{6,q}^{(6)}, \hat{C}_2^{(7)}, \hat{C}_6^{(7)}$  only to  $c_{11}^N$ ;  $\hat{C}_{7,q}^{(6)}, \hat{C}_3^{(7)}, \hat{C}_7^{(7)}$  only to  $c_{10}^N$ ; and  $\hat{C}_{8,q}^{(6)}, \hat{C}_4^{(7)}, \hat{C}_8^{(7)}$  only to  $c_6^N$ . The Wilson coefficients only contributing to a single  $c_i^N$  cannot be distinguished from each other using measurements on different targets, since they always enter in the same linear combination, unless the much smaller  $v_\mu$  suppressed relativistic corrections and the small corrections from the  $q^2$  dependence of nucleon form factors can also be taken into account (i.e., the total theoretical error on the prediction for  $\Gamma(\mu \rightarrow e)$  reaches the level where these corrections become relevant).
- The  $q_{\text{eff}}$  dependence of CLFV coefficients  $R_{MM}^{\tau\tau'}$ ,  $R_{\Sigma'\Sigma'}^{\tau\tau'}$ ,  $R_{\Sigma''\Sigma''}^{\tau\tau'}$  and  $R_{\Phi''\Phi''}^{\tau\tau'}$  comes from the  $q$  dependence of  $c_i^N$  in eqs. (3.49) and (3.64) (for heavy new physics the WET Wilson coefficients  $\mathcal{C}_i^{(d)}$  are  $q$  independent). Since  $q_{\text{eff}}$  depends only mildly on the chosen target nucleus, the  $c_i^N$  entering the predictions for the  $\mu \rightarrow e$  rate are effectively constant, i.e., independent of the nuclear target. In this limit there are only 12 combinations of  $c_i^N$ , i.e., the combinations multiplying  $R_{MM}^{\tau\tau'}$ ,  $R_{\Sigma'\Sigma'}^{\tau\tau'}$ ,  $R_{\Sigma''\Sigma''}^{\tau\tau'}$  and  $R_{\Phi''\Phi''}^{\tau\tau'}$  for  $\tau^{(')} = 0, 1$  that can be measured.

At a future time when  $\mu \rightarrow e$  conversion has been discovered in several different targets, one could use the “bottom-up” approach to efficiently encode the CLFV physics in the NRET LECs, which would then serve as constraints on generic UV models. Given existing uncertainties in nuclear response calculations — perhaps in the range of tens of percent — details like the variation of  $q_{\text{eff}}$  with target could be neglected. (If our ability to compute nuclear responses were ever to reach the few percent level, one would need to exercise more care.) In general, one

---

<sup>5</sup>We ignored for simplicity the quark flavor in this counting. A more precise statement is that a certain linear combination of  $\hat{C}_{5,u}^{(6)}, \hat{C}_{5,d}^{(6)}, \hat{C}_{5,s}^{(6)}, \hat{C}_1^{(7)}, \hat{C}_5^{(7)}$  enters  $c_1^p$ , while a different linear combination enters  $c_1^n$ , and similarly for the other  $c_i^N$ .

would not be able to determine individual LECS, but only the combinations that appear in the expressions for the  $R_{OO'}^{\tau\tau'}$ . To do more, one would need additional constraints on CLFV, beyond those available from elastic  $\mu \rightarrow e$  conversion.

The NRET employs single-nucleon currents and charges, but could in principle be extended to include a similar set of Galilean-invariant two-body operators. For certain cases, like the Rayleigh operators, these two-body currents can be important [189]. Due to the averaging properties of nuclei, most of the effects of such contributions (assuming they are not treated explicitly) would be absorbed into the one-body LECs, making them effective, as discussed in Sec. IIIG of ref. [172]. While most of the missing physics would thus be properly incorporated into the fitted LECs, one would need to account for the associated renormalization and operator mixing, before relating empirically determined LECs to the predictions of an underlying model.

### 3.5 Predictions from UV models

Next we turn to a few examples of new physics models that can lead to  $\mu \rightarrow e$  conversions. In the “top-down” approach, our results can be used to obtain predictions for  $\Gamma(\mu \rightarrow e)$  in a particular UV model. In this case, one must first match the UV model onto SMEFT by integrating out the mediators at scale  $\mu \approx m_{\text{mediator}}$ , then RG evolve in SMEFT down to  $\mu \approx m_W$ , match onto WET, and finally RG evolve down to  $\mu = 2$  GeV. At this point one can then use our results, encoded in the `MuonBridge` code suite, to obtain the prediction for the  $\mu \rightarrow e$  transition rate. In section 3.5.1 we first illustrate the expected reach of the upcoming  $\mu \rightarrow e$  experiments in terms of bounds on single SMEFT Wilson coefficients. In sections 3.5.2 and 3.5.3, on the other hand, we use concrete new physics models. From the large array of possible UV examples, we choose two that best highlight the strengths of our systematic EFT based approach:  $\mu \rightarrow e$  conversions induced by leptoquark exchanges, which lead to scalar, vector, and tensor currents (section 3.5.2), and  $\mu \rightarrow e$  conversions induced by light pseudoscalar/ALP exchanges, which can also be covered by our formalism, but now with  $q^2$ -dependent Wilson coefficients  $\hat{\mathcal{C}}_i^{(d)}$  (section 3.5.3).

#### 3.5.1 Bounds on UV Wilson coefficients

We start by considering the case where the UV theory generates a single SMEFT operator above the electroweak scale. This is a standard approach in phenomenological EFT analysis used to estimate the scales that are being probed by experiments, without consideration for the ability or inability of plausible new physics models to realize these single-operator contributions.

For concreteness, let us consider a UV theory that, after integrating out the heavy degrees of freedom at a scale  $\mu = \Lambda$  ( $\sim$  heavy mediator mass), generates just a single dimension-6 SMEFT

operator in the Warsaw basis

$$\mathcal{L}_{\text{SMEFT,UV}} = \frac{\mathcal{C}_i}{\Lambda^2} \mathcal{Q}_i. \quad (3.66)$$

To arrive at the prediction for the  $\mu \rightarrow e$  conversion rate, as described in section 3.3, one first needs to RGE evolve from the scale  $\mu = \Lambda$  to  $\mu = 2 \text{ GeV}$  using the tower of EFTs, from SMEFT to WET with  $n_f = 5$  to WET with  $n_f = 4$  flavors followed by a tree-level matching to WET with  $n_f = 3$ , as shown in fig. 3.1. We perform the one-loop RG running using `wilson` [173] and then use `MuonConverter` to obtain the prediction for the  $\mu \rightarrow e$  conversion rate. Using the projected experimental sensitivity  $B(\mu^- + \text{Al} \rightarrow e^- + \text{Al}) < 10^{-17}$ , we show in fig. 3.3 the implied bounds on  $\Lambda_{\text{CLFV},i} = \Lambda/\sqrt{\mathcal{C}_i}$ , if no signal is found. We perform the calculation for each dimension-6 CLFV SMEFT operator  $\mathcal{Q}_i$  in the Warsaw basis that can induce  $\mu \rightarrow e$  transitions.

For each operator in fig. 3.3, the bound is obtained by identifying the UV scale  $\Lambda_{\text{CLFV},i}$  that, after one-loop RGE evolution to  $\mu = 2 \text{ GeV}$ , produces a conversion rate saturating the projected single-event sensitivities of the upcoming Mu2e and COMET experiments. The magnitude of the initial Wilson coefficient, assuming  $\mathcal{C}_i = 1$ , is set by  $\Lambda_{\text{CLFV},i}^{-2}$  and scanned over ten equally spaced points in the range  $\Lambda_{\text{CLFV},i}^{-2} \in 10^{-17} - 10^{-4} \text{ GeV}^{-2}$  corresponding to new physics scales  $\Lambda_{\text{CLFV},i} \sim 100 \text{ GeV} - 10^5 \text{ TeV}$ . The resulting conversion rates are then interpolated as a function of  $\Lambda_{\text{CLFV},i}$  and a root-finding algorithm is utilized to obtain the scale at which the conversion rate crosses the projected experimental limits. The running of each operator is solved exactly via numerical integration of the one-loop RG equations from  $\mu = \Lambda$  to  $\mu = 2 \text{ GeV}$  using `wilson`. In agreement with the leading log resummation, the matchings between different thresholds are performed at tree level.

Operator-mixing induced by the one-loop running allows for non-zero limits to be placed on the purely leptonic and off-diagonal semi-leptonic SMEFT operators. This treatment is consistent as long as the logarithmically enhanced RG running contributions to dimension-six operators are numerically leading and the finite terms from loop-level matching can be ignored.

### 3.5.2 Leptoquarks

Next, we use our computational framework to analyze the  $\mu \rightarrow e$  conversion rate in the context of an explicit UV model. Specifically, we assume that the  $\mu \rightarrow e$  conversion is generated by tree-level exchange of a leptoquark scalar  $R_2$ , which then leads to vector, scalar and tensor interactions, making it an ideal showcase for quantifying the relative magnitudes and correlations between different nuclear responses. The leptoquark  $R_2$  is in the  $(\mathbf{3}, \mathbf{2}, 7/6)$  representation of the SM gauge group, so that the interaction Lagrangian is given by [190]

$$\mathcal{L} \supset -y_{2ij}^{RL} \bar{u}_R^i R_2^a \epsilon^{ab} L_L^{j,b} + y_{2ij}^{LR} \bar{e}_R^i R_2^{a*} Q_L^{j,a} + \text{h.c.}, \quad (3.67)$$

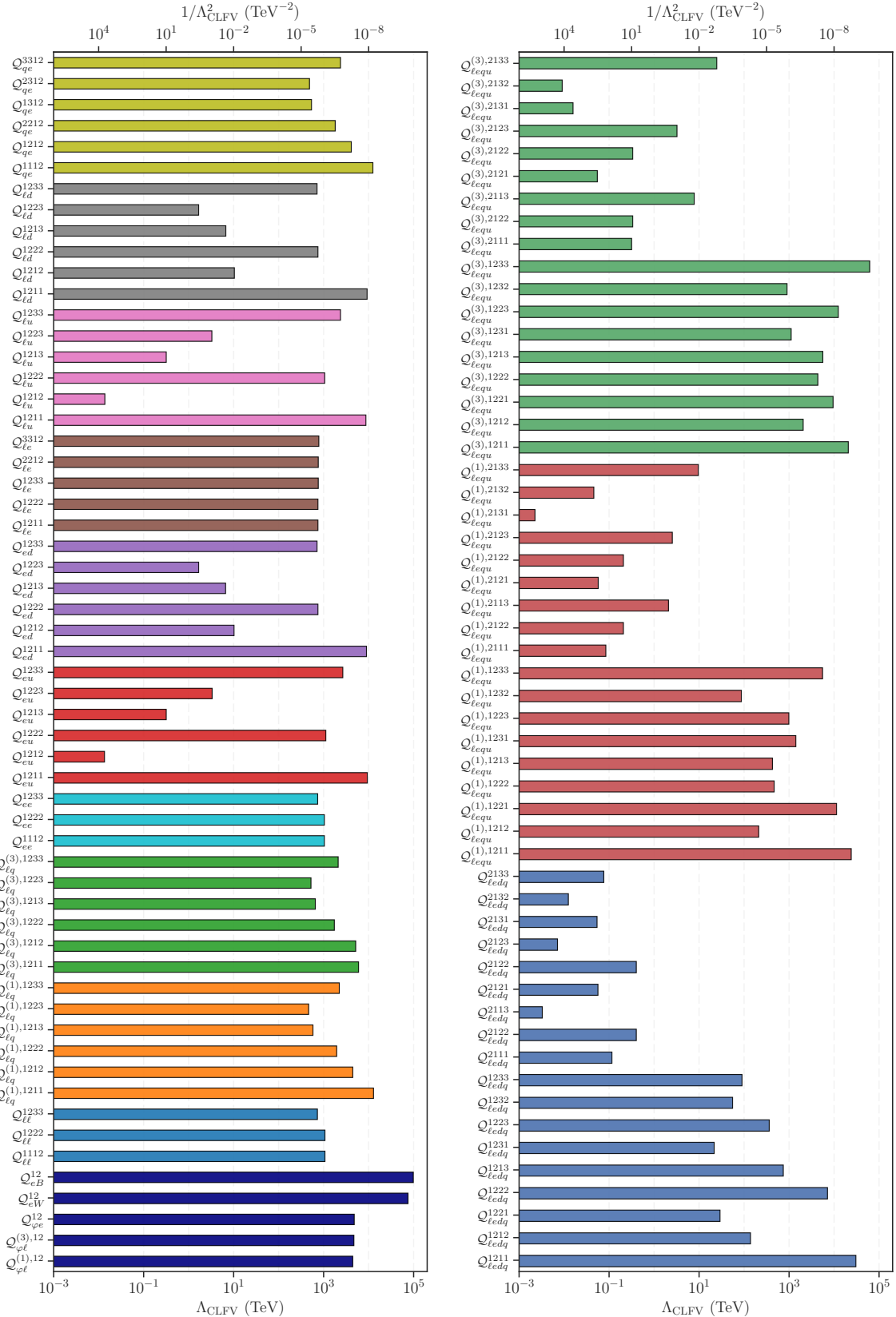


FIGURE 3.3: The energy scales probed by dimension-six SMEFT operators assuming the projected experimental limits of the future Mu2e and COMET experiments,  $B(\mu^- + \text{Al} \rightarrow e^- + \text{Al}) < 10^{-17}$ . The notation is as in [16, 17].

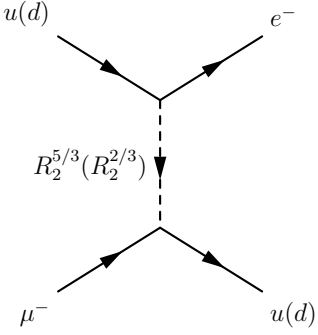


FIGURE 3.4: Diagram for tree-level contributions to  $\mu \rightarrow e$  conversion mediated by scalar leptoquark  $R_2$ . Leptoquark superscripts indicate the electric charge of the exchanged particle.

where the summation over flavor indices,  $i, j = 1, 2, 3$ , and electroweak SU(2) indices  $a, b = 1, 2$  is implicit, and we do not display the contraction of color indices.

Integrating out the leptoquark at tree level, cf. fig. 3.4, gives the following nonzero contributions to the SMEFT Wilson coefficients (we use the notation of refs. [16, 17]),

$$C_{\ell u}^{12ii} = -\frac{1}{2m_{\text{LQ}}^2} y_{2i2}^{RL} y_{2i1}^{RL*}, \quad (3.68a)$$

$$C_{qe}^{ii12} = -\frac{1}{2m_{\text{LQ}}^2} y_{22i}^{LR*} y_{21i}^{LR}, \quad (3.68b)$$

$$C_{\ell equ}^{(1),12ii} = 2C_{\ell equ}^{(3),12ii} = -\frac{1}{2m_{\text{LQ}}^2} y_{22i}^{LR*} y_{2i1}^{RL*}, \quad (3.68c)$$

$$C_{\ell equ}^{(1),21ii} = 2C_{\ell equ}^{(3),21ii} = -\frac{1}{2m_{\text{LQ}}^2} y_{2i2}^{LR} y_{21i}^{RL}, \quad (3.68d)$$

where  $m_{\text{LQ}}$  is the leptoquark mass. The Wilson coefficients in eqs. (3.68a) and (3.68b) multiply vector four-fermion operators  $(\bar{\ell}_1 \gamma_\mu \ell_2)(\bar{u}_i \gamma^\mu u_i)$  and  $(\bar{q}_i \gamma^\mu q_i)(\bar{e}_1 \gamma_\mu e_2)$ , respectively, while the Wilson coefficients in eqs. (3.68c) and (3.68d) with the superscript (1) [(3)] multiply scalar [tensor] four-fermion operators of the form  $(\bar{\ell}_1^a e_2)\epsilon_{ab}(\bar{q}_i^b u_i) [(\bar{\ell}_1^a \sigma_{\mu\nu} e_2)\epsilon_{ab}(\bar{q}_i^b \sigma^{\mu\nu} u_i)]$  and with  $1 \leftrightarrow 2$  lepton flavor indices exchanged.

The above effective interactions introduce both spin-independent as well as spin-dependent nuclear responses, when running down to low energies and matching onto NRET. Ignoring for the moment the effect of RG running, integrating out the leptoquark results in the SMEFT operators

in eq. (3.68) and gives the following nonzero contributions to the WET Wilson coefficients:

$$\hat{C}_{1,u}^{(6)} = -\hat{C}_{4,u}^{(6)} = -\frac{1}{8m_{\text{LQ}}^2} \lambda_+, \quad (3.69)$$

$$\hat{C}_{2,u}^{(6)} = -\hat{C}_{3,u}^{(6)} = -\frac{1}{8m_{\text{LQ}}^2} \lambda_-, \quad (3.70)$$

$$\hat{C}_{1,d_j}^{(6)} = \hat{C}_{2,d_j}^{(6)} = -\hat{C}_{3,d_j}^{(6)} = -\hat{C}_{4,d_j}^{(6)} = -\frac{1}{8m_{\text{LQ}}^2} \lambda'_j, \quad (3.71)$$

$$\hat{C}_{5,u}^{(6)} = -\hat{C}_{8,u}^{(6)} = 2\hat{C}_{9,u}^{(6)} = \frac{1}{8m_{\text{LQ}}^2} \lambda_{RL+}, \quad (3.72)$$

$$\hat{C}_{6,u}^{(6)} = \hat{C}_{7,u}^{(6)} = 2\hat{C}_{10,u}^{(6)} = \frac{i}{8m_{\text{LQ}}^2} \lambda_{RL-}. \quad (3.73)$$

The up-quark couplings are

$$\lambda_{\pm} = c_{1L}c_{2L}^* \pm c_{2R}c_{1R}^*, \quad \lambda_{RL\pm} = c_{2R}c_{1L} \pm c_{2L}^*c_{1R}^*, \quad (3.74)$$

where (for  $i = 1, 2$ )

$$c_{iL} = (y_2^{LR}V^\dagger)_{i1}, \quad c_{iR} = y_{21i}^{RL}, \quad (3.75)$$

The coupling to the down quarks is (for  $j = 1, 2$  down quark flavors)

$$\lambda'_j = y_{21j}^{LR}y_{22j}^{LR*}. \quad (3.76)$$

The NRET LECs that lead to coherently enhanced nuclear responses (again, ignoring RGE effects) are given by

$$\begin{aligned} c_1^N &= -\frac{1}{8m_{\text{LQ}}^2} \left\{ \lambda_+ F_1^{u/N} - \lambda_{RL+} \left[ \frac{1}{m_u} F_S^{u/N} - \frac{q}{2m_N} (\hat{F}_{T,0}^{u/N} - \hat{F}_{T,1}^{u/N} + 4\hat{F}_{T,2}^{u/N}) \right] \right\} \\ &\quad - \frac{1}{8m_{\text{LQ}}^2} \left( \lambda'_1 F_1^{d/N} + \lambda'_2 F_1^{s/N} \right), \end{aligned} \quad (3.77)$$

$$c_{11}^N = -ic_1^N (\lambda_+ \rightarrow \lambda_-, \lambda_{RL+} \rightarrow \lambda_{RL-}), \quad (3.78)$$

while the LECs that contribute to spin-dependent nuclear responses  $W_{\Sigma'\Sigma'}^{\tau\tau'}$ ,  $W_{\Sigma''\Sigma''}^{\tau\tau'}$  are

$$c_4^N = \frac{1}{8m_{\text{LQ}}^2} \left\{ \lambda_+ \left[ -F_A^{u/N} + \frac{q}{2m_N} (F_1^{u/N} + F_2^{u/N}) \right] + \lambda_{RL+} \hat{F}_{T,0}^{u/N} \right\} \\ + \frac{1}{8m_{\text{LQ}}^2} \sum_j \lambda'_j \left[ -F_A^{d_j/N} + \frac{q}{2m_N} (F_1^{d_j/N} + F_2^{d_j/N}) \right] \quad (3.79)$$

$$c_6^N = \frac{1}{8m_{\text{LQ}}^2} \frac{q}{2m_N} \left[ \lambda_+ \left( F_1^{u/N} + F_2^{u/N} - \frac{m_+}{2m_N} F_{P'}^{u/N} \right) + \frac{\lambda_{RL+}}{m_u} F_P^{u/N} \right] \\ + \frac{1}{8m_{\text{LQ}}^2} \frac{q}{m_N} \sum_j \lambda'_j \left( F_1^{d_j/N} + F_2^{d_j/N} - \frac{m_+}{2m_N} F_{P'}^{d_j/N} \right) \quad (3.80)$$

$$c_9^N = \frac{1}{8m_{\text{LQ}}^2} \left\{ \lambda_- \left[ \frac{q}{2m_N} (F_1^{u/N} + F_2^{u/N}) - F_A^{u/N} \right] + \lambda_{RL-} \hat{F}_{T,0}^{u/N} \right\} \\ + \frac{1}{8m_{\text{LQ}}^2} \sum_j \lambda'_j \left[ \frac{q}{2m_N} (F_1^{d_j/N} + F_2^{d_j/N}) - F_A^{d_j/N} \right], \quad (3.81)$$

$$c_{10}^N = \frac{i}{8m_{\text{LQ}}^2} \left[ \lambda_- \left( F_A^{u/N} - \frac{qm_-}{4m_N^2} F_{P'}^{u/N} \right) - \lambda_{RL-} \left( \hat{F}_{T,0}^{u/N} - \frac{q}{2m_N} \frac{1}{m_u} F_P^{u/N} \right) \right] \\ + \frac{i}{8m_{\text{LQ}}^2} \sum_j \lambda'_j \left( F_A^{d_j/N} - \frac{qm_-}{4m_N^2} F_{P'}^{d_j/N} \right), \quad (3.82)$$

and those that generate the coherent but velocity-suppressed  $W_{\Phi''\Phi''}^{\tau\tau'}$  nuclear response are

$$c_3^N = -\frac{1}{8m_{\text{LQ}}^2} \lambda_{RL+} \hat{F}_{T,0}^{u/N}, \quad (3.83)$$

$$c_{12}^N = -\frac{i}{8m_{\text{LQ}}^2} \lambda_{RL-} \hat{F}_{T,0}^{u/N}. \quad (3.84)$$

In addition, the NRET LECs  $c_5^N$ ,  $c_8^N$ , and  $c_{13}^N$  are nonzero but contribute only to numerically subleading nuclear response functions. The NRET LECs  $c_2^N$ ,  $c_7^N$ , and  $c_{14}^N$  are also nonzero, but do not contribute to the elastic conversion process due to the parity and time-reversal symmetries of the nuclear ground state. Numerically,

$$c_{1(11)}^p + c_{1(11)}^n = \frac{-1(+i)}{8m_{\text{LQ}}^2} \left\{ 2.91(\lambda_\pm + \lambda'_1) - [6.8(2.2) - 0.26(15)] \lambda_{RL\pm} + [2.2(2.1) \times 10^{-4} \lambda'_2] \right\}. \quad (3.85)$$

In summary, i) the LQ model leads to many different NRET coefficients, including those leading to velocity suppressed but coherently enhanced  $\Phi''$  nuclear response, and ii) it is possible that the leading, spin-independent, contribution could be accidentally small due to cancellations between different contributions, though that is not a generic situation (cf. eq. (3.85)). These two qualitative features persist also once the RGE running is included, as we demonstrate below using a numerical analysis.

The leptoquark model introduced in eq. (3.67) depends on one dimensionful quantity,  $m_{\text{LQ}}$ , and 36 dimensionless parameters (i.e., 18 complex coefficients  $y_{2ij}^{RL,LR}$ ). In matching onto SMEFT

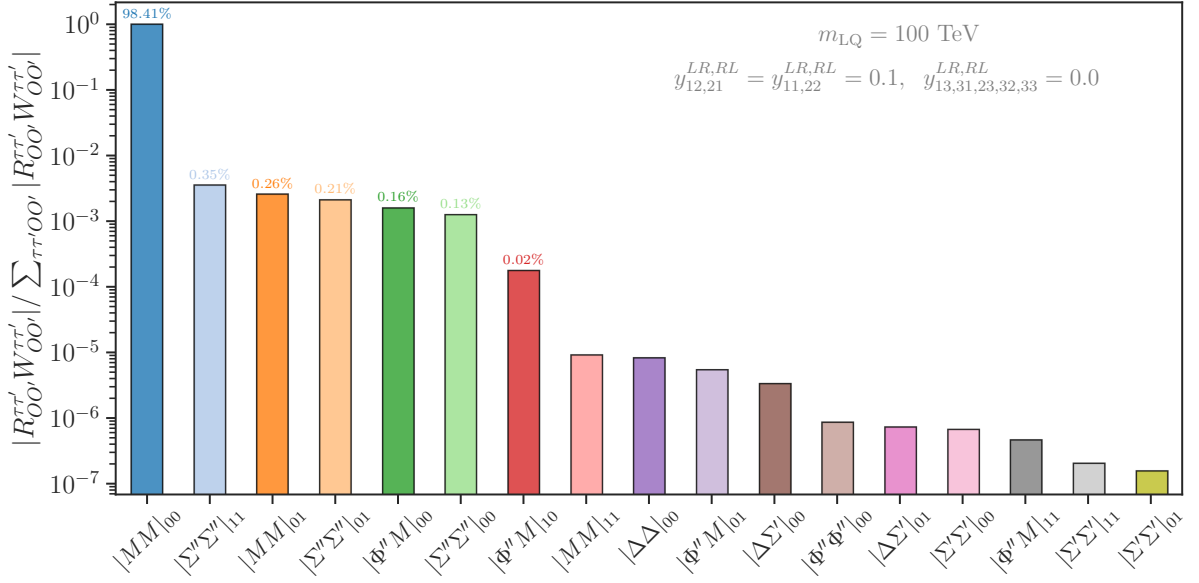


FIGURE 3.5: A decomposition of the  $\mu \rightarrow e$  conversion rate in terms of contributions from different nuclear response components classified by the type of response ( $OO'$ ) as well as the isoscalar/isovector component ( $\tau\tau'$ ), for  $^{27}\text{Al}$  target, at a single representative point in the parameter space of the  $R_2$  leptoquark model, eq. (3.67).

in eq. (3.68), we already limited the discussion to  $\mu \rightarrow e$  transitions and anticipated that only flavor-conserving quark currents are relevant in nuclear transitions.

In our numerical analysis, we focus on conversion in  $^{27}\text{Al}$  and explore the 18-dimensional complex Yukawa parameter space. The SMEFT coefficients at the scale  $\mu = m_{\text{LQ}}$ , eq. (3.68), are RG evolved to  $\mu = 2$  GeV using `wilson`, after which we utilize our WET to NRET matching expressions to compute the  $\mu \rightarrow e$  conversion rate as described in sections 3.2 and 3.4. The conversion rate is proportional to the product of leptonic  $R_{OO'}^{\tau\tau'}$  and nuclear  $W_{OO'}^{\tau\tau'}$  response functions summed over all nuclear responses ( $OO'$ ) and isospin ( $\tau, \tau' = 0, 1$ ) components (see eq. (3.25)). To better understand which nuclear responses are numerically relevant it is useful to analyze the sum in terms of its summands. We define the quantities

$$|OO'|_{\tau\tau'} \equiv \frac{|R_{OO'}^{\tau\tau'} W_{OO'}^{\tau\tau'}|}{\sum_{\tau\tau'OO'} |R_{OO'}^{\tau\tau'} W_{OO'}^{\tau\tau'}|}, \quad (OO')_{\tau\tau'} \equiv \frac{R_{OO'}^{\tau\tau'} W_{OO'}^{\tau\tau'}}{\sum_{\tau\tau'OO'} R_{OO'}^{\tau\tau'} W_{OO'}^{\tau\tau'}}, \quad (3.86)$$

such that  $|OO'|_{\tau\tau'}$  denotes the normalized, non-negative fractional contribution of the  $R_{OO'}^{\tau\tau'} W_{OO'}^{\tau\tau'}$  component to the total rate and  $(OO')_{\tau\tau'}$  denotes the normalized, signed fractional contribution. Figure 3.5 shows the relative strengths of each response at a representative point in the leptoquark Yukawa parameter space,  $m_{\text{LQ}} = 100$  TeV,  $y_{12,21}^{LR,RL} = y_{11,22}^{LR,RL} = 0.1$ ,  $y_{13,31,23,32,33}^{LR,RL} = 0$ . We find that the isoscalar component of the scalar response  $|MM|_{00}$  dominates the rate, as expected, but additionally that the coherent tensor-scalar interference response  $|\Phi''M|_{00}$  is comparable in magnitude to the longitudinal nuclear spin response  $|\Sigma''\Sigma''|_{00}$  (but where the total summed

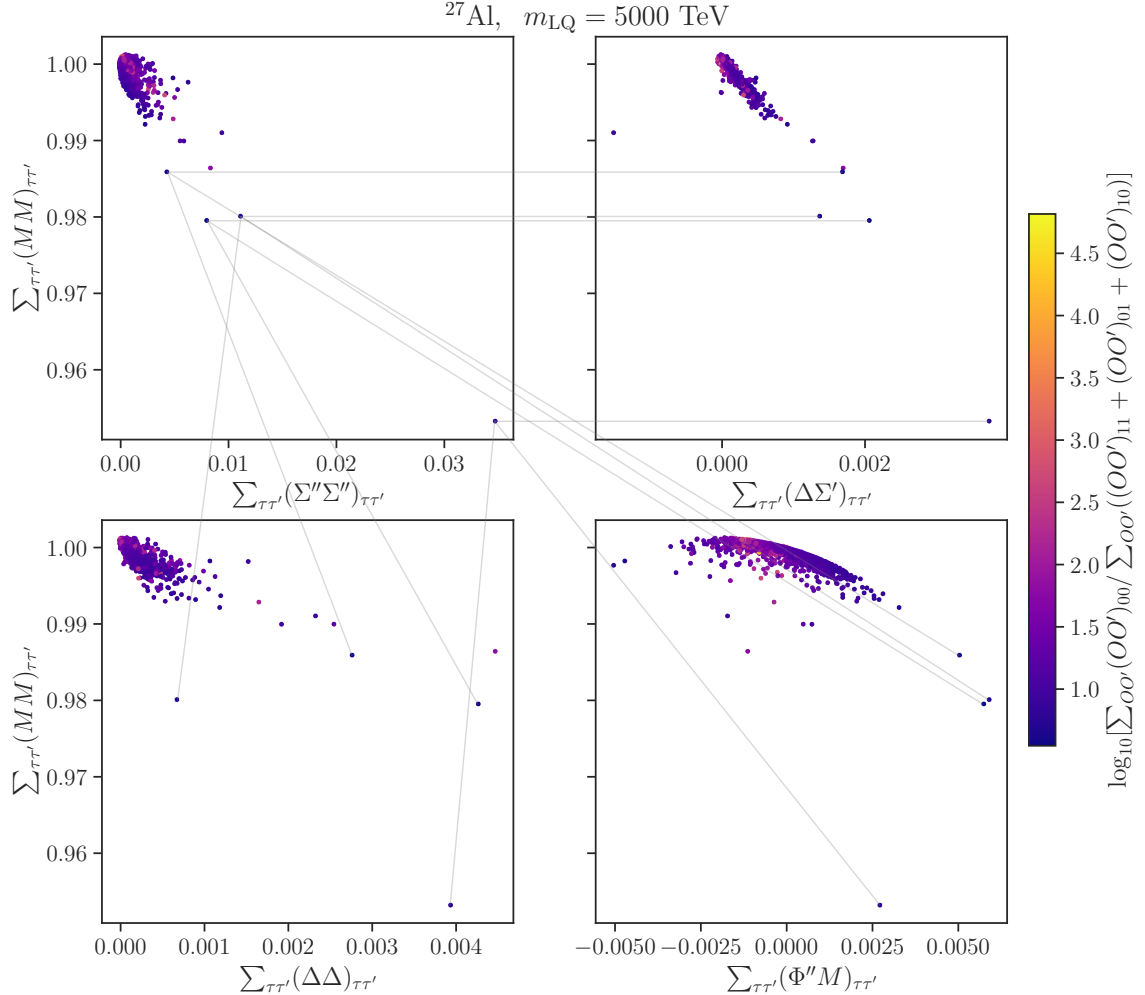


FIGURE 3.6: A comparison of the isoscalar nuclear response components over  $2 \times 10^4$  parameterizations of the  $R_2$  leptoquark model introduced in eqs. (3.67) and (3.68). Each of the 18 dimensionless complex parameters  $y_{2ij}^{RL,LR}$  are randomly sampled over the unit complex circle and the leptoquark mass is held fixed at 5000 TeV. The color denotes the logarithm of the ratio of the summed isoscalar components and the sum of isovector components for all contributing nuclear responses. Whenever the scalar response contributions fall below  $\approx 98\%$  of the total rate, the gray lines are used to illustrate how the components are distributed. The  $\mu \rightarrow e$  conversion rates for the shown points lie in the range  $10^{-17} < B(\mu^- + \text{Al} \rightarrow e^- + \text{Al}) < 10^{-11}$  (we do not denote which of the points are already excluded).

longitudinal response dominates). For  $\mu \rightarrow e$  conversion on  ${}^{63}\text{Cu}$  nuclei, at the same point in parameter space, we find that the total tensor-scalar interference response instead dominates over longitudinal spin response — the former making up  $\sum_{\tau\tau'} |\Phi''M|_{\tau\tau'} \approx 0.23\%$  of the total rate compared to  $\sum_{\tau\tau'} |\Sigma''\Sigma''|_{\tau\tau'} \approx 0.17\%$  from the latter.

In fig. 3.6 we illustrate the correlations between the leading isospin-summed nuclear response ( $MM$ ) and the next-to-leading ( $\Sigma''\Sigma''$ ), ( $\Delta\Sigma'$ ), ( $\Delta\Delta$ ), and ( $\Phi''M$ ) nuclear responses over  $2 \times 10^4$  samples of the 18-dimensional  $y_{2ij}^{RL,LR}$  parameter space. Additional nuclear response components, such as ( $\Sigma'\Sigma'$ ), ( $\Phi''\Phi''$ ), and ( $\tilde{\Phi}'\tilde{\Phi}'$ ) are also generated but contribute  $< 10^{-5}\%$  to the total rate and thus are not shown. Each point represents a unique parameterization of the

model where the 18 complex Yukawas have been sampled independently and uniformly over the unit complex circle such that

$$\left|y_{2ij}^{RL,LR}\right|^2 = \text{Re} \left( y_{2ij}^{RL,LR} \right)^2 + \text{Im} \left( y_{2ij}^{RL,LR} \right)^2 \leq 1, \quad (3.87)$$

while leptoquark mass is set to  $m_{\text{LQ}} = 5 \cdot 10^3 \text{ TeV}$ . We find that the scalar ( $MM$ ) and longitudinal-spin ( $\Sigma''\Sigma''$ ) nuclear responses dominate the total rate and are highly correlated across parameter space. The remaining nuclear responses generally provide  $< 1\%$  contributions to the total rate. However, in some parts of parameter space, where contributions from the scalar response falls below  $\approx 98\%$ , these responses become enhanced with  $\mathcal{O}(1\%)$ -level contributions that may be measurable, as depicted by the gray lines between the figure sub-panels that connect like-parameterizations.

While outside the scope of the current work, a detailed analysis exploring the similarities and differences of nuclear responses between different target nuclei (see, for example, [191]) as well as UV completions is easily accommodated by our computational framework.

### 3.5.3 ALP exchanges

The above formalism for computing  $\Gamma(\mu \rightarrow e)$  can, with trivial modifications, also be used in scenarios where the mediators are light. We illustrate this in the case of  $\mu \rightarrow e$  conversion induced by the exchange of a light axion-like particle (ALP) with mass  $m_a$ . The only required change is that now the Wilson coefficients  $\hat{C}_i^{(d)}$  in WET Lagrangian eq. (3.1) become  $q^2$  dependent. As long as one is only interested in  $\mu \rightarrow e$  conversion, the fact that WET is strictly speaking no longer the correct effective field theory, since there is an additional light degree of freedom — the ALP, makes no practical difference since all the relevant effects of the ALP are absorbed in  $\hat{C}_i^{(d)}(q^2)$ .

The ALP interactions with the SM fields start at dimension 5 and are given by

$$\mathcal{L}_{\text{ALP}} \supset -\frac{\alpha_s}{8\pi} \frac{1}{f_a} a G_{\alpha\beta}^a \tilde{G}^{a\alpha\beta} + \frac{\partial_\alpha a}{2f_a} \bar{e} \gamma^\alpha (C_\ell^V + C_\ell^A \gamma_5) \mu + \sum_{q=u,d,s} C_q^A \frac{\partial_\alpha a}{2f_a} \bar{q} \gamma^\alpha \gamma_5 q, \quad (3.88)$$

where we only display the couplings relevant for  $\mu \rightarrow e$  conversion. The tree level ALP exchange induces  $\mu \rightarrow e$  transition, inducing the following  $\hat{C}_i^{(d)}$  coefficients

$$\hat{C}_{7,q}^{(6)} = -i \frac{m_q m_-}{2f_a^2} \frac{C_q^A C_\ell^V}{q^2 + m_a^2}, \quad (3.89)$$

$$\hat{C}_{8,q}^{(6)} = \frac{m_q m_+}{2f_a^2} \frac{C_q^A C_\ell^A}{q^2 + m_a^2}, \quad (3.90)$$

$$\hat{C}_3^{(7)} = -i \frac{m_-}{2f_a^2} \frac{C_\ell^V}{q^2 + m_a^2}, \quad (3.91)$$

$$\hat{C}_4^{(7)} = \frac{m_+}{2f_a^2} \frac{C_\ell^A}{q^2 + m_a^2}, \quad (3.92)$$

where we used  $q_{\text{rel}}^2 \simeq -q^2$ , cf. eq. (3.46). Since these are higher dimension operators, suppressed by two powers of the UV scale,  $\propto 1/f_a^2$ , other dimension 6 contributions from the complete new physics model could be relevant as well, a possibility that we ignore in this example (see, however, ref. [192]). More importantly for our purposes is that the  $\hat{C}_i^{(d)}$  are, as anticipated, now explicitly  $q^2$  dependent. Since these coefficients are induced in the IR, no RGE running needs to be included in the numerical analysis. That is, the values of the  $\hat{C}_i^{(d)}$  coefficients in eqs. (3.89) and (3.92) are already given at  $\mu = 2 \text{ GeV}$ .

The resulting NRET coefficients are

$$c_6^N = \frac{q}{2m_N} \frac{m_+}{2f_a^2} \frac{C_\ell^A}{q^2 + m_a^2} \left[ - \sum_q C_q^A F_P^{q/N} + F_G^N \right],$$

$$c_{10}^N = i \frac{q}{2m_N} \frac{m_-}{2f_a^2} \frac{C_\ell^V}{q^2 + m_a^2} \left[ - \sum_q C_q^A F_P^{q/N} + F_G^N \right], \quad (3.93)$$

which both contribute to the longitudinal spin response function  $W_{\Sigma''\Sigma''}^{\tau\tau'}$ .

### 3.6 Public code: MuonBridge

Below we outline the structure and purpose of the accompanying public code available in **Python** and **Mathematica** at

<https://github.com/Berkeley-Electroweak-Physics/MuonBridge>.

The full code repository, termed **MuonBridge**, is composed of three independent sub-repositories, namely **Elastic**, **Mu2e\_NRET**, and **MuonConverter** each with dependencies on the former i.e., **MuonConverter** is dependent on **Mu2e\_NRET**, which is dependent on **Elastic**.

**Elastic** is a database containing ground-state-to-ground-state one-body density matrices computed using the nuclear shell-model code **BIGSTICK** [193, 194] for a variety of relevant isotopes for muon-to-electron conversion.

The repository `Mu2e_NRET` contains two versions: `Mu2e_NRET_v1` and `Mu2e_NRET_v2`. `Mu2e_NRET_v1`, originally developed in [172], provides functionality for computing branching ratios and decay rates for nuclear muon to electron conversion. The current release, `Mu2e_NRET_v2`, extends the original code by including the effects that arise from tensor-mediated exchanges as well as form-factor corrections induced by the muon’s velocity operator  $\vec{v}_\mu$ . These additions were necessary to support the current “top-down” WET reduction as discussed in the main text. A top-level `Python` (`Mathematica`) notebook, `Mu2e_v2.ipynb(.nb)` provides an example of typical usage and input. The `Mathematica` version offers both an interactive and manual (in the form of an association) input interface while the `Python` version requires manual input in the form of a dictionary or YAML file containing the required parameters. The parameters for both languages include:

1. A target isotope choice. For an updated list of supported target isotopes, please refer to the current repository.
2. A shell-model interaction, used to select one-body density matrices. A detailed list of supported shell-model interactions for specific target nuclei can be found in Table XIII of [172].
3. An optional harmonic oscillator length scale  $b$  in units of fm.
4. An optional response function option to generate an analytic nuclear response function  $W(y)$  (available with `Mathematica` only) and/or to generate plots of the response functions. With this option, one also specifies the isospin with one of the options: isoscalar, isovector, proton-only, or neutron-only couplings.
5. The leptonic scale  $m_L$ , which should match the leptonic scale used by `MuonConverter` so that LEC interpretation matches.
6. The relativistic LECs, i.e., the  $d_i^N$  coefficients of the Lorentz-covariant EFT defined in eq. (3.47). Only non-zero values need to be specified.
7. An optional override of the default ordinary muon capture rate to be used in the branching ratio calculation. The default values are obtained through a weighted average of the measurements compiled in [195].

Additional documentation and annotated examples of input files are included in the repository.

The main purpose of `MuonConverter` is to provide an interface between external EFT software such as `wilson` [173], `DsixTools` [17, 174], etc, and the `Mu2e_NRET` software developed in [172]. This interface extends the functionality of the original `Mu2e_NRET` code and allows for full top-down (or bottom-up) phenomenological studies of muon-to-electron conversion in the field of a target nucleus. Explicitly, in conjunction with external EFT software, `MuonConverter` can be

used to compute the influence of UV charged-lepton-flavor-violating operators on the predictions for branching and capture ratios reported by experimental collaborations.

Both versions of `MuonConverter` (Python and Mathematica) are comprised of four modular components:

1. Numerical inputs — all numerical inputs are stored within an associative array that can be modified by the user upon initialization of the `MuonConverter` class. The parameters and their default values can be found in `parameters.py(.wl)`.
2. Form factors — the form factor expressions required for the WET to NRET matching, eqs. (3.37) and (3.45), and whose numerical values are summarized in appendix B.2 can be found in `form_factors.py(.wl)`. For maximum flexibility, the default form factor values may be manually overwritten within `parameters.py(.wl)`.
3. Matching — to facilitate the WET to NRET matching, `MuonConverter` utilizes the matching expressions derived in eqs. (B.1) and (B.32) for the relativistic  $d_i$  coefficients (the  $d_i$  coefficients are automatically translated to the nonrelativistic  $c_i$ ,  $b_i$  coefficients within `Mu2e_NRET`). The matching expressions, as well as their translation to the isospin basis, can be found in `hadronization.py(.wl)`.
4. Interfacing — given an array of WET coefficients (in units of  $\text{GeV}^{-2}$ )<sup>6</sup>, the interface with `Mu2e_NRET`, utilizing external and internal basis translations as well as the matching expressions implemented in `hadronization.py(.wl)`, can be found in `MuonConverter.py(.wl)`.

To facilitate interfacing with external EFT software we provide a representation of our WET basis (defined in eqs. (3.3) and (3.13) up to dimension-six<sup>7</sup> in the naming conventions of the Wilson coefficient exchange format WCxf [28]. In addition, we provide an explicit translation between our basis and the relevant subset of flavor-violating operators in the Jenkins, Manohar, Stoffer (JMS) three-flavor WET basis [28, 175] which we will conventionally use as the ‘reference basis’ when interfacing with external codes. For more details on this translation, see appendix B.3.

As an example of typical usage, consider an arbitrary UV model defined above the electroweak scale that has been matched onto a SMEFT basis, run down to  $\sim 2 \text{ GeV}$ , matched onto a three flavor WET basis, and translated to the JMS three-flavor WET basis. The output of the previously described procedure will be a data-structure<sup>8</sup> consisting of Wilson coefficient names

---

<sup>6</sup>The dimensionful input allows for the support of multiple CLFV scales  $\Lambda, \Lambda', \Lambda'', \dots$ , if desired.

<sup>7</sup>At the time of writing, commonly used EFT software [17, 173, 174] performing RG evolution and matching above and below the electroweak scale only support operators up to dimension-six. Because our basis also includes matching expressions for dimension-seven operators, future versions of these codes supporting higher dimensional operators can be accommodated straightforwardly by `MuonConverter`.

<sup>8</sup>`MuonConverter` utilizes Python dictionaries and Mathematica associations as input.

and values in the WET-3 JMS basis, e.g.,

$$\{ \text{'VeuLL\_1211'} : 10^{-13}, \dots \}. \quad (3.94)$$

Both the **Python** and **Mathematica** versions of **MuonConverter** take Wilson coefficient names and values as well as the momentum transfer  $q^\mu \equiv (\Delta E, q_x, q_y, q_z)$  as input (in addition to the atomic and nuclear input required by **Mu2e\_NRET**, please see appendix C of [172] or the example notebooks and documentation within the repository for more information and explicit examples). It is assumed by default that the input Wilson coefficients and values are given in the WET-3 JMS basis.<sup>9</sup> Upon initialization, the input Wilson coefficient data is automatically translated to the basis defined in eqs. (3.3) and (3.13). The heart of **MuonConverter** is the matching expressions derived in eqs. (B.1) and (B.32) which relate the Wilson coefficients from an EFT of relativistic quarks and gluons to an EFT of relativistic nucleons. Using these expressions, the translated dictionary can be straightforwardly ‘hadronized’ and fed into **Mu2e\_NRET** where these coefficients are mapped to the NRET basis using the expressions derived in tables B.1 and B.4. The final output is the conversion rate  $\Gamma(\mu^- + A \rightarrow e^- + A)$  in units of  $s^{-1}$  and corresponding branching ratio  $B(\mu^- + A \rightarrow e^- + A)$ .

For example, consider the WET-3 JMS data structure given in eq. (3.94), with all coefficients except `VeuLL_1211` set to zero, in an aluminum target with momentum transfer four vector  $q^\mu = (0, 0, 0, 0.11081)$  GeV. Internally, the translation to the **MuonConverter** basis gives non-zero  $C_{1,u}^{(6)}, C_{2,u}^{(6)}, C_{3,u}^{(6)}$ , and  $C_{4,u}^{(6)}$  coefficients. These WET coefficients then generate non-zero  $d_2^{(N)}, d_4^{(N)}, d_5^{(N)}, d_6^{(N)}, d_7^{(N)}, d_{13}^{(N)}, d_{14}^{(N)}, d_{15}^{(N)}$  covariant coefficients upon hadronization. Finally, after feeding the covariant coefficients to **Mu2e\_NRET**, the conversion rate and capture ratio are given by<sup>10</sup>

$$\Gamma(\mu^- + \text{Al} \rightarrow e^- + \text{Al}) = 4.19 \times 10^{-10} \text{ s}^{-1}, \quad B(\mu^- + \text{Al} \rightarrow e^- + \text{Al}) = 6.0 \times 10^{-16}. \quad (3.95)$$

For details on the running and matching procedure down to  $\sim 2$  GeV, we refer the reader to the documentation of the respective external EFT software of choice. For additional details, documentation, and examples showcasing the usage of **MuonConverter** with external EFT software see the public repository whose link is provided at the beginning of this section.

A schematic outline of the computation performed by the **MuonBridge** software suite can be seen in fig. 3.7. The graph shows how a single CLFV SMEFT operator, defined at a scale  $\Lambda = 10^3$  TeV, is mapped through our WET basis and down to the final NRET basis, where the

---

<sup>9</sup>However, it is also possible to directly input coefficients from our WET basis, eqs. (3.3) and (3.13), by passing the following argument to the relevant functions: `basis = 'HMMRZ'`.

<sup>10</sup>Note that, because the Wilson coefficients in [172] are normalized using the weak scale, the conversion rate and the capture ratio returned by the **Mu2e\_NRET** code must be rescaled by  $v^4/\Lambda^4$  where  $v = (\sqrt{2}G_F)^{-1/2} = 246.2$  GeV is the Higgs vacuum expectation value and  $G_F$  is the Fermi constant. This rescaling is automatically incorporated into the rate computation functions within **MuonConverter**.

conversion rate is computed. The one-loop RGE from  $\mu = \Lambda$  to  $\mu = 2$  GeV generates many WET operators, however, only a small portion are numerically relevant — as depicted by the red edges of the graph.

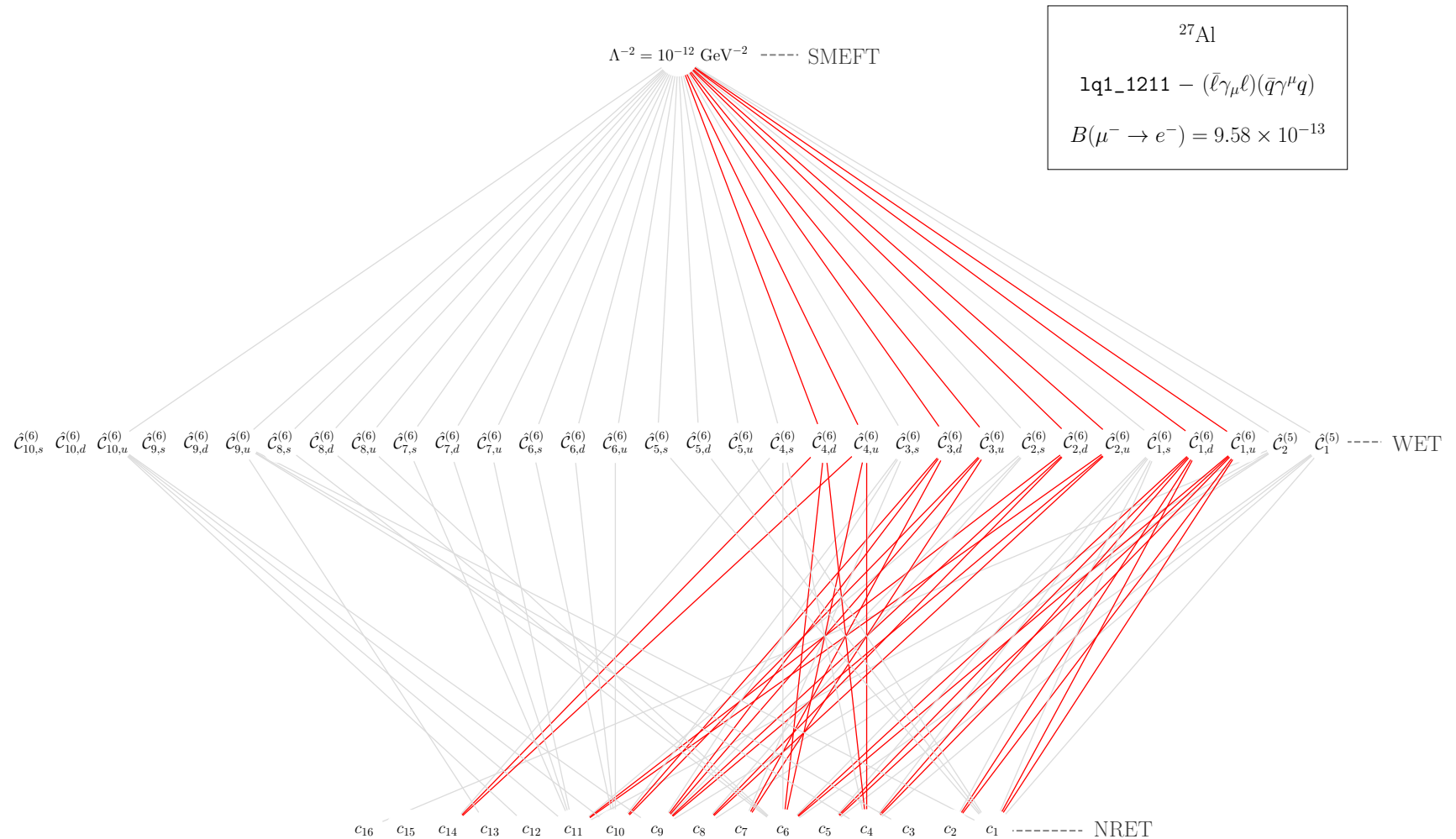


FIGURE 3.7: A simplified overview of the mapping and matching computations performed by `wilson` + `MuonBridge` for a UV theory defined by a single CLFV SMEFT operator with a Wilson coefficient set to  $1/\Lambda^2$  at scale  $\mu_{\text{UV}} = \Lambda$ . The red lines denote the largest contributions to the WET coefficients and are chosen by selecting all coefficients with an absolute value within one order-of-magnitude of the largest coefficient.

### 3.7 Conclusions

Next-generation experiments, such as Mu2e at Fermilab [129, 196] and COMET at J-PARC [128, 197], are expected to advance limits on  $\mu \rightarrow e$  conversion rate by four orders of magnitude, to about  $B(\mu^- + \text{Al} \rightarrow e^- + \text{Al}) \lesssim 10^{-17}$ . What will the new limits — or a nonzero signal — tell us about the new physics responsible for CLFV?

The experiments are done at low energy, using nonrelativistic nuclear targets, yet probe new BSM physics associated with UV energy scales. Effective field theory is a powerful technique for bridging between low energies and the UV, thereby connecting experimental constraints to BSM models. Recently, a nonrelativistic nucleon-level effective theory (NRET) was constructed and then embedded in a series of nuclei, allowing limits extracted from different nuclear targets to be meaningfully compared. The NRET can be organized according to a hierarchy of dimensionless small parameters,  $y = (qb/2)^2 > |\vec{v}_N| > |\vec{v}_\mu| > |\vec{v}_T|$ . The operator expansion through order  $\vec{v}_N$  was shown to generate the most general form of the nuclear  $\mu \rightarrow e$  conversion rate, while the retention of  $\vec{v}_\mu$  adds form factor corrections associated with the muon's lower component [171, 172]. Open-source **Mathematica** and **Python** codes named **Mu2e\_NRET\_v1** for calculating nuclear  $\mu \rightarrow e$  conversion rates were released with [172], using the NRET basis obtained by expanding through order  $\vec{v}_N$ .

In this chapter, we connected this NRET to a CLFV weak effective theory (WET) in which the degrees of freedom are the light quarks ( $u, d, s$ ), gluons, and photons. We also updated and extended the accompanying nucleon-level computer codes, to fully support this matching. These codes are collected in the repository **MuonBridge**, consisting of **MuonConverter** and **Mu2e\_NRET\_v2** computer codes (available in both **Mathematica** and **Python** versions), as well as of the **Elastic** repository (see section 3.6 for details). **MuonConverter** matches from WET to the intermediate step of relativistic covariant nucleon interactions, while the new script **Mu2e\_NRET\_v2** extends **Mu2e\_NRET\_v1** to support this matching. This was done by adding to the script's existing 16 operators the 10 additional  $\vec{v}_\mu$  suppressed NRET operators already identified in [172]. Furthermore, selected tensor-mediated interactions were added to the scalar- and vector-mediated interactions already present in **Mu2e\_NRET\_v1**. These are needed in the WET matching at dimension 7. Finally, the repository **Elastic** is a database of shell-model one-body density matrices needed for nuclear form-factor calculations. In principle, this repository can be utilized for other problems such as the calculation of dark matter direct detection rates.

Our choice for the WET basis, consisting of dimension-5, -6, and -7 operators, was motivated by the problem at hand; the operators are built out of quark, gluon and photon currents with definite parity, which simplifies the calculation of nucleon matrix elements. The basis is consistent with the complete WET basis of ref. [183], when the latter is restricted to the operators that can mediate  $\mu \rightarrow e$  conversion. **MuonBridge** contains an example of translation between our WET basis and provides the interface to external SMEFT softwares such as **wilson**

[173], and `DsixTools` [17, 174], that can be used to perform RG running, see section 3.6 for further details.

In conclusion, over the next decade the experimental community will be making a major effort to improve our understanding of CLFV. In anticipation of these experiments, it is important to develop theory tools that can treat the particle and nuclear physics of  $\mu \rightarrow e$  conversion as completely and accurately as possible. As discussed in [172], most past work on  $\mu \rightarrow e$  conversion has focused on one or two of the 16 + 10 NRET operators, employed schematic nuclear response functions, and simplified the leptonic physics through partial-wave truncations and other steps that are not well justified. The formalism developed in [171, 172] and encoded in `Mu2e_NRET_v2` addresses all of these issues, and now `MuonConverter` connects this low-energy formalism to the light-quark and gluon WET as well as to higher energy EFTs. The completeness of the WET and NRET operator bases ensures that they can faithfully encode the low-energy consequences of any UV CLFV theory.

# Chapter 4

## Muon-induced baryon number violation

**Preface:** This chapter closely follows the published work in [4] with Paddy, Matheus, Maxim, and Jure. Typically it’s assumed that if experiments such as Mu2e and COMET (also Mu3e and MEG, for their respective signals) were to see the “smoking gun” signal of mono-energetic conversion electrons, the new physics sourcing this signal must violate charged-lepton-flavor. The main goal of this project was to construct models that could mimic the mono-energetic conversion electron signal sought by Mu2e but *without* CLFV. We successfully do so – indicating that in the case of observation, additional measurements must be performed before definitively claiming new CLFVing physics.

### 4.1 Particle production in muon capture

We are interested in models of light new physics that can generate the following types of transitions at the nucleon level,

$$\mu^- + p \rightarrow e^- + \{X\}^+, \text{ or } \mu^- + n \rightarrow e^- + \{X\}^0, \quad (4.1)$$

where  $\{X\}$  denotes dark and/or visible sector final state particles, out of which an odd number are fermions. We are specifically interested in transitions with  $e^-$  in the final state since these can result in a similar signal to the usual one in the  $\mu \rightarrow e$  conversion searches but are still distinct from it when examined in detail. How much the process in eq. (4.1) will differ from the usual channel,  $\mu^- + A \rightarrow e^- + A$ , will depend on which particles are part of the  $\{X\}^+$  and  $\{X\}^0$  final states, as well as on the nature of the new interactions. For instance, the electron may be a by-product of the decays in the dark sector, in which case the kinematics of these processes no longer ensure that the electron is mono-energetic. As is well appreciated in the

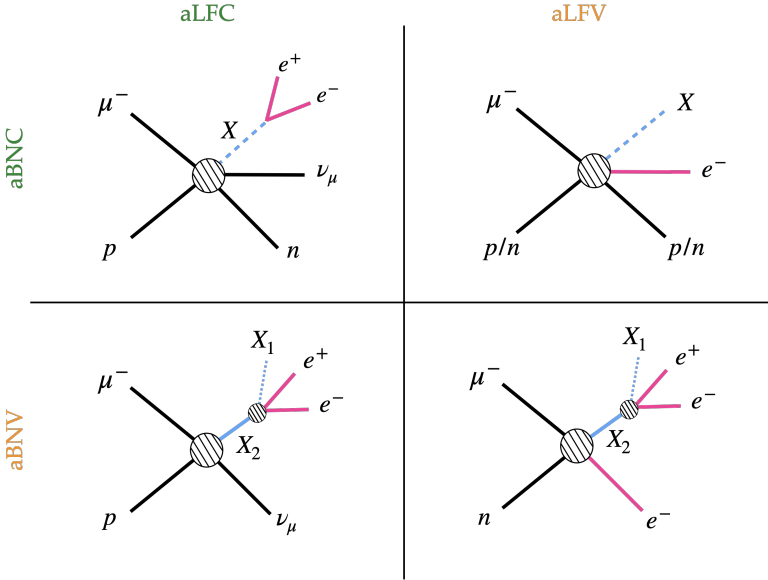


FIGURE 4.1: A schematic of the different particle production mechanisms in muon capture. Each quadrant corresponds to a different rule for baryon and lepton flavor number conservation or (apparent) violation.

literature, the fragmentation of on-shell ‘‘dark’’ states  $\{X\}$  opens up vast possibilities for the multiple production of light SM states, such as photons, electrons, and positrons.

In  $\mu \rightarrow e$  conversion, the small recoil energy of the nucleus can be neglected to a very good approximation. That is, the electron takes away essentially all of the available energy,

$$E_e^{\text{conv}} \simeq m_\mu - E_b, \quad (4.2)$$

where  $E_b \sim (Z\alpha)^2 m_\mu / 2 \sim 450 \text{ keV}$  is the binding energy of the muonic aluminum atom, and thus  $E_e^{\text{conv}} \simeq 104.98 \text{ MeV}$  [172]. The distinct signature of  $\mu \rightarrow e$  conversion is, therefore, mono-energetic electrons, with energy slightly below the muon mass and thus above the SM backgrounds. The kinematics of  $\mu \rightarrow e$  transitions that involve the production of light new physics, eq. (4.1), is different. Depending on the details of the model, i.e., which particles are present in the final state and what their masses are, the energy of the final state electron may be well below or even well above the muon mass. If the outgoing electron is significantly less energetic than  $E_e^{\text{conv}}$ , the backgrounds from the decays of muons in orbit, as well as from radiative decays followed by either Dalitz or Bethe-Heitler conversion, are expected to be prohibitively large. Furthermore, due to the small acceptance of the tracker for low-transverse momentum electrons ( $p_T \gtrsim 90 \text{ MeV}$  at Mu2e [129]), such less energetic electrons and other visible particles may be experimentally unobservable. Therefore, we will be particularly interested in new physics scenarios in which  $E_e > E_e^{\text{conv}}$ .

In what follows, we start with the general discussion of the minimal scenarios for the light particle production in muon capture, eq. (4.1), and then focus on a particular concrete example,

the model discussed in section 4.2. In general, we can divide the models into apparent baryon number conserving (**aBNC**) and apparent baryon number violating (**aBNV**) scenarios, and also into apparent lepton flavor conserving (**aLFC**) and apparent lepton flavor violating (**aLFV**) scenarios, giving four distinct classes of models. By “apparent conservation or violation”, we refer to the conservation of baryon number or lepton flavors within visible sector particles, including neutrinos. These two quantum numbers need not necessarily be violated since the dark sector particles can also carry baryon or lepton numbers. Our discussion focuses on processes involving muonic aluminum atoms ( $\mu^{-}{}^{27}\text{Al}$ ), since  ${}^{27}\text{Al}$  is the currently planned target material in the Mu2e experiment. Should other targets for muon capture be used, our models can be easily generalized to those target atoms as well. Notably, the choice of a different target only changes  $E_e^{\text{conv}}$  by at most  $\approx 5\%$ , and thus has negligible impact on the kinematics of the final state particles for the models we consider [172].

**aLFC and aBNC scenarios.** These involve charged-current (CC) reactions, such as,

$$\mu^{-} + {}^{27}\text{Al} \rightarrow (X_0 \rightarrow \nu_{\mu} e^{+} e^{-}) + {}^{27}\text{Mg}^{(*)}, \quad (4.3)$$

$$\mu^{-} + {}^{27}\text{Al} \rightarrow \nu_{\mu} + (X_0 \rightarrow e^{+} e^{-}) + {}^{27}\text{Mg}^{(*)}, \quad (4.4)$$

where  $X_0$  is an electromagnetically neutral dark sector particle. For example,  $X_0$  in eq. (4.3) could be a heavy neutral lepton,  $X_0 = N$ , produced through electroweak charge-current interaction,  $\mu^{-} p \rightarrow N n$ , that is induced via  $N$  mixing with the SM neutrinos, followed by the  $N \rightarrow \nu_{\mu} e^{+} e^{-}$  decay. The sterile-active neutrino mixing is strongly constrained for light sterile neutrinos,  $m_N \lesssim m_{\mu}$ . However, it could still induce the muon-to- $N$  capture rate as large as  $R \sim 10^{-12} - 10^{-10}$  (see eq. (4.50) below for the definition of  $R$ ). The sterile neutrino  $N$  can decay within the target, for instance, if the decay is mediated through a new dark force, such as  $N \rightarrow \nu(A' \rightarrow e^{+} e^{-})$ , where  $A'$  is a dark photon. Related NP transitions have been considered in the literature; for instance, the muon capture producing a sterile neutrino,  $\mu^{-} p \rightarrow (N \rightarrow \nu \gamma) n$  was discussed in ref. [198]. The dark photon  $A'$  can also be the dark state in the transition in eq. (4.4). In the notation of eq. (4.4),  $X_0 = A'$ , so that the dark photon gets produced in the  $\mu^{-} p \rightarrow \nu_{\mu} n A'$  transition and then decays to an electron-positron pair,  $A' \rightarrow e^{+} e^{-}$ . If the  $A'$  boson is emitted directly, as in eq. (4.4), it can be emitted from any of the lines in the diagram through couplings to muon, neutrinos, or nucleons.

In both types of transitions, eqs. (4.3) and (4.4), the energy of the outgoing electron is significantly smaller than  $m_{\mu}$  (as is the energy of the outgoing positron). The kinematic end-point is given by the back-to-back decay configuration of electron recoiling against all the other particles, resulting in  $E_e \lesssim m_{\mu}/2$ . This kinematic limitation is a result of both the fact that the above CC reactions conserve baryon number and thus the masses of final and initial nuclei are very close to each other,  $M({}^{27}\text{Mg}) - M({}^{27}\text{Al}) \sim 3 \text{ MeV}$ , as well as due to the fact that the remaining final state particles,  $e^{+}$  and  $\nu_{\mu}$ , are very light. Therefore, while the current constraints on the

couplings of new particles do not preclude several thousands of such transitions from occurring at Mu2e or COMET, identifying the new signal events would be challenging for the current experimental designs.

**aLFV and aBNC scenarios.** An example is

$$\mu^- + {}^{27}\text{Al} \rightarrow e^- + X_0 + {}^{27}\text{Al}, \quad (4.5)$$

which could be a result of a  $\mu^- \rightarrow e^- X_0$  decay, with nucleus not playing any significant role. The  $X_0$  can be stable on collider time-scales, resulting in  $\mu^- + {}^{27}\text{Al} \rightarrow e^- + {}^{27}\text{Al} + \text{inv}$  signature. A concrete realization of this scenario is an axion-like-particle,  $X_0 = a$ , coupled to the  $\bar{\mu}\gamma^5 e$  current [24, 199–203]. However, searching for  $\mu^- \rightarrow e^- a$  decays is intrinsically more challenging than searching for the signal of  $\mu \rightarrow e$  conversion, since in the former the electron is necessarily much softer,  $E_e \lesssim m_\mu/2$ . Similar conclusions apply also in the case the decays of  $X_0$  are visible, such as  $X_0 \rightarrow e^+ e^-$ .

**aLFC and aBNV scenarios.** The simplest transitions of this type are

$$\mu^- + {}^{27}\text{Al} \rightarrow \nu_\mu + (X_1 \rightarrow e^+ e^-) + {}^{26}\text{Mg}^{(*)}, \quad (4.6)$$

$$\mu^- + {}^{27}\text{Al} \rightarrow \nu_\mu + (X_2 \rightarrow X_1 e^+ e^-) + {}^{26}\text{Mg}^{(*)}, \quad (4.7)$$

where  $X_{1,2}$  are dark sector states. Compared to the previous two types of models, the main new ingredient is that the number of SM baryons changes. In principle, this releases an additional  $m_N \sim 1 \text{ GeV}$  of energy and thus one can have  $E_e > E_e^{\text{conv}}$ , as long as  $m_1 \lesssim m_n, m_p$ .

Note that the transitions in eqs. (4.6) and (4.7) need not be BNV since  $X_{1,2}$  can carry nonzero baryon number. Nevertheless, in general, the constraints on BNV processes, i.e., the bounds on the (in)stability of the proton and the bound neutrons, do place stringent bounds on aBNV processes. That is, the transitions in eqs. (4.6) and (4.7) above imply nucleon decays either through tree-level diagrams or via loop diagrams with off-shell muons, which then naively precludes any signatures at the  $\mu \rightarrow e$  conversion experiments. However, as we will show below, through a combination of judicious charge assignments and kinematic suppressions in the form of mass hierarchies, these contributions can be sufficiently suppressed either due to off-shellness, higher loop orders, or phase space suppression, ensuring phenomenologically-viable nucleon stability.

In the two examples above, the nucleon decay transitions are  $p \rightarrow \mu^{+*} \nu_\mu X_{1,2}$ . These are kinematically forbidden if the mass spectra satisfy  $m_{X_{1,2}} > m_p - m_e$ , neglecting neutrino masses and using the fact that the off-shell  $\mu^{+*}$  decays leptonically,  $\mu^+ \rightarrow e^+ \bar{\nu}_\mu \nu_e$ . Since  $X_1$  and  $X_2$  are allowed to decay, one also needs to consider the following full decay chains,

$$p \rightarrow \nu_\mu + (X_1^* \rightarrow e^+ e^-) + (\mu^{+*} \rightarrow e^+ \nu_e \bar{\nu}_\mu), \quad (4.8)$$

$$p \rightarrow \nu_\mu + (X_2^* \rightarrow X_1 e^+ e^-) + (\mu^{+*} \rightarrow e^+ \nu_e \bar{\nu}_\mu), \quad (4.9)$$

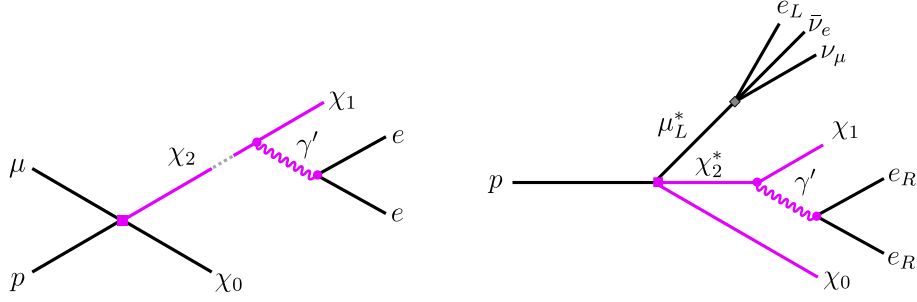


FIGURE 4.2: The scenario for muon-induced (apparent) baryon number violation considered in this work (eq. (4.14)). On the left, we show the muon capture on protons, and on the right, the tree-level proton decay channel. In both cases, the dark photon  $A'$  can be either on or off shell.

as well as their variants. As we will show below, these decays can be sufficiently suppressed in the region of parameter space where  $E_{e^+/e^-} > E_e^{\text{conv}}$ . We will illustrate this within the scenario in eq. (4.7), identifying  $X_{1,2}$  with dark sector fermions,  $X_{1,2} = \chi_{1,2}$ , and also generalizing it by replacing  $\nu_\mu$  with some generic light particle  $\chi_0$ . The muon capture and the associated nucleon decay channel schematics for this case are shown in fig. 4.2.

**aLFV and aBNV scenarios.** Transitions of this type are

$$\mu^- + {}^{27}\text{Al} \rightarrow e^- + X_1 + {}^{26}\text{Al}, \quad (4.10)$$

$$\mu^- + {}^{27}\text{Al} \rightarrow e^- + (X_2 \rightarrow X_1 e^+ e^-) + {}^{26}\text{Al}, \quad (4.11)$$

and are induced by the  $\mu^- n \rightarrow e^- X$  nucleon level transitions. Similarly to other cases, these transitions can also result in energetic electrons above the  $\mu \rightarrow e$  endpoint,  $E_{e^-} \gtrsim E_e^{\text{conv}}$ . In eq. (4.10), this occurs for  $m_{X_1} \lesssim m_n$ , and in eq. (4.11), if either  $m_{X_2} \lesssim m_n$  and/or if  $m_{X_2} \gg m_{X_1}$ .

As in the previous classes of models, also here the most stringent constraints are due to the bounds on BNV nucleon decays. For instance, if the decays of bound neutrons,  $n \rightarrow \mu^{+(*)} e^- X_0$ , are kinematically forbidden, this also means that the transition eq. (4.10) will not result in energetic electrons in Mu2e. The decay chain in eq. (4.11) is of greater phenomenological interest. Choosing  $m_{X_1} > m_n$ , the decay  $n \rightarrow \mu^{+(*)} e^- (X_1^* \rightarrow X_0 e^+ e^-)$  comes with a second virtual particle in the final state, which, combined with the phase-space suppression caused by the smallness of  $\Delta E = m_n - m_{X_0} - 3m_e$ , can make the decays of neutrons bound inside nuclei sufficiently rare, at least at tree-level. In the transition in eq. (4.11), the electron from the primary LFV vertex is soft,  $E_{e^-} < m_\mu$ . However, the positron and the electron from the  $X_2 \rightarrow X_1 e^+ e^-$  decay can be energetic enough to be observed in the experiment.

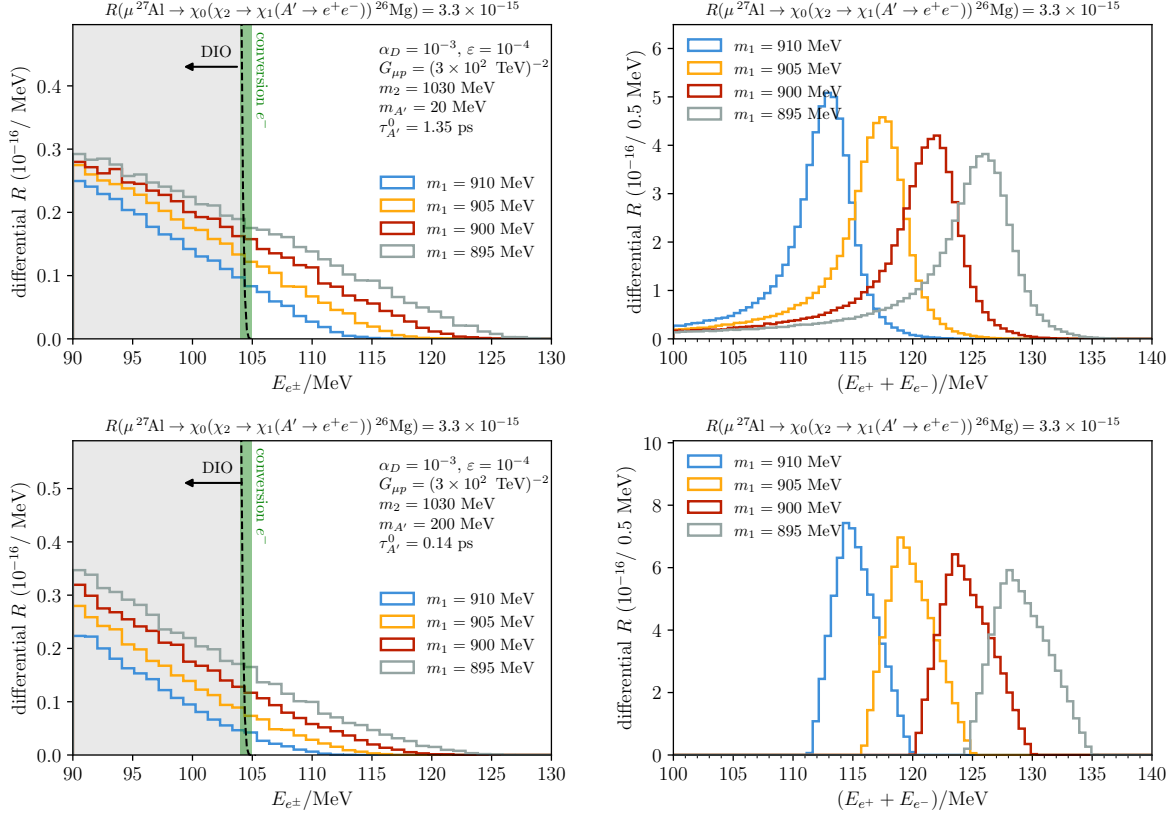
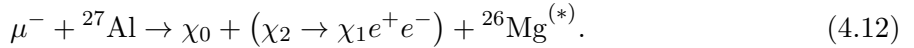


FIGURE 4.3: The energy spectrum for electrons and positrons produced in exotic muon capture for a few choices of dark particle masses. Couplings are fixed as indicated in the left panel of each row. On the left, we show the individual electron/positron energies, and on the right, their combined energy. The usual  $\mu \rightarrow e$  conversion electron energy is shown as a narrow green band around  $E_{e^-}^{\text{cap}} \simeq 104.98$  MeV, and the region where muon decay-in-orbit dominates is shaded in gray [18].

## 4.2 The effective operator

Next, we discuss in detail a concrete model of muon capture on a nucleus that results in multiple particle production. We specialize to the aLFC/aBNV scenario in eq. (4.7), but with three dark sector particles,  $\chi_{0,1,2}$ ,



The transition conserves lepton flavor number if  $\chi_0$  carries a muon lepton number (for instance,  $\chi_0$  can be  $\nu_\mu$  in which case this is exactly the scenario in eq. (4.7)). Similarly, the transition conserves baryon number if either  $\chi_0$  or  $\chi_{2,1}$  carry baryon number. We are particularly interested in the part of the parameter space that results in  $e^+e^-$  pairs with high enough energy to be observable at Mu2e and COMET.

We start by realizing the scenario within a  $U(1)_D$  extension of the SM, to which we add three dark fermions,  $\chi_{0,1,2}$  with masses  $m_{0,1,2}$ . The  $U(1)_D$  gauge symmetry is spontaneously broken,

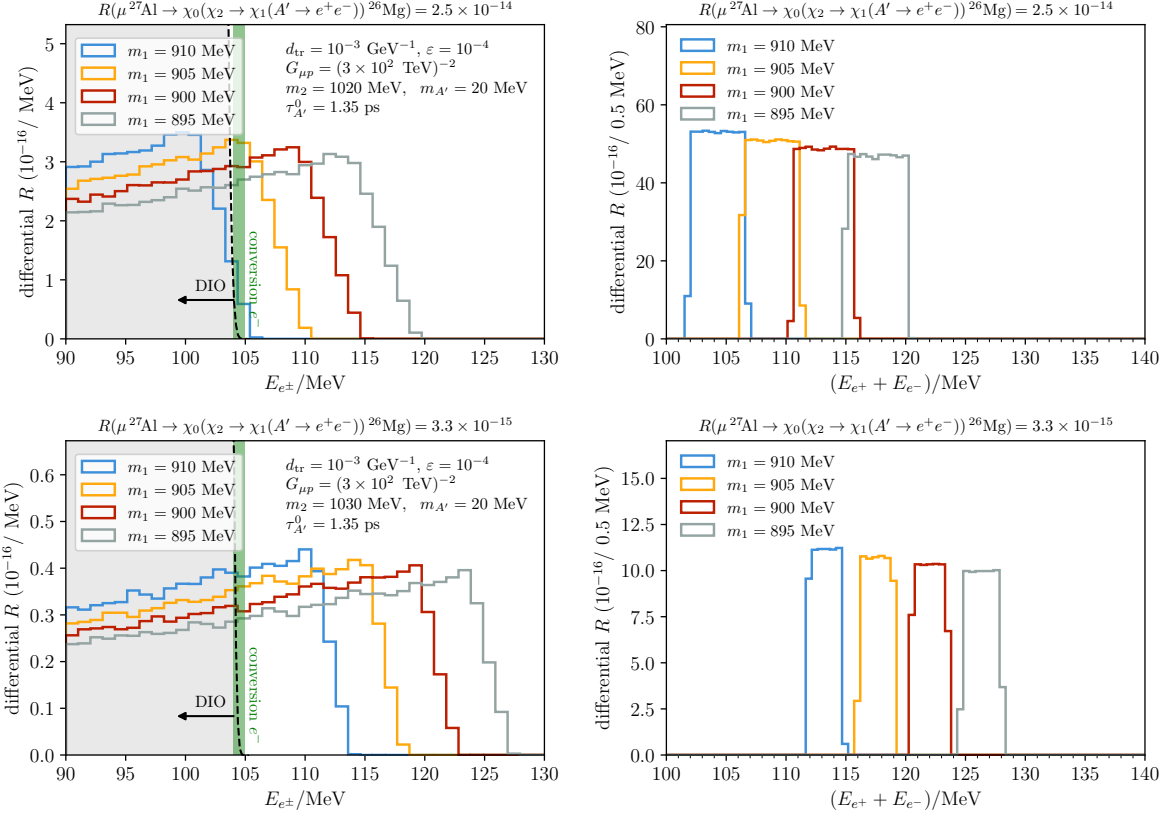


FIGURE 4.4: Same as fig. 4.3 but for  $\alpha_D \ll 1$  and  $d_{\text{tr}} = 10^{-3} \text{ GeV}^{-1}$ . The  $\chi_2 \rightarrow \chi_1 e^+ e^-$  transition is induced by the tensor interaction of eq. (4.15) and leads to a preference for more energy-asymmetric  $e^+ e^-$ .

giving rise to a dark photon  $A'$  with mass  $m_{A'}$ . Kinetic mixing gives rise to the interaction term

$$\mathcal{L} \supset e\varepsilon A'_\mu J_{\text{EM}}^\mu, \quad (4.13)$$

where  $J_{\text{EM}}^\mu$  is the SM electromagnetic current.

The flavor-violating interaction at low energies is assumed to be given by the following effective dimension 6 operator,

$$\mathcal{L} \supset \frac{G_{\mu p}}{\sqrt{2}} (\bar{p}\chi_2) (\bar{\mu}\chi_0) + \text{h.c.} \quad (4.14)$$

One can also contemplate other chiral and Lorentz structures than the one above; we discuss some variations and their impact on our conclusions in section 4.3. At the quark level, the above interaction is generated from operators of dimension 9 or higher. The underlying new-physics scale associated with the nucleon-level four-fermion operator is, therefore, more accurately estimated as  $\Lambda \sim (\Lambda_{\text{QCD}}^3/G_{\mu p})^{1/5} \sim 100 \text{ GeV}$ , which points to new color-charged particles at the electroweak scale (see section 4.3 for a more detailed discussion of UV completions).

Note that if  $\chi_0$  carries baryon number,  $B(\chi_0) = 1$ , then baryon number is conserved by the interaction in eq. (4.14). Since we are interested in scenarios where  $m_0 < m_p$ , this means that  $\chi_0$  would be the lightest baryon and remain stable. If we can consistently assign  $L(\chi_0) = 1$ ,

then lepton number is also conserved. The other possibility is that  $B(\chi_2) = B(\chi_1) = 1$ , and  $L(\chi_2) = L(\chi_1) = 1$ , which also keeps the baryon and lepton numbers conserved. In this case, the lightest baryon is  $\chi_1$ . Which of the dark sector particles carries baryon and lepton numbers has no bearing on the phenomenology that we are interested in, though. The important point for us is that there is a muon-induced exothermic transition between nucleons and dark sector particles that reduces the number of nucleons by one unit.

The heaviest dark fermions are required to interact with dark photon via the off-diagonal terms, giving rise to  $\chi_2 \rightarrow \chi_1 + A'$  decays. We consider two ways of generating such interactions, either through dimension 4 and dimension 5 operators,

$$\mathcal{L} \supset g_D (\bar{\chi}_2 \gamma^\mu \chi_1) A'_\mu + d_{\text{tr}} (\bar{\chi}_2 \sigma^{\mu\nu} \chi_1) F'_{\mu\nu} + \text{h.c..} \quad (4.15)$$

The first term arises if  $\chi_1$  and  $\chi_2$  are maximally mixed Majorana fermions (a well-known example is, e.g., inelastic dark matter [204]). The second term is a non-renormalizable transition magnetic moment between the two (Dirac or Majorana) fermions through the dark photon, where  $F'_{\mu\nu} = \partial_\mu A'_\nu - \partial_\nu A'_\mu$ . In the remainder of the paper, we will refer to the following benchmark for Mu2e signatures,

Benchmark (I)

$$\begin{aligned} m_2 &= 1030 \text{ MeV}, m_1 = 900 \text{ MeV}, \\ m_0 &= 0, m_{A'} = 20 \text{ MeV}, \\ G_{\mu p} &= (300 \text{ TeV})^{-2}, \varepsilon = 10^{-4}, \alpha_D = 10^{-3}. \end{aligned} \quad (4.16)$$

Similarly, in the case of a transition magnetic moment,

Benchmark (II)

$$\begin{aligned} m_2 &= 1030 \text{ MeV}, m_1 = 900 \text{ MeV}, \\ m_0 &= 0, m_{A'} = 20 \text{ MeV}, \\ G_{\mu p} &= (300 \text{ TeV})^{-2}, \varepsilon = 10^{-4}, d_{\text{tr}} = 10^{-3} \text{ GeV}^{-1}. \end{aligned} \quad (4.17)$$

This choice of spectrum ensures that the energy release in  $\mu \rightarrow e$  transitions can be large  $E_{e^+/e^-} > E_e^{\text{conv}}$  while guaranteeing that at least two particles must be off-shell in nucleon decay.

Given eq. (4.13) and our benchmarks, the partial width for the leptonic decay of the dark photon is given by

$$\Gamma_{A' \rightarrow e^+ e^-} = \frac{1}{3} \alpha \varepsilon^2 m_{A'} \sqrt{1 - 4r_e^2} (1 + 2r_e^2), \quad (4.18)$$

where  $r_e \equiv m_e/m_{A'}$ . For our benchmarks, this gives a lifetime of  $\tau_{A'}^0 \approx 1.4$  ps. The  $\chi_2$  lifetime depends on which interaction term in eq. (4.15) is considered. Assuming the channel is open,

the partial width for  $\chi_2$  to decay to  $\chi_1$  and  $A'$  through the vector interaction is given by

$$\Gamma_{\chi_2 \rightarrow \chi_1 A'}^V = \frac{1}{4} \alpha_D \frac{m_2^3}{m_{A'}^2} F(r_1, r_{A'}) , \quad (4.19)$$

where

$$F(r_1, r_{A'}) = (r_1^4 - 2r_{A'}^4 + r_1^2(r_{A'}^2 - 2) + r_{A'}^2(1 - 6r_1) + 1) \\ \times \sqrt{r_1^4 - 2r_1^2(r_{A'}^2 + 1) + (1 - r_{A'}^2)^2} , \quad (4.20)$$

and  $r_1 \equiv m_1/m_2$  and  $r_{A'} = m_{A'}/m_2$ . Giving a benchmark lifetime  $\tau_{\chi_2}^0 \approx 6 \times 10^{-14}$  ns. In the limit that  $r_{A'} \rightarrow 0$ , the mass splitting between  $\chi_1$  and  $\chi_2$  also vanishes ( $r_1 \rightarrow 1$ ) and the width is well defined. The tensor interaction gives the partial rate

$$\Gamma_{\chi_2 \rightarrow \chi_1 A'}^T = \frac{1}{4\pi} d_{\text{tr}}^2 m_2^3 \tilde{F}(r_1, r_{A'}) , \quad (4.21)$$

where

$$\tilde{F}(r_1, r_{A'}) = (2(1 - r_1^2)^2 - r_{A'}^2(r_{A'}^2 + r_1^2 + 6r_1 + 1)) \\ \times \sqrt{r_1^4 - 2r_1^2(r_{A'}^2 + 1) + (1 - r_{A'}^2)^2} , \quad (4.22)$$

giving a benchmark lifetime of  $\tau_{\chi_2}^0 \approx 3 \times 10^{-7}$  ns. These decays are all well below the  $\mathcal{O}(1\mu\text{s})$  signal time window at Mu2e and COMET. This is no longer true when the dark photon becomes off-shell in  $\chi_2 \rightarrow \chi_1 e^+ e^-$  decays. For instance, when  $m_{A'} = 200$  MeV, the  $\chi_2$  lifetime is of the order of  $\mu\text{s}$  and  $s$  for the couplings in eqs. (4.16) and (4.17), respectively. In comparison with the timescales of the beam and muon capture, these events will constitute a constant rate in time and may be harder to discriminate from beam-induced backgrounds.

### 4.3 UV completions

At first glance, the expected sensitivity of the Mu2e experiment at the level of  $R(\mu \rightarrow e) \sim \mathcal{O}(10^{-16})$  translates to a very impressive NP reach, on the order of  $G_{\mu p} \propto 10^{-8} G_F$ , or in terms of the effective NP scale,  $G_{\mu p}^{-1/2} \sim 10^3$  TeV. However,  $G_{\mu p}^{-1/2}$  is not a fundamental UV scale. Proton is composed of quarks, and thus we can expect

$$G_{\mu p} \sim \frac{\Lambda_{\text{QCD}}^3}{\Lambda_{\text{col}}^{d_{\text{col}}} \Lambda_{\text{sin}}^{5-d_{\text{col}}}} , \quad (4.23)$$

where the QCD scale is  $\Lambda_{\text{QCD}} \sim 0.3$  GeV, while the value of the exponent,  $d_{\text{col}}$ , depends on the details of the model. In eq. (4.23) we already anticipated that the phenomenologically favored situation is when the mediators charged under QCD are much heavier than the color singlet

No.	Decay channel	Mass range	Decay rate scaling
1)	$p \rightarrow \mu \chi_2 \chi_0$	$m_p > m_\mu + m_2 + m_0$	$\Gamma \propto \frac{G_{\mu p}^2 Q^5}{8\pi \times 16\pi^2}$
2)	$p \rightarrow \mu(\chi_2^* \rightarrow \chi_1 A') \chi_0$	$\left\{ \begin{array}{l} m_p > m_\mu + m_{A'} + m_1 + m_0, \\ m_1 + m_{A'} > m_2 \text{ or } m_2 > m_p - m_\mu - m_0 \end{array} \right.$	$\Gamma \propto \frac{G_{\mu p}^2 \alpha_D Q^7}{(16\pi^2)^2 m_2^2}$
3)	$p \rightarrow \mu(\chi_2^* \rightarrow \chi_1(A'^* \rightarrow ee)) \chi_0$	$\left\{ \begin{array}{l} m_p > m_\mu + 2m_e + m_0 \\ m_1 + 2m_e > m_2 \text{ or } m_2 > m_p - m_\mu - m_0 \\ 2m_e > m_{A'} \text{ or } m_{A'} > m_p - m_\mu - m_0 - m_1 \end{array} \right.$	$\Gamma \propto \frac{G_{\mu p}^2 \alpha_D (e\varepsilon)^2 Q^{11}}{(16\pi^2)^3 m_2^2 m_{A'}^4}$
4)	$p \rightarrow (\mu^* \rightarrow e\nu\nu) \chi_2 \chi_0$	$m_p > m_2 + m_0 + m_e \text{ and } m_\mu > m_p - m_2 - m_0$	$\Gamma \propto \frac{G_{\mu p}^2 G_F^2 Q^{11}}{8\pi \times (16\pi^2)^3 m_\mu^2}$
5)	$p \rightarrow (\mu^* \rightarrow e\nu\nu)(\chi_2^* \rightarrow \chi_1 A') \chi_0$	$\left\{ \begin{array}{l} m_p > m_1 + m_0 + m_e + m_{A'} \\ m_\mu > m_p - m_1 - m_0 - m_{A'} \\ m_2 < m_1 + m_{A'} \text{ or } m_p - m_0 - m_e < m_2 \end{array} \right.$	$\Gamma \propto \frac{G_{\mu p}^2 G_F^2 \alpha_D Q^{13}}{(16\pi^2)^4 m_\mu^2 m_2^2}$

TABLE 4.1: Proton decay channels and the corresponding constraints on the dark sector mass spectrum that we impose so as to forbid them at tree level. The naive scaling of each decay channel, assuming all final state particles are relativistic, is shown in the right-most column. Generalization to non-relativistic final state particles is straightforward – see section 4.5.1 for more details.

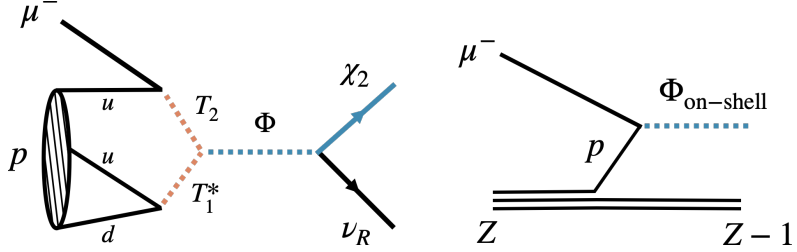


FIGURE 4.5: The left diagram shows the UV completion of section 4.3 that realizes the contact interaction  $G_{\mu p}$  of eq. (4.14). A heavy di-quark  $T_1$  and a lepto-quark  $T_2$  scalar couple to an intermediate-mass gateway particle  $\Phi$ . The diagram on the right shows how the gateway particle  $\Phi$  can be produced on-shell in muon capture with a third-body rescattering ( $Z$  represents a nucleus of atomic number  $Z$ ).

mediators, and we have thus split the two scales,  $\Lambda_{\text{col}} \gg \Lambda_{\text{sin}}$  (for simplicity, we still assume that each of the two types of mediators have a common mass).

As we will see below, credible UV models of  $\mu^- p$  annihilation to dark states will require *both* heavy new physics, above the electroweak scale, as well as light, GeV scale, states. The goal of this section is to demonstrate that such UV completions exist without providing a comprehensive study of all the models that can lead to the effective operator in eq. (4.14).

Below, we discuss in detail a triplet-triplet-singlet model that leads to a large scale  $\Lambda_{\text{col}}$  suppression in eq. (4.23) with  $d_{\text{col}} = 3$ . We find this to be rather typical, though models with smaller  $d_{\text{col}} = 2$  (and thus a higher value of  $\Lambda_{\text{col}}$  for which there is still an observable signal at Mu2e and COMET) do exist (see section 4.3.2). This model is partially inspired by UV completions behind potential dark channels for neutron decay [88, 205]. It is also important to keep in mind that other UV realizations can lead to distinct LHC and high-energy phenomenology, which can differ significantly from the model we discuss in detail.

### 4.3.1 Triplet-triplet-singlet model

A UV model that we consider in detail extends the SM with two scalar color triplets, the di-quark  $T_1$  ( $Q = -1/3, B = -2/3, L = 0$ ) and the leptoquark  $T_2$  ( $Q = -1/3, B = 1/3, L = 1$ ), which have the following couplings to the SM fermions<sup>1</sup>

$$\mathcal{L} \supset -y_{ud}(\overline{u}_R^{iC} d_R^j) \epsilon_{ijk} T_1^k - y_{\mu u}(\overline{\mu}_R^{iC} \mu_R) (T_2^*)_i + \text{h.c.}, \quad (4.24)$$

as well as by a complex color singlet scalar  $\Phi$  ( $Q = 0, B = 1, L = 1$ ), and the dark sector fermions  $\chi_0 \equiv \nu_R$  and  $\chi_2$

$$\mathcal{L} \supset \rho T_1^{k*} T_2 k \Phi^* + y_\chi \Phi (\overline{\nu}_R \chi_2^C) + \text{h.c..} \quad (4.25)$$

---

<sup>1</sup>For charge conjugate fields we use the notation from [206]. In particular,  $\psi_R = P_R \psi = \frac{1}{2}(1 + \gamma_5)\psi$ , and  $\psi_R^C = P_L \psi^C = C \bar{\psi}_R^T = [\psi_R(x)]^C$ . (Note that this differs from [207] where  $\psi_R^C$  denotes  $[\psi_L(x)]^C$ .)

All the new states are singlets under  $SU(2)_L$ . The color contractions over  $i, j, k$  indices are shown explicitly, while the Lorentz contractions are not; in the latter,  $C$  denotes the charge conjugation Dirac matrix. Note that the coupling constants,  $y_{ud}, y_{\mu u}, y_\chi$  are dimensionless, while  $\rho$  has mass dimension 1. In what follows, we require that  $\Phi$  does not develop a vacuum expectation value. If the  $\nu_R \chi_2$  bilinear carries the same global quantum numbers as  $\Phi$ , the above Lagrangian has both  $B$  and  $L$  conserved.

We are interested in the limit of very heavy  $T_{1,2}$  so that at low energies, these can be integrated out. The resulting effective interaction is

$$\mathcal{L}_{\text{eff}}^\Phi = \frac{1}{\Lambda_{\text{col}}^3} (\bar{u}_R^{iC} \mu_R) \epsilon_{ijk} (\bar{u}_R^{jC} d_R^k) \Phi^* + \text{h.c.}, \quad (4.26)$$

where

$$\frac{1}{\Lambda_{\text{col}}^3} = y_{ud} y_{\mu u} \frac{\rho}{m_{T_1}^2 m_{T_2}^2}. \quad (4.27)$$

Below the QCD confinement scale, this then leads to the effective interaction with the proton,

$$\mathcal{L}_{\text{int}}^\Phi = \lambda_{\text{eff}} \Phi^* (\bar{p}_R^C \mu_R) + \text{h.c.}, \quad (4.28)$$

with

$$\lambda_{\text{eff}} \simeq y_{ud} y_{\mu u} \frac{\rho \Lambda_{\text{QCD}}^3}{m_{T_1}^2 m_{T_2}^2}, \quad (4.29)$$

where for the matrix element between the tri-quark operator and the proton we used the NDA estimate,  $\langle 0 | \bar{u}_R^{iC} (\bar{u}_R^{jC} d_R^k) \epsilon_{ijk} | p \rangle \simeq \Lambda_{\text{QCD}}^3 \langle 0 | \bar{p}_R^C | p \rangle$ , with the parenthesis denoting a Lorentz contraction.

#### 4.3.1.1 Off-shell $\Phi$

If  $\Phi$  is heavy enough that it can also be integrated out, this gives the effective interaction

$$\mathcal{L}_{\text{eff}} = \frac{1}{\Lambda_{\text{col}}^3} \frac{1}{\Lambda_{\text{sin}}^2} (\bar{u}_R^{iC} \mu_R) \epsilon_{ijk} (\bar{u}_R^{jC} d_R^k) (\bar{\nu}_R \chi_{2R}^C) + \text{h.c.}, \quad (4.30)$$

with  $\Lambda_{\text{col}}$  given in eq. (4.27), and

$$\frac{1}{\Lambda_{\text{sin}}^2} = \frac{y_\chi}{m_\Phi^2}, \quad (4.31)$$

or in terms of interactions with the proton<sup>2</sup>

$$\mathcal{L}_{\text{int}} = \tilde{G}_{\mu p} (\bar{p}_R^C \mu_R) (\bar{\nu}_R \chi_{2R}^C), \quad (4.32)$$

---

<sup>2</sup>The structure of the dimension six operator is similar to the operator considered in eq. (4.14), but with a different Lorentz structure. This operator further suppresses nucleon decay while leading to  $\mathcal{O}(1)$  difference in the muon capture phenomenology. These quantitative differences, however, are not important for the more qualitative discussion we are focusing on here.

where  $\tilde{G}_{\mu p}$  is given in eq. (4.23) with  $d_{\text{col}} = 3$ , and  $\Lambda_{\text{col}}$  and  $\Lambda_{\text{sin}}$  given in eq. (4.27) and eq. (4.31), respectively.

For observable  $\mu^- p$  annihilation rate with  $R \simeq 3 \times 10^{-15}$ , we require, from eq. (4.50), that  $\tilde{G}_{\mu p} \simeq 10^{-6} G_F$ . In terms of the UV completion this is,

$$\begin{aligned}\tilde{G}_{\mu p} &= \frac{\lambda_{\text{eff}} y_\chi}{m_\Phi^2} = 2 \cdot 10^{-6} G_F y_\chi \left( \frac{\lambda_{\text{eff}}}{10^{-10}} \right) \left( \frac{2 \text{ GeV}}{m_\Phi} \right)^2 \\ &\sim 10^{-6} G_F y_{ud} y_{\mu u} y_\chi \left( \frac{1 \text{ TeV}}{\sqrt{m_{T_1} m_{T_2}}} \right)^4 \left( \frac{\rho}{4 \text{ TeV}} \right) \left( \frac{2 \text{ GeV}}{m_\Phi} \right)^2.\end{aligned}\quad (4.33)$$

In the numerical example in the last line, we show a possible case  $m_{T_1, T_2} \sim \rho \gg m_\Phi \gtrsim m_p$ . A light  $\Phi$  enhances the  $\mu^- p$  annihilation rate, and so would lighter  $T_{1,2}$ . However, the masses of  $T_1, T_2$  are required to be at least in the TeV range in order to evade the LHC monojet constraints. Note that the trilinear scalar coupling  $\rho$  was taken to be large. The  $\Phi$  mass receives radiative corrections of size  $m_\Phi^2 \sim \rho^2/16\pi^2$ , making our choice of  $m_\Phi$  in the GeV range somewhat fine-tuned.

The phenomenology of section 4.2 is obtained if  $\chi_2$  decays inside the detector to a lighter dark state  $\chi_1$  via  $\chi_2 \rightarrow A' \chi_1$ , and the dark photon then decays to an electron-positron pair,  $A' \rightarrow e^+ e^-$ . We assume that the  $\chi_2 \rightarrow A' \chi_1$  transition is due to a dipole operator  $d_{\text{tr}}$  in eq. (4.15), and that the states in the SM and in the triplet-triplet-singlet model, including  $\chi_{2,1}$ , are not charged under the  $U(1)_d$ . The dipole operator is generated from other heavier states charged under  $U(1)_d$  running in the loop. The possibility where  $\chi_{2,1}$  are charged under  $U(1)_d$  is discussed in section 4.3.2.

#### 4.3.1.2 On-shell $\Phi$

The  $\mu^- p$  annihilation rate can be further enhanced if the  $\Phi$  scalar is light enough to be produced on-shell, cf. fig. 4.5. In this case, the muonic atom undergoes a transition  $\mu^-(A, Z) \rightarrow \Phi(A - 1, Z - 1)$ . The phenomenologically favored kinematics is when the  $\Phi$  scalar can be produced on-shell in muon capture, while a proton decay would require both  $\Phi$  and  $\mu^+$  to be off-shell, thus suppressing the proton decay rate. This occurs for  $\Phi$  mass in the range  $m_p < m_\Phi < m_\mu + m_p$  (ignoring the differences in the nuclear binding energies), while the  $\chi_0$  and  $\chi_2$  masses satisfy  $m_p < m_\mu + m_{\chi_0} + m_{\chi_2}$ , with  $m_{\chi_0} + m_{\chi_2} < m_\Phi$ . The observable signal in the  $\mu^- p$  annihilation arises from the decay of  $\Phi$  to the dark sector states,  $\Phi \rightarrow \chi_2 \chi_0$ , followed by the subsequent decay of  $\chi_2$ , which involves visible states, such as  $\chi_2 \rightarrow \chi_1 e^+ e^-$ .

The  $2 \rightarrow 1$  process,  $\mu^- p \rightarrow \Phi$ , is enabled by the re-scatterings on the other nucleons inside a nucleus. In this sense, the  $\mu^- p \rightarrow \Phi$  annihilation is analogous to the well-known SM process of pion capture,  $\pi^- p \rightarrow n$ , which at face value is also a  $2 \rightarrow 1$  process. Following section 4.4 we compute a naive estimate for  $\Phi$  production through a ratio with the off-shell channel whose

SM-normalized rate is given in eq. (4.50). The ratio of the on- and off-shell capture rate is given roughly by

$$\frac{\Gamma_{\mu Z \rightarrow \Phi(Z-1)}}{\Gamma_{\mu Z \rightarrow \chi_0 \chi_2(Z-1)}} \sim \frac{m_{\Phi, \text{off}}^4}{y_\chi^2 E_{\chi_2} E_{\chi_0}} \frac{16\pi^2}{(M - m_{\text{Mg}})^3} \tilde{r}_{\text{p.s.}}, \quad (4.34)$$

where the phase space factor can be estimated as

$$\tilde{r}_{\text{p.s.}} \simeq \frac{(1 - x_{\Phi, \text{on}}^2)^{1/2}}{(1 - x_{02})^2 (1 + x_{02})}, \quad (4.35)$$

with  $x_{\Phi, \text{on}} = m_{\Phi, \text{on}} / (M - m_{\text{Mg}})$  and  $x_{02} = (m_{\chi_0} + m_{\chi_2}) / (M - m_{\text{Mg}})$ . Here the  $m_{\Phi, \text{on}}$  is the mass of the  $\Phi$  that is produced on-shell, while  $m_{\Phi, \text{off}}$  is the mass of the virtual  $\Phi$  leading to the three body transition. Taking  $m_{\Phi, \text{on}} = 1$  GeV and comparing to the off-shell benchmark, eqs. (4.16), (4.17) and (4.33), the on-shell rate is significantly enhanced by  $\approx 10^9 - 10^{10} \times y_\chi^{-2}$  depending on the phase space configuration of the three-body off-shell decay. Here, the additional suppression of the three body off-shell transition, beyond the naive dimensional analysis factor  $y_\chi^2 / 16\pi^2$ , comes from the suppression of the matrix element by a factor of  $Q \sim E_{\chi_0}$  and the fact that the phase space is squeezed, resulting in large  $\tilde{r}_{\text{p.s.}}$ . The on-shell capture rate is controlled by  $\lambda_{\text{eff}}$ , where  $\lambda_{\text{eff}} \lesssim 10^{-14}$  gives capture rates below current  $\mu \rightarrow e$  limits, assuming a similar signal of ‘conversion’ electrons to that of the off-shell  $\Phi$ , see, e.g., figs. 4.3 and 4.4, after  $\Phi$  decays promptly. Note that because  $R_{\text{on-shell}} \propto \lambda_{\text{eff}}^2 \propto (m_{T_1} m_{T_2})^{-4}$  the significant enhancement of the on-shell capture rate only translates to an increase of  $m_{T_{1,2}}$  by  $\approx$  an order of magnitude.

### 4.3.2 More models

Above, we discussed only one possible UV completion in detail, the triplet-triplet-singlet model. While this model is a good representative of how the experimental constraints can be evaded, primarily though compressed spectra, we expect that many other SM extensions exist that can lead to observable  $\mu - p$  annihilation while satisfying current constraints. Below, we discuss some of the possible variants of the triplet-triplet-singlet model as well as its extensions. Some of these variants have already been touched upon above.

**Alternative scenarios for  $\Phi$  produced on-shell.** In the numerical analysis, we primarily focused on the case of a heavy singlet  $\Phi$ . However, the  $\Phi$  can also be lighter, even so light that it is produced on-shell in  $\mu^- p$  annihilation. The  $\Phi$  can then decay into the dark sector states and the  $e^+ e^-$  pair, which is the same final state particle content as the one we discussed in detail in the case of heavy  $\Phi$ , but with modified kinematics. It is also possible that the dominant decay of  $\Phi$  is into other visible particles (and dark states), not the  $e^+ e^-$  pair. For instance,  $\Phi \rightarrow 4e + \text{dark states}$  or  $\Phi \rightarrow \gamma + \text{dark states}$  are both possible and can have drastically different experimental efficiencies at an experiment such as Mu2e.

**Production of kaons.** An interesting alternative for releasing more energy is  $\mu^- p$  annihilation to kaons. This could, for instance, be mediated via the following low-energy interactions,  $\mathcal{L} \supset \lambda_{\text{eff}} \Phi^* \overline{p_R^C} \mu_R + \lambda_{KK} \Phi(K^0)^2$ . For  $\Phi$  that has a mass in the range  $2m_K < m_\Phi < m_p + m_\mu$ , the muon induced conversion process is then  $\mu^- p \rightarrow \Phi + \text{nucl recoil} \rightarrow K^0 K^0$ . Proton decay, on the other hand, can only proceed via two virtual particles,  $p \rightarrow (\mu^+)^*(\Phi^* \rightarrow KK^*)$ . As before, the main idea is to use the muon mass as a means to enable baryon number violation in  $\mu p$  capture while at the same time suppressing proton decay via a judicious choice of the mass spectrum. The novelty in this scenario is that the byproducts of the capture reaction are fixed by the branching ratios of the kaon, leading to the production of pions, muons, and photons in addition to electrons and positrons. Note, however, that this scenario is quite likely challenged by the neutron star physics. In the neutron star, the final state  $K$ -mesons will get re-absorbed by nuclei, resulting in a loss of two fermions per every  $\mu^- p$  annihilation, with strong implications for the properties of the neutron stars.

**Alternative dark photon couplings.** In the main part of the text, we assumed that the  $\chi_2 \rightarrow \chi_1 A'$  transition proceeds through dimension 5 dipole operators. However, this transition can also be mediated by renormalizable interactions. To show this, we first assume that the dark photon mass arises from its coupling to dark higgs,  $h_d$ , after it acquires a vev. The interactions of the dark  $U(1)_D$  gauge boson,  $A'_\mu$ , depend on the assigned  $U(1)_D$  charges of the dark states  $\chi_{1,2}, \nu_R$ . To allow for the transition  $\chi_2 \rightarrow \chi_1 A'$ ,  $\chi_1$  and  $\chi_2$  must have the same charge. To avoid charging SM particles under the  $U(1)_D$ ,  $\nu_R$  must be oppositely charged to  $\chi_{1,2}$ , or the second term in eq. (4.25) must contain an insertion of  $h_d$ . One possibility is that none of these carry a  $U(1)_D$  charge, and thus the  $\chi_2 \rightarrow \chi_1 A'$  decay is due to the dipole interaction in eq. (4.15). If the  $\chi_i$ 's carry a  $U(1)_D$  charge, the decay takes place through the contact operator in eq. (4.15). In either case, the coupling to the dark photon is off-diagonal in  $\chi$  flavor space.

This off-diagonal form of the coupling can be achieved if there are 3 Weyl fermions in the dark sector, two of which make up a pseudo-Dirac pair. Consider 3 states  $\psi_0, \psi_1, \psi_1^c$ , with a vector-like mass  $m\psi_1\psi_1^c$  and a small Majorana mass  $\delta\psi_1\psi_1$ . This can be generated, for instance, by integrating out a massive fermion with a small Yukawa coupling with  $\psi_1$  and  $h_d$ . The mass eigenstates  $\chi_{1,2}$  are approximately equal admixtures of  $\psi_1, \psi_1^c$ . Since Majorana fermions can neither carry a charge nor have a magnetic dipole moment, the mass mixing implies that the couplings will be of the transition type. If  $\psi_i$  carry a magnetic dipole moment<sup>3</sup> the mass eigenstates  $\chi_{1,2}$  will acquire a magnetic dipole transition operator. If instead  $(\psi_0, \psi_1, \psi_1^c)$  carry charge  $(1, 1, -1)$  respectively, with the massive state which generates the Majorana mass having charge 2, then  $\chi_{1,2}$  will couple in an off-diagonal fashion to the dark photon.

---

<sup>3</sup>These dipole moments may be generated perturbatively through loops of  $U(1)_D$  charged states, in which case the typical size is  $\sim g_D^3/(16\pi^2 m_\pm)$ . Or they may be generated non-perturbatively, as for the SM baryons, in which case we expect the size to be  $\sim g_D/m_\chi$ .

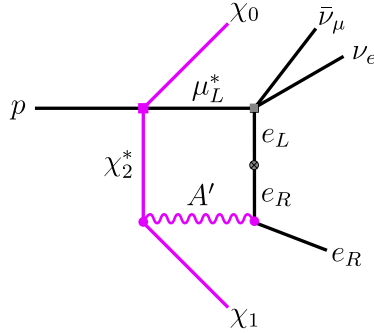


FIGURE 4.6: Loop induced proton decay from the triplet-singlet model.

Even if the SM fields are not charged under the dark gauge group, the coupling of the dark photon to the SM fields can occur through kinetic mixing of  $U(1)_D$  with  $U(1)_Y$ . This would be generated at one loop by having fields charged under both groups running in the loop. At low energies, this leads to a kinetic mixing between the dark photon and the SM photon of size  $\epsilon \sim eg_D/(16\pi^2)$ . The dark photon couplings to charged leptons are then of size  $\epsilon e$ .

**Models that lead to  $\mu^- n$  annihilation.** A completely separate set of models that can lead to energetic electrons at Mu2e and COMET are models that have the  $\mu^- n$  annihilation as the leading effect, while  $\mu^- p$  is induced only at the subleading loop level. An example are models that result in neutron-to-dark-state  $\chi_n$  transition, induced by the mass mixing  $\mathcal{L} \supset \epsilon(\bar{n}\chi_n + \bar{\chi}_n n)$ , as in ref. [88]. If the UV model contains  $\mu \rightarrow e$  CLFV interactions, then the  $\mu^- n \rightarrow e^- \chi_2$  transition becomes possible.

#### 4.3.3 Loop-induced processes

So far, we have focused on processes directly related, at tree level, to those responsible for the exotic signals at Mu2e. Within the triplet-triplet-singlet UV completion, section 4.3.1, we can also estimate the radiatively generated processes. For proton decay, these loop-induced contributions are potentially important since they can lead to proton decay with a smaller number of particles in the final state than those that we used for our estimates in section 4.5.1. The radiative corrections can also give rise to new processes, such as bound neutron decays and  $n - \chi$  mixing. Below, we address the possible constraints due to each of these processes.

**Proton decay.** If any of the final legs in fig. 4.2 (right) can be contracted to form a loop (see fig. 4.6),<sup>4</sup> this lowers the number of powers of  $Q$  suppressing the proton decay rate, and on dimensional grounds also removes the appropriate powers of  $G_F$  suppression. However, contraction of external legs requires small mass and/or coupling insertions. For instance, loop-level proton decay  $p \rightarrow (\chi_1 A')(\nu_e e^+)$  is obtained by contracting the  $\bar{\nu}_\mu$  and  $\nu_R$  external lines,

<sup>4</sup>Remember that we identified  $\chi_0 = \nu_R$ .

which requires a neutrino mass insertion. Contracting  $e^-$  with the  $e^+$  line from the weak vertex gives rise to the 5-body decay  $p \rightarrow e^+ \chi_1 \nu_e \bar{\nu}_\mu \nu_R$ , but requires an off-shell  $A'$  and is thus suppressed by small kinetic mixing, due to coupling of  $A'$  to the  $e^+e^-$  pair. Similarly, the  $p \rightarrow e^+ \chi_1 \nu_e$  decay, arising from a two-loop diagram with both  $\bar{\nu}_\mu$  contracted with  $\nu_R$  and  $e^-$  contracted with the  $e^+$  line from the weak vertex, is suppressed by the neutrino mass and by kinetic mixing. Because of these suppressions, the loop-induced proton decays always have smaller partial decay widths than the tree-level processes discussed in section 4.5.1.

**Neutron decay.** A one loop  $W$  exchange converts the  $u - \mu - T_2$  vertex in eq. (4.24) to a  $d - \nu_\mu - T_2$  one

$$(\overline{u_R^{iC}} \mu_R)(T_2^*)_i \rightarrow \frac{y_\mu y_u}{16\pi^2} \times (\overline{d_L^{iC}} \nu_\mu)(T_2^*)_i , \quad (4.36)$$

which after the  $T_{1,2}, \Phi$  are integrated out, and the higher dimension operator is run down to the weak scale, gives the effective Lagrangian

$$\mathcal{L}_{\text{int}} = \kappa \tilde{G}_{\mu p} \left( \overline{n_L^C} \nu_\mu \right) \left( \overline{\nu_R} \chi_{2R}^C \right) , \quad (4.37)$$

where

$$\kappa \simeq \frac{y_\mu y_u}{16\pi^2} \log \left( \frac{\Lambda_{\text{UV}}^2}{M_W^2} \right) \sim 10^{-10} , \quad (4.38)$$

with  $\Lambda_{\text{UV}} \sim m_{T_1}, m_{T_2}$ . The muon and up-quark Yukawa couplings arise due to mass insertions required for converting right-handed fields to left-handed ones, which then couple to the  $W$  boson.

In the same way as the  $u - \mu - T_2$  vertex leads to the proton decay inducing operator in eq. (4.30), after  $T_{1,2}$  and  $\Phi$  are integrated out, the  $d - \nu_\mu - T_2$  interaction in eq. (4.36) will induce the decay of the neutron into dark sector particles,

$$n \rightarrow (\chi_2^* \rightarrow \chi_1 A') \nu_R \bar{\nu}_\mu , \quad (4.39)$$

however, with a highly suppressed rate proportional to  $\kappa^2$ ,

$$\Gamma_n \simeq \left( \frac{g_D \kappa G_{\mu p}}{m_2} \right)^2 \frac{Q^7}{(16\pi^2)^2} . \quad (4.40)$$

Here,  $Q \approx (m_n - \epsilon_b - m_1 - m_{A'} - m_{\nu_R})/4$  is the typical momentum of the final state particles. In the expression for it, we already anticipated that the phenomenologically most relevant are the decays of neutrons bound inside nuclei, with  $\epsilon_b$  the average binding energy of a neutron inside a nucleus. This binding energy is large enough that the bound neutron decay will be kinematically forbidden for the squeezed mass spectra we consider.

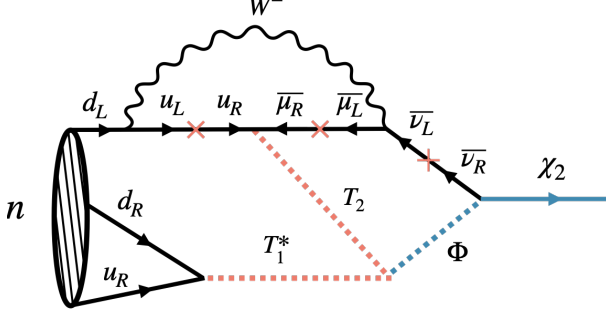


FIGURE 4.7: Neutron mixing with  $\chi_2$  generated at the two-loop level. At an additional loop, the mixing between  $\chi_1$  and  $n$  is generated by an  $A'$  line.

The bounds from searches for exotic decays of free neutrons of the type  $n \rightarrow e^+e^- + \text{inv}$  are relatively weak [208, 209]. However, if these transitions occur inside a nucleus, they would appear as decays of stable or long-lived nuclei, which then places stringent constraints on new physics models. In particular,  $^{12}\text{C} \rightarrow ^{11}\text{C} + \text{inv}$  and  $^{16}\text{O} \rightarrow ^{15}\text{O} + \text{inv}$  decays are well constrained, since the de-excitations of the daughter nucleus would leave visible signals in the underground large-volume detectors such as Borexino [210], KamLAND [211], and SNO/SNO+ [212, 213]. Since the daughter nuclei are meta-stable, the de-excitation signatures can be targeted experimentally, independently of the electron/positron pair signature that arises from the decay of  $A'$ . A lack of any positive signal places a bound  $\tau_n \gtrsim 10^{29}$  years, which should be compared with the expectations in eq. (4.40), shown in the right panel of fig. 4.8. Note that we take  $\kappa \sim 10^{-10}$  and have neglected the additional penalty from the binding energy.

In summary, the operator behind neutron decay indeed lifts part of the phase-space suppression in free proton decay but also gets suppressed in our model by  $u$ -quark and muon mass insertions. Due to the binding energy of the nucleus, it may even be kinematically forbidden in part of the parameter space.

**$n - \chi$  mixing.** Since in our specific UV completion  $\chi_0 = \nu_R$ , the diagrams such as the one in fig. 4.7 induce mixing between  $n$  and  $\chi_2$  ( $\chi_1$ ) at two-loops (three-loops), giving rise to  $n \rightarrow \chi_1$  transitions. The relevant operators are

$$\mathcal{L}_{\text{eff}} \supset m_{n\chi_1} \bar{n} \chi_1 + m_{n\chi_2} \bar{n} \chi_2 + \text{h.c.} \quad (4.41)$$

The  $m_{n\chi_1}$  parameter has greater phenomenological significance as it leads to kinematically-allowed  $n \rightarrow \chi_1$  transitions in nuclei. Let us first estimate  $m_{n\chi_2}$  in our UV completion using naive dimensional analysis,

$$\begin{aligned} m_{n\chi_2} &\sim \frac{y_u y_\mu y_\nu}{(16\pi^2)^2} (\lambda_{\text{eff}} y_\chi) v_{\text{EW}} \log^2 \left( \frac{\Lambda_{\text{UV}}^2}{m_W^2} \right) \\ &\sim y_\chi \times 10^{-28} \text{ MeV} \times \left( \frac{\lambda_{\text{eff}}}{10^{-10}} \right) \left( \frac{y_\nu}{10^{-12}} \right). \end{aligned} \quad (4.42)$$

Note that the mixing parameter is proportional to the neutrino coupling  $\kappa$  in eq. (4.38) and neutrino masses. One more loop is then required to transform  $\chi_2$  into  $\chi_1$  and is generated by an  $A'$  line that either connects to  $\nu_R$ , if charged under  $U(1)_D$ , or to an electrically charged state through kinetic mixing. We discuss the possible  $U(1)_D$  charge assignments in section 4.3.2. For now, we focus on the latter possibility, which leads to an estimate of  $m_{n\chi_1} \sim m_{n\chi_2} \times \epsilon^2 \alpha_D / 4\pi$ .

The rate for neutron disappearance inside a nucleus is given by Fermi's golden rule,

$$\Gamma_n = 2\pi |\langle \psi_f | m_{n\chi_1} | \psi_i \rangle|^2 \delta(E_f - E_i) \rho(E_f) , \quad (4.43)$$

with  $\rho(E_f)$  the density of states of the final state and  $\psi_i$  and  $\psi_f$  are the wavefunctions of the initial neutron and final state  $\chi_1$  state, respectively. The momentum of the final state, a free  $\chi_1$  particle, is determined by energy conservation with  $p_f^2/2m_1 = m_n - \epsilon_b - m_1$  and  $\epsilon_b$  is the binding energy of the neutron. Taking into account that there are  $N = A - Z$  neutrons inside a nucleus, the rate for nuclear transition induced by the  $n - \chi_1$  mixing is given by

$$\Gamma_N = \frac{N}{\pi} m_{n\chi_1}^2 m_1 p_f \xi^2 V_{\text{nucl.}} . \quad (4.44)$$

The overlap of the final state wavefunction with the neutron,  $\psi_i$ , bound inside a nucleus of volume  $V_{\text{nucl.}}$ , is encoded in the dimensionless quantity  $\xi$ , where

$$\xi^2 = \left| \frac{1}{\sqrt{V_{\text{nucl.}}}} \int d^3r \psi_i \exp(i\vec{p} \cdot \vec{r}) \right|^2 . \quad (4.45)$$

For large energy release,  $p_f^3 \gg V_{\text{nucl.}}$ , this overlap is small. Instead, we assume  $\xi \approx 1$  and arrive at an estimate for the decay time of a carbon nucleus, where  $\epsilon_b \sim 10$  MeV, due to neutron disappearance of

$$\begin{aligned} \tau_C &\simeq 10^{33} \text{ years} \times \left( \frac{850 \text{ MeV}}{m_1} \right) \left( \frac{100 \text{ MeV}}{p_f} \right) \\ &\quad \times \left( \frac{100 \text{ fm}^3}{V_{\text{nucl.}}} \right) \left( \frac{10^{-28} \text{ MeV}}{m_{n\chi_1}} \right)^2 . \end{aligned} \quad (4.46)$$

This lifetime should be compared to bounds on Pauli exclusion transitions from Borexino [214], which searched for a spontaneous formation of holes in the closed nucleon shells of  $^{12}\text{C}$ . For both the Pauli excluded transitions or a neutron conversion to  $\chi_1$  in a carbon nucleus, the remaining nucleons will refill shells, releasing an  $\mathcal{O}(10)$  MeV photon. Borexino's lack of a signal places a constraint of  $\tau_C \gtrsim 10^{27}$  years, which is easily satisfied in our model.

## 4.4 The signature

While the prediction for the aBNV transition  $\mu^- + {}^{27}\text{Al} \rightarrow \chi_0 + (\chi_2 \rightarrow \chi_1 e^+ e^-) + {}^{26}\text{Mg}^{(*)}$  requires a calculation of inelastic nuclear response function, we can make a naive estimate for its rate by using the muon capture rates in the SM. That is, an  $\mathcal{O}(1)$  fraction of muon capture on  ${}^{27}\text{Al}$  involves an emission of a neutron,  $\mu^- + {}^{27}\text{Al} \rightarrow \nu_\mu + n + {}^{26}\text{Mg}^{(*)}$ , which has similar  $1 \rightarrow 3$  decay kinematics and involves the same types of nuclear wave-functions in the initial and final state. We assume that ignoring the phase space corrections, the ratio of aBNV and SM muon captures remains roughly the same, irrespective of the initial nucleus. This implies, for instance

$$\frac{|\mathcal{M}(\mu^- {}^{27}\text{Al} \rightarrow \chi_0 \chi_2 {}^{26}\text{Mg})|^2}{|\mathcal{M}(\mu^- {}^{27}\text{Al} \rightarrow \nu_\mu n {}^{26}\text{Mg})|^2} \simeq \frac{|\mathcal{M}(\mu p \rightarrow \chi_0 \chi_2)|^2}{|\mathcal{M}(\mu p \rightarrow \nu_\mu n)|^2}. \quad (4.47)$$

Including the phase space correction, we thus have

$$\Gamma(\mu^- {}^{27}\text{Al} \rightarrow \chi_0 \chi_2 {}^{26}\text{Mg}) \simeq r_{\text{p.s.}} \frac{G_{\mu p}^2}{G_F^2} \Gamma(\mu^- {}^{27}\text{Al} \rightarrow \nu_\mu n {}^{26}\text{Mg}), \quad (4.48)$$

where we estimate the effect of phase space with the ratio of two Dalitz plot areas

$$\begin{aligned} r_{\text{p.s.}} &\simeq \frac{A_{\text{Dalitz}}(\mu^- {}^{27}\text{Al} \rightarrow \chi_0 \chi_2 {}^{26}\text{Mg})}{A_{\text{Dalitz}}(\mu^- {}^{27}\text{Al} \rightarrow \nu_\mu n {}^{26}\text{Mg})} \\ &\simeq \frac{(M - m_{\text{Mg}} - m_0 - m_2)^2 (M - m_{\text{Mg}} + m_0 + m_2)}{(M - m_{\text{Mg}} - m_n)^2 (M - m_{\text{Mg}} + m_n)}. \end{aligned} \quad (4.49)$$

In the last line, we neglected the neutrino mass. Above,  $M$  is the mass of the muonic atom,  $M = m_\mu + m_{\text{Al}} - E_b$ , with  $E_b \approx 0.463 \text{ MeV}$  the binding energy,  $m_{\text{Al}}$  the mass of the  ${}^{27}\text{Al}$  and  $m_{\text{Mg}}$  the mass of the  ${}^{26}\text{Mg}$  atom. Note that for  $m_0 + m_2 = m_n$  the above ratio is  $r_{\text{p.s.}} = 1$ . This is exact only if  $m_0$  is massless, showing the limitation of our approximations. For our benchmarks, eqs. (4.16) and (4.17), we find  $r_{\text{p.s.}} \simeq 4 \times 10^{-3}$ .

Equating  $\Gamma(\mu^- {}^{27}\text{Al} \rightarrow \nu_\mu n {}^{26}\text{Mg})$  with the full SM muon capture rate,  $\Gamma_{\mu \text{Al}} = 0.7 \times \mu\text{s}^{-1} = 4.6 \times 10^{-19} \text{ GeV}$  [215], which is in line with our other approximations, we then get for the aBNV conversion rate

$$R \equiv \frac{\Gamma_{\text{exotic}}}{\Gamma_{\mu \text{Al}}} \simeq r_{\text{p.s.}} \frac{G_{\mu p}^2}{G_F^2}. \quad (4.50)$$

The benchmarks in eqs. (4.16) and (4.17) result in a rate  $R \sim 3 \times 10^{-15}$ , well within Mu2e and COMET's sensitivities and, as we will see, safe from nucleon decay bounds.

Once produced,  $\chi_2$  eventually decays to an  $e^+ e^-$  pairs through the cascade  $\chi_2 \rightarrow \chi_1 (A' \rightarrow e^+ e^-)$ . The resulting energy spectra of the  $e^+ e^-$  pairs produced are shown for a few representative points in figs. 4.3 and 4.4. Note that the individual electron or positron energies

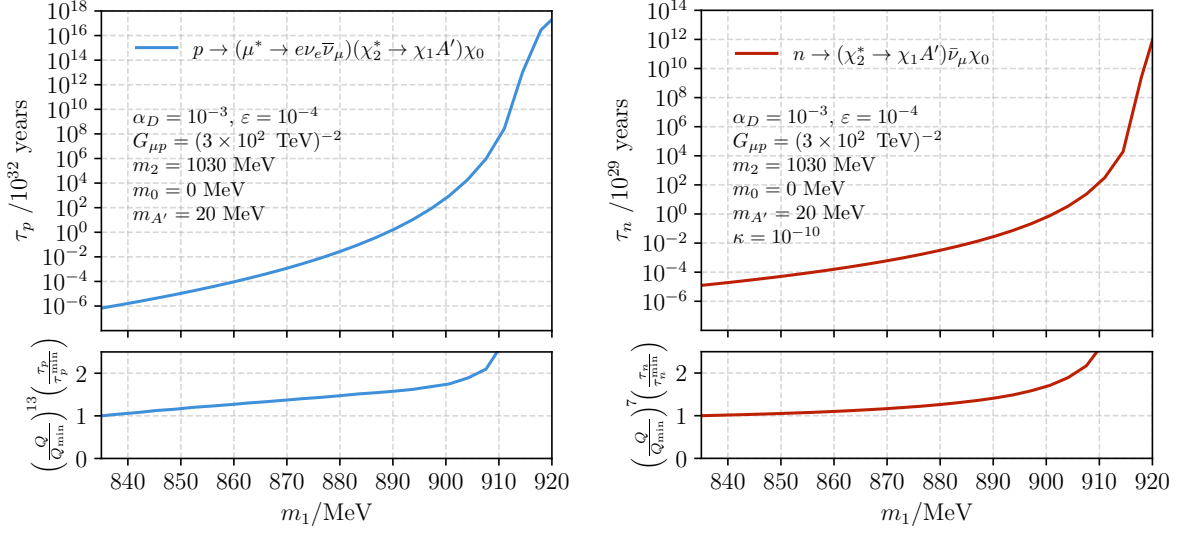


FIGURE 4.8: Estimates of the lifetime of a free proton (left) and neutron (right) as a function of the mass of the lightest dark particle  $\chi_1$  for benchmark (I). The bottom panel illustrates the scaling of the lifetime with respect to the energy release  $Q$ , which is proportional to the nucleon mass minus the sum of the masses of all final state particles that are on shell, see eqs. (4.51) and (4.52). The nucleon lifetime  $\tau_N^{\min}$  and its respective energy release  $Q_{\min}$  are calculated for the smallest value of  $\chi_1$  mass shown in the figure. We do not include loop-level proton decay channels which may dominate at the largest masses.

can be greater than  $m_\mu$  due to the additional energy released by the destruction of the proton mass. This is also manifested in the sum of the electron and positron energies, which peaks at  $E_{e+} + E_{e-} \simeq (m_2^2 - m_1^2 + m_{A'}^2) / 2m_2$ , given that  $\chi_2$  only has a small boost and thus the lab frame kinematics almost coincide with the rest frame  $\chi_2 \rightarrow \chi_1 A'$  two body decay kinematics ( $E_{e+} + E_{e-} = E_{A'}$  for  $A'$  on-shell).

Several features can help distinguish the aBNV processes from  $\mu^- \rightarrow e^-$  conversion, most notably the differing electron spectra and the presence of positrons in the aBNV case. A signal of equal magnitude with equal endpoints in the electron and positron channels that go beyond the  $\mu^- \rightarrow e^-$  endpoint would be a strong indication for aBNV processes of the type considered here. The positron signal is subject to even smaller backgrounds than the search for  $\mu^- \rightarrow e^-$  signal is; the DIO background produces only electrons, and charge misidentification is expected to be rare. Most background events are expected to arise from radiative muon capture (RMC) with either internal or external photon conversion. RMC, however, has an even lower endpoint than DIO,  $E_{\text{RMC}}^{\text{Al}} \lesssim 101.9$  MeV [216]. The positron search could be done already with the Al target, while one could also explore other targets (for a different BSM signal producing positrons, the lepton-number-violating  $\mu^- \rightarrow e^+$  conversion, see refs. [216, 217]). Finally, we note that the  $Z$  dependence of the aBNV rate will differ from the one for  $\mu^- \rightarrow e^-$  or  $\mu^- \rightarrow e^+$  conversion (see, for instance, ref. [218]). The planned upgrades of Mu2e using, e.g., Au as the target [219], could thus help distinguish between these scenarios.

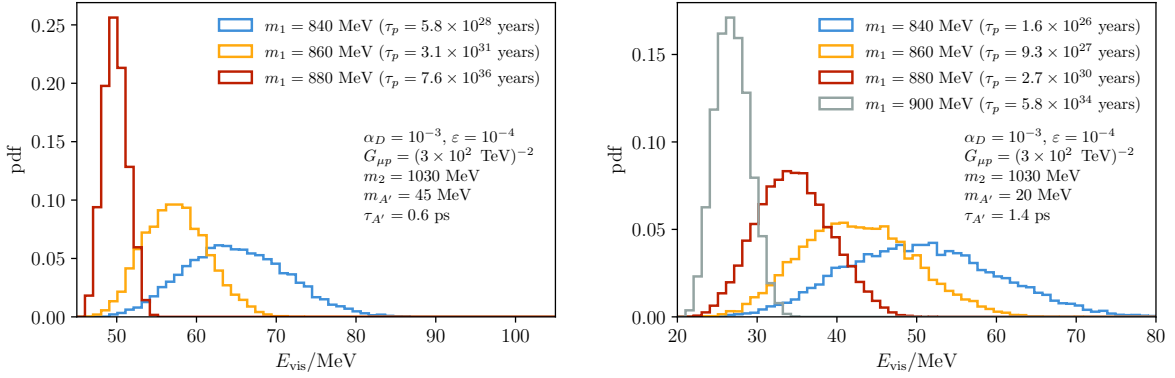


FIGURE 4.9: The normalized true total visible energy spectrum (energy of the  $e^+e^-e^-e^-$  system) in  $p \rightarrow eee\nu\nu\chi_1\chi_0$  decays for two choices of dark photon masses. The distributions look similar for the same benchmarks when using transition moments instead ( $\alpha_D \rightarrow d_{tr}$ ), although the total lifetimes increase.

One of the crucial aspects of the Mu2e experiment is the requirement of a very high degree of initial proton and pion beam extinction within the signal time window, as well as a very reliable rejection of cosmic-ray-induced events. If a certain amount of pion “contamination” is, for example, present within the signal-taking time interval, it may result in charged leptons with energy well above  $E_e^{\text{conv}}$ . The  $\pi^-$  capture on a nucleus can thus result in a  $\sim 135$  MeV photon, which can Compton-scatter and produce electrons well above  $E_e^{\text{conv}}$ . The  $\mu^-p$  annihilation electrons could, therefore, easily be misinterpreted as being due to a pion background. The above benchmarks for the  $\mu^-p$  annihilation models, which can create  $E_e \sim m_\pi$ , thus show that extra care needs to be taken. In the event of a signal, a detailed investigation would be warranted to determine definitively whether such electrons do indeed stem from the pion decays and not from exotic new physics signatures, such as those investigated in this section.

## 4.5 Constraints

### 4.5.1 Proton decay

The effective interaction in eq. (4.14) violates proton number. What is an apparent phenomenological disaster can be readily reconciled with the most stringent constraints on proton decay by a judicious choice of mass hierarchies. By such a choice, we can ensure that some of  $\chi_2, \chi_0, \mu$  must be produced off their mass shell, resulting in a higher particle multiplicity of final states and extra suppression by small coupling constants. Furthermore, the amount of open final state phase space will be small, suppressing the proton decay rate. In table 4.1, we list the possible decay channels, the necessary constraints on the mass hierarchy of the model to allow this channel, and an estimate for the proton decay width. Before discussing how these constraints

affect the allowed region of parameter space, we first discuss how they are derived. Later on, we will calculate the rate fully numerically using `MADGRAPH5_v3.5.3`.

**Scaling with energy release:** The energy released in proton decay is

$$\Delta E = (m_p - \sum_i^{N_f} m_i), \quad (4.51)$$

where  $N_f$  is the number of final state particles in the decay. Each of the final particles therefore carries a typical momentum

$$Q \simeq \Delta E / N_f, \quad (4.52)$$

with  $N_f \in [3, 7]$  depending on which decay is being considered; we leave the discussion of loop decay for later since it is UV model dependent. The typical value of  $Q$  in proton decay is  $\sim \mathcal{O}(5)$  MeV, see fig. 4.10. That is, at the upper range of  $m_1$ , the electrons will start becoming non-relativistic; we will discuss the effect of this below. In some of the decay channels, there are off-shell particles whose propagators we estimate to scale as inverse powers of the particle mass ( $m^{-1}$  for fermions and  $m^{-2}$  for bosons). For instance, the muon has 3 approximately massless decay products and scales as

$$\frac{\not{p}_\mu + m_\mu}{p_\mu^2 - m_\mu^2} \sim \frac{3Q + m_\mu}{(3Q)^2 - m_\mu^2} \sim -\frac{1}{m_\mu}, \quad (4.53)$$

whereas for  $\chi_2$  the decay products may be non-relativistic and it scales as

$$\frac{\not{p}_{\chi_2} + m_2}{p_{\chi_2}^2 - m_2^2} \sim \frac{\not{p}_{\chi_2} + m_2}{(m_{\chi_1} + m_{A'})^2 - m_2^2} \sim -\frac{1}{m_2}, \quad (4.54)$$

where we used the fact that  $\chi_1$  and  $A'$  are non-relativistic (a better approximation for  $\chi_1$  than it is for  $A'$ ). The matrix element squared acquires scalings with  $Q$  when carrying out spin/polarization sums. The final state fermions contribute to  $|\mathcal{M}|^2$  parametrically as  $\sim Q$  ( $\sim m$ ) if they are relativistic (non-relativistic), while the final state vector bosons as  $\sim Q^0$  ( $\sim Q^2/m_{A'}^2$ ). Furthermore, although we focus on the contact interaction, if the coupling is through the dipole interaction  $d_{\text{tr}}$  then  $|\mathcal{M}|^2$  picks up another factor of  $Q^2$ . The remaining  $Q$  scaling comes from the phase space integrals, where for each final state particle

$$\frac{d^3 p_i}{(2\pi)^3 2E_i} \sim \begin{cases} \frac{1}{16\pi^2} Q^2, & \text{relativistic,} \\ \frac{1}{16\pi^2} \frac{Q^3}{m_i}, & \text{non-rel.,} \end{cases} \quad (4.55)$$

The scaling of the matrix element and phase space for final state fermions is such that each one contributes  $Q^3$  in both the relativistic and non-relativistic limits. We present the results of these approximations in table 4.1, where we have assumed the final state  $A'$  is non-relativistic,

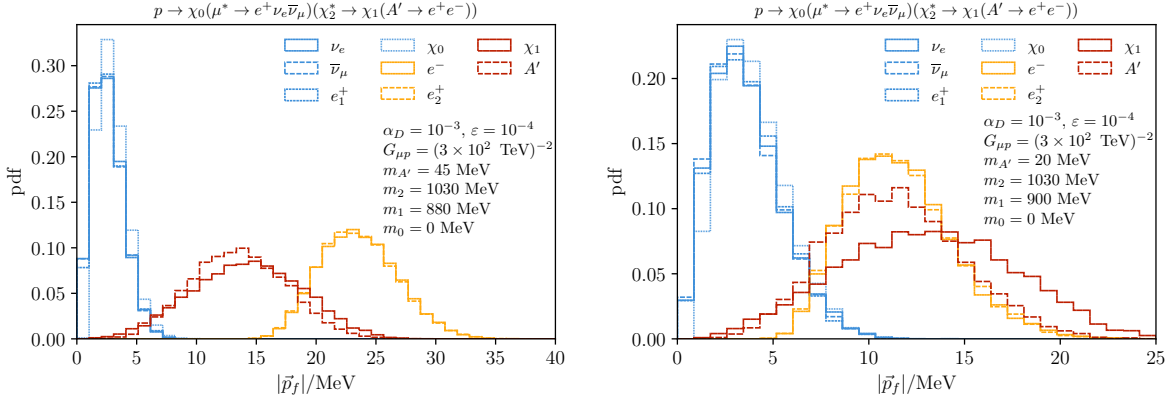


FIGURE 4.10: The momentum of the individual final state particles in  $p \rightarrow eeee\nu\nu\chi_1\chi_0$  decays for two choices of dark photon masses. Here the final state positrons  $e_1^+$  and  $e_2^+$  are distinguished at the event level by the magnitude of the three-momenta, with  $e_2^+$  always being assigned to the larger momenta.

which will be the case for the parameter space we are interested in. In table 4.1, we also list the scaling for a tree level  $p \rightarrow \mu ee\chi_1\chi_0$  decay with  $\chi_1$  heavy enough for  $A'$  to be required to be off-shell, which gives an additional  $Q^4/m_{A'}^4$  suppression for the decay width.

From these scalings, it is clear that channels 1 and 2 will lead to too rapid proton decay unless  $\alpha_D$  is taken very small, which removes the prompt signal at Mu2e. Channel 3 requires considerable tuning in the mass spectrum, so we ignore it from now on. This leaves channels 4 and 5, both of which can be small enough to avoid constraints. The benchmarks described in eqs. (4.16) and (4.17) have a decay through channel (5) with an estimated lifetime of  $\tau_p \sim 5 \times 10^{34}$  years and  $\tau_p \sim 2 \times 10^{41}$  years, respectively.

**MadGraph estimates:** To calculate the rate more accurately and study the resulting kinematics, we implement the model in MADGRAPH5\_v3.5.3 and calculate the proton lifetime by generating  $p \rightarrow (\mu^* \rightarrow e\nu_e\bar{\nu}_\mu)(\chi_2^* \rightarrow \chi_1(A' \rightarrow e\bar{e}))\chi_0$  decays. This includes contributions from real as well as virtual  $A'$ . We calculate the decay width of the new particles for each choice of couplings. For values of  $\alpha_D$  larger than about  $\alpha_D = 10^{-2}$ , the  $\chi_2$  width can lead to important corrections to the decay rate and kinematics, but we do not explore this further here. For the small values of kinetic mixing we are interested in, the width of the dark photon is always negligible. Our results are shown for  $10^5$  generated events.

The left panel of fig. 4.8 shows the resulting proton lifetime in the region of interest for the benchmark point in eq. (4.16) as a function of the  $\chi_1$  mass. The bottom row of the left panel shows the accuracy of the  $Q^{13}$  scaling. This lifetime should be compared to experimental constraints. The strongest constraints on the proton lifetime were obtained in underground neutrino detectors, where, for instance,  $\tau(p \rightarrow e^+\pi^0) > 2.4 \times 10^{34}$  years [220]. Other similar channels have been searched for, including  $\tau(p \rightarrow e^+e^+e^-) > 3.4 \times 10^{34}$  years [221]. While these channels have similar topologies to  $p \rightarrow eeee\nu\nu\chi_1\chi_0$ , namely three electromagnetic showers, the

kinematics differs significantly from our signal. In particular, the energy of the three showers must reconstruct the proton, while in our case, the energy release is, in fact, much smaller. fig. 4.9 shows the total visible energy of the exotic proton decay mode, showing that the energy released into electrons and positrons is significantly smaller than the proton mass. In this low-energy region, experimental backgrounds, such as from neutrino interactions at underground detectors, become larger, typically by factors of  $\mathcal{O}(100)$  [220]. Therefore, constraints on proton decays induced by the muon-induced baryon number violation are expected to be significantly weaker than they are for the golden  $p \rightarrow e^+ \pi^0$  and  $p \rightarrow e^+ e^+ e^-$  decay channels. While a detailed study of the resulting limit is beyond the scope of this paper, it appears that one can safely conclude that the current searches do not exclude lifetimes as small as  $10^{32}$  years.

Figure 4.10 shows the momentum distribution of the final state particles in the exotic proton decay  $p \rightarrow eee\nu\nu\chi_1\chi_0$ . As expected, the available energy  $\Delta E$  is split unevenly between the final states thanks to the large imbalance of masses of the particles involved. In fact, the final states produced in the chain  $\chi_2 \rightarrow \chi_1 + A'$  carry more energy thanks to the large mass of  $\chi_1$  and  $\chi_2$ . Similarly, positrons emitted from the  $\mu^+ \rightarrow e^+\nu\nu$  chain carry less energy than those from the decay of the on-shell dark photon. In the figure, we show the energy of both positrons, with  $e_1^+$  being the least and  $e_2^+$  the most energetic positron in the final state.

Finally, an important consideration is that the tree-level six-body proton decay channel, for which we estimated the rates above, is not the only possible proton decay mode that can be generated via  $\mu p$  annihilation interactions, once radiative corrections are included. In fact, at the loop level, many new decay channels open up, with a smaller number of final state particles, which relaxes the steep suppression of the decay rate by high powers of  $Q$ . An example is a loop correction obtained by attaching the dark photon line to any of the charged particles, which then leads to  $p \rightarrow (\chi_1\chi_0)(e^+\nu_e\bar{\nu}_\mu)$  decays. In similar ways, corresponding decay modes for bound neutrons can be found. These contributions are UV-sensitive, see section 4.3, where we showed that this reduction in  $Q$  dependence is compensated by the necessary inclusion of small couplings/masses.

#### 4.5.2 Neutron stars

Neutron star properties such as mass-radius relation and their cooling function are well understood and can be used to probe many aspects of new physics [222, 223]. Among others, neutron stars can also provide an indirect probe of the new  $\mu^-$ -nucleon interactions in eq. (4.1), due to a large abundance of muons, not only during the initial stage of the core-collapse supernova explosion but also at much later stages in the form of the quasi-degenerate Fermi fluid of  $\mu^-$ . A related topic has been addressed in the literature of “dark neutron” models [88], from where we borrow several results in our discussion (see, in particular, Refs. [224–229]).

The zero-temperature nuclear matter inside neutron stars is in chemical equilibrium due to weak interaction transitions, such as  $n \leftrightarrow p\ell^-\bar{\nu}_\ell$  and  $p\ell^- \leftrightarrow n\nu_\ell$ , where  $\ell = \{e, \mu\}$ . These ensure that the chemical potentials  $\mu_i$  for  $i = n, p, e, \mu$ , satisfy  $\mu_n - \mu_p = \mu_e = \mu_\mu$ . Thanks to the large value of  $\mu_e$  it is possible for beta-decay type reactions to create muons inside the neutron star despite their larger mass. The large value of  $\mu_e$  also makes  $\mu^-$  stable inside the neutron star. The muon fraction inside the core of the neutron star is determined by nuclear density and equation of state, and, therefore, depends on the modeling of nuclear matter.<sup>5</sup> In Ref. [230], it was estimated that the fraction of the muon to baryon number densities could be as high as  $n_\mu/n_B \sim 20\%$ , to be compared with the maximum proton fraction of about  $n_p/n_B \sim 40\%$ .

The muon-induced aBNV transitions of the form  $\mu^-n \rightarrow e^-\{X\}^0$  or  $\mu^-p \rightarrow e^-\{X\}^+$ , cf. eq. (4.1), can change the above equilibrium, since now neutrons and/or protons can be converted into dark sector states inside the neutron star. That is, in the concrete model we are considering in detail, the process  $\mu^-p \rightarrow \chi_0\chi_2$  (and the  $\nu_\mu n \rightarrow \chi_0\chi_2$  process, generated at 1-loop) will become energetically favorable and deplete the number of nucleons. The capture rate inside the neutron star is given by

$$\Gamma_{\mu^-p \rightarrow \chi_0\chi_2}^{\text{NS}} = \langle \sigma_{\mu p} v \rangle n_p \simeq G_{\mu p}^2 m_\mu m_p n_p, \quad (4.56)$$

where  $\sigma_{\mu p}$  is the cross section for scattering of muons on protons,  $v$  is their relative velocity, and  $\langle \dots \rangle$  indicates that we should average over the phase space of the particles involved. For the benchmark value of  $G_{\mu p}$ , eqs. (4.16) and (4.17), this gives

$$\Gamma_{\mu^-p \rightarrow \chi_0\chi_2}^{\text{NS}} \simeq \frac{1}{100 s} \left( \frac{G_{\mu p}}{(300 \text{ TeV})^2} \right)^2. \quad (4.57)$$

Interestingly, for dynamics on such intermediate time-scales  $\sim \mathcal{O}(\text{min} - \text{months})$  there are no stringent constraints from the properties of neutron stars, as long as  $\chi_0$  and  $\chi_2$  do not escape from the stellar interior. The constraints on properties of the proto-neutron star come from the measurements of the neutrino flux that was generated by the supernova SN-1987a explosion. This probes dynamics on the timescales  $\lesssim 10\text{s}$  of seconds. The constraints on properties of neutron stars, on the other hand, apply only to much longer timescales. Typically, there are no direct observations of young neutron stars following the supernova explosion since these are obscured by the remnants of the outer envelope of a progenitor.

The muon-induced aBNV processes in Eq. (4.1) would heat up the star, emitting visible energy in the form of  $e^+$  and  $e^-$ . The  $\mu^-p$  and/or  $\mu^-n$  annihilations would create holes in the nucleon and  $\mu^-$  Fermi seas, which then get refilled, resulting in additional energy release. If such processes

---

<sup>5</sup>In some models of nuclear matter it is hypothesized that at extremely large densities there is a stable population of heavier baryons and hyperons such as  $\Delta(1232)^-$  and  $\Sigma^-$ , which dominate the number density of negatively charged particle species, and de-leptonize the core. This can significantly reduce the muon density and, therefore, the rate of  $\mu^-p$  or  $\mu^-n$  reactions. Similar arguments apply to the higher-density models where the transition to quark matter reduces the muon chemical potential  $\mu_\mu$ .

are rather slow, *i.e.*, occurring on time-scales of millions of years, the late-time observables of neutron stars, such as the temperature [231, 232] of the coldest neutron stars [233] or the periods of pulsars [234], will be sensitive to the muon-induced aBNV.

However, for the capture rates that Mu2e and COMET are sensitive to, the nucleon depletion is fast and will lead to a new equilibrium inside the star with a lower pressure and a softer equation of state (EoS) due to the redistribution of energy over a larger number of degrees of freedom. The dark sector dynamics will determine whether or not the new EoS will support stars with radii and masses consistent with observation. These considerations are similar to what happens in mirror neutron models [224–227], with the added requirement that muons participate in the conversion reactions. It is clear that the models with stable massive fermions in the dark sector, similar to our benchmark cases, are vastly favored over the models in which the dark sector states decay to very light fermions and/or bosons. In the latter case, the newly produced dark states are not retained by the neutron stars and/or do not contribute to the Fermi pressure.

A new dark force can help restore the pressure lost to the increased number of degrees of freedom. To illustrate this, consider a scenario where  $\mathcal{O}(50\%)$  of nucleons get converted into a population of new fermions,  $\chi$ . This may be  $\chi_1$  or  $\chi_0$ , depending on the details of the model. If  $k_{F,0}$  is the original Fermi momentum of neutrons in a neutron star without dark states, then by particle number conservation,  $k_{F,0}^3 = k_{F,n}^3 + k_{F,\chi}^3$ . If half of the existing nucleons go to  $\chi$ , then  $k_{F,n} \simeq k_{F,\chi} < k_{F,0}$ , thereby reducing the pressure (which is a highly nonlinear function of  $k_F$ ).

A repulsive self-interaction between the dark sector states contributes to the pressure and could compensate for the reduction of the Fermi momentum. The change in pressure due to a single new dark particle  $\chi$  subject to a new long-range force mediated by  $A'$  is

$$\Delta P = \frac{1}{15\pi^2} \left( \frac{k_{F,n}^5 - k_{F,0}^5}{m_n} + \frac{k_{F,\chi}^5}{m_\chi} \right) + \frac{g_\chi^2 k_{F,\chi}^6}{18\pi^4 m_{A'}^2}. \quad (4.58)$$

Therefore, when  $(g_\chi^2/\pi^2 m_{A'}^2) \times (k_{F,0} m_n) \gg 1$ , this leads to a positive change in pressure compared to the one for a neutron star in the SM, indicating that it is indeed possible to counteract the loss of pressure through a repulsive force. In our scenario, the required size of  $g_\chi^2/m_{A'}^2$  will depend on the dynamics of the dark sector, the nature of  $\chi_0$ , and the origin of the new force (the mediator of this dark force may be the dark photon of section 4.2, but in general this may not be the case and could be due to a different light mediator).

An alternative possibility for adjusting the neutron star properties was pointed out in refs. [228, 229], where the large multiplicity of the dark fermions in the final state was used to correct for the loss of Fermi pressure in the nucleon fluid. In our framework this can be implemented by, *e.g.*, further decays along the “dark decay chain”, such as  $\chi_1 \rightarrow 3\chi_3$  with  $m_{\chi_3}$  not too far from  $m_{\chi_1}/3$ . This model would then not require any additional pressure from the  $A'$  exchanges.

In conclusion, dark sector models offer sufficient flexibility to compensate for the loss of nucleon Fermi pressure. Having outlined a potential reconciliation between observable exotic muon capture and the physics of neutron stars, we leave an investigation of the broader impact of muon-induced baryon number violation on neutron stars to future literature.

## 4.6 Conclusions

In this chapter, we have constructed new physics scenarios with muon-induced (apparent) baryon number violation. Using a specific example, we demonstrated that these models lead to a spectrum of higher energy electrons and positrons in the  $\mu^- A \rightarrow e^- A$  conversion experiments, such as Mu2e and COMET, while satisfying experimental bounds on proton stability. The main idea consists of tapping into the baryonic energy reservoir of the nucleus  $A$  by destroying protons or neutrons in the muon capture process. This releases energies greater than  $m_\mu$  into dark particles that eventually decay to  $e^+e^-$  pairs. The  $e^+$  or  $e^-$  can reach energies as high as  $\mathcal{O}(130)$  MeV, depending on the choice of parameters, significantly overshooting the energy of electrons produced in decay-in-orbit as well as of eventual monochromatic electrons from  $\mu^- {}^{27}\text{Al} \rightarrow e^- {}^{27}\text{Al}$  ( $E_{e^-}^{\text{Al-conv}} = 104.98$  MeV).

These signatures are not excluded by limits on the proton lifetime thanks to a coincidence between the mass of the proton and the dark particles, which forces the protons to decay via two or more off-shell states. The stability of nuclei (more specifically, that of bound neutrons) also imposes meaningful constraints due to radiative corrections. These are again bypassed due to strong phase-space suppression as well as by chiral suppression in the UV completions we considered. The crucial component for constructing models that enhance the  $\mu^-$ –nucleon annihilation while suppressing nucleon decays is that the ratio of muon to proton mass is  $m_\mu/m_p \sim 1/9$ , which is not a very small ratio. Consequently, changes in mass splittings in the dark sector at the level of  $\sim 20$  MeV (*i.e.*, at a few percent level) are very consequential for the signals discussed here and can change answers by many orders of magnitude.

While our scenarios are specifically designed to hide nucleon decay and highlight muon capture, they demonstrate that Mu2e and COMET can be sensitive to electrons that come from new physics sources other than the  $\mu \rightarrow e$  lepton flavor violating neutral currents. Such scenarios are particularly attractive in the event that high-energy electrons or positrons are detected at Mu2e. Our proposal also shows that such high-energy events may not necessarily come only from backgrounds such as the decay of late-time pions or cosmics.

Finally, we also emphasize that positrons may present a particularly interesting final state. Light dark sectors can lead to positron energies beyond those induced by radiative muon capture and by the lepton-number-violating channel  $\mu^- A \rightarrow e^+ A'^*$  [235, 236]. The latter includes a monochromatic positron with energy of about  $E_{e^+}^{\text{conv}} \simeq 92.3$  MeV for  $\mu^- {}^{27}\text{Al} \rightarrow e^+ {}^{27}\text{Na(g.s.)}$

transitions. It should be noted that past searches for  $\mu^- \rightarrow e^+$  at TRIUMF [237] and PSI [125, 238, 239] on Ti and Au targets have all reported excesses of positrons above  $E_{e^+} \gtrsim 90$  MeV but below  $E_{e^+} \lesssim m_\mu$  (see also earlier searches in [240–242]). While the modeling of radiative muon capture may be insufficient in this energy region [217], these events represent an immediate application of our scenarios. In fact, since the positron energies in these excess events are still less energetic than  $m_\mu$ , an explanation through muon-induced BNV would be feasible even for parameters that render protons and bound neutrons stable.

# Chapter 5

## Direct detection of ultralight dark matter with CLFV

**Preface:** This chapter closely follows the work in [5] with Innes, Paddy, Yann, Roni, Gordan and Jure. The main idea was to consider the phenomenological consequences of introducing an ultralight scalar field with lepton flavor violating couplings – most importantly, how the inherent time-dependence of ULDM might manifest in experiments at the intensity frontier. We find that time-dependence is UV-dependent and sourced at dimension - 5 or 6. Additionally, avoiding environmental fine-tuning requires two distinct scalar fields, one of which is required to be DM. Finally, we estimate the reach at current and future intensity frontier experiments (using time-independent or time-dependent analyses) in both the  $\mu$  and  $\tau$  CLFVing channels ( $\mu \rightarrow e\phi'$ ,  $\tau \rightarrow \ell\phi'$ ).

Dark matter (DM) remains one of the most compelling empirical pieces of evidence pointing beyond the SM. Originally proposed by Zwicky in the 1930s from anomalous galaxy cluster dynamics [243], the existence of dark matter is now robustly supported by many independent astrophysical and cosmological observations, including galactic rotation curves [244], gravitational lensing [245], cosmic microwave background (CMB) anisotropies [246], and large-scale structure formation [247]. Even with overwhelming gravitational evidence, its particle nature remains unknown despite decades of dedicated experiments [248].

In this chapter we'll focus on ultralight dark matter (ULDM), consisting of particles with sub-eV masses. Such ultralight bosonic fields, behave as coherent classical fields rather than a point-like propagating degrees of freedom and manifest unique wave-like phenomena distinct from traditional particle dark matter. The quantum coherence of ULDM on astrophysical scales naturally induces distinctive astrophysical signatures, such as modifications in galactic density profiles, coherent oscillations in fundamental constants, and as we'll see in this chapter, observable periodic signals in precision experiments.

The ultralight regime of dark matter is attractive from both theoretical and observational perspectives. It naturally arises in frameworks addressing outstanding issues in particle physics, such as the Strong CP problem and dark sector gauge extensions. Furthermore, due to their extended de Broglie wavelengths, ULDM fields can imprint distinctive phenomenological signatures at lower energies and higher precision than traditional heavy dark matter searches, opening new frontiers at the intersection of particle physics, astrophysics, and cosmology.

## 5.1 Ultralight dark matter

A prototypical production mechanism for ultralight dark matter is through vacuum misalignment of a scalar field in the early universe. Consider a real scalar field  $\phi$  with a quadratic potential of the form

$$V(\phi) = \frac{1}{2}m_\phi^2\phi^2, \quad (5.1)$$

where  $m_\phi$  is the ULDM mass. The equations of motion in an expanding Friedmann-Robertson-Walker (FRW) background are given by

$$\ddot{\phi} + 3H\dot{\phi} + m_\phi^2\phi = 0, \quad (5.2)$$

where  $H$  is the Hubble parameter and dots denote derivatives with respect to cosmic time.

At early times, when  $H \gg m_\phi$ , the Hubble friction term dominates and the field is overdamped, causing the field to remain frozen at its initial field value  $\phi_0$ . This initial displacement is set by initial conditions and typically assumed to be of order the symmetry breaking scale in axion-like models. As the universe expands the Hubble rate redshifts i.e. decreases, once  $H \sim m_\phi$  the scalar field begins to ‘thaw’ and begins to coherently oscillate about the minimum of its potential. At late times ( $H \ll m_\phi$ ), the equation of motion reduces to that of a damped harmonic oscillator,

$$\phi(t) \sim \phi_0(t) \cos(m_\phi t), \quad (5.3)$$

with an amplitude  $\phi_0(t)$ . The time-averaged energy density of the field behaves as

$$\langle \rho_\phi \rangle = \left\langle \frac{1}{2}\dot{\phi}^2 + \frac{1}{2}m_\phi^2\phi^2 \right\rangle \propto a^{-3}, \quad (5.4)$$

where  $a(t)$  is the scale factor. This scaling is characteristic of pressureless matter, motivating the interpretation of ULDM as cold dark matter at late times.

Importantly, the coherence length of the field,  $\lambda_{\text{dB}} \sim (m_\phi v)^{-1}$ , can span astrophysical distances due to the suppressed mass and small virial velocities, enhancing wave-like effects in structure formation and precision experiments. Thus, misalignment production not only generates the correct relic abundance for a broad range of initial conditions and masses, but also induces

ULDM with macroscopic coherence and a rich phenomenology distinct from particle-like dark matter candidates.

## 5.2 ULDM with flavor violating couplings

While DM searches have traditionally focused on DM masses near the weak scale, in recent years, this global effort has broadened to cover a wide range of DM masses. Such strategies incorporate techniques from diverse disciplines, including accelerator [249], condensed matter [250, 251], and atomic/molecular/optical physics [252], and their relative advantages depend greatly on the DM mass scale.

Based on the measured dark matter mass density and the Tremaine-Gunn bound [253], any self consistent theory of “ultralight” DM *must* be both bosonic and wavelike with a present day classical field value [254]

$$\phi_c(t) = \phi_0 \cos(m_\phi t + \delta), \quad (5.5)$$

where  $m_\phi$  is the DM mass,  $\delta$  is an arbitrary phase. The amplitude satisfies

$$\phi_0 = \frac{\sqrt{2\rho_\phi}}{m_\phi} \simeq 2.5 \text{ TeV} \left( \frac{10^{-15} \text{ eV}}{m_\phi} \right), \quad (5.6)$$

where  $\rho_\phi = 0.4 \text{ GeV/cm}^3$  is the local dark matter mass density [255] and  $\phi$  is said to be “misaligned” from its potential minimum [256–258]. This unique<sup>1</sup> description of ultralight DM offers a powerful first-principles starting point for *any* investigation into DM candidate masses in the range  $10^{-21} \text{ eV} < m_\phi < 1 \text{ eV}$ . Masses below  $10^{-21} \text{ eV}$  are excluded because the DM de-Broglie wavelength exceeds the scale of dwarf galaxies [259, 260].

As the field in eq. (5.5) modulates in time with frequency  $m_\phi$ , interactions between  $\phi$  and the SM fields can inherit the characteristic periodicity

$$\tau_\phi = \frac{2\pi}{m_\phi} \simeq 4 \text{ s} \left( \frac{10^{-15} \text{ eV}}{m_\phi} \right), \quad (5.7)$$

which may be appreciable on experimental timescales. While there is a large literature on DM-induced time variation in fundamental constants, particle masses, and nuclear spin-precession, these strategies assume flavor blind interactions between  $\phi$  and SM fields (see [261–263] for reviews). Ultralight DM has been studied as a catalyst for time variation in the quark and lepton mixing matrices [264–270], in the CP phase of strong interactions [271–273], and of

---

<sup>1</sup>If the functional form were to substantially deviate from eq. (5.5), the energy density would not redshift like non-relativistic pressureless matter [254], which would spoil cosmological structure formation. Alternatively, if  $\phi$  were a spin-1 field, eq. (5.5) would feature a polarization vector, but the time dependence and the amplitude would not be affected.

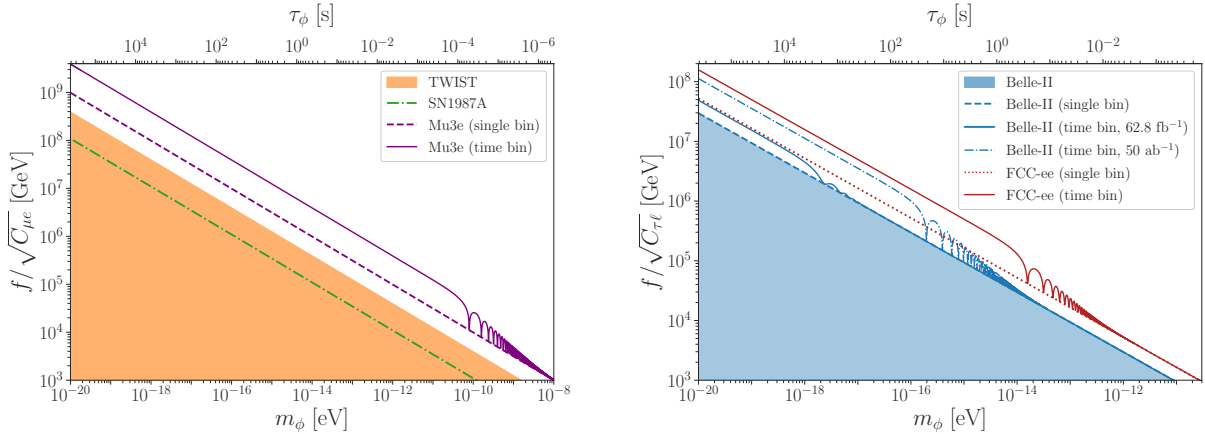


FIGURE 5.1: Present and projected constraints on LFV couplings  $f/\sqrt{C_{\mu e}}$  (left) and  $f/\sqrt{C_{\tau e}}$  (right) for time-binned and single-bin analyses, as a function of the scalar mass,  $m_\phi$  – see eqs. (5.10) and (5.12). **Left:** Present constraint from TWIST [19, 20] is shaded in yellow. The projected single-bin (dashed line) and time-binned (solid line) analysis reach from Mu3e [21, 22] are shown in purple. The astrophysical bound on  $f/\sqrt{C_{\mu e}}$  from SN1987A [23, 24] is shown here as a dot-dashed green line – see main text for details. **Right:** The constraints on  $f/\sqrt{C_{\tau e}}$  from present and projected Belle-II analyses [25] are shown here in blue: current  $62.8 \text{ fb}^{-1}$  time-integrated constraint is shaded, single-bin constraint is a dashed line and projected time-binned constraint is a solid line; the  $50 \text{ ab}^{-1}$  projected time-binned constraint is a dot-dashed line. The projected constraints from FCC-ee Tera-Z run [26] are shown in red: dotted line for single-bin analysis, and red solid line for time-binned analysis. The constraints on  $C_{\tau\mu}$  and on  $C_{\tau e}$  (denoted collectively here as  $C_{\tau\ell}$ ) almost completely overlap on this logarithmic scale.

fundamental constants (see e.g. [274]). However, to date, no study has explored its possible impact on flavor violating processes.

In this chapter, we introduce a novel DM search strategy based on flavor changing neutral current (FCNC) transitions induced by the presence of a misaligned field. We focus on charged lepton flavor violating (CLFV) decays, and find that certain classes of dark-visible interactions can viably induce time-modulation at levels that can be probed at existing and future experiments.

As numerical examples, we show projections for a possible reanalysis of existing Belle-II data [25, 275], as well as the estimates for future Mu3e [21, 22, 122] and FCC-ee [26, 276, 277] sensitivities – these results are presented in fig. 5.1. Similar analyses could be performed at other current and future CLFV experiments, including MEG-II [24, 124, 278], Mu2e [129, 136, 196, 201, 202], COMET [128, 202, 279], BES-III [280, 281], Super Tau Charm Factory [282–284], and CEPC [285].

**Time-dependent CLFV interactions.** Arguably the simplest interactions of  $\phi$  to the SM fermions arises from the dimension-5 Higgs interaction  $\phi H \bar{L}_i \ell_j$ . Once the Higgs acquires its vacuum expectation value this operator becomes  $y_{ij}\phi \bar{\ell}_i \ell_j$  and leads to decays of the charged lepton to dark matter. However, this interaction does *not* lead to observable time-dependent CLFV transitions, due to several challenges that we outline below.

1. *Time-independent Limits:* The off-diagonal interactions in the dimension-5 operators  $\phi H \bar{\ell}_i \ell_j$  predict flavor changing processes, including the decays:  $\tau \rightarrow \mu\phi$ ,  $\tau \rightarrow e\phi$ , and  $\mu \rightarrow e\phi$ , where the final state  $\phi$  is invisible to experiments. For such linear  $\phi$  couplings the decay rates are *independent* of the  $\phi_c$  background at leading order and, therefore, do not inherit time modulation. Furthermore, conventional time-averaged searches for  $\ell_i \rightarrow \ell_j +$  invisible decays yield stringent limits on the couplings [19, 24, 25, 286]

$$|y_{\tau e}|, |y_{\tau \mu}| \lesssim 2 \times 10^{-7}, \quad |y_{\mu e}| \lesssim 10^{-10}, \quad (5.8)$$

which severely limit any CLFV time-dependent effects that could arise at higher orders, via additional  $y_{ij}$  insertions.

2. *Mass-Shift Effects:* In the case of the Higgs operator,  $\phi H \bar{\ell}_i \ell_j$ , setting  $\phi$  to its background value  $\phi_c$  yields corrections to the lepton mass matrix:

$$m_{ij}(t) = \text{diag}(m_e, m_\mu, m_\tau) + y_{ij} \phi_c(t), \quad (5.9)$$

where the additional mass terms induce time dependence in SM decays. For example, the branching ratio  $\mathcal{B}(\mu \rightarrow e\nu\bar{\nu})$  acquires time modulation with an amplitude  $\propto \mathcal{O}(y_{\mu\mu}, y_{\mu e}^2)$ , due to the modified muon mass. Furthermore, these terms can also induce time-dependent exotic FCNC decays, such as  $\mu \rightarrow e\gamma$  or  $\tau \rightarrow e\gamma$ . However, the branching fractions for these processes are suppressed by both  $y_{ij}^2$  and by  $\dot{\phi}_c$ .<sup>2</sup> Thus, after taking into account the constraints from eq. (5.8), all time-varying CLFV signals are unobservably small.

Similarly, a dimension-5 axion portal operator of the form  $\partial_\mu \phi \bar{\ell}_i \gamma^\mu \gamma_5 \ell_j$  leads to time-independent dark matter decays of charged leptons.

For the charged lepton decays to be time dependent the operator must involve two insertions of dark sector fields, with at least one of these insertions being the ultra-light dark matter. If both of the insertions are the dark matter, operators of the form  $\phi^2 \bar{\ell}_i \ell_j$  then the decays can become time dependent as the decay amplitude is proportional to  $\phi_c$ . However, this raises the problem that loop corrections to  $m_\phi$  depend explicitly on the local DM density,  $\phi_c$ , leading to *position dependent* fine tuning. This problem does not exist if there are two separate fields only one of which has a classical field value.

As a concrete example we will consider interactions of the form

$$\mathcal{L}_{\text{int}} \supset \frac{i\phi (\partial_\mu \phi')}{2f^2} \bar{\ell}_i \gamma^\mu (C_{ij}^V + C_{ij}^A \gamma_5) \ell_j + \text{h.c.}, \quad (5.10)$$

---

<sup>2</sup>In the  $\tau_\phi \gg \tau_\ell$  limit the  $\phi_c$  term in eq. (5.9) merely corrects the charged lepton mass matrix, and does not result in a new source of flavor violation.

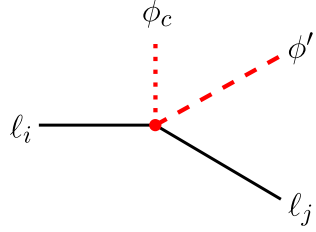


FIGURE 5.2: Model contribution to  $\ell_i \rightarrow \ell_j \phi'$ , where the interaction with the background classical field ( $\phi_c$ ) is denoted in red.

where  $\phi$  is DM and  $\phi'$  is another ultra-light dark sector field,  $C_{ij}^{V,A}$  are hermitian matrices in flavor space and the  $i,j$  indices run over all charged fermion species and  $f$  is the effective energy scale associated with the generation of this operator. In section 5.3 we show that the interaction in eq. (5.10) can be the leading DM-SM interaction if  $\phi$  and  $\phi'$  are pseudo-Nambu-Goldstone bosons of a spontaneously broken non-Abelian global symmetry, and how  $f$  relates to the physics that generates this operator. In section 5.3 we also give further examples of such quadratic interactions with the dark sector.

Since the interaction in eq. (5.10) contains two light field insertions, expanding  $\phi$  around its background value,  $\phi_c$ , results in time-dependent FCNC decays at leading order. To make this time modulation manifest, we integrate by parts and replace the  $\phi$  field with  $\phi_c$  to obtain

$$\mathcal{L}_{\text{int}} \supset \frac{\phi_c}{2f^2} \phi' \bar{\ell}_i \left[ C_{ij}^V (m_{\ell_i} - m_{\ell_j}) + C_{ij}^A (m_{\ell_i} + m_{\ell_j}) \gamma_5 \right] \ell_j, \quad (5.11)$$

where  $m_{\ell_i}$  is the mass of  $\ell_i$ . The branching fraction for  $\ell_i \rightarrow \ell_j \phi'$  decays is now explicitly calculated from the diagram in fig. 5.2 and is time-dependent,

$$\mathcal{B}(\ell_i \rightarrow \ell_j \phi') = \frac{C_{ij}^2 \phi_0^2}{64\pi f^4} \frac{m_{\ell_i}^3}{\Gamma_{\ell_i}} \cos^2(m_\phi t + \delta), \quad (5.12)$$

where  $C_{ij}^2 \equiv |C_{ij}^V|^2 + |C_{ij}^A|^2$ ,  $\Gamma_{\ell_i}$  is the total width of lepton  $\ell_i$ ,  $\phi_0$  is the field amplitude from eq. (5.6), and we have approximated all final state particles as massless except for the appearance of  $m_\phi$  in the cosine. Note that, as part of the dark sector,  $\phi'$  will be invisible on accelerator length scales.

### 5.3 UV realization(s)

#### 5.3.1 Non-Abelian pseudo-NGBs

A spontaneously broken global symmetry gives rise to massless Nambu-Goldstone Bosons (NGBs). The NGBs acquire a nonzero mass, if there is a small explicit breaking of the global symmetry. Celebrated examples of NGBs in particle physics are the QCD axion, and the light mesons

$\pi^\pm$  and  $\pi^0$ . The QCD axion is a pseudo-NGB (pNGB) of a  $U(1)_{\text{PQ}}$  Peccei-Quinn global symmetry, spontaneously broken at high scale  $f_a$  and then also explicitly broken by the QCD anomaly [287–290]. The pions are the pNGBs of spontaneous chiral symmetry breaking in QCD,  $SU(2)_L \times SU(2)_R \rightarrow SU(2)_V$ , where the initial  $SU(2)_L \times SU(2)_R$  global group is also explicitly broken by the  $m_{u,d}$  quark masses (see, e.g., [291]). The QCD axion is an example of an Abelian pNGB, while the pions are examples of non-Abelian pNGBs.

More generally, the non-Abelian pseudo-Goldstone Bosons (npNGBs) arise when the theory is invariant under an approximate non-Abelian global group  $G$ , that is spontaneously broken to its subgroup  $H$  ( $G \rightarrow H$ ), where the  $G/H$  coset consists of several pNGBs that have non-linear interactions with each other. Let us denote the npNGB parametrization of the  $G/H$  coset as  $U(\phi)$  where, under  $G$  transformations,  $U(\phi) \rightarrow V_L^\dagger U(\phi) V_R$ . In general, the left and right transformations differ so that  $V_L \neq V_R$ ; this is the case we are interested in.<sup>3</sup> We assume that the leading interactions between the npNGB dark sector and the SM has the general form

$$\mathcal{L}_{\text{int}} \supset \text{Tr}(QU^\dagger i\partial_\mu U)\bar{\ell}_i \gamma^\mu (\tilde{C}_{\ell_i \ell_j}^V + \tilde{C}_{\ell_i \ell_j}^A \gamma_5) \ell_j + \text{h.c.}, \quad (5.13)$$

where  $\ell_i$  are the SM charged leptons, and  $Q$  is the symmetry breaking spurion that transforms as  $Q \rightarrow V_R^\dagger Q V_R$  under  $G$ . Other transformation properties for  $U$  and  $Q$ , and thus different structures for the interaction term, eq. (5.13), can also be considered. The interaction in eq. (5.13) can be generated via heavy mediators, that are then integrated out at low energies, but variants of this model with light mediators can also be considered (for the phenomenology we are most interested in, though, they should still be heavier than a muon). Note that the interaction term eq. (5.13) remains invariant under shift symmetry,  $U \rightarrow e^{-i\alpha} U$ , where  $\alpha = \alpha^a T^a$  is an arbitrary constant matrix in the tangent space of the  $G/H$  coset. Due to this remaining shift symmetry the interaction in eq. (5.13) does not generate contributions to npNGB masses.

Expanding the  $U(\phi)$  exponentiation in terms of the  $\phi_a$  fields,  $U = \exp(i\phi^a T^a)$ , gives dimension-6 interaction operators with a typical form

$$\mathcal{L}_{\text{int}} \supset \left( \frac{\phi_1}{f} \frac{i\partial_\mu \phi_2}{2f} - \frac{\phi_2}{f} \frac{i\partial_\mu \phi_1}{2f} \right) \bar{\ell}_i \gamma^\mu (C_{\ell_i \ell_j}^V + C_{\ell_i \ell_j}^A \gamma_5) \ell_j + \text{h.c.}, \quad (5.14)$$

where  $f$  is the scale of spontaneous symmetry breaking, while  $\phi_1$  and  $\phi_2$  are two different npNGBs, possibly related through complex conjugation so that  $\phi_1 = \phi_2^\dagger$ , depending on the detailed structure of the  $G/H$  coset and on the form of spurion  $Q$ . Note that the above interaction term is invariant under the nonlinearly realized shift symmetry  $\phi^a T^a \rightarrow \phi^a T^a - \alpha^a T^a - \frac{1}{2}[\alpha^a T^a, i\phi^a T^a] + \dots$ , with  $\alpha^a$  constants (this is most easily seen in the exponentiated form, keeping all terms in  $\phi^a$ ).

---

<sup>3</sup>If  $V_L = V_R$ , then  $\text{Tr}\partial_\mu U \sim \partial_\mu \phi_a$  is invariant under  $G$ . At low energies, interactions of the form  $\partial\phi_a \bar{\ell}_i \gamma^\mu \ell_j$  are then also allowed – i.e., the same interaction types that are generally present for a QCD axion, or any other  $U(1)$  pNGB. We define non-Abelian pNGBs to be the models where such terms are absent, although one could also consider the case where both Abelian and non-Abelian terms are present.

It is illuminating to compare the phenomenology of the FCNC  $\ell_i \rightarrow \ell_j \phi$  decays for the two cases, when  $\phi$  a non-Abelian pNGB, and when  $\phi$  is an Abelian pNGB. For non-Abelian pNGBs the  $\ell_i \rightarrow \ell_j \phi$  decays are induced by interaction in eq. (5.10), while for Abelian pNGBs the interaction involves only a single  $\phi$  field,

$$\mathcal{L} \supset C_{\ell_i \ell_j} \left( \frac{\partial_\mu \phi}{f} \right) \bar{\ell}_i \gamma^\mu \gamma_5 \ell_j. \quad (5.15)$$

There are several important differences between the two cases. First of all, since the interaction in eq. (5.15) is linear in  $\phi$ , the  $\ell_i \rightarrow \ell_j \phi$  decay rates for Abelian pNGB case are time independent, and also do not depend on the local DM number density. In contrast, for npNGBs the two-body  $\ell_i \rightarrow \ell_j \phi$  decays arise only, if there is a background density of light  $\phi$  particles. This background density then leads to time-dependent  $\ell_i \rightarrow \ell_j \phi$  rates. The observation of such time-dependent  $\ell_i \rightarrow \ell_j \phi$  decays would be a smoking-gun signal of light npNGB dark matter. For Abelian pNGB the observation of  $\ell_i \rightarrow \ell_j \phi$  signal instead does not immediately imply that  $\phi$  is DM, and one would need to confirm that  $\phi$  is indeed the DM using other observations (for instance by searching for time-dependent interactions via its couplings to electrons).

The npNGBs have already been discussed in the literature as the possible dark matter candidates, though, in a very different mass regime that we are interested in. An example is the strongly interacting massive particle (SIMP) dark matter candidate [292–296]. While in the SIMP case the interesting mass regime is around GeV, we are interested in much lighter npNGB dark matter candidates, with masses well below eV. For other examples of heavier npNGB dark matter, see, e.g., Refs. [297–301], and for strongly-interacting dark sectors with dark pions as npNGBs, see, e.g., Refs. [302–305]. The dark sector currents of the form  $\phi \partial_\mu \phi$  coupling to SM fermion currents through light dark vectors were also considered in [306].

### 5.3.1.1 An example realization: $SU(3)_L \times SU(3)_R \rightarrow SU(3)_V$

The form of the interactions in eq. (5.13) may seem exotic. However, as noted above, there is a familiar example in the SM: the pion sector of QCD interacting through QED with leptons. The spontaneous breaking of chiral symmetry in QCD,  $SU(2)_L \otimes SU(2)_R \rightarrow SU(2)_V$  results in three light npNGBs,  $\pi^\pm$  and  $\pi^0$ . In the QCD Lagrangian the  $SU(2)_L \otimes SU(2)_R$  global symmetry is explicitly broken by the  $m_{u,d}$  quark masses, giving rise to pion masses. The  $\pi^+ i \partial_\mu \pi^-$  current couples to the electromagnetic current of the SM leptons through a tree level photon exchange, giving rise to a non-local interaction of the form  $(\pi^+ i \partial_\mu \pi^-) \partial^{-2} (\bar{\ell} \gamma^\mu \ell)$ , where the nonlocal structure  $\partial^{-2}$  is due to the photon propagator,  $-ig_{\mu\nu}/q^2$ , but in the position-space representation.

If all three light SM quark masses,  $m_u, m_d$  and  $m_s$  can be neglected, then the QCD Lagrangian has a larger global symmetry  $SU(3)_L \otimes SU(3)_R$ . This can still be viewed as being spontaneously

broken to its diagonal subgroup  $SU(3)_V$ , though, in this case the explicit breaking due to strange quark mass  $m_s$  is much larger. In this case there are eight npNGBs: the pions, kaons and eta. Let us now assume that a similar  $SU(3)_L^{\text{hid}} \otimes SU(3)_R^{\text{hid}} \rightarrow SU(3)_V^{\text{hid}}$  symmetry breaking pattern also occurs in the hidden sector. Let us also charge the dark sector under a gauged  $U(1)'$  – that may, but need not, be a subgroup of  $SU(3)_V^{\text{hid}}$ , and assume that  $\pi_D^\pm$  are the dark matter. The low energy chiral Lagrangian for the hidden sector is given by

$$\mathcal{L} = \frac{f_{\text{UV}}^2}{8} \text{Tr}(D_\mu U D^\mu U^\dagger) + \frac{f_{\text{UV}}^2}{8} \text{Tr}(\chi^\dagger U + U^\dagger \chi) + \dots, \quad (5.16)$$

where  $\chi$  is an explicit  $SU(3)_L^{\text{hid}} \otimes SU(3)_R^{\text{hid}}$  global symmetry breaking spurion (in QCD,  $\chi \propto (m_u, m_d, m_s)$ ), while ellipses denote higher terms in chiral expansion. Working in the basis where  $\chi$  is diagonal (in QCD this would be in the quark mass basis), the exponentiated npNGB matrix  $U = \exp(i\sqrt{2}\Pi_D/f_{\text{UV}})$  is given by

$$\Pi_d = \begin{pmatrix} \frac{\pi_D^0}{\sqrt{2}} + \frac{\eta_{D8}}{\sqrt{6}} & \pi_D^+ & K_D^+ \\ \pi_D^- & -\frac{\pi_D^0}{\sqrt{2}} + \frac{\eta_{D8}}{\sqrt{6}} & K_D^0 \\ K_D^- & \bar{K}_D^0 & -\sqrt{\frac{2}{3}}\eta_{D8} \end{pmatrix}, \quad (5.17)$$

where we follow the SM notation for the npNGB mass eigenstates (note that the charges in this notation need not correspond to  $A'$  charges). The covariant derivative is given by

$$D_\mu U = \partial_\mu U + ig' A'_\mu [Q, U], \quad (5.18)$$

where  $g'$  is the  $U(1)'$  gauge coupling, and  $Q$  is a  $3 \times 3$  spurion matrix. For instance, taking  $Q = q_U \lambda_6$ , where  $\lambda_6$  is the sixth Gell-Mann matrix, and  $q_U$  the charge, then the kinetic term contains

$$\begin{aligned} \frac{f_{\text{UV}}^2}{8} \text{Tr}(D_\mu U D^\mu U^\dagger) &\supset \frac{f_{\text{UV}}^2}{8} g' A'_\mu \text{Tr}([Q, U] \partial_\mu U^\dagger - \partial_\mu U [U^\dagger, Q]) + \dots \\ &= -g' q_U A'_\mu (\pi_D^+ i \partial^\mu K_D^- - K_D^- i \partial^\mu \pi_D^+ + \text{h.c.}) + \dots, \end{aligned} \quad (5.19)$$

where ellipses denote terms with no gauge fields or with two gauge fields, and the terms where  $A'$  couples to currents not involving  $\pi_D^\pm$ . Alternatively, if the spurion is  $Q = (q_U/2)\lambda_3$ , then

$$\frac{f_{\text{UV}}^2}{8} \text{Tr}(D_\mu U D^\mu U^\dagger) \supset g' q_U A'_\mu (\pi_D^+ i \partial^\mu \pi_D^- - \pi_D^- i \partial^\mu \pi_D^+) + \dots. \quad (5.20)$$

The two examples are reminiscent of the weak and QED interactions in the SM. The first choice for  $Q$ , in eq. (5.19), is akin to  $W^\pm$  interactions in the SM which change the quark flavors. The

second choice for  $Q$ , in eq. (5.20), is instead akin to QED interactions, which are flavor diagonal, though, in our example only the first two generations are charged under dark  $U(1)'$ .

We can also charge the SM fermions under this dark  $U(1)'$ , in principle with flavor violating couplings, see, e.g., [307]. In this example we do not aim to explain the structure of SM Yukawas, and so interactions will have a general flavor structure

$$\mathcal{L}_{\text{int}} = ig' c_{ij} \bar{\psi}_i A' \psi_j + \text{h.c..} \quad (5.21)$$

From now on let us focus on the example, where  $Q = q_U \lambda_6$ , eq. (5.19) and take the mass of the dark photon to be generated via a dark-Higgs mechanism, with vacuum expectation value  $v'$ , such that  $m_{A'} = g' v'$ . The tree-level exchange of  $A'$  between dark sector and SM fermions generates an interaction of the form

$$c_{ij} \frac{g'^2 f_{\text{UV}}^2}{m_{A'}^2} (\bar{\psi}_i \gamma^\mu \psi_j) \text{Tr}([Q, U] \partial_\mu U^\dagger - \partial_\mu U [U^\dagger, Q]) = \frac{c_{ij} q_U g'^2}{m_{A'}^2} (\bar{\psi}_i \gamma^\mu \psi_j) (\pi_D^+ \partial_\mu K_D^-) + \dots \quad (5.22)$$

Note that the  $f_{\text{UV}}$  scale disappears from the effective interaction. The strength of the interaction with the SM is instead controlled by  $m_{A'}/g' = v'$ , i.e., by the  $U(1)'$  spontaneous symmetry breaking scale. Matching onto the notation in eq. (5.14) gives<sup>4</sup>

$$\frac{f}{\sqrt{C_{ij}}} \sim \frac{m_{A'}}{g' \sqrt{c_{ij} q_U}} = \frac{10^9 \text{ GeV}}{\sqrt{c_{ij} q_U}} \left( \frac{m_{A'}}{10^6 \text{ GeV}} \right) \left( \frac{10^{-3}}{g'} \right). \quad (5.23)$$

Finally, for considerations related to the feasibility of cosmological evolution in the context of ultralight npNGBs, we refer the reader to ref. [308] which considers the case of  $SU(2)_L \otimes SU(2)_R$ .

### 5.3.1.2 Other examples

Beyond npNGBs there are other possibilities for quadratic interactions between dark sector and the SM. We are interested in the case where there are two different species of dark sector particles involved in the couplings to the SM currents (for the case where a single light DM field couples quadratically to the SM with flavor diagonal interactions, see, e.g., [309–314]). We are also specifically interested in the CLFV SM currents. The simplest such interaction is, for instance,

$$\left( \frac{\phi \phi'}{\Lambda_{ij}^2} \right) H \bar{L}_i \ell_j. \quad (5.24)$$

Linear interaction of  $\phi$  and  $\phi'$  may be forbidden, if these are odd under a  $Z_2$  symmetry. The main difference with respect with the npNGBs is that the masses of  $\phi$  and  $\phi'$ s are no longer protected using just the symmetries still present in the IR. Such interactions may thus face a

---

<sup>4</sup>The correspondence with the example in the main text is not exact, since we have DM that is composed out of two states,  $\pi_D^\pm$ .

large hierarchy problem, though, this may not be a problem in concrete UV models, e.g., if the dark sector possesses a softly broken supersymmetry.

Another example where multiple dark sector particles may interact with the SM current is if the dark matter is composed of light non-Abelian gauge bosons,  $G_{D\mu}^a$ , where the gauge symmetry is spontaneously completely broken. These dark gauge bosons can interact with the SM through a higher dimension operator such as

$$\frac{1}{\Lambda_{ij}^4} (G_{D\mu\nu}^a G_D^{a\mu\nu}) (H \bar{L}_i \ell_j) , \quad (5.25)$$

with  $G_{D\mu\nu}^a$  the field strength associated with the vector field  $G_{D\mu}^a$ . These interactions contain terms that are of the schematic form  $\partial G_D \partial G_D \bar{\mu} e$ ,  $\partial G_D G_D^2 \bar{\mu} e$ , and  $G^4 \bar{\mu} e$ . The  $\partial G_D \partial G_D \bar{\mu} e$  operator is not interesting for our purposes since it leads to effects that are suppressed by the small  $G_D$  mass. The other two operators, on the other hand, can lead to  $\mu \rightarrow e G_D$  decays with either two or three  $G_D$  fields set to their classical background values. The  $\mu \rightarrow e G_D$  decay rates will thus oscillate as a combination of higher harmonics  $\Gamma(\mu \rightarrow e G_D) \propto (\cos^2 m_{G_D} t + \dots \cos^3 m_{G_D} t)^2$ . The operator in eq. (5.25) can also induce time dependent  $\mu \rightarrow e G_D G_D$  decays, which can also be searched for.

## 5.4 Observing periodic signals

New physics transitions  $\ell_i \rightarrow \ell_j \phi'$  have an irreducible SM background from the tree-level  $W$ -boson mediated decays,  $\ell_i \rightarrow \ell_j \nu_i \bar{\nu}_j$ . Due to three-body kinematics, this background mimics the signal  $\ell_i \rightarrow \ell_j \phi'$  *only* when the invariant mass of the two neutrinos is close to zero, within experimental resolution (the  $\phi'$  mass is assumed to be far below the invisible mass resolution in these experiments). Time-dependent signals offer a valuable handle to distinguish signal from background, particularly because the background events do not exhibit periodic modulation. Observing a time modulation in  $\ell_i \rightarrow \ell_j \phi'$  decays would constitute compelling evidence for DM or another misaligned field with nontrivial cosmological abundance.<sup>5</sup>

We assess the statistical sensitivity to sinusoidal signals in eq. (5.12) in the presence of substantial SM backgrounds using a simplified analysis. Assuming continuous data collection over total observation time  $T$ , the data are divided into  $n_{\text{bin}} = T/\Delta t$  equal-sized bins, each of duration  $\Delta t$ , which are longer or equal to the experimental resolution. Using eq. (5.12), the predicted event rate is

$$\dot{N}_{\text{pred}}(t) = \frac{N_{\text{tot}}}{T} [\mathcal{B}_{\text{bg}} f_{\text{bg}} + 2\mathcal{B}_{\text{sig}} f_{\text{sig}} \cos^2(m_\phi t + \delta)], \quad (5.26)$$

where  $N_{\text{tot}}$  is the total number of  $\ell_i$  decays,  $\mathcal{B}_{\text{bg(sig)}}$  and  $f_{\text{bg(sig)}}$  are the background (signal) branching fractions and experimental efficiencies, respectively. Local DM with velocity  $v \sim 10^{-3}$

---

<sup>5</sup>In general,  $\phi$  could be a subdominant DM component, and still lead to a time-dependent signal.

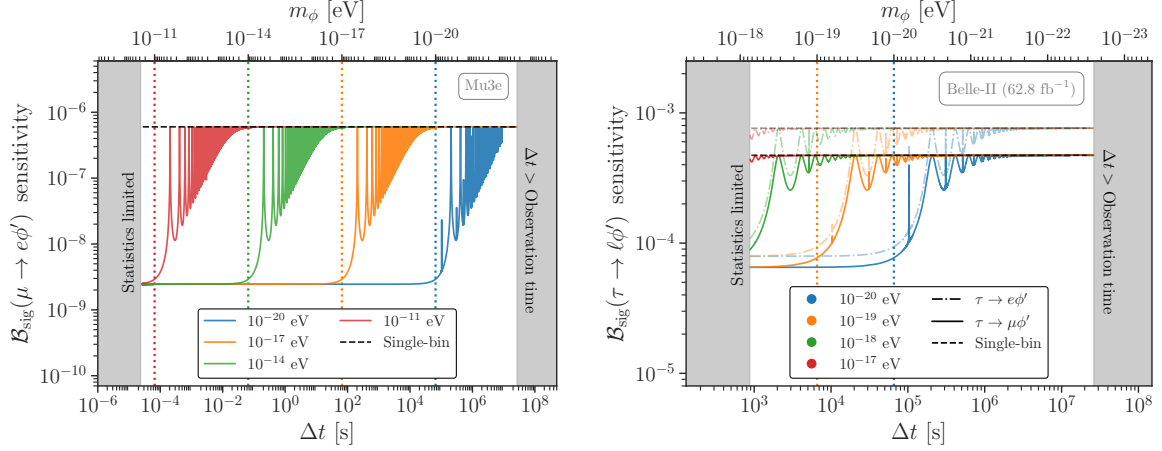


FIGURE 5.3: The 90% confidence upper limit on the signal branching  $\mathcal{B}_{\text{sig}}$  obtained from a time-dependent analysis, as a function of bin size  $\Delta t$  (solid, dashed-dotted lines) for different  $\phi$  masses at Mu3e (left) and Belle II (right), using the same assumptions as in Fig. 5.1. The dotted vertical lines denote approximately when the oscillatory signal for each mass is resolved,  $\Delta t \sim m_\phi^{-1}$ . The horizontal dashed black line denotes the upper limit for a time-independent, single-bin, analysis.

sets a characteristic coherence time

$$\tau_{\text{coh}} \sim \frac{1}{m_\phi v^2} \simeq 7 \times 10^5 \text{ s} \left( \frac{10^{-15} \text{ eV}}{m_\phi} \right) \left( \frac{10^{-3}}{v} \right)^2, \quad (5.27)$$

during which the classical DM field maintains the same phase  $\delta$ . For  $T > \tau_{\text{coh}}$ , an experiment can experience two or more coherent ‘patches’ with different phases. Further details about decoherence in our analysis may be found in section 5.6. In eq. (5.26), the *time-averaged* branching ratio for the signal channel satisfies

$$\mathcal{B}_{\text{sig}} \equiv \langle \mathcal{B}(\ell_i \rightarrow \ell_j \phi') \rangle = \frac{C_{ij}^2}{128\pi} \frac{\phi_0^2}{f^4} \frac{m_{\ell_i}^3}{\Gamma_{\ell_i}}, \quad (5.28)$$

where we have used eq. (5.12). The number of background events, assumed to be non-modulating and dominant over the signal, is given by

$$N_{\text{bg}} = N_{\text{tot}} \mathcal{B}_{\text{bg}} f_{\text{bg}} \quad , \quad \mathcal{B}_{\text{bg}} f_{\text{bg}} \gg \mathcal{B}_{\text{sig}} f_{\text{sig}}. \quad (5.29)$$

The number of events per time bin is obtained from integrating  $\dot{N}_{\text{pred}}(t)$  over each bin interval  $\Delta t$ . Using Asimov datasets<sup>6</sup> we construct a  $\chi^2$  test statistic, which depends on the quadratic sum of statistical and systematic errors in each bin, which respectively satisfy

$$\sigma_{\text{stat}} = \sqrt{N_{\text{bg}}/n_{\text{bin}}} \quad , \quad \sigma_{\text{sys}} = \alpha N_{\text{bg}}/n_{\text{bin}}, \quad (5.30)$$

<sup>6</sup>In an Asimov data set, all observed quantities are set equal to their expected values.

where  $\alpha$  is the relative systematic uncertainty. The  $\chi^2$  test statistic can then be translated to the expected bounds on  $f/\sqrt{C_{ij}}$  from eq. (5.12) using time-dependent  $\ell_i \rightarrow \ell_j \phi'$  searches. As shown in section 5.6, in the “fine-binned” (fb) limit where  $m_\phi \Delta t \ll 1$ ,  $m_\phi T \gg 1$ , the time-dependent test statistic  $\chi^2_{\text{fb}}$  can be written

$$\chi^2_{\text{fb}} = \frac{3}{2} \left[ 1 + \frac{n_{\text{bin}}}{3} \left( \frac{\sigma_{\text{sys}}}{\sigma_{\text{stat}}} \right)^2 \right] \chi^2_{\text{const}}, \quad (5.31)$$

where  $\chi^2_{\text{const}}$  is the usual time-independent test statistic. Thus, in the fine-binned limit, the sensitivity to a time-dependent signal is significantly enhanced if systematic uncertainties dominate over statistical ones. The time-dependence of the signal allows the background rate to be measured in situ, in the low signal rate bins, thus removing the associated uncertainty. In fact, in the systematics-dominated regime, section 5.4 reduces to [?]

$$\chi^2_{\text{fb}} = \frac{(\mathcal{B}_{\text{sig}} f_{\text{sig}} N_{\text{tot}})^2}{2 n_{\text{bin}} \sigma_{\text{stat}}^2}, \quad (5.32)$$

which shows complete independence from systematic uncertainties. Thus, with an appropriate analysis, it is possible to measure a time-dependent signal even in the presence of large systematic uncertainties, as long as all the systematics are time-independent.

The expected sensitivity generally depends on the choice of time-bin width  $\Delta t$  (equivalently, the number of bins  $n_{\text{bin}}$ ), as shown in fig. 5.3. The time-independent limit corresponds to  $n_{\text{bin}} = 1$  (dashed line in fig. 5.3). Sensitivity gradually decreases as  $\Delta t$  increases: small  $\Delta t$  corresponds to a regime fully resolving oscillations, whereas large  $\Delta t$  approaches a less sensitive, time-integrated analysis dominated by systematics.

In fig. 5.1, we summarize the expected sensitivity to  $\mathcal{B}(\ell_i \rightarrow \ell_j \phi')$  as a function of  $m_\phi$  for representative numerical examples detailed below. We choose the smallest feasible  $\Delta t$  (largest  $n_{\text{bin}}$ ) consistent with valid  $\chi^2$  statistics, typically requiring at least ten events per time bin. This choice consistently exceeds experimental time resolution in all examples. Further details on the procedure can be found in section 5.6.

#### 5.4.1 Numerical examples

As representative examples we consider a possible search for time-dependent  $\mu \rightarrow e \phi'$  decays at Mu3e, and for  $\tau \rightarrow \ell \phi'$  decays at Belle II and at FCC-ee. More details regarding the chosen numerical values for each example can be found in section 5.6.4.

For Mu3e, we assume  $T = 300$  days of continuous data collection, yielding  $N_{\text{tot}} \sim 3 \times 10^{15}$  muon decays. The endpoint region for  $m_\phi \simeq 0$  includes  $N_{\text{bg}} \sim 10^{13}$  background events from  $\mu \rightarrow e \nu \bar{\nu}$ , corresponding to a background fraction  $f_{\text{bg}} \sim 3 \times 10^{-3}$  [21, 22]. For these large data samples, the  $\mu \rightarrow e \phi'$  search will be dominated by systematics, which we conservatively assume are set

by theoretical uncertainties, implying a 90% CL upper bound of  $\mathcal{B}(\mu \rightarrow e\phi') < 6 \times 10^{-7}$  (Fig. 12 of ref. [315]), and thus a relative systematic uncertainty of  $\alpha \sim 10^{-4}$ . Given the dataset above, the time-dependent search for  $\mu \rightarrow e\phi'$  can result in a sensitivity to the  $\mu \rightarrow e\phi'$  branching ratio well below the systematic uncertainty for  $m_\phi \lesssim 10^{-10}$  eV (solid purple line in fig. 5.1 left).

Estimating the Belle-II sensitivity to time-dependent  $\tau \rightarrow \ell\phi'$  decays is complicated by the fact that the state-of-the-art time-integrated search for these decays relies on the combined fit to the shape of  $\tau \rightarrow \ell\nu\bar{\nu}$  background and the  $\tau \rightarrow \ell\phi'$  signal in the pseudo-rest-frame of the tau [25]. Since, in this frame, the spectrum of lepton energies in SM  $\tau \rightarrow \ell\nu\bar{\nu}$  decays is similar to the spectrum from  $\tau \rightarrow \ell\phi'$ , we approximate the sensitivity using a simplified counting experiment. For the existing Belle-II analysis [25], using data corresponding to an integrated luminosity of  $62.8 \text{ fb}^{-1}$ , we consider only the  $\tau \rightarrow \ell\nu\bar{\nu}$  events with lepton energies in the range that contains 90% of the signal leptons from  $\tau \rightarrow \ell\phi'$  decays. Taking experimental efficiencies into account gives  $f_{\text{sig}}^{e[\mu]} \sim 0.12[0.16]$  and  $f_{\text{bg}}^{e[\mu]} \sim 8[9] \times 10^{-2}$ . Using this, the background process branching  $\mathcal{B}_{\text{bg}}^{e[\mu]} \sim 3 \times 10^{-2}$ , the 90% CL upper limits set by the analysis  $\mathcal{B}(\tau \rightarrow e[\mu]\phi') < 7.6[4.7] \times 10^{-4}$  [25], and assuming that the search is systematics limited, gives the relative systematic uncertainty of  $\alpha_{e[\mu]} \sim 6[4] \times 10^{-2}$ . For simplicity, we also assume that the  $N_{\text{tot}} \sim 10^8$  taus were collected uniformly within  $T = 300$  days. Using this relatively small data-sample, the time-dependent search resolves oscillations only for  $\phi$  masses below  $m_\phi \lesssim 10^{-17}$  eV (blue solid line in fig. 5.1 right). With the full  $50 \text{ ab}^{-1}$  integrated luminosity, Belle-II will have  $N_{\text{tot}} \sim 10^{11}$ , which should significantly improve the reach in  $f^2/C_{\tau\ell}$  and sensitivity to larger  $\phi$  masses. Assuming continuous data collection over  $T = 3 \times 10^3$  days with unchanged  $f_{\text{bg}}$ ,  $f_{\text{sig}}$ , and  $\alpha$ , yields the blue dashed-dotted line in fig. 5.1 (right).

Finally, we also consider  $\tau \rightarrow \ell\phi'$  searches at FCC-ee. While running in Tera-Z mode the proposed FCC-ee experiment will produce approximately  $N_{\text{tot}} = 3.4 \times 10^{11}$  taus over  $T = 740$  days of running [26]. Using a relative systematic uncertainty of  $\alpha \sim 1.7 \times 10^{-3}$ ,  $f_{\text{bg}} \sim 0.5$ , and  $f_{\text{sig}} \sim 0.8$  we obtain the projected sensitivities shown as the red solid line in fig. 5.1 (right), resolving oscillations up to  $m_\phi \lesssim 10^{-13}$  eV.

## 5.5 Astrophysical and laboratory constraints

Light particles with CFLV interactions can modify energy transport in supernovae and conflict with the observed properties of SN1987A in the Large Magellanic Cloud (LMC) [24]. Previous bounds on such particles assumed environment-independent couplings, but our interaction from eq. (5.11) depends on  $\phi_c$  and thus requires knowledge of the DM density in the LMC. At the SN1987A location ( $\sim 1$  kpc from the LMC center [316]), the DM density is estimated to be [317]

$$\rho_\phi^{\text{LMC}} \in [0.4, 8] \text{ GeV/cm}^3 , \quad (5.33)$$

and in fig. 5.1 (left) we use the lower end of this range to place conservative limits on the quantity  $f/\sqrt{C_{\mu e}}$ , following the same procedure as outlined in ref. [203].

It is instructive to compare CLFV constraints to those on flavor-diagonal couplings. As diagonal scalar couplings vanish in our model at leading order, see eq. (5.11), we consider constraints on an ultralight pseudoscalar DM and define  $C_{\mu e}|_{\text{Mu3e}}$  as the maximum Mu3e sensitivity in fig. 5.1, reflecting a time-binned analysis with fine binning. The strongest constraints on the diagonal electron couplings are from Red Giant cooling [318]

$$C_{ee} \left( \frac{\text{GeV}}{f} \right)^2 \lesssim 2 \times 10^2 \left( \frac{m_\phi}{\text{eV}} \right), \quad (5.34)$$

while for the diagonal muon coupling, the strongest constraints come from SN1987A cooling, where [319, 320]

$$C_{\mu\mu} \left( \frac{\text{GeV}}{f} \right)^2 \lesssim 8 \times 10^4 \left( \frac{m_\phi}{\text{eV}} \right), \quad (5.35)$$

which yields the relations

$$C_{ee} \lesssim 30 C_{\mu e}|_{\text{Mu3e}}, \quad C_{\mu\mu} \lesssim 10^4 C_{\mu e}|_{\text{Mu3e}}. \quad (5.36)$$

Without fine-tuned cancellations, rotating into the charged-lepton mass basis generally produces

$$C_{\mu e} \lesssim \sqrt{C_{ee} C_{\mu\mu}} \lesssim 5 \times 10^2 C_{\mu e}|_{\text{Mu3e}} \quad (5.37)$$

where we have combined eqs. (5.34) and (5.36) in the last expression. This indicates that Mu3e searches can probe new and *natural* DM parameter space without special hierarchies between diagonal and off-diagonal couplings. Given the much weaker bounds on  $C_{\tau\tau}$ , the Belle-II searches we describe above also do not face any such fine-tuning considerations, especially for  $\tau \rightarrow \mu\phi'$  decays.

## 5.6 Additional details related to observing periodic signals

Here we present the details necessary to estimate the time-dependent sensitivity projection for the sinusoidal  $\ell_i \rightarrow \ell_j \phi'$  signal from eq. (5.12). To simplify the analysis we consider an idealized case: an experiment that can collect data continuously for a total observation time  $T > \tau_\phi$ , with a constant time resolution  $\Delta t < \tau_\phi$ , and with a constant efficiency close to unity. In a realistic experimental analysis these simplifying assumptions may not be realized, implications of which we will discuss in ??.

Since galactic DM is non-relativistic with local velocity  $\mathcal{O}(v) \sim 10^{-3}$ , its energy spread is  $\mathcal{O}(v^2) \sim 10^{-6}$ , so the the signal in eq. (5.12) is coherent over  $\mathcal{O}(10^6)$  oscillations. Therefore, in our analysis we separately consider two cases:

1. **Coherent (“slow”) oscillations:** for sufficiently slow oscillations, we can assume that the signal is coherent over the complete data collection time, which we discuss in section 5.6.1,
2. **Incoherent (“fast”) oscillations:** for faster oscillations we need to take into account the random phase variations using  $\delta$  in eq. (5.12), as discussed in section 5.6.2.

The time-integrated analysis is given in section 5.6.3.

### 5.6.1 Coherent (“slow”) oscillations

We first consider time-oscillating  $\ell_i \rightarrow \ell_j \phi'$  decays with a fixed phase. To estimate the expected upper bound on the branching ratio of the oscillating signal, we construct a  $\chi^2$  test statistic, and work with the “Asimov” data set, which assumes that each of the  $n_{\text{bin}} = T/\Delta t$  bins will contain the “predicted” event counts ( $N_{\text{pred}}$ ) under a given hypothesis. Since background processes are assumed not to oscillate, the expected number of background events is taken to be constant in each bin. Thus, in the presence of the oscillatory signal from eq. (5.12) with fixed phase  $\delta$ , the total number of predicted number of events in  $k^{\text{th}}$  time bin, with  $t \in [t_{k-1}, t_k]$ , is given by

$$N_{\text{pred},k} = \int_{t_{k-1}}^{t_k} dt \dot{N}_{\text{pred}} = \frac{N_{\text{tot}}}{T} \int_{t_{k-1}}^{t_k} dt [\mathcal{B}_{\text{bg}} f_{\text{bg}} + 2\mathcal{B}_{\text{sig}} f_{\text{sig}} \cos^2(m_\phi t + \delta)], \quad (5.38)$$

where  $N_{\text{tot}}$  is the total number of observed  $\ell_i$  decays,  $\mathcal{B}_{\text{sig}}$  ( $\mathcal{B}_{\text{bg}}$ ) is the  $\ell_i \rightarrow \ell_j \phi'$  ( $\ell_i \rightarrow \ell_j \nu \bar{\nu}$ ) *time-averaged* branching ratio, while  $f_{\text{sig(bg)}}$  is the experimental efficiency – which includes both detection efficiencies and experimental cuts. As anticipated, under the background-only hypothesis, the expected number of observed events is constant across all bins, so

$$N_{\text{bg},1} \equiv N_{\text{pred},k} \Big|_{\mathcal{B}_{\text{sig}} \rightarrow 0} = N_{\text{tot}} \mathcal{B}_{\text{bg}} f_{\text{bg}} \left( \frac{\Delta t}{T} \right), \quad (5.39)$$

where we have defined  $N_{\text{bg},1}$  to be the constant background count in each bin. In the limit of large backgrounds, we take the statistical uncertainty in each bin to satisfy  $\sigma_{\text{stat}}^2 = N_{\text{bg},1}$ , consistent with the use of the Asimov set. We also take into account systematic uncertainties, modeled by  $\sigma_{\text{sys}}^2 = \alpha^2 N_{\text{bg},1}^2$  with  $\alpha$  common to all bins – i.e., we assume that the systematic error is a fixed, time-independent, relative error. Therefore, systematics are fully correlated across all time bins, and the covariance matrix and its inverse are given by

$$C = N_{\text{bg},1} \mathbf{1} + \alpha^2 N_{\text{bg},1}^2 \mathbb{I}, \quad \text{and} \quad C^{-1} = \frac{1}{N_{\text{bg},1}} \mathbf{1} - \frac{\alpha^2}{1 + \alpha^2 N_{\text{bg},1} n_{\text{bin}}} \mathbb{I}, \quad (5.40)$$

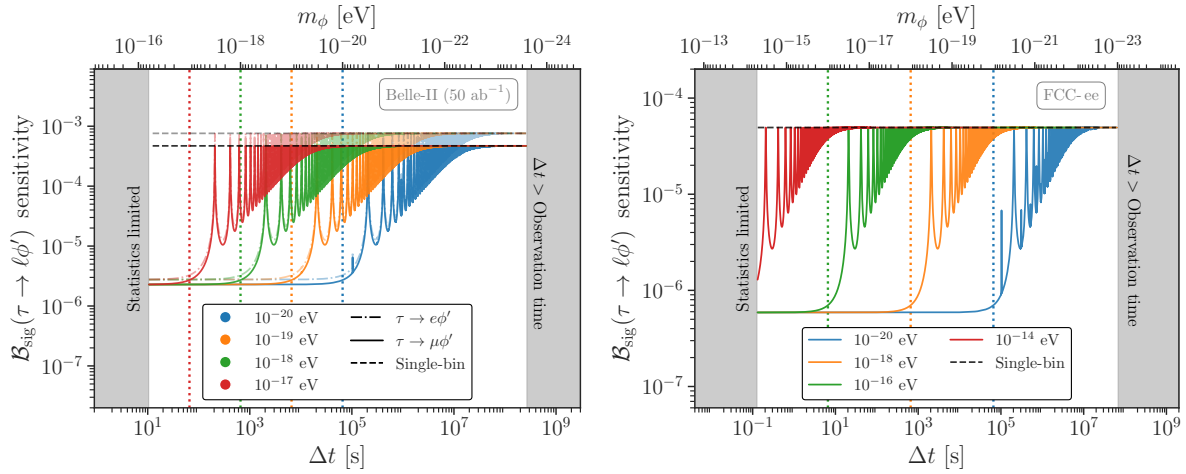


FIGURE 5.4: Same as fig. 5.3 for the full integrated luminosity at Belle-II (left) as well the projection for FCC-ee (right).

where  $\mathbf{1}$  is the  $n_{\text{bin}} \times n_{\text{bin}}$  identity matrix and  $\mathbb{I}$  is the  $n_{\text{bin}} \times n_{\text{bin}}$  constant unity matrix with 1 in every entry. The corresponding  $\chi^2$  statistic is therefore given by

$$\chi^2 = \sum_{k,p=1}^{n_{\text{bin}}} S_k C_{kp}^{-1} S_p = \frac{1}{N_{\text{bg},1}} \sum_{k=1}^{n_{\text{bin}}} S_k^2 - \frac{\alpha^2}{1 + \alpha^2 n_{\text{bin}} N_{\text{bg},1}} \left( \sum_{k=1}^{n_{\text{bin}}} S_k \right)^2, \quad (5.41)$$

where  $S_k \equiv N_{\text{obs}}^k - N_{\text{pred}}^k$  is the number of signal events in bin  $k$ . For the signal in eq. (5.38) we then have

$$\begin{aligned} S_k &= 2\mathcal{B}_{\text{sig}} f_{\text{sig}} \frac{N_{\text{tot}}}{T} \int_{(k-1)\Delta t}^{k\Delta t} dt \cos^2(m_\phi t + \delta) \\ &= \mathcal{B}_{\text{sig}} f_{\text{sig}} \frac{N_{\text{tot}}}{T} \left[ \Delta t + \frac{\sin(2km_\phi\Delta t + 2\delta) - \sin(2(k-1)m_\phi\Delta t + 2\delta)}{2m_\phi} \right], \end{aligned} \quad (5.42)$$

so using this expression, the two terms in the  $\chi^2$  in eq. (5.41) can be computed explicitly, and satisfy

$$\begin{aligned} \sum_{k=1}^{n_{\text{bin}}} S_k &= \mathcal{B}_{\text{sig}} f_{\text{sig}} N_{\text{tot}} \left[ 1 + \frac{\sin(2m_\phi T + 2\delta) - \sin(2\delta)}{2m_\phi T} \right], \\ \sum_{k=1}^{n_{\text{bin}}} S_k^2 &= \mathcal{B}_{\text{sig}}^2 f_{\text{sig}}^2 \left( \frac{N_{\text{tot}}}{2m_\phi T} \right)^2 \left\{ n_{\text{bin}} [1 + 4\Delta t^2 m_\phi^2 - \cos(2m_\phi \Delta t)] \right. \\ &\quad \left. + 8m_\phi \Delta t \sin(m_\phi T) \cos(m_\phi T + 2\delta) + \cos(2m_\phi T + 4\delta) \sin(2m_\phi T) \tan(m_\phi \Delta t) \right\}. \end{aligned} \quad (5.43)$$

Using these expressions it is possible to calculate the  $\chi^2$  statistic for any choice of binning (for any value  $n_{\text{bin}}$ ). Given  $\Delta t$ ,  $T$ ,  $N_{\text{tot}}$ , and  $\alpha$ , we obtain a 90% confidence sensitivity estimate on  $\mathcal{B}_{\text{sig}}$  by requiring the branching ratio to be non-negative and utilizing the one-sided upper bound obtained by solving  $\chi^2[\mathcal{B}_{\text{sig}}] = Z_{90}$ , where  $Z_{90} = 2.706$  is the solution to  $\text{erf}(\sqrt{Z_{90}/2}) \equiv 0.9$  –

for more details see section 5.6.3.

The behavior of numerical results in figs. 5.3 and 5.4 can be understood by considering various limiting cases:

1. *Single bin.* First, let us consider a single time bin analysis, so that one does not resolve the oscillating signal. In this case, the  $\chi^2$  statistic in eq. (5.38) evaluates to

$$\chi_1^2 = \frac{\mathcal{B}_{\text{sig}}^2 f_{\text{sig}}^2 N_{\text{tot}}}{\mathcal{B}_{\text{bg}} f_{\text{bg}} (1 + \alpha^2 \mathcal{B}_{\text{bg}} f_{\text{bg}} N_{\text{tot}})} \left( 1 + \frac{\sin(2m_\phi T + 2\delta) - \sin 2\delta}{2m_\phi T} \right)^2. \quad (5.45)$$

It is useful to compare  $\chi_1^2$  with the  $\chi^2$  for a signal constant in time,

$$\chi_{\text{const}}^2[\mathcal{B}] = \frac{n_{\text{bin}} S_{\text{bin}}^2}{\sigma_{\text{stat}}^2 + n_{\text{bin}} \sigma_{\text{sys}}^2} = \frac{(\mathcal{B} f_{\text{sig}} N_{\text{tot}})^2}{N_{\text{tot}} \mathcal{B}_{\text{bg}} f_{\text{bg}} + \alpha^2 (N_{\text{tot}} \mathcal{B}_{\text{bg}} f_{\text{bg}})^2} \quad (5.46)$$

where  $\mathcal{B}$  is the time-averaged  $\ell_i \rightarrow \ell_j \phi'$  branching ratio. The first equality follows from eq. (5.41) for a constant signal in each bin,  $S_i = S_{\text{bin}}$ , while the second equality uses that  $S_{\text{bin}} = \mathcal{B} f_{\text{sig}} N_{\text{tot}} / n_{\text{bin}}$ . In the limit of fast oscillations, i.e., for the case where the duration of the experiment is much longer than the oscillation period,  $m_\phi T \gg 1$ , one has  $\mathcal{B}_{\text{sig}} = \langle 2\mathcal{B}_{\text{sig}} \cos^2(m_\phi t + \delta) \rangle$ , giving for  $\chi_1^2$  in item 1

$$\chi_1^2 \rightarrow \chi_{\text{const}}^2[\mathcal{B}_{\text{sig}}]. \quad (5.47)$$

That is, averaging  $\chi_1^2$  over time gives the value of  $\chi^2$  for a time-independent signal. In the limit of slow oscillations,  $m_\phi T \ll 1$ , item 1 becomes

$$\chi_1^2 \rightarrow \chi_{\text{const}}^2[\mathcal{B}_{\text{sig}} \cos^2(\delta)] + \mathcal{O}(m_\phi T). \quad (5.48)$$

The  $\chi^2$  test statistic is then sensitive to the phase  $\delta$  of the classical field  $\phi_c$ , resulting in a  $\chi^2$  that may be larger or smaller than the time-averaged signal with amplitude  $\mathcal{B}_{\text{sig}}$ . For  $\delta = \pi/2$  the signal (and thus the  $\chi^2$ ) vanishes at leading order in  $m_\phi T$ ; the first non-zero contribution to the signal is of order  $(m_\phi T)^4$ , resulting in a highly suppressed, but non-zero  $\chi^2$ .

2. *Coarse binning.* If the signal oscillates in the duration of the experiment ( $m_\phi T \gg 1$ ), but the oscillation time is shorter than the bin size ( $m_\phi \Delta t \gg 1$ ) the sensitivity to oscillations is decreased. In this limit the result for  $\chi^2$  is the same as the single bin result, eq. (5.47), because the binning is too coarse

$$\chi_{\text{cb}}^2 = \chi_{\text{const}}^2[\mathcal{B}_{\text{sig}}]. \quad (5.49)$$

3. *Fine binning.* If the binning is sufficiently small to resolve the oscillations ( $m_\phi \Delta t \ll 1$ ) and the experiment runs long enough ( $m_\phi T \gg 1$ ), then the  $\chi^2$  becomes

$$\chi_{\text{fb}}^2 = \frac{3}{2} \left( 1 + \frac{\alpha^2 N_{\text{tot}} \mathcal{B}_{\text{bg}} f_{\text{bg}}}{3} \right) \chi_{\text{const}}^2[\mathcal{B}_{\text{sig}}] = \frac{3}{2} \left( 1 + \frac{n_{\text{bin}} \sigma_{\text{sys}}^2}{3 \sigma_{\text{stat}}^2} \right) \chi_{\text{const}}^2[\mathcal{B}_{\text{sig}}]. \quad (5.50)$$

When the systematic uncertainties can be ignored ( $\alpha^2 N_{\text{tot}} f_{\text{bg}} \ll 1$ ) this fine binning performs slightly better than the course binning,  $\chi_{\text{fb}}^2 = 3\chi_{\text{cb}}^2/2$ . When systematic uncertainties dominate, however, fine binning does substantially better, resulting in a  $\chi^2$  that is not limited by the systematic uncertainty,

$$\chi_{\text{fb}}^2 = \frac{1}{2N_{\text{tot}} \mathcal{B}_{\text{bg}} f_{\text{bg}}} (\mathcal{B}_{\text{sig}} f_{\text{sig}} N_{\text{tot}})^2 = \frac{n_{\text{bin}}}{2} \frac{S_{\text{avg},1}^2}{\sigma_{\text{stat}}^2}, \quad (5.51)$$

where  $S_{\text{avg},1} \equiv \langle S_i \rangle = \mathcal{B}_{\text{sig}} f_{\text{sig}} N_{\text{tot}} / n_{\text{bin}}$ . This result is intuitive: it is possible to measure a time-dependent signal even in the presence of large systematic uncertainties, as long as all the systematics are time independent.

### 5.6.2 Incoherent (“fast”) oscillations

For a given DM mass  $m_\phi$ , the galactic halo’s typical velocity dispersion sets a characteristic coherence time,  $\tau_{\text{coh}} \simeq (m_\phi v^2)^{-1}$ , during which the classical DM background remains effectively in phase. When  $m_\phi \gtrsim (v^2 T)^{-1}$ , the total observation time  $T$  spans multiple coherence patches. To estimate the sensitivity to a DM signal in this regime, we account for decoherence by subdividing the observation period into  $n_{\text{patch}} = \lceil T/\tau_{\text{coh}} \rceil = \lceil T m_\phi v^2 \rceil \simeq \lceil 10^{-6} m_\phi T \rceil$  equally spaced patches, where  $\lceil \dots \rceil$  represents the ceiling function. Each patch  $p \in \{1, 2, \dots, n_{\text{patch}}\}$  is assigned a phase  $\delta_p$  determined by minimizing the  $\chi^2$  statistic over the allowed phase variations. In the case  $T/\tau_{\text{coh}} \in \mathbb{Z}$ , the  $\chi^2$  is minimized when each patch maintains the same phase  $\delta_{\text{patch}}$ , corresponding to the minimization with respect to  $\delta$  over a single patch. For simplicity, in each patch we set  $\delta_p = \delta_{\text{patch}}$  despite the possibility of a single partial patch not fully residing within the observation window  $T$  (assuming that the first patch starts at the beginning of the observation time). Including this additional minimization on the final partial patch does not meaningfully impact our derived sensitivities. To further simplify the analysis, we restrict the maximum size of each time bin to be the coherence time,  $\Delta t \leq \tau_{\text{coh}}$ , and limit the binning scheme to evenly divide the duration of a single patch, ensuring that no time bin traverses multiple patches.

Under these approximations, the  $\chi^2$  statistic becomes

$$\begin{aligned} \chi^2 &= \frac{1}{N_{\text{bg},1}} \sum_{p=1}^{n_{\text{patch}}} \sum_{k=1}^{n_{\text{bin}}^p} S_k^2[\delta_p] - \frac{\alpha^2}{1 + \alpha^2 n_{\text{bin}} N_{\text{bg},1}} \left( \sum_{p=1}^{n_{\text{patch}}} \sum_{k=1}^{n_{\text{bin}}^p} S_k[\delta_p] \right)^2 \\ &\simeq n_{\text{patch}} \left[ \frac{1}{N_{\text{bg},1}} \sum_{k=1}^{n_{\text{bin}}^{\text{patch}}} S_k^2[\delta_{\text{patch}}] - n_{\text{patch}} \frac{\alpha^2}{1 + \alpha^2 n_{\text{bin}} N_{\text{bg},1}} \left( \sum_{k=1}^{n_{\text{bin}}^{\text{patch}}} S_k[\delta_{\text{patch}}] \right)^2 \right] + \chi_{\text{partial}}^2, \end{aligned} \quad (5.52)$$

where the number of bins per patch is given by  $n_{\text{bin}}^{\text{patch}} = \tau_{\text{coh}}/\Delta t = T/n_{\text{patch}}\Delta t = (m_\phi v^2 \Delta t)^{-1}$  and  $\chi_{\text{partial}}^2$  refers to the additional contribution to the  $\chi^2$  stemming from partial patches at the end of the observation time. Because of the fixed binning within each patch, a given  $\Delta t$  is not guaranteed to fit within a partial patch, introducing an error from integrating the signal over an additional amount of time  $dt_{\text{extra}}$  equivalent to

$$dt_{\text{extra}} = \left( \left\lceil \frac{\tau_{\text{coh}}(1 - n_{\text{patch}}) + T}{\Delta t} \right\rceil - \frac{\tau_{\text{coh}}(1 - n_{\text{patch}}) + T}{\Delta t} \right) \Delta t, \quad (5.53)$$

which vanishes as  $\Delta t \rightarrow 0$  ( $n_{\text{bin}}^{\text{patch}} \rightarrow \infty$ ). In the numerical examples presented in the main text, this error is accounted for explicitly in the computation of  $\chi_{\text{partial}}^2$  via subtraction of the extra contribution introduced by  $dt_{\text{extra}}$ . The  $\chi^2$  statistic and the derived sensitivity are computed analogously to the fully coherent case (using section 5.6.1).

### 5.6.3 Time-independent signal

The  $\chi^2$  square statistic for a time-independent  $\ell_i \rightarrow \ell_j \phi'$  branching ratio  $\mathcal{B}_{\text{const}}$  is given by  $\chi_{\text{const}}^2[\mathcal{B}_{\text{const}}]$  in eq. (5.46). Again requiring  $\mathcal{B}_{\text{const}}$  to be non-negative the one-sided upper bound at  $X\%$  confidence level (CL) for  $\mathcal{B}_{\text{const}}$ , denoted as  $\mathcal{B}_{\text{const}}^{X\% \text{CL}}$ , is obtained by solving

$$\chi_{\text{const}}^2[\mathcal{B}_{\text{const}}] = Z_X \quad \text{with} \quad \text{erf}(\sqrt{Z_X/2}) \equiv (X/100). \quad (5.54)$$

For instance,  $Z_{90} = 2.706$  and  $Z_{95} = 3.841$ . This yields

$$\mathcal{B}_{\text{const}}^{X\% \text{CL}} = \frac{1}{f_{\text{sig}}} \sqrt{Z_X \mathcal{B}_{\text{bg}} f_{\text{bg}} \left( \frac{1}{N_{\text{tot}}} + \mathcal{B}_{\text{bg}} f_{\text{bg}} \alpha^2 \right)} = \frac{1}{f_{\text{sig}} N_{\text{tot}}} \sqrt{Z_X n_{\text{bin}} (\sigma_{\text{stat}}^2 + n_{\text{bin}} \sigma_{\text{sys}}^2)}. \quad (5.55)$$

In the main text, Eq. (5.55) was used to determine the systematic uncertainty parameter  $\alpha$  for different experiments, given a quoted upper bound  $\mathcal{B}_{\text{const}}^{X\% \text{CL}}$ . For instance, for a systematic-dominated analysis ( $\alpha^2 N_{\text{tot}} \mathcal{B}_{\text{bg}} f_{\text{bg}} \gg 1$ ), eq. (5.55) gives  $\mathcal{B}_{\text{const}}^{X\% \text{CL}} \simeq \alpha \sqrt{Z_X} (\mathcal{B}_{\text{bg}} f_{\text{bg}} / f_{\text{sig}})$ .

### 5.6.4 Discussion of time-dependent results

For time-dependent analysis we show in fig. 5.3 in the main text, and in fig. 5.4 in section 5.6, the derived upper limits on the signal branching ratio of  $\mu \rightarrow e\phi'$ ,  $\tau \rightarrow \mu\phi'$  and  $\tau \rightarrow \ell\phi'$ , respectively, as a function of the bin size in time (time resolution)  $\Delta t$  for different DM masses. For each mass and  $\Delta t$ , the phase  $\delta$  is chosen by profiling the  $\chi^2$  over  $\delta$  and selecting the value that minimizes the test statistic, ensuring the most conservative estimate. We see that for coarse time bins, in which the oscillatory nature of the signal cannot be resolved ( $m_\phi \Delta t \gg 1$ ), the derived sensitivity is systematics limited. As  $\Delta t$  decreases and the time bins become finer, the oscillations start to be resolved, eventually becoming fully resolved around  $\Delta t \sim m_\phi^{-1}$  (indicated by the vertical dotted lines). In this regime ( $m_\phi \Delta t \ll 1$ ), the sensitivity is no longer systematics limited but instead becomes constrained by statistics.

The translated sensitivities on the scale  $f$  as a function of DM mass, using the most optimal time binning for each mass within the region of validity (between the gray regions denoted in fig. 5.3), can be found in fig. 5.1. That is, in the limit of fine-binning, given  $T, N_{\text{tot}}, \mathcal{B}_{\text{bg}}, f_{\text{bg}}$ ,  $f_{\text{sig}}$ , and  $\alpha$ , the 90% CL sensitivity estimates on  $\mathcal{B}_{\text{sig}}$  are obtained by demanding that  $\chi^2 \leq Z_{90}$ . Using eq. (5.12) and item 3, this requirement translates in the lower bound

$$\frac{f}{\sqrt{C_{ij}}} \geq \frac{8.9 \times 10^{-12} \text{ GeV}}{\sqrt{m_\phi}} \left( \frac{m_{\ell_i}^3}{\Gamma_{\ell_i}} \right)^{1/4} \left( \frac{N_{\text{tot}} f_{\text{sig}}^2}{\mathcal{B}_{\text{bg}} f_{\text{bg}}} \left[ \frac{3 + \mathcal{B}_{\text{bg}} f_{\text{bg}} \alpha^2 N_{\text{tot}}}{1 + \mathcal{B}_{\text{bg}} f_{\text{bg}} \alpha^2 N_{\text{tot}}} \right] \right)^{1/8}, \quad (5.56)$$

where  $\Gamma_{\ell_i}$  denotes the SM decay width of  $\ell_i$ . Likewise in the limit of coarse-binning (or a single-bin analysis) the lower limit on  $f$  is given by

$$\frac{f}{\sqrt{C_{ij}}} \geq \frac{9.7 \times 10^{-12} \text{ GeV}}{\sqrt{m_\phi}} \left( \frac{m_{\ell_i}^3}{\Gamma_{\ell_i}} \right)^{1/4} \left( \frac{N_{\text{tot}} f_{\text{sig}}^2}{\mathcal{B}_{\text{bg}} f_{\text{bg}} (1 + \mathcal{B}_{\text{bg}} f_{\text{bg}} \alpha^2 N_{\text{tot}})} \right)^{1/8}. \quad (5.57)$$

Note that the derivation leading to item 3 has several implicit assumptions, all of which can fail:

- We assume that the data is collected continuously over the full observation time. More realistic experimental setups, where the observation window is broken into discrete chunks of continuous data-taking, can be taken into account with minimal and straightforward modifications to the analysis described above. Alternatively one could also use the Lomb-Scargle periodogram to search for the time-dependent signal [321].
- We assume that each time bin contains a sufficient number of events such that the statistic is  $\chi^2$  distributed. In our numerical analysis, we impose these boundaries as hard limits; for each experiment, we give estimates for improved sensitivity only for  $m_\phi \in [1/T, n_{\text{bin}}^{\text{max}}/T]$ , where  $n_{\text{bin}}^{\text{max}} = N_{\text{tot}} f_{\text{bg}} / 10$  is the largest number of bins such that each bin contains at

least 10 events (background + signal). The regions outside the observational window  $m_\phi \in [1/T, n_{\text{bin}}^{\max}/T]$  are shaded in gray in figs. 5.3 and 5.4.

- In item 3 we assume that the DM phase is fully coherent over the full observation time  $T$ . In a full experimental analysis, one must also properly account for the effect of phase coherence. As described in section 5.6.2, in our analysis, we account for DM decoherence approximately by considering  $n_{\text{patch}} = T/\tau_{\text{coh}}$  equally spaced coherent patches where each patch maintains the same phase over its duration, chosen conservatively through a minimization of the test statistic over  $\delta$ .

#### 5.6.4.1 Experimental details

In this subsection we give further details about the treatment of experimental projections.

- **Mu3e  $\mu \rightarrow e\phi'$ :** A defining feature of the  $\mu \rightarrow e\phi'$  signal are monoenergetic positrons at energy  $E_e \simeq m_\mu/2$ . This mono-energetic line lies at the endpoint of the SM decay  $\mu \rightarrow e\nu\bar{\nu}$  ( $\mathcal{B}_{\mu \rightarrow e\nu\bar{\nu}} = \mathcal{B}_{\text{bg}} \simeq 1$ ), given by the kinematic configuration of two neutrinos collinear that are back-to-back with the positron. The size of the background from the SM is determined by the detector's energy resolution. In our projections we take the positrons to be in the endpoint region, if their energy is within 3 MeV of the kinematic endpoint; this choice corresponds to the anticipated detector's intrinsic energy resolution [21, 22, 122], and is also comparable with the signal region used in the analysis in [315], where it was defined to be within  $\simeq 4$  MeV of the endpoint, but also with a cut on the direction of positrons relative to muon spin. In this narrow window, the estimated background level is  $N_{\text{bg}} \simeq 1.1 \times 10^{13}$ , which is what we use in our projections. For comparison, widening the endpoint energy window to twice the resolution (i.e., 6 MeV) would increase the background yield to approximately  $5.7 \times 10^{13}$  events. Assuming, for simplicity, that the detection and reconstruction efficiencies are  $\simeq 1$ , we have  $f_{\text{bg}} \simeq N_{\text{bg}}/N_{\text{tot}} = 3.3 \times 10^{-3}$ . We also assume that the systematic uncertainties are dominated by the theory prediction on the SM background. This gives an expected 90%CL upper limit on  $\mu \rightarrow e\phi'$  branching ratio of  $\mathcal{B}_{\text{const}}^{90\%} = 6 \times 10^{-7}$  (as determined in Ref. [315, Fig. 12]). From it we deduce the systematic uncertainty parameter  $\alpha$ , assuming that approximately all of the signal events fall into this kinematic endpoint ( $f_{\text{sig}} \simeq 1$ ) as well as systematics domination ( $\alpha^2 N_{\text{tot}} \mathcal{B}_{\text{bg}} f_{\text{bg}} \gg 1$ ) in eq. (5.55), giving  $\alpha \simeq (\mathcal{B}_{\text{const}}^{90\%} f_{\text{sig}})/(\sqrt{Z_{90}} \mathcal{B}_{\text{bg}} f_{\text{bg}}) = 1.1 \times 10^{-4}$ .
- **Belle-II  $\tau \rightarrow \ell\phi'$ :** During the 2019-2020 run, Belle-II recorded roughly  $N_{\text{tot}} \simeq 1.2 \times 10^8$  taus [25] (we assume that these were collected continuously over 300 days). Of these, approximately  $\mathcal{B}_{\tau \rightarrow e\nu\bar{\nu}} = 17.8\%$  (for  $\ell = e$ ) and  $\mathcal{B}_{\tau \rightarrow \mu\nu\bar{\nu}} = 17.4\%$  (for  $\ell = \mu$ ) decay via the SM channel  $\tau \rightarrow \ell\nu\bar{\nu}$  [34]. The Belle-II analysis also requires the tag hemisphere to

contain three charged particles,  $\tau \rightarrow 3h\nu_\tau$ ,  $h = \pi, K$ , with a branching  $\mathcal{B}_{\tau \rightarrow 3h\nu} = 15.2\%$  [34]. The irreducible SM background (available for the analysis) thus has a branching of

$$B_{\text{bg}}^{e[\mu]} \simeq 2.7 \times 10^{-2} \left( \frac{\mathcal{B}_{\tau \rightarrow \ell\nu\bar{\nu}}}{0.178[0.174]} \right) \left( \frac{\mathcal{B}_{\tau \rightarrow 3h\nu}}{0.152} \right). \quad (5.58)$$

In the tau pseudo-rest frame the distribution of charged lepton energy  $E_\ell^*$  for these SM decays resembles the one expected from the exotic  $\tau \rightarrow \ell\phi'$  decays, since the poor reconstruction of the tau rest frame smears the mono-energetic signature. In Belle-II shape information was used to distinguish between background and signal. In our estimates we instead use a simplified strategy, and define signal regions as the energy windows  $E_e^*/(m_\tau/2) \in [0.66, 1.48]$  and  $E_\mu^*/(m_\tau/2) \in [0.71, 1.38]$  defined to retain  $\epsilon_{\text{cut}}^{\text{sig}} \simeq 90\%$  of the  $\tau \rightarrow \ell\phi'$  signal events,  $N_{\text{sig}}$ , and straddle symmetrically the peak of the signal distribution. These windows simultaneously capture about  $\epsilon_{\text{cut}}^{\text{bg},e} \simeq 59\%$  and  $\epsilon_{\text{cut}}^{\text{bg},\mu} \simeq 56\%$  of the SM background events,  $N_{\text{bg}}$ , for electrons and muons, respectively. Moreover, the minimal reconstruction efficiency for the signal channel is estimated at  $\epsilon_{\text{rec}}^{\text{sig},e} \simeq 13.4\%$  for electrons and  $\epsilon_{\text{rec}}^{\text{sig},\mu} \simeq 17.4\%$  for muons [322, Table 4.4], while for the background  $\epsilon_{\text{rec}}^{\text{bg},e} \simeq 12.7\%$  and  $\epsilon_{\text{rec}}^{\text{bg},\mu} \simeq 16.2\%$  [25, 322]. Combining the kinematic cuts and the reconstruction efficiencies yields

$$f_{\text{bg}}^{e[\mu]} \simeq 7.5 \times 10^{-2} [9.1 \times 10^{-2}] \left( \frac{\epsilon_{\text{cut}}}{0.59[0.56]} \right) \left( \frac{\epsilon_{\text{rec}}}{0.127[0.162]} \right), \quad (5.59)$$

$$f_{\text{sig}}^{e[\mu]} \simeq 0.12 [0.16] \left( \frac{\epsilon_{\text{cut}}}{0.9} \right) \left( \frac{\epsilon_{\text{rec}}}{0.134[0.174]} \right). \quad (5.60)$$

These agree within 30% with the values one would obtain if the results in Fig. 1 in [25] were used instead. Using the relation  $\alpha \simeq (\mathcal{B}_{\text{const}}^{90\%} f_{\text{sig}})/(\sqrt{Z_{90}} \mathcal{B}_{\text{bg}} f_{\text{bg}})$  in eq. (5.55) with the 90% confidence-level limits  $\mathcal{B}_{\text{const}}^{90\%} \simeq 7.6 \times 10^{-4}$  for electrons and  $4.7 \times 10^{-4}$  for muons [25, Tab. III], we obtain systematic uncertainty parameters of  $\alpha \simeq 2.7 \times 10^{-2}$  and  $\alpha \simeq 1.9 \times 10^{-2}$  for the electron and muon channels, respectively. For the full Belle-II analysis utilizing the entire  $50 \text{ ab}^{-1}$  integrated luminosity dataset, we provide sensitivity projections using the same analysis outlined above (with an appropriately rescaled  $N_{\text{tot}}$ ) assuming that the time integrated analysis will remain systematics dominated at the present value. While this is very likely to be too conservative, given that improvements in both the systematics and the observables used to distinguish between signal and background are likely [323], the approximation suffices for our purposes: the rough estimate of the reach for the time-dependent analysis.

- **FCC-ee  $\tau \rightarrow \ell\phi'$**  : While running in Tera-Z mode the proposed FCC-ee experiment will produce approximately  $N_{\text{tot}} = 2N_{\tau\bar{\tau}} \simeq 2 \times 1.7 \times 10^{11}$  taus over  $T = 740$  days of running [26]. While the changes in the boost of the taus, coverage of the detector, and energy resolution will doubtless lead to changes in signal and background separation, to date

there have not been detailed studies of the expected reach for the  $\tau \rightarrow \ell\phi'$  channel at FCC. Here, for simplicity, we assume a similar analysis and background contamination to that of Belle-II, and take the reconstruction efficiency to be  $\epsilon_{\text{rec}}^{\text{sig, bg}} \simeq 90\%$ . Ignoring small differences between  $e$  and  $\mu$  this gives

$$f_{\text{bg}} \simeq 0.53 \left( \frac{\epsilon_{\text{cut}}}{0.59} \right) \left( \frac{\epsilon_{\text{rec}}}{0.9} \right), \quad (5.61)$$

$$f_{\text{sig}} \simeq 0.81 \left( \frac{\epsilon_{\text{cut}}}{0.9} \right) \left( \frac{\epsilon_{\text{rec}}}{0.9} \right). \quad (5.62)$$

As a surrogate for the expected bound on  $\tau \rightarrow \ell\phi'$  we use the expected systematics dominated (absolute) precision on the leptonic branching fraction of  $\sigma(\mathcal{B}_\ell) = 3 \times 10^{-5}$ . It is hoped that, even if the final precision is systematically limited, it will not be far from this value [324]. Using  $\alpha \simeq \sigma(\mathcal{B}_\ell)f_{\text{sig}}/(\mathcal{B}_{\text{bg}}f_{\text{bg}})$  with  $\mathcal{B}_{\text{bg}}$  in eq. (5.58), we find  $\alpha \simeq 1.7 \times 10^{-3}$ .

## 5.7 Conclusions

In this chapter we demonstrated that FCNC decays may offer a new window into ultralight DM candidates. Crucially, the presence of FCNC couplings to charged SM leptons can induce time modulation with DM mass frequency in  $\tau \rightarrow \ell\phi'$  and  $\mu \rightarrow e\phi'$  decays, where  $\phi'$  is a light dark sector scalar. Since observing time dependence in these decays would be smoking-gun evidence of DM, we find that rare lepton decay experiments can also serve as potential dark matter direct detection experiments without any instrumental modifications. Furthermore, such time-oscillating signals can improve the experimental reach compared to time-independent searches, if the latter are dominated by systematic uncertainties, see Fig. 5.1.

While our analysis focused on flavor violation in charged lepton decays, the same approach directly extends both to other observables in the lepton sector (such as  $\mu \rightarrow e$  conversion in the field of a nucleus), as well as to flavor violation in the quark sector. We leave a more detailed analysis of these phenomena for future work.

## Part II

# Differentiable Hadronization Models

# Chapter 6

## Introduction

### 6.1 Monte Carlo Event Generators

The macroscopic nature of detectors at high energy collider experiments limits their ability to resolve truly ‘exclusive’ final states below a fundamental scale set by the spatial resolution of the innermost tracking layers, typically 10–100  $\mu\text{m}$  from the interaction point. What experiments actually record is a coarse-grained, macroscopic projection of the underlying microscopic dynamics originating at the hard scale  $\sim \sqrt{s}$ . General-purpose Monte Carlo (MC) event generators bridge this gap by precisely simulating the microscopic evolution of a collision – from the partonic hard scattering through parton showering, hadronization, and decays – producing fully exclusive final states from which the inclusive features observed by detectors can emerge. The central idea is that the macroscopic detector response can be understood as the aggregate consequence of an ensemble of such exclusive microscopic events.

Generically, general-purpose MC event generators such as PYTHIA [29, 30], SHERPA [325], HERWIG [326], etc. simulate the fully exclusive evolution of high energy particle collisions using  $\sim 3–5$  modular algorithmic prescriptions which, when stitched together, make predictions for exclusive particle final states in the form of an event record that can be translated into experimental observables. Another useful definition of MC generators is exclusive final state event simulation. More conservatively, the definition of an event generator is the code which executes the simulation. The event generators are monolithic codebases written in C++ with hundreds of thousands of lines of code<sup>1</sup>.

From a functional perspective, an event generator,  $\mathcal{G}$ , is a set of sequential higher-order (or composite) functions where the outputs of sub-programs are fed in as arguments to other sub-programs. The sub-programs are commonly broken down as:

---

<sup>1</sup>PYTHIA v8.315 has roughly  $\approx 564,000$  (338,000 C++) lines of code, SHERPA v3.0.1 has  $\approx 397,000$  (242,000 C++) lines of code, and HERWIG v7.3.0 has  $\approx 379,000$  (224,000 C++) lines of code. Values obtained using the `cloc` command line tool.

1. **Hard process**,  $\mathcal{M}$ : This stage encapsulates the perturbative calculation of short-distance matrix elements typically computed at fixed-order accuracy (LO, NLO, or NNLO) in QCD or electroweak theory. The hard process defines the initial partonic final state based on the scattering amplitude squared,  $|\mathcal{M}|^2$ , which provides differential cross sections and sets the initial conditions for subsequent evolution. Practically, this calculation is often interfaced with dedicated fixed-order squared matrix element generator tools such as MADGRAPH [138, 327], POWHEG [328, 329], or MC@NLO [330].
2. **Parton shower**,  $\mathcal{P}$ : The parton shower implements the perturbative evolution of partonic final states from the hard process down to scales approaching  $\Lambda_{\text{QCD}}$ . It resums collinear and soft logarithms via stochastic splitting algorithms (e.g., DGLAP or dipole-based showers), effectively dressing the hard process with additional radiation. Crucially, the parton shower probabilistically generates branching histories guided by Sudakov form factors and splitting kernels, typically interfaced through algorithms implemented in generators such as PYTHIA [29], HERWIG [331], or SHERPA [332].
3. **Hadronization**,  $\mathcal{H}$ : At scales around  $\Lambda_{\text{QCD}}$ , non-perturbative QCD effects become dominant, and colored partons must transition into color-neutral hadrons. Hadronization models, such as the Lund string model [333] or cluster model [334–337], provide probabilistic mechanisms to map final-state partons onto hadronic spectra, accounting for longitudinal and transverse momentum distributions, baryon-to-meson ratios, and hadron multiplicities. This step is inherently phenomenological, tuned extensively to experimental data from  $e^+e^-$  colliders and hadron colliders.
4. **Hadron decays**,  $\mathcal{D}$ : After formation, unstable hadrons decay into stable or semi-stable particles according to experimentally measured branching ratios and decay kinematics. This step systematically employs particle decay databases (e.g., HEPMC tables [338], EVTGEN [339, 340]) to produce physically accurate final-state particle distributions, including resonance decay channels, weak and electromagnetic decays, and spin correlations where relevant.
5. **Detector simulation**,  $\mathcal{S}$ : Finally, the stable particles from hadron decays are propagated through detailed numerical simulations of detector geometries and materials. Software frameworks such as GEANT4 [341–343] simulate particle interactions with detector components, modeling energy deposition, particle tracking, calorimetric response, and efficiencies of reconstruction algorithms. This step transforms idealized theoretical final states into realistic experimental observables, enabling direct comparison between simulated events and detector-level experimental data. While not typically included within general-purpose event generators, the importance of detector simulations for direct comparison with experimental data in the broader simulation pipeline warrants their inclusion in an expanded definition of ‘event generator’.

The output of the generator is an array of particle data – the so-called *event record*,  $\mathcal{E}$  e.g. particle properties, four-momenta, color-connections, etc. Note that the event record contains both the final output particle information as well as the internal representations used by each algorithm to propagate results. Schematically we have

$$\mathcal{G} : \underbrace{\mathcal{S}(\mathcal{D}(\mathcal{H}(\mathcal{P}(\mathcal{M}))))}_{\text{Simulation}} = \mathcal{E} \simeq \underbrace{\begin{pmatrix} \{\text{id}, E, p_x, p_y, p_z, \dots\}_1 \\ \{\text{id}, E, p_x, p_y, p_z, \dots\}_2 \\ \vdots \\ \{\text{id}, E, p_x, p_y, p_z, \dots\}_N \end{pmatrix}}_{\text{Event record}} . \quad (6.1)$$

From the event record, an infinite number of observables  $O$  can be defined. Each observable can be generically defined as a function of the full or partial event record

$$O \equiv f(\mathcal{E}) . \quad (6.2)$$

The event record can equivalently be thought of as a high-dimensional probability distribution over particle phase space. The observables  $O$  form slices or projections/marginalizations<sup>2</sup> on this high-dimensional distribution. As such, each observable is then also a random variable with an associated probability distribution over phase space variables. In practice, the analysis of probability distributions is almost always done with histograms  $O \rightarrow \{O_i\}$ , with each bin also qualifying as an independent observable. The structure of these observable distributions is intimately tied to the underlying simulation.

As discussed briefly above, event simulation can broadly be partitioned into perturbative (hard process, parton shower) and non-perturbative (hadronization, hadron decays) components. The non-perturbative components, especially hadronization, require phenomenological modeling. Almost by definition, these phenomenological models contain free parameters that must be *tuned* to data. Tuning involves taking a set of measured experimental observables and varying parameters of the model to achieve the best global agreement. In this way, tuning constitutes an inverse problem: one observes the statistical imprint left by the non-perturbative QCD dynamics and seeks to infer the model parameters that best reproduce it. However, because the mapping from model parameters to observables is generally many-to-one and entangled across different observables, tuning is inherently underconstrained. This ambiguity, compounded by the fact that no model of hadronization is derived from first principles, introduces a fundamental uncertainty into the simulation. Understanding how different hadronization models navigate this inverse problem, and the degree to which their uncertainties propagate to predictions, is essential for interpreting experimental results and improving the reliability of Monte Carlo event generators.

---

<sup>2</sup>Thank you Manuel, for all knowledge related to marginalization.

## 6.2 Landscape of hadronization models

In part II we will primarily be interested in improving the non-perturbative modeling of *hadronization*. Colliders probe energy scales where quarks and gluons interact perturbatively. As described above, hard scattering events often produce colored partons that evolve via parton showers, radiating additional quarks and gluons. At the detector level, far below the QCD confinement scale, only color-neutral composite particles such as mesons, baryons, and occasionally exotic hadrons (e.g. tetraquarks or pentaquarks) are observed. To bridge this gap, Monte Carlo event generators must model the nonperturbative process that converts colored final state particles from the parton shower into observable hadrons. Many phenomenological models of hadronization exist, however, in modern event generators two models are favored: the *Lund string model* (implemented in PYTHIA) and the *cluster model* (implemented in HERWIG, SHERPA). In the rest of part II, we'll focus exclusively on the Lund string model, but, before moving onto a detailed discussion of the Lund model it is good to pay homage to the many hadronization models that have been considered over the years. I provide a brief summary for a selection of these models below.

**Artru–Mennessier** Proposed in 1974, the Artru–Mennessier model [344] is one of the earliest semi-classical string-based descriptions of hadronization. Unlike the cluster model or the later Lund framework, it assumes that string breakups occur uniformly per unit area of the string worldsheet, with hadron formation governed by a constant fragmentation probability modulated by an exponential suppression factor to regulate low-mass divergences. The model produces hadrons as continuous-mass string fragments, rather than discrete resonance states, and treats breakpoints as causally disconnected vertices distributed in light-cone spacetime. While it lacked explicit fragmentation functions or an iterative MC prescription, it correctly predicts features like uniform rapidity densities and linear energy scaling. Importantly, Artru and Mennessier's model served as the conceptual precursor to the Lund model, providing key physical insight into the geometric structure of hadronization and the emergence of soft hadrons from QCD string dynamics.

**Lund** Developed in the late 1970s and notably implemented in PYTHIA, the Lund model [333] provides a string-based framework for hadronization, refining and extending earlier ideas introduced by Artru–Mennessier. It models hadron formation as the sequential fragmentation of a relativistic string stretched between color-connected partons, with breakups occurring at spacelike-separated vertices along the string worldsheet. Unlike the continuous fragment spectrum of Artru–Mennessier, the Lund model generates discrete hadrons according to a universal fragmentation function that governs the probability distribution of energy-momentum sharing

between successive string breaks. The model introduces an explicit parametrization for longitudinal momentum fractions and transverse momentum smearing, enabling accurate predictions of jet shapes and hadron spectra. Due to its theoretical coherence and empirical success, the Lund model remains the dominant phenomenological framework for string fragmentation.

**Feynman and Field** Proposed in the late 1970s, the Feynman and Field model [345] offers a phenomenological description of hadronization based on independent fragmentation of color-singlet systems. In this framework, each high-energy parton fragments independently into hadrons according to a universal fragmentation function, with no long-range correlations or dynamical color structure between jets. Unlike the string-based Artru–Mennessier and Lund models, this approach does not model confinement as a collective string-like phenomenon, but instead treats hadron formation as an uncorrelated sequence of parton splittings. While successful in capturing basic features of inclusive hadron spectra, the model lacks a geometrical or dynamical picture of color reconnection or inter-jet correlations, limiting its applicability in describing the full structure of multi-jet events.

**Cluster** Introduced in the early 1980s and notably implemented in event generators such as HERWIG and SHERPA, the cluster model [334–336] provides a distinct alternative to string-based models. Rather than modeling hadronization through elongated strings, the cluster model first groups final-state partons produced in perturbative parton showers into color-singlet clusters with invariant masses typically on the order of a few GeV. These clusters subsequently decay isotropically into hadrons or resonances, governed primarily by kinematics and phase space considerations. The major technical difference compared to stringy models is the explicit two-step approach – a parton shower followed by cluster formation and decay. The approach results in simpler implementation but occasionally less accurate description of detailed hadron momentum correlations and heavy-flavor fragmentation.

**UCLA** Proposed in the mid-2000s, the UCLA model [346] introduces a Lorentz-invariant formulation of hadronization based on a spacetime area law (STAL). Unlike the Lund model, which uses a probabilistic fragmentation function in light-cone variables, UCLA assigns an exponential suppression to hadron formation based on the invariant area swept out by quark world-lines. This geometric approach incorporates quark mass effects more directly than cluster or Lund models, without relying on discrete hadron spectra or extensive parameter tuning. While not as widely implemented, it provides a distinct perspective by emphasizing covariant spacetime structure as the organizing principle behind hadronization.

**Statistical** Statistical hadronization models [347, 348], developed in the 1990s and early 2000s, were motivated by the success of thermodynamic models in describing hadron yields in heavy-ion

collisions at the SPS and RHIC. These models assume that hadrons form via thermal freeze-out from a chemically equilibrated partonic system, with species abundances governed by temperature, chemical potentials, and volume. Unlike fragmentation-based approaches, statistical models do not model exclusive kinematic structure but instead reproduce inclusive multiplicities by maximizing entropy subject to conserved quantum numbers. Their predictive success, particularly in capturing the yields of strange and multi-strange hadrons, suggests that at sufficiently high energy densities, hadronization reflects statistical hydrochemical equilibrium.

**Coalescence** Coalescence models [349, 350], developed in the early 2000s in response to RHIC data, provide an alternative to fragmentation in dense QCD matter by modeling hadron formation through the local recombination of nearby quarks in phase space. These models were introduced to explain surprising observations in central heavy-ion collisions – such as the enhanced baryon-to-meson ratios at intermediate  $p_T$  and the scaling of elliptic flow with the number of constituent quarks. Unlike string or cluster models, coalescence assumes hadronization occurs directly from partonic degrees of freedom without requiring extended color flux tubes. While they lack the ability to generate fully exclusive final states, coalescence models are important for understanding hadron production in strongly interacting, collectively flowing QCD media.

### 6.3 The Lund string model

Before continuing we should note that in the rest of part II, almost all methods are validated on the ‘simplest’ hadronizing system, namely, a  $q\bar{q}$  system hadronizing to purely pionic final states,  $\pi^0, \pi^\pm$ . This system contains all of the essential features of the non-gluonic Lund string model with additional features, such as full hadronic final states, being straightforward, but tedious, generalizations. Strings with gluons will be discussed in section 6.3.3 – the hadronization dynamics of these systems is explicit [351] but somewhat non-trivial, especially in the context of machine-learning-based methods attempting to extract hadronization dynamics from data. In chapters 7 and 8 we will denote explicitly which hadronizing systems each method has been validated on. Below we summarize in detail the dynamics and hadronization of a  $q\bar{q}$  string.

#### 6.3.1 The $q\bar{q}$ string

In QCD the potential between a static quark and anti-quark as a function of the separation distance,  $r$ , is found to be [352, 353]

$$V_{q\bar{q}}(r) \approx -\frac{4\alpha_s}{3} \frac{1}{r} + \kappa r. \quad (6.3)$$

At short distances ( $r < 0.1$  fm), the  $1/r$  piece (stemming from one-gluon exchange) dominates and the quarks behave as free ‘Coulomb-like’ charged particles. At long distances, the linear

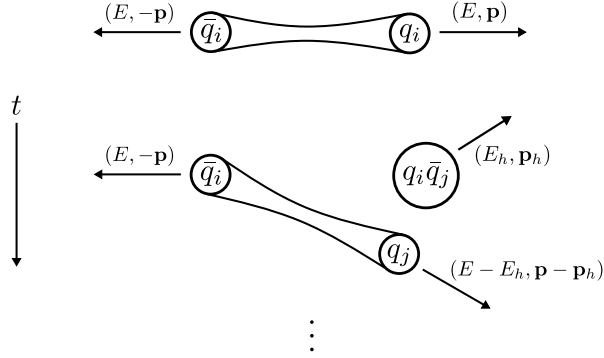


FIGURE 6.1: A cartoon illustration of a single fragmentation during  $\bar{q}q$  hadronization.

component dominates – representing the collapse of gluonic field lines into a thin color flux tube or string with a constant tension (linear energy density)  $\kappa \simeq 1 \text{ GeV/fm} \simeq 0.2 \text{ GeV}^2$ . In the Lund string model, the QCD potential is approximated as the purely linear (or string-like) piece

$$V_{\text{Lund}}(r) \approx \kappa r. \quad (6.4)$$

The idea that hadrons might be connected by strings predates QCD itself and was first inspired by the observed Regge trajectories – empirical linear relations between the squared masses and spins of mesons and baryons,  $J \sim \alpha' m^2$  [354, 355]. This empirical evidence suggested that hadrons could be understood as rotating relativistic objects with a constant energy per unit length, naturally leading to a string-like interpretation of the strong force. In the late 1960s/early 1970s, Nambu, Nielsen, and Susskind independently proposed that the strong interaction could be modeled by a relativistic string, whose quantized vibrational modes corresponded to hadronic resonances [356–358]. In this picture, the linear confinement potential in eq. (6.4) emerges as a macroscopic manifestation of the same string tension that governs the Regge slope,  $\alpha' \simeq 1/(2\pi\kappa)$ , linking the dynamics of the QCD flux tube to the early “string” models of hadrons.

To gain some intuition for the implications of eq. (6.4), consider the center-of-mass frame of a  $q_i \bar{q}_i$  system where the (massless) partons, each with flavor index  $i$  and initial energy  $E$ , travel with equal and opposite momenta along the  $z$ -axis. As the separation increases the confining force causes an approximately uniform cylindrical string (flux tube) of color field to form between the quark pair. In the absence of string breaks, our  $q\bar{q}$  system would follow an infinite “yo-yo” motion whereby the the systems energy oscillates between the kinetic energy of the quarks and the energy contained in the string.

### 6.3.2 Hadronizing a $q\bar{q}$ string

If we allow for string breaking during the separation process the energy in the string can be used to create  $q'\bar{q}'$  pairs out of the vacuum. This production breaks the original string into two fragments: a composite hadron  $h \equiv q_i \bar{q}'$  (or  $q' \bar{q}_i$ ) and another  $q' \bar{q}_i$  (or  $q_i \bar{q}'$ )-string system. The

ejected hadron inherits kinematics according to the model (and whose microscopic description in this model would be that of a mini-string following stable yo-yo motion as described above, i.e., yo-yo-hadrons). The remaining string system continues its evolution and potentially fragments further into more hadrons, see fig. 6.1 for a schematic depiction of a single string break.

In the string model, hadronization is typically implemented in momentum space as an iterative stochastic walk through production (string-break) vertices,  $v_i$ . Because each string end is massless, they both follow lightlike trajectories, motivating the use of light-cone coordinates. Given an arbitrary four-momentum  $p^\mu = (E, \vec{p})$ , the light-cone momenta are defined as:

$$p^\pm = E \pm p_z \quad (6.5)$$

and satisfy (in  $1 + 1$  dimensions)

$$p^+ p^- = m^2. \quad (6.6)$$

Under Lorentz boosts, like cone momenta have simple transformation properties

$$p^{\pm'} = k^{\pm 1} p^\pm, \quad \text{where } k = \sqrt{\frac{1+\beta}{1-\beta}} \quad (6.7)$$

with  $\beta$  denoting the boost velocity.

The string itself has total light-cone momenta (defined at  $t = 0$ ):

$$P^+ = p_q^+ + p_{\bar{q}}^+, \quad P^- = p_q^- + p_{\bar{q}}^- \quad (6.8)$$

which in the string rest frame (both ends with equal energy,  $E$ , and opposite momenta along the  $z$ -axis,  $p_z$ ) becomes

$$P^+ = 2E, \quad P^- = 2E, \quad P^+ P^- = M^2 = 4E^2 \quad (6.9)$$

where  $M$  is the string mass.

To further describe the fragmentation in dimensionless, string-normalized coordinates we also introduce light-cone momentum fractions,  $x^\pm$ , representing the light-cone separation between two breaks and defined as

$$x_i^\pm = \frac{p_i^\pm}{P^\pm}$$

for the  $i$ -th hadron. These satisfy:

$$x_i^+ x_i^- = \frac{m_i^2}{M^2}.$$

For a specified hadron mass, we thus have a fixed relationship between  $x_i^+$  and  $x_i^-$ . Note that the momentum fractions are normalized to the quark turning points such that  $0 \leq x^\pm \leq 1$ .

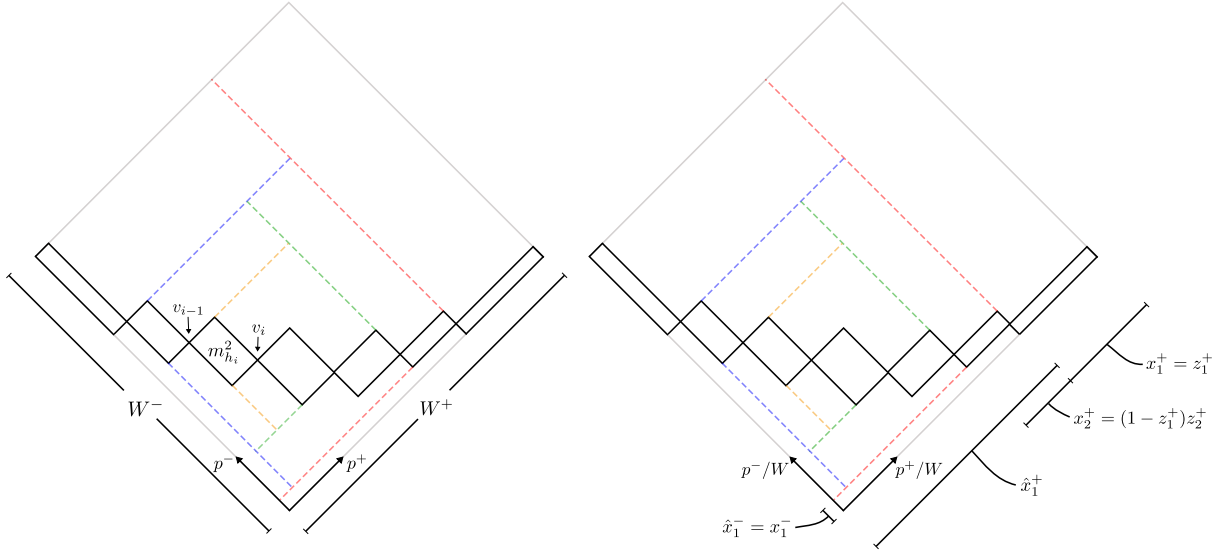


FIGURE 6.2: A depiction of the  $q\bar{q}$  string in momentum space. See the text for details.

Figure 6.2 shows an example of a fully hadronized string in energy-momentum space where  $\hat{x}^\pm$  represent light-cone vertex coordinates, describing the location of production vertices.

Very broadly, the full hadronization of a string can be categorized into two independent, but also correlated/conditionally dependent, sectors:

1. Flavor production: a prescription for string break flavor must be prescribed followed by the correct assignment of relative hadron abundances from combination of two string breaks to match data/theoretical expectations.
2. Kinematics: four-momenta assignments must be made for each of the produced hadrons.

We can finally introduce the longitudinal momentum fraction,  $z^\pm$ , defined as the fraction of longitudinal momentum (light-cone momentum  $p_i^\pm$ ) absorbed by the  $i$ -th hadron from the remaining longitudinal momentum in the string system. This is similar but distinct from the light-cone momentum fractions we defined above, they are related

$$x_1^+ = z_1^+, \quad x_i^+ = z_i^+ \prod_{j=1}^{i-1} (1 - z_j) \quad \text{for } i > 1. \quad (6.10)$$

From the transformations defined above, we see that  $z^\pm$  is manifestly invariant under boosts. The distribution from which  $z$  is sampled is called the Lund left-right symmetric scaling (fragmentation) function and is proportional to the following

$$f(z)dz \propto \frac{(1-z)^a}{z} \exp\left(-b \frac{m_h^2}{z}\right) dz \quad (6.11)$$

where  $a$  and  $b$  are tuneable phenomenological parameters fit to empirical data. Generically, the Lund  $a$  parameter can also be flavor dependent – consider a fragmentation starting from a

string end with flavor  $\alpha$  and a string breaking sourced by a  $q\bar{q}$  pair of flavor  $\beta$ , the resulting Lund distribution is given by

$$\begin{aligned} f_{\alpha\beta}(z)dz &\propto \frac{z^{a_\alpha}}{z} \times \frac{(1-z)^{a_\beta}}{z^{a_\beta}} \times \exp\left(-b\frac{m_T^2}{z}\right) dz \\ &= \frac{(1-z)^{1-a_\beta}}{z^{1+a_\beta-a_\alpha}} \exp\left(-b\frac{m_T^2}{z}\right) dz. \end{aligned} \quad (6.12)$$

Within PYTHIA, all string breaks are flavor-blind except those involving di-quarks<sup>3</sup>. For heavy quarks (charm,  $c$ , and bottom/beauty,  $b$ ), the Lund fragmentation function receives a quark mass-dependent Bowler modification

$$f_{\alpha\beta}(z)dz \propto \frac{1}{z^{r_\beta b m_\beta^2}} \frac{(1-z)^{1-a_\beta}}{z^{1+a_\beta-a_\alpha}} \exp\left(-b\frac{m_T^2}{z}\right) dz \quad (6.13)$$

where  $r_\beta$  is an arbitrary tuneable parameter.

The full iterative program for the hadronization of a  $q\bar{q}$  string in the  $(1+1)$ - $D$  Lund string model can be summarized as follows:

1. Randomly select from which string end the fragmentation will take place.
2. Select new  $q'\bar{q}'$  and hadron to be produced.
3. Sample  $z$  according to the Lund fragmentation function.
4. Compute production vertices.
5. Update all momenta.
6. Proceed through steps 1–5 until the center of mass energy of the new string system falls below a given cut off threshold  $M_{\min}^2$ .

Finally, to convert from the momentum fractions to (in principle observable) hadron four-momenta, consider the four-vectors

$$P_{q/\bar{q}}^\mu \equiv E(1, 0, 0, \pm 1), \quad (6.14)$$

and remember that the  $i$ -th ( $i \in 1, \dots, N_h$ ) hadron coordinate can be described generically by

$$x_i^+ = \hat{x}_{i-1}^+ - \hat{x}_i^+, \quad (6.15)$$

---

<sup>3</sup>A bug was recently found (originally by me, then confirmed by Manuel, followed by Steve, Christian, and finally Torbjorn) in the PYTHIA codebase, originating almost 20 years ago when the codebase was rewritten from Fortran to C++. The bug was related to how the  $a$  parameter was being updated for flavorful breaks – specifically strange and diquark breaks (although by default `zLund:aExtraS = 0`). Ultimately, and thankfully, the repercussions of this bug are minimal – as of PYTHIA v8.315 the bug is fixed. For more details, refer to the PYTHIA update history page where a short note is provided by Torbjorn nicely outlining the implications.

$$x_i^- = \hat{x}_i^- - \hat{x}_{i-1}^- \quad (6.16)$$

with  $\hat{x}_0^+ = 1, \hat{x}_0^- = 0$ . The hadron momentum is then fully described by the system of equations

$$p_i^\mu = x_i^+ P_q^\mu + x_i^- P_{\bar{q}}^\mu \quad (6.17)$$

or simply

$$E_i = E(x_i^+ + x_i^-), \quad p_{z,i} = E(x_i^+ - x_i^-) \quad (6.18)$$

constrained by the condition

$$m_i^2 = p_i^2 = x_i^+ x_i^- M^2. \quad (6.19)$$

In practice, given the mass of the new hadron  $m_i$  and longitudinal momentum fraction  $z_i$ , we'll compute the new vertex  $i$  via

$$x_i^+ = z_i^+ \prod_{j=1}^{i-1} (1 - z_j^+) \quad \text{for } i > 1 \quad (6.20)$$

$$x_i^- = \frac{m_i^2}{x_i^+ M^2} \quad (6.21)$$

where  $z_0^+ = 0$ . Finally, the position  $(\hat{x}_i^+, \hat{x}_i^-)$  of the  $i$ -th vertex can also be found recursively using the expressions above

$$\hat{x}_i^+ = \hat{x}_{i-1}^+ - x_i^+ = (1 - z_i) \hat{x}_{i-1}^+ \quad (6.22)$$

$$\hat{x}_i^- = \hat{x}_{i-1}^- + x_i^- . \quad (6.23)$$

Eventually the algorithm reaches a point where energy and momentum conservation of the outgoing hadrons becomes relevant for modeling the dynamics. For example, we will eventually reach a point where the remaining string mass is too small to produce any hadrons that we have access to – while not totally necessary, but is typically implemented in practice, the algorithm should stop the fragmentation chain before reaching this point such that an algorithm tailored for finite-mass string hadronization can be called. A potentially good condition for this would be to stop right around when the remaining area is roughly the size of two of the largest hadron masses (or the mean of all remaining viable hadron masses) that can be produced. Remember that the last vertex that we select is actually producing the final two hadrons, which in many of our examples is just two pions. This gives a rough stopping condition of the form

$$\hat{x}_n^+ (1 - \hat{x}_n^-) M^2 \approx (2m_\pi)^2. \quad (6.24)$$

If the string fragments in such a way that this final condition cannot be satisfied, the full chain is typically thrown away, i.e. rejected and the full system is re-hadronized from scratch. Within

PYTHIA, this final partitioning of hadron energy and momentum is implemented via a function called `finalTwo`. As we'll see in chapters 7 and 8, the implications of this final filtering are very important (and somewhat sinister) in the context of reweighting and the extraction of a data-driven fragmentation functions from data.

### 6.3.2.1 Incorporating transverse momentum

In the Lund string model, each string break corresponds to the non-perturbative creation of a  $q'\bar{q}'$  pair from the vacuum. This is modeled as a quantum tunneling process through the linear confining potential of the string. According to the uncertainty principle, this pair can have non-zero momentum transverse to the string axis. Since they are produced locally, momentum conservation requires that the transverse momenta of the quark and anti-quark be equal and opposite i.e. each string break introduces a local transverse momentum kick, with

$$\vec{k}_\perp^{(q')} = -\vec{k}_\perp^{(\bar{q}')}. \quad (6.25)$$

The resulting hadron inherits this transverse momentum when a quark from one break and an anti-quark from the next recombine.

The tunneling probability for producing a quark of mass  $m_q$  and transverse momentum  $p_\perp$  is given by the Schwinger-like exponential suppression:

$$\mathcal{P}(m_q, p_\perp) \propto \exp\left(-\frac{\pi(m_q^2 + p_\perp^2)}{\kappa}\right) \quad (6.26)$$

where  $\kappa \sim 1 \text{ GeV/fm} \simeq 0.2 \text{ GeV}^2$  is the string tension. Note that heavier quarks and large transverse momenta are exponentially suppressed. Thus, strange quark production is rarer than up/down, and charm production is even more highly suppressed.

Fortunately, the iterative algorithm only requires minimal changes and can be largely summarized with the transformation:  $m^2 \rightarrow m_\perp^2 \equiv m^2 + p_T^2$  where  $m_\perp$  is the transverse mass.

In light-cone coordinates, transverse momentum components completely factorize from the longitudinal components (they are orthogonal). All light-cone variable definition remain the same as defined previously with the key change coming from the on-shell condition:

$$p^+ p^- = m^2 + p_T^2 \equiv m_\perp^2. \quad (6.27)$$

Likewise, the momentum fractions become

$$x^+ x^- = \frac{m_\perp^2}{M^2}. \quad (6.28)$$

Because  $p_T$  completely factorizes (in terms of it's generation) the  $p_T$  of the  $i$ -th hadron can be computed recursively via the string end transverse momentum  $\vec{k}_T$

$$\vec{p}_{T,i} = \vec{k}_{T,i} - \vec{k}_{T,i-1}, \quad \text{with} \quad \vec{k}_{T,0} = 0. \quad (6.29)$$

Clearly the first hadron will have the same  $p_T$  as the first string break  $\vec{k}_{T,1}$ , while the second hadron will inherit  $p_T$  that is the vector sum of the first string break (whose conjugate end imparted some equal and opposite  $\vec{k}_T$  on the leftover string system) and the  $\vec{k}'_T$  of the new string break.

Even though the fragmentation happens longitudinally, the string area law (which governs hadron production probability) becomes sensitive to the full mass of the hadron, including transverse motion. So transverse momentum acts like an effective mass penalty - heavier hadrons or those with larger  $p_T$  are suppressed. As you may have guessed, the fragmentation function becomes:

$$f(z, p_{\perp}^2) \propto \frac{1}{z} (1-z)^a \exp\left(-b \frac{m_{\perp}^2}{z}\right). \quad (6.30)$$

Note that this implies that when determining kinematics, we first need to generate the string end transverse momentum components before determining the longitudinal component. In practice, the transverse momentum of the produced hadron is sampled at each string break, assuming that the distribution is azimuthally symmetric. The transverse momentum is sampled from a Gaussian:

$$f(\vec{p}_{\perp}) \propto \exp\left(-\frac{p_{\perp}^2}{\sigma^2}\right) \quad \text{with} \quad \sigma^2 \approx \frac{\kappa}{\pi} \quad (6.31)$$

where  $\sigma$  is a tuneable parameter fit from experimental data. In PYTHIA, the default value is typically  $\sigma \sim 0.3 \text{ GeV}$ .

### 6.3.2.2 The $q\bar{q}$ hadronization as a data-structure

It is useful, especially for chapter 8, to summarize and define a fully hadronized  $q\bar{q}$  as a data-structure – below, we summarize one explicit realization.

String breaks can be described by a seven dimensional vectors containing: the light-cone momentum fraction of the hadron,  $z$ ; the two-dimensional momentum kick  $\Delta\vec{p}_T = (\Delta p_x, \Delta p_y)$  of the emitted hadron; the hadron mass  $m_{ij}$ ; a boolean that encodes whether the string break occurred at the positive or the negative end of the string, stored within PYTHIA as `fromPos`; and the transverse momentum of the string before the breaking,  $\vec{p}_T^{\text{string}} = (p_x^{\text{string}}, p_y^{\text{string}})$

$$\vec{s}_{hcb} = \{z, \Delta\vec{p}_T, m, \text{fromPos}, \vec{p}_T^{\text{string}}\}_{h,c,b}. \quad (6.32)$$

In general, the energy of the string in its center-of-mass frame,  $E_{\text{string}}$ , would also be included in this list. We are able to use the shorter list in eq. (6.32), since the fragmentations in the Lund

string model do not depend explicitly on  $E_{\text{string}}$ . Additional information must also be included in the case where gluons are attached to the string, and the initial state changes between events. The indices  $h$ ,  $c$ , and  $b$  indicate the history, fragmentation chain, and string break the vector belongs to, as defined below. Note that  $\vec{s}_{hcb}$  contains redundant information, since the transverse momentum of the string fragment after the hadron emission,  $(\vec{p}_T^{\text{string}})_{hcb}$ , can be reconstructed from the  $(\Delta \vec{p}_T)_{hcb}$  of all previous hadron emissions. However, we find it convenient to keep  $\vec{p}_T^{\text{string}}$  explicitly as a datum in  $\vec{s}_{hcb}$ .

A sequence of string breaks forms a fragmentation chain,

$$\vec{S}_{hc} = \{\vec{s}_{hc1}, \dots, \vec{s}_{hcN_{h,c}}\}, \quad (6.33)$$

while a vector of rejected fragmentation chains and the accepted fragmentation chain form a fragmentation history,<sup>4</sup>

$$\vec{\mathbf{S}}_h = \{\vec{S}_{h1}, \dots, \vec{S}_{hN_h}\}. \quad (6.34)$$

Here, the indices are defined as:  $h = 1, \dots, N_{\text{data}}$  is the fragmentation history index, with  $N_{\text{data}}$  the total number of events in a run;  $c = 1, \dots, N_h$  is the fragmentation chain index for a particular fragmentation history  $h$ , which has  $N_h - 1$  rejected fragmentation chains and one accepted fragmentation chain; and  $b = 1, \dots, N_{h,c}$  is the string break index, that runs over the fragmentation chain  $c$  with a total of  $N_{h,c}$  string breaks. The form of eq. (6.34) assumes the simplified scenario of this work, where only one string is hadronized per event. When there are multiple strings per event then the fragmentation history is simply expanded to be the vector of accepted and rejected fragmentation chains for all strings, including the energy of each string.

In summary, a measurable event,  $e_h$ , where the index  $h = 1, \dots, N_{\text{data}}$  runs over all events in a run, is fully described by specifying the accepted fragmentation chain

$$e_h \equiv e(\vec{\mathbf{S}}_h) \equiv e(\vec{S}_{hN_h}). \quad (6.35)$$

Explicitly,  $e_h$  is an unordered list of  $N_{\text{had}} = N_{h,N_h} + 2$  laboratory frame four momenta,  $(E_i, \vec{p}_i)$ , and masses,  $m_i$ , of the produced hadrons,<sup>5</sup>

$$e_h = \{\{m_{h1}, E_{h1}, \vec{p}_{h1}\}, \dots, \{m_{hN_{\text{had}}}, E_{hN_{\text{had}}}, \vec{p}_{hN_{\text{had}}}\}\}. \quad (6.36)$$

This unordered list is constructed from the accepted fragmentation chain quantities,  $\vec{S}_{hN_h}$ , by boosting the momenta of the produced hadrons to the laboratory frame. If two simulation

---

<sup>4</sup>For the accepted fragmentation chain, `finalTwo` proceeds to generate two additional hadrons from the remaining string. Thus, the total number of hadrons will be the number of string breaks contained in the accepted chain plus the additional two hadrons, which are not counted as string breaks in this work. This is because their kinematic distribution does not depend on the  $a$  and  $b$  Lund parameters as long as the low-energy threshold that determines whether `finalTwo` is applied remains fixed, and thus do not need to be reweighted for the example we consider here.

<sup>5</sup>Additional information could be optionally included for each hadron such as flavor composition or charge.

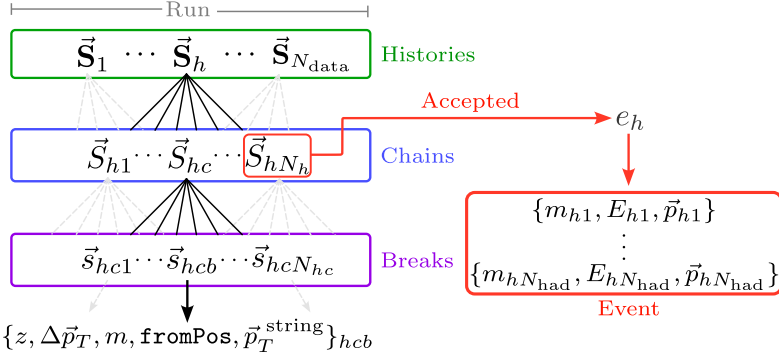


FIGURE 6.3: Schematic detailing the different components of a simulated run. String breaks are grouped into fragmentation chains, while collections of rejected and accepted fragmentation chains form fragmentation histories. Observable events are obtained from the last, accepted fragmentation chain. A collection of multiple events is a run.

histories differ only by their rejected chains, they result in the same event and are equal to the event given by the accepted fragmentation chain. An example schematic of all the components for a fragmentation history, and run, are shown in fig. 6.3.

### 6.3.3 Hadronizing a $qg\bar{q}$ string

Within the Lund string model, gluons are incorporated as quasi-local internal excitations of the  $q\bar{q}$  string. The simplest  $qg\bar{q}$  configuration involves a modification to the prototypical  $q\bar{q}$  system (in which each quark is traveling with equal and opposite momentum along the  $z$ -axis in the center of mass frame) where the midpoint of the string field between the  $q\bar{q}$  endpoints is given a momentum kick along the  $+x$ -axis. In the Lund string model, this excitation along the string is used as a model for a gluon. All  $qg\bar{q}$  systems, other than those where  $q$  and  $\bar{q}$  travel collinearly, can be transformed into a frame where this system is reproduced. In the absence of string breaks, the impulse produces a local excitation or ‘kink’ on the string traveling in the  $+x$  direction and losing energy at a rate of  $2\kappa$ . Once the kink loses all of its initial energy, two wave fronts are dispersed, emanating from the center of the string towards the string ends, eventually displacing both string ends along the transverse  $+x$ -direction until the string is fully extended. After full extension, the wave fronts reemerge, now reverberating towards the center of the string, eventually meeting again to form another point-like kink that now travels in the  $-x$ -direction. Finally, the string ends and the kink meet at the center of the string where the string ends pass one another and the same oscillatory motion repeats. This motion is typically referred to as the ‘dancing butterfly’, in contrast to the ‘yo-yo’ motion of the  $q\bar{q}$  string.

Fragmentation of the  $qg\bar{q}$  configuration in the Lund model proceeds similarly to that of the  $q\bar{q}$  string under the assumption that a string piece satisfying an on-mass-shell condition,  $(E + p_z)_{\text{string}}(E - p_z)_{\text{string}} = m_{\perp,h}^2$ , can be projected onto a hadronic state regardless of whether the string piece contains bends or kinks. The main difference between the fragmentations of the  $q\bar{q}$  and  $qg\bar{q}$  systems stems from the non-local nature of the gluon throughout the evolution

of the string. The butterfly motion described above can be parameterized by five distinct string regions, two regions for each strand containing the  $q$  and  $\bar{q}$  endpoints (for a total of four) with the two regions of each endpoint strand distinguished by the motion before/after the full string extension and a fifth region corresponding to the string strand between the two outgoing/incoming wave fronts after the energy from the gluon has dispersed. While the gluon can be considered as a local excitation or ‘kink’ the fragmentation may equivalently be described by the fragmentation of two ‘half-string’ systems<sup>6</sup> formed by the  $qg$  and  $g\bar{q}$  portions of the string. For a sufficiently hard gluon emission, the hadronization of the  $qg\bar{q}$  system will take place completely within this regime of the motion. If the system fragments ‘slowly’ enough such that the gluon has dispersed along the string i.e. if the gluon emission is soft compared to the outgoing dipole, the usual  $q\bar{q}$  fragmentation apparatus may be used, albeit with a slightly more sophisticated parameterization of world-sheet areas in light-cone coordinates required for the description of hadron formation across string regions (i.e. across non-flat or bent regions of the string world-sheet).

For additional implementation details with an explicit parameterization of the  $qg\bar{q}$  worldsheet as well as a comprehensive discussion detailing potential ambiguities related to longitudinal fragmentation in multi-parton configurations we refer the reader to [351].

## 6.4 Machine learning and differentiable event simulation

At its core, modern machine learning is a framework for optimizing complex, parameterized functions to match data. Given a model  $f_\theta$  with parameters  $\theta$  and a dataset  $\mathcal{D}$ , model output can be systematically improved through the minimization of a scalar-valued loss function  $\mathcal{L}(\theta; \mathcal{D})$  that quantifies the discrepancy between model predictions and the observed data. Modern machine learning architectures and infrastructures are capable of optimizing anywhere from a few to *trillions* of parameters [359, 360]. This scalability and flexibility makes machine learning particularly attractive for scientific modeling tasks that are traditionally heuristic or computationally intensive.

Differentiable programming generalizes this paradigm by allowing arbitrary programs (not just neural networks) to be treated as differentiable functions. This perspective opens the door to embedding physical principles directly into the training loop and enables end-to-end optimization of complex scientific pipelines. This is particularly relevant for components of Monte Carlo event generators that historically rely on hand-tuned models or non-differentiable algorithms. In chapters 7 and 8 we will primarily be focused on the development of differential-programming and machine-learning based algorithms that can remedy these potential bottlenecks in the context of hadronization. These efforts represent early but meaningful steps toward the long-term

---

<sup>6</sup>A half string system can equivalently be described by two  $qq'$ ,  $\bar{q}\bar{q}'$  subsystems with energies  $E_{q,\bar{q}} + E_g/2$  where fragmentations only occur along the  $q$  or  $\bar{q}$  ends, respectively.

goal of a fully differentiable, physics-informed event simulator – one that can be directly tuned and constrained by data through gradient-based optimization. Such tools provide a path toward more accurate, differentiable, and data-driven simulations of high energy collisions – bridging the gap between theory and experiment.

The rest of part II is organized as follows: in chapter 7 we discuss reweighting frameworks in the context of hadron kinematics and flavor production in the Lund string model and in chapter 8 we discuss ML-based solutions to the inverse problem of hadronization.

# Chapter 7

## The reweighting revolution

**Preface:** This chapter is based on a collection of works presented in [7, 12] with the MLHAD team (Ben A., Christian, Phil, Steve, Manuel, Michael, Ahmed, and Jure) and [10] with the crossover MLHADML group (Nick, Phil, Steve, Ben N., Andrzej, Manuel, and Ahmed). The work in [7, 12] outlines the development and validation of a comprehensive and powerful reweighting framework for hadronization in PYTHIA – specifically alternate parameterization weight computations for hadron kinematics and production, respectively. In [10] we emphasize that these frameworks effectively allow for the simulation to be fully differentiable with respect to model parameters – and that the differentiation can be performed externally to the simulator. To illustrate and validate this idea we embed the kinematic reweighting framework into differentiable programming library (minimally, all that is needed is an autodifferentiation engine) and explore/tune over a fully differential two-parameter subspace of the model. Myself and collaborators refer to this ongoing reformulation of event simulation in terms of reweightable, and hence differentiable, algorithms as the *reweighting revolution*<sup>a</sup>.

---

<sup>a</sup>Thank you Phil, for the coinage.

As mentioned in chapter 6, almost all collider tests of the SM rely on predictions obtained using event generators [361, 362]. An important part of these tests is the estimation of uncertainties on those predictions, which can often be obtained by varying input parameters to the event generator. Closely related is the task of tuning these parameters to data to improve agreement. Both procedures—uncertainty quantification and tuning—have traditionally relied on repeated full simulations for each parameter variation, often at significant computational cost. An important and practical consideration is therefore the efficiency of the algorithms used in these tasks. Already, efficient reweighting methods exist for the hard process and the parton shower [363–367], and various weighting techniques are used to match and merge the hard process and

parton shower, although typically not in the context of variations [328, 330, 368–378]. Similar methods for estimating uncertainties in hadronization have, up to now, remained elusive. The standard procedure to handle hadronization uncertainties, prior to the works presented here, was to perform repeated simulations with different sets of values for the relevant hadronization model’s parameters, where the values are chosen such that the model’s predictions remain compatible with the reference data [379–381]. In this manuscript, we remedy this by introducing an efficient solution for reweighting kinematic parameters of hadronization and provide an implementation for the complete hadronization model of the PYTHIA Monte Carlo event generator. This framework facilitates both fast uncertainty estimates and efficient tuning within a single infrastructure. Moreover, we extend this framework beyond kinematics to incorporate hadron flavor reweighting, which will be introduced and developed below.

In standard practice, both tuning and uncertainty estimation in hadronization are carried out by generating multiple event samples with different parameter values, followed by statistical comparisons against experimental data. While this is straightforward, it is computationally expensive, especially if the predictions are further simulated at the detector level (material interactions, detector response, etc.). It is therefore advantageous to instead use a single set of fully simulated events and compute relative probabilities for different hadronization parameter choices. This reuse of events avoids redundant detector simulation and accelerates both the tuning and uncertainty quantification workflows.

Conceptually, computing the relative probability of a given event under different model parameters is straightforward. In practice, reorganizing an existing Monte Carlo algorithm to expose this structure can be technically challenging. In section 7.2, we present a method based on the veto algorithm to compute such relative weights for hadronization kinematics parameterized by the Lund fragmentation function. The approach closely parallels previous reweighting methods developed for the parton shower [363, 365–367, 373]. In section 7.3, we present a distinct method for computing relative weights in the context of flavor production which does not rely on a veto-based construction. Instead, the flavor reweighting is complicated by the need to account for a large set of nested conditional probabilities governing hadron species selection.

## 7.1 Statistical reweighting

In Monte Carlo event generation, statistical reweighting refers to the procedure of retroactively modifying the relative importance of generated events to reflect a different theoretical or parametric hypothesis without regenerating the full event sample. Given a set of unweighted or weighted events generated under a baseline model characterized by parameters  $\theta$ , one can compute weights  $w(x)$  that rescale the contribution of each event  $x$  to reconstruct a distribution under a target model with parameters  $\theta'$ . For example, suppose one wishes to study how an observable  $O(x)$ , such as charge multiplicity, thrust, flavor asymmetries, etc., changes under a

modified parameterization of the underlying simulation. The reweighted histogram is obtained by applying event-by-event weights, typically derived as a ratio of distributions used during event generation:

$$w(x) = \frac{P(O(x); \theta')}{P(O(x); \theta)} \quad (7.1)$$

where  $P(O; \theta)$  denotes the underlying distribution(s) which produced the observable  $O(x)$  under model  $\theta$ . The weight allows for simulated dataset at some base parameterization  $\theta$  to be reinterpreted as if run in new simulator with parameterization  $\theta'$ . Below we'll explore some power applications of reweighting in the context of hadronization.

## 7.2 Automated hadron kinematic variations

In this section we introduce the the algorithmic prescription for hadronization kinematic reweighting. The kinematics of hadrons in the Lund string model are controlled by the Lund fragmentation function in eq. (6.30). In practice this distribution is only known up to a normalizing constant and must be sampled via standard accept-reject (a.k.a. veto) algorithms, summarized below.

### 7.2.1 Accept-reject sampling

Consider a random variable  $x$  over the domain  $\mathcal{X}$  with a probability density  $P(x; \boldsymbol{\theta})$  known up to a normalizing constant with  $N$  tuneable parameters  $\boldsymbol{\theta} \equiv \{\theta_1, \dots, \theta_N\}$ . Assume the maximum  $\hat{P}$  is known (or can be estimated numerically) such that  $P(x) \leq \hat{P}$  for all  $x \in \mathcal{X}$ . Samples of  $x$  can be obtained by:

1. Uniformly sampling a trial value  $x_1 \in \mathcal{X}$ .
2. Computing the acceptance probability

$$P_{\text{accept}}^1(x_1; \boldsymbol{\theta}) = \frac{P(x_1; \boldsymbol{\theta})}{\hat{P}}. \quad (7.2)$$

3. Sampling an additional uniformly distributed value  $s_1 \in [0, \hat{P}]$ .
4. If  $P_{\text{accept}}^1(x_1) \leq s_1$  accept the trial  $x_1$ , otherwise, reject and return to step 1. Repeat  $n$ -trials until  $P^n(x_n) \leq s_n$  i.e. until a trial is accepted.

Note that  $\hat{P}$  is unbounded from above, allowing the efficiency of the accept-reject algorithm to be tuned, with values larger than the minimum  $\hat{P}_{\min} \equiv \max[P(x)]$  decreasing the efficiency. A single element of an accept-reject sampling will have one accepted value  $x_{\text{accept}}$  and  $n - 1$  rejected trials  $\mathbf{x}_{\text{reject}} \equiv \{x_{\text{reject}}^1, \dots, x_{\text{reject}}^{n-1}\}$ .

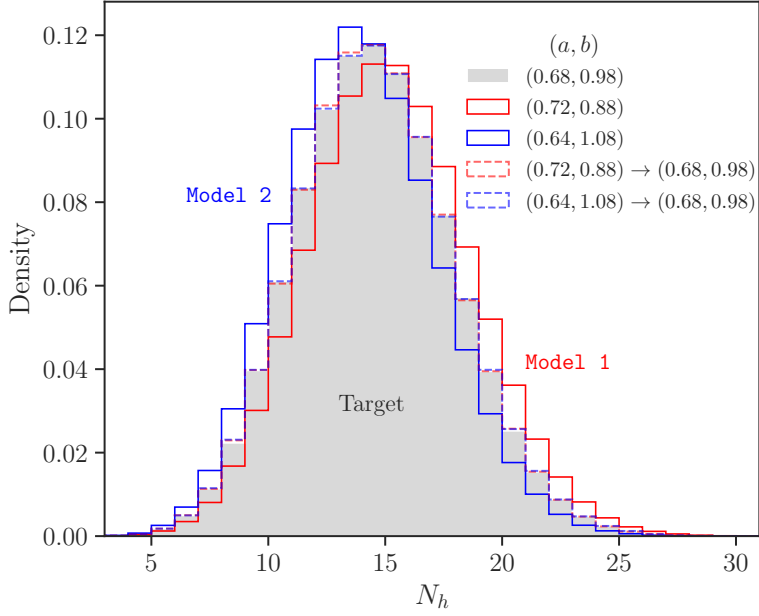


FIGURE 7.1: Observable distributions for hadron multiplicity  $N_h$  at three distinct parameterizations of the Lund  $a, b$  parameters, using a sample of  $N = 10^6$  events. Dotted histograms denote the reweighted distributions.

### 7.2.2 Alternative accept-reject sampling

Given a sample  $\mathbf{x}$ , a different sample using the same probability model but with different parameters  $\boldsymbol{\theta}' \neq \boldsymbol{\theta}$  can be obtained by assigning each trial  $x_i \in \mathbf{x}$  a statistical weight [365]. The total weight of each element is obtained by assigning the accepted value the relative acceptance probability

$$w_{\text{accept}} \equiv \frac{P_{\text{accept}}(x_{\text{accept}}; \boldsymbol{\theta}')}{P_{\text{accept}}(x_{\text{accept}}; \boldsymbol{\theta})} = \frac{P(x_{\text{accept}}; \boldsymbol{\theta}')}{P(x_{\text{accept}}; \boldsymbol{\theta})}, \quad (7.3)$$

and each rejected trial value the relative rejection probability

$$w_{\text{reject}}^j \equiv \frac{1 - P_{\text{accept}}(x_{\text{reject}}^j; \boldsymbol{\theta}')}{1 - P_{\text{accept}}(x_{\text{reject}}^j; \boldsymbol{\theta})} = \frac{\hat{P} - P(x_{\text{reject}}^j; \boldsymbol{\theta}')}{\hat{P} - P(x_{\text{reject}}^j; \boldsymbol{\theta})}. \quad (7.4)$$

The full weight,  $w$ , of an element in the sample is given by

$$w = w_{\text{accept}} \prod_{j=1}^{n-1} w_{\text{reject}}^j. \quad (7.5)$$

These weights encode the likelihood ratio between two alternative parameterizations of the same distribution with  $w < 1$  and  $w > 1$  implying the sample is less or more probable in the new parameterization  $\boldsymbol{\theta}'$ .

### 7.2.3 Kinematic reweighting in the Lund string model

As an explicit example of the prescription described above, consider the hadronization of a  $q\bar{q}$  system outlined in section 6.3.2. Given an initial string, each fragmentation will have an ensemble of a single accepted  $z$  value,  $z_{\text{accept}}$ , and typically many rejected trial  $z$  values,  $z_{\text{reject}}^i$ . If we consider a sample consisting of  $N$  hadronization events the relevant data-structure for reweighting the kinematics is given by

$$\mathbf{z} = \begin{pmatrix} \mathbf{z}_1 & \\ \vdots & \\ \mathbf{z}_N & \end{pmatrix}, \quad \mathbf{z}_1 = \begin{pmatrix} \{m_\perp^{h_1}, z_{\text{accept}}^{h_1}, z_{\text{reject}}^{1,h_1}, \dots, z_{\text{reject}}^{n_{h_1},h_1}\} \\ \{m_\perp^{h_2}, z_{\text{accept}}^{h_2}, z_{\text{reject}}^{1,h_2}, \dots, z_{\text{reject}}^{n_{h_2},h_2}\} \\ \{m_\perp^{h_3}, z_{\text{accept}}^{h_3}, z_{\text{reject}}^{1,h_3}, \dots, z_{\text{reject}}^{n_{h_3},h_3}\} \\ \vdots \\ \{m_\perp^{h_4}, z_{\text{accept}}^{h_4}, z_{\text{reject}}^{1,h_4}, \dots, z_{\text{reject}}^{n_{h_4},h_4}\} \end{pmatrix}_1, \quad (7.6)$$

where  $n_{h_i}$  refers to the total number of rejections for the  $i$ -th fragmentation/hadron. Note that because `finalTwo`, can fail (roughly 10 – 15% of the time for a  $q\bar{q}$  string system with total energy of 50 GeV), the hadron multiplicity,  $N_h$ , of an event is not necessarily equal to the total number of accepted  $z$ -values. In other words, not only do we need to keep track of all rejected  $z$  values but also all rejected chains.

Consider the variation of the Lund  $a$  and  $b$  parameters. Given a dataset generated using a base parameterization  $\boldsymbol{\theta}_B \equiv \{a, b\}_B$ , the weights for each event, given for a single sampling in eq. (8.12), can be computed and stored in an event-weight array  $\mathbf{w}$  for an alternate set of parameters,  $\boldsymbol{\theta}_P \equiv \{a, b\}_P$ . Explicitly,

$$\mathbf{w} = \begin{pmatrix} w_1 & w_2 & \dots & w_N \end{pmatrix}^T, \text{ where} \quad (7.7)$$

$$w_n = \prod_{i=1}^{\tilde{N}_{h,n}} \left( \frac{f(z_{\text{accept}}^{h_i}; \{a, b\}_P)}{f(z_{\text{accept}}^{h_i}; \{a, b\}_B)} \right) \times \prod_{j=1}^{n_{h_i}} \left( \frac{\hat{f} - f(z_{\text{reject}}^{j,h_i}; \{a, b\}_P)}{\hat{f} - f(z_{\text{reject}}^{j,h_i}; \{a, b\}_B)} \right), \quad (7.8)$$

where  $\hat{f}$  is the oversampling factor associated with the sampling of  $z$  and  $\tilde{N}_{h,n}$  denotes the total number of distinct accept-reject samplings in the  $n^{\text{th}}$  event (including those when `finalTwo` fails).

To validate the reweighting prescription we generate events from a ‘particle gun’<sup>1</sup>. We simulate  $10^6$  of the specified hadronization events with  $E = 50$  GeV using three parameterizations of the Lund fragmentation function:  $\boldsymbol{\theta}_1 \equiv \text{Model 1} = \{a = 0.72, b = 0.88\}$ ,  $\boldsymbol{\theta}_2 \equiv \text{Model 2} = \{a = 0.64, b = 1.08\}$ , and the PYTHIA default  $\boldsymbol{\theta}_{\text{exp}} \equiv \text{Target} = \{a = 0.68, b = 0.98\}$ . The rejection sampling uses an over-sampling factor of  $\hat{f} = 10$ , each accept-reject array is zero-padded to a fixed length of  $200^2$ , and each event is zero-padded to a fixed length of 75.

#### 7.2.4 Reweighting metrics

As discussed above in section 7.1, care must be taken to ensure the reweighting between two alternate parameterizations is not plagued by low coverage or highly variable weights. In practice, the efficacy/performance of a reweighting between two parameterizations can be summarized by two metrics

$$\mu \equiv \sum_{i=1}^N \frac{w_i}{N}, \quad N_{\text{eff}} = \frac{\left(\sum_{i=1}^N w_i\right)^2}{\sum_{i=1}^N w_i^2}. \quad (7.9)$$

The two metrics provide complementary reweighting diagnostics – the first gives a measure of possible lack of coverage or ‘unitarity violation’ between the two parameterizations and the second reflects the possible loss in statistical power of the reweighted sample. For two parameterizations with sufficiently good coverage we expect  $\mu \approx 1$ . Likewise,  $N_{\text{eff}}/N \approx 1$ , with  $N$  being the total number of samples used during reweighting, would signal very little statistical power lost to reweighting.

In figure 7.2 we show both of these reweighting metrics across the  $(a, b)$  parameter plane for both **Model 1** and **Model 2**. We express  $\mu$  (left column) as  $\ln(|1 - \mu|/\sigma_{1-\mu})$ , where  $\sigma_{1-\mu}$  is the uncertainty on  $1 - \mu$ , to better assess consistency with  $\mu = 1$ . Written this way and for the sample sizes considered in this work,  $\ln(|1 - \mu|/\sigma_{1-\mu})$  in the approximate range  $(-1, 1)$  are considered as reflecting adequate reweighting. In general, values closer to 0 imply better coverage, values  $\gg 0$  are inconsistent with 0 due to lack of coverage, and values  $\ll 0$  indicate weights with large variance and signal poor reweighting performance. We see that the target parameterizations (green stars) sit in regions where the reweighting metrics indicate good coverage and effective statistics in both base models (red dots). We also see that the full parameter range of interest contains large regions with poor coverage and effective statistics. If one were to use this prescription to perform a black-box fit (where a good estimate of model parameters is

---

<sup>1</sup>See, for example, `main234` within the `Pythia/examples` sub-directory of release 8.312.

<sup>2</sup>We do not allow for  $> 199$  rejections. This is a convention chosen to reduce the memory footprint of the accept-reject datasets required for reweighting. We have checked empirically that this choice does not effect fit performance.

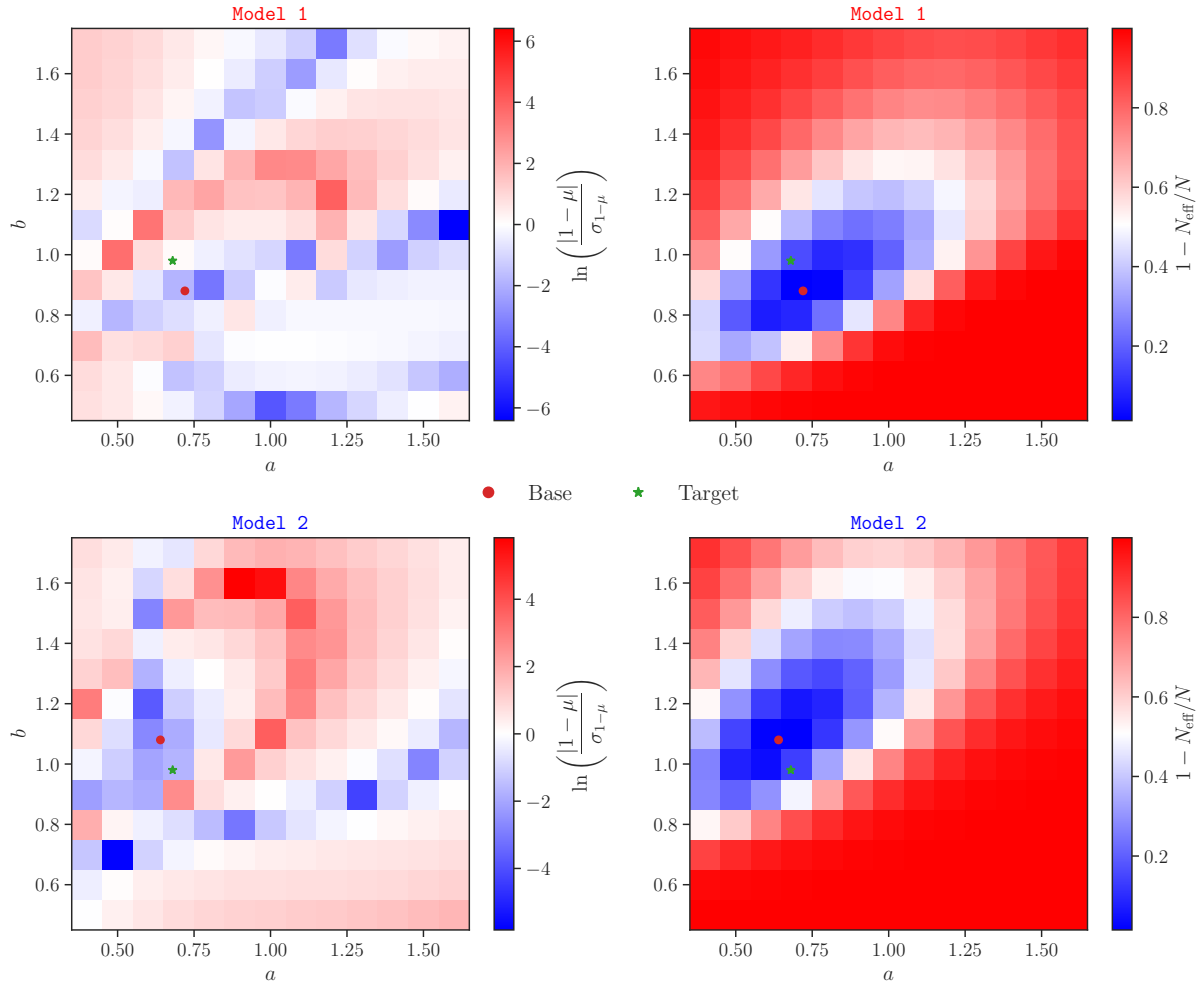


FIGURE 7.2: The reweighting metrics defined in eq. 7.9 over the  $(a, b)$  parameter plane for the **Model 1** and **Model 2** base parameterizations denoted by the red dots. The green star denotes the ‘experimental’ or target parameterization. For both metrics, values closer to zero imply better coverage and effective statistics.

unknown) over the full parameter range, the use of multiple base parameterizations that, when combined, provide adequate coverage over the full parameter volume would be required.

Additional validation plots, weight distributions, and event generation efficiency improvements for realistic event simulations ( $pp$ ,  $e^+e^-$ ) can be seen in ref. [7].

### 7.3 Automated hadron production variations

In this section we introduce the the algorithmic prescription for hadronization flavor production reweighting. While two different computational methods for obtaining the weights for flavor parameter variations were developed in ref. [12], termed the *analytic* and the *stochastic* prescriptions, for simplicity we will focus on a toy example utilizing the analytic prescription. Both prescriptions are designed to reweight distributions of physical observables from one point in

parameter space to another, but differ in how they account for the rejected proposals for produced particles. In the *analytic prescription*, the rejected proposals are explicitly integrated out to produce closed-form equations for the weights. The weights then depend on the parameters being varied, and the different filter efficiencies involved in the simulation chain. The explicit, analytic integration is what gives the prescription its name.

As described in section 6.3.2.1, string breaking occurs via a tunneling process, in which a quark and anti-quark pair tunnels through a classically forbidden region of size  $2m_\perp/\kappa$  before they can come on-shell [382]. The governing equation for the tunneling probability  $\mathcal{P}$  is

$$\frac{d\mathcal{P}}{d^2 p_T} \propto \exp(-\pi(m^2 + p_\perp^2)/\kappa) = \exp(-\pi m^2/\kappa) \exp(-\pi p_\perp^2/\kappa). \quad (7.10)$$

In principle, the relative production rates of light flavored quarks can be estimated directly from eq. (7.10) by inserting the values for quark masses. However, it is not obvious which definition of the quark masses to use: current or constituent mass or something else [30]. In the Lund approach, the difference between the  $u$  and  $d$  quark masses is ignored, while the suppression of the generation of  $s$ -quarks relative to  $u$  and  $d$  quarks is encoded in a parameter ( $\rho$ ) that is fit (“tuned”) to data. The simplest model of baryon production<sup>3</sup> is obtained by allowing diquark–anti-diquark ( $Q\bar{Q}$ ) breakups by the same mechanism [386]. The resulting procedure involves four basic parameters for string breaks with default values set to those found in [31], each restricted to values between 0 and 1 inclusive:

$\rho$  : The suppression of  $s\bar{s}$  string breaks relative to  $u\bar{u}$  or  $d\bar{d}$ .<sup>4</sup>

$\xi$  : The overall suppression of a diquark–anti-diquark splitting relative to a  $q\bar{q}$  one.<sup>5</sup>

$x$  : Suppression of diquarks with strange quark content in addition to the normal suppression from  $\rho$ .<sup>6</sup>

$y$  : Suppression of spin-1 diquarks relative to spin-0 ones, in addition to the factor of 3 due to spin counting.<sup>7</sup>

The hadron species are not fully determined by the string breaks. For example, neighboring string breaks of  $u\bar{u}$ ,  $d\bar{d}$  type result in a  $u\bar{d}$  pair connected by a string piece in the middle. This pair can become a  $\pi^+$  or a  $\rho^+$  meson, with probabilities determined by yet another parameter, called  $y_{ud}$ , governing the relative production ratio of vector (spin-1) to pseudoscalar (spin-0)

---

<sup>3</sup>Several more involved models for baryon production, the popcorn model [383] and the junction model [384, 385], are also implemented in PYTHIA and can be optionally activated by a user.

<sup>4</sup>The PYTHIA name and default value for this parameter is `StringFlav:probStoUD = 0.217`.

<sup>5</sup>The PYTHIA name and default value for this parameter is `StringFlav:probQQtoQ = 0.081`.

<sup>6</sup>The PYTHIA name and default value for this parameter is `StringFlav:probSQtoQQ = 0.915`.

<sup>7</sup>The PYTHIA name and default value for this parameter is `StringFlav:probQQ1toQQ0 = 0.0275`.

mesons for  $u$  and  $d$  types.<sup>8</sup> A similar parameter governing the relative production ratio of vector to pseudoscalar mesons for  $s$  types is here denoted  $y_s$ .<sup>9</sup>

The  $\eta$  and  $\eta'$  mesons add a further complication to the algorithm. These particles are overproduced, and must be suppressed to match data. This suppressed production is achieved in the MC simulation through individual tuneable parameters, which we denote in this paper as  $\epsilon_\eta$  and  $\epsilon_{\eta'}$ , respectively. They are both suppression probabilities, “filters”, meaning that for the value  $\epsilon_\eta = 0$  no  $\eta$  mesons get produced, while for  $\epsilon_\eta = 1$  no rejection takes place, and similarly for  $\eta'$ .<sup>10</sup> This adds a filtering step to the algorithm, where an  $\eta$  or  $\eta'$  meson may first get chosen, but then gets rejected by the filter, after which the string breaking procedure must start over again.

Baryon production from a string piece with a quark and a diquark at the ends, is similar in principle. The string break probabilities follow a similar selection scheme as for quark–antiquark breaks, and the final hadron can be rejected by a filter. In this case, the filter enforces the  $SU(6)$  spin-flavor symmetry. That is, if all three light quarks were produced in equal amounts, the resulting hadrons should follow  $SU(6)$  spin-flavor symmetry. This is ensured using  $SU(6)$  Clebsch–Gordan coefficients for individual quark–diquark combinations, making up the baryons in the octet and the decuplet. See section 2.5 and appendix B of ref. [12] for more details. As before, cases may arise where no hadron is chosen, and the string breaking procedure must start over again.

It is useful to view the string hadronization process as a Markov chain process: each string break corresponds to a probabilistic decision, conditioned on the previous state, and feeds into the next. Rejections and filters act as intermediate selection steps but preserve the sequential structure as long as the rejected decisions are still accounted for. This perspective naturally lends itself to factorized weight calculations, as we develop below. In the following sub-sections we will give a step-by-step explanation of how a reweighting strategy can be formulated as a modification to the existing string break algorithm.

### 7.3.1 Flavor reweighting in the Lund string model

As a simple example, let’s consider a case where strings are only allowed to break only into  $q\bar{q}$  pairs of the lightest quark flavors,  $u$ ,  $d$ , or  $s$ . That is, in this example we do not allow a creation of diquarks, and thus no baryons. This example can be visualized with a very simple decision tree, as shown in fig. 7.3.

---

<sup>8</sup>The PYTHIA name and default value for the parameter  $y_{ud}$  is `StringFlav:mesonUDvector = 0.5`. This default makes it twice as likely to sample, *e.g.*, a  $\pi^+$  with respect to a  $\rho^+$ . This parameter includes spin counting, hence its maximal possible value is set to 3.

<sup>9</sup>The PYTHIA name and default value for the parameter  $y_s$  is `StringFlav:mesonSvector = 0.55`.

<sup>10</sup>The PYTHIA names and default value for the parameters  $\epsilon_\eta$  and  $\epsilon_{\eta'}$  are `StringFlav:etaSup = 0.60` and `StringFlav:etaPrimeSup = 0.12`, respectively.

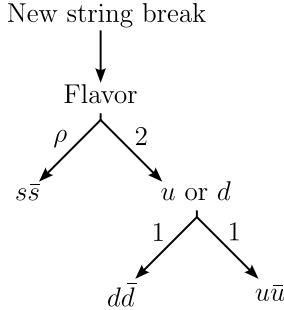


FIGURE 7.3: Illustration of the decision flow in the simple case of string breaks without diquarks. There are three possibilities,  $u\bar{u}$ ,  $d\bar{d}$ , and  $s\bar{s}$ , the latter with a probability  $\rho/(2 + \rho)$ , and the two former with a probability of  $1/2$ , given that no  $s\bar{s}$  pair was produced. All probabilities can be read off directly from the decision flow chart.

As shown in the decision tree and described above, an  $s\bar{s}$  break is suppressed by a factor  $\rho$  with respect to  $u\bar{u}$  or  $d\bar{d}$  breaks, giving a probability of  $p = \rho/(2 + \rho)$  for an  $s\bar{s}$  break. The probability that a string with a total of  $N$  breaks produces exactly  $n$   $s\bar{s}$  breaks is thus given by

$$\mathcal{P}_{ns}(\rho) = \binom{N}{n} p^n (1 - p)^{N-n}, \quad (7.11)$$

where  $\binom{N}{n}$  is the binomial coefficient. This is the result of independently sampling  $N$  indistinguishable string breaks, where each string break is either an  $s\bar{s}$  break (with probability  $p$ ) or not (with probability  $1 - p$ ). The event weights can be directly determined by probabilities of the type computed as in eq. (7.11). Schematically, the event weight after a change of parameters is simply

$$w \equiv \frac{\mathcal{P}_{\text{breaks}}(\text{params.'})}{\mathcal{P}_{\text{breaks}}(\text{params.})}. \quad (7.12)$$

These weights can be straightforwardly combined with weights originating from other parameter variations, such as those considered in eq. (7.8), through multiplication. In this simplified example, a change  $\rho \mapsto \rho'$  gives  $p \mapsto p' = \rho'/(2 + \rho')$ , giving a weight

$$\begin{aligned} w &= \frac{\mathcal{P}_{ns}(\rho')}{\mathcal{P}_{ns}(\rho)} = \left(\frac{p'}{p}\right)^n \left(\frac{1-p'}{1-p}\right)^{N-n} \\ &= \left(\frac{\rho'}{\rho}\right)^n \left(\frac{2+\rho}{2+\rho'}\right)^N \end{aligned} \quad (7.13)$$

The weight of eq. (7.13) is the basic component of both the analytic and stochastic prescriptions. The main benefit of this weight is that it can be calculated for arbitrary variations of the  $\rho$  parameter – it acts as a local Jacobian between the original and target parameterizations of the string break probability space – as long as  $N$  and  $n$  are retained through the event generation process, *i.e.*, a technical implementation only requires storing two additional integers per event

( $N$  and  $n$ ). In effect, the stored per-event integers act as a minimal sufficient statistic for computing reweighting factors under arbitrary changes to the flavor parameters. In practice, however, the hadronic composition is not fully determined by determining the amount of  $s\bar{s}$  breaks in an event once filters are included.

### 7.3.1.1 Incorporating rejection weights a.k.a. filtering

To avoid overproduction of  $\eta$  and  $\eta'$  mesons, filters are used between string-break selection and the final production of the hadron. The filtering is dictated by the parameters  $\epsilon_\eta$  and  $\epsilon_{\eta'}$ , respectively. The situation is further complicated by the existence of mixing, in particular in the pseudoscalar sector, and to a smaller extent the vector-meson sector.

Starting from an  $s$ -quark string end, the full algorithm for producing a meson from a string break is as follows:

1. Select the string break flavor,  $\bar{s}$  with weight  $\rho$  and  $\bar{u}$  or  $\bar{d}$  with a combined weight 2.
2. If a  $\bar{u}$  or  $\bar{d}$  is chosen, a kaon is produced. Further logic determines its spin as well as mixing, but there are no rejections along this algorithm branch.
3. If an  $\bar{s}$  is chosen, spin must be selected to choose whether a vector meson or a pseudoscalar meson is created. This is determined by the  $y_s$  parameter.
4. If a vector meson is chosen, further logic determines mixing. This has almost negligible effect for  $s\bar{s}$  vector states. There are no rejections along this algorithm branch.
5. If a pseudoscalar meson is selected, an  $\eta'$  is chosen with probability  $\sin^2(\alpha)$  and  $\eta$  with probability  $\cos^2(\alpha)$ , where  $\alpha$  is an angle needed to specify the probability of projecting on to a given meson state.<sup>11</sup>
6. If an  $\eta'$  was chosen, accept it with probability  $\epsilon_{\eta'}$ . If rejected, return back to step 1.
7. If an  $\eta$  was chosen, accept it with probability  $\epsilon_\eta$ . If rejected, return back to step 1.

To get a better intuition for the reweighting with filters, let's consider a simplified example where we only allow for production of pseudoscalars, and additionally, out of  $\eta, \eta'$  only allow the production of  $\eta$  mesons. This gives the simpler procedure shown in fig. 7.4, where the observables of interest are only functions of the number of accepted  $s\bar{s}$  breaks and the number of  $u\bar{u}$  and  $d\bar{d}$  breaks with no knowledge of any rejected  $s\bar{s}$  breaks. In this simplified algorithm, the probability to break into  $s\bar{s}$ , is now effectively reduced by the presence of a rejection to

$$p_{s\bar{s}|s,\text{eff}} = \frac{p_{s\bar{s}|s}\epsilon_\eta}{(1 - p_{s\bar{s}|s}) + p_{s\bar{s}|s}\epsilon_\eta} = \frac{\rho\epsilon_\eta}{2 + \rho\epsilon_\eta}, \quad (7.14)$$

---

<sup>11</sup>The angle  $\alpha$  is related to the normal mixing angle  $\alpha = \theta + 54.7$  degrees, see the review of the quark model in [139] for terminology and details. In PYTHIA this parameter is called `StringFlav:thetaPS` and has a default value of -15 degrees.

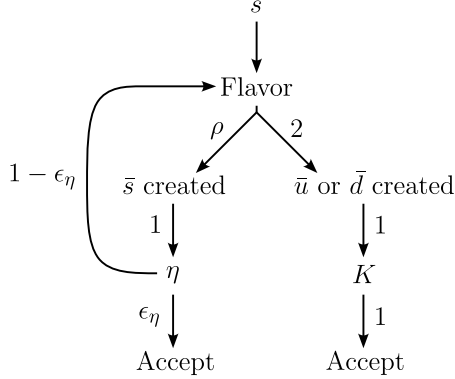


FIGURE 7.4: Flowchart depicting the introduction of rejection/filtering in a simplified example beginning with an  $s$ -quark end-point. In this toy example, vector mesons and the  $\eta'$  meson are not included, so a string break following an  $s$ -quark can only result in an  $\eta$  (for  $s\bar{s}$  breaks) or kaons (for  $u\bar{u}$  or  $d\bar{d}$  breaks). Because of this simplification, this example does not conserve isospin.

where the last expression is derived by replacing  $p_{s\bar{s}|s} = \rho/2 + \rho$ . In appendix A.1 of [12] we derive the more general case where a break can produce one of  $K$  states with probabilities  $\{p_k\}_{k=1}^K$  each of which has a filter efficiency  $\{\epsilon_k\}_{k=1}^K$ . In that case, the effective probability becomes

$$p_{k,\text{eff}} = \frac{p_k \epsilon_k}{\sum_{k=1}^K p_k \epsilon_k}, \quad (7.15)$$

with  $\sum_k p_{k,\text{eff}} = 1$  by definition. We can recover eq. (7.14) by setting  $K = 2$ , identifying  $k = 1$  with  $s\bar{s}|s$  (where  $p_{s\bar{s}|s} = \frac{\rho}{2+\rho}$  and  $\epsilon_{s\bar{s}|s} = \epsilon_\eta$ ) and  $k = 2$  with  $s\bar{u}+s\bar{d}|s$  (where  $p_{s\bar{u}+s\bar{d}|s} = 1 - p_{s\bar{s}|s} = \frac{2}{2+\rho}$  and  $\epsilon_{s\bar{u}+s\bar{d}|s} = 1$ ).

In example without filtering we introduced the reweighting of simple string breaks as a consequence of the ability to express the number of  $s\bar{s}$  breaks  $n$  as a binomially distributed variable. This was possible because the string breaks didn't depend on the previous step (*i.e.*, each break was a Bernoulli trial). The above discussion, and eq. (7.14) in particular, show that even in the presence of filtering, simple reweighting is still possible; one just needs to replace the probability  $p$  in eq. (7.13) with an appropriately chosen effective probability  $p_{\text{eff}}$ . Analytic expressions for reweighting factors, however, become very involved very quickly with effective probabilities introduced for many different kinds of rejections. For instance, the full effective probability to produce an  $s\bar{s}$ -pair, starting from an  $s$ -quark,  $p_{s\bar{s}|s,\text{eff}}$ , correcting for all rejections in the

algorithm outlined above, but still omitting baryon production, is given by

$$\begin{aligned}
p_{s\bar{s}|s,\text{eff}} &= p_{s\bar{s}_1|s,\text{eff}} + p_{s\bar{s}_0|s,\text{eff}} \\
&= p_{s\bar{s}_1|s,\text{eff}} + p_{\eta|s,\text{eff}} + p_{\eta'|s,\text{eff}} \\
&= \frac{p_{s\bar{s}_1|s}\epsilon_{s\bar{s}_1}}{\sum_k p_{k|s}\epsilon_k} + \frac{p_{\eta|s}\epsilon_\eta}{\sum_k p_{k|s}\epsilon_k} + \frac{p_{\eta'|s}\epsilon_{\eta'}}{\sum_k p_{k|s}\epsilon_k} \\
&= \frac{\rho[y_s + (\epsilon_\eta \cos^2(\alpha) + p_{\eta'} \sin^2(\alpha))(1 - y_s)]}{2 + \rho[y_s + (\epsilon_\eta \cos^2(\alpha) + \epsilon_{\eta'} \sin^2(\alpha))(1 - y_s)]} \\
&= \frac{\rho_{\text{eff}}}{2 + \rho_{\text{eff}}}, \text{ where } \rho_{\text{eff}} = \rho[y_s + (\epsilon_\eta \cos^2(\alpha) + \epsilon_{\eta'} \sin^2(\alpha))(1 - y_s)].
\end{aligned} \tag{7.16}$$

Above, the  $p_{s\bar{s}_1,\eta,\eta'}$ s are the probabilities of sampling, given an  $s$  break, a vector  $s\bar{s}$  pair,  $\eta$  meson, or  $\eta'$  meson, respectively. Filter efficiencies lead to an additional suppression, as intended, with  $\rho_{\text{eff}} \leq \rho$ . Note that eq. (7.14) is recovered when taking  $y_s = 0$  and  $\alpha = 0$ .

### 7.3.2 From analytic to stochastic weights

Rather than calculating increasingly complex effective probabilities for each filter, we can instead keep track of rejected and accepted proposals directly. This leads to a *stochastic weight formulation* that bypasses the need for analytic expressions of  $p_{\text{eff}}$ . For illustrative purposes, we still limit the discussion only to variations in the  $\rho$  parameter and keep the number of filter efficiencies fixed. Note, though, that the results obtained below generalize rather straightforwardly; the equivalence between analytic and stochastic weights in the general case is shown in appendix A.3 of ref. [12].

The stochastic weight is defined in a manner similar in spirit to the modified accept-reject algorithm introduced in section 7.2. For an accepted string break which has  $N_R$  associated rejected breaks we have:

$$w_{\text{stochastic}}^{\text{break}} = \left( \prod_{n=1}^{N_R} w_n \right) w_A = \left( \prod_{n=1}^{N_R} \frac{p'_n}{p_n} \right) \frac{p'_A}{p_A}. \tag{7.17}$$

Here,  $n = \{1, \dots, N_R\}$  labels the  $N_R$  rejected hadron candidates, and  $A$  denotes the accepted one. Each term  $w_i = p'/p$  reflects the ratio between the target and sampled probabilities for that break.<sup>12</sup>

For example, consider a simulation sequence where an  $\eta$  meson is accepted after having rejected one  $\eta$  and one  $\eta'$  meson. The stochastic weight for this sequence is

$$w_{\text{stochastic}}^{\text{break}} = w_\eta^2 w_{\eta'} = \left( \frac{(1 - y'_s)\rho' \cos^2(\alpha')}{(1 - y_s)\rho \cos^2(\alpha)} \frac{(2 + \rho)}{(2 + \rho')} \right)^2 \left( \frac{(1 - y'_s)\rho' \sin^2(\alpha')}{(1 - y_s)\rho \sin^2(\alpha)} \frac{(2 + \rho)}{(2 + \rho')} \right), \tag{7.18}$$

---

<sup>12</sup>Obtained from eq. (7.13) by setting  $n, N = 1$  and considering the appropriate sampled and target probabilities for the string breaks  $p_{n,A}$  and  $p'_{n,A}$ , respectively.

which for unchanged  $y_s$  and  $\alpha$  reduces to

$$w_{\text{stochastic}}^{\text{break}} = \left( \frac{\rho'}{\rho} \frac{(2 + \rho)}{(2 + \rho')} \right)^3, \quad (7.19)$$

i.e., recovering the form of eq. (7.13). The key observation is that for any physical observable, reweighting using  $w_{\text{stochastic}}^{\text{break}}$  yields equivalent results to incorporating the filter explicitly in terms of  $p_{\text{eff}}$ . The reason is that physical observables depend only on accepted fragmentations.

## 7.4 Autodifferentiable kinematic reweighting

We now return to kinematic reweighting and describe how the kinematic weights in eq. (7.8) allow make rejection sampling differentiable with respect to the parameters of the model. Assuming that  $P(x)$  in eq. (7.2) is smooth, the accept-reject reweighting prescription is inherently differentiable and facilitates the computation of *weight gradients* with respect to  $\theta'$ . If  $P(x)$  is sampled repeatedly within a larger simulation pipeline, we may also compute gradients of simulation outputs (which may be arbitrarily complicated functions of the sampled values of  $x$ ) via weighted binned or *unbinned* distributions. In practice, this requires the ability to efficiently compute and store numerical gradients. To efficiently compute gradients, the entire computation must be organized to enable low-overhead access to derivative information from the outset. Tracking derivatives throughout a computation is known as automatic differentiation, or autodifferentiation (autodiff for short). The prefix `auto-` reflects the fact that the derivatives of each operation are made available automatically during execution. Software systems that implement this functionality are called autodifferentiation engines, and all modern differentiable programming libraries, such as PyTorch [387] (used in this work), are built around them. In these frameworks, the parameters of interest can be implemented as differentiable (learnable) objects within custom classes (such as a PyTorch `Module`) whose forward function facilitates the extraction of weights (and their gradients) for a given batch of training data. We refer to this melding as *Rejection Sampling with Autodifferentiation* (RSA). Importantly, RSA does not require any modification to the standard accept-reject sampling described in section 7.2.1, but instead utilizes the computation of alternative parameter weights outlined in section 7.2.2 to define and compute derivatives on accept-reject samples with respect to their parameters.

### 7.4.1 Fitting a hadronization model

A practical use-case for our studies is to consider the fitting or tuning of parameters inside of Monte Carlo event generators [30, 325, 326]. Tuning consists of simulating a large number of events with a ‘base’ parameterization  $\theta$ , comparing the output distributions to experimental data, and updating the base parameterization to a new parameterization  $\theta'$  following a prescribed procedure [31, 388–391]. The first and third steps present as the primary bottlenecks

encountered when performing full event-generator tunes. The generation of simulated events at each parameter point can take  $\mathcal{O}(\text{hours}/\text{million events})$  of CPU time. This makes even a modest tuning exercise (a few parameters scanned over a hypercube consisting of 5–10 parameter values per dimension) computationally prohibitive. The computational demand can be further compounded by the non-trivial task of choosing an updated parameterization, with inefficient choices significantly increasing computation time. Below, we describe a novel tuning paradigm, utilizing RSA, that alleviates this computational burden through statistical reweighting<sup>13</sup> and utilizes modern autodifferentiation and optimization paradigms to choose updated parameterizations. This approach is similar but distinct to that of DCTR [392] which also performs event reweighting and parameter tuning, but utilizes a deep neural network classifier (instead of the exact analytic unnormalized density function) to extract event weights and perform parameter tuning. Other machine-learning-inspired tuning paradigms, such as those described in [393], do not utilize reweighting. Below we will illustrate the efficacy of parameter estimation using RSA in the context of fitting a hadronization model.

To showcase RSA, we focus on the two parameters which render rejection-based sampling necessary,  $a$  and  $b$ , and keep  $\sigma_{p_T}$  fixed to its default value, 0.335. To fit the  $a$  and  $b$  parameters of the Lund fragmentation function using RSA requires a post-hoc reweighting data-structure, which will allow for the extraction of alternate weights after event generation. The data-structure is comprised of three components: 1. the fragmentation-chain-level rejection sampling data e.g. the accepted and rejected longitudinal momentum fraction samples  $\mathbf{z}$  as well as the transverse mass  $m_T$  of the fragmenting hadron, see eq. (6.30); 2. the desired measurable observables from simulated hadronization events produced by the base parameterization  $\mathbf{y}_{\text{sim}}$  and 3. values of the same observables measured experimentally  $\mathbf{y}_{\text{exp}}$ .

Again, our simulation will consist of the hadronization of a simple string system based on the probabilistic model described in section 6.3. Both **Model 1** and **Model 2** will be used as base parameterizations during the fits. An example of the training data can be seen in eq. (7.6). Note that in practice, for use in differential programming libraries, each array  $\mathbf{z}_i$  must be zero-padded to a fixed length. In principle, the series of rejections could also be stored with the random number seed used during event generation.

Because RSA utilizes reweighting to explore the model parameter space, at least one sample of events, generated using a base parameterization  $\boldsymbol{\theta}_B \equiv \{a, b\}_B$ , is required for tuning. When fitting to experimental data (or when a good guess for initial parameters is unknown) multiple base parameterizations would be desirable/required. Given the unnormalized Lund fragmentation function,  $f(z; \boldsymbol{\theta})$ , the forward pass of training proceeds by first computing the event-weight array  $\mathbf{w}$  for the proposed parameters,  $\boldsymbol{\theta}_P \equiv \{a, b\}_P$ , shown in eqs. (7.7) and (7.8). Once the event-weight array has been computed, a ‘cost’ or ‘loss’ function must be defined and minimized

---

<sup>13</sup>For a detailed discussion and explicit timing comparisons between reweighted and re-simulated events we refer the reader to ref. [7].

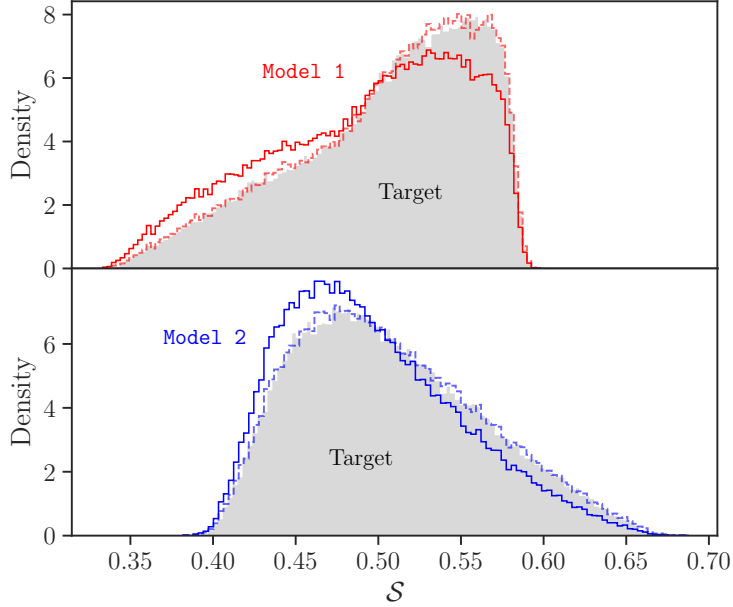


FIGURE 7.5: Observable distributions the classifier score  $\mathcal{S}$  (right) at three distinct parameterizations of the Lund  $a, b$  parameters, using a sample of  $N = 10^6$  events. Dotted histograms denote the reweighted distributions.

to allow for the determination of the next set of parameters  $\boldsymbol{\theta}_P$ . The loss will parameterize the difference between  $\mathbf{y}_{\text{exp}}$  and the weighted  $\mathbf{y}_{\text{sim}}$  ensembles, see section 7.4.3. Once the loss has been computed, PyTorch’s automatic numerical differentiation engine `autograd` paired alongside a chosen optimization algorithm (`Adam`, `SGD`, …, etc.) can be used to choose the next model parameterization i.e. fragmentation function  $f(z; \boldsymbol{\theta})$ .

#### 7.4.2 Observables

We categorize observables as either ‘high-level’ or ‘low-level’. High-level data utilizes currently available event-level/jet-level observables such as (charged) hadron multiplicity, event-shape variables like thrust, etc. Low-level data, on the other hand, assumes access to all hadron-level data that can in principle be extracted from experimental data, such as the energy and momenta of all hadrons within an event.

For tuning, we consider two observables – one high-level and one low-level. The high-level observable is the hadron multiplicity  $N_h$  that counts the total number of hadrons in the hadronization chain accepted by `finalTwo`. The multiplicity distributions are shown in the left panel of fig. 7.1 for the three model parameterizations as well as the reweighted distributions following eq. (7.8). The second observable is the low-level *truth score*  $\mathcal{S}$ . The truth score is the output of a trained DeepSets classifier [394, 395] that distinguishes between full low-level input from simulated (base) and experimental (truth/target) data. The classifier consists of a per-particle multi-layer-perceptron (MLP) encoder  $\phi$ , an aggregation function chosen to be simple addition,

and a MLP decoder  $\rho$ . Both the encoder and decoder networks consist of three layers and 64 hidden nodes. The input consists of low-level pion observables e.g. four-momenta that were preprocessed into transverse momentum, polar angle, and pseudorapidity  $\Theta_h^i \equiv (p_{T,i}, \phi_i, \eta_i)$  measured relative to the initial  $z$ -axis where

$$\begin{aligned} p_{T,i} &= \sqrt{p_{x,i}^2 + p_{y,i}^2}, \\ \phi_i &= \tan^{-1}(p_{y,i}/p_{x,i}), \\ \eta_i &= -\log [\tan^{-1}(p_z/2p_{T,i})]. \end{aligned} \quad (7.20)$$

The classifier was first trained with labeled data minimizing the binary-cross-entropy loss (BCE) between simulated and experimental data. After training, the score is given by

$$\mathcal{S}(\Theta_h^1, \dots, \Theta_h^{N_h}) = \rho \left( \sum_i^{N_h} \phi(\Theta_h^i) \right). \quad (7.21)$$

As an observable, the score  $\mathcal{S}$  effectively compresses the full-phase space kinematics  $\{\Theta_h^1, \dots, \Theta_h^{N_h}\}$  of all  $N_h$  hadrons in an event into a single scalar representation with hadron permutation-invariance that can be applied to any dataset irrespective of the actual parameter values considered for generation. The right panel of fig. 7.5 shows the score distributions as well as the reweighted distributions for the two cases in which the classifier is initially trained to distinguish between **Model 1** (top) or **Model 2** (bottom) from Target which we will refer to as scores  $\mathcal{S}_1$  and  $\mathcal{S}_2$ , respectively. Finally, when fitting, we consider multiplicity and scores individually as one-dimensional distributions as well as together to form two- and three-dimensional distributions, e.g.

$$\mathbf{y}_{\text{sim}}^d = \begin{pmatrix} \mathbf{y}_1 = C(\{N_{h,1}, \mathcal{S}_{1,1}, \mathcal{S}_{2,1}\}, d) \\ \vdots \\ \mathbf{y}_N = C(\{N_{h,N}, \mathcal{S}_{1,N}, \mathcal{S}_{2,N}\}, d) \end{pmatrix} \quad (7.22)$$

where  $C(\mathbf{O}, d)$  implies  $\mathbf{O}$  choose  $d$ , with  $d = 1, 2$  or  $3$  the number of observables considered, and keeping the same choice for all  $\{\mathbf{y}_{\text{sim}}^d\}_{n=1}^N$ .

### 7.4.3 Results

The algorithmic prescription for parameter estimation using RSA described in section 7.4.1 offers an efficient method for analyzing and exploring model parameter space. In addition to the standard binned and unbinned observables used in modern tuning exercises, RSA facilitates the exploration of parameter space using *machine-learning-based observables* (such as the score  $\mathcal{S}$ ). This facilitates a systematic study and comparison of metric spaces utilizing high- versus low-level observables. Here we first validate the algorithm through the construction of loss

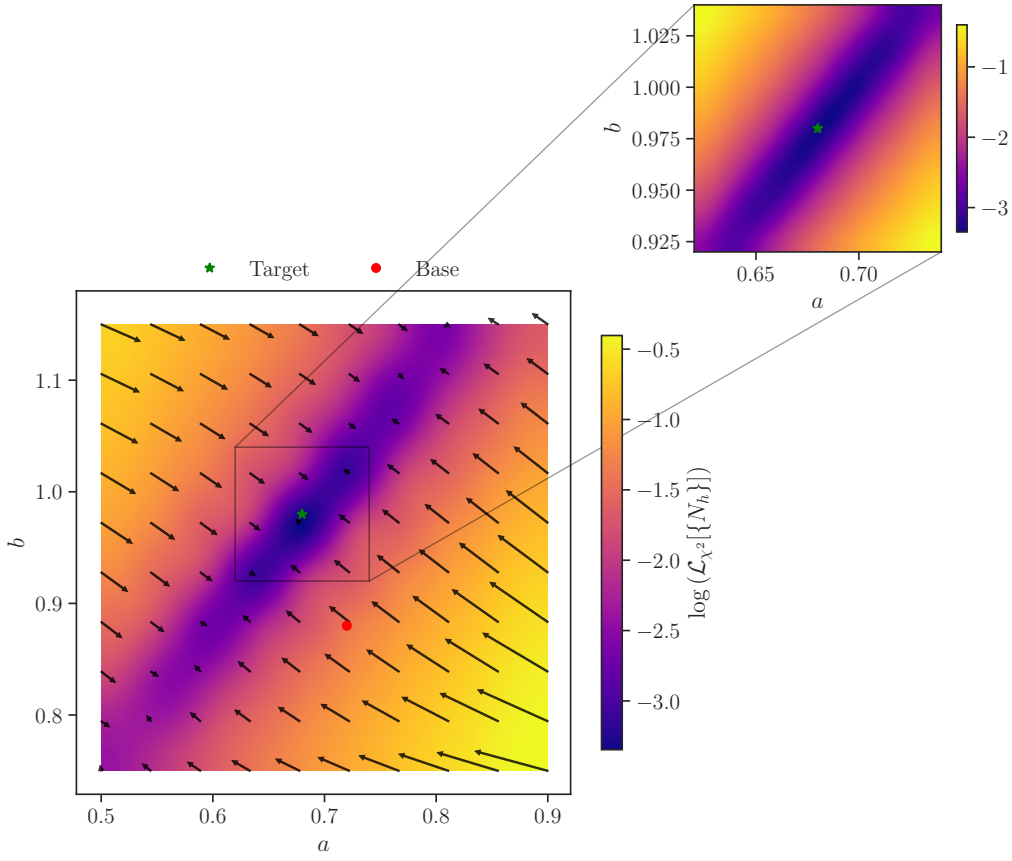


FIGURE 7.6: An example of the two-dimensional Lund  $a$  and  $b$  parameter plane loss landscape for the pseudo- $\chi^2$  loss defined in eq. (7.23). The red dot denotes the initial base parameterization from which we reweigh from and the green cross denotes the target parameterization from which the observable distribution was generated from. Both subplots are generated by computing the loss and gradients over a grid of 100  $(a, b)$  pairs. For each parameterization the losses and gradients are averaged over four mini-batches of  $5 \times 10^4$  events for a total ‘batch size’ of  $2 \times 10^5$  events.

landscapes for a variety of metrics and then turn to the investigation of fit performance using high- versus low-level observables.

#### 7.4.3.1 Loss landscapes

Given an accept-reject data-sample for an arbitrary parameterization  $\boldsymbol{\theta}$ , as described in section 7.2.3, and a set of observables  $\mathbf{y}_{\text{exp}}, \mathbf{y}_{\text{sim}}$ , RSA with reweighting can be used as a powerful exploratory device over the parameter volume. Once a metric comparing  $\mathbf{y}_{\text{exp}}$  and  $\mathbf{y}_{\text{sim}}$  is defined, a ‘loss landscape’ that illustrates the magnitude and gradients of the metric over  $\boldsymbol{\theta}$  can be created quickly using reweighting. Below we construct loss landscapes for various losses and observables.

**Pseudo- $\chi^2$**  For binned observables, a commonly used metric to determine fit efficacy is the pseudo- $\chi^2$  [31, 390]. Given a differentiable binning of  $\mathbf{y}_{\text{sim}}$ ,  $\mathbf{y}_{\text{exp}}$  and weights  $\mathbf{w}$  the pseudo- $\chi^2$  loss can be expressed as:

$$\mathcal{L}_{\chi^2}(\mathbf{y}_{\text{sim}}, \mathbf{y}_{\text{exp}}; \mathbf{w}) = \sum_{i=1}^{n_{\text{bins}}} \frac{(y_{\text{sim}}^{(i)} - y_{\text{exp}}^{(i)})^2}{\sigma_{\text{sim},i}^2 + \sigma_{\text{exp},i}^2} \quad (7.23)$$

where  $y^{(i)}$  represents the normalized count density in the  $i^{\text{th}}$  bin and  $\sigma$  denotes the statistical uncertainty of the  $i^{\text{th}}$  simulated and experimental bin. Note that this loss is well-defined for arbitrary multi-dimensional observable distributions. The landscape of the pseudo- $\chi^2$  for multiplicity  $N_h$  distributions over the parameter plane can be seen in fig. 7.6.

**1D Wasserstein distance** For unbinned observables, we utilize the optimal-transport-based Wasserstein, or Earth mover’s distance (EMD). Unlike  $f$ -divergences (like the  $\chi^2$ ), the EMD does not require overlapping support. Tuning with the EMD is similar to a WGAN [396], only here, the EMD is computed explicitly and thus there is no trainable ‘critic’ (making the optimization more stable)<sup>14</sup>. A similar use of the EMD is found in ref. [398], which used this setup to learn surrogate models for likelihood ratios. The EMD loss is defined as

$$\mathcal{L}_{\text{EMD}}(\mathbf{y}_{\text{sim}}, \mathbf{y}_{\text{exp}}; \mathbf{w}) = \sum_{n=1}^N \sum_{m=1}^M f_{n,m}^* d_{n,m}, \quad (7.24)$$

where the elements of the flow matrix  $f_{n,m}^*$  encode the fractional amount of weight to be transferred between event  $\mathbf{y}_{\text{sim},n}$  and  $\mathbf{y}_{\text{exp},m}$  and  $d_{n,m} = \|\mathbf{y}_{\text{sim},n} - \mathbf{y}_{\text{exp},m}\|_2$  is the distance between these two events. Here,  $M$  is the number of events observed in the experimental dataset. The top panel of fig. 7.7 shows the EMD loss landscapes for both the multiplicity  $N_h$  (top left) and the score  $\mathcal{S}_1$  (top right).

**Multi-dimensional sliced Wasserstein distance** To fit across multiple observables, such as multiplicity and classifier scores, we employ the sliced Wasserstein distance [399, 400]. The observable vector is randomly projected onto a large number  $N_P$  of random vectors  $\theta_i$  over the full observable space:

$$\mathcal{L}_{\text{SWD}}(\mathbf{y}_{\text{sim}}, \mathbf{y}_{\text{exp}}; \mathbf{w}) = \frac{1}{N_P} \sum_{i=1}^{N_P} \mathcal{L}_{\text{EMD}}(\mathbf{y}_{\text{sim},\theta_i}, \mathbf{y}_{\text{exp},\theta_i}; \mathbf{w}). \quad (7.25)$$

We apply slicing for two and three dimensional combinations of both low- and high-level observables, over one classifier score and multiplicity as well as over two classifier scores based of two  $(a, b)$  parameterizations and multiplicity. We chose  $N_P = 128$  (with little sensitivity

---

<sup>14</sup>A GAN-based reweighting and fitting has been explored in ref. [397].

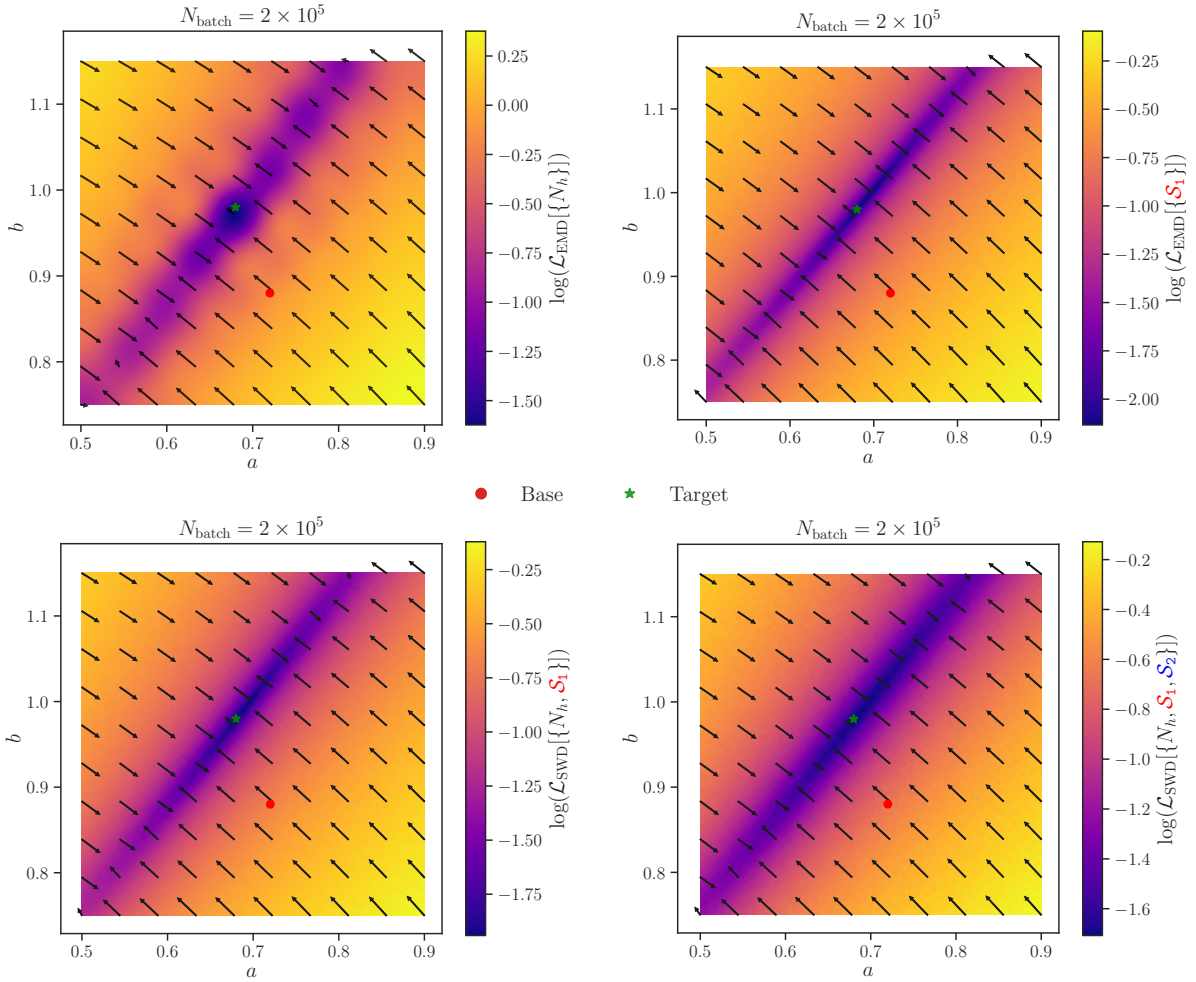


FIGURE 7.7: Two-dimensional Lund  $a$  and  $b$  parameter plane loss landscape for one-dimensional and sliced Wasserstein distances over various dimensionalities of low and high-level observables, with the same grid and mini-batching as in fig. 7.6.

to small changes) and prescaled each observable to have zero mean and unit variance. The bottom panel of fig. 7.7 shows the sliced Wasserstein loss landscapes for both the 2D observable combining multiplicity with the **Model 1** score  $\{N_h, \mathcal{S}_1\}$  (bottom left) and the 3D observable combining multiplicity with the **Model 1** and **Model 2** scores  $\{N_h, \mathcal{S}_1, \mathcal{S}_2\}$  (bottom right).

Note that in all cases (for all losses and observables), the loss landscapes in figs. 7.6 and 7.7 reveal a valley in the  $(a, b)$  plane illuminating an unavoidable degeneracy in model parameter space and correlation between the  $a$  and  $b$  parameters. For more details see the discussions in refs. [31, 390].

#### 7.4.3.2 Confidence Intervals

To demonstrate that the classifier score observables  $\mathcal{S}_1$  and  $\mathcal{S}_2$  have learned to distinguish data based off of more than the high-level event multiplicity alone, we apply our Wasserstein tuning on the 1D, 2D, and 3D observables mentioned in section 7.4.2 and compare their performance.

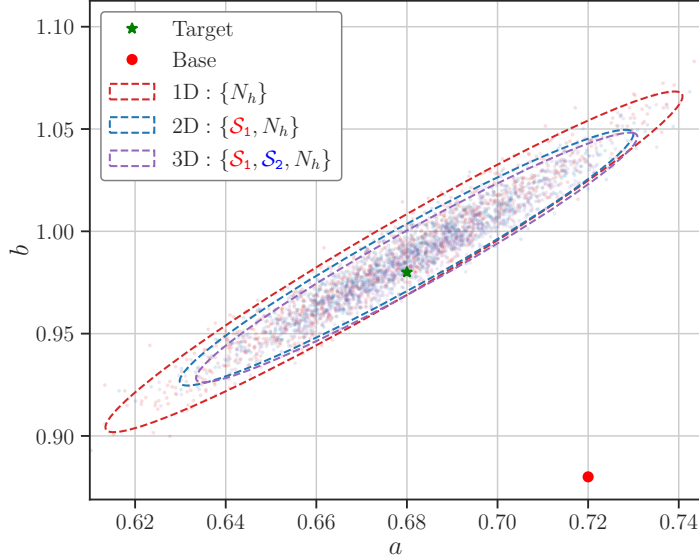


FIGURE 7.8: The 95% confidence ellipses on  $a$ ,  $b$  parameters estimated from 1,000 bootstrapped training runs over 300 epochs and identical tuning hyperparameters. Demonstrates the increasing accuracy of slicing over multiple low and high-level observables, from only  $N_h$  (red),  $\{\mathcal{S}_1, N_h\}$  (blue), and  $\{\mathcal{S}_1, \mathcal{S}_2, N_h\}$  (purple).

For each observable we perform 1,000 independent tunes, each using a single bootstrapped sample [401] of 25,000 events (both from the target and [Model 1](#) parameterizations) randomly sampled from the full datasets. Each run is initialized at  $\theta_{\text{init}} = \text{Model 1}$  with the same training hyperparameters and trained over 300 epochs with the same bootstrapped dataset after each parameter update using the [AdamW](#) optimizer. In fig. 7.8 we show the 95% confidence ellipses over all bootstrapped tunes in the  $(a, b)$  plane. The one-dimensional observable tunes utilize the 1D Wasserstein loss while the higher-dimensional observables utilize the sliced Wasserstein loss as described in section 7.4.3.1. We observe that the higher-dimensional observables (1D versus 2D versus 3D) produce a steady narrowing of confidence ellipses, indicating better fit performance.

## 7.5 Conclusions

In this chapter we introduced two reweighting frameworks for hadronization (both of which are available for use in the PYTHIA codebase, as of v8.311). These reweighting tools alone provide significant efficiency improvements for pipelines relying on many parameterization-dependent datasets such as uncertainty quantification and parameter tuning. Care must be taken to ensure valid usage, however – the accuracy of these frameworks depends crucially on sufficient coverage: when the target distribution deviates too far from the baseline, extreme weight values signal poor modeling. To identify such cases, we provide a set of diagnostic metrics in eq. (7.9).

When coverage is sufficient, these methods offer a fast and practical alternative for uncertainty estimation in hadronization models, especially in the context of full detector simulations.

We also described a proof-of-principle investigation into the implications and applications of incorporating these frameworks into existing differential programming libraries. While we presented RSA in the context of differentiable kinematic variations, it is clear that similar methods can also be used straightforwardly for flavor variations. We validated the framework in the context of two-parameter variations – we note that reweighting in high-dimensional parameter spaces may present additional challenges such as: 1. magnified statistical dilution and loss of coverage due to ‘the curse of dimensionality’ and 2. difficulties related to selecting non-degenerate observables and high-fidelity loss functions. A thorough study of the scaling of weight-based derivatives in such regimes remains an open direction. Additionally, while not a fundamental issue, the memory footprint of the current post-hoc framework, due to the necessity of zero-padding, can become computationally prohibitive for large oversampling factors or high multiplicity final states (large string energies). This can be mitigated through oversampling factor tuning, seed storage, or the direct computation and in-place storage of gradients during event generation which would completely eliminate the need for external datasets all-together.

Finally, in principle, by embedding each of the reweighting frameworks into differential libraries offers a path towards a fully differentiable hadronization simulation. More ambitiously, the success of the presented frameworks hint towards a future with fully differentiable event simulators. Additional work must be done to understand what components of the simulator can and cannot be molded into reweightable forms.

The methods developed here serve as a promising foundation for the next generation of event simulators, offering a scalable approach to accurate, differentiable, data-driven modeling, parameter estimation, and uncertainty quantification.

# Chapter 8

## Data-driven hadronization models

**Preface:** This chapter is based on the collection of works in [6, 8, 11, 27] with the MLHAD team (Ben, Christian, Phil, Steve, Manuel, Michael, Ahmed, and Jure). The original work [6] with Phil, Ahmed, and Jure was the first naive attempt to embed a generative network into a hadronization pipeline. The works thereafter [8, 11, 27] can be summarized as the development of ML-based algorithmic solutions to the inverse problem of hadronization. Specifically, two algorithms are introduced –MAGIC and HOMER– that facilitate the extraction of microscopic string dynamics, in the form of the Lund fragmentation function, directly from macroscopic experimental observables through the deformation of a base solution (*i.e.*, default PYTHIA). I typically refer to the outputs of these algorithms as *data-driven* or *differentiable* hadronization models.

Hadronization is one of the least understood ingredients in the simulation of particle collisions. While the Lund-string [402, 403] and cluster-fragmentation [334–336] models give reasonable overall descriptions of hadronization, there are still significant discrepancies between both the two models [404] and the models and data [405]. Augmenting these phenomenological models with a *data-driven* description of hadronization may help to improve predictions.

Hadronization models serve two distinct purposes. The first purpose is rooted in direct physics motivation – we aim to enhance our understanding of QCD behavior beyond the approximations afforded by lattice quantum chromodynamics (QCD) and perturbative QCD under specific limits. For this purpose, reliance on models is essential. The second purpose is to provide a realistic description of final state particles in high energy collisions. This description allows for the detailed study of detector responses, as well as realistic modeling of both background and signals for high momentum transfer processes. This modeling is critical in most high energy particle physics analyses both for interpreting the results as well as estimating systematic uncertainties.

In the first scenario, discrepancies between models offer an opportunity to utilize measurements to deepen our understanding of physics. In this context, substituting a physics model with a machine learned (ML) model may obscure these discrepancies or mask the foundational physics phenomena. However, a carefully designed ML model could also provide insights into the physics model by supplying a detailed description across all phase space of the physics model at a granular level. In the second scenario, discrepancies with data do not provide deeper insights into the hadronization process but rather produce more ambiguous interpretations of experimental data with larger associated systematic uncertainties. Here, data-driven models can reduce these uncertainties while retaining the same physics motivation present in the original models.

To develop these data-driven models the existing phenomenology can be augmented, keeping the underlying strings or clusters as the building blocks, but perturbing their dynamics to accommodate all relevant experimental observables. This is a problem well suited for ML methods, which can form a flexible basis for adjusting the underlying model dynamics to match experimental data. The first attempts at providing an ML description of simplified hadronizing systems have been carried out using both (MLHAD) conditional sliced Wasserstein autoencoders (cSWAEs) [6] and (HADML) generative adversarial networks (GANs) [406, 407]. These two architectures have reproduced key features of the Lund string model in PYTHIA [30] and the cluster model in HERWIG [326, 408], respectively, but both rely on training data that is not available at the experimental level.

As discussed in chapter 6, within the Lund string model the phenomenology of hadronization is largely determined by the probabilities with which different hadron species are produced, *i.e.*, 1. the forms of the probability distributions for the hadron momenta traditionally determined by eqs. (6.26) and (6.30), 2. the method of determining the color singlet systems, and 3. the process of flavor selection. Here, we set aside 2 and 3 to focus on 1, the kinematics of string fragmentations, for which we want to ultimately develop a *data-driven* determination of the probability distributions.

In sections 8.1.1 and 8.2 we describe two distinct algorithmic prescriptions allowing for the extraction of data-driven fragmentation functions from experimental observables.

## 8.1 MAGIC

Microscopic Alterations Generated by Infrared Collections (MAGIC) [8] is a normalizing flow (NF)-based prescription for extracting fragmentation functions from data, aimed at addressing the inverse problem of hadronization. The basic idea is to first train a NF to replicate the Lund fragmentation function, as implemented in PYTHIA, as closely as possible – this provides a differentiable and overparameterized representation of the Lund fragmentation function. The

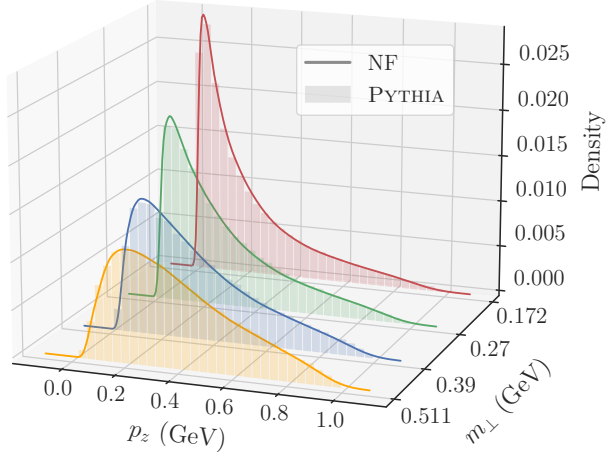


FIGURE 8.1: A comparison between the (histograms) PYTHIA and (solid lines) MLHAD NF generated single emission  $p_z$  distributions produced at four different fixed values of  $m_\perp$  which were not used in the training of the model.

base model can then be fine-tuned directly by minimizing the difference between observables produced by the base model and those from experimental data, with respect to the NF network parameters. The resulting MAGIC-based deformation provides a fragmentation function that retains physical interpretability, *i.e.*, by still describing hadronization as a series of iterative fragmentations, while simultaneously enabling a more flexible, data-driven modeling of non-perturbative QCD effects.

Normalizing flows (NFs) are generative ML models that can produce high-quality continuous approximations of probability distributions from a limited set of data samples [409–411]. They accomplish this by concatenating a series of  $N$  independent, bijective transformations,  $F(\mathbf{z}) = f_N(f_{N-1}(\dots f_2(f_1(\mathbf{z}))\dots))$ , which then map a latent space probability distribution  $\mathcal{P}_Z(\mathbf{z})$  to a target distribution  $\mathcal{P}_X(\mathbf{x})$ . The latent space is typically chosen such that it can be easily sampled. The form of the bijective functions  $f_i$  is adjusted by modifying the model parameters  $\boldsymbol{\theta}$  and any external parameters, including provided conditional labels  $\mathbf{c}$ .

Since each  $f_i$  is a continuous function, the composite function  $F$  is also continuous. This allows for density estimation over the full phase space including regions sparsely populated by the training data. In section 8.1.1 we use this feature to introduce a method for fine-tuning the form of the microscopic fragmentation function using measured observable quantities.

The MLHAD NF architecture is able to reproduce pseudo-data generated using a simplified version of the PYTHIA Lund string hadronization model. This pseudo-data is produced using the same simplified model as in [6], in which only light-quark flavors are allowed as endpoints, and isospin symmetry is required, *i.e.*, only neutral and charged pions at a single mass are generated. The MLHAD NF is trained on a dataset of  $N$  hadron emissions from a string with energy  $E_{\text{ref}} = 200 \text{ GeV}$ . That is, the training dataset consists of  $N$  two-dimensional arrays of first hadron emission kinematics  $\mathbf{x}_n = \{p_{z,n}, p_{\perp,n}\}$ , where  $n \in \{1, \dots, N\}$  and  $p_z$  and  $p_\perp$  are,

respectively, the longitudinal and transverse components of the emitted hadron’s momentum in the-center-of-mass frame of the string. To generate hadron kinematics for strings with energies other than  $E_{\text{ref}}$ , we use the rescaling property of the Lund string fragmentation function to render  $p_z$  independent of the string energy, transforming the generated value of  $p_z$  according to  $p_z \rightarrow p_z E_{\text{ref}}/E$ , where  $E$  is the energy of the quark in the initial string’s center-of-mass frame [6].

Unlike in [6], we train the MLHAD NF on a dataset containing different transverse masses,  $m_\perp$ . For this, we construct labeled training datasets  $\{x_n, c_n\}_{n=1}^N$ , where

$$c_n \equiv \frac{m_{\perp,\max} - m_{\perp,n}}{m_{\perp,\max} - m_{\perp,\min}}, \quad (8.1)$$

$m_{\perp,\min} = m_{\pi^\pm} \approx 0.140 \text{ GeV}$  and  $m_{\perp,\max} = 1.3 \text{ GeV}$  are, respectively, the minimal and maximal values of  $m_\perp$  used in training. The maximum is chosen such that none of the hadronization chains considered will produce an  $m_\perp$  above this value. That is, the conditional labels  $c_n$  are functions of hadronic transverse mass  $m_\perp$  such that  $c_n \in [0, 1]$ , where the boundaries correspond to the minimum and maximum  $m_\perp$ . Here,  $m_\perp$  is used rather than mass to ensure the independence of the  $z$  and  $p_\perp$  probability distributions for a given  $m_\perp$  value, see eq. (6.30). The training dataset is split into 15 different conditional labels, where each label corresponds to a different fixed  $m_\perp$ . For each conditional label  $5 \times 10^5$  first hadron emissions are used, for a total of  $N = 7.5 \times 10^6$  emissions in the full training dataset.

Figure 8.1 shows a comparison between PYTHIA generated kinematic distributions and the learned MLHAD NF kinematic distributions for different values of the transverse mass (we have set the NF model parameters  $\theta$  to their fixed average values). We observe that the NF model can fully reproduce the  $p_z$  of the hadronizing  $q\bar{q}$  system of the Lund string model for arbitrary hadron mass. The result of a full hadronization chain, where hadrons are sequentially emitted from the string fragments, is shown in fig. 8.2; the string fragmentation terminates at  $E_{\text{cutoff}} = 25 \text{ GeV}$  in this case in order to avoid complications from `finalTwo`. We observe excellent agreement between the hadron multiplicities produced by PYTHIA and the MLHAD NF.

### 8.1.1 Fine-tuning microscopic fragmentation kinematics

In this section we show how the MLHAD NF model trained on single hadron emission pseudo-data can be used to adjust the microscopic model of single hadron emission kinematics, so that it reproduces experimental data that has no direct single hadron emission measurements. To do this we introduce a method for fine tuning NF-based models of hadronization, termed Microscopic Alterations Generated from Infrared Collections<sup>1</sup> (MAGIC). The MAGIC training method allows for the fine tuning of *microscopic* dynamics to describe a set of *macroscopic* observables.

---

<sup>1</sup>Here, infrared collections refer to any hadronization-sensitive high-level observable distribution that can be obtained from experiment.

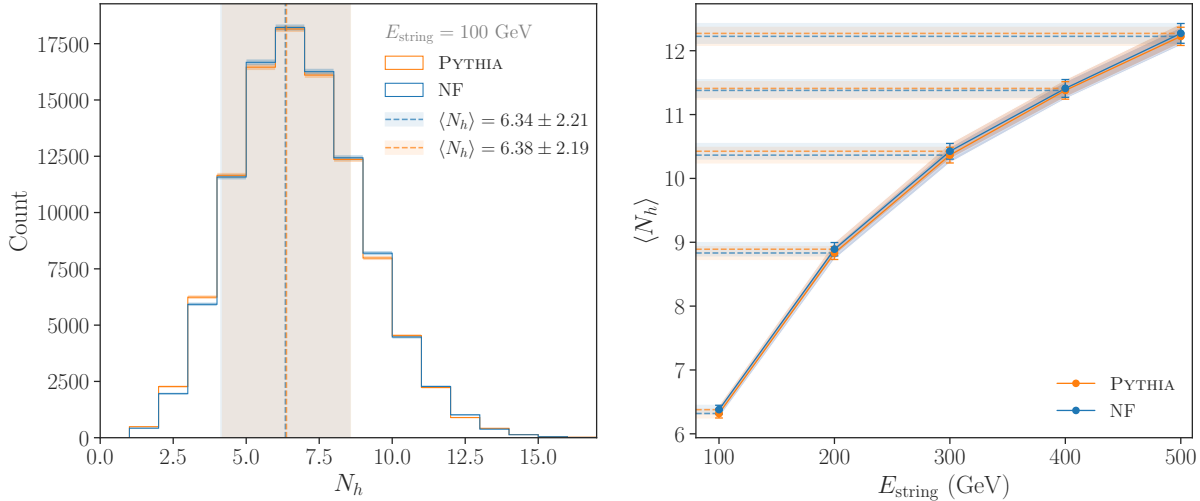


FIGURE 8.2: (left) Comparison of hadron multiplicity distributions generated with (orange) PYTHIA and the (blue) MLHAD NF, constructed from hadronizations of  $10^5$  strings, all with an initial energy of  $E_{\text{string}} = 100 \text{ GeV}$  and an energy cutoff of  $E_{\text{cutoff}} = 25 \text{ GeV}$ . (right) Scaling of average hadron multiplicity  $\langle N_h \rangle$  is given as a function of the starting string energy. Each marker represents an averaging of hadron multiplicity over the hadronization of  $5 \times 10^3$  strings. The dotted lines show the average multiplicity  $\langle N_h \rangle$  and the bands the corresponding  $1\sigma$  range.

Practically, the microscopic dynamics are produced from an underlying phenomenological model, while the macroscopic observables are from experiment.

MAGIC is a natural extension of the traditional tuning techniques, such as manual tuning [31] or automated regression techniques [390–392, 412]. Crucially, while approaches such as deep neutral networks using classification for tuning and reweighting (DCTR) [392] do parameter reweighting and tuning, they do not directly modify the underlying parametric Lund model used for training. MAGIC is able to increase the flexibility of the model beyond the parametric form, eqs. (6.26) and (6.30), while remaining physically meaningful by keeping the emission-by-emission paradigm described in section 6.3.

This method works by adding data-driven perturbations to an analytic solution, the Lund symmetric fragmentation function of eq. (6.30) in the case of hadronization, by augmenting it with an over-parameterized function such as an NF that can be modified arbitrarily to accommodate data. The Lund symmetric fragmentation function already provides a good description of experimental data; the idea is to learn data-driven perturbations to obtain even better agreement with experiment.

As a toy example we take a simplified one-dimensional NF model, consisting of a weighted mixture of Gaussian distributions, trained on the  $z$  component of the momentum of first-emission hadrons, as described in appendix C. MAGIC consists of two training phases: in the first phase, the NF is trained on simulated kinematics as described in section 8.1; in the second phase, the NF is modified to match the experimental data. The initial NF model, or base model, provides high fidelity sampling of single-hadron emission kinematics  $\mathbf{x} = p_z$ . Here we omit  $p_\perp$ , in contrast

to section 8.1, for simplicity of the model. From these  $\mathbf{x}$  kinematics, one can obtain predictions for measurable, hadronization-sensitive observables  $\mathbf{y}$ , *e.g.*, hadron multiplicity. In the second phase of training, the base model is fine-tuned by reweighting the dataset of  $\mathbf{y}$  values generated by the base model to statistically match the experimentally observable dataset. This second phase explicitly relies on the ability to reweight distributions.

The training data for the second phase of MAGIC consists of three components: 1. the hadronization-chain-level kinematics  $\mathbf{x}$ , *i.e.*, the hadron kinematics  $p_z$  from simulated emissions produced by the base model; 2. the desired measurable observables from simulated hadronization chains produced by the base model  $\mathbf{y}_{\text{sim}}$ , *e.g.*, the hadron multiplicity  $N_h$  predicted by the base model; and 3. values of the same observables measured experimentally  $\mathbf{y}_{\text{exp}}$ . As a proof of principle, we use just a single observable, the total number of hadrons for a single hadronization chain, *i.e.*, the hadron multiplicity such that  $\mathbf{y}$  is  $N_h$ .

An example of the training data, consisting of  $N$  hadronization chains, is therefore<sup>2</sup>

$$\mathbf{x} = \begin{pmatrix} \mathbf{x}_1 = \{p_{z,h_1}, p_{z,h_2}, p_{z,h_3}\}_1 \\ \mathbf{x}_2 = \{p_{z,h_1}, p_{z,h_2}, p_{z,h_3}, p_{z,h_4}\}_2 \\ \vdots \\ \mathbf{x}_N = \{p_{z,h_1}, p_{z,h_2}\}_N \end{pmatrix}, \quad \mathbf{y}_{\text{sim}} = \begin{pmatrix} \mathbf{y}_1 = N_{h,1} = 3 \\ \mathbf{y}_2 = N_{h,2} = 4 \\ \vdots \\ \mathbf{y}_N = N_{h,N} = 2 \end{pmatrix}. \quad (8.2)$$

The fine tuning modifies the hadronization model, *i.e.*, the distribution governing  $p_z$  for each emission, to minimize the difference between the two ensembles  $\mathbf{y}_{\text{sim}}$  and  $\mathbf{y}_{\text{exp}}$ . We do not match specific measured hadronization chains to a given hadronization history but instead compare the two ensembles at the statistical level.

Note that MAGIC does not regenerate hadron emissions for each perturbation of the NF, instead MAGIC reweights the hadronization chains, which is computationally advantageous with resimulating taking  $\mathcal{O}(\text{minutes per thousands of events})$  versus reweighting taking  $\mathcal{O}(\text{seconds per thousands of events})$  in our toy simulation. We make use of the fact that NFs give explicit access to the model likelihood and reweight events that were originally sampled from the base model to events sampled from the updated model. Each hadronization-chain weight can be computed in terms of the likelihood ratio between the updated, or perturbed, model likelihood  $\mathcal{P}_X(\mathbf{x}_n, \boldsymbol{\theta}_P)$ , and the base model likelihood  $\mathcal{P}_X(\mathbf{x}_n, \boldsymbol{\theta}_B)$ . Written in terms of single emissions, the likelihood  $\mathcal{P}_X(\mathbf{x}_n, \boldsymbol{\theta})$  can be factorized as,

$$\mathcal{P}_X(\mathbf{x}_n, \boldsymbol{\theta}) = \prod_{i=1}^{N_{h,n}} \mathcal{P}_X(\mathbf{x}_{n,i}, \boldsymbol{\theta}), \quad (8.3)$$

---

<sup>2</sup>While not denoted explicitly in eq. (8.2), each array  $\mathbf{x}_i$  is zero-padded to a fixed length of size  $\max(\mathbf{y}_{\text{sim}}) = \max(N_{h,n})$ .

where  $N_{h,n}$  is the number of hadrons in hadronization chain  $n$ , and  $\mathbf{x}_{n,i}$  is emission  $i$  of chain  $n$ .

We introduce a hadronization-chain weight array  $\mathbf{w}$ , where each weight is computed as the product of the likelihood ratios for all emissions in a chain

$$\mathbf{w} = \begin{pmatrix} w_1 \\ w_2 \\ \vdots \\ w_N \end{pmatrix}, \text{ where } w_n = \prod_{i=1}^{N_{h,n}} \frac{\mathcal{P}_X(\mathbf{x}_{n,i}, \boldsymbol{\theta}_P)}{\mathcal{P}_X(\mathbf{x}_{n,i}, \boldsymbol{\theta}_B)}. \quad (8.4)$$

Explicitly for this example,  $\mathbf{x}_{n,i}$  is just the  $p_z$  of hadron  $i$  from hadronization chain  $n$ . The reduction in training time associated with this use of hadronization-chain weights is crucial for the technical feasibility of the MAGIC approach to fine-tuning.

The learning objective of the fine-tuning phase is to minimize the statistical distance between  $\mathbf{y}_{\text{sim}}$ , weighted by  $\mathbf{w}$ , and the target distribution  $\mathbf{y}_{\text{exp}}$ . In our toy example, we use the Wasserstein distance [413–416], or Earth mover’s distance (EMD), as a measure of the similarity between the two samples<sup>3</sup> and define the loss function as

$$\mathcal{L}_{\text{EMD}}(\mathbf{y}_{\text{sim}}, \mathbf{y}_{\text{exp}}) = \sum_{n=1}^N \sum_{m=1}^M f_{n,m}^* d_{n,m}, \quad (8.5)$$

where the elements of the flow matrix  $f_{n,m}$  encode the fractional amount of weight to be transferred between event  $\mathbf{y}_{\text{sim},n}$  and  $\mathbf{y}_{\text{exp},m}$  and  $d_{n,m} = \|\mathbf{y}_{\text{sim},n} - \mathbf{y}_{\text{exp},m}\|_2$  is the distance between these two hadronization chains. Here,  $M$  is the number of hadronization chains observed in the experimental dataset.

Once the loss has been computed, back-propagation algorithms update the NF parameters  $\boldsymbol{\theta}$  using PYTORCH’s automatic differentiation engine `autograd`. The `autograd` engine utilizes differential programming paradigms with dynamic computational graphs to yield the gradients of the loss function with respect to all parameters  $\nabla_{\boldsymbol{\theta}} \mathcal{L}_{\text{EMD}}$  by tracking the impact of the hadronization-chain weights  $\mathbf{w}(\boldsymbol{\theta})$  on the loss. We can then find a model likelihood that produces the targeted observable distribution because updating  $\boldsymbol{\theta}$  corresponds to updating every  $\mathcal{P}_X(\mathbf{x}_{n,i}, \boldsymbol{\theta})$ . The only dynamical object in the fine-tuning phase of MAGIC is the hadronization-chain weight array  $\mathbf{w}$ ; the base model,  $\mathbf{x}$ ,  $\mathbf{y}_{\text{sim}}$ , and  $\mathbf{y}_{\text{exp}}$  all remain fixed.

In our toy example, we use a one-dimensional NF base model, see appendix C, trained on  $N = 5 \times 10^5$  PYTHIA generated hadronization chains with the Lund string parameter  $a$  set to

---

<sup>3</sup>In many cases, when training from real experimental distributions, one may only have access to binned datasets. The MAGIC paradigm may equivalently be used in these scenarios by simply utilizing a binned statistical distance such as  $\chi^2$ .

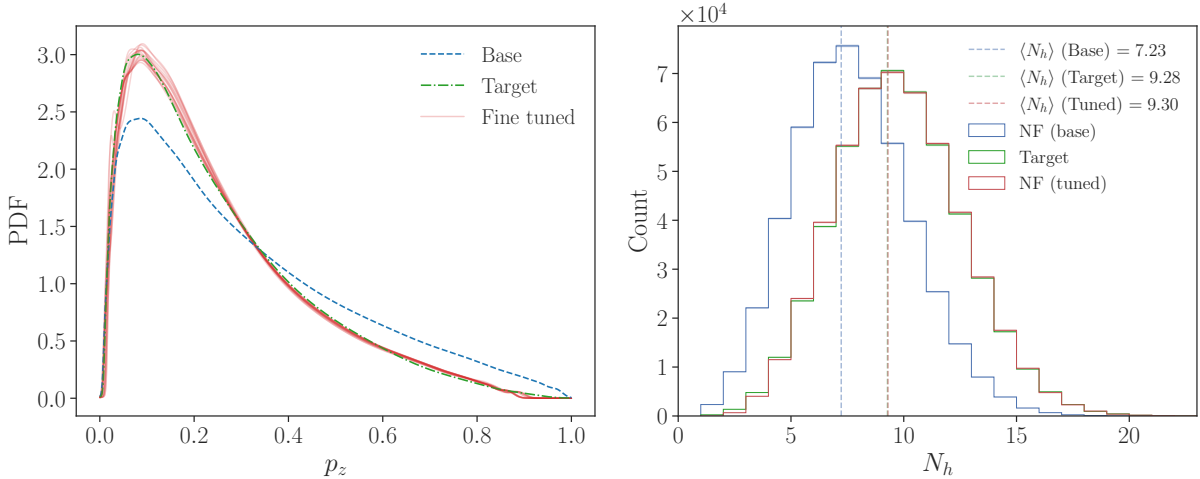


FIGURE 8.3: **Left:** Comparison between the single emission kinematic distribution  $p_z$  of the (blue dashed) base model, the (green dashed-dotted) distribution used to generate  $\mathbf{y}_{\text{exp}}$ , and (red) an ensemble of solutions learned using MAGIC. **Right:** Comparison of hadronization-chain level hadron multiplicity between the (blue) base, (red) one of the fine tuned, and the (green) target distributions where each histogram is constructed from  $5 \times 10^5$  hadronization chains. The mean of each histogram is shown as a vertical dashed line.

0.68. Each of the transverse momentum components of the emitted hadrons is sampled from a Gaussian distribution, and the correlation between  $p_z$  and  $p_\perp$  is neglected for simplicity. We create a pseudo-experimental hadron multiplicity observable  $\mathbf{y}_{\text{exp}}$  with  $M = 5 \times 10^5$  samplings of a second NF trained on PYTHIA hadronization chains, produced with  $a = 1.5$ .<sup>4</sup>

We then perform 15 independent MAGIC fine-tunings<sup>5</sup> of the base model, where each fine-tuning is trained over three epochs in batches of  $10^4$  samples with the learning rate fixed to  $\delta = 2.5 \times 10^{-2}$  in the first epoch, and reduced to  $\delta = 1 \times 10^{-2}$  for the remaining two epochs. The results of the independent trainings can be seen in the left panel in fig. 8.3; we see that the fine-tuned models all successfully learn the softer hadron emission spectrum used to generate the pseudo-experimental values of hadron multiplicity. In the right of fig. 8.3, we see that the corresponding hadron multiplicity distributions also agree.

We note some observations regarding the application of MAGIC. First, the fine-tuned models of  $p_z$  shown in fig. 8.3 do not exactly match the target, and are not unique. This is expected, and is ultimately a consequence of finite training data and time. In multi-dimensional MAGIC fine-tunings, where the conditionally dependent fragmentation function  $f(p_z|p_T)$  and transverse momentum distributions  $\mathcal{P}(p_x, p_y)$  were fine-tuned with just a single observable, we found that qualitatively different solutions are obtained, all of which are able to reproduce the observable distributions matching those of the target. This degeneracy is presumably broken once

<sup>4</sup>We do not use PYTHIA directly to generate the targeted pseudo-experimental multiplicity training dataset due to the included correlations between  $p_z$  and  $p_\perp$ , unlike the simplified base model.

<sup>5</sup>Training using MAGIC is computationally inexpensive, for example, the training for the presented toy example can be performed on a modern laptop CPU with training times of  $\mathcal{O}(1 \text{ hour})$  to achieve similar accuracy to the results shown in fig. 8.3.

additional sufficiently-orthogonal observables are included in  $\mathbf{y}$ . Because the base NF model is capable of learning arbitrarily correlated multi-dimensional distributions, it is expected that the MAGIC fine-tuning can also modify correlations between microscopic distributions assuming that the macroscopic distributions are sensitive to these correlations. In general, more care must be taken in multi-dimensional MAGIC tunes to ensure appropriate coverage across the full domain of the distribution, particularly when the microscopic distribution contains more degrees of freedom than the macroscopic distribution.

The MAGIC fine-tuned models could be included within existing event generation pipelines, either directly as a kinematic generator or as a reweighter that utilizes the learned likelihood ratio between the base, *e.g.*, the default PYTHIA, and fine-tuned models, to provide event weights similar to those of [7]. We leave a full exploration and incorporation of the MAGIC method within PYTHIA for future work.

## 8.2 HOMER

Histories and Observables for Monte Carlo Reweighting (HOMER) [9, 11] is an alternate prescription (or solution to the inverse problem of hadronization) for fine-tuning fragmentation level kinematics from experimental observables. This basic idea<sup>6</sup> is to utilize an observable-level classifier to parameterize a weight that encodes the likelihood ratio between two sets of observables (simulation versus data). This weight can then be used to solve a numerical regression problem which learns to distribute the full event-level (macroscopic) weight provided by the classifier into a product of “string break weights”. That is, each string break is weighted in such a way that the product of the assigned weights comes to the effective likelihood ratio between the observed and simulated data. Doing this procedure over large datasets eventually converges to a stable minimum where the product of string break weights match the classifier weight. These learned string break weights can then be used to extract a fragmentation function by reweighting  $z$  samples according to the learned string break weights. In many aspects, HOMER can be regarded as the reweighting revolution’s (see chapter 7) solution to the inverse problem of hadronization.

The HOMER method is a framework to learn a hadronization model from data without requiring an explicit parametric functional form; here, the model is a modified Lund string fragmentation function  $f(z)$ , *i.e.*, eq. (6.30). We demonstrate the functionality of the HOMER method using synthetic data generated with PYTHIA, which allows us to examine how well the extracted string fragmentation function  $f_{\text{HOMER}}(z)$  approximates the actual function used by the synthetic data  $f_{\text{data}}(z)$ . This actual  $f_{\text{data}}(z)$  is not available in data, even synthetic data, where the ordering of the hadron emissions cannot be measured and leads to an ambiguity in the possible fragmentation chains that could produce an observable event.

---

<sup>6</sup>Thanks to Manuel, the mastermind and codemaster behind HOMER.

The starting point of HOMER is a simulated hadronization model, *e.g.*, PYTHIA with a reasonable set of parameters, which is assumed to already give a decent approximation of the data. HOMER then uses data in a two step procedure to transform this baseline model to match the data. In our case, the simulator is PYTHIA, but with the initial string fragmentation function,  $f_{\text{sim}}(z)$ , using different parameters than those used to generate the synthetic data,  $f_{\text{data}}(z)$ . The simulator produces events, which can then be compared to data. As a reminder of the terminology defined in section 6.3.2.2, an event  $e_i$  is a list of observables,  $\vec{x}_i$ , which describe a *single collision*, *e.g.*, a single instance of  $e^+e^- \rightarrow u\bar{u}$  annihilation. A collection of events  $\{\vec{x}_1, \dots, \vec{x}_N\}$  is called a run. While two possibilities for observables were considered in ref. [27], namely high-level observables and point-cloud-based observables, for simplicity and brevity, we will only consider HOMER in the context of ubinned high-level observables (section 8.2.2) constructed from particle level information, such as thrust, multiplicity, *etc.* and summarized in appendix D.

Additionally, the HOMER method has also been generalized to the case of multi-parton configurations [11]. Again, for simplicity, we will focus on the case of a  $q\bar{q}$  string system and mention briefly the generalizations required to handle multi-parton strings.

### 8.2.1 Details about the HOMER method

In the Lund string fragmentation model, the probability of a given string break  $\vec{s}_{hcb}$  depends on the  $\vec{p}_T^{\text{string}}$  of the string fragment that is emitting the hadron. We write this conditional probability as

$$p(\vec{s}_{hcb}) \equiv p(\{z, \Delta\vec{p}_T, m, \text{fromPos}\}_{h,c,b} | \{\vec{p}_T^{\text{string}}\}_{h,c,b}). \quad (8.6)$$

HOMER aims to learn a fragmentation weight  $w_s^{\text{data}}(\vec{s}_{hcb})$  for individual hadron emissions. This is achieved by taking an initial guess for the fragmentation probability function  $p_{\text{sim}}(\vec{s}_{hcb})$  from the *baseline simulation model*, *e.g.*, PYTHIA, and reweighting it to a data-driven fragmentation function

$$p_{\text{sim}}(\vec{s}_{hcb}) \rightarrow w_s^{\text{infer}}(\vec{s}_{hcb}) p_{\text{sim}}(\vec{s}_{hcb}). \quad (8.7)$$

The baseline simulation model is taken as eq. (6.30), with parameters chosen to differ sufficiently from those used to produce the synthetic data.  $N_{\text{sim}}$  baseline simulation model events are generated. The baseline simulation model events are then compared with the experimental run dataset that contains  $N_{\text{data}}$  events. In obtaining  $w_s^{\text{infer}}(\vec{s}_{hcb})$ , HOMER only uses information that is experimentally accessible.

In the HOMER method, the inference process is divided into three steps. In Step 1 the ratio of probabilities for a given event  $e_h$  to occur in data compared to the baseline simulation model,

$$w_{\text{exact}}(e_h) = \frac{p_{\text{data}}(e_h)}{p_{\text{sim}}(e_h)}, \quad (8.8)$$

is estimated with a classifier,  $w_{\text{class}}(e_h) \approx w_{\text{exact}}(e_h)$ . The classifier weights of Step 1 are then used in Step 2 to infer single emission weights,  $w_s^{\text{infer}}(\vec{s}_{hcb})$ . These single emission weights are finally combined in Step 3 to give the predicted weight for a fragmentation history,  $w_{\text{HOMER}}(\vec{S}_h)$ . In the following, we provide details for each of these three steps.

Since the data used in this work is synthetic data produced with PYTHIA, the exact weights,  $w_{\text{exact}}(e_h)$ , are known. These weights are controlled by the ratio of probabilities for an event produced either using the “sim” or “data” values of parameters for the Lund fragmentation function of eq. (6.30); the corresponding fragmentation functions for these two parameter sets are denoted as  $f_{\text{sim}}(z)$  and  $f_{\text{data}}(z)$ , respectively. For a single emission the exact weight is then simply given by

$$w_s^{\text{exact}}(\vec{s}_{hcb}) = \frac{f_{\text{data}}(z)}{f_{\text{sim}}(z)}, \quad (8.9)$$

and thus is a known analytic function, up to the normalization constants for each  $f(z)$  (see [7] for details). The exact weights for an event,  $w_{\text{exact}}(e_h)$ , are then built from the exact single emission weights  $w_s^{\text{exact}}(\vec{s}_{hcb})$ .

### 8.2.1.1 Step 1: event classifier

To estimate  $w_{\text{exact}}(e_h)$ , we train a ML algorithm to distinguish between data and the events produced from the baseline simulation model. This classifier can only have access to measurable quantities – the kinematic and flavor information for the observable hadrons in each event – and not to the full fragmentation history. In practice, the experimental measurements that can be made realistically now or in the near future never use this full information, but, rather, collections of high-level observables. To study the performance of HOMER with such observables, we consider two limits: unbinned and binned scenarios. The unbinned scenario requires dedicated experimental measurements in the same vein as ref. [417], while the binned scenario uses only information that is already available from LEP measurements archived on HEPDATA [418].

**The unbinned scenario.** In this scenario, the information available for an event consists of values for observables  $\mathcal{O}_i$ , such as the charged multiplicity, thrust, *etc.*, for every event. A full list of the  $N_{\text{obs}} = 13$  observables we use is given in section 8.2.2. More precisely, in this scenario the information for each event  $e_h$  is given by a vector

$$\vec{x}_h = \{\mathcal{O}_1(e_h), \dots, \mathcal{O}_{N_{\text{obs}}}(e_h)\}. \quad (8.10)$$

The available information for an experimental run is therefore represented by a collection of all  $\vec{x}_h$ , giving the input vector  $\vec{X}_{\text{data}} = \{\vec{x}_1, \dots, \vec{x}_{N_{\text{data}}}\}$ . Similarly, the  $N_{\text{sim}}$  baseline simulation model events are collected in the baseline simulation model input vector,  $\vec{X}_{\text{sim}} = \{\vec{x}_1, \dots, \vec{x}_{N_{\text{sim}}}\}$ .

The Step 1 classifier is trained using the standard Binary Cross-Entropy (BCE) loss function, which for balanced classes is

$$\mathcal{L}_{\text{unbin}} = -\frac{1}{N_{\text{sim}}} \sum_{h=1}^{N_{\text{sim}}} \ln(1 - y(\vec{x}_h)) - \frac{1}{N_{\text{data}}} \sum_{h=1}^{N_{\text{data}}} \ln(y(\vec{x}_h)), \quad (8.11)$$

where  $y(\vec{x}_h) \in [0, 1]$  is the output of a classifier for the input vector  $\vec{x}_h$ , and  $N_{\text{sim}}$  and  $N_{\text{data}}$  are the number of training samples per class, which we assume to be equal in eq. (8.11). If needed, we weight the classes to ensure that each class has the same weighted number of events. This choice of the loss function guarantees that when the classifier training converges, we can obtain a good estimator for the event weight of eq. (8.8) from the output of the classifier,

$$w_{\text{class}}(e_h) \equiv \frac{y(\vec{x}_h)}{1 - y(\vec{x}_h)}, \quad (8.12)$$

so that  $w_{\text{exact}}(e_h) \approx w_{\text{class}}(e_h)$ .

**The binned scenario.** Here, the classifier input is still the vectors of observables for each event,  $\vec{x}_h$  of eq. (8.10). However, measured data is partitioned into disjoint bins  $n_i$  of observable  $\mathcal{O}_i$  values. The classifier is trained using a loss function constructed from the binned measured data and the reweighted baseline simulation model,

$$\mathcal{L}_{\text{bin}} = \sum_{\mathcal{O}_i} \frac{N_{\text{data}}}{n_i} \sum_{k=1}^{n_i} \frac{(p_k^{\mathcal{O}_i} - \bar{p}_k^{\mathcal{O}_i}(y))^2}{p_k^{\mathcal{O}_i}}, \quad (8.13)$$

where the summation is over all the observables up to index  $N_{\text{obs}}$ . The classifier attempts to minimize the difference between the measured distributions and the reweighted distributions of the baseline simulation model. That is, for each observable  $\mathcal{O}_i$ , the fractions of events  $p_k^{\mathcal{O}_i}$  in a particular bin are given by,

$$\{p_1^{\mathcal{O}_i}, \dots, p_{n_i}^{\mathcal{O}_i}\} = \frac{1}{N_{\text{data}}} \{N_1^{\text{data}}|_{\mathcal{O}_i}, \dots, N_{n_i}^{\text{data}}|_{\mathcal{O}_i}\}, \quad (8.14)$$

and similarly for the expected fractions of events,  $\bar{p}_k^{\mathcal{O}_i}$ , estimated from the baseline simulation model. For this, each event  $e_h$  is weighted with  $w_{\text{class}}(e_h) = y(\vec{x}_h)/(1 - y(\vec{x}_h))$ , so that  $\mathcal{L}_{\text{bin}}$  is minimized for  $w_{\text{class}}(e_h) \approx w_{\text{exact}}(e_h)$ . For instance, if the observable  $\mathcal{O}_i$  is the charged multiplicity,  $n_{\text{ch}}$ , then  $N_1^{\text{data}}|_{n_{\text{ch}}}$  gives the number of events in the run that have  $n_{\text{ch}} = 2$ ,  $N_2^{\text{data}}|_{n_{\text{ch}}}$  the number of events in the run that have  $n_{\text{ch}} = 4$ , etc., and similarly for simulation, but now for weighted distributions.

By construction, the loss function  $\mathcal{L}_{\text{bin}}$  in eq. (8.13) again guarantees that the output of a converged classifier can be used to approximate the event weights of eq. (8.8), using the output of the classifier from eq. (8.12). The use of classifiers for reweighting simulated events so that

their distributions match the measured event distributions is a common technique (see, *e.g.*, [392, 397, 419, 420]). The novelty of the current approach is in establishing a relationship between event weights and the underlying fragmentation function, made possible via the application of eq. (8.20). This is exploited in Step 2 to infer an estimator for  $w_s$ .

### 8.2.1.2 Step 2: inference of fragmentation weights

The goal of this step is to construct the appropriate single emission weights  $w_s$  such that the probability for each string break that produces the emission,  $p_{\text{data}}(\vec{S}_{hcb})$  of eq. (8.7), will reproduce data by reweighting the baseline simulation model string breaks. However, there are two complications. First, in PYTHIA, the baseline fragmentation history also contains the string fragmentation chains that do not pass the `finalTwo` filter (as explained in chapter 6). That is, the `finalTwo` filter divides the fragmentation chains  $\{\vec{S}_{hc}\}$  in two: chains that pass the `finalTwo` filter, a set consisting of  $\{\vec{S}_{hc}^{\text{Accepted}}\}$ , and those that do not, set  $\{\vec{S}_{hc}^{\text{Rejected}}\}$ . Second, the measurable event quantities, *i.e.*, the momenta of the outgoing hadrons of  $e_h$ , given by eq. (6.36), form an unordered list, since there is no information about the sequence of causally disconnected string breaks. This means that two fragmentation chains,  $\vec{S}_{hN_h}$  and  $\vec{S}'_{hN_h}$ , which give rise to exactly the same hadron four momenta except with a different order of emissions, are physically indistinguishable. That is, the two fragmentation chains give rise to the same observable event,  $e_h = e(\vec{S}_{hN_h}) = e(\vec{S}'_{hN_h})$ .

The probability for an event in the baseline simulation model is thus given by

$$\begin{aligned} p_{\text{sim}}(e_h) &= \left( \sum_{N_h=1}^{\infty} (p_{\text{sim}}^{\text{Rejected}})^{N_h-1} \right) \times \left( \sum_{e(\vec{S}_{hN_h})=e_h} p_{\text{sim}}(\vec{S}_{hN_h}) \right) \\ &= \frac{1}{1 - p_{\text{sim}}^{\text{Rejected}}} \sum_{e(\vec{S}_{hN_h})=e_h} p_{\text{sim}}(\vec{S}_{hN_h}) = \frac{1}{p_{\text{sim}}^{\text{Accepted}}} \sum_{e(\vec{S}_{hN_h})=e_h} p_{\text{sim}}(\vec{S}_{hN_h}), \end{aligned} \quad (8.15)$$

where the second summation of the first line is over the set of accepted fragmentation chains that lead to the same observable event  $e_h$ . The total probability of producing the event  $e_h$  also contains the probability of rejecting fragmentation chains. Since the specifics of the rejected chains do not matter, as they are statistically independent of the accepted chain, the accepted chain has no dependence on past rejected chain(s) and the probability that enters  $p_{\text{sim}}(e_h)$  is the probability of rejecting *any* chain. This is given by summing over the set of rejected chains,

$$p_{\text{sim}}^{\text{Rejected}} = \sum_{\vec{S}_{jk} \in \{\vec{S}_{hc}^{\text{Rejected}}\}} p_{\text{sim}}(\vec{S}_{jk}), \quad (8.16)$$

where the summation over  $N_h$  in eq. (8.15) counts the number of fragmentation chains that are rejected in the simulation before  $\vec{S}_{hN_h}$  is accepted.<sup>7</sup> Similarly, the total probability for the accepted fragmentation chains is given by

$$p_{\text{sim}}^{\text{Accepted}} = 1 - p_{\text{sim}}^{\text{Rejected}} = \sum_{\vec{S}_{jk} \in \{\vec{S}_{hc}^{\text{Accepted}}\}} p_{\text{sim}}(\vec{S}_{jk}), \quad (8.17)$$

Note that the probabilities for individual fragmentation chains are products of string breaks,

$$p_{\text{sim}}(\vec{S}_{hc}) = \prod_{b=1}^{N_b} p_{\text{sim}}(\vec{s}_{hcb}). \quad (8.18)$$

We use the label ‘‘data’’ for the probabilities that describe the measured distributions and the equivalent expressions of eqs. (8.15) to (8.18), *i.e.*,  $p_{\text{data}}(e_h)$ ,  $p_{\text{data}}^{\text{Rejected}}$ ,  $p_{\text{data}}^{\text{Accepted}}$  and  $p_{\text{data}}(\vec{S}_{hc})$ , respectively. With real measured data, these probabilities may only be approximate, but for the synthetic data that we use as an example in this paper, we know these exact probabilities must exist. Below, we describe how the best estimate for  $p_{\text{data}}(\vec{s}_{hcb})$  is found.

For Step 2, rather than directly working with  $p_{\text{data}}(\vec{s}_{hcb})$  and  $p_{\text{sim}}(\vec{s}_{hcb})$ , we introduce weights by which the baseline simulation model results need to be reweighted in order to match the measured data. The exact weight for a single emission is given by, see also eq. (8.9),

$$w_s^{\text{exact}}(\vec{s}_{hcb}) = \frac{p_{\text{data}}(\vec{s}_{hcb})}{p_{\text{sim}}(\vec{s}_{hcb})}, \quad (8.19)$$

and the corresponding weight for the event  $e_h$  is given by<sup>8</sup>

$$w_{\text{exact}}(e_h) = \frac{p_{\text{sim}}^{\text{Accepted}}}{p_{\text{data}}^{\text{Accepted}}} \langle w_{\text{exact}}(\vec{S}_{hN_h}) \rangle_{e(\vec{S}_{hN_h})=e_h}, \quad (8.20)$$

with

$$w_{\text{exact}}(\vec{S}_{hN_h}) = \prod_{b=1}^{N_{\text{had}}-2} w_s^{\text{exact}}(\vec{s}_{hN_h b}), \quad (8.21)$$

where  $N_{\text{had}}$  is the number of hadrons in the event. Here, the number of hadrons is two larger than the number of string breaks in the accepted simulation chain due to `finalTwo`, *i.e.*, in our notation  $N_{\text{had}} - 2 = N_{h,N_h}$ . In eq. (8.20), the product of single weights is averaged over fragmentation chains that produce the same event, see also eq. (8.15).

To achieve  $w_{\text{exact}}(\vec{s}_{hcb}) \approx w_{\text{infer}}(\vec{s}_{hcb})$ , several approximations can be made. First, it is unlikely to encounter two fragmentation chains simulated with very similar observable kinematics. In

---

<sup>7</sup>Note that the  $N_h$  index for  $\vec{S}_{hN_h}$  in eq. (8.15) is a dummy index, and thus the  $p_{\text{Rejected}}$  is truly independent from the second term in eq. (8.15).

<sup>8</sup>In a Bayesian context, the weight in terms of  $e$  is the evidence ratio between models obtained by marginalizing over all possible histories  $h$  that are compatible with  $e$ .

HOMER we can thus replace the average in eq. (8.20) with the weight for a single fragmentation chain<sup>9</sup>

$$w_{\text{infer}}(e_h, \theta) = \frac{p_{\text{sim}}^{\text{Accepted}}}{p_{\text{infer}}^{\text{Accepted}}(\theta)} w_{\text{infer}}(\vec{S}_{hN_h}, \theta), \quad (8.22)$$

where

$$w_{\text{infer}}(\vec{S}_{hN_h}, \theta) = \prod_{b=1}^{N_{\text{had}}-2} w_s^{\text{infer}}(\vec{s}_{hN_h b}, \theta). \quad (8.23)$$

To find the form of  $w_{\text{infer}}(e_h, \theta)$ , we parameterize  $w_s^{\text{infer}}$  using a neural network  $g$  with parameters  $\theta$ ,

$$w_s^{\text{infer}}(\vec{s}_{hcb}, \theta) = g_\theta(\vec{s}_{hcb}). \quad (8.24)$$

The two acceptance probabilities in eq. (8.22) are therefore given by

$$p_{\text{sim}}^{\text{Accepted}} = \frac{N_{\text{Accepted}}}{N_{\text{tot}}}, \quad p_{\text{infer}}^{\text{Accepted}}(\theta) = \frac{\sum_{\vec{S}_{jk} \in \{\vec{S}_{hc}^{\text{Accepted}}\}} w_{\text{infer}}(\vec{S}_{jk}, \theta)}{\sum_{\vec{S}_{jk} \in \{\vec{S}_{hc}\}} w_{\text{infer}}(\vec{S}_{jk}, \theta)}, \quad (8.25)$$

where  $N_{\text{Accepted}} = N_{\text{sim}}$  is the number of accepted fragmentation chains in the simulation with  $N_{\text{sim}}$  events, while  $N_{\text{tot}}$  is the total number of chains in the fragmentation history, including the rejected ones.

The neural network of eq. (8.24) takes as input the seven-dimensional string break vector,  $\vec{s}_{hcb}$  given by eq. (6.32), and outputs the weight  $w_s^{\text{infer}}$  for this string break. Since the event weight,  $w_{\text{infer}}(e_h, \theta)$ , involves products of multiple weights, see eq. (8.22), it is easier to learn the logarithm of  $w_s$ . In fact, it is numerically expedient to introduce  $\ln g_\theta(\vec{s})$  as a difference of two neutral networks

$$\ln g_\theta(\vec{s}) = g_1(z, \Delta \vec{p}_T, m, \text{fromPos}, \vec{p}_T^{\text{string}}; \theta) - g_2(\vec{p}_T^{\text{string}}; \theta), \quad (8.26)$$

where  $\theta$  denotes the parameters of the neural network.

This choice of parameterization is not strictly necessary, however, it does allow us to impose the conditional structure eq. (8.6) explicitly in the loss function, see discussion surrounding eq. (8.33) below. The estimator for the fragmentation chain weight,  $w_{\text{infer}}(\vec{S}_{hN_h}, \theta)$ , is obtained by combining all individual  $g_\theta$  contained in that chain, *c.f.* eq. (8.23). We do this by treating each chain  $\vec{S}_{hc}$  as a string-break point cloud, not to be confused with the hadron-level point cloud discussed in section 8.2.1.1, and implementing eq. (8.26) as a module in a Message-Passing Graph Neural Network (MPGNN) written using the PYTORCH GEOMETRIC library[421, 422].

---

<sup>9</sup>Approximating eq. (8.20) with eq. (8.22), while accurate enough for the case of  $q\bar{q}$  strings of fixed energy, was found empirically to break down when gluons are added to the string. A modified version of HOMER will therefore be needed in order to handle more general string hadronization cases [11].

The loss function for  $g_\theta$  has two terms

$$\mathcal{L}_{\text{infer}} = \mathcal{L}_C + \mathcal{L}_{12}, \quad (8.27)$$

where  $\mathcal{L}_C$ , given in eq. (8.31) below, ensures that the event-level weights  $w_{\text{infer}}(e_h, \theta)$  reproduce the weights  $w_{\text{class}}(e_h)$  of eq. (8.8) well, which were learned in Step 1. The second term,  $\mathcal{L}_{12}$ , given in eq. (8.33) below, is a regularization term that ensures a proper convergence of the  $g_1$  and  $g_2$  NNs towards a solution that satisfies the conditional structure imposed by the string breaks within the Lund string model. In the remainder of this section, we motivate the forms of these two loss functions.

The main ingredient that makes Step 2 of the HOMER method possible is that in Step 1 we obtained a good approximation for the event weights,  $w_{\text{class}}(e_h)$ . All we need to ensure in Step 2 is that  $w_{\text{infer}}(e_h, g_\theta)$  reproduces well  $w_{\text{class}}(e_h)$ , and thus  $w_{\text{exact}}(e_h)$ , by minimizing the appropriate loss function. One possibility is to treat this as a regression problem and minimize an MSE loss

$$\mathcal{L}_R = \frac{1}{N_{\text{sim}}} \sum_{h=1}^{N_{\text{sim}}} (w_{\text{class}}(e_h) - w_{\text{infer}}(e_h, g_\theta))^2. \quad (8.28)$$

However, for a finite dataset the MSE loss may not force  $w_{\text{infer}}(e_h, g_\theta)$  to behave as a likelihood ratio. A conceptually clearer approach is to view the problem of constructing  $w_{\text{infer}}(e_h, \theta)$  as yet another classification problem, where the learnable function observes both data and simulation to obtain the necessary likelihood-ratio. If we had access to histories for both simulation and measurements we could obtain the NN parameters in  $g_\theta$  by minimizing the BCE loss

$$\mathcal{L}_C^{\text{BCE}} = -\mathbb{E}_{\text{sim}} \left[ \ln \left( \frac{1}{1 + w_{\text{infer}}(e_h, g_\theta)} \right) \right] - \mathbb{E}_{\text{data}} \left[ \ln \left( \frac{w_{\text{infer}}(e_h, g_\theta)}{1 + w_{\text{infer}}(e_h, g_\theta)} \right) \right], \quad (8.29)$$

where the two expectation values  $\mathbb{E}$  are over simulation and data, respectively. The above loss function is minimized when  $w_s^{\text{infer}}(\vec{s}_{hcb}) = p_{\text{data}}(\vec{s}_{hcb})/p_{\text{sim}}(\vec{s}_{hcb})$ . While the fragmentation histories are not accessible in data, the expectation value over data in eq. (8.29) can be approximated through the use of the event weights that were learned in Step 1. That is, for any observable  $\mathcal{O}$  the expectation value over events is given by

$$\mathbb{E}_{\text{data}}[\mathcal{O}(e_h)] = \mathbb{E}_{\text{sim}}[w(e_h)\mathcal{O}(e_h)]. \quad (8.30)$$

This allows us to rewrite the BCE loss function as

$$\mathcal{L}_C = -\frac{1}{N_{\text{sim}}} \sum_{h=1}^{N_{\text{sim}}} \left( \ln \left( \frac{1}{1 + w_{\text{infer}}(e_h, g_\theta)} \right) + w_{\text{class}}(e_h) \ln \left( \frac{w_{\text{infer}}(e_h, g_\theta)}{1 + w_{\text{infer}}(e_h, g_\theta)} \right) \right), \quad (8.31)$$

which is minimized when  $w_{\text{infer}}(e_h, g_\theta) = w_{\text{class}}(e_h)$ . That is, we can achieve the same objective as the regression problem by taking the expectation value over simulated events, where we consider

each event twice,<sup>10</sup> once unweighted and then once again weighted by  $w_{\text{class}}$ . This approach regularizes the problem by ensuring that the likelihood ratio behaves well both for simulated events and for measured events, where for the latter the distributions are approximated via the reweighted simulations.

The second term in the loss function,  $\mathcal{L}_{12}$ , treats  $g_1$  and  $g_2$  differently, and ensures that the individual string break weights,  $w_s^{\text{infer}}(\vec{s}_{hcb}, \theta)$ , are given by the ratios of conditional probabilities, see also eq. (8.19),

$$w_s^{\text{infer}}(\vec{s}_{hcb}, \theta) \approx w_s^{\text{exact}}(\vec{s}_{hcb}) = \frac{p_{\text{data}}\left(p(\{z, \Delta\vec{p}_T, m, \text{fromPos}\}_{h,c,b} | \{\vec{p}_T^{\text{string}}\}_{h,c,b})\right)}{p_{\text{sim}}\left(p(\{z, \Delta\vec{p}_T, m, \text{fromPos}\}_{h,c,b} | \{\vec{p}_T^{\text{string}}\}_{h,c,b})\right)}. \quad (8.32)$$

The form of the loss function that ensures this property is given by,

$$\mathcal{L}_{12} = - \sum_{\vec{s}_{hbc}} \left( \ln \left( \frac{1}{1 + \exp [g_2(\vec{s}_{hbc})]} \right) + \exp [g_1(\vec{s}_{hbc})] \ln \left( \frac{\exp [g_2(\vec{s}_{hbc})]}{1 + \exp [g_2(\vec{s}_{hbc})]} \right) \right). \quad (8.33)$$

In the limit of infinite baseline model simulation, *i.e.*, training data,  $\mathcal{L}_{12}$  is minimized by  $g_1$  and  $g_2$  that satisfy

$$\begin{aligned} \exp [g_2(\vec{p}_T^{\text{string}})] &= \int d\Omega p_{\text{sim}}(z, \Delta\vec{p}_T, m, \text{fromPos} | \vec{p}_T^{\text{string}}) \\ &\quad \times \exp [g_1(z, \Delta\vec{p}_T, m, \text{fromPos}, \vec{p}_T^{\text{string}})], \end{aligned} \quad (8.34)$$

where  $\Omega$  denotes the variables that are being sampled, *i.e.*, all the variables except the transverse momentum of the string,  $\vec{p}_T^{\text{string}}$ .

In the infinite simulation sample limit, the following relations hold,

$$\exp [g_1(z, \Delta\vec{p}_T, m, \text{fromPos}, \vec{p}_T^{\text{string}})] \rightarrow \frac{p_{\text{class}}(\{z, \Delta\vec{p}_T, m, \text{fromPos}, \vec{p}_T^{\text{string}}\})}{p_{\text{sim}}(\{z, \Delta\vec{p}_T, m, \text{fromPos}, \vec{p}_T^{\text{string}}\})}, \quad (8.35a)$$

$$\exp [g_2(\vec{p}_T^{\text{string}})] \rightarrow \frac{p_{\text{class}}(\vec{p}_T^{\text{string}})}{p_{\text{sim}}(\vec{p}_T^{\text{string}})}, \quad (8.35b)$$

$$\exp (g_1 - g_2) \rightarrow w_s, \quad (8.35c)$$

where  $p_{\text{class}}$  refers to the probability distributions obtained with  $w_s^{\text{class}}$  such that we have  $w_{\text{infer}}(e_h, g_\theta) = w_{\text{class}}(e_h)$  and  $p_{\text{class,sim}}(\vec{p}_T^{\text{string}})$  are the marginal distributions over the transverse momenta of the string. These are obtained by integrating out all the other variables. Equation (8.35c) is the limit of  $\mathcal{L}_C$ , and  $\mathcal{L}_{12}$  enforces eq. (8.34) which produces the limits of eqs. (8.35a) and (8.35b). Combined, this results in the limiting behavior for  $\mathcal{L}_{\text{infer}}$ , the loss function of eq. (8.27). We observe that in this infinite simulation sample limit, the parameterization of eq. (8.26) and the presence of the  $\mathcal{L}_{12}$  term in  $\mathcal{L}_{\text{infer}}$  ensure that we are computing

---

<sup>10</sup>A feature of using the same data twice is that statistical fluctuations cancel out, see, *e.g.*, [423].

the weight between two conditional distributions, as dictated by how PYTHIA samples string breaks, avoiding other more expensive solutions, see *e.g.*, [424].

### 8.2.1.3 Step 3: HOMER output

Once the weights for each individual string fragmentation  $w_s^{\text{infer}}(\vec{s}_{hcb}, \theta)$  are known, it is straightforward to reweight any baseline simulation model fragmentation history. The output of HOMER is the weight, which is a product of the weights for all the string fragmentations in the baseline model simulation fragmentation history, including the rejected string fragmentations,

$$w_{\text{HOMER}}(\vec{\mathbf{S}}_h) = \prod_{c=1}^{N_h} \prod_{b=1}^{N_{hc}} w_s^{\text{infer}}(\vec{s}_{hcb}, \theta), \quad (8.36)$$

where  $N_{hc}$  are the string breaks contained in chain  $c$ . Compared to the event weight  $w_{\text{exact}}(e_h)$  of eq. (8.20), which contains averaging over histories that lead to the same event, the HOMER output is a weight for each individual fragmentation history. The event weight is the average of the compatible history weights. That is,

$$w_{\text{exact}}(e_h) \simeq w_{\text{HOMER}}(e_h) \equiv \langle w_{\text{HOMER}}(\vec{\mathbf{S}}_h) \rangle_{e(\vec{\mathbf{S}}_h)=e_h}. \quad (8.37)$$

Note that the event weight inferred in Step 2, *i.e.*,  $w_{\text{infer}}(e_h)$  of eq. (8.22), differs from  $w_{\text{HOMER}}(\vec{\mathbf{S}}_h)$ , because of averaging over rejected fragmentations. That is,  $w_{\text{infer}}(e_h)$  in eq. (8.22) contains the ratio  $p_{\text{sim}}^{\text{Accepted}}/p_{\text{infer}}^{\text{Accepted}}(\theta)$ , while  $w_{\text{HOMER}}(\vec{\mathbf{S}}_h)$  is a weight for a particular instance of a simulated fragmentation history. Once averaged over all fragmentation histories that produce the same event, the two weights  $w_{\text{infer}}(e_h)$  and  $w_{\text{HOMER}}(\vec{\mathbf{S}}_h)$  coincide. However, the weight  $w_{\text{HOMER}}(\vec{\mathbf{S}}_h)$  can be calculated from a single baseline simulation model fragmentation history, *i.e.*, for our baseline simulation model this weight can be calculated directly from a single PYTHIA event. This is critical for any practical application of the method, where the correction can be applied on an event by event level for the baseline simulation model.

More importantly, as we have shown, the expectation values that enter the calculation of event weights can be estimated efficiently using simulated Monte Carlo samples where we have access to the simulated histories. This allows us to accurately estimate the new fragmentation function *without explicit access to the analytic form of the baseline fragmentation function*.

That is, the new fragmentation function  $f_{\text{data}}$  is implicitly defined through  $w_s^{\text{infer}}(\vec{s}_{hcb}, \theta)$ . The value of  $f_{\text{data}}$  for a particular bin in the lightcone momentum fraction,  $z \in [z_i, z_{i+1})$ , and in the squared transverse mass,  $m_T^2 \in [m_{T,j}^2, m_{T,j+1}^2)$ , can be obtained by reweighting a sample of string breaks  $\vec{s}_{hcb}$  that were simulated using the baseline model. Explicitly, we have

$$f_{\text{data}}(z_i, m_{T,j}^2) = \mathbb{E}_{\vec{s}_{hcb} \sim \text{sim}} [w_s^{\text{infer}}(\vec{s}_{hcb})] \Big|_{z \in [z_i, z_{i+1}), m_T^2 \in [m_{T,j}^2, m_{T,j+1}^2]}, \quad (8.38)$$

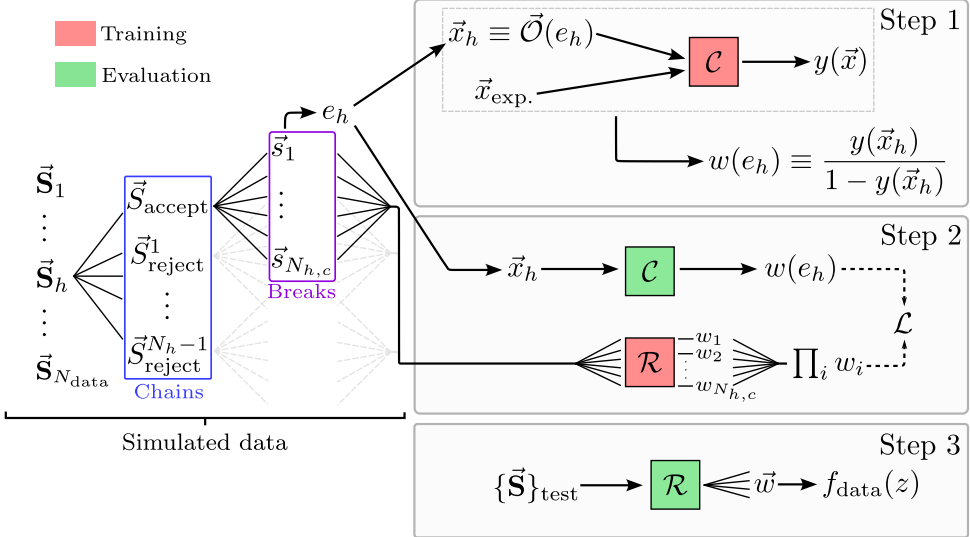


FIGURE 8.4: Summary flowchart of the HOMER method. Here  $\mathcal{C}$  is the event-level classifier and  $\mathcal{R}$  is the weight-level regressor that transforms the event-level weights into string break-level weights.

where the averaging of the weights  $w_s^{\text{infer}}$  is performed only over the string breaks that correspond to the particular  $(z, m_T^2)$  bin. In section 7.4.3 we also consider  $\langle f(z) \rangle$ , the fragmentation function averaged over all the sampled  $m_T^2$  values, which is thus given by

$$\langle f_{\text{data}}(z_i) \rangle = \mathbb{E}_{\vec{s}_{hcb} \sim \text{sim}} [w_s^{\text{infer}}(\vec{s}_{hcb})] \Big|_{z \in [z_i, z_{i+1}]} . \quad (8.39)$$

Note that in both of the above expressions the only requirement on the baseline fragmentation function is that it can be sampled.

We emphasize that we are exploiting the fact that, for simulated events, we have both the underlying fragmentation history, as produced by the model, and observable quantities that can be compared with measurements. If we learn how to reweight a given history to match the measured event distribution, we are effectively updating the fragmentation model.

To recapitulate, HOMER learns a data-driven fragmentation function  $f_{\text{data}}(z)$  by estimating the likelihood ratio  $w_s$  for each string break, eq. (8.19), which depends on the yet-to-be-determined  $f_{\text{data}}(z)$  and the baseline simulation model fragmentation function  $f_{\text{sim}}(z)$ . The HOMER method divides the task of learning  $f_{\text{data}}(z)$  into three steps. In Step 1, event-level observables  $\vec{x}_h = \vec{x}_h(e_h)$  are used to estimate the event-level weights  $w_{\text{exact}}(e_h)$ . In Step 2, the event-level weights  $w_{\text{exact}}(e_h)$  are used to train two neural networks  $g_1$  and  $g_2$ . These two neural nets then provide  $w_s$  for each string break such that the reproduced  $w(e_h)$  best matches the target value,  $w_{\text{exact}}(e_h)$ . The string break weights are then used to reweight the baseline simulation model output, including rejected fragmentations, in Step 3. The loss function that is used in the training of the  $g_{1,2}$  networks is given in eqs. (8.27), (8.31) and (8.33). A summary flowchart of the HOMER method can be seen in fig. 8.4.

### 8.2.2 High-level observables

The high-level observables that we use as inputs to the classifier in Step 1 are the same 13 high-level observables that were used in the Monash tune [31], though now only for light flavors:

- Event shape observables:  $1 - T$ ,  $B_T$ ,  $B_W$ ,  $C$  and  $D$ ; their definitions are collected in appendix D.
- Particle multiplicity  $n_f$ , the total number of visible particles in the event, and charged particle multiplicity  $n_{\text{ch}}$ , the number of charged particles in the event.
- The first three moments of the  $|\ln x|$  distribution, the second and the third moment are computed around the mean, where  $x$  is the momentum fraction of a particle. Explicitly  $x = 2|\vec{p}|/\sqrt{s}$  where  $\sqrt{s}$  is the center of mass of the collision and  $\vec{p}$  the momentum of the particle. This is computed both for all visible particles,  $\ln x_f$ , and for just the charged particles,  $\ln x_{\text{ch}}$ .

These 13 high-level observables must all be calculated on an event-by-event basis. However, experimental measurements are currently only available for aggregate distributions of these observables, *i.e.*, histograms. While in ref. [11], both binned and unbinned observables are considered in the HOMER pipeline, below in section 8.2.3 focus on unbinned observables to showcase the impressive performance. For many more details and a thorough analysis of the HOMER method in the context of binned, unbinned, and point-cloud-based observables, please see ref. [11].

### 8.2.3 Extracting fragmentation functions with HOMER: unbinned high-level observables

To showcase the use of the HOMER method we used PYTHIA to generate two different sets of  $2 \times 10^6$  events, in each case hadronizing a  $u\bar{u}$  string with a center-of-mass frame energy of  $\sqrt{s} = 90$  GeV, while permitting only emission of pions for simplicity. The two sets were generated using two different sets of values for the Lund parameters. The baseline simulation model dataset was generated using the default Monash values for the parameters,  $a_{\text{sim}} = 0.68$ ,  $b = 0.98$ ,  $\sigma_T = 0.335$ , while the synthetic measured data were generated for a changed value of  $a_{\text{data}} = 0.30$ , with all the other parameters kept the same. The choice of parameters was based on the benchmarks studied in ref. [7], where we found the reweighting from “sim” to “data” for this change in the Lund  $a$  parameter to be non-trivial yet still achievable with good coverage, albeit with low effective statistics. Both the synthetic measured data and baseline simulation model datasets were generated using PYTHIA, in order to be able to perform a closure test. In future applications, only the baseline simulation model dataset need be generated using PYTHIA, or

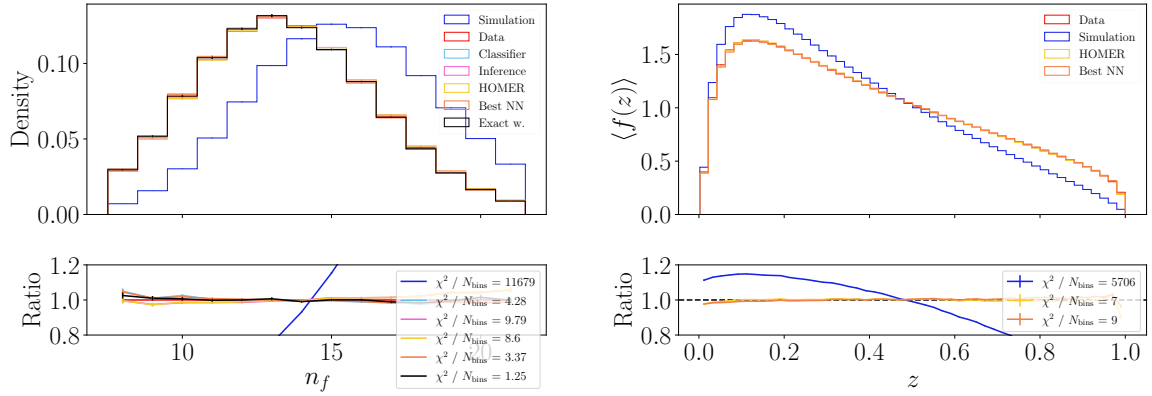


FIGURE 8.5: **Left:** Performance of the Step 1 classifier depicted in the context of reweighting performance of the total hadron multiplicity,  $n_f$ . We see very nice agreement between the HOMER-reweighted (yellow) simulation (blue) compared to the desired data distribution (red). For more details on the curves labeled ‘Classifier’, ‘Inference’, ‘Best NN’ see ref. [27]. **Right:** Distributions for the fragmentation function averaged over all string break variables except (left)  $z$ . We see that the HOMER extracted fragmentation function (yellow) agree nicely with the fragmentation function used to generate the synthetic data (red). All weights are from the model trained with the unbinned high-level observables.

another generator of choice, while the actual experimentally measured observables will be used for Step 1.

The two  $2 \times 10^6$  event datasets were both split in half, with  $N_{\text{train}} = 10^6$  and  $N_{\text{test}} = 10^6$  events in each dataset used for training and testing, respectively. All the figures below were obtained using the testing datasets, which were also used to verify the absence of any significant overfitting both in Step 1 and Step 2 of the HOMER method. In more realistic applications, where HOMER is to be tuned to data instead of performing a closure test using simulated datasets, the datasets should be divided into three subsets for training, testing and visualization. This will avoid overfitting of the test dataset.

### 8.2.3.1 Results: Steps 1 (classifier) and 2 (regressor)

The accuracy of the event-level weights produced from the Step 1 classifier trained on unbinned event-by-event high-level observables can be seen in fig. 8.5 left, where we show the reweighted prediction for hadron multiplicity using the Step 1 classifier weights. Excellent agreement can be seen between reweighted multiplicity distribution using the Step 1 classifier weights (yellow) and the multiplicity distribution given by the ‘data’ (red). The agreement is further emphasized by comparing the reduced  $\chi^2$ ’s of the distributions using the the classifier (yellow) versus exact weights (black).

The Step 2 HOMER fragmentation function can be seen in fig. 8.5 right. We see near perfect agreement between the HOMER extracted fragmentation function (yellow) and the fragmentation function used to generate the synthetic data (red). As mentioned previously, to see additional validation and in depth comparisons between binned, unbinned, and point-cloud-based observables using the HOMER method, please see ref. [27].

We now turn to key modifications of the HOMER method necessary for the successful extraction of data-driven fragmentation functions in string configurations containing gluons [11].

#### 8.2.4 HOMER with gluons

Two serious complications arise with the addition of gluons (see section 6.3.3 for a brief description of how gluons are incorporated into the Lund string model). First, the information gap between event-level and fragmentation-level information is increased. That is, the relation between  $f(z)$  and the measurable quantities is more complicated for strings with gluons, even if the kinematics of the string and the number of gluons are held fixed. Second, introducing a variable number of gluons and kinks on the string, with varying kinematics, means that the treatment of the `finalTwo` filter must be reevaluated. Step 2 of the HOMER method must be modified to handle these complications.

##### 8.2.4.1 Increase in information gap and decrease in effective statistics

First, we consider the case of a string of fixed kinematics with a fixed number of gluons. The presence of multiple string regions, defined by the gluon kinks, leads to a more complex relationship between fragmentation-level variables, mainly the individual  $z$  values per emission, and the event-level variables, the hadron four-momenta. This has practical consequences; as the event-level variables become less predictive, the mean-squared-error between  $w_{\text{class}}$  and  $w_{\text{HOMER}}$  increases

To address this problem, we approximate the expectation value in eq. (8.20) with an average over a neighborhood of fragmentation chains,

$$\langle w_{\text{infer}}(\vec{S}_{jN_j}) \rangle_{e_j=e_h} \approx \frac{\sum_{\vec{S}_{jN_j}} w_{\text{infer}}(\vec{S}_{jN_j}) \mathcal{N}_{\sigma_s}(|\vec{t}_h - \vec{t}_j|)}{\sum_{\vec{S}_{jN_j}} \mathcal{N}_{\sigma_s}(|\vec{t}_h - \vec{t}_j|)}, \quad (8.40)$$

where  $\mathcal{N}_{\sigma_s}$  is a Gaussian function of width  $\sigma_s$  and  $\vec{t}_h$  is a scaled vector of high-level observables  $\vec{x}_h$  for event  $e_h$

$$\vec{t}_h = \frac{\vec{x}_h - \min[\{\vec{x}_h\}]}{\max[\{\vec{x}_h\}] - \min[\{\vec{x}_h\}]}, \quad (8.41)$$

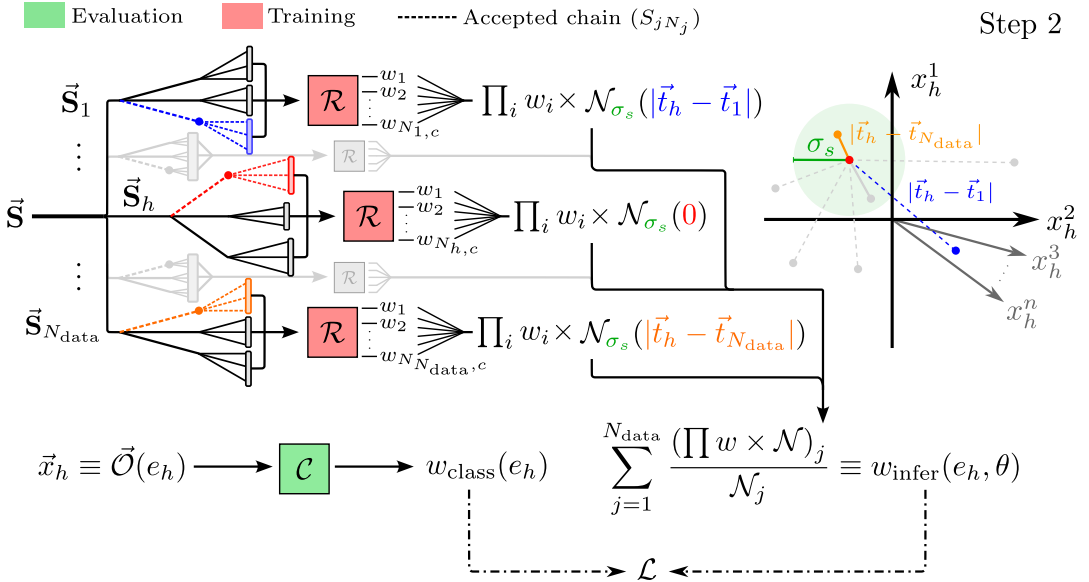


FIGURE 8.6: Flowchart of the modified Step 2 for the HOMER method with gluons.

such that each component of  $\vec{t}$  is between 0 and 1.<sup>11</sup> The similarity between two events  $e_1$  and  $e_2$  is thus measured by the distance  $|\vec{t}_1 - \vec{t}_2|$ , and the averaging of eq. (8.40) is performed over events that are within  $\sigma_s$  of  $e_h$  using this metric. This introduces some bias in the estimate of  $\langle w_{\text{infer}}(\vec{S}_{j N_j}) \rangle_{e_j = e_h}$ , which we find to be negligible as long as  $\sigma_s$  is sufficiently small.

With this approximation, the Step 2 estimate of  $w_{\text{infer}}(e_h, \theta)$  of eq. (8.20) is replaced by a smearing procedure

$$w_{\text{infer}}(e_h, \theta) = \frac{p_{\text{sim}}^{\text{Accepted}}}{p_{\text{data}}^{\text{Accepted}}(\theta)} \frac{\sum_{\vec{S}_{j N_j}} w_{\text{infer}}(\vec{S}_{j N_j}, \theta) \mathcal{N}_{\sigma_s}(|\vec{t}_h - \vec{t}_j|)}{\sum_{\vec{S}_{j N_j}} \mathcal{N}_{\sigma_s}(|\vec{t}_h - \vec{t}_j|)}, \quad (8.42)$$

while the rest of Step 2 remains unchanged. Here,  $w_{\text{infer}}(\vec{S}_{h N_h}, \theta)$  is still given by a product of single emission weights from eq. (8.23).

#### 8.2.4.2 Varying initial states

Strings of varying kinematics and with varying numbers of gluons introduce new challenges. Since the `finalTwo` efficiency depends on these initial state quantities, it is no longer practical to calculate  $p_{\text{sim}}^{\text{Accepted}}$  in eq. (8.42) once for each possible initial state. Instead, the smearing procedure is modified to estimate also the `finalTwo` efficiency by averaging over complete

<sup>11</sup>Here,  $\min[\{\vec{x}_h\}]$  denotes a vector where each component is the minimum of each high-level observable contained in  $\vec{x}_h$ , and  $\max[\{\vec{x}_h\}]$  a vector containing each maximum. The high-level observables that we use are listed in section 7.4.3.

simulated histories, including the rejected chains

$$w_{\text{infer}}(e_h, \theta) = \frac{\sum_j w_{\text{HOMER}}(\vec{S}_j) \mathcal{N}_{\sigma_s}(|\vec{t}_h - \vec{t}_j|)}{\sum_j \mathcal{N}_{\sigma_s}(|\vec{t}_h - \vec{t}_j|)}, \quad (8.43)$$

where the summation is over simulated histories. Specifically, in eq. (8.42)  $w_{\text{infer}}$  is only calculated using the final accepted fragmentation chain  $\vec{S}_{jN_j}$ , while here all the fragmentation chains of the history  $\vec{S}_j$  are used. The factor  $\mathcal{N}_{\sigma_s}(|\vec{t}_h - \vec{t}_j|)$  constrains the possible contributions from accepted fragmentation chains; only those that result in high-level observables similar to the one for the event  $e_h$  contribute. The rejected fragmentation chains are not constrained at all by the  $\mathcal{N}_{\sigma_s}$  factor, so that the summation over  $j$  results in a good estimate of the effect of the `finalTwo` filter, at the cost of a decreased effective sample size due to the increased variance of the weights,  $\sum w_{\text{HOMER}}^2$ .

Equation (8.43) is a main result; it is the required modification of Step 2 in HOMER to allow strings with gluons and of varying kinematics. With this modification, displayed in fig. 8.6, the HOMER weights are now utilized for both Step 2 and Step 3, first with smearing for training and then without smearing for reweighting any generated events with a fixed data-driven fragmentation function. We emphasize that while Step 2 of HOMER  $w_{\text{infer}}(e_h)$  is now calculated using eq. (8.43) rather than eq. (8.20), all the other parts of HOMER remain the same. In particular, we use the same loss functions and neural network architectures as in ref. [27].

#### 8.2.4.3 Selecting the hyperparameter $\sigma_s$

The width  $\sigma_s$  of the smearing kernel in eq. (8.43) is a hyperparameter that can be optimized such that the weights  $w_{\text{HOMER}}(\vec{S}_h)$  lead to the best description of data. For very large  $\sigma_s$ ,  $\sigma_s \rightarrow \infty$ , the inferred weights converge as  $w_{\text{infer}}(e_h) \rightarrow 1$ , *i.e.*,  $w_{\text{infer}}$  becomes a random classifier with no information about the event. In the opposite limit,  $\sigma_s \rightarrow 0$ , the smearing reverts to the original HOMER approximation, see the discussion above for eq. (8.24), albeit now with a very poor approximation for the effect of the `finalTwo` filter. We thus expect that there is a small but nonzero value of  $\sigma_s$  that provides an optimal choice.

To find the optimal value of  $\sigma_s$ , we use a  $\chi^2$ -inspired goodness of fit metric

$$\chi^2(\mathcal{O}, \sigma_s) = \frac{1}{N_{\text{bins}}} \sum_{k=1}^{N_{\text{bins}}} \frac{(p_{\text{data},k}^{\mathcal{O}} - p_{\text{pred},k}^{\mathcal{O}}(\sigma_s))^2}{(\sigma_{\text{data},k}^{\mathcal{O}})^2 + (\sigma_{\text{pred},k}^{\mathcal{O}}(\sigma_s))^2}, \quad (8.44)$$

where we choose the observable  $\mathcal{O}$  to be the output of the classifier in Step 1, *i.e.*,  $\mathcal{O} = -2 \ln w_{\text{class}}$  in analogy to the test statistic used for hypothesis tests [425]. The value of  $\mathcal{O}$  for each event is used to separate data into  $N_{\text{bins}}$  bins, where  $p_{\text{data},k}^{\mathcal{O}}$  in eq. (8.44) denotes the fraction of experimental events in bin  $k$ , and  $p_{\text{pred},k}^{\mathcal{O}}(\sigma_s)$  is the corresponding predicted fraction obtained using HOMER weights  $w_{\text{HOMER}}$ . The  $p_{\text{pred},k}^{\mathcal{O}}$  fractions depend on the hyperparameter  $\sigma_s$  since

$w_{\text{HOMER}}$  weights change depending on what value of  $\sigma_s$  is used in the smearing of eq. (8.43). Both the measurement  $\sigma_{\text{data},k}^{\mathcal{O}}$  and the simulation uncertainties  $\sigma_{\text{pred},k}^{\mathcal{O}}(\sigma_s)$  are used in the definition of the goodness-of-fit metric to adequately account for the impact of low statistics in some of the bins.

Minimization of  $\chi^2(\mathcal{O}, \sigma_s)/N_{\text{bins}}$  gives the optimal value of the smearing hyperparameter  $\sigma_s^*$ . This optimization procedure may be numerically expensive since one needs to determine HOMER weights for several  $\sigma_s$  values. In practice, the procedure can be accelerated via parallelization and a judicious exploration of possible  $\sigma_s$  values. Note that the value of  $\sigma_s^*$  depends on the size of data samples used to extract  $w_{\text{HOMER}}$ ; for larger samples,  $\sigma_s$  can be smaller and still result in sufficiently efficient smearing. This is particularly important since, due to memory constraints, we always compute the smearing on relatively small batches of  $10^4$  events. A systematic exploration of the impact of sample and batch size on  $\sigma_s^*$  is left for future work.

### 8.3 Conclusions

In this chapter, we introduced two proposed solutions to the inverse problem of hadronization: MAGIC [8] and HOMER [11, 27]. While both methodologies target the same problem, their approaches are distinct.

MAGIC follows a two-step fine-tuning procedure. First, a base normalizing flow model is trained to replicate the microphysical output of PYTHIA directly. This base model is then fine-tuned using a non-convex adversarial loss function that minimizes discrepancies between model output and ‘experimental’ observables. Once trained, the NF can either fully replace the PYTHIA fragmentation sampler or be used indirectly to reweight events, similar to HOMER.

HOMER employs a three-step procedure. A classifier is first trained to distinguish high- or low-level observables between simulation and ‘experiment’. This classifier is then used to define event weights that parameterize the composite likelihood ratio between the two datasets. A separate regression model is then trained to partition the classifier-derived event weights into individual string-break weights. After training, HOMER effectively provides a string-break reweighter that, when applied to event ensembles, exactly mimics the use of an alternate fragmentation function.

A broad (but soft) distinction between the two methods lies in the order of operations: MAGIC starts from the microscopic model and tunes to match macroscopic observables, while HOMER begins with macroscopic observables and tunes the microscopic dynamics. HOMER’s forward-mode reweighting strategy is well-suited for integration into the full simulation pipeline, in contrast to MAGIC, whose ideal fine-tuning use-case requires full replacement of PYTHIA’s kinematic sampler, making it more invasive. As a sampler of kinematics, however, a MAGIC fine-tuned model can also be used in the same way as HOMER—acting as a reweighter of simulation events. Finally, HOMER is trained with an explicit convex loss function, in contrast to MAGIC, which

can improve convergence during optimization. Whether this feature is necessary for achieving production-level data-driven hadronization remains an open question.

Both methods have, so far, only been validated on closure-like tests with toy simulated data. In this respect, HOMER is significantly more developed, having been tested and validated on both  $q\bar{q}$  systems and arbitrary gluon configurations, whereas MAGIC has only been validated on the simplest  $q\bar{q}$  system. Further validation on generic hadron production is required before either method can be used for full kinematic modeling. In the context of arbitrary gluon configurations, HOMER sees a degradation of performance. This can likely be traced to an explosion of degeneracies in the space of observables (*i.e.*, many distinct string histories map to the same observable), in combination with non-trivial `finalTwo` filtering dynamics. While MAGIC hasn't been tested in this context both approaches should be expected to be constrained by the availability and informativeness of the observables on which they are trained – this is an ongoing focus of the MLHAD collaboration. Additional approaches which factorize the effects of `finalTwo` filtering should also be investigated in future work.

Taken together, MAGIC and HOMER offer promising and complementary approaches to the inverse problem of hadronization. Continued development and refinement of these methods provide a promising path toward production-grade data-driven models of hadronization.

# Chapter 9

## Conclusions

This dissertation presented a collection of studies in two areas: new physics signatures in charged lepton flavor violating rare decays, and the development of differentiable, data-driven models for hadronization. Both efforts aim to improve the interpretability, flexibility, and precision of theoretical predictions at high-intensity and high-energy experiments.

In chapters 2 to 5, we studied a range of rare lepton decay signatures sourced by both heavy and light new physics across multiple experimental frontiers. In chapter 2, we analyzed multi-electron muon decays, including both SM backgrounds and exotic signals such as  $\mu \rightarrow 5e$  mediated by new dark sector states. We quantified the reach of Mu3e using full detector-level simulations and proposed search strategies for signal discrimination. In chapter 3, we constructed a tower of matched EFTs connecting UV CLFV operators to nuclear-scale observables for  $\mu \rightarrow e$  conversion, including a full implementation of the required matching and running via the `MuonBridge` code. In chapter 4, we proposed and analyzed a novel baryon-number-violating signature induced by muon capture in the presence of dark sector states, identifying viable UV completions and estimating signal rates at experiments such as Mu2e and COMET. Chapter 5 examined ultralight dark matter with CLFV couplings, highlighting the possibility of direct detection via time-dependent rate modulation in high-intensity muon and tau experiments. Collectively, these studies highlight the role of rare lepton decays as precision probes of new physics across a wide range of scales and couplings, from high-scale UV completions to ultralight, time-varying backgrounds. Continued improvements in experimental sensitivity, particularly at high-intensity facilities, will continue to extend the reach of these channels and maintain their status as powerful and theoretically clean probes of beyond-the-Standard-Model physics.

In chapters 7 and 8, we shifted focus to Monte Carlo event generators and the ongoing work to develop differentiable and data-driven hadronization models. We described a suite of differentiable reweighting and tuning methods that allow efficient uncertainty quantification and parameter

tuning. We also introduced machine-learning-based generative models for hadronization, constructed by deforming the approximate solution already given by default tunes of PYTHIA. These data-driven models can be tuned directly from hadron-level observables and establish the viability of replacing hand-tuned hadronization procedures with scalable, differentiable alternatives. Future work will involve generalizing these techniques to more realistic string topologies, full  $e^+e^-$  and  $pp$  events, and incorporating equivalent data-driven models of flavor – all building towards the goal of constructing the first data-driven model of hadronization trained on real experimental data.

Stepping back, the methods and results presented in part II contribute toward a longer-term goal: the development of fully differentiable event generators. Such generators would enable end-to-end optimization of the entire simulation chain, with components grounded in physical structure yet flexible enough to be tuned systematically from data. Embedding differentiable, interpretable modules into these pipelines will be essential for robust uncertainty quantification, precise parameter estimation, and improved control over modeling systematics – especially in the high-precision era of collider physics. The ongoing integration of machine learning and differentiable programming into Monte Carlo event generators, such as the work presented here, is driving a paradigm shift in how theoretical models interface with experimental data.

# Bibliography

- [1] Ramandeep S Vilkhu. *Modeling Electrical Neural Stimulation for Brain-Computer Interfaces*. Stanford University, 2024.
- [2] Matheus Hostert, Tony Menzo, Maxim Pospelov, and Jure Zupan. New physics in multi-electron muon decays. *JHEP*, 10(0):006, 2023. doi: 10.1007/JHEP10(2023)006.
- [3] Wick Haxton, Kenneth McElvain, Tony Menzo, Evan Rule, and Jure Zupan. Effective theory tower for  $\mu \rightarrow e$  conversion. *JHEP*, 11:076, 2024. doi: 10.1007/JHEP11(2024)076. URL <https://arxiv.org/abs/2406.13818>.
- [4] Patrick J. Fox, Matheus Hostert, Tony Menzo, Maxim Pospelov, and Jure Zupan. Muon-induced baryon number violation. *Phys. Rev. D*, 110(7):075015, 2024. doi: 10.1103/PhysRevD.110.075015.
- [5] Innes Bigaran, Patrick J. Fox, Yann Gouttenoire, Roni Harnik, Gordan Krnjaic, Tony Menzo, and Jure Zupan. Direct detection of ultralight dark matter via charged lepton flavor violation, 2025. URL <https://arxiv.org/abs/2503.07722>.
- [6] Phil Ilten, Tony Menzo, Ahmed Youssef, and Jure Zupan. Modeling hadronization using machine learning. *SciPost Phys.*, 14(3):027, 2023. doi: 10.21468/SciPostPhys.14.3.027.
- [7] Christian Bierlich, Philip Ilten, Tony Menzo, Stephen Mrenna, Manuel Szewc, Michael K. Wilkinson, Ahmed Youssef, and Jure Zupan. Reweighting Monte Carlo predictions and automated fragmentation variations in Pythia 8. *SciPost Phys.*, 16(5):134, 2024. doi: 10.21468/SciPostPhys.16.5.134.
- [8] Christian Bierlich, Phil Ilten, Tony Menzo, Stephen Mrenna, Manuel Szewc, Michael K. Wilkinson, Ahmed Youssef, and Jure Zupan. Towards a data-driven model of hadronization using normalizing flows. *SciPost Phys.*, 17(2):045, 2024. doi: 10.21468/SciPostPhys.17.2.045.
- [9] Christian Bierlich, Phil Ilten, Tony Menzo, Stephen Mrenna, Manuel Szewc, Michael K. Wilkinson, Ahmed Youssef, and Jure Zupan. Describing hadronization via histories and observables for Monte-Carlo event reweighting. *SciPost Phys.*, 18(2):054, 2025. doi: 10.21468/SciPostPhys.18.2.054. URL <https://arxiv.org/abs/2410.06342>.

- [10] Nick Heller, Phil Ilten, Tony Menzo, Stephen Mrenna, Benjamin Nachman, Andrzej Siodmok, Manuel Szewc, and Ahmed Youssef. Rejection Sampling with Autodifferentiation - Case study: Fitting a Hadronization Model, 11 2024.
- [11] Benoit Assi, Christian Bierlich, Philip Ilten, Tony Menzo, Stephen Mrenna, Manuel Szewc, Michael K. Wilkinson, Ahmed Youssef, and Jure Zupan. Characterizing the hadronization of parton showers using the homer method, 2025. URL <https://arxiv.org/abs/2503.05667>.
- [12] Benoît Assi, Christian Bierlich, Philip Ilten, Tony Menzo, Stephen Mrenna, Manuel Szewc, Michael K. Wilkinson, Ahmed Youssef, and Jure Zupan. Post-hoc reweighting of hadron production in the lund string model, 2025. URL <https://arxiv.org/abs/2505.00142>.
- [13] Adam Davis, Tony Menzo, Ahmed Youssef, and Jure Zupan. Earth mover's distance as a measure of CP violation. *JHEP*, 06:098, 2023. doi: 10.1007/JHEP06(2023)098.
- [14] Chaja Baruch, Patrick J. Fitzpatrick, Tony Menzo, Yotam Soreq, Sokratis Trifinopoulos, and Jure Zupan. Searching for exotic scalars at fusion reactors, 2 2025.
- [15] J. M. Poutissou, L. Felawka, C. H. Quentin Ingram, R. MacDonald, David F. Measday, M. Salomon, and J. Spuller. A New Limit on the Decay  $\mu^+ \rightarrow e^+ \gamma \gamma$ . *Nucl. Phys. B*, 80:221–229, 1974. doi: 10.1016/0550-3213(74)90514-8.
- [16] B. Grzadkowski, M. Iskrzynski, M. Misiak, and J. Rosiek. Dimension-Six Terms in the Standard Model Lagrangian. *JHEP*, 10:085, 2010. doi: 10.1007/JHEP10(2010)085.
- [17] Alejandro Celis, Javier Fuentes-Martin, Avelino Vicente, and Javier Virto. DsixTools: The Standard Model Effective Field Theory Toolkit. *Eur. Phys. J. C*, 77(6):405, 2017. doi: 10.1140/epjc/s10052-017-4967-6.
- [18] Andrzej Czarnecki, Xavier Garcia i Tormo, and William J. Marciano. Muon decay in orbit: spectrum of high-energy electrons. *Phys. Rev. D*, 84:013006, 2011. doi: 10.1103/PhysRevD.84.013006.
- [19] R. Bayes et al. Search for two body muon decay signals. *Phys. Rev. D*, 91(5):052020, 2015. doi: 10.1103/PhysRevD.91.052020.
- [20] J. R. Musser et al. Measurement of the Michel parameter rho in muon decay. *Phys. Rev. Lett.*, 94:101805, 2005. doi: 10.1103/PhysRevLett.94.101805.
- [21] Ann-Kathrin Perrevoort. *Sensitivity Studies on New Physics in the Mu3e Experiment and Development of Firmware for the Front-End of the Mu3e Pixel Detector*. PhD thesis, U. Heidelberg (main), 2018.

- [22] Ann-Kathrin Perrevoort. Searching for Charged Lepton Flavour Violation with Mu3e †. *Phys. Sci. Forum*, 8(1):30, 2023. doi: 10.3390/psf2023008030.
- [23] Georg G. Raffelt. Astrophysical methods to constrain axions and other novel particle phenomena. *Phys. Rept.*, 198:1–113, 1990. doi: 10.1016/0370-1573(90)90054-6.
- [24] Lorenzo Calibbi, Diego Redigolo, Robert Ziegler, and Jure Zupan. Looking forward to lepton-flavor-violating ALPs. *JHEP*, 09:173, 2021. doi: 10.1007/JHEP09(2021)173.
- [25] I. Adachi et al. Search for Lepton-Flavor-Violating  $\tau$  Decays to a Lepton and an Invisible Boson at Belle II. *Phys. Rev. Lett.*, 130(18):181803, 2023. doi: 10.1103/PhysRevLett.130.181803.
- [26] G. Bernardi et al. The Future Circular Collider: a Summary for the US 2021 Snowmass Process, 3 2022.
- [27] Christian Bierlich, Phil Ilten, Tony Menzo, Stephen Mrenna, Manuel Szewc, Michael K. Wilkinson, Ahmed Youssef, and Jure Zupan. Describing Hadronization via Histories and Observables for Monte-Carlo Event Reweighting, 10 2024.
- [28] Jason Aebischer et al. WCxf: an exchange format for Wilson coefficients beyond the Standard Model. *Comput. Phys. Commun.*, 232:71–83, 2018. doi: 10.1016/j.cpc.2018.05.022.
- [29] Torbjorn Sjostrand, Stephen Mrenna, and Peter Z. Skands. PYTHIA 6.4 Physics and Manual. *JHEP*, 05:026, 2006. doi: 10.1088/1126-6708/2006/05/026.
- [30] Christian Bierlich et al. A comprehensive guide to the physics and usage of PYTHIA 8.3. *SciPost Phys. Codeb.*, 2022:8, 2022. doi: 10.21468/SciPostPhysCodeb.8.
- [31] Peter Skands, Stefano Carrazza, and Juan Rojo. Tuning PYTHIA 8.1: the Monash 2013 Tune. *Eur. Phys. J. C*, 74(8):3024, 2014. doi: 10.1140/epjc/s10052-014-3024-y.
- [32] Howard E. Haber and Gordon L. Kane. The Search for Supersymmetry: Probing Physics Beyond the Standard Model. *Phys. Rept.*, 117:75–263, 1985. doi: 10.1016/0370-1573(85)90051-1.
- [33] Stephen P. Martin. A Supersymmetry primer. *Adv. Ser. Direct. High Energy Phys.*, 18:1–98, 1998. doi: 10.1142/9789812839657\_0001.
- [34] S. Navas et al. Review of particle physics. *Phys. Rev. D*, 110(3):030001, 2024. doi: 10.1103/PhysRevD.110.030001.
- [35] J. Wess and B. Zumino. Supergauge Transformations in Four-Dimensions. *Nucl. Phys. B*, 70:39–50, 1974. doi: 10.1016/0550-3213(74)90355-1.

- [36] Pierre Fayet. Supersymmetry and Weak, Electromagnetic and Strong Interactions. *Phys. Lett. B*, 64:159, 1976. doi: 10.1016/0370-2693(76)90319-1.
- [37] Paul Langacker. Grand Unified Theories and Proton Decay. *Phys. Rept.*, 72:185, 1981. doi: 10.1016/0370-1573(81)90059-4.
- [38] R. L. Workman and Others. Review of particle physics. *Prog. Theor. Exp. Phys.*, 2024: 083C01, 2024. doi: 10.1093/ptep/ptae083. See section on *Grand Unified Theories*.
- [39] Jogesh C. Pati and Abdus Salam. Lepton Number as the Fourth Color. *Phys. Rev. D*, 10:275–289, 1974. doi: 10.1103/PhysRevD.10.275. [Erratum: Phys.Rev.D 11, 703–703 (1975)].
- [40] H. Georgi and S. L. Glashow. Unity of All Elementary Particle Forces. *Phys. Rev. Lett.*, 32:438–441, 1974. doi: 10.1103/PhysRevLett.32.438.
- [41] Harald Fritzsch and Peter Minkowski. Unified Interactions of Leptons and Hadrons. *Annals Phys.*, 93:193–266, 1975. doi: 10.1016/0003-4916(75)90211-0.
- [42] Raphael Bousso and Joseph Polchinski. Quantization of four form fluxes and dynamical neutralization of the cosmological constant. *JHEP*, 06:006, 2000. doi: 10.1088/1126-6708/2000/06/006.
- [43] Steven B. Giddings, Shamit Kachru, and Joseph Polchinski. Hierarchies from fluxes in string compactifications. *Phys. Rev. D*, 66:106006, 2002. doi: 10.1103/PhysRevD.66.106006.
- [44] Sujay Ashok and Michael R. Douglas. Counting flux vacua. *JHEP*, 01:060, 2004. doi: 10.1088/1126-6708/2004/01/060.
- [45] Frederik Denef and Michael R. Douglas. Distributions of flux vacua. *JHEP*, 05:072, 2004. doi: 10.1088/1126-6708/2004/05/072.
- [46] Gerard 't Hooft and M. J. G. Veltman. Regularization and Renormalization of Gauge Fields. *Nucl. Phys. B*, 44:189–213, 1972. doi: 10.1016/0550-3213(72)90279-9.
- [47] Gerard 't Hooft. Dimensional regularization and the renormalization group. *Nucl. Phys. B*, 61:455–468, 1973. doi: 10.1016/0550-3213(73)90376-3.
- [48] William A. Bardeen, A. J. Buras, D. W. Duke, and T. Muta. Deep Inelastic Scattering Beyond the Leading Order in Asymptotically Free Gauge Theories. *Phys. Rev. D*, 18: 3998, 1978. doi: 10.1103/PhysRevD.18.3998.
- [49] Paul A. M. Dirac. The quantum theory of the electron. *Proc. Roy. Soc. Lond. A*, 117: 610–624, 1928. doi: 10.1098/rspa.1928.0023.

- [50] C. D. Anderson. The Positive Electron. *Phys. Rev.*, 43:491–494, 1933. doi: 10.1103/PhysRev.43.491.
- [51] S. H. Neddermeyer and C. D. Anderson. Note on the Nature of Cosmic Ray Particles. *Phys. Rev.*, 51:884–886, 1937. doi: 10.1103/PhysRev.51.884.
- [52] C. M. G. Lattes, H. Muirhead, G. P. S. Occhialini, and C. F. Powell. PROCESSES INVOLVING CHARGED MESONS. *Nature*, 159:694–697, 1947. doi: 10.1038/159694a0.
- [53] Hideki Yukawa. On the Interaction of Elementary Particles I. *Proc. Phys. Math. Soc. Jap.*, 17:48–57, 1935. doi: 10.1143/PTPS.1.1.
- [54] C. S. Wu, E. Ambler, R. W. Hayward, D. D. Hoppes, and R. P. Hudson. Experimental Test of Parity Conservation in  $\beta$  Decay. *Phys. Rev.*, 105:1413–1414, 1957. doi: 10.1103/PhysRev.105.1413.
- [55] F. Reines and C. L. Cowan. Detection of the free neutrino. *Phys. Rev.*, 92:830–831, 1953. doi: 10.1103/PhysRev.92.830.
- [56] Martin Breidenbach, Jerome I. Friedman, Henry W. Kendall, Elliott D. Bloom, D. H. Coward, H. C. DeStaeler, J. Drees, Luke W. Mo, and Richard E. Taylor. Observed behavior of highly inelastic electron-proton scattering. *Phys. Rev. Lett.*, 23:935–939, 1969. doi: 10.1103/PhysRevLett.23.935.
- [57] Jerome I. Friedman. Deep inelastic scattering: Comparisons with the quark model. *Rev. Mod. Phys.*, 63:615–629, 1991. doi: 10.1103/RevModPhys.63.615.
- [58] J. J. Aubert et al. Experimental Observation of a Heavy Particle *J. Phys. Rev. Lett.*, 33: 1404–1406, 1974. doi: 10.1103/PhysRevLett.33.1404.
- [59] J. E. Augustin et al. Discovery of a Narrow Resonance in  $e^+e^-$  Annihilation. *Phys. Rev. Lett.*, 33:1406–1408, 1974. doi: 10.1103/PhysRevLett.33.1406.
- [60] S. W. Herb et al. Observation of a Dimuon Resonance at 9.5 GeV in 400 GeV Proton-Nucleus Collisions. *Phys. Rev. Lett.*, 39:252–255, 1977. doi: 10.1103/PhysRevLett.39.252.
- [61] F. Abe et al. Observation of top quark production in  $\bar{p}p$  collisions. *Phys. Rev. Lett.*, 74: 2626–2631, 1995. doi: 10.1103/PhysRevLett.74.2626.
- [62] S. Abachi et al. Observation of the top quark. *Phys. Rev. Lett.*, 74:2632–2637, 1995. doi: 10.1103/PhysRevLett.74.2632.
- [63] G. Arnison et al. Experimental Observation of Isolated Large Transverse Energy Electrons with Associated Missing Energy at  $\sqrt{s} = 540$  GeV. *Phys. Lett. B*, 122:103–116, 1983. doi: 10.1016/0370-2693(83)91177-2.

- [64] M. Banner et al. Observation of Single Isolated Electrons of High Transverse Momentum in Events with Missing Transverse Energy at the CERN anti-p p Collider. *Phys. Lett. B*, 122:476–485, 1983. doi: 10.1016/0370-2693(83)91605-2.
- [65] S. Schael et al. Precision electroweak measurements on the  $Z$  resonance. *Phys. Rept.*, 427: 257–454, 2006. doi: 10.1016/j.physrep.2005.12.006.
- [66] Georges Aad et al. Observation of a new particle in the search for the Standard Model Higgs boson with the ATLAS detector at the LHC. *Phys. Lett. B*, 716:1–29, 2012. doi: 10.1016/j.physletb.2012.08.020.
- [67] Serguei Chatrchyan et al. Observation of a New Boson at a Mass of 125 GeV with the CMS Experiment at the LHC. *Phys. Lett. B*, 716:30–61, 2012. doi: 10.1016/j.physletb.2012.08.021.
- [68] Roel Aaij et al. Test of lepton universality in beauty-quark decays. *Nature Phys.*, 18(3): 277–282, 2022. doi: 10.1038/s41567-023-02095-3. [Addendum: Nature Phys. 19, (2023)].
- [69] R. Aaij et al. Test of lepton universality in  $b \rightarrow s\ell^+\ell^-$  decays. *Phys. Rev. Lett.*, 131(5): 051803, 2023. doi: 10.1103/PhysRevLett.131.051803.
- [70] Yasmine Sara Amhis et al. Averages of b-hadron, c-hadron, and  $\tau$ -lepton properties as of 2018. *Eur. Phys. J. C*, 81(3):226, 2021. doi: 10.1140/epjc/s10052-020-8156-7.
- [71] G. Caria et al. Measurement of  $\mathcal{R}(D)$  and  $\mathcal{R}(D^*)$  with a semileptonic tagging method. *Phys. Rev. Lett.*, 124(16):161803, 2020. doi: 10.1103/PhysRevLett.124.161803.
- [72] Andrzej Czarnecki, William J. Marciano, and Alberto Sirlin. Radiative Corrections to Neutron and Nuclear Beta Decays Revisited. *Phys. Rev. D*, 100(7):073008, 2019. doi: 10.1103/PhysRevD.100.073008.
- [73] Chien-Yeah Seng, Mikhail Gorchtein, Hiren H. Patel, and Michael J. Ramsey-Musolf. Reduced Hadronic Uncertainty in the Determination of  $V_{ud}$ . *Phys. Rev. Lett.*, 121(24): 241804, 2018. doi: 10.1103/PhysRevLett.121.241804.
- [74] J. C. Hardy and I. S. Towner. Superallowed  $0^+ \rightarrow 0^+$  nuclear  $\beta$  decays: 2020 critical survey, with implications for  $V_{ud}$  and CKM unitarity. *Phys. Rev. C*, 102(4):045501, 2020. doi: 10.1103/PhysRevC.102.045501.
- [75] T. Aaltonen et al. High-precision measurement of the  $W$  boson mass with the CDF II detector. *Science*, 376(6589):170–176, 2022. doi: 10.1126/science.abk1781.
- [76] S. Schael et al. Electroweak Measurements in Electron-Positron Collisions at W-Boson-Pair Energies at LEP. *Phys. Rept.*, 532:119–244, 2013. doi: 10.1016/j.physrep.2013.07.004.

- [77] Morad Aaboud et al. Measurement of the  $W$ -boson mass in pp collisions at  $\sqrt{s} = 7$  TeV with the ATLAS detector. *Eur. Phys. J. C*, 78(2):110, 2018. doi: 10.1140/epjc/s10052-017-5475-4. [Erratum: Eur.Phys.J.C 78, 898 (2018)].
- [78] Reuven Balkin, Eric Madge, Tony Menzo, Gilad Perez, Yotam Soreq, and Jure Zupan. On the implications of positive  $W$  mass shift. *JHEP*, 05:133, 2022. doi: 10.1007/JHEP05(2022)133.
- [79] A. J. Krasznahorkay et al. Observation of Anomalous Internal Pair Creation in Be8 : A Possible Indication of a Light, Neutral Boson. *Phys. Rev. Lett.*, 116(4):042501, 2016. doi: 10.1103/PhysRevLett.116.042501.
- [80] A. J. Krasznahorkay et al. New evidence supporting the existence of the hypothetic X17 particle, 10 2019.
- [81] A. J. Krasznahorkay, M. Csatlós, L. Csige, J. Gulyás, A. Krasznahorkay, B. M. Nyakó, I. Rajta, J. Timár, I. Vajda, and N. J. Sas. New anomaly observed in He4 supports the existence of the hypothetical X17 particle. *Phys. Rev. C*, 104(4):044003, 2021. doi: 10.1103/PhysRevC.104.044003.
- [82] S. Bertelli et al. Characterization of the PADME positron beam for the X17 measurement. *JHEP*, 08:121, 2024. doi: 10.1007/JHEP08(2024)121.
- [83] K. Afanaciev et al. Search for the X17 particle in  ${}^7\text{Li}(\text{p}, \text{e}^+\text{e}^-){}^8\text{Be}$  processes with the MEG II detector. *Eur. Phys. J. C*, 85(7):763, 2025. doi: 10.1140/epjc/s10052-025-14345-0.
- [84] D. Banerjee et al. Search for a Hypothetical 16.7 MeV Gauge Boson and Dark Photons in the NA64 Experiment at CERN. *Phys. Rev. Lett.*, 120(23):231802, 2018. doi: 10.1103/PhysRevLett.120.231802.
- [85] D. Banerjee et al. Improved limits on a hypothetical X(16.7) boson and a dark photon decaying into  $e^+e^-$  pairs. *Phys. Rev. D*, 101(7):071101, 2020. doi: 10.1103/PhysRevD.101.071101.
- [86] A. Serebrov et al. Measurement of the neutron lifetime using a gravitational trap and a low-temperature Fomblin coating. *Phys. Lett. B*, 605:72–78, 2005. doi: 10.1016/j.physletb.2004.11.013.
- [87] A. T. Yue, M. S. Dewey, D. M. Gilliam, G. L. Greene, A. B. Laptev, J. S. Nico, W. M. Snow, and F. E. Wietfeldt. Improved Determination of the Neutron Lifetime. *Phys. Rev. Lett.*, 111(22):222501, 2013. doi: 10.1103/PhysRevLett.111.222501.
- [88] Bartosz Fornal and Benjamin Grinstein. Dark Matter Interpretation of the Neutron Decay Anomaly. *Phys. Rev. Lett.*, 120(19):191801, 2018. doi: 10.1103/PhysRevLett.120.191801. [Erratum: Phys.Rev.Lett. 124, 219901 (2020)].

- [89] Zurab Berezhiani. Neutron lifetime puzzle and neutron–mirror neutron oscillation. *Eur. Phys. J. C*, 79(6):484, 2019. doi: 10.1140/epjc/s10052-019-6995-x.
- [90] D. P. Aguillard et al. Measurement of the Positive Muon Anomalous Magnetic Moment to 127 ppb, 6 2025.
- [91] Tatsumi Aoyama, Toichiro Kinoshita, and Makiko Nio. Theory of the Anomalous Magnetic Moment of the Electron. *Atoms*, 7(1):28, 2019. doi: 10.3390/atoms7010028.
- [92] V. Tishchenko et al. Detailed Report of the MuLan Measurement of the Positive Muon Lifetime and Determination of the Fermi Constant. *Phys. Rev. D*, 87(5):052003, 2013. doi: 10.1103/PhysRevD.87.052003.
- [93] Richard H. Parker, Chenghui Yu, Weicheng Zhong, Brian Estey, and Holger Müller. Measurement of the fine-structure constant as a test of the Standard Model. *Science*, 360:191, 2018. doi: 10.1126/science.aap7706.
- [94] Léo Morel, Zhibin Yao, Pierre Cladé, and Saïda Guellati-Khélifa. Determination of the fine-structure constant with an accuracy of 81 parts per trillion. *Nature*, 588(7836):61–65, 2020. doi: 10.1038/s41586-020-2964-7.
- [95] G. Abbiendi et al. Search for lepton flavor violation in e+ e- collisions at  $s^{**}(1/2) = 189$ -GeV - 209-GeV. *Phys. Lett. B*, 519:23–32, 2001. doi: 10.1016/S0370-2693(01)01086-3.
- [96] S. L. Glashow. Partial Symmetries of Weak Interactions. *Nucl. Phys.*, 22:579–588, 1961. doi: 10.1016/0029-5582(61)90469-2.
- [97] Steven Weinberg. A Model of Leptons. *Phys. Rev. Lett.*, 19:1264–1266, 1967. doi: 10.1103/PhysRevLett.19.1264.
- [98] Abdus Salam. Weak and Electromagnetic Interactions. *Conf. Proc. C*, 680519:367–377, 1968. doi: 10.1142/9789812795915\_0034.
- [99] Peter W. Higgs. Broken Symmetries and the Masses of Gauge Bosons. *Phys. Rev. Lett.*, 13:508–509, 1964. doi: 10.1103/PhysRevLett.13.508.
- [100] F. Englert and R. Brout. Broken Symmetry and the Mass of Gauge Vector Mesons. *Phys. Rev. Lett.*, 13:321–323, 1964. doi: 10.1103/PhysRevLett.13.321.
- [101] G. S. Guralnik, C. R. Hagen, and T. W. B. Kibble. Global Conservation Laws and Massless Particles. *Phys. Rev. Lett.*, 13:585–587, 1964. doi: 10.1103/PhysRevLett.13.585.
- [102] Peter W. Higgs. Spontaneous Symmetry Breakdown without Massless Bosons. *Phys. Rev.*, 145:1156–1163, 1966. doi: 10.1103/PhysRev.145.1156.

- [103] Stuart Raby. *Introduction to the Standard Model and Beyond: Quantum Field Theory, Symmetries and Phenomenology*. Cambridge University Press, 2021.
- [104] Yuval Grossman and Yossi Nir. *The Standard Model: From Fundamental Symmetries to Experimental Tests*. Princeton University Press, 10 2023. ISBN 978-0-691-23910-1.
- [105] Y. Fukuda et al. Evidence for oscillation of atmospheric neutrinos. *Phys. Rev. Lett.*, 81: 1562–1567, 1998. doi: 10.1103/PhysRevLett.81.1562.
- [106] Q. R. Ahmad et al. Measurement of the rate of  $\nu_e + d \rightarrow p + p + e^-$  interactions produced by  ${}^8\text{B}$  solar neutrinos at the Sudbury Neutrino Observatory. *Phys. Rev. Lett.*, 87:071301, 2001. doi: 10.1103/PhysRevLett.87.071301.
- [107] Julian Heeck. Interpretation of Lepton Flavor Violation. *Phys. Rev. D*, 95(1):015022, 2017. doi: 10.1103/PhysRevD.95.015022.
- [108] John Ellis, Malcolm Fairbairn, and Patrick Tunney. Anomaly-Free Models for Flavour Anomalies. *Eur. Phys. J. C*, 78(3):238, 2018. doi: 10.1140/epjc/s10052-018-5725-0.
- [109] B. C. Allanach, Joe Davighi, and Scott Melville. An Anomaly-free Atlas: charting the space of flavour-dependent gauged  $U(1)$  extensions of the Standard Model. *JHEP*, 02:082, 2019. doi: 10.1007/JHEP02(2019)082. [Erratum: JHEP 08, 064 (2019)].
- [110] Martin Bauer, Patrick Foldenauer, and Joerg Jaeckel. Hunting All the Hidden Photons. *JHEP*, 07:094, 2018. doi: 10.1007/JHEP07(2018)094.
- [111] Julian Heeck and Werner Rodejohann. Gauged  $L_\mu - L_\tau$  Symmetry at the Electroweak Scale. *Phys. Rev. D*, 84:075007, 2011. doi: 10.1103/PhysRevD.84.075007.
- [112] Peter Ballett, Matheus Hostert, Silvia Pascoli, Yuber F. Perez-Gonzalez, Zahra Tabrizi, and Renata Zukanovich Funchal.  $Z'$ 's in neutrino scattering at DUNE. *Phys. Rev. D*, 100 (5):055012, 2019. doi: 10.1103/PhysRevD.100.055012.
- [113] Lorenzo Calibbi and Giovanni Signorelli. Charged Lepton Flavour Violation: An Experimental and Theoretical Introduction. *Riv. Nuovo Cim.*, 41(2):71–174, 2018. doi: 10.1393/ncr/i2018-10144-0.
- [114] J. Hisano, T. Moroi, K. Tobe, and Masahiro Yamaguchi. Lepton flavor violation via right-handed neutrino Yukawa couplings in supersymmetric standard model. *Phys. Rev. D*, 53: 2442–2459, 1996. doi: 10.1103/PhysRevD.53.2442.
- [115] Steven Weinberg. Baryon and Lepton Nonconserving Processes. *Phys. Rev. Lett.*, 43: 1566–1570, 1979. doi: 10.1103/PhysRevLett.43.1566.

- [116] W. Buchmuller and D. Wyler. Effective Lagrangian Analysis of New Interactions and Flavor Conservation. *Nucl. Phys. B*, 268:621–653, 1986. doi: 10.1016/0550-3213(86)90262-2.
- [117] S. Davidson, Y. Kuno, Y. Uesaka, and M. Yamanaka. Probing  $\mu e\gamma\gamma$  contact interactions with  $\mu \rightarrow e$  conversion. *Phys. Rev. D*, 102(11):115043, 2020. doi: 10.1103/PhysRevD.102.115043.
- [118] Marco Ardu and Sacha Davidson. What is Leading Order for LFV in SMEFT? *JHEP*, 08:002, 2021. doi: 10.1007/JHEP08(2021)002.
- [119] Simon Knapen, Kevin Langhoff, Toby Opferkuch, and Diego Redigolo. Angling for insights: illuminating light new physics at Mu3e through angular correlations. *JHEP*, 07:194, 2024. doi: 10.1007/JHEP07(2024)194.
- [120] Yohei Ema, Patrick J. Fox, Matheus Hostert, Tony Menzo, Maxim Pospelov, Anupam Ray, and Jure Zupan. Long-lived Axion-Like Particles from Tau Decays, 7 2025.
- [121] U. Bellgardt et al. Search for the Decay  $\mu^+ \rightarrow e^+ e^+ e^-$ . *Nucl. Phys. B*, 299:1–6, 1988. doi: 10.1016/0550-3213(88)90462-2.
- [122] K. Arndt et al. Technical design of the phase I Mu3e experiment. *Nucl. Instrum. Meth. A*, 1014:165679, 2021. doi: 10.1016/j.nima.2021.165679.
- [123] A. M. Baldini et al. Search for the lepton flavour violating decay  $\mu^+ \rightarrow e^+ \gamma$  with the full dataset of the MEG experiment. *Eur. Phys. J. C*, 76(8):434, 2016. doi: 10.1140/epjc/s10052-016-4271-x.
- [124] A. M. Baldini et al. The design of the MEG II experiment. *Eur. Phys. J. C*, 78(5):380, 2018. doi: 10.1140/epjc/s10052-018-5845-6.
- [125] Wilhelm H. Bertl et al. A Search for muon to electron conversion in muonic gold. *Eur. Phys. J. C*, 47:337–346, 2006. doi: 10.1140/epjc/s2006-02582-x.
- [126] R. A. Burnham et al. Search for  $\mu e$  Conversion in Ti. *Phys. Rev. Lett.*, 59:970–973, 1987. doi: 10.1103/PhysRevLett.59.970.
- [127] N. Teshima. Status of the DeeMe Experiment, an Experimental Search for  $\mu-e$  Conversion at J-PARC MLF. *PoS*, NuFact2019:082, 2020. doi: 10.22323/1.369.0082.
- [128] R. Abramishvili et al. COMET Phase-I Technical Design Report. *PTEP*, 2020(3):033C01, 2020. doi: 10.1093/ptep/ptz125.
- [129] L. Bartoszek et al. Mu2e Technical Design Report, 10 2014.

- [130] K. Hayasaka et al. Search for Lepton Flavor Violating Tau Decays into Three Leptons with 719 Million Produced Tau+Tau- Pairs. *Phys. Lett. B*, 687:139–143, 2010. doi: 10.1016/j.physletb.2010.03.037.
- [131] I. Adachi et al. Search for lepton-flavor-violating  $\tau^- \rightarrow \mu^- \mu^+ \mu^-$  decays at Belle II. *JHEP*, 09:062, 2024. doi: 10.1007/JHEP09(2024)062.
- [132] K. Uno et al. Search for lepton-flavor-violating tau decays to  $\ell\alpha$  at Belle, 3 2025.
- [133] Bernard Aubert et al. Searches for Lepton Flavor Violation in the Decays  $\tau^\pm \rightarrow e^\pm \gamma$  and  $\tau^\pm \rightarrow \mu^\pm \gamma$ . *Phys. Rev. Lett.*, 104:021802, 2010. doi: 10.1103/PhysRevLett.104.021802.
- [134] A. M. Baldini et al. Search for lepton flavour violating muon decay mediated by a new light particle in the MEG experiment. *Eur. Phys. J. C*, 80(9):858, 2020. doi: 10.1140/epjc/s10052-020-8364-1.
- [135] A. E. Pifer, T. Bowen, and K. R. Kendall. A High Stopping Density mu+ Beam. *Nucl. Instrum. Meth.*, 135:39–46, 1976. doi: 10.1016/0029-554X(76)90823-5.
- [136] R. M. Carey et al. Proposal to search for  $\mu^- N \rightarrow e^- N$  with a single event sensitivity below  $10^{-16}$ , 10 2008.
- [137] R. J. Abrams et al. Mu2e Conceptual Design Report, 11 2012.
- [138] J. Alwall, R. Frederix, S. Frixione, V. Hirschi, F. Maltoni, O. Mattelaer, H. S. Shao, T. Stelzer, P. Torrielli, and M. Zaro. The automated computation of tree-level and next-to-leading order differential cross sections, and their matching to parton shower simulations. *JHEP*, 07:079, 2014. doi: 10.1007/JHEP07(2014)079.
- [139] R. L. Workman et al. Review of Particle Physics. *PTEP*, 2022:083C01, 2022. doi: 10.1093/ptep/ptac097.
- [140] M. Fael and C. Greub. Next-to-leading order prediction for the decay  $\mu \rightarrow e^- (e^+ e^-) \nu \bar{\nu}$ . *JHEP*, 01:084, 2017. doi: 10.1007/JHEP01(2017)084.
- [141] G. M. Pruna, A. Signer, and Y. Ulrich. Fully differential NLO predictions for the rare muon decay. *Phys. Lett. B*, 765:280–284, 2017. doi: 10.1016/j.physletb.2016.12.039.
- [142] Pulak Banerjee, T. Engel, A. Signer, and Y. Ulrich. QED at NNLO with McMule. *SciPost Phys.*, 9:027, 2020. doi: 10.21468/SciPostPhys.9.2.027.
- [143] Bertrand Echenard, Rouven Essig, and Yi-Ming Zhong. Projections for Dark Photon Searches at Mu3e. *JHEP*, 01:113, 2015. doi: 10.1007/JHEP01(2015)113.
- [144] Wilhelm H. Bertl et al. Search for the Decay  $\mu^+ \rightarrow e^+ e^+ e^-$ . *Nucl. Phys. B*, 260:1–31, 1985. doi: 10.1016/0550-3213(85)90308-6.

- [145] S. N. Gninenko and N. V. Krasnikov. The Muon anomalous magnetic moment and a new light gauge boson. *Phys. Lett. B*, 513:119, 2001. doi: 10.1016/S0370-2693(01)00693-1.
- [146] Chien-Yi Chen, Hooman Davoudiasl, William J. Marciano, and Cen Zhang. Implications of a light “dark Higgs” solution to the  $g - 2$  discrepancy. *Phys. Rev. D*, 93(3):035006, 2016. doi: 10.1103/PhysRevD.93.035006.
- [147] Brian Batell, Nicholas Lange, David McKeen, Maxim Pospelov, and Adam Ritz. Muon anomalous magnetic moment through the leptonic Higgs portal. *Phys. Rev. D*, 95(7):075003, 2017. doi: 10.1103/PhysRevD.95.075003.
- [148] Chien-Yi Chen, Maxim Pospelov, and Yi-Ming Zhong. Muon Beam Experiments to Probe the Dark Sector. *Phys. Rev. D*, 95(11):115005, 2017. doi: 10.1103/PhysRevD.95.115005.
- [149] S. N. Gninenko and N. V. Krasnikov. Probing the muon  $g_\mu - 2$  anomaly,  $L_\mu - L_\tau$  gauge boson and Dark Matter in dark photon experiments. *Phys. Lett. B*, 783:24–28, 2018. doi: 10.1016/j.physletb.2018.06.043.
- [150] Yonatan Kahn, Gordan Krnjaic, Nhan Tran, and Andrew Whitbeck. M<sup>3</sup>: a new muon missing momentum experiment to probe  $(g - 2)_\mu$  and dark matter at Fermilab. *JHEP*, 09:153, 2018. doi: 10.1007/JHEP09(2018)153.
- [151] A. Aguilar-Arevalo et al. Improved search for two body muon decay  $\mu^+ \rightarrow e^+ X_H$ . *Phys. Rev. D*, 101(5):052014, 2020. doi: 10.1103/PhysRevD.101.052014.
- [152] R. Eichler et al. Limits for Shortlived Neutral Particles Emitted  $\mu^+$  or  $\pi^+$  Decay. *Phys. Lett. B*, 175:101, 1986. doi: 10.1016/0370-2693(86)90339-4.
- [153] Bob Holdom. Two U(1)’s and Epsilon Charge Shifts. *Phys. Lett. B*, 166:196–198, 1986. doi: 10.1016/0370-2693(86)91377-8.
- [154] Brian Batell, Maxim Pospelov, and Adam Ritz. Probing a Secluded U(1) at B-factories. *Phys. Rev. D*, 79:115008, 2009. doi: 10.1103/PhysRevD.79.115008.
- [155] Brian Petersen. First Physics Results from the FASER Experiment. In *57th Rencontres de Moriond on Electroweak Interactions and Unified Theories*, 5 2023.
- [156] Aielet Efrati, Adam Falkowski, and Yotam Soreq. Electroweak constraints on flavorful effective theories. *JHEP*, 07:018, 2015. doi: 10.1007/JHEP07(2015)018.
- [157] G. Azuelos et al. A New Upper Limit of the Decay  $\mu \rightarrow e\gamma\gamma$ . *Phys. Rev. Lett.*, 51:164, 1983. doi: 10.1103/PhysRevLett.51.164.
- [158] R. D. Bolton et al. Search for Rare Muon Decays with the Crystal Box Detector. *Phys. Rev. D*, 38:2077, 1988. doi: 10.1103/PhysRevD.38.2077.

- [159] J. D. Bowman, T. P. Cheng, Ling-Fong Li, and H. S. Matis. New Upper Limit for mu → e gamma gamma. *Phys. Rev. Lett.*, 41:442–445, 1978. doi: 10.1103/PhysRevLett.41.442.
- [160] C. M. York, C. O. Kim, and W. Kernan. Search for the reaction  $\mu^+ + e^- \rightarrow \gamma + \gamma$ . *Phys. Rev. Lett.*, 3:288–291, Sep 1959. doi: 10.1103/PhysRevLett.3.288. URL <https://link.aps.org/doi/10.1103/PhysRevLett.3.288>.
- [161] Iftah Galon and Jure Zupan. Dark sectors and enhanced  $h \rightarrow \tau\mu$  transitions. *JHEP*, 05:083, 2017. doi: 10.1007/JHEP05(2017)083.
- [162] Aram Hayrapetyan et al. Search for the lepton-flavor violating decay of the Higgs boson and additional Higgs bosons in the  $e\mu$  final state in proton-proton collisions at  $\sqrt{s} = 13$  TeV, 5 2023.
- [163] Georges Aad et al. Search for the Higgs boson decays  $H \rightarrow ee$  and  $H \rightarrow e\mu$  in  $pp$  collisions at  $\sqrt{s} = 13$  TeV with the ATLAS detector. *Phys. Lett. B*, 801:135148, 2020. doi: 10.1016/j.physletb.2019.135148.
- [164] ATLAS Collaboration. A detailed map of Higgs boson interactions by the ATLAS experiment ten years after the discovery. *Nature*, 607(7917):52–59, 2022. doi: 10.1038/s41586-022-04893-w. [Erratum: Nature 612, E24 (2022)].
- [165] Roni Harnik, Joachim Kopp, and Jure Zupan. Flavor Violating Higgs Decays. *JHEP*, 03:026, 2013. doi: 10.1007/JHEP03(2013)026.
- [166] Albert Puig and Jonas Eschle. phasespace: n-body phase space generation in python. *Journal of Open Source Software*, oct 2019. doi: 10.21105/joss.01570. URL <https://doi.org/10.21105/joss.01570>.
- [167] First Results from the Search for Dark Photons with the FASER Detector at the LHC, 2023. URL <https://cds.cern.ch/record/2853210>.
- [168] B. Döbrich, E. Minucci, and T. Spadaro. Search for dark photon decays to  $\mu^+\mu^-$  at NA62, 3 2023.
- [169] Philip Ilten, Yotam Soreq, Mike Williams, and Wei Xue. Serendipity in dark photon searches. *JHEP*, 06:004, 2018. doi: 10.1007/JHEP06(2018)004.
- [170] C. Antel et al. Feebly Interacting Particles: FIPs 2022 workshop report. In *Workshop on Feebly-Interacting Particles*, 5 2023.
- [171] Evan Rule, W. C. Haxton, and Kenneth McElvain. Nuclear-Level Effective Theory of  $\mu \rightarrow e$  Conversion. *Phys. Rev. Lett.*, 130(13):131901, 2023. doi: 10.1103/PhysRevLett.130.131901.

- [172] W. C. Haxton, Evan Rule, Ken McElvain, and Michael J. Ramsey-Musolf. Nuclear-level effective theory of  $\mu \rightarrow e$  conversion: Formalism and applications. *Phys. Rev. C*, 107(3):035504, 2023. doi: 10.1103/PhysRevC.107.035504.
- [173] Jason Aebischer, Jacky Kumar, and David M. Straub. Wilson: a Python package for the running and matching of Wilson coefficients above and below the electroweak scale. *Eur. Phys. J. C*, 78(12):1026, 2018. doi: 10.1140/epjc/s10052-018-6492-7.
- [174] Javier Fuentes-Martin, Pedro Ruiz-Femenia, Avelino Vicente, and Javier Virto. DsixTools 2.0: The Effective Field Theory Toolkit. *Eur. Phys. J. C*, 81(2):167, 2021. doi: 10.1140/epjc/s10052-020-08778-y.
- [175] Elizabeth E. Jenkins, Aneesh V. Manohar, and Peter Stoffer. Low-Energy Effective Field Theory below the Electroweak Scale: Operators and Matching. *JHEP*, 03:016, 2018. doi: 10.1007/JHEP03(2018)016.
- [176] Elizabeth E. Jenkins, Aneesh V. Manohar, and Michael Trott. Renormalization Group Evolution of the Standard Model Dimension Six Operators I: Formalism and lambda Dependence. *JHEP*, 10:087, 2013. doi: 10.1007/JHEP10(2013)087.
- [177] Elizabeth E. Jenkins, Aneesh V. Manohar, and Michael Trott. Renormalization Group Evolution of the Standard Model Dimension Six Operators II: Yukawa Dependence. *JHEP*, 01:035, 2014. doi: 10.1007/JHEP01(2014)035.
- [178] Rodrigo Alonso, Elizabeth E. Jenkins, Aneesh V. Manohar, and Michael Trott. Renormalization Group Evolution of the Standard Model Dimension Six Operators III: Gauge Coupling Dependence and Phenomenology. *JHEP*, 04:159, 2014. doi: 10.1007/JHEP04(2014)159.
- [179] Ilaria Brivio and Michael Trott. The Standard Model as an Effective Field Theory. *Phys. Rept.*, 793:1–98, 2019. doi: 10.1016/j.physrep.2018.11.002.
- [180] Wouter Dekens and Peter Stoffer. Low-energy effective field theory below the electroweak scale: matching at one loop. *JHEP*, 10:197, 2019. doi: 10.1007/JHEP10(2019)197. [Erratum: *JHEP* 11, 148 (2022)].
- [181] Zvi Bern, Julio Parra-Martinez, and Eric Sawyer. Structure of two-loop SMEFT anomalous dimensions via on-shell methods. *JHEP*, 10:211, 2020. doi: 10.1007/JHEP10(2020)211.
- [182] Stefano Di Noi and Luca Silvestrini. RGESolver: a C++ library to perform renormalization group evolution in the Standard Model Effective Theory. *Eur. Phys. J. C*, 83(3):200, 2023. doi: 10.1140/epjc/s10052-023-11189-4.

- [183] Yi Liao, Xiao-Dong Ma, and Quan-Yu Wang. Extending low energy effective field theory with a complete set of dimension-7 operators. *JHEP*, 08:162, 2020. doi: 10.1007/JHEP08(2020)162.
- [184] W. C. Haxton and Evan Rule. Distinguishing charged lepton flavor violation scenarios with inelastic  $\mu \rightarrow e$  conversion, 4 2024.
- [185] A. Liam Fitzpatrick, Wick Haxton, Emanuel Katz, Nicholas Lubbers, and Yiming Xu. The Effective Field Theory of Dark Matter Direct Detection. *JCAP*, 02:004, 2013. doi: 10.1088/1475-7516/2013/02/004.
- [186] Fady Bishara, Joachim Brod, Benjamin Grinstein, and Jure Zupan. DirectDM: a tool for dark matter direct detection, 8 2017.
- [187] Fady Bishara, Joachim Brod, Benjamin Grinstein, and Jure Zupan. From quarks to nucleons in dark matter direct detection. *JHEP*, 11:059, 2017. doi: 10.1007/JHEP11(2017)059.
- [188] Ayala Glick-Magid. Non-relativistic nuclear reduction for tensor couplings in dark matter direct detection and  $\mu \rightarrow e$  conversion, 12 2023.
- [189] Grigory Ovanesyan and Luca Vecchi. Direct detection of dark matter polarizability. *JHEP*, 07:128, 2015. doi: 10.1007/JHEP07(2015)128.
- [190] I. Doršner, S. Fajfer, A. Greljo, J. F. Kamenik, and N. Košnik. Physics of leptoquarks in precision experiments and at particle colliders. *Phys. Rept.*, 641:1–68, 2016. doi: 10.1016/j.physrep.2016.06.001.
- [191] Julian Heeck, Robert Szafron, and Yuichi Uesaka. Isotope dependence of muon-to-electron conversion. *Nucl. Phys. B*, 980:115833, 2022. doi: 10.1016/j.nuclphysb.2022.115833.
- [192] Kaori Fuyuto and Emanuele Merighetti. ALP contributions to  $\mu \rightarrow e$  conversion, 7 2023.
- [193] Calvin W. Johnson, W. Erich Ormand, and Plamen G. Krastev. Factorization in large-scale many-body calculations. *Comput. Phys. Commun.*, 184:2761–2774, 2013. doi: 10.1016/j.cpc.2013.07.022.
- [194] Calvin W. Johnson, W. Erich Ormand, Kenneth S. McElvain, and Hongzhang Shan. BIGSTICK: A flexible configuration-interaction shell-model code, 1 2018.
- [195] T. Suzuki, D. F. Measday, and J. P. Roalsvig. Total nuclear capture rates for negative muons. *Phys. Rev. C*, 35:2212–2224, Jun 1987. doi: 10.1103/PhysRevC.35.2212. URL <https://link.aps.org/doi/10.1103/PhysRevC.35.2212>.
- [196] R. H. Bernstein. The Mu2e Experiment. *Front. in Phys.*, 7:1, 2019. doi: 10.3389/fphy.2019.00001.

- [197] J. C. Angélique et al. COMET - A submission to the 2020 update of the European Strategy for Particle Physics on behalf of the COMET collaboration, 12 2018.
- [198] David McKeen and Maxim Pospelov. Muon Capture Constraints on Sterile Neutrino Properties. *Phys. Rev. D*, 82:113018, 2010. doi: 10.1103/PhysRevD.82.113018.
- [199] Xavier Garcia i Tormo, Douglas Bryman, Andrzej Czarnecki, and Matthew Dowling. Bounds on majoron emission from muon to electron conversion experiments. *Phys. Rev. D*, 84:113010, 2011. doi: 10.1103/PhysRevD.84.113010.
- [200] Yuichi Uesaka. Model identification in  $\mu^- \rightarrow e^-$  conversion with invisible boson emission using muonic atoms. *Phys. Rev. D*, 102(9):095007, 2020. doi: 10.1103/PhysRevD.102.095007.
- [201] Simon Knapen, Kevin Langhoff, Toby Opferkuch, and Diego Redigolo. A Robust Search for Lepton Flavour Violating Axions at Mu3e, 11 2023.
- [202] Richard J. Hill, Ryan Plestid, and Jure Zupan. Searching for new physics at  $\mu \rightarrow e$  facilities with  $\mu^+$  and  $\pi^+$  decays at rest. *Phys. Rev. D*, 109(3):035025, 2024. doi: 10.1103/PhysRevD.109.035025.
- [203] Lorenzo Calibbi, Florian Goertz, Diego Redigolo, Robert Ziegler, and Jure Zupan. Minimal axion model from flavor. *Phys. Rev. D*, 95(9):095009, 2017. doi: 10.1103/PhysRevD.95.095009.
- [204] David Tucker-Smith and Neal Weiner. Inelastic dark matter. *Phys. Rev. D*, 64:043502, 2001. doi: 10.1103/PhysRevD.64.043502.
- [205] Bartosz Fornal and Benjamín Grinstein. Neutron's dark secret. *Mod. Phys. Lett. A*, 35(31):2030019, 2020. doi: 10.1142/S0217732320300190.
- [206] Professor Tsutomu Yanagida (auth.) Professor Masataka Fukugita. *Physics of Neutrinos: and Application to Astrophysics*. Texts and Monographs in Physics. Springer-Verlag Berlin Heidelberg, 1 edition, 2003. ISBN 978-3-642-07851-4, 978-3-662-05119-1.
- [207] Herbi K. Dreiner, Howard E. Haber, and Stephen P. Martin. Two-component spinor techniques and Feynman rules for quantum field theory and supersymmetry. *Phys. Rept.*, 494:1–196, 2010. doi: 10.1016/j.physrep.2010.05.002.
- [208] X. Sun et al. Search for dark matter decay of the free neutron from the UCNA experiment:  $n \rightarrow \chi + e^+ e^-$ . *Phys. Rev. C*, 97(5):052501, 2018. doi: 10.1103/PhysRevC.97.052501.
- [209] M. Klopf, E. Jericha, B. Märkisch, H. Saul, T. Soldner, and H. Abele. Constraints on the Dark Matter Interpretation  $n \rightarrow \chi + e^+ e^-$  of the Neutron Decay Anomaly with the PERKEO II experiment. *Phys. Rev. Lett.*, 122(22):222503, 2019. doi: 10.1103/PhysRevLett.122.222503.

- [210] H. O. Back et al. New limits on nucleon decays into invisible channels with the BOREXINO counting test facility. *Phys. Lett. B*, 563:23–34, 2003. doi: 10.1016/S0370-2693(03)00636-1.
- [211] T. Araki et al. Search for the invisible decay of neutrons with KamLAND. *Phys. Rev. Lett.*, 96:101802, 2006. doi: 10.1103/PhysRevLett.96.101802.
- [212] S. N. Ahmed et al. Constraints on nucleon decay via ‘invisible’ modes from the Sudbury Neutrino Observatory. *Phys. Rev. Lett.*, 92:102004, 2004. doi: 10.1103/PhysRevLett.92.102004.
- [213] A. Allega et al. Improved search for invisible modes of nucleon decay in water with the SNO+detector. *Phys. Rev. D*, 105(11):112012, 2022. doi: 10.1103/PhysRevD.105.112012.
- [214] H. O. Back et al. New experimental limits on violations of the Pauli exclusion principle obtained with the Borexino counting test facility. *Eur. Phys. J. C*, 37:421–431, 2004. doi: 10.1140/epjc/s2004-01991-1.
- [215] T. Suzuki, David F. Measday, and J. P. Roalsvig. Total Nuclear Capture Rates for Negative Muons. *Phys. Rev. C*, 35:2212, 1987. doi: 10.1103/PhysRevC.35.2212.
- [216] Beomki Yeo, Yoshitaka Kuno, MyeongJae Lee, and Kai Zuber. Future experimental improvement for the search of lepton-number-violating processes in the  $e\mu$  sector. *Phys. Rev. D*, 96(7):075027, 2017. doi: 10.1103/PhysRevD.96.075027.
- [217] MyeongJae Lee and Michael MacKenzie. Muon to Positron Conversion. *Universe*, 8(4):227, 2022. doi: 10.3390/universe8040227.
- [218] Léo Borrel, David G. Hitlin, and Sophie Middleton. A New Determination of the (Z,A) Dependence of Coherent Muon-to-Electron Conversion, 1 2024.
- [219] K. Byrum et al. Mu2e-II: Muon to electron conversion with PIP-II. In *Snowmass 2021*, 3 2022.
- [220] A. Takenaka et al. Search for proton decay via  $p \rightarrow e^+\pi^0$  and  $p \rightarrow \mu^+\pi^0$  with an enlarged fiducial volume in Super-Kamiokande I-IV. *Phys. Rev. D*, 102(11):112011, 2020. doi: 10.1103/PhysRevD.102.112011.
- [221] M. Tanaka et al. Search for proton decay into three charged leptons in 0.37 megaton-years exposure of the Super-Kamiokande. *Phys. Rev. D*, 101(5):052011, 2020. doi: 10.1103/PhysRevD.101.052011.
- [222] Dima G. Yakovlev and C. J. Pethick. Neutron star cooling. *Ann. Rev. Astron. Astrophys.*, 42:169–210, 2004. doi: 10.1146/annurev.astro.42.053102.134013.

- [223] James M. Lattimer and Maddapa Prakash. Neutron Star Observations: Prognosis for Equation of State Constraints. *Phys. Rept.*, 442:109–165, 2007. doi: 10.1016/j.physrep.2007.02.003.
- [224] David McKeen, Ann E. Nelson, Sanjay Reddy, and Dake Zhou. Neutron stars exclude light dark baryons. *Phys. Rev. Lett.*, 121(6):061802, 2018. doi: 10.1103/PhysRevLett.121.061802.
- [225] T. F. Motta, P. A. M. Guichon, and A. W. Thomas. Implications of Neutron Star Properties for the Existence of Light Dark Matter. *J. Phys. G*, 45(5):05LT01, 2018. doi: 10.1088/1361-6471/aab689.
- [226] Gordon Baym, D. H. Beck, Peter Geltenbort, and Jessie Shelton. Testing dark decays of baryons in neutron stars. *Phys. Rev. Lett.*, 121(6):061801, 2018. doi: 10.1103/PhysRevLett.121.061801.
- [227] James M. Cline and Jonathan M. Cornell. Dark decay of the neutron. *JHEP*, 07:081, 2018. doi: 10.1007/JHEP07(2018)081.
- [228] Alessandro Strumia. Dark Matter interpretation of the neutron decay anomaly. *JHEP*, 02:067, 2022. doi: 10.1007/JHEP02(2022)067.
- [229] Leonardo Darini. Dark matter implications of the neutron anomaly. *Eur. Phys. J. C*, 83(5):364, 2023. doi: 10.1140/epjc/s10052-023-11497-9.
- [230] Nai-Bo Zhang and Bao-An Li. Constraints on the muon fraction and density profile in neutron stars. *Astrophys. J.*, 893:61, 2020. doi: 10.3847/1538-4357/ab7dbc.
- [231] David McKeen, Maxim Pospelov, and Nirmal Raj. Cosmological and astrophysical probes of dark baryons. *Phys. Rev. D*, 103(11):115002, 2021. doi: 10.1103/PhysRevD.103.115002.
- [232] David McKeen, Maxim Pospelov, and Nirmal Raj. Neutron Star Internal Heating Constraints on Mirror Matter. *Phys. Rev. Lett.*, 127(6):061805, 2021. doi: 10.1103/PhysRevLett.127.061805.
- [233] Sebastien Guillot, G. G. Pavlov, C. Reyes, A. Reisenegger, L. Rodriguez, B. Rangelov, and O. Kargaltsev. Hubble Space Telescope Nondetection of PSR J2144–3933: The Coldest Known Neutron Star. *Astrophys. J.*, 874(2):175, 2019. doi: 10.3847/1538-4357/ab0f38.
- [234] Itzhak Goldman, Rabindra N. Mohapatra, and Shmuel Nussinov. Bounds on neutron-mirror neutron mixing from pulsar timing. *Phys. Rev. D*, 100(12):123021, 2019. doi: 10.1103/PhysRevD.100.123021.
- [235] Tanja Geib, Alexander Merle, and Kai Zuber.  $\mu^- - e^+$  conversion in upcoming LFV experiments. *Phys. Lett. B*, 764:157–162, 2017. doi: 10.1016/j.physletb.2016.11.029.

- [236] Jeffrey M. Berryman, André de Gouvêa, Kevin J. Kelly, and Andrew Kobach. Lepton-number-violating searches for muon to positron conversion. *Phys. Rev. D*, 95(11):115010, 2017. doi: 10.1103/PhysRevD.95.115010.
- [237] S. Ahmad et al. Search for Muon - Electron and Muon - Positron Conversion. *Phys. Rev. D*, 38:2102, 1988. doi: 10.1103/PhysRevD.38.2102.
- [238] C. Dohmen et al. Test of lepton flavor conservation in  $\mu^- \rightarrow e^-$  conversion on titanium. *Phys. Lett. B*, 317:631–636, 1993. doi: 10.1016/0370-2693(93)91383-X.
- [239] J. Kaulard et al. Improved limit on the branching ratio of  $\mu^- \rightarrow e^+$  conversion on titanium. *Phys. Lett. B*, 422:334–338, 1998. doi: 10.1016/S0370-2693(97)01423-8.
- [240] G. Conforto, M. Conversi, and L. di Lella. Search for Neutrinoless Coherent Nuclear Capture of mu- Mesons. *Nuovo Cim.*, 26:261, 1962. doi: 10.1007/BF02787041.
- [241] D. A. Bryman, M. Blecher, K. Gotow, and R. J. Powers. Search for the reaction  $\mu^- \text{Cu} \rightarrow e^+ \text{Co}$ . *Phys. Rev. Lett.*, 28:1469–1471, 1972. doi: 10.1103/PhysRevLett.28.1469.
- [242] R. Abela, G. Backenstoss, W. Kowald, J. Wuest, H. G. Seiler, M. Seiler, and L. M. Simons. New Upper Limit For  $\mu^- \rightarrow e^+$  Conversion. *Phys. Lett. B*, 95:318–322, 1980. doi: 10.1016/0370-2693(80)90495-5.
- [243] F. Zwicky. Die Rotverschiebung von extragalaktischen Nebeln. *Helv. Phys. Acta*, 6:110–127, 1933. doi: 10.1007/s10714-008-0707-4.
- [244] Vera C. Rubin and W. Kent Ford, Jr. Rotation of the Andromeda Nebula from a Spectroscopic Survey of Emission Regions. *Astrophys. J.*, 159:379–403, 1970. doi: 10.1086/150317.
- [245] Douglas Clowe, Marusa Bradac, Anthony H. Gonzalez, Maxim Markevitch, Scott W. Randall, Christine Jones, and Dennis Zaritsky. A direct empirical proof of the existence of dark matter. *Astrophys. J. Lett.*, 648:L109–L113, 2006. doi: 10.1086/508162.
- [246] N. Aghanim et al. Planck 2018 results. VI. Cosmological parameters. *Astron. Astrophys.*, 641:A6, 2020. doi: 10.1051/0004-6361/201833910. [Erratum: Astron. Astrophys. 652, C4 (2021)].
- [247] Max Tegmark et al. The 3-D power spectrum of galaxies from the SDSS. *Astrophys. J.*, 606:702–740, 2004. doi: 10.1086/382125.
- [248] Marco Cirelli, Alessandro Strumia, and Jure Zupan. Dark Matter, 6 2024.
- [249] Philip Ilten et al. Experiments and Facilities for Accelerator-Based Dark Sector Searches. In *Snowmass 2021*, 6 2022.

- [250] Yonatan Kahn and Tongyan Lin. Searches for light dark matter using condensed matter systems. *Rept. Prog. Phys.*, 85(6):066901, 2022. doi: 10.1088/1361-6633/ac5f63.
- [251] Andrea Mitridate, Tanner Trickle, Zhengkang Zhang, and Kathryn M. Zurek. Snowmass white paper: Light dark matter direct detection at the interface with condensed matter physics. *Phys. Dark Univ.*, 40:101221, 2023. doi: 10.1016/j.dark.2023.101221.
- [252] Joerg Jaeckel, Gray Rybka, and Lindley Winslow. Report of the Topical Group on Wave Dark Matter for Snowmass 2021, 9 2022.
- [253] S. Tremaine and J. E. Gunn. Dynamical Role of Light Neutral Leptons in Cosmology. *Phys. Rev. Lett.*, 42:407–410, 1979. doi: 10.1103/PhysRevLett.42.407.
- [254] Michael S. Turner. Coherent scalar-field oscillations in an expanding universe. *Phys. Rev. D*, 28:1243–1247, Sep 1983. doi: 10.1103/PhysRevD.28.1243. URL <https://link.aps.org/doi/10.1103/PhysRevD.28.1243>.
- [255] Pablo F. de Salas and Axel Widmark. Dark matter local density determination: recent observations and future prospects. *Rept. Prog. Phys.*, 84(10):104901, 2021. doi: 10.1088/1361-6633/ac24e7.
- [256] John Preskill, Mark B. Wise, and Frank Wilczek. Cosmology of the Invisible Axion. *Phys. Lett. B*, 120:127–132, 1983. doi: 10.1016/0370-2693(83)90637-8.
- [257] L. F. Abbott and P. Sikivie. A Cosmological Bound on the Invisible Axion. *Phys. Lett. B*, 120:133–136, 1983. doi: 10.1016/0370-2693(83)90638-X.
- [258] Michael Dine and Willy Fischler. The Not So Harmless Axion. *Phys. Lett. B*, 120:137–141, 1983. doi: 10.1016/0370-2693(83)90639-1.
- [259] Tim Zimmermann, James Alvey, David J. E. Marsh, Malcolm Fairbairn, and Justin I. Read. Dwarf galaxies imply dark matter is heavier than  $2.2 \times 10^{-21}$  eV, 5 2024.
- [260] María Benito, Gert Hütsi, Kristjan Müürsepp, Jorge Sánchez~Almeida, Juan Urrutia, Ville Vaskonen, and Hardi Veermäe. Fuzzy dark matter fails to explain the dark matter cores, 2 2025.
- [261] D. Antypas et al. New Horizons: Scalar and Vector Ultralight Dark Matter, 3 2022.
- [262] Lam Hui. Wave Dark Matter. *Ann. Rev. Astron. Astrophys.*, 59:247–289, 2021. doi: 10.1146/annurev-astro-120920-010024.
- [263] M. S. Safranova, D. Budker, D. DeMille, Derek F. Jackson Kimball, A. Derevianko, and C. W. Clark. Search for New Physics with Atoms and Molecules. *Rev. Mod. Phys.*, 90(2):025008, 2018. doi: 10.1103/RevModPhys.90.025008.

- [264] Asher Berlin. Neutrino Oscillations as a Probe of Light Scalar Dark Matter. *Phys. Rev. Lett.*, 117(23):231801, 2016. doi: 10.1103/PhysRevLett.117.231801.
- [265] Vedran Brdar, Joachim Kopp, Jia Liu, Pascal Prass, and Xiao-Ping Wang. Fuzzy dark matter and nonstandard neutrino interactions. *Phys. Rev. D*, 97(4):043001, 2018. doi: 10.1103/PhysRevD.97.043001.
- [266] Gordan Krnjaic, Pedro A. N. Machado, and Lina Necib. Distorted neutrino oscillations from time varying cosmic fields. *Phys. Rev. D*, 97(7):075017, 2018. doi: 10.1103/PhysRevD.97.075017.
- [267] Francesco Capozzi, Ian M. Shoemaker, and Luca Vecchi. Neutrino Oscillations in Dark Backgrounds. *JCAP*, 07:004, 2018. doi: 10.1088/1475-7516/2018/07/004.
- [268] Abhish Dev, Gordan Krnjaic, Pedro Machado, and Harikrishnan Ramani. Constraining feeble neutrino interactions with ultralight dark matter. *Phys. Rev. D*, 107(3):035006, 2023. doi: 10.1103/PhysRevD.107.035006.
- [269] Marta Losada, Yosef Nir, Gilad Perez, Inbar Savoray, and Yoge Shpilman. Time dependent CP-even and CP-odd signatures of scalar ultralight dark matter in neutrino oscillations. *Phys. Rev. D*, 108(5):055004, 2023. doi: 10.1103/PhysRevD.108.055004.
- [270] Michael Dine, Gilad Perez, Wolfram Ratzinger, and Inbar Savoray. Nelson-Barr ultralight dark matter. *Phys. Rev. D*, 111(1):015049, 2025. doi: 10.1103/PhysRevD.111.015049.
- [271] Dean Lee, Ulf-G. Meißner, Keith A. Olive, Mikhail Shifman, and Thomas Vonk.  $\theta$  - dependence of light nuclei and nucleosynthesis. *Phys. Rev. Res.*, 2(3):033392, 2020. doi: 10.1103/PhysRevResearch.2.033392.
- [272] Xin Zhang, Nick Houston, and Tianjun Li. Nuclear decay anomalies as a signature of axion dark matter. *Phys. Rev. D*, 108(7):L071101, 2023. doi: 10.1103/PhysRevD.108.L071101.
- [273] Jorge Alda, Carlo Broggini, Giuseppe Di Carlo, Luca Di Luzio, Denise Piatti, Stefano Rigolin, and Claudio Toni. Weak nuclear decays deep-underground as a probe of axion dark matter. *Phys. Rev. D*, 111(3):035022, 2025. doi: 10.1103/PhysRevD.111.035022.
- [274] Thomas Bouley, Philip Sørensen, and Tien-Tien Yu. Constraints on ultralight scalar dark matter with quadratic couplings. *JHEP*, 03:104, 2023. doi: 10.1007/JHEP03(2023)104.
- [275] W. Altmannshofer et al. The Belle II Physics Book. *PTEP*, 2019(12):123C01, 2019. doi: 10.1093/ptep/ptz106. [Erratum: PTEP 2020, 029201 (2020)].
- [276] A. Abada et al. FCC Physics Opportunities: Future Circular Collider Conceptual Design Report Volume 1. *Eur. Phys. J. C*, 79(6):474, 2019. doi: 10.1140/epjc/s10052-019-6904-3.

- [277] Mogens Dam. Tau-lepton Physics at the FCC-ee circular  $e^+e^-$  Collider. *SciPost Phys. Proc.*, 1:041, 2019. doi: 10.21468/SciPostPhysProc.1.041.
- [278] Yongssoo Jho, Simon Knapen, and Diego Redigolo. Lepton-flavor violating axions at MEG II. *JHEP*, 10:029, 2022. doi: 10.1007/JHEP10(2022)029.
- [279] Yoshitaka Kuno. A search for muon-to-electron conversion at J-PARC: The COMET experiment. *PTEP*, 2013:022C01, 2013. doi: 10.1093/ptep/pts089.
- [280] M. Ablikim et al. Future Physics Programme of BESIII. *Chin. Phys. C*, 44(4):040001, 2020. doi: 10.1088/1674-1137/44/4/040001.
- [281] M. Ablikim et al. Design and Construction of the BESIII Detector. *Nucl. Instrum. Meth. A*, 614:345–399, 2010. doi: 10.1016/j.nima.2009.12.050.
- [282] Antonio Pich. Tau physics opportunities at the super tau-charm facility. *Int. J. Mod. Phys. A*, 39(26n27):2442002, 2024. doi: 10.1142/S0217751X24420028.
- [283] M. N. Achasov et al. Experiments at the Super Charm-Tau factory. *Phys. Usp.*, vol(1): 55–70, 2024. doi: 10.3367/UFNr.2023.10.039583.
- [284] M. Achasov et al. STCF conceptual design report (Volume 1): Physics & detector. *Front. Phys. (Beijing)*, 19(1):14701, 2024. doi: 10.1007/s11467-023-1333-z.
- [285] Xiaocong Ai et al. Flavor Physics at CEPC: a General Perspective, 12 2024.
- [286] A. Jodidio et al. Search for Right-Handed Currents in Muon Decay. *Phys. Rev. D*, 34: 1967, 1986. doi: 10.1103/PhysRevD.34.1967. [Erratum: Phys.Rev.D 37, 237 (1988)].
- [287] R. D. Peccei and Helen R. Quinn. CP Conservation in the Presence of Instantons. *Phys. Rev. Lett.*, 38:1440–1443, 1977. doi: 10.1103/PhysRevLett.38.1440.
- [288] R. D. Peccei and Helen R. Quinn. Constraints Imposed by CP Conservation in the Presence of Instantons. *Phys. Rev. D*, 16:1791–1797, 1977. doi: 10.1103/PhysRevD.16.1791.
- [289] Frank Wilczek. Problem of Strong  $P$  and  $T$  Invariance in the Presence of Instantons. *Phys. Rev. Lett.*, 40:279–282, 1978. doi: 10.1103/PhysRevLett.40.279.
- [290] Steven Weinberg. A New Light Boson? *Phys. Rev. Lett.*, 40:223–226, 1978. doi: 10.1103/PhysRevLett.40.223.
- [291] J. F. Donoghue, E. Golowich, and Barry R. Holstein. *Dynamics of the standard model*, volume 2. CUP, 2014. doi: 10.1017/CBO9780511524370.

- [292] Yonit Hochberg, Eric Kuflik, Hitoshi Murayama, Tomer Volansky, and Jay G. Wacker. Model for Thermal Relic Dark Matter of Strongly Interacting Massive Particles. *Phys. Rev. Lett.*, 115(2):021301, 2015. doi: 10.1103/PhysRevLett.115.021301.
- [293] Yonit Hochberg, Eric Kuflik, and Hitoshi Murayama. SIMP Spectroscopy. *JHEP*, 05:090, 2016. doi: 10.1007/JHEP05(2016)090.
- [294] Soo-Min Choi, Yonit Hochberg, Eric Kuflik, Hyun Min Lee, Yann Mambrini, Hitoshi Murayama, and Mathias Pierre. Vector SIMP dark matter. *JHEP*, 10:162, 2017. doi: 10.1007/JHEP10(2017)162.
- [295] Yonit Hochberg, Eric Kuflik, Robert Mcgehee, Hitoshi Murayama, and Katelin Schutz. Strongly interacting massive particles through the axion portal. *Phys. Rev. D*, 98(11):115031, 2018. doi: 10.1103/PhysRevD.98.115031.
- [296] Yonit Hochberg, Eric Kuflik, and Hitoshi Murayama. Twin Higgs model with strongly interacting massive particle dark matter. *Phys. Rev. D*, 99(1):015005, 2019. doi: 10.1103/PhysRevD.99.015005.
- [297] Gordan Krnjaic and Kris Sigurdson. Big Bang Darkleosynthesis. *Phys. Lett. B*, 751:464–468, 2015. doi: 10.1016/j.physletb.2015.11.001.
- [298] Reuven Balkin, Maximilian Ruhdorfer, Ennio Salvioni, and Andreas Weiler. Dark matter shifts away from direct detection. *JCAP*, 11:050, 2018. doi: 10.1088/1475-7516/2018/11/050.
- [299] Reuven Balkin, Gilad Perez, and Andreas Weiler. Little composite dark matter. *Eur. Phys. J. C*, 78(2):104, 2018. doi: 10.1140/epjc/s10052-018-5552-3.
- [300] David Marzocca and Alfredo Urbano. Composite Dark Matter and LHC Interplay. *JHEP*, 07:107, 2014. doi: 10.1007/JHEP07(2014)107.
- [301] Michele Frigerio, Alex Pomarol, Francesco Riva, and Alfredo Urbano. Composite Scalar Dark Matter. *JHEP*, 07:015, 2012. doi: 10.1007/JHEP07(2012)015.
- [302] Asher Berlin, Nikita Blinov, Stefania Gori, Philip Schuster, and Natalia Toro. Cosmology and Accelerator Tests of Strongly Interacting Dark Matter. *Phys. Rev. D*, 97(5):055033, 2018. doi: 10.1103/PhysRevD.97.055033.
- [303] Elias Bernreuther, Felix Kahlhoefer, Michael Krämer, and Patrick Tunney. Strongly interacting dark sectors in the early Universe and at the LHC through a simplified portal. *JHEP*, 01:162, 2020. doi: 10.1007/JHEP01(2020)162.
- [304] Graham D. Kribs, Adam Martin, Bryan Ostdiek, and Tom Tong. Dark Mesons at the LHC. *JHEP*, 07:133, 2019. doi: 10.1007/JHEP07(2019)133.

- [305] Sophie Renner and Pedro Schwaller. A flavoured dark sector. *JHEP*, 08:052, 2018. doi: 10.1007/JHEP08(2018)052.
- [306] Jordi Folch Eguren, Sophie Klingel, Emmanuel Stamou, Mustafa Tabet, and Robert Ziegler. Flavor phenomenology of light dark vectors. *JHEP*, 08:111, 2024. doi: 10.1007/JHEP08(2024)111.
- [307] Aleks Smolkovič, Michele Tammaro, and Jure Zupan. Anomaly free Froggatt-Nielsen models of flavor. *JHEP*, 10:188, 2019. doi: 10.1007/JHEP10(2019)188. [Erratum: *JHEP* 02, 033 (2022)].
- [308] Azadeh Maleknejad and Evan McDonough. Ultralight pion and superheavy baryon dark matter. *Phys. Rev. D*, 106(9):095011, 2022. doi: 10.1103/PhysRevD.106.095011.
- [309] Abhishek Banerjee, Gilad Perez, Marianna Safronova, Inbar Savoray, and Aviv Shalit. The phenomenology of quadratically coupled ultra light dark matter. *JHEP*, 10:042, 2023. doi: 10.1007/JHEP10(2023)042.
- [310] Xucheng Gan, Da Liu, Di Liu, Xuheng Luo, and Bingrong Yu. Detecting Ultralight Dark Matter with Matter Effect, 4 2025.
- [311] Yuval Grossman, Bingrong Yu, and Siyu Zhou. Axion forces in axion backgrounds, 3 2025.
- [312] Ken Van Tilburg. Wake forces in a background of quadratically coupled mediators. *Phys. Rev. D*, 109(9):096036, 2024. doi: 10.1103/PhysRevD.109.096036.
- [313] Carl Beadle, Sebastian A. R. Ellis, Jérémie Quevillon, and Pham Ngoc Hoa Vuong. Quadratic coupling of the axion to photons. *Phys. Rev. D*, 110(3):035019, 2024. doi: 10.1103/PhysRevD.110.035019.
- [314] Aurélien Hees, Olivier Minazzoli, Etienne Savalle, Yevgeny V. Stadnik, and Peter Wolf. Violation of the equivalence principle from light scalar dark matter. *Phys. Rev. D*, 98(6): 064051, 2018. doi: 10.1103/PhysRevD.98.064051.
- [315] P. Banerjee, A. M. Coutinho, T. Engel, A. Gurgone, A. Signer, and Y. Ulrich. High-precision muon decay predictions for ALP searches, 11 2022.
- [316] N. Panagia, R. Gilmozzi, F. Macchetto, H. M. Adorf, and R. P. Kirshner. Properties of the SN 1987A Circumstellar Ring and the Distance to the Large Magellanic Cloud. *Astrop. J. Lett.*, 380:L23, 1991. doi: 10.1086/186164.
- [317] Matthew R. Buckley, Eric Charles, Jennifer M. Gaskins, Alyson M. Brooks, Alex Drlica-Wagner, Pierrick Martin, and Geng Zhao. Search for Gamma-ray Emission from Dark Matter Annihilation in the Large Magellanic Cloud with the Fermi Large Area Telescope. *Phys. Rev. D*, 91(10):102001, 2015. doi: 10.1103/PhysRevD.91.102001.

- [318] Francesco Capozzi and Georg Raffelt. Axion and neutrino bounds improved with new calibrations of the tip of the red-giant branch using geometric distance determinations. *Phys. Rev. D*, 102(8):083007, 2020. doi: 10.1103/PhysRevD.102.083007.
- [319] Robert Bollig, William DeRocco, Peter W. Graham, and Hans-Thomas Janka. Muons in Supernovae: Implications for the Axion-Muon Coupling. *Phys. Rev. Lett.*, 125(5):051104, 2020. doi: 10.1103/PhysRevLett.125.051104. [Erratum: Phys.Rev.Lett. 126, 189901 (2021)].
- [320] Andrea Caputo, Georg Raffelt, and Edoardo Vitagliano. Muonic boson limits: Supernova redux. *Phys. Rev. D*, 105(3):035022, 2022. doi: 10.1103/PhysRevD.105.035022.
- [321] Jacob T. VanderPlas. Understanding the lomb scargle periodogram. *The Astrophysical Journal Supplement Series*, 236(1):16, May 2018. ISSN 1538-4365. doi: 10.3847/1538-4365/aab766. URL <http://dx.doi.org/10.3847/1538-4365/aab766>.
- [322] Marcela Garcia Hernandez. *Search for new physics in charged lepton flavor violating processes at the Belle II experiment*. PhD thesis, Cinvestav-IPN, CINVESTAV, IPN, 2023.
- [323] E. De La Cruz-Burelo, M. Hernandez-Villanueva, and A. De Yta-Hernandez. New method for beyond the Standard Model invisible particle searches in tau lepton decays. *Phys. Rev. D*, 102(11):115001, 2020. doi: 10.1103/PhysRevD.102.115001.
- [324] Mogens Dam. The  $\tau$  challenges at FCC-ee. *Eur. Phys. J. Plus*, 136(9):963, 2021. doi: 10.1140/epjp/s13360-021-01894-y.
- [325] Enrico Bothmann et al. Event Generation with Sherpa 2.2. *SciPost Phys.*, 7(3):034, 2019. doi: 10.21468/SciPostPhys.7.3.034.
- [326] Johannes Bellm et al. Herwig 7.0/Herwig++ 3.0 release note. *Eur. Phys. J. C*, 76(4):196, 2016. doi: 10.1140/epjc/s10052-016-4018-8.
- [327] Simone Alioli, Paolo Nason, Carlo Oleari, and Emanuele Re. A general framework for implementing NLO calculations in shower Monte Carlo programs: the POWHEG BOX. *JHEP*, 06:043, 2010. doi: 10.1007/JHEP06(2010)043.
- [328] Paolo Nason. A New method for combining NLO QCD with shower Monte Carlo algorithms. *JHEP*, 11:040, 2004. doi: 10.1088/1126-6708/2004/11/040.
- [329] Stefano Frixione, Paolo Nason, and Carlo Oleari. Matching NLO QCD computations with Parton Shower simulations: the POWHEG method. *JHEP*, 11:070, 2007. doi: 10.1088/1126-6708/2007/11/070.

- [330] Stefano Frixione and Bryan R. Webber. Matching NLO QCD computations and parton shower simulations. *JHEP*, 06:029, 2002. doi: 10.1088/1126-6708/2002/06/029.
- [331] Joon-Bin Lee, M. R. Masouminia, Michael H. Seymour, and Un-ki Yang. Generalized angular-order parton showers in Herwig 7. *JHEP*, 08:064, 2024. doi: 10.1007/JHEP08(2024)064.
- [332] Steffen Schumann and Frank Krauss. A Parton shower algorithm based on Catani-Seymour dipole factorisation. *JHEP*, 03:038, 2008. doi: 10.1088/1126-6708/2008/03/038.
- [333] Bo Andersson. *The Lund Model*, volume 7 of *Cambridge Monographs on Particle Physics, Nuclear Physics and Cosmology*. Cambridge University Press, 7 2023. ISBN 978-1-00-940129-6, 978-1-00-940125-8, 978-1-00-940128-9, 978-0-521-01734-3, 978-0-521-42094-5, 978-0-511-88149-7. doi: 10.1017/9781009401296.
- [334] Richard D. Field and Stephen Wolfram. A QCD Model for e+ e- Annihilation. *Nucl. Phys. B*, 213:65–84, 1983. doi: 10.1016/0550-3213(83)90175-X.
- [335] Thomas D. Gottschalk. An Improved Description of Hadronization in the {QCD} Cluster Model for  $e^+e^-$  Annihilation. *Nucl. Phys. B*, 239:349–381, 1984. doi: 10.1016/0550-3213(84)90253-0.
- [336] B.R. Webber. A QCD Model for Jet Fragmentation Including Soft Gluon Interference. *Nucl. Phys. B*, 238:492–528, 1984. doi: 10.1016/0550-3213(84)90333-X.
- [337] Alexander Kupco. Cluster hadronization in HERWIG 5.9. In *Workshop on Monte Carlo Generators for HERA Physics (Plenary Starting Meeting)*, pages 292–300, 4 1998.
- [338] Andy Buckley, Philip Ilten, Dmitri Konstantinov, Leif Lönnblad, James Monk, Witold Pokorski, Tomasz Przedzinski, and Andrii Verbytskyi. The HepMC3 event record library for Monte Carlo event generators. *Comput. Phys. Commun.*, 260:107310, 2021. doi: 10.1016/j.cpc.2020.107310.
- [339] D. J. Lange. The EvtGen particle decay simulation package. *Nucl. Instrum. Meth. A*, 462:152–155, 2001. doi: 10.1016/S0168-9002(01)00089-4.
- [340] Anders Ryd, David Lange, Natalia Kuznetsova, Sophie Versille, Marcello Rotondo, David P. Kirkby, Frank K. Wuerthwein, and Akimasa Ishikawa. EvtGen: A Monte Carlo Generator for B-Physics, 5 2005.
- [341] S. Agostinelli et al. GEANT4 - A Simulation Toolkit. *Nucl. Instrum. Meth. A*, 506:250–303, 2003. doi: 10.1016/S0168-9002(03)01368-8.
- [342] John Allison et al. Geant4 developments and applications. *IEEE Trans. Nucl. Sci.*, 53:270, 2006. doi: 10.1109/TNS.2006.869826.

- [343] Naomi Ratcliffe, Roger Barlow, Adriana Bungau, Cristian Bungau, and Robert Cywinski. GEANT4 Target Simulations for Low Energy Medical Applications. In *4th International Particle Accelerator Conference*, page THPWA039, 2013.
- [344] X. Artru and G. Mennessier. String model and multiproduction. *Nucl. Phys. B*, 70:93–115, 1974. doi: 10.1016/0550-3213(74)90360-5.
- [345] R. D. Field and R. P. Feynman. A Parametrization of the Properties of Quark Jets. *Nucl. Phys. B*, 136:1, 1978. doi: 10.1016/0550-3213(78)90015-9.
- [346] S. Abachi, C. Buchanan, A. Chien, S. Chun, and B. Hartfiel. UCLA space-time area law model: A Persuasive foundation for hadronization. *Eur. Phys. J. C*, 49:569–580, 2007. doi: 10.1140/epjc/s10052-006-0185-3.
- [347] Peter Braun-Munzinger, Krzysztof Redlich, and Johanna Stachel. Particle production in heavy ion collisions, 4 2003.
- [348] F. Becattini, M. Gazdzicki, A. Keranen, J. Manninen, and R. Stock. Chemical equilibrium in nucleus nucleus collisions at relativistic energies. *Phys. Rev. C*, 69:024905, 2004. doi: 10.1103/PhysRevC.69.024905.
- [349] R. J. Fries, Berndt Muller, C. Nonaka, and S. A. Bass. Hadronization in heavy ion collisions: Recombination and fragmentation of partons. *Phys. Rev. Lett.*, 90:202303, 2003. doi: 10.1103/PhysRevLett.90.202303.
- [350] V. Greco, C. M. Ko, and P. Levai. Parton coalescence and anti-proton / pion anomaly at RHIC. *Phys. Rev. Lett.*, 90:202302, 2003. doi: 10.1103/PhysRevLett.90.202302.
- [351] Torbjörn Sjöstrand. Jet fragmentation of multiparton configurations in a string framework. *Nuclear Physics B*, 248(2):469–502, 1984. ISSN 0550-3213. doi: [https://doi.org/10.1016/0550-3213\(84\)90607-2](https://doi.org/10.1016/0550-3213(84)90607-2). URL <https://www.sciencedirect.com/science/article/pii/0550321384906072>.
- [352] G. S. Bali and K. Schilling. Static quark - anti-quark potential: Scaling behavior and finite size effects in SU(3) lattice gauge theory. *Phys. Rev. D*, 46:2636–2646, 1992. doi: 10.1103/PhysRevD.46.2636.
- [353] Gunnar S. Bali, Klaus Schilling, and Armin Wachter. Complete O ( $v^{**2}$ ) corrections to the static interquark potential from SU(3) gauge theory. *Phys. Rev. D*, 56:2566–2589, 1997. doi: 10.1103/PhysRevD.56.2566.
- [354] T. Regge. Introduction to complex orbital momenta. *Nuovo Cim.*, 14:951, 1959. doi: 10.1007/BF02728177.

- [355] G. F. Chew and Steven C. Frautschi. Regge Trajectories and the Principle of Maximum Strength for Strong Interactions. *Phys. Rev. Lett.*, 8:41–44, 1962. doi: 10.1103/PhysRevLett.8.41.
- [356] Yoichiro Nambu. DUAL MODEL OF HADRONS, 2 1970.
- [357] Holger Bech Nielsen and P. Olesen. A Parton view on dual amplitudes. *Phys. Lett. B*, 32: 203–206, 1970. doi: 10.1016/0370-2693(70)90474-0.
- [358] Leonard Susskind. Dual symmetric theory of hadrons. 1. *Nuovo Cim. A*, 69:457–496, 1970. doi: 10.1007/BF02726485.
- [359] Nan Du, Yanping Huang, Andrew M. Dai, Simon Tong, Dmitry Lepikhin, Yuanzhong Xu, Maxim Krikun, Yanqi Zhou, Adams Wei Yu, Orhan Firat, Barret Zoph, Liam Fedus, Maarten Bosma, Zongwei Zhou, Tao Wang, Yu Emma Wang, Kellie Webster, Marie Pellat, Kevin Robinson, Kathleen Meier-Hellstern, Toju Duke, Lucas Dixon, Kun Zhang, Quoc V Le, Yonghui Wu, Zhifeng Chen, and Claire Cui. Glam: Efficient scaling of language models with mixture-of-experts, 2022. URL <https://arxiv.org/abs/2112.06905>.
- [360] Jesmin Jahan Tithi, Hanjiang Wu, Avishai Abuhatzera, and Fabrizio Petrini. Scaling intelligence: Designing data centers for next-gen language models, 2025. URL <https://arxiv.org/abs/2506.15006>.
- [361] Andy Buckley et al. General-purpose event generators for LHC physics. *Phys. Rept.*, 504: 145–233, 2011. doi: 10.1016/j.physrep.2011.03.005.
- [362] J. M. Campbell et al. Event Generators for High-Energy Physics Experiments. In *2022 Snowmass Summer Study*, 3 2022.
- [363] W. T. Giele, D. A. Kosower, and P. Z. Skands. Higher-Order Corrections to Timelike Jets. *Phys. Rev.*, D84:054003, 2011. doi: 10.1103/PhysRevD.84.054003.
- [364] Z. Bern, L. J. Dixon, F. Febres Cordero, S. Höche, H. Ita, D. A. Kosower, and D. Maitre. Ntuples for NLO Events at Hadron Colliders. *Comput. Phys. Commun.*, 185:1443–1460, 2014. doi: 10.1016/j.cpc.2014.01.011.
- [365] S. Mrenna and P. Skands. Automated Parton-Shower Variations in Pythia 8. *Phys. Rev. D*, 94(7):074005, 2016. doi: 10.1103/PhysRevD.94.074005.
- [366] Johannes Bellm, Simon Plätzer, Peter Richardson, Andrzej Siódlok, and Stephen Webster. Reweighting Parton Showers. *Phys. Rev. D*, 94(3):034028, 2016. doi: 10.1103/PhysRevD.94.034028.
- [367] Enrico Bothmann, Marek Schönherr, and Steffen Schumann. Reweighting QCD matrix-element and parton-shower calculations. *Eur. Phys. J. C*, 76(11):590, 2016. doi: 10.1140/epjc/s10052-016-4430-0.

- [368] Mats Bengtsson and Torbjorn Sjöstrand. Coherent Parton Showers Versus Matrix Elements: Implications of PETRA - PEP Data. *Phys. Lett.*, B185:435, 1987. doi: 10.1016/0370-2693(87)91031-8.
- [369] Gabriela Miu and Torbjorn Sjostrand.  $W$  production in an improved parton shower approach. *Phys. Lett. B*, 449:313–320, 1999. doi: 10.1016/S0370-2693(99)00068-4.
- [370] E. Norrbin and T. Sjöstrand. QCD radiation off heavy particles. *Nucl. Phys.*, B603: 297–342, 2001. doi: 10.1016/S0550-3213(01)00099-2.
- [371] Leif Lonnblad. Correcting the color dipole cascade model with fixed order matrix elements. *JHEP*, 05:046, 2002. doi: 10.1088/1126-6708/2002/05/046.
- [372] Michelangelo L. Mangano, Mauro Moretti, Fulvio Piccinini, and Michele Treccani. Matching matrix elements and shower evolution for top-quark production in hadronic collisions. *JHEP*, 01:013, 2007. doi: 10.1088/1126-6708/2007/01/013.
- [373] Stefan Hoeche, Steffen Schumann, and Frank Siegert. Hard photon production and matrix-element parton-shower merging. *Phys. Rev.*, D81:034026, 2010. doi: 10.1103/PhysRevD.81.034026.
- [374] Stefan Hoche, Frank Krauss, Marek Schonherr, and Frank Siegert. NLO matrix elements and truncated showers. *JHEP*, 08:123, 2011. doi: 10.1007/JHEP08(2011)123.
- [375] Leif Lönblad and Stefan Prestel. Unitarising Matrix Element + Parton Shower merging. *JHEP*, 02:094, 2013. doi: 10.1007/JHEP02(2013)094.
- [376] Leif Lönnblad and Stefan Prestel. Merging Multi-leg NLO Matrix Elements with Parton Showers. *JHEP*, 03:166, 2013. doi: 10.1007/JHEP03(2013)166.
- [377] Rikkert Frederix and Stefano Frixione. Merging meets matching in MC@NLO. *JHEP*, 12: 061, 2012. doi: 10.1007/JHEP12(2012)061.
- [378] Rikkert Frederix and Ioannis Tsinikos. On improving NLO merging for  $t\bar{t}W$  production. *JHEP*, 11:029, 2021. doi: 10.1007/JHEP11(2021)029.
- [379] Adil Jueid, Jochem Kip, Roberto Ruiz de Austri, and Peter Skands. The Strong Force meets the Dark Sector: a robust estimate of QCD uncertainties for anti-matter dark matter searches, 3 2023.
- [380] Adil Jueid, Jochem Kip, Roberto Ruiz de Austri, and Peter Skands. Impact of QCD uncertainties on antiproton spectra from dark-matter annihilation. *JCAP*, 04:068, 2023. doi: 10.1088/1475-7516/2023/04/068.

- [381] Simone Amoroso, Sascha Caron, Adil Jueid, Roberto Ruiz de Austri, and Peter Skands. Estimating QCD uncertainties in Monte Carlo event generators for gamma-ray dark matter searches. *JCAP*, 05:007, 2019. doi: 10.1088/1475-7516/2019/05/007.
- [382] Bo Andersson, G. Gustafson, and B. Soderberg. A General Model for Jet Fragmentation. *Z. Phys. C*, 20:317, 1983. doi: 10.1007/BF01407824.
- [383] Bo Andersson, G. Gustafson, and T. Sjostrand. Baryon Production in Jet Fragmentation and  $\Upsilon$  Decay. *Phys. Scripta*, 32:574, 1985. doi: 10.1088/0031-8949/32/6/003.
- [384] T. Sjostrand and Peter Z. Skands. Baryon number violation and string topologies. *Nucl. Phys. B*, 659:243, 2003. doi: 10.1016/S0550-3213(03)00193-7.
- [385] Jesper R. Christiansen and Peter Z. Skands. String Formation Beyond Leading Colour. *JHEP*, 08:003, 2015. doi: 10.1007/JHEP08(2015)003.
- [386] Bo Andersson, G. Gustafson, and T. Sjostrand. A Model for Baryon Production in Quark and Gluon Jets. *Nucl. Phys. B*, 197:45–54, 1982. doi: 10.1016/0550-3213(82)90153-5.
- [387] Adam Paszke, Sam Gross, Francisco Massa, Adam Lerer, James Bradbury, Gregory Chanan, Trevor Killeen, Zeming Lin, Natalia Gimelshein, Luca Antiga, Alban Desmaison, Andreas Kopf, Edward Yang, Zachary DeVito, Martin Raison, Alykhan Tejani, Sasank Chilamkurthy, Benoit Steiner, Lu Fang, Junjie Bai, and Soumith Chintala. Pytorch: An imperative style, high-performance deep learning library. In *Advances in Neural Information Processing Systems 32*, pages 8024–8035. Curran Associates, Inc., 2019. URL <http://papers.neurips.cc/paper/9015-pytorch-an-imperative-style-high-performance-deep-learning-library.pdf>.
- [388] Peter Z. Skands. The Perugia Tunes. In *1st International Workshop on Multiple Partonic Interactions at the LHC*, pages 284–297, 5 2009.
- [389] Andy Buckley, Hendrik Hoeth, Heiko Lacker, Holger Schulz, and Jan Eike von Seggern. Systematic event generator tuning for the LHC. *Eur. Phys. J. C*, 65:331–357, 2010. doi: 10.1140/epjc/s10052-009-1196-7.
- [390] Philip Ilten, Mike Williams, and Yunjie Yang. Event generator tuning using Bayesian optimization. *JINST*, 12(04):P04028, 2017. doi: 10.1088/1748-0221/12/04/P04028.
- [391] Mohan Krishnamoorthy, Holger Schulz, Xiangyang Ju, Wenjing Wang, Sven Leyffer, Zachary Marshall, Stephen Mrenna, Juliane Müller, and James B. Kowalkowski. Apprentice for Event Generator Tuning. *EPJ Web Conf.*, 251:03060, 2021. doi: 10.1051/epjconf/202125103060.

- [392] Anders Andreassen and Benjamin Nachman. Neural Networks for Full Phase-space Reweighting and Parameter Tuning. *Phys. Rev. D*, 101(9):091901, 2020. doi: 10.1103/PhysRevD.101.091901.
- [393] Marco Lazzarin, Simone Alioli, and Stefano Carrazza. MCNNTUNES: Tuning Shower Monte Carlo generators with machine learning. *Comput. Phys. Commun.*, 263:107908, 2021. doi: 10.1016/j.cpc.2021.107908.
- [394] Manzil Zaheer, Satwik Kottur, Siamak Ravanbakhsh, Barnabas Poczos, Ruslan Salakhutdinov, and Alexander Smola. Deep sets, 2018. URL <https://arxiv.org/abs/1703.06114>.
- [395] Patrick T. Komiske, Eric M. Metodiev, and Jesse Thaler. Energy Flow Networks: Deep Sets for Particle Jets. *JHEP*, 01:121, 2019. doi: 10.1007/JHEP01(2019)121.
- [396] Martin Arjovsky, Soumith Chintala, and Léon Bottou. Wasserstein gan, 2017. URL <https://arxiv.org/abs/1701.07875>.
- [397] Krish Desai, Benjamin Nachman, and Jesse Thaler. Moment Unfolding, 7 2024.
- [398] Chu-Cheng Pan, Xiang Dong, Yu-Chang Sun, Ao-Yan Cheng, Ao-Bo Wang, Yu-Xuan Hu, and Hao Cai. SwdFold:A Reweighting and Unfolding method based on Optimal Transport Theory, 6 2024.
- [399] Julien Rabin, Gabriel Peyré, Julie Delon, and Marc Bernot. Wasserstein barycenter and its application to texture mixing. In *Scale Space and Variational Methods in Computer Vision: Third International Conference, SSVM 2011, Ein-Gedi, Israel, May 29–June 2, 2011, Revised Selected Papers 3*, pages 435–446. Springer, 2012.
- [400] Soheil Kolouri, Kimia Nadjahi, Umut Simsekli, Roland Badeau, and Gustavo Rohde. Generalized sliced wasserstein distances. *Advances in neural information processing systems*, 32, 2019.
- [401] B. Efron. Bootstrap Methods: Another Look at the Jackknife. *The Annals of Statistics*, 7(1):1 – 26, 1979. doi: 10.1214/aos/1176344552. URL <https://doi.org/10.1214/aos/1176344552>.
- [402] Bo Andersson, G. Gustafson, G. Ingelman, and T. Sjostrand. Parton Fragmentation and String Dynamics. *Phys. Rept.*, 97:31–145, 1983. doi: 10.1016/0370-1573(83)90080-7.
- [403] Bo Andersson. The Lund model. *Camb. Monogr. Part. Phys. Nucl. Phys. Cosmol.*, 7: 1–471, 1997.
- [404] Gennaro Corcella, Roberto Franceschini, and Doojin Kim. Fragmentation Uncertainties in Hadronic Observables for Top-quark Mass Measurements. *Nucl. Phys. B*, 929:485–526, 2018. doi: 10.1016/j.nuclphysb.2018.02.012.

- [405] Nadine Fischer and Torbjörn Sjöstrand. Thermodynamical String Fragmentation. *JHEP*, 01:140, 2017. doi: 10.1007/JHEP01(2017)140.
- [406] Aishik Ghosh, Xiangyang Ju, Benjamin Nachman, and Andrzej Siódmiak. Towards a deep learning model for hadronization. *Phys. Rev. D*, 106(9):096020, 2022. doi: 10.1103/PhysRevD.106.096020.
- [407] Jay Chan, Xiangyang Ju, Adam Kania, Benjamin Nachman, Vishnu Sangli, and Andrzej Siódmiak. Fitting a deep generative hadronization model. *JHEP*, 09:084, 2023. doi: 10.1007/JHEP09(2023)084.
- [408] M. Bahr et al. Herwig++ Physics and Manual. *Eur. Phys. J. C*, 58:639–707, 2008. doi: 10.1140/epjc/s10052-008-0798-9.
- [409] Ivan Kobyzev, Simon J.D. Prince, and Marcus A. Brubaker. Normalizing Flows: An Introduction and Review of Current Methods. *IEEE Transactions on Pattern Analysis and Machine Intelligence*, 43(11):3964–3979, nov 2021. doi: 10.1109/tpami.2020.2992934.
- [410] Danilo Rezende and Shakir Mohamed. Variational Inference with Normalizing Flows. In Francis Bach and David Blei, editors, *Proceedings of the 32nd International Conference on Machine Learning*, volume 37 of *Proceedings of Machine Learning Research*, pages 1530–1538, Lille, France, 07–09 Jul 2015. PMLR. URL <https://proceedings.mlr.press/v37/rezende15.html>.
- [411] Laurent Dinh, David Krueger, and Yoshua Bengio. NICE: Non-linear Independent Components Estimation. In Yoshua Bengio and Yann LeCun, editors, *3rd International Conference on Learning Representations*, 2015. URL <http://arxiv.org/abs/1410.8516>.
- [412] P. Abreu et al. Tuning and test of fragmentation models based on identified particles and precision event shape data. *Z. Phys. C*, 73:11–60, 1996. doi: 10.1007/s002880050295.
- [413] Patrick T. Komiske, Eric M. Metodiev, and Jesse Thaler. The Hidden Geometry of Particle Collisions. *JHEP*, 07:006, 2020. doi: 10.1007/JHEP07(2020)006.
- [414] Cédric Villani. *Optimal transport, old and new*. Springer, Berlin, 2008.
- [415] Filippo Santambrogio. *Optimal Transport for Applied Mathematicians*. Springer, Switzerland, 2015.
- [416] Aaditya Ramdas, Nicolás García Trillos, and Marco Cuturi. On wasserstein two-sample testing and related families of nonparametric tests. *Entropy*, 19(2):47, 2017.
- [417] Georges Aad et al. Simultaneous Unbinned Differential Cross-Section Measurement of Twenty-Four Z+jets Kinematic Observables with the ATLAS Detector. *Phys. Rev. Lett.*, 133(26):261803, 2024. doi: 10.1103/PhysRevLett.133.261803.

- [418] Eamonn Maguire, Lukas Heinrich, and Graeme Watt. HEPData: a repository for high energy physics data. *J. Phys. Conf. Ser.*, 898(10):102006, 2017. doi: 10.1088/1742-6596/898/10/102006.
- [419] A. Rogozhnikov. Reweighting with Boosted Decision Trees. *J. Phys. Conf. Ser.*, 762(1):012036, 2016. doi: 10.1088/1742-6596/762/1/012036.
- [420] Sascha Diefenbacher, Engin Eren, Gregor Kasieczka, Anatolii Korol, Benjamin Nachman, and David Shih. DCTRGAN: Improving the Precision of Generative Models with Reweighting. *JINST*, 15(11):P11004, 2020. doi: 10.1088/1748-0221/15/11/P11004.
- [421] Matthias Fey and Jan Eric Lenssen. Fast graph representation learning with pytorch geometric, 2019. URL <https://arxiv.org/abs/1903.02428>.
- [422] Matthias Fey, Jinu Sunil, Akihiro Nitta, Rishi Puri, Manan Shah, Blaž Stojanovič, Ramona Bendias, Alexandria Barghi, Vid Kocijan, Zecheng Zhang, Xinwei He, Jan Eric Lenssen, and Jure Leskovec. Pyg 2.0: Scalable learning on real world graphs, 2025. URL <https://arxiv.org/abs/2507.16991>.
- [423] Siyu Chen, Alfredo Glioti, Giuliano Panico, and Andrea Wulzer. Boosting likelihood learning with event reweighting. *JHEP*, 03:117, 2024. doi: 10.1007/JHEP03(2024)117.
- [424] Benjamin Nachman and Jesse Thaler. Neural conditional reweighting. *Phys. Rev. D*, 105(7):076015, 2022. doi: 10.1103/PhysRevD.105.076015.
- [425] Jerzy Neyman and Egon Sharpe Pearson. On the Problem of the Most Efficient Tests of Statistical Hypotheses. *Phil. Trans. Roy. Soc. Lond. A*, 231(694-706):289–337, 1933. doi: 10.1098/rsta.1933.0009.
- [426] Julian Heeck and Volodymyr Takhistov. Inclusive Nucleon Decay Searches as a Frontier of Baryon Number Violation. *Phys. Rev. D*, 101(1):015005, 2020. doi: 10.1103/PhysRevD.101.015005.
- [427] R. Kleiss, W. James Stirling, and S. D. Ellis. A New Monte Carlo Treatment of Multiparticle Phase Space at High-energies. *Comput. Phys. Commun.*, 40:359, 1986. doi: 10.1016/0010-4655(86)90119-0.
- [428] Johan Alwall, Claude Duhr, Benjamin Fuks, Olivier Mattelaer, Deniz Gizem Öztürk, and Chia-Hsien Shen. Computing decay rates for new physics theories with FeynRules and MadGraph 5\_aMC@NLO. *Comput. Phys. Commun.*, 197:312–323, 2015. doi: 10.1016/j.cpc.2015.08.031.
- [429] Lynton Ardizzone, Till Bungert, Felix Draxler, Ullrich Köthe, Jakob Kruse, Robert Schmier, and Peter Sorrenson. Framework for Easily Invertible Architectures (FrEIA), 2018. URL <https://github.com/vislearn/FrEIA>.

- [430] S. Brandt, C. Peyrou, R. Sosnowski, and A. Wroblewski. The Principal axis of jets. An Attempt to analyze high-energy collisions as two-body processes. *Phys. Lett.*, 12:57–61, 1964. doi: 10.1016/0031-9163(64)91176-X.
- [431] Edward Farhi. A QCD Test for Jets. *Phys. Rev. Lett.*, 39:1587–1588, 1977. doi: 10.1103/PhysRevLett.39.1587.
- [432] S. Catani, G. Turnock, and B. R. Webber. Jet broadening measures in  $e^+e^-$  annihilation. *Phys. Lett. B*, 295:269–276, 1992. doi: 10.1016/0370-2693(92)91565-Q.
- [433] Yuri L. Dokshitzer, A. Lucenti, G. Marchesini, and G. P. Salam. On the QCD analysis of jet broadening. *JHEP*, 01:011, 1998. doi: 10.1088/1126-6708/1998/01/011.
- [434] G. Parisi. Super Inclusive Cross-Sections. *Phys. Lett. B*, 74:65–67, 1978. doi: 10.1016/0370-2693(78)90061-8.
- [435] John F. Donoghue, F. E. Low, and So-Young Pi. Tensor Analysis of Hadronic Jets in Quantum Chromodynamics. *Phys. Rev. D*, 20:2759, 1979. doi: 10.1103/PhysRevD.20.2759.

## Appendix A

# Estimating decay rates and scattering cross sections

Consider the decay of a mother particle,  $A$ , with mass  $M$  to an  $n$ -particle final state in the rest frame of the mother. The decay width can be written as

$$\begin{aligned}\Gamma(A \rightarrow a_1 a_2 \cdots a_n) &= \frac{1}{2M} \int d\Phi_n |\mathcal{M}|^2 \\ &\sim \frac{1}{2M} \times \Phi_n \times \langle |\mathcal{M}|^2 \rangle\end{aligned}\tag{A.1}$$

Assuming massless final states the phase space volume is given by [426, 427]

$$\Phi_n(M) = \frac{1}{2^{4n-5} \pi^{2n-3}} \frac{M^{2n-4}}{(n-1)!(n-2)!}\tag{A.2}$$

such that

$$\Gamma \sim \frac{2^{5-4n} \pi^{3-2n}}{2M} \times \frac{M^{2n-4}}{(n-1)!(n-2)!} \times \langle |\mathcal{M}|^2 \rangle.\tag{A.3}$$

Similarly, consider  $2 \rightarrow n$  scattering in the COM frame with energy  $\sqrt{s} \equiv W$ . The cross section can be written as

$$\begin{aligned}\sigma(AB \rightarrow a_1 a_2 \cdots a_n) &= \frac{1}{F} \int d\Phi_n |\mathcal{M}|^2 \\ &\sim \frac{1}{2s} \times \Phi_n(W) \times \langle |\mathcal{M}|^2 \rangle\end{aligned}\tag{A.4}$$

where  $F = 4E_A E_B |\vec{v}_A - \vec{v}_B|$  is the flux – in the COM frame,  $E_A = E_B = \sqrt{s}/2$ ,  $|\vec{v}_A - \vec{v}_B| \rightarrow 1$  such that  $F \rightarrow 2s$ . This gives

$$\sigma \sim \frac{2^{5-4n} \pi^{3-2n}}{2s} \times \frac{s^{n-2}}{(n-1)!(n-2)!} \times \langle |\mathcal{M}|^2 \rangle.\tag{A.5}$$

The squared matrix element can be written as a modular product of Feynman diagram components [428]

$$\langle |\mathcal{M}|^2 \rangle \simeq \frac{N_{\text{color}}}{N_{\text{spin}}} \times \left| \prod_{\text{internal}} P(E) \right|^2 \times \prod_{\text{external}} \mathcal{P}(E) \times \prod_{\text{vertices}} \left( \sum_i C_i \Gamma_i \right)^2 \quad (\text{A.6})$$

where  $N_{\text{spin}}$  denotes the average over initial spin states,  $N_{\text{color}}$  tracks the color multiplicity of the diagram,  $P(E)$  denotes a product over internal propagators,  $\mathcal{P}(E)$  is the product over the polarization tensors of the external particles, and  $\sum_i C_i \Gamma_i$  denotes the sum over the products of coupling constants and Lorentz structures. Note that for higher-dimensional operators, the coefficient  $C$  will have mass dimension

$$C_i \rightarrow \frac{C_i^{(d)}}{\Lambda^{d-4}}. \quad (\text{A.7})$$

Common propagators and polarization tensors along with corresponding ‘rough forms’ useful for estimations can be found in table A.1. In the COM frame the scalings of higher dimensional operators simplify significantly. The propagators drop out (because they are encoded via eq. (A.7)), such that for a matrix element sourced by  $d$ -dimensional operator ( $d > 4$ ) the matrix element can be roughly estimated in terms of the characteristic energy scale  $E$  ( $E \equiv M, \sqrt{s}$  for decay rates and cross sections, respectively)

$$\mathcal{M} \sim E^{d-N} \Lambda^{4-d} = E^{d-n-1} \Lambda^{4-d} \quad (\text{A.8})$$

where  $N$  is the total number of external particles. For example, defining  $\Gamma_{d,n}^{\mathcal{O}}, \sigma_{d,n}^{\mathcal{O}}$  as the decay rates and cross sections sourced by a  $d$ -dimensional operator  $\mathcal{O}^{(d)}$  to an  $n$ -particle final state we can estimate straightforwardly (remember that we are assuming to be in the COM frame and all final state particle re assumed to be approximately massless)

$$\Gamma_{5,3}^{\bar{\psi}\psi\phi\phi} \sim \left(\frac{2}{3}\right)^2 \frac{M}{256\pi^3} \left(C_{(5)} \frac{M}{\Lambda}\right)^2 \approx 6 \times 10^{-5} C_{(5)}^2 \frac{M^3}{\Lambda^2} \quad (\text{A.9})$$

$$\sigma_{5,2}^{\bar{\psi}\psi\phi\phi} \sim \frac{1}{16\pi} \left(\frac{C_{(5)}}{\Lambda}\right)^2 \quad (\text{A.10})$$

$$\Gamma_{5,2}^{\partial^\mu \phi \bar{\psi} \gamma_\mu \psi} \sim \frac{1}{16\pi} \left(\frac{C_{(5)}}{\Lambda}\right)^2 M^3 \quad (\text{A.11})$$

$$\Gamma_{6,3}^{\bar{\psi}\psi\bar{\psi}\psi} \sim \left(\frac{2}{3}\right)^2 \frac{M}{256\pi^3} \left(C_{(6)} \frac{M^2}{\Lambda^2}\right)^2 \quad (\text{A.12})$$

$$\Gamma_{12,7}^{\bar{\psi}\psi\bar{\psi}\psi\bar{\psi}\psi\bar{\psi}\psi} \sim \frac{C_{(12)}^2}{4.7 \times 10^{15} \times \pi^{11}} \frac{M^{17}}{\Lambda^{16}} \quad (\text{A.13})$$

Spin	Propagator $P$	Polarization tensor $\mathcal{P}$
0	$\frac{i}{p^2 - m^2} \approx \frac{1}{E^2 - m^2}$	1
1/2	$\frac{-i(\not{p} + m)}{p^2 - m^2} \approx \frac{E}{E^2 - m^2}$	2E
1	$\frac{-i}{p^2 - m^2} \left( g_{\mu\nu} - \frac{p_\mu p_\nu}{m^2} \right) \approx \frac{1 - E^2/m^2}{E^2 - m^2}$	$\begin{cases} 1 + E^2/m^2 & \text{for } m \neq 0 \\ 1 & \text{for } m = 0 \end{cases}$

TABLE A.1: Propagators and polarization tensors for spin-0, 1/2, and 1 particles.

## Appendix B

# Additional details on matching and form factor numerics

### B.1 Intermediate results for WET to NRET matching

In this appendix we collect further details on the matching from WET to NRET effective theories, where, following ref. [172] we use as an intermediate step a set of Lorentz covariant CLFV operators that are the products of flavor-changing lepton currents and single-nucleon currents. In appendix B.1.1 we first show the results for the nonperturbative matching from WET to these covariant interactions, followed in appendix B.1.2 by the nonrelativistic reduction to NRET. Some of the results were derived in ref. [172] and are here merely reproduced for convenience (tables B.1 and B.3), while tables B.2 and B.4 contain new results, required for tensor currents.

#### B.1.1 From WET to covariant nucleon interactions

In this subsection we collect the results for the  $d_j^{(N)}$  coefficients in the effective covariant interaction Lagrangian, eq. (3.47). The basis of covariant operators that we use is given in the first columns of tables B.1 and B.2. The  $d_j^{(N)}$  coefficients in the covariant single-nucleon interaction

Lagrangian in eq. (3.47) are explicitly given by

$$d_1^N = \sum_q \frac{1}{m_q} \hat{\mathcal{C}}_{5,q}^{(6)} F_S^{q/N} + \hat{\mathcal{C}}_1^{(7)} F_G^N + \hat{\mathcal{C}}_5^{(7)} F_\gamma^N, \quad (\text{B.1})$$

$$\begin{aligned} d_2^N &= -i \frac{m_-}{2m_N} \sum_q \hat{\mathcal{C}}_{3,q}^{(6)} F_{P'}^{q/N} + \sum_q \frac{1}{m_q} \hat{\mathcal{C}}_{7,q}^{(6)} F_P^{q/N} - \hat{\mathcal{C}}_3^{(7)} F_{\tilde{G}}^N - \hat{\mathcal{C}}_7^{(7)} F_{\tilde{\gamma}}^N \\ &\quad - i \frac{m_+ m_-}{2m_N} \sum_q \hat{\mathcal{C}}_{11,q}^{(7)} F_{P'}^{q/N}, \end{aligned} \quad (\text{B.2})$$

$$d_3^N = \sum_q \frac{1}{m_q} \hat{\mathcal{C}}_{6,q}^{(6)} F_S^{q/N} + \hat{\mathcal{C}}_2^{(7)} F_G^N + \hat{\mathcal{C}}_6^{(7)} F_\gamma^N, \quad (\text{B.3})$$

$$\begin{aligned} d_4^N &= \frac{m_+}{2m_N} \sum_q \hat{\mathcal{C}}_{4,q}^{(6)} F_{P'}^{q/N} + \sum_q \frac{1}{m_q} \hat{\mathcal{C}}_{8,q}^{(6)} F_P^{q/N} - \hat{\mathcal{C}}_4^{(7)} F_{\tilde{G}}^N - \hat{\mathcal{C}}_8^{(7)} F_{\tilde{\gamma}}^N \\ &\quad - i \frac{m_+ m_-}{2m_N} \sum_q \hat{\mathcal{C}}_{12,q}^{(7)} F_{P'}^{q/N}, \end{aligned} \quad (\text{B.4})$$

$$d_5^N = \sum_q \hat{\mathcal{C}}_{1,q}^{(6)} F_1^{q/N} + m_+ \sum_q \hat{\mathcal{C}}_{9,q}^{(7)} F_1^{q/N} - \sum_q \frac{q_{\text{rel.}}^2}{2m_N} \hat{\mathcal{C}}_{13,q}^{(7)} \left( \hat{F}_{T,1}^{q/N} - 4\hat{F}_{T,2}^{q/N} \right), \quad (\text{B.5})$$

$$d_6^N = -\frac{1}{2} \sum_q \hat{\mathcal{C}}_{1,q}^{(6)} F_2^{q/N} - \frac{1}{2} m_+ \sum_q \hat{\mathcal{C}}_{9,q}^{(7)} F_2^{q/N}, \quad (\text{B.6})$$

$$d_7^N = \sum_q \hat{\mathcal{C}}_{3,q}^{(6)} F_A^{q/N} + m_+ \sum_q \hat{\mathcal{C}}_{11,q}^{(7)} F_A^{q/N}, \quad (\text{B.7})$$

$$d_8^N = 0, \quad (\text{B.8})$$

$$d_9^N = -\frac{\alpha}{\pi} \hat{\mathcal{C}}_1^{(5)} \frac{m_L}{q_{\text{rel.}}^2} \sum_q Q_q F_1^{q/N} - m_L \sum_q \hat{\mathcal{C}}_{9,q}^{(7)} F_1^{q/N}, \quad (\text{B.9})$$

$$d_{10}^N = \frac{\alpha}{2\pi} \hat{\mathcal{C}}_1^{(5)} \frac{m_L}{q_{\text{rel.}}^2} \sum_q Q_q F_2^{q/N} + \frac{m_L}{2} \sum_q \hat{\mathcal{C}}_{9,q}^{(7)} F_2^{q/N}, \quad (\text{B.10})$$

$$d_{11}^N = -m_L \sum_q \hat{\mathcal{C}}_{11,q}^{(7)} F_A^{q/N}, \quad (\text{B.11})$$

$$d_{12}^N = 0, \quad (\text{B.12})$$

$$d_{13}^N = \sum_q \hat{\mathcal{C}}_{2,q}^{(6)} F_1^{q/N} - im_- \sum_q \hat{\mathcal{C}}_{10,q}^{(7)} F_1^{q/N} - \sum_q \frac{q_{\text{rel.}}^2}{2m_N} \hat{\mathcal{C}}_{14,q}^{(7)} \left( \hat{F}_{T,1}^{q/N} - 4\hat{F}_{T,2}^{q/N} \right), \quad (\text{B.13})$$

$$d_{14}^N = -\frac{1}{2} \sum_q \hat{\mathcal{C}}_{2,q}^{(6)} F_2^{q/N} + \frac{i}{2} m_- \sum_q \hat{\mathcal{C}}_{10,q}^{(7)} F_2^{q/N}, \quad (\text{B.14})$$

$$d_{15}^N = \sum_q \hat{\mathcal{C}}_{4,q}^{(6)} F_A^{q/N} - im_- \sum_q \hat{\mathcal{C}}_{12,q}^{(7)} F_A^{q/N}, \quad (\text{B.15})$$

$$d_{16}^N = 0, \quad (\text{B.16})$$

$$d_{17}^N = \frac{\alpha}{\pi} \hat{\mathcal{C}}_2^{(5)} \frac{m_L}{q_{\text{rel.}}^2} \sum_q Q_q F_1^{q/N} + m_L \sum_q \hat{\mathcal{C}}_{10,q}^{(7)} F_1^{q/N}, \quad (\text{B.17})$$

$$d_{18}^N = -\frac{\alpha}{2\pi} \hat{\mathcal{C}}_2^{(5)} \frac{m_L}{q_{\text{rel.}}^2} \sum_q Q_q F_2^{q/N} - \frac{1}{2} m_L \sum_q \hat{\mathcal{C}}_{10,q}^{(7)} F_2^{q/N}, \quad (\text{B.18})$$

$$d_{19}^N = m_L \sum_q \hat{\mathcal{C}}_{12,q}^{(7)} F_A^{q/N}, \quad (\text{B.19})$$

$$d_{20}^N = 0, \quad (\text{B.20})$$

$$d_{21}^N = \sum_q \hat{\mathcal{C}}_{9,q}^{(6)} \hat{F}_{T,0}^{q/N}, \quad (\text{B.21})$$

$$d_{22}^N = - \sum_q \hat{\mathcal{C}}_{9,q}^{(6)} \hat{F}_{T,1}^{q/N}, \quad (\text{B.22})$$

$$d_{23}^N = - \sum_q \hat{\mathcal{C}}_{9,q}^{(6)} \hat{F}_{T,2}^{q/N}, \quad (\text{B.23})$$

$$d_{24}^N = 0, \quad (\text{B.24})$$

$$d_{25}^N = \sum_q \hat{\mathcal{C}}_{10,q}^{(6)} \hat{F}_{T,0}^{q/N}, \quad (\text{B.25})$$

$$d_{26}^N = - \sum_q \hat{\mathcal{C}}_{10,q}^{(6)} \hat{F}_{T,1}^{q/N}, \quad (\text{B.26})$$

$$d_{27}^N = - \sum_q \hat{\mathcal{C}}_{10,q}^{(6)} \hat{F}_{T,2}^{q/N}, \quad (\text{B.27})$$

$$d_{28}^N = 0, \quad (\text{B.28})$$

$$d_{29}^N = -m_L \sum_q \hat{\mathcal{C}}_{13,q}^{(7)} \left( \hat{F}_{T,0}^{q/N} - \frac{q_{\text{rel.}}^2}{m_N^2} \hat{F}_{T,2}^{q/N} \right), \quad (\text{B.29})$$

$$d_{30}^N = -m_L \sum_q \hat{\mathcal{C}}_{14,q}^{(7)} \left( \hat{F}_{T,0}^{q/N} - \frac{q_{\text{rel.}}^2}{m_N^2} \hat{F}_{T,1}^{q/N} \right), \quad (\text{B.30})$$

$$d_{31}^N = \frac{m_L}{4} \sum_q \hat{\mathcal{C}}_{16,q}^{(7)} \hat{F}_{T,0}^{q/N}, \quad (\text{B.31})$$

$$d_{32}^N = \frac{m_L}{4} \sum_q \hat{\mathcal{C}}_{15,q}^{(7)} \hat{F}_{T,0}^{q/N}. \quad (\text{B.32})$$

Note that all the form factors depend on  $q_{\text{rel.}}^2 = -q^2$ , eq. (3.46), see a more detailed discussion in appendix B.2. As before, we shortened the notation above by introducing  $m_{\pm} = m_\mu \pm m_e$ , cf. eq. (3.65). Note that  $m_-$  vanishes in the limit when electron and muon masses are the same,  $m_e \rightarrow m_\mu$ .

Six of the single-nucleon coefficients,  $d_8^N$ ,  $d_{12}^N$ ,  $d_{16}^N$ ,  $d_{20}^N$ ,  $d_{24}^N$ , and  $d_{28}^N$  are zero. They are associated with the second-class currents — nucleon currents that have opposite time-reversal parity from the quark currents that generate them.

### B.1.2 NRET decomposition of covariant interactions

When performing the nonrelativistic reduction of the covariant interactions in eq. (3.47), we follow closely ref. [172]. In particular, we work to linear orders in  $v_N$  and  $v_\mu$ , while the nonrelativistic reduction is performed on matrix elements  $\langle e, N' | \mathcal{L}_{\text{eff}}^{\text{cov}} | \mu, N \rangle$ . The results in ref. [172] were limited to the first 20  $\mathcal{L}_{\text{int}}^{j,N}$ , since these involve scalar and vector currents. Working to

linear order in  $v_N$ , but to  $\mathcal{O}(v_\mu^0)$ , the nonrelativistic reduction of  $\mathcal{L}_{\text{int}}^{j,N}$ ,  $j = 1, \dots, 20$ , gives rise to the NRET operator combinations listed in table B.1 (with slight abuse of notation,  $N$  now denotes the corresponding Dirac four-component spinors, see caption for details). We observe that these involve only a subset of the 16 operators constituting the complete  $\mathcal{O}(v_N)$  NRET operator basis in eq. (3.22): the operators  $\mathcal{O}_3$ ,  $\mathcal{O}_{12}$ ,  $\mathcal{O}'_{13}$ , and  $\mathcal{O}_{15}$  do not appear. If the contributions of  $\mathcal{O}(\vec{v}_\mu)$  are added, thereby including contributions from the muon's lower component, the additional NRET operators in eq. (3.36) are generated, with the results collected in table B.3. Note that extending the nonrelativistic reduction to  $\mathcal{O}(v_\mu)$  does not generate the missing NRET operators. The net effect of  $\vec{v}_\mu$  is to modify [at  $\mathcal{O}(\sim 5\%)$ ] the nuclear response functions  $W_i^{\tau\tau'}$ , all of which were already present in the expansion to order  $\mathcal{O}(\vec{v}_N)$ : this is a consequence of the fact that the emitted electron is ultra-relativistic, which guarantees that the contribution of  $\vec{v}_\mu$  to the leptonic current will always be just a correction. The results of the above nonrelativistic reduction at  $\mathcal{O}(v_N)$  were encoded in Mu2e\_NRET\_v1 version of the public code that accompanied ref. [172].

Motivated by the dimension  $d \leq 7$  light-quark interactions described in section 3.2, we add to the covariant interaction in eq. (3.47) an additional 12 operators that take the form of products of tensor currents. The additional  $\mathcal{L}_{\text{int}}^{j,N}$  interactions are listed in the first column in table B.2, which also gives the results of the nonrelativistic reduction, working at  $\mathcal{O}(v_N)$ . The four NRET operators previously missing now appear. When  $\vec{v}_\mu$  corrections are included, this generates the additional NRET contributions listed in table B.4. The extended nucleon-level Dirac basis, consisting of  $20+12=32$  operators, is employed in the updated script, Mu2e\_NRET\_v2.

`Mu2e_NRET_v2` thus includes 32 Dirac interactions associated with scalar, vector, or tensor exchanges. The NRET reduction used in the new script also includes the lower-component contributions of  $\vec{v}_\mu$ , extending the NRET basis used in `Mu2e_NRET_v1` by an additional 10 operators, for a total of 26. When the nuclear physics multipole expansion is performed for the additional operators, new nuclear multipoles arise. These appear in Eq. (B7) of [172]. Matrix elements of the new multipole operators can still be evaluated analytically, if the Slater determinants used in the shell model are constructed in a harmonic oscillator single-particle basis. But unlike the original 16 NRET operators, the results are no longer expressible in the form of  $e^{-2y}p(y)$  where  $p(y)$  is a finite polynomial in  $y$ .

## B.2 Numerical value of nucleon form factors

In the numerical results of section 3.5, we evaluated the nucleon form factors in eqs. (3.37) and (3.45) at  $q_{\text{rel.}}^2 = -q_{\text{eff}}^2$ , where  $q_{\text{eff}} = 110.81 \text{ MeV}$  for  ${}^{27}\text{Al}$ . We summarize these numerical values below in table B.5. For more details on the expressions leading to these numerical values, please see appendix D of [3].

### B.3 WET translation

In Tables [B.6](#) and [B.7](#) we list and outline explicitly the translation between a variant of the dimension-6 WET-3 flavor basis of Jenkins, Manohar, and Stoffer [\[175\]](#) to our basis in eqs. [\(3.4\)](#) and [\(3.8\)](#). These naming convention and translations are used within `MuonConverter` to interface with the existing SMEFT/WET software.

TABLE B.1: Dirac forms of the CLFV amplitudes  $\mathcal{L}_{\text{int}}^j$  are related to linear combinations of the Pauli forms (the operators  $\mathcal{O}_i$ ). Bjorken and Drell spinor and gamma matrix conventions are used. Here  $\chi_e = \begin{pmatrix} \xi_s & \vec{\sigma}_L \cdot \hat{q} \xi_s \end{pmatrix}^\top$ ,  $\chi_\mu = \begin{pmatrix} \xi_s & 0 \end{pmatrix}^\top$ , and  $N = \begin{pmatrix} \xi_s & \frac{\vec{\sigma}_N \cdot \vec{v}_N}{2} \xi_s \end{pmatrix}^\top$ . The Dirac forms are expanded to first order in  $\vec{v}_N$  to maintain consistency with their use between Schrödinger wave functions.

$j$	$\mathcal{L}_{\text{int}}^j$	Pauli operator reduction	$\sum_i c_i \mathcal{O}_i$
1	$\bar{\chi}_e \chi_\mu \bar{N} N$	$1_L 1_N$	$\mathcal{O}_1$
2	$\bar{\chi}_e \chi_\mu \bar{N} i \gamma^5 N$	$1_L \left( i \frac{\vec{q}}{2m_N} \cdot \vec{\sigma}_N \right)$	$\frac{q}{2m_N} \mathcal{O}_{10}$
3	$\bar{\chi}_e i \gamma^5 \chi_\mu \bar{N} N$	$(-\hat{q} \vec{\sigma}_L) 1_N$	$-\mathcal{O}_{11}$
4	$\bar{\chi}_e i \gamma^5 \chi_\mu \bar{N} i \gamma^5 N$	$(-\hat{q} \vec{\sigma}_L) \left( i \frac{\vec{q}}{2m_N} \cdot \vec{\sigma}_N \right)$	$-\frac{q}{2m_N} \mathcal{O}_6$
5	$\bar{\chi}_e \gamma^\mu \chi_\mu \bar{N} \gamma_\mu N$	$1_L 1_N$ $- (\hat{q} 1_L - i \hat{q} \times \vec{\sigma}_L) \cdot \left( \vec{v}_N + i \frac{\vec{q}}{2m_N} \times \vec{\sigma}_N \right)$	$\mathcal{O}_1$ $+ i \mathcal{O}'_2 - \mathcal{O}_5 - \frac{q}{2m_N} (\mathcal{O}_4 + \mathcal{O}_6)$
6	$\bar{\chi}_e \gamma^\mu \chi_\mu \bar{N} i \sigma_{\mu\alpha} \frac{q^\alpha}{m_N} N$	$- (\hat{q} 1_L - i \hat{q} \times \vec{\sigma}_L) \cdot \left( -i \frac{\vec{q}}{m_N} \times \vec{\sigma}_N \right)$	$\frac{q}{m_N} (\mathcal{O}_4 + \mathcal{O}_6)$
7	$\bar{\chi}_e \gamma^\mu \chi_\mu \bar{N} \gamma_\mu \gamma^5 N$	$1_L (\vec{v}_N \cdot \vec{\sigma}_N) - (\hat{q} 1_L - i \hat{q} \times \vec{\sigma}_L) \cdot \vec{\sigma}_N$	$\mathcal{O}_7 + i \mathcal{O}_{10} - \mathcal{O}_9$
8	$\bar{\chi}_e \gamma^\mu \chi_\mu \bar{N} \sigma_{\mu\alpha} \frac{q^\alpha}{m_N} \gamma^5 N$	$1_L \left( -i \frac{\vec{q}}{m_N} \cdot \vec{\sigma}_N \right)$	$-\frac{q}{m_N} \mathcal{O}_{10}$
9	$\bar{\chi}_e i \sigma^{\mu\nu} \frac{q_\nu}{m_L} \chi_\mu \bar{N} \gamma_\mu N$	$- \frac{q}{m_L} 1_L 1_N$ $- \left( -i \frac{\vec{q}}{m_L} \times \vec{\sigma}_L \right) \cdot \left( \vec{v}_N + i \frac{\vec{q}}{2m_N} \times \vec{\sigma}_N \right)$	$-\frac{q}{m_L} \mathcal{O}_1$ $- \frac{q}{m_L} \left( \mathcal{O}_5 + \frac{q}{2m_N} (\mathcal{O}_4 + \mathcal{O}_6) \right)$
10	$\bar{\chi}_e i \sigma^{\mu\nu} \frac{q_\nu}{m_L} \chi_\mu \bar{N} i \sigma_{\mu\alpha} \frac{q^\alpha}{m_N} N$	$- \left( -i \frac{\vec{q}}{m_L} \times \vec{\sigma}_L \right) \cdot \left( -i \frac{\vec{q}}{m_N} \times \vec{\sigma}_N \right)$	$\frac{q}{m_L} \frac{q}{m_N} (\mathcal{O}_4 + \mathcal{O}_6)$
11	$\bar{\chi}_e i \sigma^{\mu\nu} \frac{q_\nu}{m_L} \chi_\mu \bar{N} \gamma_\mu \gamma^5 N$	$\left( -\frac{q}{m_L} 1_L \right) \vec{v}_N \cdot \vec{\sigma}_N - \left( -i \frac{\vec{q}}{m_L} \times \vec{\sigma}_L \right) \cdot \vec{\sigma}_N$	$-\frac{q}{m_L} (\mathcal{O}_7 + \mathcal{O}_9)$
12	$\bar{\chi}_e i \sigma^{\mu\nu} \frac{q_\nu}{m_L} \chi_\mu \bar{N} \sigma_{\mu\alpha} \frac{q^\alpha}{m_N} \gamma^5 N$	$\left( -\frac{q}{m_L} 1_L \right) \left( -i \frac{\vec{q}}{m_N} \cdot \vec{\sigma}_N \right)$	$\frac{q}{m_L} \frac{q}{m_N} \mathcal{O}_{10}$
13	$\bar{\chi}_e \gamma^\mu \gamma^5 \chi_\mu \bar{N} \gamma_\mu N$	$(\hat{q} \cdot \vec{\sigma}_L) 1_N - \vec{\sigma}_L \cdot \left( \vec{v}_N + i \frac{\vec{q}}{2m_N} \times \vec{\sigma}_N \right)$	$-i \mathcal{O}_{11} - \mathcal{O}_8 - \frac{q}{2m_N} \mathcal{O}_9$
14	$\bar{\chi}_e \gamma^\mu \gamma^5 \chi_\mu \bar{N} i \sigma_{\mu\alpha} \frac{q^\alpha}{m_N} N$	$- \vec{\sigma}_L \cdot \left( -i \frac{\vec{q}}{m_N} \times \vec{\sigma}_N \right)$	$\frac{q}{m_N} \mathcal{O}_9$
15	$\bar{\chi}_e \gamma^\mu \gamma^5 \chi_\mu \bar{N} \gamma_\mu \gamma^5 N$	$(\hat{q} \cdot \vec{\sigma}_L) (\vec{v}_N \cdot \vec{\sigma}_N) - \vec{\sigma}_L \cdot \vec{\sigma}_N$	$-i \mathcal{O}_{14} - \mathcal{O}_4$
16	$\bar{\chi}_e \gamma^\mu \gamma^5 \chi_\mu \bar{N} \sigma_{\mu\alpha} \frac{q^\alpha}{m_N} \gamma^5 N$	$(\hat{q} \cdot \vec{\sigma}_L) \left( -i \frac{\vec{q}}{m_N} \cdot \vec{\sigma}_N \right)$	$i \frac{q}{m_N} \mathcal{O}_6$
17	$\bar{\chi}_e \sigma^{\mu\nu} \frac{q_\nu}{m_L} \gamma^5 \chi_\mu \bar{N} \gamma_\mu N$	$\left( -i \frac{\vec{q}}{m_L} \cdot \vec{\sigma}_L \right) 1_N$ $- i \frac{q}{m_L} (\vec{\sigma}_L - \hat{q} \hat{q} \cdot \vec{\sigma}_L) \cdot \left( \vec{v}_N + i \frac{\vec{q}}{2m_N} \times \vec{\sigma}_N \right)$	$-\frac{q}{m_L} \mathcal{O}_{11}$ $- \frac{q}{m_L} \left( i \mathcal{O}_8 + i \frac{q}{2m_N} \mathcal{O}_9 + i \mathcal{O}'_{16} \right)$
18	$\bar{\chi}_e \sigma^{\mu\nu} \frac{q_\nu}{m_L} \gamma^5 \chi_\mu \bar{N} i \sigma_{\mu\alpha} \frac{q^\alpha}{m_N} N$	$- i \frac{q}{m_L} (\vec{\sigma}_L - \hat{q} \hat{q} \cdot \vec{\sigma}_L) \cdot \left( -i \frac{\vec{q}}{m_N} \times \vec{\sigma}_N \right)$	$i \frac{q}{m_L} \frac{q}{m_N} \mathcal{O}_9$
19	$\bar{\chi}_e \sigma^{\mu\nu} \frac{q_\nu}{m_L} \gamma^5 \chi_\mu \bar{N} \gamma_\mu \gamma^5 N$	$\left( -i \frac{\vec{q}}{m_L} \cdot \vec{\sigma}_L \right) (\vec{v}_N \cdot \vec{\sigma}_N)$ $- i \frac{q}{m_L} (\vec{\sigma}_L - \hat{q} \hat{q} \cdot \vec{\sigma}_L) \cdot \vec{\sigma}_N$	$-\frac{q}{m_L} \mathcal{O}_{14}$ $- \frac{q}{m_L} (i \mathcal{O}_4 + i \mathcal{O}_6)$
20	$\bar{\chi}_e \sigma^{\mu\nu} \frac{q_\nu}{m_L} \gamma^5 \chi_\mu \bar{N} \sigma_{\mu\alpha} \frac{q^\alpha}{m_N} \gamma^5 N$	$\left( -i \frac{\vec{q}}{m_L} \cdot \vec{\sigma}_L \right) \left( -i \frac{\vec{q}}{m_N} \cdot \vec{\sigma}_N \right)$	$\frac{q}{m_L} \frac{q}{m_N} \mathcal{O}_6$

TABLE B.2: Nonrelativistic reduction of tensor currents and their correspondence to the upper-component operators  $\mathcal{O}_i$ .

$j$	$\mathcal{L}_{\text{int}}^j$	Pauli Operator Reduction	$\sum_i c_i \mathcal{O}_i$
21	$\bar{\chi}_e \sigma^{\mu\nu} \chi_\mu \bar{N} \sigma_{\mu\nu} N$	$-\frac{q}{m_N} 1_L 1_N - 2i\hat{q} \cdot (\vec{v}_N \times \vec{\sigma}_N) + 2\vec{\sigma}_L \cdot \vec{\sigma}_N + 2\vec{\sigma}_L \cdot [\hat{q} \times (\vec{v}_N \times \vec{\sigma}_N)]$	$-\frac{q}{m_N} \mathcal{O}_1 - 2\mathcal{O}_3 + 2\mathcal{O}_4 - 2i\mathcal{O}'_{13}$
22	$\bar{\chi}_e \sigma^{\mu\nu} \chi_\mu \frac{i}{2m_N} \bar{N} \gamma_{[\mu} q_{\nu]} N$	$-\frac{q}{m_N} 1_L 1_N$	$-\frac{q}{m_N} \mathcal{O}_1$
23	$\bar{\chi}_e \sigma^{\mu\nu} \chi_\mu \frac{i}{m_N^2} \bar{N} q_{[\mu} k_{12,\nu]} N$	$4\frac{q}{m_N} 1_L 1_N$	$4\frac{q}{m_N} \mathcal{O}_1$
24	$\bar{\chi}_e i \sigma^{\mu\nu} \chi_\mu \frac{1}{m_N} \bar{N} \gamma_{[\mu} \not{q} \gamma_{\nu]} N$	$-4i\frac{q}{m_N} (\hat{q} \times \vec{\sigma}_L) \cdot (\hat{q} \times \vec{\sigma}_N)$	$-4i\frac{q}{m_N} (\mathcal{O}_4 + \mathcal{O}_6)$
25	$\bar{\chi}_e i \sigma^{\mu\nu} \gamma_5 \chi_\mu \bar{N} \sigma_{\mu\nu} N$	$2\vec{\sigma}_L \cdot (\hat{q} \times \vec{\sigma}_N) - 2i\hat{q} \cdot \vec{\sigma}_N + \frac{q}{m_N} i\hat{q} \cdot \vec{\sigma}_L - 2\vec{\sigma}_L \cdot (\vec{v}_N \times \vec{\sigma}_N)$	$-2i\mathcal{O}_9 - 2\mathcal{O}_{10} + \frac{q}{m_N} \mathcal{O}_{11} - 2\mathcal{O}_{12}$
26	$\bar{\chi}_e i \sigma^{\mu\nu} \gamma_5 \chi_\mu \frac{i}{2m_N} \bar{N} \gamma_{[\mu} q_{\nu]} N$	$\frac{q}{m_N} i\hat{q} \cdot \vec{\sigma}_L 1_N$	$\frac{q}{m_N} \mathcal{O}_{11}$
27	$\bar{\chi}_e i \sigma^{\mu\nu} \gamma_5 \chi_\mu \frac{i}{m_N^2} \bar{N} q_{[\mu} k_{12,\nu]} N$	$-4\frac{q}{m_N} i\hat{q} \cdot \vec{\sigma}_L 1_N$	$-4\frac{q}{m_N} \mathcal{O}_{11}$
28	$\bar{\chi}_e i \sigma^{\mu\nu} \gamma_5 \chi_\mu \frac{1}{m_N} \bar{N} \gamma_{[\mu} \not{q} \gamma_{\nu]} N$	$-4\frac{q}{m_N} \vec{\sigma}_L \cdot (i\hat{q} \times \vec{\sigma}_N)$	$-4\frac{q}{m_N} \mathcal{O}_9$
29	$\frac{i}{2m_L} \bar{\chi}_e \gamma^{[\mu} q^{\nu]} \chi_\mu \bar{N} \sigma_{\mu\nu} N$	$\frac{q}{m_L} \left( \frac{q}{2m_N} 1_L 1_N + i\hat{q} \cdot (\vec{v}_N \times \vec{\sigma}_N) + (\hat{q} \times \vec{\sigma}_L) \cdot (\hat{q} \times \vec{\sigma}_N) \right)$	$\frac{q}{m_L} \left( \frac{q}{2m_N} \mathcal{O}_1 + \mathcal{O}_3 + \mathcal{O}_4 + \mathcal{O}_6 \right)$
30	$\frac{i}{2m_L} \bar{\chi}_e \gamma^{[\mu} q^{\nu]} \gamma_5 \chi_\mu \bar{N} \sigma_{\mu\nu} N$	$\frac{q}{m_L} \left( \vec{\sigma}_L \cdot (i\hat{q} \times \vec{\sigma}_N) + \frac{q}{2m_N} \hat{q} \cdot \vec{\sigma}_L 1_N + \hat{q} \cdot \vec{\sigma}_L i\hat{q} \cdot (\vec{v}_N \times \vec{\sigma}_N) \right)$	$\frac{q}{m_L} \left( \mathcal{O}_9 - i\frac{q}{2m_N} \mathcal{O}_{11} - i\mathcal{O}_{15} \right)$
31	$\frac{1}{m_L} \bar{\chi}_e \gamma^{[\mu} \not{q} \gamma^{\nu]} \chi_\mu \bar{N} \sigma_{\mu\nu} N$	$4\frac{q}{m_L} \left( -i(\hat{q} \cdot \vec{\sigma}_L)(\hat{q} \cdot \vec{\sigma}_N) + \vec{\sigma}_L \cdot [i\hat{q} \times (\vec{v}_N \times \vec{\sigma}_N)] \right)$	$4\frac{q}{m_L} (i\mathcal{O}_6 + \mathcal{O}'_{13})$
32	$\frac{1}{m_L} \bar{\chi}_e \gamma^{[\mu} \not{q} \gamma^{\nu]} \gamma_5 \chi_\mu \bar{N} \sigma_{\mu\nu} N$	$4\frac{q}{m_L} \left( -i\hat{q} \cdot \vec{\sigma}_N + \vec{\sigma}_L \cdot (\vec{v}_N \times \vec{\sigma}_N) - \hat{q} \cdot \vec{\sigma}_L \hat{q} \cdot (\vec{v}_N \times \vec{\sigma}_N) \right)$	$4\frac{q}{m_L} (-\mathcal{O}_{10} + \mathcal{O}_{12} + \mathcal{O}_{15})$

TABLE B.3: As in table B.1, but listing the additional terms generated for scalar- and vector-mediated interactions when the linear expansion in velocities includes  $\vec{v}_\mu$ , so that

$$\chi_\mu = \begin{pmatrix} \xi_s \\ \frac{\vec{\sigma}_L \cdot \vec{v}_\mu}{2} \xi_s \end{pmatrix}.$$

$j$	$\mathcal{L}_{\text{int}}^j$	Pauli operator reduction	$\sum_i b_i \mathcal{O}_i^f$
1	$\bar{\chi}_e \chi_\mu \bar{N} N$	$-\frac{1}{2} \hat{q} \cdot \vec{v}_\mu 1_N - \frac{i}{2} \hat{q} \cdot [\vec{v}_\mu \times \vec{\sigma}_L] 1_N$	$i\mathcal{O}_2^{f'} - \mathcal{O}_3^f$
3	$\bar{\chi}_e i \gamma^5 \chi_\mu \bar{N} N$	$\frac{i}{2} \vec{v}_\mu \cdot \vec{\sigma}_L 1_N$	$i\mathcal{O}_7^f$
5	$\bar{\chi}_e \gamma^\mu \chi_\mu \bar{N} \gamma_\mu N$	$\frac{1}{2} \hat{q} \cdot \vec{v}_\mu 1_N + \frac{i}{2} \hat{q} \cdot [\vec{v}_\mu \times \vec{\sigma}_L] 1_N$	$-i\mathcal{O}_2^{f'} + \mathcal{O}_3^f$
7	$\bar{\chi}_e \gamma^\mu \chi_\mu \bar{N} \gamma_\mu \gamma^5 N$	$-\frac{1}{2} \vec{v}_\mu \cdot \vec{\sigma}_N - \frac{i}{2} [\vec{v}_\mu \times \vec{\sigma}_L] \cdot \vec{\sigma}_N$	$-\mathcal{O}_8^f - i\mathcal{O}_{12}^f$
9	$\bar{\chi}_e i \sigma^{\mu\nu} \frac{q_\nu}{m_L} \chi_\mu \bar{N} \gamma_\mu N$	$\frac{q}{2m_L} (\hat{q} \cdot \vec{v}_\mu 1_N + i \hat{q} \cdot [\vec{v}_\mu \times \vec{\sigma}_L] 1_N)$	$\frac{q}{m_L} (-i\mathcal{O}_2^{f'} + \mathcal{O}_3^f)$
11	$\bar{\chi}_e i \sigma^{\mu\nu} \frac{q_\nu}{m_L} \chi_\mu \bar{N} \gamma_\mu \gamma^5 N$	$\frac{q}{2m_L} (\vec{v}_\mu \cdot \vec{\sigma}_N + i [\vec{v}_\mu \times \vec{\sigma}_L] \cdot \vec{\sigma}_N - i \hat{q} \cdot [\vec{v}_\mu \times \vec{\sigma}_L] \hat{q} \cdot \vec{\sigma}_N - \hat{q} \cdot \vec{v}_\mu \hat{q} \cdot \vec{\sigma}_N)$	$\frac{q}{m_L} (\mathcal{O}_8^f + i\mathcal{O}_{12}^f + i\mathcal{O}_{15}^f + \mathcal{O}_{16}^{f'})$
13	$\bar{\chi}_e \gamma^\mu \gamma^5 \chi_\mu \bar{N} \gamma_\mu N$	$\frac{1}{2} \vec{v}_\mu \cdot \vec{\sigma}_L 1_N$	$\mathcal{O}_7^f$
15	$\bar{\chi}_e \gamma^\mu \gamma^5 \chi_\mu \bar{N} \gamma_\mu \gamma^5 N$	$\frac{i}{2} [\hat{q} \times \vec{v}_\mu] \cdot \vec{\sigma}_N - \frac{1}{2} (\hat{q} \times [\vec{v}_\mu \times \vec{\sigma}_L]) \cdot \vec{\sigma}_N - \frac{1}{2} \vec{v}_\mu \cdot \vec{\sigma}_L \hat{q} \cdot \vec{\sigma}_N$	$\mathcal{O}_5^f + i\mathcal{O}_{13}^{f'}$ $+ i\mathcal{O}_{14}^f$
17	$\bar{\chi}_e \sigma^{\mu\nu} \frac{q_\nu}{m_L} \gamma^5 \chi_\mu \bar{N} \gamma_\mu N$	$\frac{iq}{2m_L} \vec{v}_\mu \cdot \vec{\sigma}_L 1_N$	$\frac{iq}{m_L} \mathcal{O}_7^f$
19	$\bar{\chi}_e \sigma^{\mu\nu} \frac{q_\nu}{m_L} \gamma^5 \chi_\mu \bar{N} \gamma_\mu \gamma^5 N$	$\frac{q}{2m_L} ([\hat{q} \times \vec{v}_\mu] \cdot \vec{\sigma}_N + (i \hat{q} \times [\vec{v}_\mu \times \vec{\sigma}_L]) \cdot \vec{\sigma}_N)$	$\frac{q}{m_L} (-i\mathcal{O}_5^f + \mathcal{O}_{13}^{f'})$

TABLE B.4: As in table B.2, but listing the additional terms generated for tensor-mediated interactions when the linear expansion in velocities includes  $\vec{v}_\mu$ .

$j$	$\mathcal{L}_{\text{int}}^j$	Pauli Operator Reduction	$\sum_i b_i \mathcal{O}_i^f$
21	$\bar{\chi}_e \sigma^{\mu\nu} \chi_\mu \bar{N} \sigma_{\mu\nu} N$	$(i \hat{q} \times \vec{v}_\mu) \cdot \vec{\sigma}_N - [\hat{q} \times (\vec{v}_\mu \times \vec{\sigma}_L)] \cdot \vec{\sigma}_N - (\vec{v}_\mu \cdot \vec{\sigma}_L) (\hat{q} \cdot \vec{\sigma}_N)$	$2\mathcal{O}_5^f + 2i\mathcal{O}_{13}^{f'} + 2i\mathcal{O}_{14}^f$
25	$\bar{\chi}_e i \sigma^{\mu\nu} \gamma_5 \chi_\mu \bar{N} \sigma_{\mu\nu} N$	$i \vec{v}_\mu \cdot \vec{\sigma}_N - (\vec{v}_\mu \times \vec{\sigma}_L) \cdot \vec{\sigma}_N$	$2i\mathcal{O}_8^f - 2\mathcal{O}_{12}^f$
29	$\frac{i}{2m_L} \bar{\chi}_e \gamma^{[\mu} q^{\nu]} \chi_\mu \bar{N} \sigma_{\mu\nu} N$	$-\frac{q}{m_L} \left( (i \hat{q} \times \frac{\vec{v}_\mu}{2}) \cdot \vec{\sigma}_N - [\hat{q} \times (\frac{\vec{v}_\mu}{2} \times \vec{\sigma}_L)] \cdot \vec{\sigma}_N \right)$	$-\frac{q}{m_L} (\mathcal{O}_5^f + i\mathcal{O}_{13}^{f'})$
30	$\frac{i}{2m_L} \bar{\chi}_e \gamma^{[\mu} q^{\nu]} \gamma_5 \chi_\mu \bar{N} \sigma_{\mu\nu} N$	$\frac{q}{m_L} \left( \frac{\vec{v}_\mu}{2} \cdot \vec{\sigma}_N + i \left( \frac{\vec{v}_\mu}{2} \times \vec{\sigma}_L \right) \cdot \vec{\sigma}_N - i \hat{q} \cdot \left( \frac{\vec{v}_\mu}{2} \times \vec{\sigma}_L \right) \hat{q} \cdot \vec{\sigma}_N - \hat{q} \cdot \frac{\vec{v}_\mu}{2} \hat{q} \cdot \vec{\sigma}_N \right)$	$\frac{q}{m_L} (\mathcal{O}_8^f + i\mathcal{O}_{12}^f + i\mathcal{O}_{15}^f + \mathcal{O}_{16}^{f'})$
31	$\frac{1}{m_L} \bar{\chi}_e \gamma^{[\mu} q^{\nu]} \chi_\mu \bar{N} \sigma_{\mu\nu} N$	$-2i \frac{q}{m_L} \vec{v}_\mu \cdot \vec{\sigma}_L \hat{q} \cdot \vec{\sigma}_N$	$-4 \frac{q}{m_L} \mathcal{O}_{14}^f$
32	$\frac{1}{m_L} \bar{\chi}_e \gamma^{[\mu} q^{\nu]} \gamma_5 \chi_\mu \bar{N} \sigma_{\mu\nu} N$	$2 \frac{q}{m_L} \left( \hat{q} \cdot (\vec{v}_\mu \times \vec{\sigma}_L) \hat{q} \cdot \vec{\sigma}_N - i \hat{q} \cdot \vec{v}_\mu \hat{q} \cdot \vec{\sigma}_N \right)$	$4 \frac{q}{m_L} (-\mathcal{O}_{15}^f + i\mathcal{O}_{16}^{f'})$

parameter	value	parameter	value	parameter	value
$\mu_p$	2.792847	$\mu_n$	-1.91304	$\mu_s$	-0.036(21)
$[r_E^p]^2$	0.7071(7) fm <sup>2</sup>	$[r_E^n]^2$	-0.1155(17) fm <sup>2</sup>	$[r_E^s]^2$	-0.0045(14) fm <sup>2</sup>
$[r_M^p]^2$	0.724(45) fm <sup>2</sup>	$[r_M^n]^2$	0.743(16) fm <sup>2</sup>	$[r_M^s]^2$	-0.010(11) fm <sup>2</sup>
$g_A$	1.2754(13)	$\Delta\Sigma_{ud}$	0.397(40)	$\Delta s$	-0.045(9)
$\langle r_A^2 \rangle_{u-d}$	0.392(28) fm <sup>2</sup> ,	$\langle r_A^2 \rangle_{u+d}$	0.49(31) fm <sup>2</sup>	$\langle r_A^2 \rangle_s$	0.48(48) fm <sup>2</sup>
$F_{P'}^{u/p}(0)$	119(7)	$F_{P'}^{d/p}(0)$	-130(17)	$F_{P'}^{s/p}(0)$	-1.6(1.0)
$\Delta_{\text{GT}}^8$	0.50(14)				
$\tilde{\sigma}_{\pi N}$	48(6) MeV	$\hat{c}_5$	-0.51(8)	$\sigma_s^N$	43.3(4.8) MeV
$F_S^{u/p}(0)$	0.72(14) GeV <sup>-1</sup>	$F_S^{d/p}(0)$	0.59(14) GeV <sup>-1</sup>	$F_S^{s/p}(0)$	0.17(14) GeV <sup>-1</sup>
$F_G^N(0)$	-50.4(6) MeV	$F_G'^N(0)$	-0.14(5) GeV <sup>-1</sup>	$\alpha_s(2 \text{ GeV})$	0.297(6)
$g_T^u$	0.784(30)	$g_T^d$	-0.204(15)	$g_T^s$	-2.7(1.6) · 10 <sup>-3</sup>
$\hat{F}_{T,0}^{u/p}(0)$	0.54(11) GeV <sup>-2</sup>	$\hat{F}_{T,0}^{d/p}(0)$	-0.11(2) GeV <sup>-2</sup>	$\hat{F}_{T,0}^{s/p}(0)$	-0.0014(9) GeV <sup>-2</sup>
$\hat{F}_{T,1}^{u/p}(0)$	-3.0(2.0)	$\hat{F}_{T,1}^{d/p}(0)$	1.0(6)	$\hat{F}_{T,1}^{s/p}(0)$	0.018(10)
$\hat{F}_{T,1}^{u/p}(0)$	-14.0(1.6) GeV <sup>-2</sup>	$\hat{F}_{T,1}^{d/p}(0)$	5.0(6) GeV <sup>-2</sup>	$\hat{F}_{T,1}^{s/p}(0)$	0.082(52) GeV <sup>-2</sup>
$\hat{F}_{T,2}^{u/p}(0)$	-0.1(2)	$\hat{F}_{T,2}^{d/p}(0)$	0.6(3)	$\hat{F}_{T,2}^{s/p}(0)$	0.004(3)
$\hat{F}_{T,2}^{u/p}(0)$	-1.8(2) GeV <sup>-2</sup>	$\hat{F}_{T,2}^{d/p}(0)$	2.1(2) GeV <sup>-2</sup>	$\hat{F}_{T,2}^{s/p}(0)$	0.015(13) GeV <sup>-2</sup>
$r_{ud}$	0.474(65)	$r_s$	27.33(72)		
$F_\gamma^p(0)$	$4.7(2.6) \cdot 10^{-7}$ GeV	$F_\gamma^n(0)$	$1.5(0.5) \cdot 10^{-6}$ GeV		
$F_{\tilde{\gamma}}^p(0)$	$3.83(3) \cdot 10^{-6}$ GeV	$F_{\tilde{\gamma}}^n(0)$	$-3.9(7) \cdot 10^{-7}$ GeV		

TABLE B.5: Numerical values of input parameters that enter the expressions for matrix elements of vector, axial, scalar, pseudoscalar, and tensor quark currents, CP-even and CP-odd gluonic currents, as well as the CP-even and CP-odd Rayleigh operators. See the main text and appendix D of [3] for details and references.

TABLE B.6: The WCxf-compatible operators and Wilson coefficient naming schemes for MuonConverter (left) and the WET-3 JMS basis [28] (right). The translation between the two bases can be found in table B.7.

MuonConverter	
WC name	Operator
Tegamma_12 - $\hat{\mathcal{C}}_1^{(5)}$	$(\bar{e}\sigma^{\alpha\beta}\mu)F_{\alpha\beta}$
ATegamma_12 - $\hat{\mathcal{C}}_2^{(5)}$	$(\bar{e}\sigma^{\alpha\beta}i\gamma_5\mu)F_{\alpha\beta}$
VVe <u>_1211</u> - $\hat{\mathcal{C}}_{1,u}^{(6)}$	$(\bar{e}\gamma_\alpha\mu)(\bar{u}\gamma^\alpha u)$
VVe <u>_1211</u> - $\hat{\mathcal{C}}_{1,d}^{(6)}$	$(\bar{e}\gamma_\alpha\mu)(\bar{d}\gamma^\alpha d)$
VVe <u>_1222</u> - $\hat{\mathcal{C}}_{1,s}^{(6)}$	$(\bar{e}\gamma_\alpha\mu)(\bar{s}\gamma^\alpha s)$
AVVe <u>_1211</u> - $\hat{\mathcal{C}}_{2,u}^{(6)}$	$(\bar{e}\gamma_\alpha\gamma_5\mu)(\bar{u}\gamma^\alpha u)$
AVVe <u>_1211</u> - $\hat{\mathcal{C}}_{2,d}^{(6)}$	$(\bar{e}\gamma_\alpha\gamma_5\mu)(\bar{d}\gamma^\alpha d)$
AVVe <u>_1222</u> - $\hat{\mathcal{C}}_{2,s}^{(6)}$	$(\bar{e}\gamma_\alpha\gamma_5\mu)(\bar{s}\gamma^\alpha s)$
VAVVe <u>_1211</u> - $\hat{\mathcal{C}}_{3,u}^{(6)}$	$(\bar{e}\gamma_\alpha\mu)(\bar{u}\gamma^\alpha\gamma_5 u)$
VAVVe <u>_1211</u> - $\hat{\mathcal{C}}_{3,d}^{(6)}$	$(\bar{e}\gamma_\alpha\mu)(\bar{d}\gamma^\alpha\gamma_5 d)$
VAVVe <u>_1222</u> - $\hat{\mathcal{C}}_{3,s}^{(6)}$	$(\bar{e}\gamma_\alpha\mu)(\bar{s}\gamma^\alpha\gamma_5 s)$
AVAVVe <u>_1211</u> - $\hat{\mathcal{C}}_{4,u}^{(6)}$	$(\bar{e}\gamma_\alpha\gamma_5\mu)(\bar{u}\gamma^\alpha\gamma_5 u)$
AVAVVe <u>_1211</u> - $\hat{\mathcal{C}}_{4,d}^{(6)}$	$(\bar{e}\gamma_\alpha\gamma_5\mu)(\bar{d}\gamma^\alpha\gamma_5 d)$
AVAVVe <u>_1222</u> - $\hat{\mathcal{C}}_{4,s}^{(6)}$	$(\bar{e}\gamma_\alpha\gamma_5\mu)(\bar{s}\gamma^\alpha\gamma_5 s)$
SSe <u>_1211</u> - $\hat{\mathcal{C}}_{5,u}^{(6)}$	$(\bar{e}\mu)(\bar{u}u)$
SSe <u>_1211</u> - $\hat{\mathcal{C}}_{5,d}^{(6)}$	$(\bar{e}\mu)(\bar{d}d)$
SSe <u>_1222</u> - $\hat{\mathcal{C}}_{5,s}^{(6)}$	$(\bar{e}\mu)(\bar{s}s)$
ASe <u>_1211</u> - $\hat{\mathcal{C}}_{6,u}^{(6)}$	$(\bar{e}i\gamma_5\mu)(\bar{u}u)$
ASe <u>_1211</u> - $\hat{\mathcal{C}}_{6,d}^{(6)}$	$(\bar{e}i\gamma_5\mu)(\bar{d}d)$
ASe <u>_1222</u> - $\hat{\mathcal{C}}_{6,s}^{(6)}$	$(\bar{e}i\gamma_5\mu)(\bar{s}s)$
SAe <u>_1211</u> - $\hat{\mathcal{C}}_{7,u}^{(6)}$	$(\bar{e}\mu)(\bar{u}i\gamma_5 u)$
SAe <u>_1211</u> - $\hat{\mathcal{C}}_{7,d}^{(6)}$	$(\bar{e}\mu)(\bar{d}i\gamma_5 d)$
SAe <u>_1222</u> - $\hat{\mathcal{C}}_{7,s}^{(6)}$	$(\bar{e}\mu)(\bar{s}i\gamma_5 s)$
AAe <u>_1211</u> - $\hat{\mathcal{C}}_{8,u}^{(6)}$	$(\bar{e}i\gamma_5\mu)(\bar{u}i\gamma_5 u)$
AAe <u>_1211</u> - $\hat{\mathcal{C}}_{8,d}^{(6)}$	$(\bar{e}i\gamma_5\mu)(\bar{d}i\gamma_5 d)$
AAe <u>_1222</u> - $\hat{\mathcal{C}}_{8,s}^{(6)}$	$(\bar{e}i\gamma_5\mu)(\bar{s}i\gamma_5 s)$
TTe <u>_1211</u> - $\hat{\mathcal{C}}_{9,u}^{(6)}$	$(\bar{e}\sigma^{\alpha\beta}\mu)(\bar{u}\sigma_{\alpha\beta} u)$
TTe <u>_1211</u> - $\hat{\mathcal{C}}_{9,d}^{(6)}$	$(\bar{e}\sigma^{\alpha\beta}\mu)(\bar{d}\sigma_{\alpha\beta} d)$
TTe <u>_1222</u> - $\hat{\mathcal{C}}_{9,s}^{(6)}$	$(\bar{e}\sigma^{\alpha\beta}\mu)(\bar{s}\sigma_{\alpha\beta} s)$
ATTTe <u>_1211</u> - $\hat{\mathcal{C}}_{10,u}^{(6)}$	$(\bar{e}i\sigma^{\alpha\beta}\gamma_5\mu)(\bar{u}\sigma_{\alpha\beta} u)$
ATTTe <u>_1211</u> - $\hat{\mathcal{C}}_{10,d}^{(6)}$	$(\bar{e}i\sigma^{\alpha\beta}\gamma_5\mu)(\bar{d}\sigma_{\alpha\beta} d)$
ATTTe <u>_1222</u> - $\hat{\mathcal{C}}_{10,s}^{(6)}$	$(\bar{e}i\sigma^{\alpha\beta}\gamma_5\mu)(\bar{s}\sigma_{\alpha\beta} s)$

WET-3 JMS [28, 175]	
WC name	Operator
egamma_12	$\bar{e}_L\sigma^{\alpha\beta}\mu_R F_{\alpha\beta}$
VeuLL_1211	$(\bar{e}_L\gamma_\alpha\mu_L)(\bar{u}_L\gamma^\alpha u_L)$
VedLL_1211	$(\bar{e}_L\gamma_\alpha\mu_L)(\bar{d}_L\gamma^\alpha d_L)$
VedLL_1222	$(\bar{e}_L\gamma_\alpha\mu_L)(\bar{s}_L\gamma^\alpha s_L)$
VeuRR_1211	$(\bar{e}_R\gamma_\alpha\mu_R)(\bar{u}_R\gamma^\alpha u_R)$
VedRR_1211	$(\bar{e}_R\gamma_\alpha\mu_R)(\bar{d}_R\gamma^\alpha d_R)$
VedRR_1222	$(\bar{e}_R\gamma_\alpha\mu_R)(\bar{s}_R\gamma^\alpha s_R)$
VeuLR_1211	$(\bar{e}_L\gamma_\alpha\mu_L)(\bar{u}_R\gamma^\alpha u_R)$
VedLR_1211	$(\bar{e}_L\gamma_\alpha\mu_L)(\bar{d}_R\gamma^\alpha d_R)$
VedLR_1222	$(\bar{e}_L\gamma_\alpha\mu_L)(\bar{s}_R\gamma^\alpha s_R)$
VueLR_1112	$(\bar{e}_R\gamma_\alpha\mu_R)(\bar{u}_L\gamma^\alpha u_L)$
VdeLR_1112	$(\bar{e}_R\gamma_\alpha\mu_R)(\bar{d}_L\gamma^\alpha d_L)$
VdeLR_2212	$(\bar{e}_R\gamma_\alpha\mu_R)(\bar{s}_L\gamma^\alpha s_L)$
SeuRL_1211	$(\bar{e}_L\mu_R)(\bar{u}_R u_L)$
SedRL_1211	$(\bar{e}_L\mu_R)(\bar{d}_R d_L)$
SedRL_1222	$(\bar{e}_L\mu_R)(\bar{s}_R s_L)$
SeuRR_1211	$(\bar{e}_L\mu_R)(\bar{u}_L u_R)$
SedRR_1211	$(\bar{e}_L\mu_R)(\bar{d}_R d_R)$
SedRR_1222	$(\bar{e}_L\mu_R)(\bar{s}_L s_R)$
TeuRR_1211	$(\bar{e}_L\sigma^{\alpha\beta}\mu_R)(\bar{u}_L\sigma_{\alpha\beta} u_R)$
TedRR_1211	$(\bar{e}_L\sigma^{\alpha\beta}\mu_R)(\bar{d}_L\sigma_{\alpha\beta} d_R)$
TedRR_1222	$(\bar{e}_L\sigma^{\alpha\beta}\mu_R)(\bar{s}_L\sigma_{\alpha\beta} s_R)$

TABLE B.7: The translation between the MuonConverter basis and the WET-3 JMS basis.

MuonConverter	WET-3 translation
Tegamma_12	$4\pi^2 \text{ egamma\_12}$
ATegamma_12	$-4\pi^2 i \text{ egamma\_12}$
VVeu_1211	$(\text{VeuLL\_1211} + \text{VeuRR\_1211} + \text{VeuLR\_1211} + \text{VueLR\_1112})/4$
VWed_1211	$(\text{VedLL\_1211} + \text{VedRR\_1211} + \text{VedLR\_1211} + \text{VdeLR\_1112})/4$
VWed_1222	$(\text{VedLL\_1222} + \text{VedRR\_1222} + \text{VedLR\_1222} + \text{VdeLR\_2212})/4$
AVVeU_1211	$(-\text{VeuLL\_1211} + \text{VeuRR\_1211} - \text{VeuLR\_1211} + \text{VueLR\_1112})/4$
AVWed_1211	$(-\text{VedLL\_1211} + \text{VedRR\_1211} - \text{VedLR\_1211} + \text{VdeLR\_1112})/4$
AVWed_1222	$(-\text{VedLL\_1222} + \text{VedRR\_1222} - \text{VedLR\_1222} + \text{VdeLR\_2212})/4$
VAVeU_1211	$(-\text{VeuLL\_1211} + \text{VeuRR\_1211} + \text{VeuLR\_1211} - \text{VueLR\_1112})/4$
VAVed_1211	$(-\text{VedLL\_1211} + \text{VedRR\_1211} + \text{VedLR\_1211} - \text{VdeLR\_1112})/4$
VAVed_1222	$(-\text{VedLL\_1222} + \text{VedRR\_1222} + \text{VedLR\_1222} - \text{VdeLR\_2212})/4$
AVAVeU_1211	$(\text{VeuLL\_1211} + \text{VeuRR\_1211} - \text{VeuLR\_1211} - \text{VueLR\_1112})/4$
AVAVed_1211	$(\text{VedLL\_1211} + \text{VedRR\_1211} - \text{VedLR\_1211} - \text{VdeLR\_1112})/4$
AVAVed_1222	$(\text{VedLL\_1222} + \text{VedRR\_1222} - \text{VedLR\_1222} - \text{VdeLR\_2212})/4$
SSeu_1211	$(\text{SeuRL\_1211} + \text{SeuRR\_1211})/4$
SSed_1211	$(\text{SedRL\_1211} + \text{SedRR\_1211})/4$
SSed_1222	$(\text{SedRL\_1222} + \text{SedRR\_1222})/4$
ASeu_1211	$-i(\text{SeuRL\_1211} + \text{SeuRR\_1211})/4$
ASed_1211	$-i(\text{SedRL\_1211} + \text{SedRR\_1211})/4$
ASed_1222	$-i(\text{SedRL\_1222} + \text{SedRR\_1222})/4$
SAeu_1211	$i(\text{SeuRL\_1211} - \text{SeuRR\_1211})/4$
SAed_1211	$i(\text{SedRL\_1211} - \text{SedRR\_1211})/4$
SAed_1222	$i(\text{SedRL\_1222} - \text{SedRR\_1222})/4$
AAeu_1211	$(\text{SeuRL\_1211} - \text{SeuRR\_1211})/4$
AAed_1211	$(\text{SedRL\_1211} - \text{SedRR\_1211})/4$
AAed_1222	$(\text{SedRL\_1222} - \text{SedRR\_1222})/4$
TTeu_1211	$\text{TeuRR\_1211}/4$
TTed_1211	$\text{TedRR\_1211}/4$
TTed_1222	$\text{TedRR\_1222}/4$
ATTeu_1211	$-i\text{TeuRR\_1211}/4$
ATTed_1211	$-i\text{TedRR\_1211}/4$
ATTed_1222	$-i\text{TedRR\_1222}/4$

## Appendix C

# Normalizing flows

Normalizing flows (NFs) [409–411] are a class of generative ML architectures that can produce high fidelity continuous approximations of complex probability distributions using a finite collection of data samples. This is achieved by learning a composition of  $n$  independent bijective transformations that relate a probability distribution  $\mathcal{P}_Z(\mathbf{z})$  on a chosen latent space  $Z$  to the target distribution  $p_X(\mathbf{x})$  on target space  $X$ .

More precisely, given a multivariate random variable  $\mathbf{z} \in \mathbb{R}^d$  and an invertible map  $f : \mathbb{R}^d \rightarrow \mathbb{R}^d$ , the probability distribution for the random variable  $\mathbf{x} = f(\mathbf{z})$  is given by

$$\mathcal{P}_{X,f}(\mathbf{x}) = \mathcal{P}_Z(\mathbf{z}) |\det J_f(\mathbf{z})|^{-1}, \quad (\text{C.1})$$

where  $J_f = \partial f / \partial \mathbf{z}$  is the Jacobian of the differentiable transformation  $f$ . The full map  $F$  produced by the NF architecture is composed from a sequence of  $n$  such transformations  $\mathbf{z} \equiv$

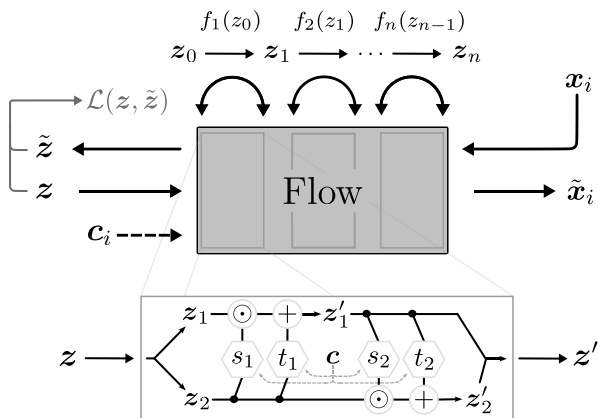


FIGURE C.1: (top) Schematic of the input and output of the NF architecture. Here  $\mathbf{x}_i$  and  $\tilde{\mathbf{z}}$  represent, respectively, the input and output samples obtained from the network when mapping in the forward direction and  $\mathbf{z}$  and  $\tilde{\mathbf{x}}_i$  represent, respectively, input and output samples of the network obtained when traversing the network in the backward direction. The backward direction is used for event generation while the forward direction is used for training. The forward (backward) direction consists of a series of  $n$  successive transformations  $f_{i+1}(\mathbf{z}_i)$  ( $f_i^{-1}(\mathbf{x}_i)$ ).

$\mathbf{z}_0 \rightarrow \mathbf{z}_1 \equiv f_1(\mathbf{z}_0) \rightarrow \cdots \rightarrow \mathbf{x} \equiv \mathbf{z}_n \equiv f_n(\mathbf{z}_{n-1})$ , as shown in fig. C.1, with the final distribution given by

$$\mathcal{P}_X(\mathbf{x}) = \mathcal{P}_Z(\mathbf{z}) \prod_{i=1}^n |\det J_{f_i}(\mathbf{z}_{i-1})|^{-1}. \quad (\text{C.2})$$

The NF architecture provides a continuous map from the latent space  $Z$  to the target space  $X$  and vice versa. In order to train the network to generate high fidelity mappings of samples from the latent distribution  $\mathcal{P}_Z(\mathbf{z})$  to samples of the target distribution  $\mathcal{P}_X(\mathbf{x})$  we require a learning objective that will drive our model distribution  $\mathcal{P}_X(\mathbf{x}; \boldsymbol{\theta})$  towards  $\mathcal{P}_X(\mathbf{x})$ . Given training samples  $\mathbf{x}_a$  of  $N$  data points,  $\mathbf{x}_a = \{\mathbf{x}_1, \mathbf{x}_2, \dots, \mathbf{x}_N\}$ , with conditional labels  $\mathbf{c}_a = \{\mathbf{c}_1, \mathbf{c}_2, \dots, \mathbf{c}_N\}$ , we use the minimization of the negative log likelihood as our learning objective,

$$\begin{aligned} \mathcal{L}_{\text{NF}} &= \mathbb{E}_{\mathcal{P}_X(\mathbf{x}, \mathbf{c})} [-\log \mathcal{P}_X(\mathbf{x}; \boldsymbol{\theta}, \mathbf{c})] = -\sum_{a=1}^N \log \mathcal{P}_X(\mathbf{x}_a; \boldsymbol{\theta}, \mathbf{c}_a) \\ &= \sum_{a=1}^N \left\{ -\log \mathcal{P}_Z(F^{-1}(\mathbf{x}_a; \boldsymbol{\theta}, \mathbf{c}_a)) + \log |\det J_{F^{-1}}(\mathbf{x}_a; \boldsymbol{\theta}, \mathbf{c}_a)| \right\}, \end{aligned} \quad (\text{C.3})$$

where  $F(\mathbf{x}; \boldsymbol{\theta}, \mathbf{c})$  denotes the full network, parameterized by weights  $\boldsymbol{\theta}$  and conditioned on labels  $\mathbf{c}$ . For a latent space sampled from a two-dimensional normal distribution, the loss function is given by

$$\mathcal{L}_{\text{NF}} = \sum_{a=1}^N \left\{ \frac{1}{2} \|F^{-1}(\mathbf{x}_a; \boldsymbol{\theta}, \mathbf{c}_a)\|_2^2 - \log |\det J_F(F^{-1}(\mathbf{x}_a; \boldsymbol{\theta}, \mathbf{c}_a))| \right\}. \quad (\text{C.4})$$

where  $\|\cdot\|_2^2$  denotes the squared  $\ell^2$ -norm. Because each operation is differentiable, the gradient of  $\mathcal{L}_{\text{NF}}$  with respect to each model parameter  $\boldsymbol{\theta}$  may be computed using standard auto-differentiation software and optimized through stochastic gradient descent. Intuitively, the loss function in eq. (C.4) ensures that the latent variables obtained from mapping the training data samples through the network, *i.e.*, , propagated from  $\mathbf{x}_a \rightarrow \mathbf{z}_a$ , are normally distributed.

For practical applications, the latent distribution  $\mathcal{P}_Z(\mathbf{z})$  is chosen such that it can be easily evaluated and sampled, while the transformations  $f_i$  are chosen such that (1) they are expressive enough to sufficiently approximate the transformation  $\mathcal{P}_Z(\mathbf{z}) \rightarrow \mathcal{P}_X(\mathbf{x})$  and (2) they have computationally inexpensive Jacobians. For example, in the one-dimensional examples presented in section 8.1.1, we use a uniform latent distribution,  $\mathbf{z} \sim \mathcal{U}_{[0,1]}$ , and a mixture of Gaussian cumulative distribution functions as the transformations  $f_i$ . For the two-dimensional examples presented in section 8.1.1, we use a two-dimensional unit Gaussian latent distribution,  $\mathbf{z} \sim \mathcal{N}(\vec{0}, \mathbb{I}_{2 \times 2})$ , and real-valued non-volume preserving (real NVP) transformations, as implemented in the FREIA software library [429], for  $f_i$ . In the following subsections, we provide additional details regarding the architectures used in the one and two-dimensional models presented in the main text.

## C.1 One-dimensional normalizing flows

For one-dimensional distributions and a single map  $f : \mathbb{R}^1 \rightarrow \mathbb{R}^1$ , the transformation formula of eq. (C.1) can be rewritten as

$$\log \mathcal{P}_{X,f} = \log \mathcal{P}_Z(f(x)) + \log \left| \frac{df(x)}{dx} \right|. \quad (\text{C.5})$$

In one-dimension we can utilize a cumulative distribution function (CDF) as the invertible transformation  $f$ . Because CDFs are continuous, non-decreasing functions, they are guaranteed to have a unique inverse. Additionally, because CDFs satisfy

$$\lim_{x \rightarrow -\infty} \text{CDF}(x) = 0 \text{ and } \lim_{x \rightarrow \infty} \text{CDF}(x) = 1, \quad (\text{C.6})$$

a function that consists of a linear sum of CDFs is a CDF itself, *i.e.*, ,

$$\lim_{x \rightarrow \infty} \left( \sum_i w_i \text{CDF}_i(x) \right) = \sum_i w_i \left( \lim_{x \rightarrow \infty} \text{CDF}_i(x) \right) = \sum_i w_i = 1, \quad (\text{C.7})$$

as long as the weights  $\mathbf{w}$  are normalized such that the right most equality is true and

$$\lim_{x \rightarrow -\infty} \left( \sum_i w_i \text{CDF}_i(x) \right) = \sum_i w_i \left( \lim_{x \rightarrow -\infty} \text{CDF}_i(x) \right) = \sum_i w_i \times 0 = 0. \quad (\text{C.8})$$

In the main text we use a weighted linear mixture of  $K$  Gaussian CDFs,  $\Phi(x; \mu_i, \sigma_i)$ , as the invertible transformation where the weights  $w_i$ , means  $\mu_i$ , and standard deviations  $\sigma_i$  of each Gaussian component are tunable parameters learned by the network. This setup is commonly referred to as a Gaussian mixture model (GMM). The transformation and its derivative can be written explicitly as

$$f(x) = \sum_i^K w_i \Phi(x; \mu_i, \sigma_i) = \frac{1}{2} \sum_i^K w_i \left[ 1 + \text{erf} \left( \frac{x - \mu_i}{\sqrt{2}\sigma_i} \right) \right], \quad (\text{C.9})$$

$$\frac{df(x)}{dx} = \sum_i^K w_i \mathcal{N}(x; \mu_i, \sigma_i), \quad (\text{C.10})$$

where we have used the fact that  $d\Phi(x; \mu_i, \sigma_i)/dx = \mathcal{N}(x; \mu, \sigma)$ .

Once a latent distribution  $\mathcal{P}_Z$  is specified, the network can be trained by maximizing eq. (C.5)). After training, samples can be obtained in the inverse direction via inverse transform sampling. For  $n$  successive transformations eq. (C.5), is modified to

$$\log \mathcal{P}_X(x) = \log \mathcal{P}_Z(F(x)) + \sum_{i=1}^n \log \left| \frac{df_i(x_{i-1})}{dx} \right|. \quad (\text{C.11})$$

To increase the flexibility of the network, we insert a total of  $n - 1$  intermediate non-linear functions  $y_i$  between each transformation  $f_i$  and  $f_{i+1}$  such that the full transformation  $F$  is given by  $F = f_n(y_{n-1}(f_{n-1}(\cdots(y_1(f_1(x)))\cdots)))$  and the sum in eq. (C.11) runs from  $i = 1, \dots, 2n - 1$ .

Specifically, we use a logit transformation defined as

$$y(x) = \text{logit}\left(\frac{\alpha}{2} + (1 - \alpha)x\right), \text{ where } \text{logit}(x) = \log \frac{1}{1 - x}, \quad (\text{C.12})$$

with the derivative

$$\frac{dy(x)}{dx} = \frac{1 - \alpha}{x(1 - x)}. \quad (\text{C.13})$$

Here,  $\alpha$  is a hyperparameter of the network that is set to 0.01. The full architecture used in section 8.1.1 utilizes a uniformly distributed latent distribution  $\mathcal{P}_Z \sim \mathcal{U}_{[0,1]}$  and  $n = 5$  transformations  $f_i$ , where each transformation contains  $K = 500$  Gaussian components. The learnable parameters are the Gaussian means and variances and the weights of the components, which are constrained to sum to unity per transformation.

## C.2 Two-dimensional flows

In section 8.1.1 we use two-dimensional real NVP transformations for  $f_i$ . Real NVP transformations consist of modular blocks containing two affine coupling layers. That is, given an input  $\mathbf{z}_{i-1}$ , the coupling block splits the input into two channels<sup>1</sup>  $\mathbf{z}_{i-1} = \{\mathbf{z}_{i-1,1}, \mathbf{z}_{i-1,2}\}$  and applies a sequential affine transformation to each channel as follows

$$\begin{aligned} \mathbf{z}_{i,1} &= \mathbf{z}_{i-1,1} \odot \exp(s_{i,1}(\mathbf{z}_{i-1,2})) + t_{i,1}(\mathbf{z}_{i-1,2}), \\ \mathbf{z}_{i,2} &= \mathbf{z}_{i-1,2} \odot \exp(s_{i,2}(\mathbf{z}_{i,1})) + t_{i,2}(\mathbf{z}_{i,1}), \end{aligned} \quad (\text{C.14})$$

where  $s_{i,a}$  and  $t_{i,a}$  are scale and translation transformation operators, respectively, parameterized by fully-connected multi-layer-perceptrons, while  $\odot$  denotes the element-wise direct product.

Once passed through the coupling layer, the output  $\mathbf{z}_i = \{\mathbf{z}_{i,1}, \mathbf{z}_{i,2}\}$  of the two channels is concatenated to the final output  $f_i(\mathbf{z}_{i-1}) = \mathbf{z}_i$ . The full architecture consists of  $n$  sequential coupling blocks. Note that in the inverse direction,

$$\begin{aligned} \mathbf{z}_{i,2} &= (\mathbf{z}_{i+1,2} - t_{i,2}(\mathbf{z}_{i+1,1})) \odot \exp(-s_{i,2}(\mathbf{z}_{i+1,1})), \\ \mathbf{z}_{i,1} &= (\mathbf{z}_{i+1,1} - t_{i,1}(\mathbf{z}_{i,2})) \odot \exp(-s_{i,1}(\mathbf{z}_{i,2})), \end{aligned} \quad (\text{C.15})$$

---

<sup>1</sup>Because we will deal with two-dimensional random variables, in our case both  $\mathbf{z}_1, \mathbf{z}_2$  are one-dimensional. Which component of  $\mathbf{z}$  is assigned as  $\mathbf{z}_1$  or  $\mathbf{z}_2$  is randomly chosen for each real NVP but is kept consistent over the complete dataset and stored for inference.

the  $s_{i,a}$  and  $t_{i,a}$  transformations are still evaluated in the forward direction and thus do not require a tractable inverse.

By construction, the Jacobian matrix  $J_f$  for each coupling block is upper triangular, which allows for an efficient computation of its determinant

$$\begin{aligned} \det J_f(\mathbf{z}) &= \det \frac{\partial f_{ij}}{\partial \mathbf{z}} = \det \begin{pmatrix} \text{diag}\{\exp(s_{i,1}(\mathbf{z}_{i,2}))\} & \cdots \\ 0 & \text{diag}\{\exp(s_{i,2}(\mathbf{z}_{i+1,1}))\} \end{pmatrix} \\ &= \prod \exp(s_{i,1}(\mathbf{z}_{i,2})) \prod \exp(s_{i,2}(\mathbf{z}_{i+1,1})). \end{aligned} \quad (\text{C.16})$$

Because the transformations  $s_{i,a}$  and  $t_{i,a}$  can be arbitrarily complicated, the full architecture can be conditioned by concatenating labels  $\mathbf{c}$  to the inputs of  $s_{i,a}$  and  $t_{i,a}$ , *i.e.*,  $s_{i,a}(\mathbf{z}), t_{i,a}(\mathbf{z}) \rightarrow s_{i,a}(\mathbf{z}, \mathbf{c}), t_{i,a}(\mathbf{z}, \mathbf{c})$ .

## Appendix D

# Observables

In this appendix we collect the definitions of shape observables  $1 - T$ ,  $B_T$ ,  $B_W$ ,  $C$  and  $D$  that were used in section 8.2.2. Here, thrust is defined as[430, 431]

$$T = \frac{\sum_i |\vec{p}_i \cdot \vec{n}_T|}{\sum_i |\vec{p}_i|}, \quad (\text{D.1})$$

where the sum is over particles  $i$  with three momenta  $\vec{p}_i$ , and the unit vector  $\vec{n}_T$  is chosen such that the above expression is maximized. The thrust takes values between 0.5 for spherical events and 1.0 for 2-jet events with narrow jets. The thrust axis  $\vec{n}_T$  divides the space into two hemispheres,  $S_{\pm}$ , which are then used in the definitions of other shape variable.

The two jet broadening variables are obtained by computing for each hemisphere[432, 433]

$$B_{\pm} = \frac{\sum_{i \in S_{\pm}} |\vec{p}_i \times \vec{n}_T|}{2 \sum_i |\vec{p}_i|}. \quad (\text{D.2})$$

The total jet broadening is then defined as

$$B_T = B_+ + B_-, \quad (\text{D.3})$$

while the wide jet broadening is defined as

$$B_W = \max(B_+, B_-). \quad (\text{D.4})$$

The  $C$  and  $D$  parameters, on the other hand, are related to the eigenvalues of the linearized momentum tensor[434, 435]

$$\Theta^{ij} = \frac{1}{\sum_a |\vec{p}_a|} \sum_a \frac{p_a^i p_a^j}{|\vec{p}_a|}, \quad i, j = 1, 2, 3, \quad (\text{D.5})$$

where the summation is over different particles, with three momenta  $\vec{p}_a$ , while  $p_a^i$  denotes component  $i$  of the momentum. The three eigenvalues of  $\Theta^{ij}$  are denoted  $\lambda_{1,2,3}$ , and the  $C$  and  $D$  parameters are

$$C = 3(\lambda_1\lambda_2 + \lambda_2\lambda_3 + \lambda_3\lambda_1), \quad D = 27\lambda_1\lambda_2\lambda_3. \quad (\text{D.6})$$